ANALYTICAL CHEMISTRY

JULY 15, 1994

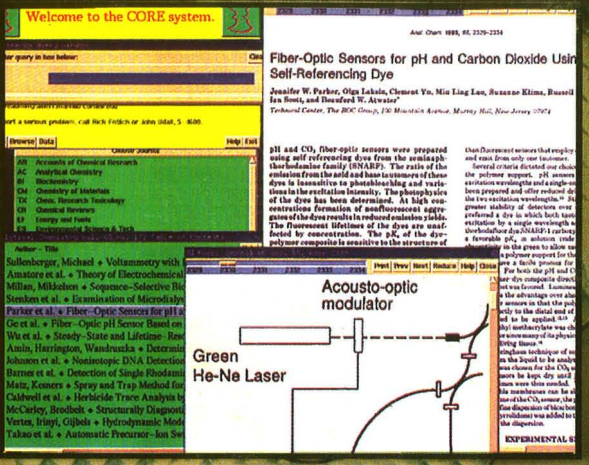

ELECTRONIC CHEMICAL JOURNALS

747 A

BOTTOM LINE:

The more you read the higher you go.

Success for your company and your career means having the right information at the right time. And that's where *C&EN* comes in.

Week after week, *C&EN* delivers up-to-the minute news on every aspect of the chemical enterprise, from business to government, and research to education. Plus, you get an in-depth reporting of trends that puts it all in perspective.

You'll find practical information that enhances day-to-day business dealings, as well as long-range planning — information you can use to hold a competitive edge.

There's only one sure way to get the comprehensive chemistry news you need. Reading *C&EN* puts you on top. For subscription information, call toll-free:

1-800-333-9511.

Success for your company and your career.

CHEMICAL & ENGINEERING NEWS
C&EN

The mirror to your success

ISO 9001 CERTIFIED

25 YEARS CHROMPACK

Reproducible capillary GC columns

As capillary gas chromatographer, you want to be able to rely on the results of your analysis. If you choose for our reliable columns, this need is fulfilled. Because we produce our columns to very tight specifications and test each one before shipment. So we can guarantee every single column. Our ISO 9001 certification of all production processes verifies this unique one-by-one testing procedure.
So reflect on our capillary GC columns for a moment, and envision the success you will have when you can totally rely on your analytical results.

For a free, full-color brochure, just contact your nearest Chrompack office.

CHROMPACK

Chrompack Inc.
1130 Route 202, Raritan, NJ 08869
Phone, toll free (800) 526-3687
Fax, (908) 722-8365

From chromatographers for chromatographers

CIRCLE 1 ON READER SERVICE CARD

Contents

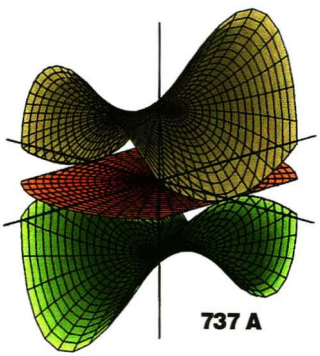

737 A

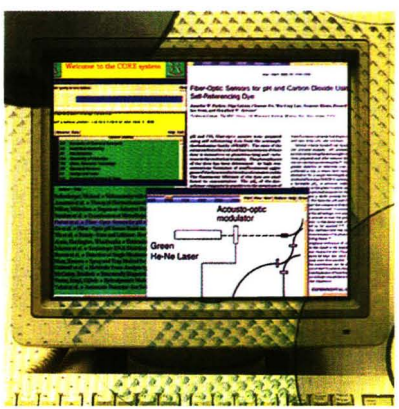

747 A

REPORT

737 A
High-pressure ionization and ion trap MS
Ion sources operated at high pressures are natural candidates for coupling with quadrupole ion traps because of pumping requirements and high ion injection efficiencies. In the second of a two-part series, Scott A. McLuckey, Gary J. Van Berkel, and Douglas E. Goeringer of Oak Ridge National Laboratory and Gary L. Glish of the University of North Carolina review how this combination can address challenges in MS.

A/C INTERFACE

747 A
ON THE COVER. Electronic chemical journals
The hype over the information superhighway has generated interest in electronic transmission of chemical information. Michael E. Lesk of Bellcore describes a collaborative experiment by the ACS, Chemical Abstracts Service, Bellcore, and the Online Computer Library Center to make chemical journals available on the desktop and predicts what electronic services may be available in the future.

EDITOR: **ROYCE W. MURRAY**
University of North Carolina

ASSOCIATE EDITORS: **Catherine C. Fenselau,** University of Maryland Baltimore County, **William S. Hancock,** Hewlett Packard, **James W. Jorgenson,** University of North Carolina, **Robert A. Osteryoung,** North Carolina State University, **Edward S. Yeung,** Iowa State University/Ames Laboratory

Editorial Headquarters
Research section
Department of Chemistry
Venable and Kenan Laboratories
University of North Carolina
Chapel Hill, NC 27599-3290
Phone: 919-962-2541
Fax: 919-962-2542
E-mail: Murray @ uncvx1.oit.unc.edu

Editorial Headquarters
A-page section
1155 Sixteenth St., N.W.
Washington, DC 20036
Phone: 202-872-4570
Fax: 202-872-4574
E-mail: acx96 @ acs.org

Managing Editor: Mary Warner
Senior Editor: Louise Voress
Associate Editors: Grace K. Lee, Felicia Wach
Editorial Assistant: Deborah Noble
Contributing Editor: Marcia Vogel
Head, Graphics and Production: Leroy L. Corcoran
Division Art Director: Alan Kahan
Art Director: Peggy Corrigan
Designer: Michele Telschow
Production Editors: Kathleen Savory, Elizabeth Wood
Electronic Composition: Wanda R. Gordon

ANALYTICAL CHEMISTRY

JULY 15, 1994
VOLUME 66 NUMBER 14

ANCHAM
66(14) 719 A–764 A/2201–2424 (1994)
ISSN 0003-2700

Registered in U.S. Patent and Trademark Office
©Copyright 1994 by the American Chemical Society

DEPARTMENTS

727 A
In This Issue

731 A
Analytical Currents

734 A
News
WPAC addresses quality concerns. • Dow to sell Camille. • ChromatoFast and Varian to market FastGC. • Ultrasound for safer air bags. • Alfred O. C. Nier passes away. • Nominations. • For Your Information.

745 A
Software
Introduction to HPLC, designed to teach basic LC, has the qualities of a textbook and the advantages of rapid indexing and animation, according to reviewer John W. Dolan. • Peter Griffiths and coworkers evaluate Spec-ID Plus, a Windows-based application that allows an unknown spectrum to be identified.

756 A
Meetings
Conferences. • Short Courses and Workshops.

757 A
Product Review
FT-IR PAS steps up to depth profiling. Photoacoustic spectroscopy can coax spectra out of intractable solids, and new step-scanning technology for FT-IR spectrometers permits depth-specific analyses. We review the basic theory involved and compare representative commercial instruments and accessories.

RESEARCH

Articles

2201
Dynamics and Response of Polymer-Coated Surface Acoustic Wave Devices: Effect of Viscoelastic Properties and Film Resonance
Stephen J. Martin, Gregory C. Frye, and Stephen D. Senturia*

2220
Solvent Extraction–Flow Injection without Phase Separation through the Use of the Differential Flow Velocities within the Segmented Flow
Charles A. Lucy and Ken K.-C. Yeung*

2226
High-Performance Evolved Gas Analysis System for Catalyst Characterization
P. A. Barnes, G.M.B. Parkes, and E. L. Charsley*

2232
Micellar Catalysis and Product Stabilization in Hydrazone Formation Reactions and Micellar-Modified Determination of Hydrazine and Phenylhydrazine
Anatoly K. Yatsimirsky, Natalia T. Yatsimirskaya, and Svetlana B. Kashina*

2240
Biodegradation of Soluble Redox Polymers. 1. (0.017Ferrocene)amylose
*Boris B. Gnedenko and Alexander D. Ryabov**

2245
Metalloporphyrin Derivatives as Neutral Carriers for PVC Membrane Electrodes
De Gao, Jun-Zhong Li, Ru-Qin Yu, and Guo-Dong Zheng*

continued on p. 723 A

Publications Division
Director: Robert H. Marks
Head, Special Publications: Anthony Durniak
Head, Journals: Charles R. Bertsch
Head, Publications Marketing: David Schulbaum

Journals Dept., Columbus, Ohio
Editorial Office Manager: Mary E. Scanlan
Journals Editing Manager: Kathleen E. Duffy
Associate Editor: Lorraine Gibb
Assistant Editor: Brenda S. Wooten

Advisory Board: Phyllis Brown, Bruce Chase, Joseph G. Gordon, David M. Haaland, Joel M. Harris, Franz Hillenkamp, Kiyokatsu Jinno, Dennis C. Johnson, Richard A. Keller, Peter Kissinger, Gary E. Maciel, Scott M. McLuckey, Milos V. Novotny, Geraldine Richmond, Ralph Riggin, James A. Yergey *Ex Officio:* Janet Osteryoung

A-page Advisory Panel: Frank V. Bright, Raymond E. Clement, Therese M. Cotton, Norman J. Dovichi, Royce C. Engstrom, Mary Ellen P. McNally, John W. Olesik, J. Michael Ramsey, Robert D. Voyksner

Copyright Permission: An individual may make a single reprographic copy of an article in this publication for personal use. Reprographic copying beyond that permitted by Section 107 or 108 of the U.S. Copyright Law is allowed, provided that the appropriate per-copy fee is paid through the Copyright Clearance Center, Inc., 222 Rosewood Dr., Danvers, MA 01923. For reprint permission, write Copyright Administrator, Publications Division, ACS, 1155 Sixteenth St., N.W., Washington, DC 20036.

BPA International Business Publication Membership Applied for August 1993.

Analytical Chemistry (ISSN 0003-2700) is published semimonthly by the American Chemical Society, 1155 Sixteenth St., N.W., Washington, DC 20036. Second-class postage paid at Washington, DC, and additional mailing offices. Postmaster: Send address changes to *Analytical Chemistry*, Member & Subscriber Services, P.O. Box 3337, Columbus, OH 43210.

Canadian GST Reg. No. R127571347.

ห้องสมุดกรมวิทยาศาสตร์บริการ
14 ส.ค. 2537

Ideas flourish in this environment.

Global warming...hazardous waste... water scarcity...ecosystem ecology... risk communication... You'll explore today's most important environmental concerns in the critically-acclaimed *Environmental Science and Technology.* Rated #1 of all environmental science journals in the latest *Science Citation Index, ES&T* provides breakthrough ideas, insightful analyses, and up-to-the-minute research every month.

Research Journal and Professional Magazine in One

Scientifically rigorous, *ES&T* combines peer-reviewed research with a lively magazine section to present the latest thinking in environmental science and protection in a reader-friendly format. International in scope, *ES&T* offers research articles, critical reviews, and special reports which examine environmental problems—and their solutions—in key geographic regions worldwide.

Strong Editorial Commitment

Editor
William H. Glaze, *University of North Carolina, Chapel Hill*

Associate Editors
W. Giger, *EAWAG, Switzerland*
R.A. Hites, *Indiana University*
C.T. Miller, *University of North Carolina, Chapel Hill*
J.L. Schnoor, *University of Iowa*
J.H. Seinfeld, *California Institute of Technology*
J. Suflita, *University of Oklahoma*

ACS PUBLICATIONS
Essential Resources for the Chemical Sciences

Free Trial Issue

Call today and we'll send you a copy of *ES&T* absolutely free with no obligation. Once you've reviewed it, you'll see why it pays to subscribe!

Call toll free 1-800-333-9511 today. Outside the continental U.S., please call 614-447-3776. FAX 614-447-3671.

1994 Subscription Rates

	U.S.	Canada, Mexico	Europe*	All Other Countries*
Members** One Year	$ 44	$ 66	$ 102	$118
Nonmembers** (personal) One Year	$ 90	$112	$148	$164
Nonmembers** (institutional) One Year	$497	$519	$555	$571

Member subscription rates for personal use only.
*Includes air service.
**2- and 3-year rates available; call for details.

Contents

2250
Response Mechanism of Polymer Membrane-Based Potentiometric Polyion Sensors
*Bin Fu, Eric Bakker, Jong H. Yun, Victor C. Yang, and Mark E. Meyerhoff**

2260
Quantitative Diffuse Reflectance and Diffuse Transmittance Infrared Spectroscopy of Surface-Derivatized Silica Powders
Farnaz Boroumand, Hubert van den Bergh, and Jacques E. Moser*

2267
In Vivo Percutaneous Absorptiometry by a Laser Photoacoustic Method Using a Novel Open-Ended Cell Combined with Light Guide
*Ryuichi Takamoto, Shinya Yamamoto, Ryujiro Namba, Tasuku Takamatsu, Masahiro Matsuoka, and Tsuguo Sawada**

2272
Laser-Induced Photofragmentation/Photoionization Spectrometry: A Method for Detecting Ambient Oxides of Nitrogen
*J. B. Simeonsson, G. W. Lemire, and R. C. Sausa**

2279
Particle- and Vapor-Phase Contributions to Metallic Impurities in Electronic-Grade Chlorine
Tracey Jacksier, Richard Udischas, Hwa-Chi Wang, and Ramon M. Barnes*

2285
Electrospray-Condensation Particle Counter: A Molecule-Counting LC Detector for Macromolecules
Kenneth C. Lewis, Daniel M. Dohmeier, James W. Jorgenson, Stanley L. Kaufman, Fahimeh Zarrin, and Frank D. Dorman*

2293
Elucidation of Species in Alcohol–Water Mixtures Using Near-IR Spectroscopy and Multivariate Statistics
M. Kathleen Alam and James B. Callis*

2302
Investigation of Molecular Weight and Terminal Group Effects on the Time-of-Flight Secondary Ion Mass Spectra of Polyglycols
*Lucinda R. Hittle, Diane E. Altland, Andrew Proctor, and David M. Hercules**

2313
MS/MS and MS/MS/MS Analyses in a Multisector Time-of-Flight Mass Spectrometer
*Toru Sakurai, Hiroyuki Ito, and Takekiyo Matsuo**

2318
Spontaneous Injection in Microcolumn Separations
*Harvey A. Fishman, Nabeel M. Amudi, Thomas T. Lee, Richard H. Scheller, and Richard N. Zare**

2330
Class-Selective Collisionally Activated Dissociation/Ion–Molecule Reactions of 4-Quinolone Antibiotics
*Armando Colorado and Jennifer Brodbelt**

2336
Factors Controlling Precision and Accuracy in Isotope-Ratio-Monitoring Mass Spectrometry
Dawn A. Merritt and J. M. Hayes

2348
Electrospray Ionization Ion Mobility Spectrometry
*Doug Wittmer, Yong Hong Chen, Brian K. Luckenbill, and Herbert H. Hill, Jr.**

2356
Determination of Nanogram Levels of Peptide Drug in Rabbit and Human Plasma Using High-Performance Liquid Chromatography Coupled with Electrospray Ionization Mass Spectrometry
J. Crowther, V. Adusumalli, T. Mukherjee, K. Jordan, P. Abuaf, N. Corkum, G. Goldstein, and J. Tolan*

2362
Quantitative Measurement of Cyclosporin A in Blood by Time-of-Flight Mass Spectrometry
David C. Muddiman, Arkady I. Gusev, Andrew Proctor, David M. Hercules, Raman Venkataramanan, and Warren Diven*

2369
Open Channel Electrochromatography on a Microchip
*Stephen C. Jacobson, Roland Hergenröder, Lance B. Koutny, and J. Michael Ramsey**

2374
Target Factor Modeling of Migration Behavior in Capillary Electrophoresis
*Rachhpal S. Sahota and Morteza G. Khaledi**

continued on p. 725 A

Registered names and trademarks used in this publication, even without specific indication thereof, are not to be considered unprotected by law.

1994 subscription rates include air delivery outside the U.S., Canada, and Mexico. Canadian subscriptions are subject to 7% GST.

	Members	Nonmembers (personal)	Nonmembers (institutional)
U.S.	$ 37	$ 79	$ 481
Canada and Mexico	72	114	516
Europe	127	169	571
Other countries	154	196	598

Nonmember rates in Japan: Rates above do not apply to nonmember subscribers in Japan, who must enter subscription orders with Maruzen Company Ltd., 3–10. Nihonbashi 2-chome, Chuo-ku, Tokyo 103, Japan. Tel: (03) 272-7211.

For multi-year and other rates, call toll free 800-227-5558 in the U.S. and Canada; in the Washington, DC, metropolitan area and outside the U.S., call 202-872-4363; fax 202-872-4615.

Single issues, current year, $21.00 except review issue, $50.00, and LabGuide, $50.00; **back issues and volumes and microform editions** available by single volume or back issue collection. For information or to order, call the number listed for subscription orders by phone; or write the Microform & Back Issues Office at the Washington address.

Subscription orders by phone may be charged to VISA, MasterCard, or American Express. Call toll free 800-333-9511 in the continental U.S.; in the Washington, DC, metropolitan area and outside the continental U.S., call 202-872-8065. Mail orders for new and renewal subscriptions should be sent with payment to American Chemical Society, Department L-0011, Columbus, OH 43268-0011.

Changes of address must include both old and new addresses with ZIP code and a recent mailing label. Send all address changes to the ACS Columbus address. Please allow 6 weeks for change to become effective. **Claims for missing numbers** will not be allowed if loss was due to failure of notice of change of address to be received in the time specified; if claim is dated (a) North America—more than 90 days beyond issue date, (b) all other foreign—more than 180 days beyond issue date. Hard copy claims are handled at the ACS Columbus address.

ACS membership information: Lorraine Bowlin (202-872-4567)

THE END OF INSCRUTABLE DISQUISITION.

The task of keeping up with the latest advances in chemical research can be daunting.

However, there is an easy way to gain a vital overview of basic research and applications in all areas of chemistry. Subscribe to *Accounts of Chemical Research* (ACR). ACR publishes leading researchers' reports of their own work. Concise, critical articles help end controversies, relate recent advances to earlier work, and project their future significance.

Place your order today by calling 1-800-333-9511. Outside the U.S. call 614-447-3776.

Accounts of Chemical Research is published monthly by the American Chemical Society. Fred W. McLafferty, Cornell University, Editor. B.A. Baird, Cornell University, and J.E. McMurry, Cornell University, Associate Editors. Subscription rates in the U.S. for ACS Members are $29 for one year, $52 for two years. Nonmembers are $191 for one year. Call for rates outside the U.S.

ACS PUBLICATIONS
Essential Resources for the Chemical Sciences

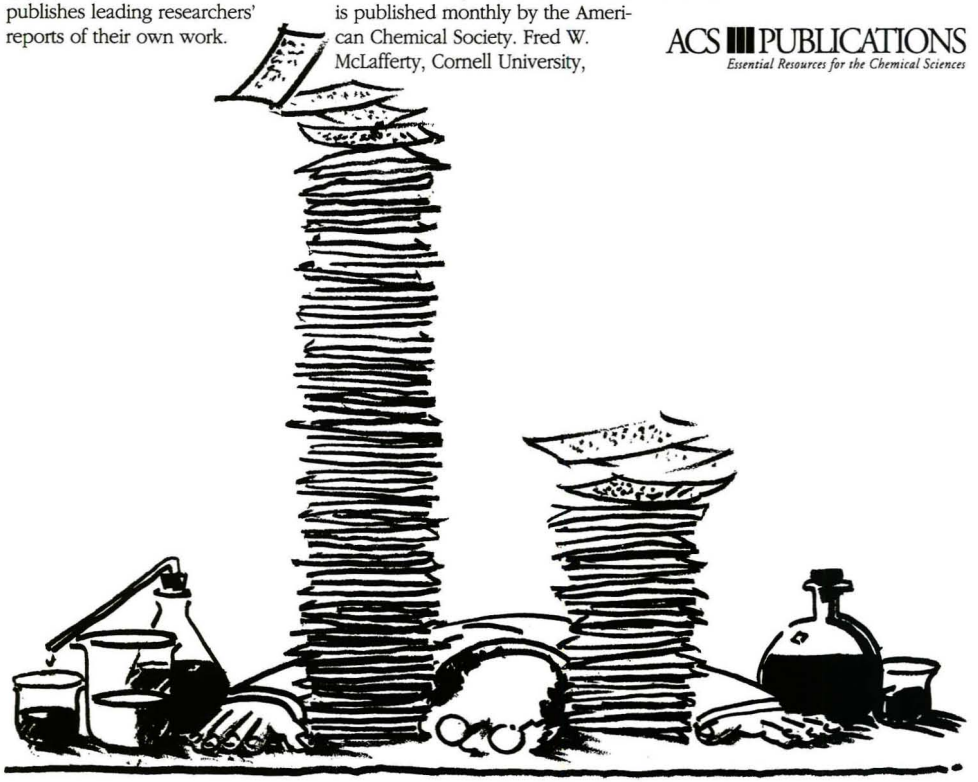

Contents

2382
Postcolumn Radionuclide Detection of Low-Energy β Emitters in Capillary Electrophoresis
*Scott Tracht, Verna Toma, and Jonathan V. Sweedler**

2390
Eluent Modifiers for the Liquid Chromatographic Separation of Carboxylic Acids Using Conductivity Detection
*John Morris and James S. Fritz**

2397
Enhanced Extraction of Phenobarbital from Serum with a Designed Artificial Receptor
*Jane N. Valenta, Robert P. Dixon, Andrew D. Hamilton, and Stephen G. Weber**

Correspondence

2404
Ion Chromatograpy as Potential Reference Methodology for the Determination of Total Calcium and Magnesium in Human Serum
Linda M. Thienpont, Jean E. Van Nuwenborg, and Dietmar Stöckl*

Technical Notes

2409
Improved Method for the Determination of the Oxygen Isotopic Composition of Cellulose
*Peter E. Sauer and Leonel d.S.L.O. Sternberg**

2412
Binding Studies of Vancomycin to the Cytoplasmic Peptidoglycan Precursors by Affinity Capillary Electrophoresis
Jinping Liu, Kevin J. Volk, Mike S. Lee, Michael Pucci, and Sandra Handwerger*

2417
Isolation of Marine Dissolved Organic Matter: Evaluation of Sequential Combinations of XAD Resins 2, 4, and 7
Rubén J. Lara and David N. Thomas*

2420
Enzymatic Profiling of Immobilized Cells Using CZE
*Karen J. Miller and Fred E. Lytle**

Author Index **2424**

Instructions for authors of AC Research and guidelines for the Instrumentation, Report, Analytical Approach, and A/C Interface features are published in the Jan. 1 issue, p. 185. Please consult these instructions prior to submitting a manuscript for consideration for publication.

Manuscripts for publication in AC Research (4 copies of text and illustrative material) should be submitted to the Editor at the University of North Carolina address. Please include a signed copyright status form; a copy of this document appears on p. 191 of the Jan. 1 issue. Manuscripts for publication in the A-page section should be submitted to the Washington editorial staff.

Supplementary material is noted in the table of contents with a ■. It is available as photocopy ($10.00 for up to 3 pages and $1.50 per page for additional pages, plus $2.00 for foreign postage) or as 24X microfiche ($10.00, plus $1.00 for foreign postage). Canadian residents should add 7% GST. See supplementary material notice at end of journal article for number of pages. Orders *must* state whether for photocopy or for microfiche and give complete title of article, names of authors, journal, issue date, and page numbers. Prepayment is required and prices are subject to change. Order from Microforms & Back Issues Office at the ACS Washington address.

The American Chemical Society and its editors assume no responsibility for the statements and opinions advanced by contributors. Views expressed in the editorials are those of the editors and do not necessarily represent the official position of the American Chemical Society.

The paper used in this publication meets the minimum requirements of American National Standard for Information Sciences—Permanence of Paper for Printed Library Materials, ANSI Z39.48-1984.

Journals Department
American Chemical Society
2540 Olentangy River Road
P.O. Box 3330
Columbus, OH 43210
614-447-3600, Ext. 3171
TELEX 6842086 Fax 614-447-3745

Member & Subscriber Services
American Chemical Society
P.O. Box 3337
Columbus, OH 43210
614-447-3776
800-333-9511

Advertising Office: Centcom Ltd., 1599 Post Road East, P.O. Box 231, Westport, CT 06881

Biochemistry. Critical research. On time. On target. On your must-read list!

Biochemistry is a must-read for researchers in chemistry, biochemistry, and molecular and cell biology. Every week (in over 12,000 pages a year), *Biochemistry* gives you fast-breaking, state-of-the-art research articles on a variety of important topics such as:

- Bioenergetics
- Carbohydrate chemistry
- Enzyme and protein biochemistry
- Gene structure and function
- Immunochemistry
- Lipid and cell membrane biochemistry
- Molecular and cell biology
- Virology

Before you begin your next research project or write your next proposal, subscribe to *Biochemistry* for the most relevant theories and methodologies in your field of endeavor.

Editor
Gordon G. Hammes
Duke University Medical Center

Associate Editors
Mary Barkley
Louisiana State University
Marc G. Caron
Duke University Medical Center
Earl W. Davie
University of Washington
Perry A. Frey
University of Wisconsin, Madison
Paul L. Modrich
Duke University Medical Center
William W. Parson
University of Washington
Joseph J. Villafranca
Bristol-Myers Squibb Co.
Leslie Wilson
University of California, Santa Barbara

ACS PUBLICATIONS
Essential Resources for the Chemical Sciences

1994 Subscription Rates

	U.S.	Canada, Mexico	Europe*	All Other Countries*
ACS Members				
One Year	$ 108	$ 200	$ 351	$ 422
Two Years	$ 194	$ 378	$ 680	$ 822
Nonmembers				
One Year	$1,328	$1,420	$1,571	$1,642

*Air service included.

Call toll free 1-800-333-9511 today. Outside the U.S., please call 614-447-3776. Or mail or fax your order to: American Chemical Society, Member & Subscriber Services, P.O. Box 3337, Columbus, OH 43210. FAX 614-447-3671.

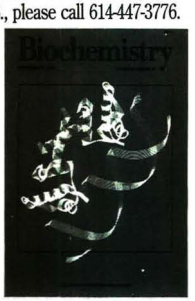

In This Issue

Brief introductions to the research articles in this issue

A membrane sensor for heparin

Heparin, a macromolecular polyanion, is used in clinical practice as an anticoagulant in surgery, kidney dialysis, and other important medical procedures. Mark Meyerhoff and co-workers at The University of Michigan describe the fabrication of a potentiometric polymer membrane-based sensor electrode for heparin and describe its nonequilibrium response behavior to clinically relevant blood concentrations of the drug. They find that polymer membrane composition plays a key role in achieving analytically useful results. (p. 2250)

Quantifying CsA with TOFMS

The recent success in organ transplantation can be attributed primarily to the development of immunosuppressive agents such as cyclosporin A (CsA). Routine therapeutic monitoring of CsA in whole blood is needed to optimize drug therapy because of the narrow therapeutic index and the large inter- and intraindividual variation in the pharmacokinetics of CsA. HPLC is the standard method for this analysis because it can specifically measure only the parent CsA. David M. Hercules and colleagues of the University of Pittsburgh explore the use of TOF-SIMS and MALDI-TOFMS to measure CsA. They analyze samples from patients receiving CsA therapy by both TOFMS methods; the results are comparable to those obtained using HPLC. (p. 2362)

Separating real drugs with artificial receptors

Antibodies, enzymes, and other types of biological receptors have all been used as the active components of affinity chromatography systems for selective determination of drugs and similar analytes. Stephen Weber and co-workers at the University of Pittsburgh have used a solution of chloroform containing a synthetic receptor for barbiturate drugs to extract phenobarbital efficiently from spiked human serum samples. They discuss the experimental parameters affecting the volume of solvent required for extraction. (p. 2397)

Ion chromatography as a reference method for calcium and magnesium

In clinical chemistry, reference methods serve as a link for transferring accuracy from definitive methods to routine methods, allowing the results from routine methods to be traceable to the "true" quantity of an analyte in a clinical sample. Because ion chromatography has been successfully used for the determination of serum analytes, Linda M. Thienpont of the University of Ghent (Belgium) and colleagues investigate its use as a potential reference method. They find that results from five control samples are comparable to those obtained with other reference methods. (p. 2404)

Binding studies using affinity CE

Glycopeptide antibiotics such as vancomycin are of considerable interest because of their specific molecular recognition abilities. Jinping Liu of Bristol-Myers Squibb and colleagues use affinity CE to study the ability of vancomycin to bind three cytoplasmic peptidoglycan precursors in bacterial species. The results are consistent with modification of the stem peptide terminus, providing additional evidence for the understanding of one mechanism of bacterial resistance. (p. 2412)

Polymer-coated SAW devices

Surface acoustic wave (SAW) devices use interdigital transducers photolithographically patterned on the surface of a piezoelectric crystal to excite and detect surface waves. Since the invention of SAW chemical sensors, a number of polymer films have been examined as chemically sensitive films or interfaces. Stephen J. Martin of Sandia National Laboratories and colleagues investigate the dynamics and response of polymer-coated SAW devices, examining the acoustically thin and thick regimes separately, and use a perturbational approach to relate velocity and attenuation responses to film translational and strain modes generated by the SAW. (p. 2201)

Catalysts by evolved gas analysis

Many catalysts are prepared by thermal decomposition of complex precursors, which must be characterized before and during decomposition. P. A. Barnes and co-workers at Leeds Metropolitan University (U.K.) describe a high-resolution system for characterization of such materials. Based on evolved gas analysis (EGA), the system can perform controlled transformation rate thermal analysis and stepwise isothermal analysis as well as conventional linear temperature program EGA. Because all three modes are available on the same system, they can be directly compared under identical sample conditions. (p. 2226)

Following depolymerization electrochemically

The pattern of random degradation in a polymeric material—the regions in which the material degrades easily or appears to be protected—can provide clues about the polymer's secondary and tertiary structures, which are often formed by self-assembly as the polymer chain grows and folds over on itself. Boris Gnedenko of Moscow State University (Russia) and Alexander Ryabov of Plekhanov Russian Economic Academy describe a method for following random enzymatic cleavage of redox-labeled amylose (starch) by cyclic voltammetry. The key, they say, is to produce a water-soluble ferrocene-modified polymer with a low degree of substitution on the starch molecule so that the labeled molecule still interacts naturally with the depolymerase enzyme. (p. 2240)

ห้องสมุดกรมวิทยาศาสตร์บริการ

Metalloporphyrins and the search for a smoke detector

Anion membrane electrodes with liquid ion exchangers generally follow the Hofmeister sequence for anion selectivity. To create electrodes that select preferentially for thiocyanate ion, a compound found in the urine of smokers, Ru-Qin Yu of Hunan University (China) and colleagues have used a synthetic lipophilic metalloporphyrin, a compound analogous to vitamin B_{12} and heme, as the active neutral carrier for a PVC membrane electrode. They examine the role of the porphyrin's coordination state on the anion selectivity order and evaluate the performance of the prototype electrode as a clinical instrument for determining SCN^- concentrations in smokers and nonsmokers. (p. 2245)

Time-of-flight SIMS of polyglycols

Polyglycols are an important class of polymers used in the pharmaceutical and cosmetics industries as lubricants, fillers, and matrices for drug transport. They are perhaps the most universally analyzed polymers and have been examined by a host of MS techniques. David M. Hercules of the University of Pittsburgh and colleagues extend this study by using TOF-SIMS to characterize polyglycols ranging in size from 400 to 100,000 Da to determine the fragmentation mechanisms responsible for ion formation. The predominant fragmentation mechanisms involve scission of the C–O bonds, similar to the fragmentation pathways observed for aliphatic ethers in other types of MS. (p. 2302)

Multisector MS/MS and MS/MS/MS

TOFMS, in combination with MALD, is widely used for analysis of biomolecules, and tandem TOFMS can be used for structural elucidation based on dissociation of precursor ions. Takekiyo Matsuo and colleagues at Osaka University (Japan) report on MS/MS and MS/MS/MS analyses using a multisector TOF mass spectrometer comprising four electric sector analyzers. Product ion spectra can be obtained by measuring the total flight time and the kinetic energy of the products without an additional separation process or any special timing circuits. MS/MS and MS/MS/MS product ion spectra from mercury/cesium complex cluster ions are obtained, and both metastable and sequential decay of the cluster are directly observed. (p. 2313)

Class analysis of quinolones

Since their discovery in the early 1960s, 4-quinolones have been used as broad-spectrum antibiotics. A general class-specific method for determination of these compounds has been elusive because the great variety of structures and substituents alters their characteristic properties. Armando Colorado and Jennifer Brodbelt of the University of Texas demonstrate how collisionally activated dissociation and ion–molecule reactions can be used for class analysis of the 4-quinolones. Collisionally activated dissociation promotes dehydration of the quinolone, which then undergoes an additional reaction with an auxillary reagent. The auxillary reagents have structures that allow formation of a cyclic adduct with the analyte. (p. 2330)

Isotope-ratio-monitoring MS

Isotope ratio monitoring refers to a potentially large range of techniques in which conventional inlet systems are avoided, widely varying ion currents are accepted, and all of the sample is utilized. Analysis times can drop from tens of minutes to tens of seconds, and subnanomole samples can be accommodated. Dawn A. Merritt and J. M. Hayes of Indiana University examine the performance of systems in which picomole quantities of sample are mixed with a carrier gas and passed through an isotope-ratio mass spectrometer system. Two different mass spectrometers, both equipped with electron-impact ion sources and Faraday cup collector systems, are used. (p. 2336)

Building a better ES needle

Although initial investigations of using ion mobility spectrometry (IMS) for detection in liquid-phase separations have been encouraging, the lack of response for high molecular weight compounds indicates that the electrospray (ES) nebulizer used as the ionization source is not behaving in a manner analagous to that observed in ESIMS. Herbert H. Hill, Jr., and colleagues of Washington State University and Millipore Corp. describe an improved ESI source for IMS developed by modifying the ES needle. They electrically insulate its tip to extend the voltage range with which a stable ES can be achieved, cool the needle to eliminate problems associated with solvent volatilization in the spray needle, and remove the needle from the ion drift region to reduce neutralization of charged drops and ions. (p. 2348)

High flow rate for ESIMS

By interfacing HPLC directly to ESIMS instrumentation, trace levels of peptide drug can be measured in relatively complex samples such as plasma, serum, and urine. J. Crowther and colleagues at the Immunobiology Research Institute have adapted a commercial ESI interface to provide a flow rate ~ 10-fold higher than normal to improve the sensitivity of quantitative LC/MS determinations of a pentapeptide drug in rabbit and human plasma. The modified interface permits the use of standard HPLC columns and adds organic modifier to the eluent to avoid problems with highly aqueous media in the mass spectrometer. (p. 2356)

More precise oxygen isotope analysis

The stable isotopes of oxygen in organic material are of interest to plant physiologists and paleoclimatologists who use isotopic ratios to constrain water relations and climate models. Because changes of 1–2‰ may be of biological or climatic importance, improving the variability of existing analytical techniques is desirable. Leonel d. S.L.O. Sternberg of the University of Miami and Peter E. Sauer of the University of Colorado have modified a procedure for oxygen isotope analysis of cellulose by using Zn rather than isoquinoline to remove HCl from the reaction products of the sample and $HgCl_2$. Precision for the Zn method is ±0.2‰ compared with ±0.9‰ for the isoquinoline method. (p. 2409)

Phase separator not required

More than 100 different applications of solvent extraction–flow injection and almost as many phase separators exist today. Manifolds eliminate the need for phase separation, but they commonly use on-tube detection, which suffers from signal problems because of the segmented flow. Alternate techniques require computer control or monitor only one phase, making them unsuitable for many applications. Charles A. Lucy and Ken K.-C. Yeung of the University of Calgary (Canada) exploit the film-

forming characteristics of two-phase segmented flow to develop a simple solvent extraction–flow injection instrument that does not require a phase separator or an on-tube detector. (p. 2220)

Molecule-counting detector

The lack of a sensitive universal detector for large molecules separated by capillary methods has limited the development of capillary LC. Tagging reactions often produce multiple products that give rise to multiple peaks, and UV absorption yields rather poor detection limits for separations in which the pathlength is often the diameter of the capillary. James W. Jorgenson of the University of North Carolina and colleagues describe a detection system in which the chromatographic effluent is electrosprayed, neutralized, and swept by a stream of air into a condensation particle counter. Individual particles are detected by light scattering from droplets condensed on the particles. When used for SEC of proteins, the detector has a linear range of 4 orders of magnitude with detection limits as low as 0.1 μg/mL. (p. 2285)

Spontaneous injection

In microcolumn separations, simply touching the capillary to the sample solution can cause an extraneous injection of up to 3 nL for a 75-μm i.d. column. Richard N. Zare and colleagues at Stanford University characterize a predominant mechanism of spontaneous extraneous injection in CE. By combining fluorescence imaging, video microscopy, and measurements from CE, they demonstrate that spontaneous injection is caused primarily by an interfacial pressure difference formed at the inlet of the capillary. Several parameters must be controlled to achieve small injections in a quantitative manner. (p. 2318)

Electrochromatography on a chip

Microfabrication of conventional chemical instrumentation is being used to develop compact, inexpensive instrumentation for field surveys, on-line process control, and remote sensing. J. Michael Ramsey and co-workers at Oak Ridge National Laboratory describe a microchip fabricated to perform electrochromatography in open channels. The surface of the channels is chemically modified with octadecylsilane to function as a stationary phase for open-channel chromatography, and electroosmotic flow is used to load the sample into the microchip and pump the mobile phase. Laser-induced fluorescence is used to monitor the separations directly and the void time indirectly. Plate heights as low as 4.1 and 5.0 μm are generated for unretained and retained components, respectively. (p. 2369)

Modeling CE migration behavior

The choice of the type and concentration of buffer modifiers can play an important role in improving the quality of CE separations. As a result, the development of effective methodologies to model and optimize solute migration is important for wider acceptance of CE. Rachhpal S. Sahota and Morteza G. Khaledi of North Carolina State University describe a target-factor-based approach that is effective in reducing the initial number of experiments required for modeling as well as in recognizing the optimum conditions for running the experiments. (p. 2374)

Carboxylic acids by LC

Chromatographic separation of carboxylic acids has traditionally involved the use of a gel-type column of large dimensions and an acidic aqueous eluent to repress ionization of the analytes. John Morris and James S. Fritz of Ames Laboratory and Iowa State University show that these conditions are not necessary. A macroporous resin column with a predominantly aqueous eluent and no added acid gives excellent separation. Addition of an alcohol to the mobile phase further increases the separation. The resulting eluent is amenable to conductivity detection. (p. 2390)

What's in the ocean?

There is much speculation about the amount and form of dissolved organic matter in the oceans. Rubén J. Lara and David N. Thomas of the Alfred Wegener Institute for Polar and Marine Research (Germany) compare the sorptive behavior of XAD2, XAD4, and XAD7 resins for dissolved organic carbon derived from marine phytoplankton. Arranging the resins in varying sequences proves to be critical for determining the efficiency of dissolved organic carbon isolation. The researchers find that 32, 21, and 2% of dissolved organic carbon is firmly retained by XAD2, XAD4, and XAD7, respectively. (p. 2417)

Enzymatic profiling using CZE

The small sampling and detection volumes of CZE make it useful for studying cells, including individual neurons and human erythrocytes. Karen J. Miller and Fred E. Lytle of Purdue University describe a method for immobilizing microorganisms within a capillary to characterize those cells using CZE. Baker's yeast cells are immobilized on a CZE capillary with a mid-capillary frit constructed using a single 50-μm particle with "through pores". Cells trapped on the capillary are profiled using different amino acid β-naphthylamide–aminopeptidase substrates. An aminopeptidase profile can be obtained using just 500 cells. (p. 2420)

Spectroscopy of micellar catalysis

Micellar solutions act as catalysts for condensation reactions that are strongly reversible in water without the need for strong acids and organic solvents. Anatoly K. Yatsimirsky of the Universidad Nacional Autónoma de México and colleagues use a spectrophotometer to follow the kinetics of hydrazone formation reactions in micellar sodium dodecyl sulfate solution. They derive the binding constants of reagents and products to the surfactant micelles as well as the rate constants of the condensation reactions within the micelles. (p. 2232)

DRIFTing sands

Diffuse reflectance IR Fourier transform spectroscopy is often used as a qualitative analytical method for powders and other solids with minimal sample preparation, but quantitative use requires extremely careful sampling. Farnaz Boroumand and colleagues at the Ecole Polytechnique Fédérale de Lausanne (Switzerland) explore some of the experimental parameters affecting quantitative diffuse transmittance and reflectance measurements of surface-derivatized silica powders taken by placing a photopyroelectric detector in direct contact with the sample. They find that the surface morphology, mechanical pressure applied to the powder, and the type of surface chemical derivatization affect the success of the experiments. (p. 2260)

The sound is more than skin-deep

Photoacoustic spectroscopy (PAS) S/N increases as the gas volume surrounding the sample in the PAS detector is reduced. Tsuguo Sawada of the University of Tokyo (Japan) and colleagues

Get A First Look At The Last Word In Materials Chemistry.

Staying informed on advancements in materials chemistry demands resources that let you read the latest research almost as it happens. *Chemistry of Materials* helps you do just that. Through a rigorous system of peer review, *Chemistry of Materials* brings what's new into clear, concise focus:

- **New directions** in molecular and ionic conductors, chemical processing of ceramics, non-linear optical materials, biomaterials, liquid crystals, and surface modified electrodes.
- **New materials** including semi- and superconductors, composites, catalysts, ceramics, nanoporous solids and advanced polymers.
- **New processes,** from MOCVD and plasma or laser-assisted deposition, to sol-gel processing.

Whether you're involved in advanced materials, R&D, chemical engineering, colloid and surface chemistry, analytical, physical, polymer chemistry or other related fields, *Chemistry of Materials* offers you an up-to-the-minute view of materials science and technology from a molecular-level perspective.

A one-year subscription is only $50 for ACS members in the U.S. and includes 12 monthly issues. Nonmembers and abroad, call for subscription prices.

To Subscribe:
Call 1-800-333-9511
Outside the U.S.
call 614-447-3776
Or write:
American Chemical Society
Publications Marketing
1155 16th Street, NW
Washington, D.C. 20036

ACS PUBLICATIONS
Essential Resources for the Chemical Sciences

EDITOR: Leonard V. Interrante
Rensselaer Polytechnic Institute

ASSOCIATE EDITORS Dennis W. Hess,
Lehigh University
Gary E. Wnek
Rensselaer Polytechnic Institute

In This Issue

have developed a miniaturized open-ended PAS cell that consists of a fiber-optic light guide that has been adapted at one end as a PAS sample chamber with an attached acoustic pipe. The pipe design has been optimized to reduce dead volume near the microphone. The light guide delivers UV light at low intensity for in vivo skin absorptiometry testing of ointments. The PAS absorptiometry test is compared with conventional in vitro and in vivo methods as a nondestructive alternative. (p. 2267)

Monitoring air pollutants

Atmospheric nitrogen oxide compounds play key roles in atmospheric reaction cycles such as the production of acid rain and photochemical smog and the regulation of species such as OH and ozone in the atmosphere. In recent years considerable interest has been focused in developing real-time, laser-based monitors that can detect such pollutants. J. B. Simeonsson, G. W. Lemire, and R. C. Sausa of the U.S. Army Research Laboratory have developed a laser-induced photofragmentation/photoionization spectrometric method to detect trace concentrations of NO, NO_2, HNO_3, and CH_3NO_2 under ambient conditions. Use of a single laser and optogalvanic ion detection greatly simplifies the instrumental requirements of the method. (p. 2272)

Analyzing electronic-grade chlorine

Monitoring metal contaminants in electronic specialty gases such as chlorine is essential because their purity can influence the yield and reliability of devices produced. Because current filtration and hydrolysis techniques are indirect, time consuming, and prone to contamination, Tracey Jacksier of Air Liquide and colleagues have developed a new analytical scheme. They use a particle counter in tandem with a sealed ICP system to establish particle size, particle concentration, and elemental composition of impurities in a chlorine gas stream and correlate the total particle volume (deduced from particle counts) and the total impurity emission. (p. 2279)

Alcohol/water interactions

Because retention time in reversed-phase LC depends on the behavior of the mobile-phase mixture, complexation behavior in alcohol/water mixtures has important implications in explaining nonlinear solute retention. M. Kathleen Alam and James B. Callis of the University of Washington use near-IR spectroscopy and multivariate statistics to provide data on the intermolecular interactions of alcohols and water. Although a 1:1 alcohol/water complex is observed at high alcohol concentrations, a complex involving a higher number of water molecules becomes important at low alcohol concentrations. (p. 2293)

Radionuclide detection using CE

Radioisotopes have been used as an analytical tool in biochemical applications for many years, in part because they offer attomole sensitivity and excellent selectivity. Jonathan V. Sweedler and co-workers at the University of Illinois describe a postcolumn radionuclide detection system for CE. Eluant from an electrophoresis capillary is directed onto a peptide binding membrane that had been previously coated with a solid scintillator. The membrane is moved in a preselected pattern relative to the fixed capillary outlet during electrophoresis, and light emission from scintillation is imaged onto a charge-coupled device by using a series of 35-mm camera lenses. Detection limits are 88 zmol for ^{32}P-labeled analytes, 17 amol for ^{35}S-labeled analytes, and 8 fmol for ^{3}H-labeled analytes. (p. 2382)

Synopses of significant analytical articles from other publications

What sputters up must come down

Bombarding a sample with an inert gas ion beam causes its surface to sputter. But the sputtered material, some of which lands in a ring around the point of bombardment, may have an altered chemical composition from the original material. Robert D. Govier and Edward H. Piepmeier of Oregon State University have used electron spectroscopy for chemical analysis (ESCA) with an ion beam etching accessory (an Ar^+ gun) to study successive layers of the craters and the deposited ring material created by bombarding a brass sample with a gas jet glow-discharge source.

They found that the surface of the crater was depleted of zinc early in the sputtering process. The deposited ring had a top surface that was enriched in copper; underlying layers of the deposit were enriched in zinc. They theorized that zinc, which has a higher sputtering yield than copper, is sputtered preferentially and is therefore redeposited in the ring around the crater earlier than copper. In addition, anomalies in the Zn/Cu ratio of the layers of sputtered material compared with the bulk sample ratio led them to conclude that zinc also resputters preferentially from the deposited material. (*Appl. Spectrosc.* **1994**, *48*, 426–35)

Dyes for sensitive near-IR

Interest in the use of near-IR fluorescence spectroscopy in chemistry and biochemistry is growing because of the high sensitivity that can be achieved. Complete utilization of the technique is limited, however, by the relatively small number of fluorochromes with high fluorescence efficiencies appropriate to the near-IR region. The commonly used di- and tricarbocyanine dyes exhibit small fluorescence quantum yields when compared with many visible fluorescence dyes. Steven A. Soper and Quincy L. Mattingly of Louisiana State University have used steady-state and picosecond laser fluorescence to study nonradiative pathways in tricarbocyanine dyes in an effort to design near-IR fluorochromes with high fluorescence efficiencies.

Their results indicate that several factors should be considered when designing these fluorochromes, such as inclusion of charged functionalities to prevent aggregation, exclusion of heavy atoms in the dye structure, structural reinforcement within the polymethine chain to reduce the rate of internal conversion, and inclusion of organized media in the aqueous environment. (*J. Am. Chem. Soc.* **1994**, *116*, 3744–52)

MALDI membranes

MALDI-MS, which offers a mass range that approaches 300,000 Da and picomolar sensitivity, has quickly become one of the most useful MS methods for characterizing proteins and other large biomolecules. Several research groups have attempted to analyze proteins adsorbed onto membranes used for conventional electrophoretic methods via MALDI-MS, but not all membranes work well with the matrix.

E. J. Zaluzec, D. A. Gage, John Allison, and J. Throck Watson of Michigan State University tested several types of membranes to find the ones best suited to MALDI techniques. They mounted the membranes with adsorbed proteins onto a probe, coated them with the matrix compound, and performed MALDI-TOFMS. They found that polyvinylidene difluoride (PVDF) and nitrocellulose both retained proteins strongly and prevented them from mixing with the matrix compound for cocrystallization. Nylon-66 and positive charge-modified nylon membranes, however, provided low-picomolar sensitivity without decreasing mass accuracy. (*J. Am. Soc. Mass Spectrom.* **1994**, *5*, 230–37)

Analyzing ion mobility spectra

Ion mobility spectrometry is based on the drift of gas-phase ions through air or nitrogen in the presence of a weak field at constant temperature and pressure. Ion mobility spectra, however, often consist of broad peaks and simple patterns without obvious details associated with structural characteristics, which can hinder the analysis of spectra derived from mixed vapors. Dennis M. Davis and colleagues at the U.S. Army Edgewood Research, Development, and Engineering Center and New Mexico State University have developed a Gaussian deconvolution algorithm for analyzing ion mobility spectra of binary mixtures.

The deconvolution algorithm was examined for sensitivity toward parameters and for boundaries of operation using ion mobility spectra of binary mixtures. An ion–molecule cluster ion that is not obvious in traditional spectral analysis was disclosed by deconvolution analysis and confirmed by independent ion mobility spectrometry/MS. (*Anal. Chim. Acta.* **1994**, *289*, 263–72)

Anticancer drug binding to DNA

Actinomycin D (AMD), a potent anticancer agent that is much larger than many of the other drugs that bind to DNA, has been shown by single-crystal X-ray diffraction (XRD) to have three different binding conformations, which may explain its high potency. Shigehiro Kamitori and Fusao Takusagawa of the University of Kansas used XRD and molecular modeling to study complexes of AMD bound to an eight-base oligomer of DNA that contained the AMD target binding sequence.

The researchers found that crystals with one space group contained AMD–DNA complexes with two independent structures that showed an exact two-fold symmetry. Molecular modeling studies

showed that the two structures were related to a third structure that had been determined from XRD of crystals with a different space group.

The central phenoxazone and threonine groups of AMD intercalate into the minor groove of the DNA helix and form hydrogen bonds with its bases and backbone. The drug's two depsipeptide rings lie on either side of the minor groove, and the drug can apparently change its conformation to fit these rings into topographically different DNA helices without breaking bonds. The researchers speculate that this phenomenon may eventually help explain the drug's tendency to inhibit RNA transcription more strongly than DNA replication. (*J. Am. Chem. Soc.* **1994**, *116*, 4154–65)

MALDI of vitamin B_{12}

One characteristic feature of MALDI is the low abundance of fragment ions observed in the resulting mass spectrum. This can be a disadvantage, however, in cases where the generation of fragment ions can provide insight into analyte structure. Although researchers have generally believed that little or no fragmentation of analyte molecules occurs during MALDI on a sufficiently fast time scale to be observed as nonmetastable ions in a TOF mass spectrum, they have found that sufficiently high analyte ion internal energies are accessed during MALDI to initiate ion fragmentation on somewhat longer time scales.

Gary R. Kinsel, Lisa M. Preston, and David H. Russell of Texas A&M University have designed a series of experiments to probe the extent and mechanism of ion excitation in MALDI. They investigated the influence of changes in experimental parameters on the degree of fragmentation of vitamin B_{12}, whose labile structure makes it senstitive to internal excitation, and conclude that the specific matrix chosen to perform MALDI strongly influences the degree of analyte ion excitation. (*Biol. Mass Spectrom.* **1994**, *23*, 205–11)

Sweating it out

In situ estimates of athletes' physical and biochemical conditions are required to evaluate their training regimes. Blood lactate is an important index for estimating physical condition. The blood lactate concentration of an athlete undergoing exhaustive exercise increases following the onset of a more energy-productive anaerobic metabolism. Once a certain level of lactate concentration is reached, however, exhaustion occurs followed by a rapid decline in exercise capacity.

Previously, lactate concentration has been monitored by taking blood from an athlete during exercise; however, noninvasive monitoring would be more desirable. As an alternative to blood analysis, Isao Karube and co-workers from the University of Tokyo (Japan) analyzed the metabolites present in sweat. Analyses were conducted using either amperometric biosensors or commercial ion-selective electrodes. The data were compared with previously reported results for blood and sweat analysis. (*Anal. Chim. Acta* **1994**, *289*, 27–34)

Microelectrode arrays

Microelectrode arrays consist of numerous small electrodes organized into a regular pattern within the surface of an electrochemically inert matrix. The inert matrix provides mechanical stability, defines the fluid dynamic properties, and ensures electrical correspondence between the microelectrodes. To achieve the optimal fractional active area, graphite particles must be incorporated into the matrix to achieve connectivity between the microelectrodes. However, there are two disadvantages to using graphite powder. First, when the electrodes are polished, a loss of graphite occurs at the surface, resulting in a loss of electrical connectivity. Second, because graphite is a useful electrode material for faradaic reactions, its use is undesirable in the fabrication of metal microelectrode arrays.

Advantages could be gained if matrices that are both electrically conductive and electrochemically inert are used. Ti_4O_7, a ceramic material, is an appropriate candidate because of its high conductivity and stability in corrosive media. Lin He, Hugo F. Franzen, Joseph E. Vitt, and Dennis C. Johnson of Ames Laboratory and Iowa State University report on the generation of ruthenium microelectrodes within conductive Ti_4O_7 matrices as part of a larger project to synthesize composite electrode materials using a minimum of precious metals. A rotated disk electrode constructed from ruthenium and Ti_4O_7 exhibits virtually no dependence on rotational velocity for the oxidation of I^- to I_2, thereby demonstrating that this material functions as an ideal microelectrode array. (*J. Electrochem. Soc.* **1994**, *141*, 1014–20)

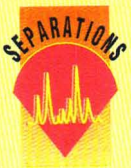

Flow-injection immunosensor for herbicides

The growing availability of antibodies for compounds of environmental interest has resulted in an increased use of immunoassays rather than traditional chromatographic methods for determining water pollutants. Monika Wortberg and co-workers at Westfälische Wilhelms-Universität (Germany) have developed a flow-injection immunosensor for triazine herbicides based on principles of immunoaffinity chromatography.

The affinity column consists of triazine herbicide derivatives immobilized on oxirane acrylic beads; the beads are saturated with monoclonal antiherbicide antibodies labeled with a fluorescent Eu(III) chelate. Antibodies are replaced with analyte upon exposure, and the resulting fluorescence is detected using a postcolumn laser fluorimeter. The detection limit for atrazine is 1 μg/L, and the linear dynamic range covers 3 orders of magnitude. The affinity column is stable at room temperature for at least two weeks. (*Anal. Chim. Acta* **1994**, *289*, 177–86)

Building a better SOC trap

The distribution of semivolatile organic compounds (SOCs), such as PCBs, PAHs, and polychlorinated dibenzodioxins, between the vapor and particle phases is an important determinant of the compound's environmental fate and transport. SOCs are commonly sampled with a high-volume air sampler, but artifacts inherent in its design make it difficult to determine true vapor–particle partitioning.

To address this problem, Mark S. Krieger and Ronald A. Hites of Indiana University have developed an alternate sampling technique—diffusion denuders that use short sections of capillary GC tubing as the sampling tubes—and used it to quantitatively measure SOCs and to determine heats of desorption of PAHs. They simultaneously sampled PCBs with the denuders and a filter/polyurethane foam sampler and found that the total vapor and particle concentrations measured were not statistically different. This indicated the accuracy of the denuder measurement. Breakthrough experiments demonstrate that 80% of the PCBs are collected in the first 25% of the denuder, and 99% are collected in the first 75%. (*Environ. Sci. Technol.* **1994**, *28*, 1129–33)

Progress.

New strategies for the design of catalytic antibodies. Large-scale **bioprocessing** of solids. **Bioseparations.** Sustaining **protein synthesis** in the absence of rapid cell division. Acid metabolites in shake flasks and stirred **bioreactors.** Metabolism of hybridoma **cells cultured** in media supplemented with whey or fetal calf serum. From **basic science** to innovative **new applications of research,** today's discoveries are transforming the biotechnology and bioprocess industries. There's **one source** that covers the latest advances...reported in detail...reported first. So you can know the newest breakthroughs in **molecular and cellular biology.** So you can apply the best new R&D on everything from **formulation** and **product delivery** to **bioinstrumentation** and **tissue engineering.** To move ahead. To break new ground. To make a difference. That's progress.

Biotechnology Progress.

Published bimonthly by the American Chemical Society and the American Institute of Chemical Engineers

EDITOR Jerome S. Schultz, *Center for Biotechnology & Bioengineering, University of Pittsburgh* **ASSOCIATE EDITOR, Reviews,** Michael C. Flickinger, *University of Minnesota*

	US	CANADA & MEXICO	EUROPE*	ALL OTHER COUNTRIES*
ACS/AIChE Members	$ 30	$ 35	$ 40	$ 44
Nonmembers	$340	$345	$350	$354

*Air Service Included

To subscribe to this forefront research journal,

CALL 1-800-333-9511

(Outside the U.S. call 614-447-3776. Fax 614-447-3671)

ACS PUBLICATIONS

Essential Resources for the Chemical Sciences

WPAC addresses quality concerns

The Working Party on Analytical Chemistry (WPAC) of the Federation of European Chemical Societies (FECS) is an association that promotes the field of analytical chemistry. One goal of WPAC is to bring European analytical chemists and their laboratories into the world market of analytical services. This goal requires meeting standards of competence and performance, such as the EN 45000 and ISO 9000 standards, ISO/IEC Guide 25, and Good Laboratory Practices.

One way that WPAC seeks to attain this goal is to maintain a close relationship with the European Analytical Chemistry Accreditation System (Eurachem). Toward this end, Eurachem's endeavors include publications to help analysts conform to the standards and workshops on proficiency testing. In addition, a discussion paper on calibration and traceability with information on primary, certified, and working reference materials is being drafted. Standards for microbiological and R&D laboratories are also under consideration.

WPAC member countries have given valuable input to the programs on education and training in quality, both nationally and within the European Union. In fact, at a Eurachem meeting last fall, organizers decided that the "observer" status of several eastern European countries—the Czech Republic, Hungary, Poland, Russia, the Slovak Republic, and Slovenia—would be upgraded to associate member in recognition of their contributions to quality assurance goals.

WPAC gives its full support to the goal of uniform quality assurance across Europe. It intends to promote cooperation with Eurachem and urges its members to install or support national Eurachem organizations. WPAC also strongly supports education programs that focus on quality as well as testing and registration of analytical chemists. For more information on these educational initiatives, see *Anal. Chem.* **1994**, *66*, 98 A–101 A. For general information about WPAC and Eurachem, contact Bauke te Nijenhuis, Royal Gist Brocades, P.O. Box 1, 2600 MA Delft, The Netherlands (31-15-799111) or Robert Kellner, Institute for Analytical Chemistry, University of Technology Vienna, Getreidemarkt 9/A-1060 Vienna, Austria (43-1-58801-4831; fax 43-1-56-78-13).

Dow to sell Camille

The Dow Chemical Company (Midland, MI) is selling its Camille Products line to Sagian, Inc. (Indianapolis, IN), a full-service systems integration firm that specializes in the chemical processing industry. Camille Products sells integrated hardware and software systems for data acquisition and process control in laboratory, pilot plant, and small- to mid-sized process operations. Dow is selling Camille because, as a software and hardware company, it no longer fits in with Dow's business strategy as a chemical products company.

Dow developed Camille in 1979 to satisfy the need for automated process control and data acquisition in its own laboratories and pilot plants. Camille began selling its products outside of Dow in 1987, building a substantial user base in the chemical, plastics, pharmaceutical, and other processing industries. More than 475 systems have been installed in Dow facilities, making it one of Sagian's largest future customers.

In searching for a buyer, Dow wanted a company with the experience and resources that could keep Camille at the forefront of data acquisition and control. Because of Sagian's strategic focus in this industry, Dow is confident that there will be no disruption to customers currently using Camille systems.

ChromatoFast and Varian to market FastGC

ChromatoFast, Inc. (Ann Arbor, MI) has entered an alliance with Varian Associates (Palo Alto, CA) to market GC instruments with FastGC, an accessory developed by the University of Michigan's Richard Sacks and three former graduate students, the founders of ChromatoFast. FastGC allows analyses to be completed 10–100 times faster than is currently possible with conventional instruments. Al Lauer, head of Varian's instrument business, says that "The partnership with ChromatoFast is another example of Varian's commitment to providing tools that increase productivity in our customers' laboratories."

With FastGC, a sample is cooled onto a cryotrap, then rapidly heated and inserted into the gas chromatograph as a sharp plug to allow analysis in seconds rather than minutes. FastGC will be incorporated into Varian's Star CX GC systems and can be retrofitted in the 3400 and 3600 model gas chromatographs. Shipping will begin later this year.

Ultrasound for safer air bags

NIST has signed a cooperative R&D agreement with Morton Automotive Safety Products (Ogden, UT), the leading supplier of air bag inflators to the automotive industry, to study the feasibility of using ultrasound to inspect the inflators for weld defects. Morton's personnel will be trained to use an electromagnetic acoustic transducer (EMAT), a detector developed at NIST, to look for the flaws. The EMAT bounces sound waves up and down within the complicated geometry of the inflator. Under normal circumstances the waves build up amplitude at the resonance frequencies. When a defect is encountered, however, the sound wave is scattered and is no longer in phase. In proof of concept studies, this clearly decreases the resonance observed and thus indirectly enhances the sensitivity of the ultrasound signal. Morton hopes to eventually install the detectors on the assembly line to provide QA for its products.

NOMINATIONS

■ Chemical Publication of the Century

The ACS Division of Chemical Information requests nominations for the "Chemical Publication of the Century." Nominations should be in the form of a poster to be presented at Sci/Mix at the ACS national meeting in Chicago in August 1995.

Posters should demonstrate how the publication has contributed to the advancement of chemistry, chemical engineering, or a related field. Journal articles, separately authored chapters in books, patents, and other publications in existence since Jan. 1, 1901, may be nominated. A maximum of two posters nominating any one publication will be accepted.

The poster should include some or all of the following information about the publication: historical context; a brief summary of its technical content; its impact on the field and on society in general; the way in which it contributed to communicating the advancement; the way in which it provides a "window into the soul" of the author; unique features worthy of emulation; and continuing significance.

For further information, contact David Saari, American Cyanamid Co., Agricultural Research Division, Clarksville Rd., P.O. Box 400, Princeton, NJ 08543-0400 (609-799-0400, ext. 2512; fax 609-275-3576; internet saarid@pt.cyanamid.com).

■ Reminder about 1995 Division of Analytical Chemistry awards

The Division of Analytical Chemistry is seeking nominations for the Division's Award in Chemical Instrumentation, Award for Excellence in Teaching, and Awards in Spectrochemical Analysis and Electrochemistry. Each award consists of a $4000 honorarium, a plaque, and a travel allowance to the fall 1995 ACS national meeting. Eligibility for the awards is not restricted to members of the Division of Analytical Chemistry; nominating and seconding letters may also come from individuals who are not members. All nominations must be submitted by Sept. 1 to Janet Osteryoung, Dept. of Chemistry, Box 8204, North Carolina State University, Raleigh, NC 27695-8204. For additional information, see the March 15 issue (p. 351 A).

Alfred O. C. Nier

Photo ca. 1984

The Journal regrets to report the death of Alfred O. C. Nier, professor emeritus at the School of Physics and Astronomy at the University of Minnesota, on May 16. Through his pioneering work on the mass spectrometer in the 1930s Nier was able to determine that the age of the Earth is 5 billion years, separate ^{235}U and ^{238}U for the Manhattan Project, and measure the masses of most of the elements in the periodic table. Nier was most recently honored as a participant in the 5th James L. Waters Annual Symposium Recognizing Pioneers in Analytical Instrumentation: Mass Spectrometry, held in conjunction with Pittcon '94 earlier this year in Chicago.

FOR YOUR INFORMATION

■ Measurement cooperation

NIST, the National Research Council of Canada, the Standards Council of Canada, the National Center for Metrology (Mexico), and the Director General for Standards of Mexico have formed NORAMET and the North American Calibration Cooperation (NACC) to promote closer cooperation in metrology and calibration laboratory accreditation. NORAMET will provide regional collaboration in measurement standards and services. NACC will work to develop national calibration laboratory accreditation programs and to negotiate agreements with similar organizations throughout the world. For information, contact the Office of International and Academic Affairs at NIST (301-975-3089; fax 301-975-3530; internet oiaa@micf.nist.gov).

Spend a Year Collecting Information, Testing New Theories and Conferring With International Experts.

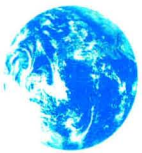

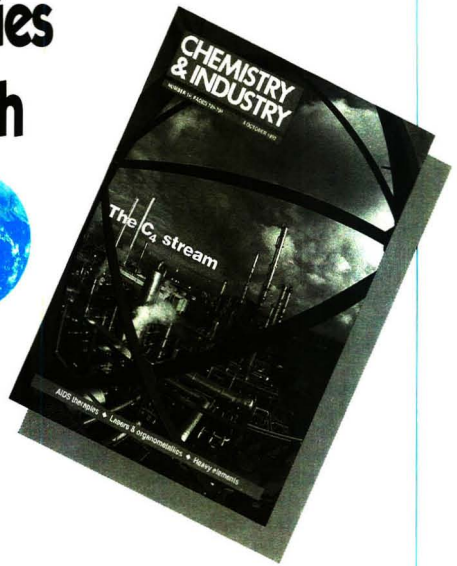

Stay on top of the industry's latest developments with an annual subscription to *Chemistry & Industry*. Discover the best source of global news, views and information — made, written and read by people like you. People involved in every aspect of the chemical industry, from academic and government scientists to R&D management, policy makers and opinion shapers from across Europe and around the world. Meet them all in the pages of *Chemistry & Industry*, the official publication of the Society of Chemical Industry, UK.

Twice a month, read the latest news, research and commentary about:

- applied chemistry
- food science
- biotechnology
- environmental issues
- science policy
- new materials
- pharmaceuticals
- energy

Subscribe today for the timely, innovative and international perspective that's exclusively *Chemistry & Industry*.

As lively as it is informative, *Chemistry & Industry* delivers a glimpse of future policy and research directions. Regular features include a quick-scan survey of European patent news, a section devoted to late-breaking research findings and reviews of the most current books and software.

IT'S THE NEWS YOU NEED FOR THE WORK YOU DO. SEND OR CALL FOR MORE INFORMATION.

Special subscription price for American Chemical Society members: $59 (non-members, $341). Air-shipped from Britain for expedited delivery in the U.S. Contact the American Chemical Society, P.O. Box 3337, Columbus, OH 43210. Phone: 800-333-9511 (U.S. only) or 614-447-3776 (outside the U.S.). Fax: 614-447-3671.

For orders outside the U.S., Canada and Mexico, please contact the Society of Chemical Industry, The Distribution Centre, Blackhorse Road, Letchworth, Herts SG6 1HN, England.

EXCLUSIVE OFFER: ONLY $59 ANNUALLY FOR ACS MEMBERS!

Report

Ion Trap Mass Spectrometry

Using High-Pressure Ionization

Plasma and electrospray ionization sources can be coupled with the ion trap to meet inorganic and organic analytical challenges

Scott A. McLuckey
Gary J. Van Berkel
Douglas E. Goeringer
Oak Ridge National Laboratory
Gary L. Glish
University of North Carolina

Given the preceding discussion in Part 1 of this series on the use of ion injection/quadrupole ion trap MS in the July 1 issue (p. 689 A), it should be apparent that the ion trap may or may not be an appropriate mass analyzer for a given analytical problem, depending on the relative importance of the mass analyzer characteristics. Ion sources operated at high pressures, however, are natural candidates for coupling with a quadrupole ion trap because of pumping requirements and because ion injection efficiencies are highest for ions with low kinetic energy. The latter characteristic obviates the electrical isolation challenges associated with certain techniques, such as coupling high-pressure ionization sources with sector mass spectrometers.

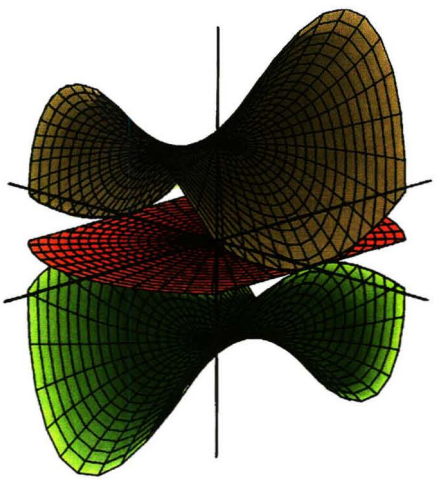

Many high-pressure ion sources are used with MS. In recent years, several of these have been coupled with the ion trap to address analytical challenges in both organic and inorganic MS. In this article, we will review this work briefly, drawing from our own experiences with atmospheric sampling glow discharge ionization (ASGDI), a form of ionization that occurs at ~ 1 torr, and electrospray (ES), an atmospheric pressure technique. Our discussion is divided into these two pressure regimes and includes descriptions of organic and inorganic applications.

Ionization at 1 torr

Organic MS. Our involvement with quadrupole ion traps and specifically with ion injection experiments grew from a project aimed at the development of a highly sensitive and specific detector for trace quantities of high explosives (such as nitroaromatic compounds, nitrate esters, and heterocyclic nitramines) in air. The strategy was to use an atmospheric sampling ionization technique with negative ion tandem MS. Because species commonly found in high explosives often form stable negative ions (*1*), negative ion analysis significantly reduces background noise.

The quadrupole ion trap seemed to be a particularly attractive analyzer because of its small size, its ability to operate at high pressures, and its high MS/MS efficiencies (*2*). It was apparent, however, that an in situ ionization method would lack the specificity and sensitivity required for the ion trap to compete with a beam-type scanning technology that uses negative ions. Low part-per-billion by volume (ppbv) detection limits have been demonstrated for in situ positive ionization ion trap MS in direct air-sampling scenarios (*3*). Lower detection limits are desirable because the saturated headspace room-temperature vapor pressures of many explosives of interest can be orders of magnitude lower than 1 ppbv (*4*). Negative ionization via electron capture can provide lower detection limits because of

0003-2700/94/0366-737A/$04.50/0
© 1994 American Chemical Society

its selectivity, thereby reducing background, and because of the higher rates associated with electron capture relative to ionization by ion–molecule reactions for these species (*5*). However, efficient negative ion formation, particularly when direct electron capture is desired, is difficult to achieve within the ion-trapping volume because of the wide disparity in mass for electrons and ions (*6*). Conditions appropriate for trapping electrons lead to essentially zero well depths for ions, whereas appropriate conditions for trapping ions lead to values of m/z_{min} that are orders of magnitude greater than the m/z of the electron (see Equation 1 in Part 1). Therefore, it is difficult to accumulate enough slow electrons within the ion trap to achieve efficient ionization of the analyte. Consequently, we were forced to consider another means of ionization to take advantage of the virtues of the ion trap.

In previous work we had already applied an ASGDI source (*7*) with beam-type tandem MS (*8*) to the detection of explosives in air. This form of ionization is particularly well suited to the problem because it samples directly from the air, which supports the glow discharge. There is, of course, a high density of slow electrons within the discharge that yields high electron capture rates for the explosives of interest (*9*). Furthermore, at the pumping speed and analyte number densities associated with the ASGDI source, ionization is under kinetic control—which minimizes matrix effects upon ionization—instead of thermodynamic control. Given the poor efficiency of anion formation within the ion trap, we interfaced an ASGDI source with the ion trap (*10*). The glow discharge source can be used to ionize the analyte directly, as in explosives detection, or it can be used to form reagent anions that are injected into the ion trap to effect in situ negative chemical ionization (*6*).

Figure 1 shows a schematic of this combination. The filament assembly normally mounted on the entrance end cap was removed. A three-element lens system was used to focus ions issuing from the ion source onto the entrance end-cap aperture during ion accumulation and to prevent ions from reaching the entrance aperture at all other times.

The ASGDI/ion trap combination, with air in the vacuum system at 0.1 mtorr and helium added to bring the total pressure to ~ 1 mtorr, provides subpicogram and low part-per-trillion detection limits for the organic high explosives of interest and yields MS/MS efficiencies of 40–100% for the precursor ions derived from these species. Figure 2, for example, shows virtually 100% MS/MS efficiency for the precursor ion derived from pentaerythritol tetranitrate (PETN), a plastic explosive. These performance characteristics are highly desirable in an explosives vapor detection system. However, the influence of matrix ions on the ions of interest and the mutual influence of like ions can seriously compromise the actual application of the ion trap in detecting targeted compounds in an automated system.

Matrix ions, if permitted to accumulate with the ions of interest, can greatly affect the number of analyte ions that can be accumulated, because of the limited ion storage capacity of the ion trap. This is especially problematic when the analyte ions represent only a small fraction of the accumulated ions. A means to allow for the accumulation of the ions of interest is therefore desirable when the ions of interest represent a small fraction of the ion beam injected into the ion trap.

Explosives detection is just such a scenario, and we used it to illustrate this effect and to show that the ejection of matrix ions during ion accumulation could allow for the concentration of the ions of interest in an ion injection experiment (*11*). We applied a single-frequency large-amplitude signal to the end caps to continuously eject a wide range of low m/z ions formed from the discharge gases while the molecular anion of 2,4,6-trinitrotoluene (TNT) accumulated. However, it is much more desirable to use tailored signals that allow for the accumulation or ejection of arbitrary ranges of m/z so that ions of widely different m/z can accumulate simultaneously. Such a capability is necessary for the ion trap to retain its duty cycle advantage.

Recently, stored waveform inverse FT (SWIFT) (*12*) and filtered-noise fields (*13*) have been used with ion injection/ion trap experiments to provide this capability. We have evaluated filtered-noise fields applied to the ASGDI/ion trap explosives detection experiment for the simultaneous accumulation of the molecular anion of TNT and three anions observed from sulfur, S_2^-, S_3^-, and S_4^-. Figure 3 shows the resulting mass spectra acquired with and without a filtered-noise field that allows for the selective accumulation of the targeted ions. Note that in the absence of the filtered-noise field, the

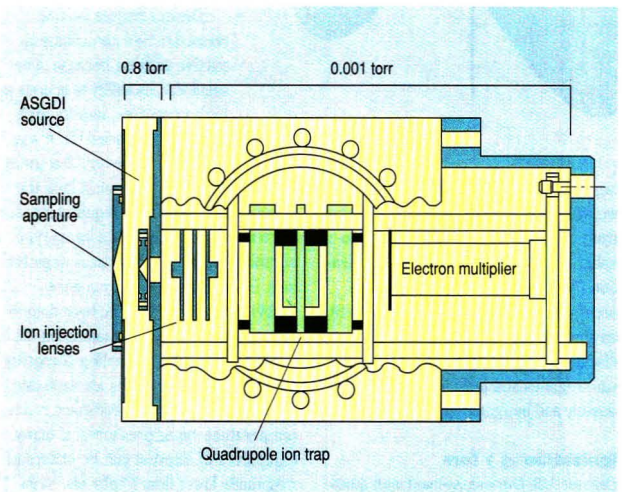

Figure 1. Side-view schematic of an ASGDI source coupled with a quadrupole ion trap.

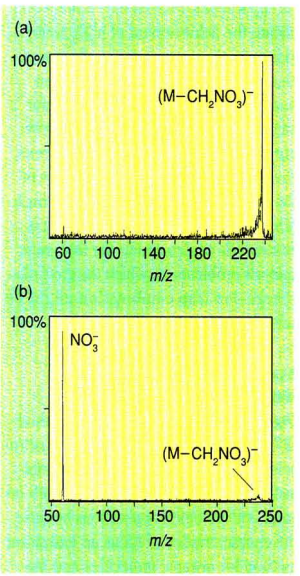

Figure 2. Ion trap MS/MS data for the $(M-CH_2NNO_2)^-$ precursor ion derived from PETN by using ASGDI.

Spectrum acquired (a) after precursor ion isolation and before collisional activation and (b) after collisional activation.

more abundant and slightly space-charge broadened matrix ion signals somewhat obscured the sulfur-derived ions. In addition, the matrix ions adversely affected the accumulation of the TNT molecular anion. These and other results have shown that mass-selective ion accumulation techniques can be used to make the full dynamic range of the ion trap available in an ion injection experiment even for ions of low abundance in the injected ion beam.

A second potentially troublesome aspect associated with detecting targeted compounds with the ion trap is the need for optimization of collisional activation conditions. The major tuning variables for such experiments are the well depth, the frequency of the dipolar potential applied to the end caps, the amplitude of the potential applied to the end caps, and the duration of resonance excitation. The optimum well depth, amplitude, and duration for a targeted ion are largely independent of the number of ions and therefore can be established in the laboratory and used in the field. However, the electric field of other ions can affect the frequencies of ion motion, although they are largely determined by the parameters in Equation 4 in Part 1. Ions of similar *m/z* are most influential because they occupy similar wells (i.e., they overlap most in space). Frequency shifts associated with space charge can be large enough to move an entire ion population of a particular *m/z* out of resonance with a radio frequency (rf) potential tuned to the frequency of a single ion. In explosives detection, for example, it is not possible to predict a priori the quantity of analyte and hence the number of ions likely to be encountered. It is therefore desirable to use an ion activation method that is independent of both *m/z* and the number of precursor ions.

Recently, several approaches that address this space charge problem, such as rapid forward- and reverse-frequency scan to determine optimum frequency and 1.7-kHz bandwidth signals (*14*), have been demonstrated. Random noise (*15, 16*) and a low-frequency dipolar field applied to the end caps (*17*) have been shown to be effective in dissociating ions independent of *m/z* and ion number. The latter approach effectively shifts the entire potential well off-center. The ions gain kinetic energy from the trapping field because suddenly they are no longer at the bottom of the well. When the field is reversed, the potential well is shifted off-center again, but in the other direction, once more placing the ions away from the bottom of the well. These techniques, together with mass-selective ion accumulation, should now make direct mixture analysis for targeted compounds with the ion trap practical in the field.

The ASGDI source is a form of chemical ionization source. However, conventional filament-based chemical ionization sources have been interfaced with a quadrupole ion trap by Pedder et al. (*18*) and by Bier et al. (*19*). (A notable aspect of the work of Pedder et al. is the use of a dc quadrupole to gate the ions into the ion trap. This allows the ion source to be mounted off-axis with respect to the entrance end cap, as opposed to the line-of-sight configuration of Figure 1.) Perhaps the main advantage of an external chemical ionization source over in situ chemical ionization used with the ion trap derives from the separation of neutral analyte from the mass analysis region. External ion sources greatly reduce the likelihood for ion–molecule reactions and memory effects (*19*). Furthermore, the pressure regions are much different, which can significantly affect ion chemistry.

Inorganic MS. By far, most ion trap work has been directed toward the MS of organic and biological species. However, the unusual characteristics of the ion trap might also prove to be useful in some inorganic MS applications, and inquiries along these lines have begun. For example, high MS/MS efficiencies, which can

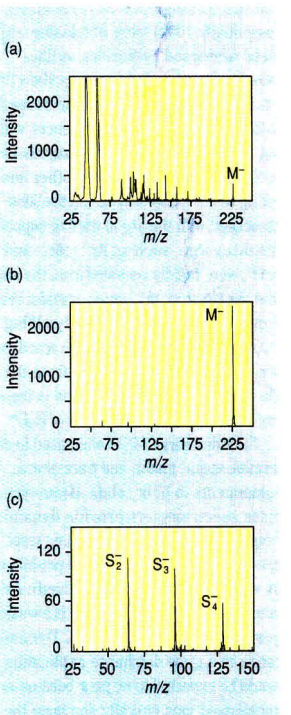

Figure 3. Ion trap mass spectra obtained by using ASGDI of the headspace vapors of a mixture of TNT and black powder in air with an ion accumulation time of 1 s.

Results obtained (a) without selective ejection of matrix ions and (b) using a filtered-noise field to allow for selective accumulation of the molecular anion of TNT and S_2^-, S_3^-, and S_4^-. (c) Expanded-scale version of (b) to show sulfur ions in more detail. (Adapted from Reference 13.)

be obtained for many organic ions, would be useful in eliminating or reducing the number of polyatomic ions that interfere with the analysis of atomic species. Isobaric interferences can limit some glow discharge MS analyses (*20*). Two approaches can overcome this problem: use sufficiently high resolving powers to separate the isobars in either sector MS (*21*) or FT-ICR MS (*22*), or destroy polyatomic isobars by using collision-induced dissociation instrumentation (*23, 24*).

An rf glow discharge ionization source was substituted for the ASGDI source of Figure 1 to explore the strengths and limitations of the ion trap for inorganic analyses (*25, 26*). A particularly promising result was that high MS/MS efficiencies (essentially 100%) were obtainable with metal oxides and hydroxides, as illustrated in Figure 4. These results show that ion trap collisional activation can be used to destroy polyatomic interferences without significantly affecting the signals associated with atomic ions. Another interesting result is that several intense ions associated with the argon used to support the discharge, such as Ar^{2+}, Ar_2^+, and ArH^+, were rapidly removed from the ion trap via electron and proton transfer reactions with background gases, yielding H_3O^+ as the terminal ion. These reactions served to remove the charge from the ion trap because the m/z_{min} used in these experiments exceeded the m/z of H_3O^+.

Glow discharge MS is often used to determine major, minor, and trace atomic components in bulk solids. Beam-type mass spectrometers provide dynamic ranges extending up to 10^9 (i.e., trace components present at the part-per-billion by weight level can be determined). As noted in Part 1, dynamic range is a weakness of ion trap techniques. Dynamic range in a glow discharge application would be expected to be poor because argon-derived ions typically dominate the spectrum. However, the rapid reactions with background gases tend to remove these ions and mass-selective ion accumulation techniques can provide a dynamic range of at least 10^5 (*26*).

The relatively high levels of chemical and background noise in these early experiments precluded greater extension of the dynamic range. Further extension might be possible, but only at the expense of the mass range of accumulated ions. Ions derived from minor or trace components must be accumulated by allowing ions within only relatively narrow mass ranges to be stored during a given ion injection period. The accumulation of ions over a small mass range is also desirable from the point of view of the measurement precision of isotope abundances. The best ion statistics are obtained by allowing accumulation of the isotopes of interest and excluding all others. There is a tradeoff, therefore, between dynamic range and duty cycle when a variety of elements are to be determined in a given sample, because a series of ion trap experiments is necessary to fully characterize a sample with many components of widely differing concentrations.

Dynamic range, abundance sensitivity, and abundance measurement precision are more important in inorganic MS applications than in most organic and biological applications. Ion–ion interactions complicate the achievement of high performance in these areas for ion trap techniques; however, the limitations of ion traps have not yet been determined nor has much attention been paid to improving their performance in these areas. Given the desirable characteristics of the quadrupole ion trap, such as high MS/MS efficiencies and small size, it is worthwhile to determine the inorganic analysis problems for which the glow discharge–ion trap combination might be suitable.

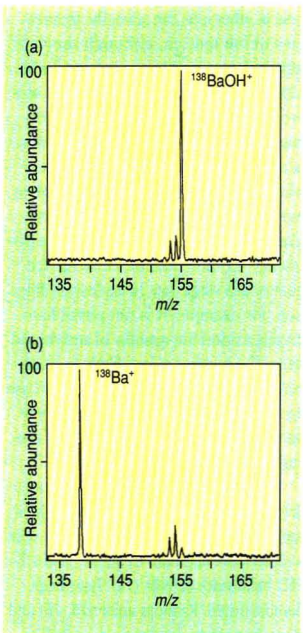

Figure 4. Ion trap MS/MS data derived from the $BaOH^+$ precursor ion.

(a) The spectrum of isolated $BaOH^+$ isotopes prior to collisional activation. (b) The spectrum obtained after collisional activation of $^{138}BaOH^+$. (Adapted from Reference 25.)

Atmospheric pressure ionization

Organic MS. ES is the ionization method (*27–29*) used most often with the quadrupole ion trap. We expect that this combination will be used extensively in both organic and biological applications because the characteristics of ES as an ionization method for organic molecules and biomolecules play directly to the strengths of the ion trap. For example, although the total ion current produced by the ES is as high as 1 μA, ~ 10^{-11}–10^{-10} A actually reach the analyzer (*28*). The current associated with the analyte may be a small fraction of the current injected into the analyzer. Therefore, the potential duty cycle advantage offered by the ion trap is realized because of the long ion accumulation times required. The duty cycle advantage coupled with the transmission advantage in tandem MS experiments allows the ion trap, in favorable cases, to provide detection limits several orders of magnitude lower than those provided in an analogous scanning beam-type instrument experiment.

The sensitivity of ESMS to both solution chemistry and gas-phase ion chemistry results in the tendency for researchers to observe the most thermodynamically stable ions. Therefore, ES is particularly prone to matrix effects, and mixture analysis problems are ordinarily addressed by using some form of separation before ionization so that analyte species are subjected to ES one at a time (*30*). The selectivity of ES for species present as ions in solution usually leads to the concentration of charge in the analyte species. The most intense matrix ions appear at relatively low m/z and can be readily discrimi-

nated against with proper adjustment of m/z_{min}. Consequently, ES matrix ions are far less troublesome than those associated with the plasma ion sources described elsewhere in this article.

As in other ion injection experiment, the bath gas serves to remove kinetic energy from the ion to facilitate trapping and focuses the ions at the bottom of the potential well. The bath gas plays an additional role that is particularly significant in the ES/ion trap experiment: It provides a mechanism for energy transfer to and from the surroundings. Without ion–ion interactions, trapped ions assume the temperature of the bath gas (i.e., the bath gas thermalizes the ions both internally and kinetically). In contrast to most other forms of MS, ions in the ion trap are not isolated within the analyzer; therefore, the internal energy distribution of the ions that issue from the ion source can change upon storage. Thus, loosely bound species dissociate within the ion trap if they are not kinetically stable at the temperatures they assume upon storage.

The significance for ES is that extensive desolvation can occur within the ion trap (*31*); therefore, the need for desolvation within the ES ion source is eliminated. Indeed, in our laboratory we performed all of the ES/ion trap work with a homemade ES source that does not use dry countercurrent gas flow or heating to assist in desolvation. Although ions derived from relatively small molecules are observed without significant solvation, multiply-charged biomolecules, such as proteins, can be observed as highly solvated ions. Figure 5a, for example, shows the ES ion trap mass spectrum of horse skeletal muscle apomyoglobin acquired without desolvating the ions in the ion source. However, ion trap collisional activation can be used to desolvate the ions once they are trapped, as illustrated in Figure 5b (*32*). The ability to desolvate ions within the ion trap, as opposed to declustering them in the ion source, is desirable because it allows solvated and loosely bound complexes, such as myoglobin (*33*) and duplex fragments of DNA (*34*), to be studied in MS^n experiments. Declustering within the ion trap can be accelerated non-mass-selectively during ion accumulation by using broadband excitation without dissociating covalently bound species. This technique is useful for improving S/N and signal-to-background levels in total ion electropherograms obtained with capillary electrophoresis (CE) coupled with ES ion trap MS (*35*).

Most ES ion trap mass spectrometer configurations have used ion injection through an end-cap electrode, and all have used the commercially available "stretched" electrode geometry (*36*). (A preliminary report has been published that describes ion injection diagonally along an ion trap asymptote [*37*].) Most of the recently developed high-performance ion trap techniques have been applied to ions formed by ES, such as high-mass multiply-charged ions. These include extended m/z range via resonance ejection (*38*), MS^n, high mass resolution via slow scanning (*39*), and high-resolution precursor ion selection (*40*). Collision-induced dissociation, using both single-frequency resonance excitation and random noise (*15*), and proton transfer (*41, 42*) have served as the reactions between MS stages. In some cases, both reactions have been used in a single MS^n experiment (*42*). Ion trap collisional activation studies have shown that, via MS^n, extensive sequence information can be obtained for peptides (*43*) and oligonucleotides (*44*). Analyte quantities required to obtain this information can be as much as 2 orders of magnitude less than those required with a scanning beam-type tandem mass spectrometer.

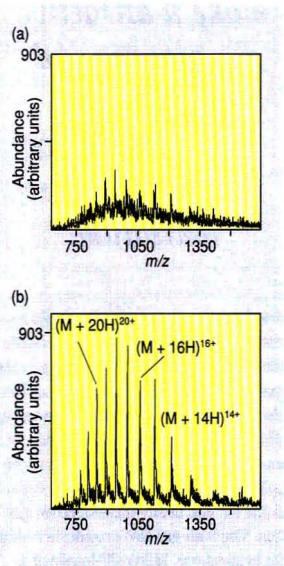

Figure 5. Electrospray ion trap mass spectra of horse skeletal muscle apomyoglobin.

Spectrum acquired (a) without desolvating the ions in the ion source and (b) using ion trap collisional activation to desolvate the ions once they have been trapped. (Adapted from Reference 32.)

Much of the ES ion trap work has used direct infusion of the analyte-containing solution to introduce the sample. However, ES is particularly well suited as an interface between condensed-phase separations and MS (*30*). Given the susceptibility of ES to matrix effects (*45*), a separation step is often desirable for mixture analysis. Indeed, many important analytical applications of ES, such as the analysis of tryptic digests, mandate a separation step. Therefore, several studies have evaluated the utility of the ion trap in HPLC (*32*) and CE (*46*) applications on line with ESMS and ESMS/MS. The CE study demonstrated excellent S/N in full-scan mass spectra acquired for peptides admitted onto the CE column in quantities > 10 fmol. The duty cycle advantage of the ion trap clearly benefits this application. The high efficiency of ion trap MS/MS can provide even greater sensitivity than that obtained with scanning beam-type mass spectrometers in on-line ESMS/MS applications. However, single-frequency collisional activation is of limited utility in on-line separation applications because of the tuning requirements and potential for frequency shifts due to ion–ion interactions. The development of non-mass-selective ion activation methods can overcome this problem. Alternatively, interface-induced fragmentation or fragmentation induced upon ion injection (*47*) can be used in on-line separations to obtain structural information. These are not MS/MS experiments and may be compromised in cases of co-eluting mixture components, but they are satisfactory when separations are adequate.

On-line separation coupled with ES and ion trap MS has not yet become a routine analytical tool. This is largely because an ion trap system designed for such work is not commercially available. However, the work already done with highly modified

versions of commercially available ion traps demonstrates that the ion trap will be a powerful tool in many organic and biological applications.

Inorganic MS. The inductively coupled plasma (ICP) operated with atmospheric pressure argon as the support gas is the most widely used source of ions for trace elemental analysis (*48*). Barinaga and Koppenaal have recently reported coupling an ICP mass spectrometer with a quadrupole ion trap (*49*). The instrument's geometry consists of an ICP ion source followed by a linear quadrupole mass filter mated to a quadrupole ion trap. The linear quadrupole can be operated as a mass filter, as a high-pass filter, or as a notch filter to provide some filtering before ion injection. The sophisticated mass-selective ion accumulation techniques recently applied in organic analysis applications were not available for this work.

Many of the considerations for coupling other forms of ionization for elemental analysis to the ion trap, such as glow discharge and laser ablation (*50*), also apply to the ICP. The challenges posed by ion–ion interactions are particularly important in ICP/ion trap MS, given the intense ion currents derived from the plasma gas and matrix. Nevertheless, this preliminary work noted solution concentration detection limits in the sub-part-per-billion range. This level of performance is possible because of the discrimination against many normally abundant matrix ions observed in beam-type ICPMS. For example, argon-related ions, such as Ar^+, Ar_2^+, ArO^+, and ArN^+, and the other major matrix ions, such as ClO^+, were virtually absent from the mass spectrum because of mechanisms for ion destruction, including dissociation and charge transfer reactions. Similar observations were also made in glow discharge/ion trap work.

The dramatically reduced abundance of matrix ions also facilitates the analysis of elements that are isobaric with the matrix ions. For example, mass spectra obtained with a beam-type ICPMS system and with the ion trap were compared by using solutions containing iron, arsenic, and vanadium (*49*). Background mass spectra obtained with the quadrupole mass filter showed intense signals for the matrix ions $^{35}ClO^+$, ArO^+, and $Ar^{35}Cl^+$, among others, which are isobaric with the major isotopes of vanadium, iron, and arsenic, respectively. The ion trap background mass spectrum, on the other hand, was essentially devoid of the matrix ions, allowing the spectrum of the analyte to be acquired free of interferences. The elimination of Ar^+ and ArH^+ also allowed for the analysis of calcium and potassium. These results, along with those obtained with rf glow discharge ionization, clearly show that the ion trap is potentially useful for the removal of both polyatomic interferences and argon ions and suggest that the ion trap might play a role in ICPMS.

Summary

The quadrupole ion trap, operated with a relatively high-pressure bath gas, occupies a unique place among mass analyzers. As an ion storage device, it shares many characteristics with the ICR instrument, but the use of a light bath gas and mass-selective instability for mass analysis contrasts with normal ICR operation. The bath gas facilitates the capture of ions injected into the oscillating quadrupole field and cools the ions to the center of the ion trap before mass-selective ejection. The bath gas also provides a conduit for heating ions. Mild collisional activation conditions can dissociate clusters, such as solvated analyte ions, formed by ES. Dissociation of covalently bound ions can be used to obtain structural information as part of a tandem MS experiment or to destroy polyatomic species in elemental analyses.

Characteristics of the ion trap make it attractive for organic and biological applications that use high-pressure ionization.

The moderate background pressure requirements of the ion trap using mass-selective instability make it a natural mass analyzer to be coupled with high-pressure ionization methods. The ion trap can provide a significant advantage in efficiency over beam-type mass spectrometers, which translates into lower detection limits. Lower detection limits can be realized from superior duty cycle and MS/MS efficiency, although transmission for single-stage MS is comparable. The greatest advantage in efficiency can be obtained with weak ion beams that require long ion accumulation times and therefore high duty cycles. This, in part, makes the ion trap particularly attractive for ES. Bright ion sources can provide similar advantages if major ion beam components can be ejected during ion accumulation to minimize the deleterious effects caused by ion–ion interactions.

The relatively high charge densities found in the ion trap complicate the achievement of high mass accuracy, high abundance sensitivity, and wide dynamic range. Methods to control charge densities, such as mass-selective ion accumulation, are currently being evaluated and show promise for enhancing ion trap performance in these areas.

The characteristics of the ion trap already make it particularly attractive for many organic and biological applications that use high-pressure ionization methods. The use of external ion sources, such as ES and chemical ionization, is expected to become widespread. The application of the ion trap as a mass analyzer in inorganic analyses is only now beginning to be evaluated. The results obtained from glow discharge and ICP studies have already demonstrated the capability for discriminating strongly against species that sometimes interfere in analyses performed with beam-type mass analyzers. Additional research will show what role the ion trap might play in inorganic MS analyses.

Research performed in our laboratory was sponsored by the U.S. Department of Energy Offices of Basic Energy Sciences and Safeguards and Securities and the National Institutes of Health under grant GM45372. The Oak Ridge National Laboratory is managed for the U.S. Department of Energy by Martin Marietta Energy Systems, Inc., under contract DE-AC05-84OR21400.

References

(1) Yinon, J. *Mass Spectrom. Rev.* **1982**, *1*, 257.
(2) McLuckey, S. A.; Glish, G. L.; Kelley, P. E. *Anal. Chem.* **1987**, *59*, 1670.
(3) Wise, M. B.; Thompson, C. V.; Buchanan, M. V.; Merriweather, R.; Guerin, M. R. *Spectroscopy* **1993**, *8*, 14.
(4) Dionne, B. C.; Roundbehler, D. P.; Achter, E. K.; Hobbs, J. R.; Fine, D. H. *J. Energ. Mater.* **1986**, *4*, 447.
(5) Harrison, A. G. *Chemical Ionization Mass Spectrometry*; CRC Press: Boca Raton, FL, 1992.
(6) Eckenrode, B. A.; Glish, G. L.; McLuckey, S. A. *Int. J. Mass Spectrom. Ion Processes* **1990**, *99*, 151.
(7) McLuckey, S. A.; Glish, G. L.; Asano, K. G.; Grant, B. C. *Anal. Chem.* **1988**, *60*, 2220.
(8) McLuckey, S. A.; Glish, G. L.; Grant, B. C. *Anal. Chem.* **1990**, *62*, 56.
(9) Chambers, D. M.; McLuckey, S. A.; Glish, G. L. *Anal. Chem.* **1993**, *65*, 778.
(10) McLuckey, S. A.; Glish, G. L.; Asano, K. G. *Anal. Chim. Acta* **1989**, *225*, 25.
(11) McLuckey, S. A.; Goeringer, D. E.; Glish, G. L. *J. Am. Soc. Mass Spectrom.* **1991**, *2*, 11.
(12) Julian, R. K., Jr.; Cox, K. A.; Cooks, R. G. *Anal. Chem.* **1993**, *65*, 1827.
(13) Goeringer, D. E.; Asano, K. G.; McLuckey, S. A.; Hoekman, D.; Stiller, S. W. *Anal. Chem.* **1994**, *66*, 313.
(14) Yates, N. A.; Yost, R. A. *Proceedings of the 39th ASMS Conference on Mass Spectrometry and Allied Topics*; Nashville, TN, 1991; p. 132.
(15) McLuckey, S. A.; Goeringer, D. E.; Glish, G. L. *Anal. Chem.* **1992**, *64*, 1455.
(16) Van Berkel, G. J.; Goeringer, D. E. *Anal. Chim. Acta* **1993**, *277*, 41.
(17) Wang, M.; Wells, G. *Proceedings of the 41st ASMS Conference on Mass Spectrometry and Allied Topics*; San Francisco, CA, 1993; p. 463.
(18) Pedder, R. E.; Yost, R. A.; Weber-Grabau, M. *Proceedings of the 37th ASMS Conference on Mass Spectrometry and Allied Topics*; Miami Beach, FL, 1989; p. 468
(19) Bier, M. E.; Louris, J. N.; Taylor, D. M.; Schwartz, J. C.; Uhrich, M. D. *Proceedings of the 41st ASMS Conference on Mass Spectrometry and Allied Topics*; San Francisco, CA, 1993; p. 456.
(20) King, F. L.; Harrison, W. W. *Mass Spectrom. Rev.* **1990**, *9*, 285.
(21) VG9000 Glow Discharge Mass Spectrometer; VG Isotopes: Cheshire, England, 1986.
(22) Barshick, C. M.; Eyler, J. R. *J. Am. Soc. Mass Spectrom.* **1992**, *3*, 122.
(23) King, F. L.; Harrison, W. W. *Int. J. Mass Spectrom. Ion Processes* **1989**, *89*, 171.
(24) Duckworth, D. C.; Marcus, R. K. *Appl. Spectrosc.* **1990**, *44*, 649.
(25) McLuckey, S. A.; Glish, G. L.; Duckworth, D. C.; Marcus, R. K. *Anal. Chem.* **1992**, *64*, 1606.
(26) Duckworth, D. C.; Barshick, C. M.; Smith, D. H.; McLuckey, S. A. *Anal. Chem.* **1994**, *66*, 92.
(27) Fenn, J. B.; Mann, M.; Meng, C. K.; Whitehouse, C. M. *Science* **1990**, *246*, 64.
(28) Smith R. D.; Loo, J. A.; Edmonds, C. G.; Barinaga, C. J.; Udseth, H. R. *Anal. Chem.* **1990**, *62*, 882.
(29) Fenn, J. B.; Mann, M.; Meng, C. K.; Wong, S. F.; Whitehouse, C. M. *Mass Spectrom. Rev.* **1990**, *9*, 37.
(30) Huang, E. C.; Wachs, T.; Conboy, J. J.; Henion, J. D. *Anal. Chem.* **1990**, *62*, 713 A.
(31) McLuckey, S. A.; Asano, K. G.; Glish, G. L.; Bartmess, J. E. *Int. J. Mass Spectrom. Ion Processes* **1991**, *109*, 171.
(32) McLuckey, S. A.; Van Berkel, G. J.; Glish, G. L.; Huang, E. C.; Henion, J. D. *Anal. Chem.* **1991**, *63*, 375.
(33) Ramsey, R. S.; McLuckey, S. A. *J. Am. Soc. Mass Spectrom.* **1944**, *5*, 324.
(34) Doktycz, M.; Habibi-Goudarzi, S.; McLuckey, S. A., submitted for publication in *Anal. Chem.*
(35) Ramsey, R. S.; Goeringer, D. E.; McLuckey, S. A. *Anal. Chem.* **1993**, *65*, 3521.
(36) Louris, J.; Schwartz, J.; Stafford, G.; Syka, J.; Taylor, D. *Proceedings of the 40th Conference on Mass Spectrometry and Allied Topics*; Washington, DC, 1992; p. 1003.
(37) Voyksner, R. D.; Lin, H-Y. *Proceedings of the 41st Conference on Mass Spectrometry and Allied Topics*; San Francisco, CA, 1993; p. 461.
(38) Van Berkel, G. J.; Glish, G. L.; McLuckey, S. A. *Anal. Chem.* **1990**, *62*, 1284.
(39) Schwartz, J. C.; Syka, J.E.P.; Jardine, I. *J. Am. Soc. Mass Spectrom.* **1991**, *2*, 198.
(40) Schwartz, J. C.; Jardine, I. *Rapid Commun. Mass Spectrom.* **1992**, *6*, 313.
(41) McLuckey, S. A.; Van Berkel, G. J.; Glish, G. L. *J. Am. Chem. Soc.* **1990**, *112*, 5668.
(42) McLuckey, S. A.; Glish, G. L.; Van Berkel, G. J. *Anal. Chem.* **1991**, *63*, 1971.
(43) McLuckey, S. A.; Van Berkel, G. J.; Glish, G. L.; Schwartz, J. C. In *Modern Mass Spectrometry: Practical Aspects of Ion Trap Mass Spectrometry*; March, R. E., Ed.; CRC Press: Boca Raton, FL, 1994; Vol. 2, Chapter 7.
(44) McLuckey, S. A.; Habibi-Goudarzi, S. *J. Am. Chem. Soc.* **1993**, *115*, 12085.
(45) Tang, L.; Kebarle, P. *Anal. Chem.* **1993**, *65*, 3654.
(46) Schwartz, J. C.; Jardine, I. *Proceedings of the 40th ASMS Conference on Mass Spectrometry and Allied Topics*; Washington, DC, 1992; p. 707.
(47) Van Berkel, G. J.; McLuckey, S. A.; Glish, G. L. *Anal. Chem.* **1991**, *63*, 1098.
(48) Koppenaal, D. W. *Anal. Chem.* **1992**, *64*, 320.
(49) Barinaga, C. J.; Koppenaal, D. W. *Rapid Commun. Mass Spectrom.* **1994**, *8*, 71.
(50) Gill, C. G.; Daigle, B.; Blades, M. W. *Spectrochim. Acta* **1991**, *46B*, 1227.

Scott A. McLuckey (left) received his B.S. degree from Westminster College (PA) in 1978 and his Ph.D. from Purdue University in 1982. He joined the research staff at Oak Ridge National Laboratory (ORNL) where he is currently head of the Analytical Spectroscopy Section in the Chemical and Analytical Sciences Division (Oak Ridge, TN 37831). His research focuses on fundamental and applied aspects of tandem MS, the chemistry of multiply-charged biomolecules, and quadrupole ion trap MS.

Gary J. Van Berkel (second from left) received his B.A. degree from Lawrence University (WI) in 1982 and his Ph.D. from Washington State University in 1987. He then joined ORNL and is now a member of the research staff in the Chemical and Analytical Sciences Division (Oak Ridge, TN 37831). His research interests include development of instrumentation and methods for MS; solution chemistry aspects of ESMS; and ESMS methods for biomedical, environmental, and geochemical applications.

Douglas E. Goeringer (second from right) received his B.S. degree from Southwestern Oklahoma State University in 1973 and his Ph.D. from Purdue University in 1979. He joined the research staff at ORNL in 1979 (Chemical and Analytical Sciences Division, Oak Ridge, TN 37831). His research interests include fundamentals and instrumentation for quadrupole ion trap MS and the application of lasers in analytical MS.

Gary L. Glish (right) is associate professor of chemistry at the University of North Carolina at Chapel Hill (C348 Kenan Laboratory, CB3290, University of North Carolina, Chapel Hill, NC 27599). He received his B.S. degree from Wabash College (IN) in 1976 and his Ph.D. from Purdue University in 1980. He was a member of the research staff at ORNL for 12 years before assuming his faculty position at the University of North Carolina. His research interests include developing new techniques and instrumentation for MS and applying them to the study of gas-phase ion chemistry.

New Elements.

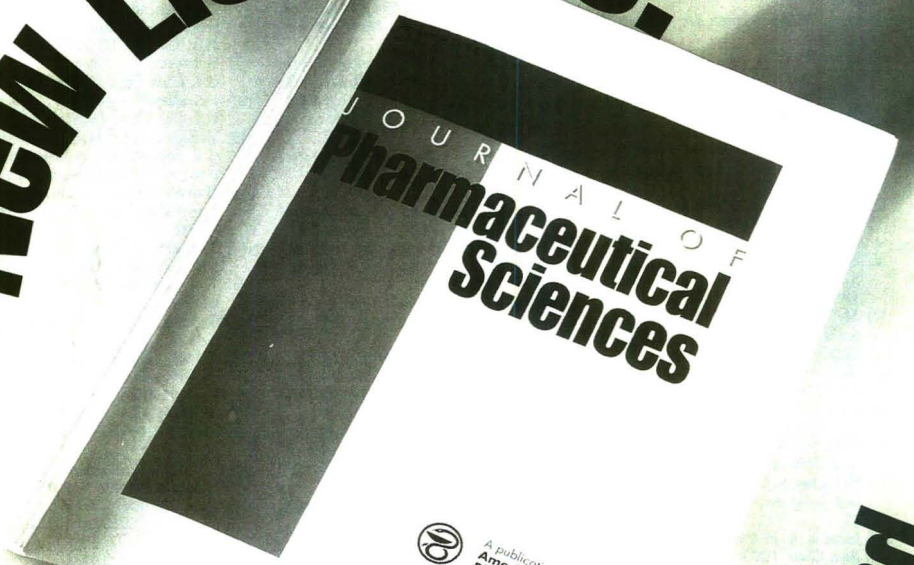

A Stronger Bond.

The American Chemical Society and The American Pharmaceutical Association Working Together As Co-Publishers

APhA and ACS are working to provide unprecedented exposure of pharmaceutical sciences to the broader scientific community. The *Journal of Pharmaceutical Sciences* is now expanding its coverage of:

- Chemical processing of pharmaceuticals
- Chemical stability of drugs
- Pharmacokinetics
- Biopharmaceutics
- Pro-drug developments
- Metabolic disposition of bioactive agents
- Dosage form design
- Protein-peptide chemistry
- Biotechnology and much more.

A New Editor, New Focus, Special Low Member Price!

New Editor Dr. William I. Higuchi has brought a new focus to the *Journal of Pharmaceutical Sciences*. It's been modified and expanded to serve chemists and scientists in pharmaceutical science research, technology and targeted drug delivery. Dr. Higuchi is Distinguished Professor and Chair, Department of Pharmaceutics and Pharmaceutical Chemistry at the University of Utah.

Best of all, the *Journal* is now available at a low member price–just $30 a year! Members: $30/year, Individual nonmembers: $85/year, Institutions: $278/year.

Call toll-free, 1-800-333-9511 and subscribe today! Outside the U.S. call 614-447-3776. Fax to 614-447-3671.

APhA Members order through APhA. To order directly, call 1-800-237-APhA or FAX to 202-783-2351.

Money-Back Guarantee: ACS offers a prompt, pro-rata refund policy covering all unmailed issues.

Editor

William I. Higuchi
Department of Pharmaceutics and Pharmaceutical Chemistry
University of Utah

Associate Editors

David J. W. Grant
University of Minnesota

Ho-Leung Fung
State University of New York at Buffalo

Bradley D. Anderson
University of Utah

C. Russell Middaugh
Merck and Co.

Editorial Advisory Board

Gregory E. Amidon, James E. Axelson, Meir Bialer, Ronald T. Borchardt, David W.A. Bourne, Robert L. Bronaugh, Stephen R. Byrn, John F. Carpenter, Jens T. Carstensen, Win Loung Chiou, Jeffrey L Cleland, James C. Cloyd, Kenneth A. Connors, Michael G. Cordingley, Daan J.A. Crommelin, William J. Curatolo, David J. Cutler, William E. Evans, David Fitzgerald, Jeffrey L. Fox, William Foye, Emilio Gelpi, Detlef Groger, Iris H. Hall, Manabu Hanano, James N. Herron, Nair Rodriguez-Hornedo, William J. Jusko, Stanley A. Kaplan, Gerald B. Kasting, Kristine Knutson, William J. Lambert, Robert S. Langer, Abraham M. Lenhoff, Andrew T. McPhail, Kamal K. Midha, Tsuneji Nagai, Michael S. Roberts, Malcom Rowland, Gautam Sanyal, Jiaxiang Shen, Miklos Simonyi, Valentino J. Stella, Raj G. Suryanarayanan, Felix Theeuwes, John A.Thomson, Daniel L. Weiner, Dominic J. Wells, Peter York, George Zografi

AMERICAN CHEMICAL SOCIETY
1155 Sixteenth Street, NW Washington, DC 20036

AMERICAN PHARMACEUTICAL ASSOCIATION
2215 Constitution Avenue, NW Washington, DC 20037

Animating the Basics

Introduction to HPLC
SAVANT Audiovisuals
P.O. Box 3670
Fullerton, CA 92634
800-472-8268; 714-870-7880;
714-526-7400 (fax)
$495

This program is the first in a series of five modules designed to teach basic LC. The program is written with a programming tool called ToolBook (Asymetrix Corp.), and the result is software that handles much like a textbook but has the added advantages of rapid indexing and animation. Computer requirements are consistent with today's equipment: a 286-based PC, 1 MB of RAM, 2.5 MB of disk space, a color VGA monitor, Windows 3.0, and a mouse. My experience is that ToolBook is rather slow on a 286 machine—I have used it on 386- and 486-based computers with no problems.

Once the program is loaded it runs from an icon, as in most Windows programs. After a couple of pages of introductory material, the user is presented with a table of contents listing the chapters (chromatography, eluents, columns, equipment, method development, final quiz, and an index of printable pages). The user can jump to any topic by clicking on the desired item with a mouse, or the material can be covered a page at a time, just like reading a book. Keywords that may need more explanation (e.g., capacity factor) are highlighted with a box, and clicking on the box brings up a dialog box with more explanatory material. Many of the pages have additional illustrative material that can be accessed by clicking on a labeled button.

One of the strongest points this program has to offer is its animation. The user can model changes in flow rate, particle size, and solvent strength as well as observe a change in a simple chromatogram. The equipment chapter makes especially good use of animation, demonstrating how pumps, injectors, and detectors work. The animation reinforces the written explanations and provides variety to help keep the reader's interest.

From a technical perspective, this program provides solid coverage of LC basics. The chromatography chapter explains how LC differs from other chromatography techniques and clearly defines retention, selectivity, plate number, and other chromatography fundamentals. The properties required for LC solvents and some of the reasons for choosing one solvent over another are covered in the eluents chapter. The section on columns covers column hardware and physical characteristics such as particle size. It goes on to illustrate each chromatographic mode with a diagrammatic model and sample chromatograms. The equipment unit explains the function of each module, and the animated illustrations make the functions clear. Method development is briefly explained. The principles needed to select the proper method and starting conditions and to refine the separation prior to validation are given.

The program makes good use of simple quizzes at several places. These simple multiple-choice questions reinforce the material covered and also act as a teaching tool, because correct answers are confirmed and a helpful explanation is given with each incorrect answer. The quiz material is duplicated in the manual.

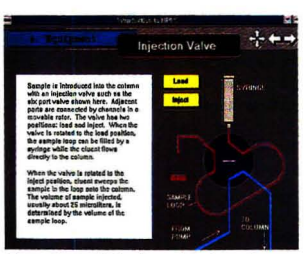

The animated injection valve shows how this component operates in both "load" and "inject" cycles.

This software would be very useful for people who are not proficient in chromatography or computers. I skimmed through the program in about an hour, covering every page but not reading every word of text. I expect that a beginning technician would benefit from studying the material for 3–4 hours in 30-min or 1-h blocks.

As with all software, the inevitable bugs and some design irritants occur. The installation procedure, although effective, is out of date. Installation requires manually making a directory, copying disks, and setting up a program item. Most Windows-based programs do all of this automatically when the user types "a: install" in the Run command of the File menu. Another problem is the requirement to manually change to 640 × 480 VGA resolution—the program works adequately at 800 × 600 VGA resolution, but it does not fill the screen. If the program is started in another video mode, the user is advised to switch to the 640 × 480 mode but, again, this should be done automatically. I thought the use of color was a bit overdone in this module, although I did not get the same impression with another module in the series that I had looked at earlier, so this may mean that I needed to become more accustomed to the presentation medium.

I only found two real bugs in the program. The preferred solvents table listed several solvent properties, but the TLV column did not contain any numbers with the color combination selected for my computer. A more severe problem was the inability to print any of the information at the end of the program. Several tries at printing with my HP LaserJet II resulted in hard hangs, which required rebooting my computer.

In summary, this program is well worth the purchase price as a technician training tool, especially for companies that have a

regular turnover of technical staff. It gives a basic introduction for the novice and a good review for experienced individuals who may be rusty. I wish a program this complete and clear had been available when I was a novice.

Reviewed by John W. Dolan, LC Resources, Amity, OR

Spectral searching

Spec-ID Plus
Nicolet Instrument
5225 Verona Rd.
P.O. Box 44451
Madison, WI 53744-4451
608-271-3333, 800-356-8088;
608-273-5046 (fax)
$1435 (U.S.); foreign prices vary

The Spec-ID Plus IR spectral identification package, a Windows-based application, allows an unknown spectrum to be identified by matching approximate parameters of user-selected bands to entries in the Aldrich library of condensed- or vapor-phase reference spectra stored on CD-ROM. Many of the reference spectra in the Aldrich condensed-phase library have been measured with samples prepared as Nujol (paraffinic mineral oil) mulls; those regions where Nujol absorbs in the reference spectra are indicated on the screen display in a different color and are ignored in the normal program operation.

The computer requirements are minimal: an Intel 286-based processor, Windows 3.0, at least 2 MB of RAM and 10 kB of free hard disk space, a mouse or other compatible pointing device and, of course, a CD-ROM drive. By using the mouse, the user defines rectangular regions to represent locations and approximate intensities of bands in the transmittance spectrum of the unknown. In the default operational mode, the ordinate axis of the spectrum is divided into three regions representing "strong," "medium," and "weak" absorption bands. The number of reference spectra that contain bands in the rectangular region with peak transmittance values within these arbitrarily defined limits is displayed. Each of these "matches" can be examined sequentially by scrolling through the reference spectral match list.

The manual suggests that the number of spectral regions be increased until the number of listed spectral matches is reduced to ~ 10. However, we found that between 20 and 200 spectral matches are usually needed for many authentic compounds to appear on the list, including those that contain unique functional groups such as S–H. Searches using three or four spectral regions to identify molecules such as tetrachloroethylene and cyclopentanol were not very successful. Tetrachloroethylene was never listed, and cyclopentanol was eventually found in a list of 27 compounds.

When personnel from Nicolet entered band parameters for the four strongest bands in the spectrum of cyclopentanol taken directly from the reference spectral library, they obtained a list of seven compounds, including cyclopentanol. However, we found that when the frequency limits for the four bands were changed by only 1–2 cm^{-1}, cyclopentanol disappeared from the list. Choice of band position is extremely important for correct spectral identification.

The biggest problem with the current version of the software is that transmittance spectra are compared instead of absorbance spectra; therefore, the relative band intensities depend on the concentration and pathlength of the analyte. Thus, unless the user's sample has been prepared to yield a transmittance spectrum that is very similar to that of the appropriate reference spectrum, there is a good chance that the authentic match will not be listed. By using a software option, the program can ignore all intensity information, but the number of matches increases by a factor of 3–10.

Of even more relevance is the fact that the transmittance values that are input to the program must match within 5% of the transmittance of corresponding bands in the reference spectrum unless the option to use no intensity information is selected. This deficiency means that the sample must be prepared so that the product of concentration and pathlength is within 5% of the values in the reference spectrum of that compound. Because one cannot look this up before preparing the sample (because the identity of the analyte is not known), the chances of having the authentic analyte listed as a possible match are quite slim. For example, we selected four bands that led to cyclopentanol being correctly listed in the possible matches. We converted the transmittance values of these bands to absorbance, divided by 2, and then converted back to transmittance. (This operation is equivalent to the concentration–pathlength product for the reference spectrum being halved.) When these data were entered into Spec-ID Plus, no compounds were listed as potential matches. In practice, therefore, the only way that the user can find the authentic compound listed is to use the option in which intensity information is ignored and to input the wavenumbers of at least seven or eight bands with relatively wide (~40 cm^{-1}) spectral windows for each one.

The biggest advantage of Spec-ID Plus is that it allows the user to purchase a digitized version of the Aldrich Libraries of IR spectra at a reasonable cost. It would be helpful if these reference spectra could be readily printed for side-by-side comparison with the spectrum of the unknown. The vast majority of IR spectrometers have the capability of outputting spectra in the JCAMP-DX format. Standard spectral searching with the Aldrich databases can be accomplished relatively easily compared with the manual input required for the Spec-ID Plus package.

Considering the limitations and cost, the software package does not appear to have a significant advantage over manual methods for comparing hard-bound copies of reference spectra. However, Nicolet plans to introduce a revised version of this software that will address many of these concerns.

Reviewed by Nathan C. Chaffin, Nelson W. Daniel, Jr., Ian R. Lewis, John Jegla, and Peter R. Griffiths, Department of Chemistry, University of Idaho

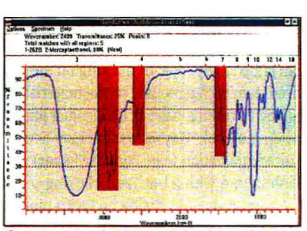

Spectra from the internal database that have bands corresponding to the defined ranges (shown as red boxes) can be retrieved.

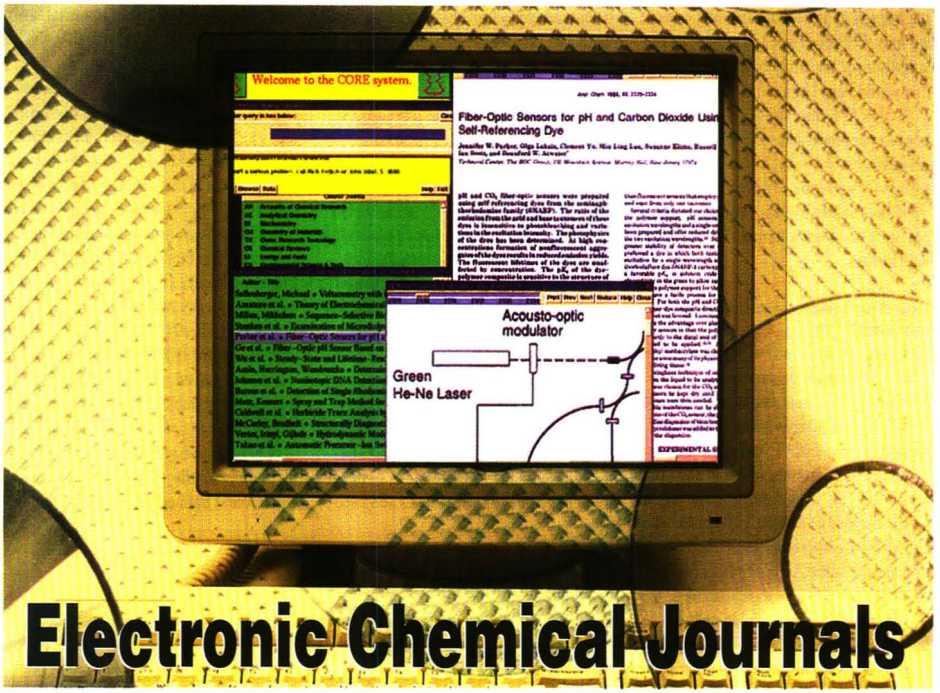

Electronic Chemical Journals

We can anticipate a future in which information appears on the desktop computer screen, arrives in greater quantity, and becomes more important to the chemist than it is today

Maintaining the quality of electronic information distribution is a particularly relevant issue for scientists today. Even if the widespread enthusiasm for the Internet threatens the traditional print-on-paper modality, we still need the reviewing, archiving, and other processes that make chemical literature reliable and useful. In this third in a series of articles addressing issues of management and information technology within the analytical laboratory, Michael E. Lesk of Bellcore describes a collaborative experiment undertaken by Cornell University, the American Chemical Society (ACS), Chemical Abstracts Service (CAS), Bellcore, and the Online Computer Library Center (OCLC) to make chemical journals available on the desktop. Both image and text formats for the journal articles are provided. Currently about 200,000 pages are available in this system, representing two years' worth of publications from 20 primary journals.

Raymond E. Dessy
Series Coordinator

The hype over the Internet and the information superhighway in the past year has also generated considerable interest in electronic transmission of chemical information and technical journals. Scientists have become excited about bulletin boards, Mosaic pages (a hypertext system including contributions from all over the world), and other instantaneous methods of exchanging information. At the same time, they have become aware of the potential dangers of unreviewed and unedited electronic distribution methods, which can overwhelm users and rapidly spread material not worth reading or writing.

If the quality of the papers available electronically can be maintained, bench chemists should find that they have quick access to reference data, new procedures, and discussions of techniques—advantages that might permit them to improve the quality of their work. If infor-

Michael E. Lesk
Bellcore

0003-2700/94/0366-747A/$04.50/0
© 1994 American Chemical Society

mation quality is not maintained, however, we may find reference to the literature substituting for analytical experiments that would have been more valuable.

In this A/C Interface we will examine how electronics can be used effectively to disseminate chemical information. We will also discuss the relative value of electronic journals to users as well as the importance of different formats for providing information.

Building electronic information systems

Electronic information can be provided in two basic formats: image and ASCII. Recent interest in electronic journals has focused on page images in research projects such as Tulip (*1*) for materials science, Stellar for astrophysics, and Red Sage for medicine (*2*). In addition, commercial products such as the IEEE journals sold by University Microfilms and the biomedical journals in the Adonis system involve CD-ROM distribution of page images.

ASCII text is also available online through STN International for ACS journals and for journals of several other publishers. Many full-text publications in disciplines outside science are also sold. The best known is probably the Lexis/Nexis system of Mead Data Central, which provides access to the text of legal decisions and newspapers, among other files. In general, these systems do not provide access to any illustrations included in the original publications.

Currently ACS, CAS, Bellcore, Cornell University, and OCLC are collaborating in an experimental project called CORE (Chemical Online Retrieval Experiment). We are interested in several questions: How can one build systems that display information for chemists in a way that is efficient to create and easy to implement in typical environments? How effective are the various forms of electronic information, compared with each other and with paper? How do chemists actually use online information?

In this project we have been developing a system for electronic access to ACS journals. We have access to the original text as stored from the primary journal creation and for the *Chemical Abstracts* indexing, as well as paper copies of the same journals. These paper copies have been scanned to provide image representations of the pages. We assemble the online file used in our experiments from all this material.

We have both ASCII and image formats for ACS journals. We analyze scanned pages, look for the illustrations, and extract them; readers can thus read either the full pages in the image format or the ASCII material with accompanying graphics. This can be accomplished using three different interfaces, each of which differs in its emphasis on image versus ASCII display.

One issue we confronted is which standard formats to use in representing the information. Although ACS uses a standard format in its primary journal file, this format was defined some years ago before the now-favored standard general markup language (SGML) was adopted. We therefore convert the material, attempting to put it into a format that will be as useful as possible for the future.

Figure 1 shows samples of the input and output for the beginning of one article. The input is a displayed form of the record structure used by ACS; the output is encoded in SGML. SGML, of course, is only a syntactic standard. It can be used only with an accompanying document type definition that specifies the codes and meanings used. In our case, we have adopted a variant of the American Association of Publishers (AAP) Electronic Manuscript Standard (EMS). Readers may well ask why we need a variant, and this is an instructive example of the problems that arise in this type of electronic experiment.

Chemical journals contain a great deal of information that AAP did not anticipate when it first defined its manuscript stan-

Excerpt of original records

```
segment 1165: this record 148 bytes total so far 301136
...
field 01256 mode 3 len 9 value AC900886X
field 01413 mode 3 len 117 value Observation of Elemental Anomalies at the Surface of
Palladium after Electrochemical Loading of Deuterium or Hydrogen
field 01562 mode 6 len 4 value 7
...
field 00089 mode 3 len 14 value Rolison, D. R.
field 00089 mode 3 len 14 value O'Grady, W. E.
field 00615 mode 9 len 16 GOK 0 4 0 1 1 40 0 1 2 40 0 3 3 44 0 3
field 01243 mode 3 len 25 value Debra R. Rolison##fnt#*##
field 01243 mode 3 len 18 value William E. O'Grady
field 01256 mode 3 len 9 value AC900886X
field 01562 mode 6 len 4 value 7
field 01806 mode 3 len 93 value Surface Chemistry Branch, Code 6170, Naval Research
Laboratory, Washington, D.C. 20375-5000
segment 1172: this record 1356 bytes total so far 303324
field 01413 mode 3 len 130 value In this work, the results from surface-sensitive analyses
are reported for Pd after electrolysis of light water and heavy water.
```

Processed version

```
<article><fm><pubfm><ti> Anal. Chem. </ti><cdn> ANCHAM </cdn> <issn> 00032700
</issn> <vol> 063 </vol> <iss> 017 </iss> <pp><spn> 1697 </spn><epn> 1702
</epn></pp> <acsn> AC063:1697Ro </acsn><jc> AC </jc>
<aid> AC900886X </aid> <pubname> American Chemical Society </pubname>
<copyrite> American Chemical Society, 91 </copyrite> <year> 1991 </year>
<prdates><acd> Accepted May 23, 1991. </acd>
<rcd> R <scp> ECEIVED </scp> for review November 9, 1990. </rcd></prdates> <msc> A
</msc></pubfm>
<tig><atl> Observation of Elemental Anomalies at the Surface of Palladium after
Electrochemical Loading of Deuterium or Hydrogen </atl></tig>
<aug><au><fnm> Debra </fnm><mnm> R. </mnm><snm> Rolison
<fnr>*</fnr></snm></au>
<au><fnm> William </fnm><mnm> E. </mnm><snm> O'Grady </snm></au>
<aff> Surface Chemistry Branch, Code 6170, Naval Research Laboratory, Washington,
D.C. 20375-5000 </aff></aug>
<abs><p><sen> In this work, the results from surface-sensitive analyses are reported for
Pd after electrolysis of light water and heavy water. </sen><sen> Pd foils used to
electrolyze D<d>2</d>O or H<d>2</d>O (with Li<d>2</d>SO<d>4</d> electrolyte and
using the electrode configuration of Pons and Fleischmann) show a near-surface
enrichment of Rh and Ag as detected by X-ray photoelectron spectroscopy (XPS). </sen>
```

Figure 1. Translation of ACS record structure to SGML format.

dard. For example, CAS has several different types of indexing elements, including not only the basic name and subject terms but also pre- and postmodifying elements. Creators of the AAP format simply did not anticipate this kind of complex indexing, which the typical book does not contain. Within the text of the article, there are many special characters (e.g., the different kinds of filled and half-filled boxes and triangles used to indicate different lines in a plot). Each of these needs some kind of code definition and/or instruction for printing.

We have defined special codes for many commonly used symbols, but to avoid the need for further definition of a great many characters that combine accent marks with ordinary letters, we have been forced to classify some of these special characters as overprints. There are also fields of information, such as tables of definitions of abbreviations, that were not anticipated. To avoid losing information, we have defined extra codes rather than reduce some of these special cases to simple printing instructions.

Perhaps the most frustrating need to extend the AAP EMS arose from the citation of references. In AAP style, the same names that are used in the main text are used to define titles, authors, or publishers' names within references. The expectation is that the software that interprets the article will rely on context (the enclosing <bb> tab for bibliographic reference) to interpret names such as <ati> for article title differently. Unfortunately, we encountered software that couldn't do that, so we were forced to produce a unique set of names for fields within a bibliographic citation. In the end what we have is information that is more portable than if we had never heard of SGML, but it cannot be fed directly into formatting programs that know only AAP EMS.

Once there is a standard format for storing the article text, we then have to ask whether we can display it on the users' terminals. In our case, we simplify this problem by requiring a fairly high-quality user workstation, expecting that what is now high quality will, in the future, become standard. We use X-windows as the display protocol, so the workstation must run X, and we need a bitmap area larger than 640 × 480 for the interfaces that display full-page images.

Nevertheless, we still run into considerable difficulty with the fonts available on the workstations. There is no standard set of fonts across X-terminals, the Macintosh X emulators, and the various workstations that run X. There is not even standardization across different software systems on the same workstation. Thus we find ourselves defining new fonts, and that requires learning yet another set of procedures because different window systems have different processes for font definition. In short, it is still difficult to take any user's modern workstation and install software that can display complex documents without some degree of systems administration support.

In our experiment, a complete file of images is also prepared. The images are scanned at 300 dpi, one bit per pixel, and stored in TIFF with Group IV compression. (TIFF is the Tag Image File Format, and Group IV is the new facsimile encoding standard; both are common image representation formats.) Despite slight differences among some image processing programs and minor difficulties with machines that have different byte orders within a word, TIFF conversion has generally gone smoothly, and it has been easy to code around machine differences.

Our major problem with the image file is its size; the typical page is about 100 KB after compression, so at the moment we require about 25 GB of storage. These images are stored on a write once, read multiply (WORM) "jukebox." This device is a multiplatter optical disk system that selects platters like its 1950s namesake. To accelerate retrieval of the images, we also maintain a file of lower resolution images,

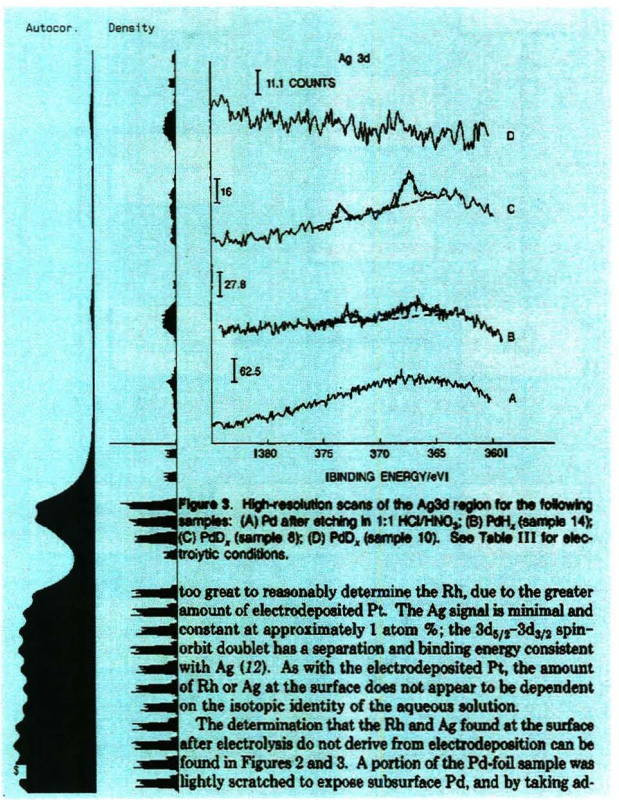

Figure 3. High-resolution scans of the Ag3d region for the following samples: (A) Pd after etching in 1:1 HCl/HNO_3; (B) PdH_x (sample 14); (C) PdD_x (sample 8); (D) PdD_x (sample 10). See Table III for electrolytic conditions.

too great to reasonably determine the Rh, due to the greater amount of electrodeposited Pt. The Ag signal is minimal and constant at approximately 1 atom %; the $3d_{5/2}$–$3d_{3/2}$ spin–orbit doublet has a separation and binding energy consistent with Ag (*12*). As with the electrodeposited Pt, the amount of Rh or Ag at the surface does not appear to be dependent on the isotopic identity of the aqueous solution.

The determination that the Rh and Ag found at the surface after electrolysis do not derive from electrodeposition can be found in Figures 2 and 3. A portion of the Pd-foil sample was lightly scratched to expose subsurface Pd, and by taking ad-

Figure 2. Sample column showing detection of figure.

many of which we store on a magnetic Winchester disk. These images are stored at 100 dpi, with 2 bits per pixel, so that some anti-aliasing can be done. This step removes some of the jagged edges inherent in binary images, which significantly improves readability for users with color or gray-scale displays.

The next important step in preparing the file is to provide the graphic illustrations to go with the ASCII version of the text. There are four kinds of illustrative material: figures, tables, equations, and everything else, which we call schemes. The tables and the equations are included in the tapes available from the primary journal creation. However, to avoid the problems described earlier in setting complex material and fonts, we have resorted to two expedients.

We format the tables as the material is processed, then send it to the user as monospaced material, in which all characters are of equal width. This avoids the need to know the width tables of the unspecified fonts on the user's machine. For equations, we also format the material as it is converted, this time going all the way to bitmaps. The bitmaps are displayed as if they were any other images.

Unfortunately, the figures and schemes are not on the ACS tapes and must be obtained from the scanned page images. This involves segmenting the pages, so that we know which parts of each page are graphical. Figure 2 shows a sample column, and to the left of it are two plots. The function shown immediately to the left of the column is the bit density per horizontal scan line, which can be thought of as an ordinary plot rotated 90°.

This column was produced, in essence, simply by removing all the white bits from each line and leaving as many black bits as were present. Note the regular sequence of peaks corresponding to the text lines and the irregularities where there is a graphic. Each line peak is doubled, as a result of the many letters such as o and d that have holes. Text is detected by looking for regularities in the bit density function; the leftmost column shows an autocorrelation of the density function at an offset of the line spacing (which is found by looking for the peak of the autocorrelation function). This function separates text from graphics.

When we encounter a graphic, we must identify it by using the following heuristic rules. Tables contain at least three full-width horizontal lines. Equations are wide but short and combine a centered main text with an optional equation number at the right margin. Figures contain the word "Figure" at the beginning of the caption, which is simply matched as a bitmap in the appropriate font for each journal. Whatever graphics are left after these rules have been applied are classified as schemes.

When a page is classified, the extracted graphics are shrunk to 150 dpi for display convenience and matched up with the article (so that clicking on the ref-

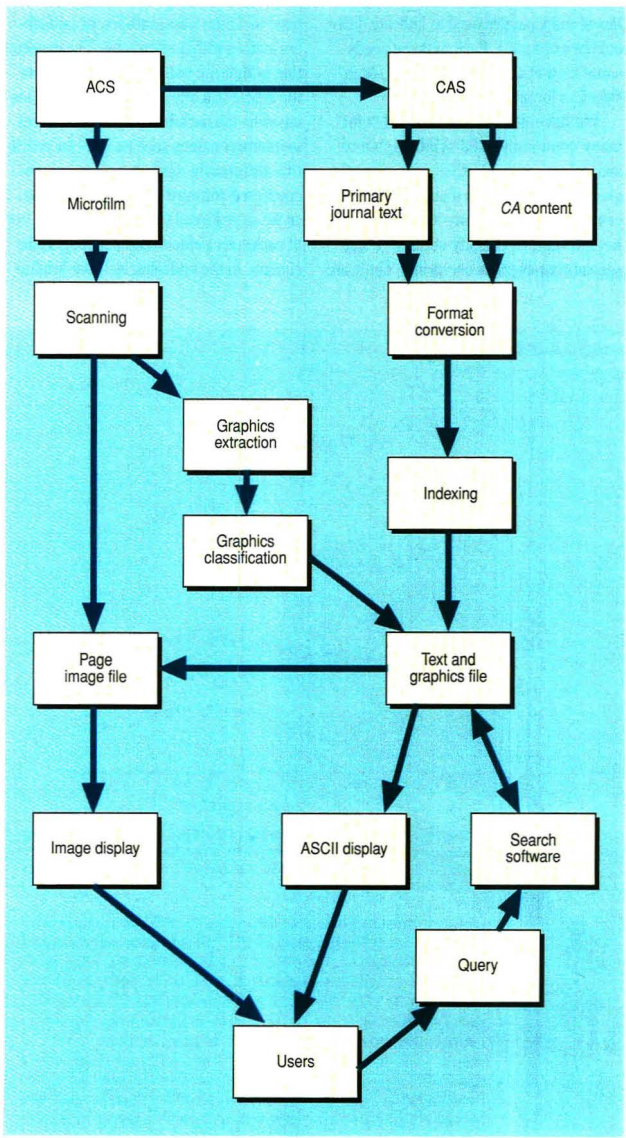

Figure 3. Data flow in the CORE project.

erence to Figure *N* will produce the correct image). Unfortunately, this matching process now depends on counting the figures through the article, and thus even a small error rate in basic figure detection is likely to throw off a large number of figure correspondences, even if most of the actual figures are right. On average, each journal page contains a figure or a scheme that takes about 20–25% of the page.

The overall processing flow is shown in Figure 3. At the end, there are two complete files, one in ASCII and one in image format. All searching is done on the ASCII file; the user can then display results from either file.

Electronic interfaces

We have done experiments comparing the ability of chemists to do simple tasks using the paper journals and both electronic formats. In these experiments, the two electronic formats used were "Pixlook" (image display) and "SuperBook" (text display).

Pixlook is a simple image system that uses the ASCII file to search and to provide tables of contents. It has two modes: browsing and searching. In the browsing interface, the user selects a journal and a specific issue and gets a list of titles in that issue. The full-page bitmap for any page then can be called up by clicking on the specific article title. The image appears first in the 100 dpi resolution so that a full page almost fits on a Sun-type screen. Selecting an "enlarge" button provides the 300 dpi bitmap. When we had Sparc-1 machines, we pre-fetched and decoded the high-resolution bitmap while the user was considering the low-resolution bitmap. Now that the high-resolution image may be on a jukebox, this concurrent step is not necessary. The full-resolution images are easy to read but can show only a small part of any page.

Figure 4 shows the process of browsing in the image system. In this case, an issue from *Analytical Chemistry* has been selected, and the user has looked through the table of contents and chosen the article starting on p. 2329. Another window has been opened to show an enlarged part of the full page. Note that the enlarged image is clear but small; the full-page image is barely readable. The alternative use of Pixlook is to perform a search and then use the list of retrieved articles in the same way that one uses the table of contents. This use is illustrated in Figure 5, in which the search was done on the name "Corey." An article beginning on p. 442 of *The Journal of Organic Chemistry* has been selected for display.

In this interface, users can perform four operations. First, they can move from page to page within one article, using the scrollbar shown at the top of each full-page display. This scrollbar also tells the user how long each article is. Second, they can move from article to article, either within a table of contents or within a list of hits. Third, they can search on a word or group of words and find a list of articles. There is no way to locate the words found this way within an article, although the articles are usually short enough that this is not too much of a problem. Finally, they can view any number of articles at once, within the limits of the screen size.

The searching system for this interface is provided by the Newton software written by OCLC, and the standard Boolean primitives (and, or, not) are available. An important property of this interface is that the figures dominate the user's first glimpse of the article. The page appears first at the 100 dpi resolution, in which the text may be hard to read, but the figures are usually clear.

The text-oriented alternative, shown in Figure 6, is SuperBook. The screen is split into a table of contents area, organized by subject and shown on the left, and the current page, shown on the right. Footnotes, tables, and graphics appear as icons in the right margin of the text page. A search window is tucked away at the bottom left.

In this example, the user searched for "hollow cathode" and found that term highlighted in the text. In the right margin of the text a graphic is indicated by the thumbnail picture. By clicking on the small picture, the user has added the enlarged picture to the screen along with scrollbars because it does not fit.

The table of contents is hierarchically divided, and the user can expand or contract any part of it by clicking on that line. The number of hits on any search is shown next to the line in question, thus giving the user a clear picture of where in the text relevant material appears. Clicking on a line in the table of contents brings the text page to that point. The text page can also be moved by clicking on the options for the next or previous hit on the search term(s).

The text is more clearly shown on the screen in SuperBook than in Pixlook, and

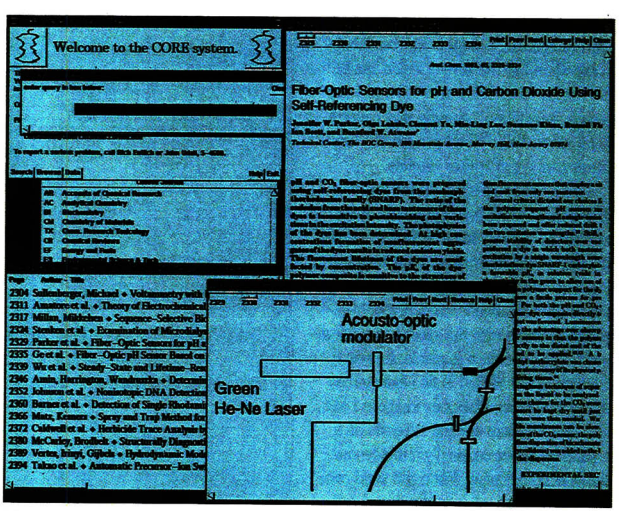

Figure 4. Browsing the Pixlook image system.

motion across article boundaries is easier because the complete text is always shown in the table of contents. As shown in the example, highlighting is used to locate the exact appearance of particular words. However, users do not find the display familiar because it emphasizes the text, and people often browse through articles by looking first at the graphics.

We also have another interface called Scepter, written by OCLC, which combines access to text, figures, and page images. Scepter, which is being used at Cornell, was not used in the experiments described below. It provides access to all text, graphics, and page images, and the user is given menus of everything within an article. An example of Scepter is shown in Figure 7. Note the use of thumbnails to list the figures in the article—all can be seen at once in this example, unlike SuperBook where the figure icons are distributed through the text. Similarly, the reader may call up the list of references, tables, or any other part of an article.

The ease of use of all the electronic systems could still be improved. Even those with 1000 × 1000 screens cannot see an entire page at an easily readable resolution. Our strategy of using 2 bits of gray scale helps considerably, and with this technique the entire printed part of the page fits on a large screen and can be read with some effort. However, we felt it necessary to provide the ability to zoom in and discovered that this feature is regularly used. When users zoom in, the readability is excellent but the screen is too small; they must constantly move around the screen. In addition, zooming may cause a delay of perhaps 15 s because the large images are on an optical jukebox.

As mentioned before, we are pushing the limits of X-windows compatibility as well as the security features in the various operating systems and window managers. For many new users some workstation reconfiguration is needed, if only to install the fonts with the special characters needed for chemical journals. Network bandwidth (10 MB/s) is also inadequate. An uncompressed full-page image is 1 MB, and this will take several seconds on a typical Ethernet, especially if the destination machine is slow. We could send compressed images, but that requires installing additional software on the user workstations, some of which don't have much CPU power and many of which require unusual programming environments.

Comparisons of electronic journal interfaces and paper

Our experiments were run by Dennis Egan with 36 Cornell students as subjects. The students ranged from undergraduates to graduate students and were divided into three groups. One-third of them used the journals on paper; one-third used the images, and one-third used SuperBook (the electronic approaches used earlier versions of the systems shown in the figures). The students had five types of tasks to perform. These ranged from relatively easy (find a particular fact in a given article) to quite hard (find a synthetic pathway whose starting and ending compounds are analogous to but not identical to those in a pathway given somewhere in the collection of articles). In these experiments we used a 1000-article sample taken from issues 1–12 of the *Journal of the American Chemical Society* published in 1988.

The tasks were designed by two chemistry professors in an effort to simulate what chemists do in a library. The easiest task was the "citation" search, a simple request for a fact in an article whose complete citation was given. Such a query might be: "In the article 'Total Synthesis of Ginkgolide B' by E. J. Corey, M. Kang, M. C. Desai, A. R. Ghosh, and I. N. Houpis (*J. Am. Chem. Soc.* **1988**, *110*, 649–51), what is reported as a medically important property of ginkgolide?"

A similar task was the "search," which had an equally specific question but left the student the job of finding the right article. An example might be: "What is the calculated P–O bond distance in hydroxyphosphine?" One of the most interesting tasks was named "browsing." Here the students were presented with a list of eight topics (e.g., "bridgehead halides") and one issue of the journal and were asked to check which of the eight topics were mentioned in this one issue. We also made an effort to evaluate serendipity in this task. After the students had finished, the journal was removed (in whatever format) and a new list of eight additional topics was presented. Again, students had to report on what they thought had been mentioned, on the basis of whatever they remembered about the issue.

The remaining tasks were the "essay," a request to write a couple of paragraphs about a topic (e.g., "phospholipids"), and the "analogous transformation," which required the students to suggest how you might convert one organic compound into another. Both compounds were shown

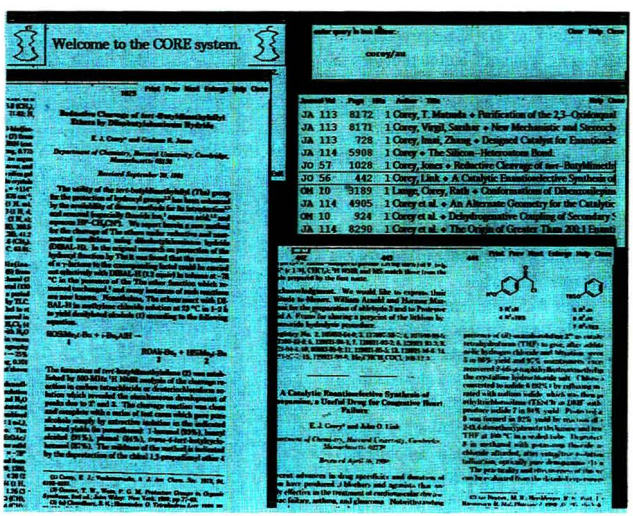

Figure 5. Result of a search using Pixlook.

as structural diagrams, and neither appeared in exactly that form in the collection of articles. To successfully complete this task, the students had to find a similar transformation and apply it to the given example.

We found that either electronic system was much better than paper whenever searching was important. (For more detail on the results, see Reference 3.) Although the students with the paper journals had access to *Chemical Abstracts*, they were not expert in its use and they could do electronic searches more effectively. For example, in the search task subjects were told they could give up after 15 min. More than half the students with the paper journals gave up; three-quarters of the people with electronic searching found the right answer.

By contrast, the electronic journals showed no great advantage for tasks that only involved reading. The citation task, for example, specifies which article to read. All the experimental groups could perform this task correctly about three-quarters of the time, and all took about 5 min to read the article and report the answer. Various problems (e.g., inadequate emphasis on graphics in the SuperBook system or confusion about which article was being read) caused electronic reading on occasion to be less satisfactory than paper. For example, the organic compound transformation task depends heavily on seeing the right diagram in the journals. SuperBook, which keys to the text display and requires a click to see the image, was less effective for this task.

The browsing task resulted in roughly equal scores for all the groups, no matter which format they had. However, the students with paper made different kinds of errors than the students with electronic journals. Those with paper journals tended to miss many relevant documents, whereas those with electronic journals claimed to have found relevant documents that in fact had not been accepted as relevant by the professors who made the lists. That is, the students with paper found far fewer documents they considered relevant than the students with electronics. Part of this may result from general difficulties in formulating searches, but part is the difficulty of searching on paper. Although the students had access to *Chemical Abstracts*, as mentioned before, they were not familiar with the techniques needed to use this resource with maximal effectiveness. For example, they apparently did not know how to use the Trivial Name Index, so they could not look up substance names.

Despite all these problems, we conclude that the typical user can actually accomplish a mix of tasks with electronic journals more successfully than with paper journals. The first complaint of the users is that we don't have enough journals—not that what we have is useless. The image display method is a useful bridge between the traditional format and new electronic systems, provided the user workstations are adequate. Image systems are also relatively free of software that must be specialized to deal with particular journals or subject areas. For example, in our work we have needed a special font to handle the symbols used in ACS journals, and we have considered whether "He," "In," "As," and "I" should be on the stoplist (the list of words not processed by the retrieval system) because they are the chemical symbols for helium, indium, arsenic, and iodine. Image systems are thus easier to code and provide to users, despite the fact that they are more demanding of hardware.

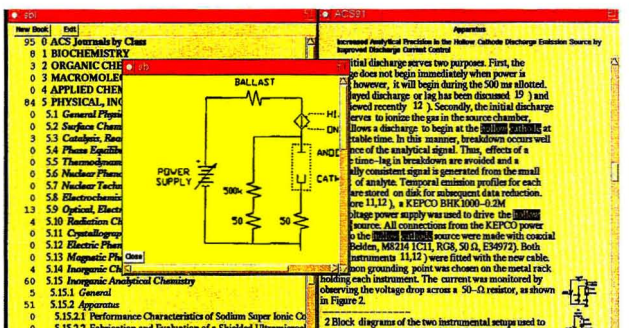

Figure 6. SuperBook screen with table of contents and text.

Conclusions and predictions

We now have some experience with the users at Cornell, although it is somewhat limited because the file they have seen thus far usually lacks the most recent journals and anything before 1991. What we find is that these users are very visually oriented. Given a choice, they would look first at the illustrations in an article, even before the title. Reading the text is the very last thing the users do; it comes after the figures, the authors, the title and abstract, the tables, and even the references. Browsing is more likely to be done than searching. Many of the readers are not looking for anything in particular; they are just looking to see what is there.

Note that while browsing in paper journals, looking at the figures also dominates peoples' behavior. They flip through issues, looking at the graphics and stopping when they see something interesting. Like many other kinds of science and engineering, chemistry is often a visual subject (*4*). Publishers of journals know this and attempt to cater to it in their paper publications. Color is being used increasingly, for example, to make figures more intelligible. In the same way, the faster spread of Mosaic relative to that of the Wide Area Information System (WAIS) is another testimony to the attractiveness of graphics and illustrations. WAIS offers relevant feedback but normally provides only an ASCII display; Mo-

saic pages, formatted with hypertext links, normally contain some pictures. Some museums, for example, provide pages that have a description of their contents as well as illustrations of some exhibits.

Electronics will help here. The incremental cost of color illustrations or even sound recordings is much lower in an electronic context than with paper. Already Mosaic pages contain pictures and sounds in a great many contexts, and we can expect this kind of interface to spread. The limitations of paper journals will be overcome. For example, we can anticipate journal articles that contain data visualization, such as synthesized animations of molecular structure, and even the ability for the user to manipulate such images (e.g., rotating a 3D molecular picture in the article). Such software is already widely available outside of journals, and published articles could easily reference it. Users should thus find the new electronic journals more attractive than today's paper publications.

Another important item for readers is quality control. Scientists rely heavily on the names of the authors, even in peer-reviewed journals. In a file that was not reviewed, they would probably rely entirely on the work of people they already knew. This would not help enlarge access to chemical information and would reduce exposure for new researchers below the attention their work might deserve.

So what of the future? No one doubts that electronic information will continue to supplement and replace primary journals on paper, just as it has begun to replace secondary services on paper. But what kinds of electronic services will these be? Let me briefly touch on two possible trends.

If journals become electronic, for example, their size could increase easily. There would be little difficulty for a prestigious journal to become twice or four times as large. This might push marginal journals out of existence, as their papers went to better known publications, or it might just cause a great deal more junk to appear. Suppose the larger and better known journals take over from the smaller journals. Will this frustrate people—for example, those in new interdisciplinary areas—who are having trouble finding places to publish? Or will smaller journals thrive in the electronic world because, with procedures somewhere between those of a traditional journal and those of a bulletin board, they might have lower costs? My guess is that we will find the small journals retreating into such an intermediate state, becoming much like some informal conference proceedings currently published.

Although journals may get larger, the articles in them may get smaller. Computers incur little overhead distributing small items and, provided the journals can handle the reviewing, authors may move toward publishing many small snippets rather than saving up their data for a large article. Traditionally, the desire to increase the number of one's publications has been cited as the reason to produce smaller articles. On the other hand, it is easy with computers to quickly link together several publications on a topic so that the readers can assemble for themselves the equivalent longer article that might have been published in the past.

The chemical laboratory will change to include more facilities for accessing the literature. This will mean, in many cases, upgrading the networks in the laboratories and increasing the amount of computer support provided to the chemists. This will benefit not only those who are searching the literature but also those who will access databases of chemical properties and programs that suggest syntheses or analyze spectra. The networks within the laboratory as well as the network connections from the lab are probably going to be upgraded. Currently a typical local net, whether Appletalk, token ring, or Ethernet, runs at 10 Mb/s (megabits/s) or lower, and connections out of many laboratories may be dialed up only at 9.6 Kb/s or 14.4 Kb/s. There will be an increasing demand for 100 Mb/s either on optical fiber or high-quality twisted pair (called FDDI and CDDI, respectively) within the lab and external connections ranging from ISDN (Integrated Services Digital Network) at 56 Kb/s to the Internet at 1.5 Mb/s.

Considerably higher speeds are practical but currently expensive. The National Science Foundation is upgrading parts of the national research network backbone to 155 Mb/s ATM (asynchronous transmission mode). However, given that most bench workstations are not supercomputers, higher speeds are likely to be a few years off. Perhaps many chemists will find it more important to upgrade the display quality and speed of their local workstations than to try to match the state of the art in network connectivity.

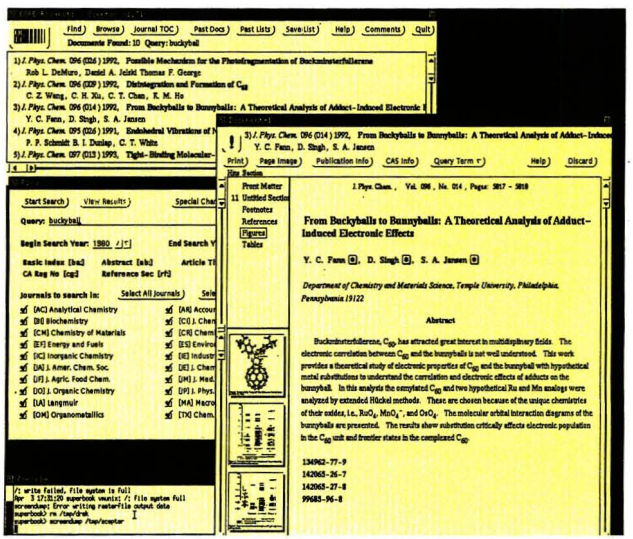

Figure 7. Scepter screen.

Laboratory management must consider the tradeoffs between connectivity and local resources, between sharing programs/databases and buying multiple copies and, in general, between computing and traditional instrumentation. With time, more instruments will be connected to general-purpose machines that are also useful for literature searches, but that again will make them more complex and increase the demand for computer support to the laboratory. Laboratory staff also will have to decide whether to attempt to standardize machines, giving up some local optimization in the interest of lower support costs.

Laboratory management must consider the tradeoffs between connectivity and local resources and between computing and traditional instrumentation.

What will the chemist get for all this effort and money spent on computer support used for searching the literature? At this point, it is only possible to speculate. Presumably, chemists will be able to pick out appropriate techniques more rapidly, work more efficiently, and match their problems to solutions more perfectly. The economic models used may affect this; we do not yet know whether publishers will charge by the byte, the minute, the page, the month, or the chemist. From the standpoint of using the literature effectively, chemists hope that publishers will use a charging system that encourages browsing and reading, not something that pushes only toward single searches.

Printing journal articles to read and study elsewhere will be possible, which may encourage the most effective use of existing material. One suspects that as integrated systems are developed, chemists will move toward accessing databases and analytical programs as well as general literature searching.

Finally, electronic publication will make searching in the library much easier. Does this mean that library work will increase while the fraction of time chemists devote to bench research declines? For example, the rise of computers in architecture has meant that simulation has replaced model building. If chemists start to rely too heavily on the literature and too little on actual bench measurement, there is a danger that people will believe everything they read and believe too much. In this scenario, the role of librarians will increase, chemists will spend more time in the library, and they may lose some of their bench skills. Is this any more serious than the replacement of many wet chemical analytical procedures with MS and other spectroscopic and chromatographic methods? I expect that we will reach a balance; I hope that we reach it fast enough to avoid a major disaster in the process and that innovation does not suffer as people find answers in the literature rather than thinking of new things themselves.

We can anticipate a future in which information arrives on the screen, arrives in greater quantity, and becomes more important to the chemist than it is today.

References

(1) McKnight, C. *ASLIB Proc.* **1993**, *45*, 7–10.
(2) Hoffman, M. M. et al. *J. Am. Soc. Inf. Sci.* **1993**, *44*, 44 and 452.
(3) Egan, D. E. et al. *Proceedings of Hypertext '91*; Association for Computing Machinery: New York, 1991.
(4) Ferguson, E. *Engineering and the Mind's Eye*; MIT Press: Cambridge, MA, 1992.

After receiving a Ph.D. in chemical physics, Michael E. Lesk joined the computer science research group at Bell Laboratories. Since 1984 he has managed the computer science research group at Bellcore (Rm 2A-385, 445 South St., Morristown, NJ 07960-1910; e-mail: lesk@bellcore.com). He is best known for work in electronic libraries and for writing Unix system utilities, including those for table printing (tbl), lexical analyzers (lex), and intersystem mail (uucp). His other interests include document production and retrieval software, computer networks, computer languages, and human–computer interfaces.

Helping Your Child Learn Science

Here's a practical guide for stimulating a child's interest in science. Presenting safe and simple activities suitable for children from preschool through the early elementary grades, *Helping Your Child Learn Science* suggests activities with bubbles, bugs, plants, crystals, and television. Most of the activities cost little or nothing and require no special equipment.

This handy volume explores opportunities for learning science in such places as zoos, museums, planetariums, aquariums, and farms. It presents definitions and descriptions of science and provides suggestions for helping children understand and learn scientific ideas.

Appendices offer practical tips encouraging schools to develop good science programs, descriptions of nine scientific concepts, and a list of recommended science books and magazines. Originally available from the U. S. Department of Education.

Nancy Paulu and **Margery Martin**
76 pages (1993) Paperbound
ISBN 0-8412-2626-1
$11.95

ORDER FROM
American Chemical Society
Distribution Office Dept 65
1155 Sixteenth Street, NW
Washington, DC 20036
Or CALL TOLL FREE
800-227-5558
(In Washington, DC, 872-4363) and use your credit card!

Conferences

36th Rocky Mountain Conference on Analytical Chemistry
July 31–Aug. 5. Denver, CO
Contact: Patricia Sulik, Rocky Mountain Instrumental Laboratories, 456 S. Link Lane, Ft. Collins, CO 80524 (phone/fax 303-530-1169)

2nd Changchun International Symposium on Analytical Chemistry
Aug. 2–6. Changchun, P.R. China
Contact: Qinhan Jin, Dept. of Chemistry, Jilin University, Changchun 130023, P.R. China (86-431-822331, ext. 2433; fax 86-431-823907)

108th AOAC International Annual Meeting and Exposition
Sept. 12–15. Portland, OR
Contact: Margaret Ridgell, AOAC International, 2200 Wilson Blvd., Suite 400, Arlington, VA 22201-3301 (703-522-3032; fax 703-522-5458)

21st Conference of the Federation of Analytical Chemistry and Spectroscopy Societies
Oct. 2–7. St. Louis, MO
Contact: FACSS, 198 Thomas Johnson Dr., Suite S-2, Frederick, MD 21702-4317 (301-846-4797; fax 301-694-6860)

Biosensors and Biological Techniques in Environmental Analysis
Sept. 12–14. Paris, France
Contact: M-C. Hennion, ESPCI, 10 rue Vauquelin, 75005 Paris, France

5th International Symposium on Pharmaceutical and Biomedical Analysis
Sept. 21–24. Stockholm, Sweden
Contact: Swedish Academy of Pharmaceutical Sciences, P.O. Box 1136, S-111 81 Stockholm, Sweden (46-8-245085; fax 46-8-205511)

5th International Symposium on Advances in Electrochemical Science and Technology
Nov. 24–26. Madras, India
Contact: The Secretary, Society for Advancement of Electrochemical Science and Technology, Karaikudi 623 006, India (91 4565 2368)

4th International Conference on Plasma Source MS
Sept. 11–16. Durham, U.K.
Contact: Grenville Holland, Department of Geological Sciences, Science Laboratories, South Rd., Durham City DH1 3LE, U.K. or Mark Nicholls, Finnigan MAT, Paradise, Hemel Hempstead, Hertfordshire HP2 4TG, U.K. (44-442-233555; fax 44-442-233666)

3rd International Symposium on MS
Sept. 13–18. San Francisco, CA
Contact: Marilyn F. Schwartz, University of California, San Francisco, Box 0446, San Francisco, CA 94143-0446 (415-476-2582; fax 415-476-0688)

11th Montreux Symposium on LC/MS
Nov. 9–11. Montreux, Switzerland
Contact: M. Fre–Häusler, Postfach 46, CH-4123 Allschwil 2, Switzerland (41-61-4812789; fax 41-61-4820805)

16th International Symposium on Capillary Chromatography
Sept. 16–20. Riva del Garde, Italy
Contact: P. Sandra, I.O.P.M.S., Kennedypark 20, B-8500 Kortrijk, Belgium (32-56-204960; fax 32-56-204859)

IICS '94 International Chromatography Symposium
Sept. 19–22. Turin, Italy
Contact: Century International Inc., P.O. Box 493, 25 Lee Rd., Medfield, MA 02052-0493 (508-359-8777; fax 508-359-8778)

5th International Symposium on Chiral Discrimination
Sept. 25–28. Stockholm, Sweden
Contact: Swedish Academy of Pharmaceutical Sciences, P.O. Box 1136, S-111 81 Stockholm, Sweden (46-8-245085; fax 46-8-205511)

7th International Diffuse Reflectance Conference
Aug. 14–19. Chambersburg, PA
Contact: Phil Williams, Grain Research Laboratory, 1404-303 Main St., Winnipeg, Manitoba, Canada R3C 3G8 (204-983-3344; fax 204-983-0724)

Colloquium Spectroscopicum Internationale XXIX
Aug. 27–Sept. 1. Leipzig, Germany
Contact: Gesellschaft Deutscher Chemiker, Abt. Tagungen, P.O. Box 90 04 40, D-60444 Frankfurt/Main, Germany (49-69-7917-358 or -360); fax 49-69-7917-475)

Short Courses and Workshops

Mass Spectrometry: Principles and Practice
July 25–29. East Lansing, MI
Contact: ACS, Dept. of Continuing Education, 1155 16th St., N.W. Washington, DC 20036 (800-227-5558; 202-872-4508; fax 202-872-6336)

Evaluation of Measurement Uncertainty in Chemical Analysis
Sept. 5–6. Graz, Austria
Contact: Wolfhard Wegscheider, Technische Universitat Graz, Technikerstrasse 4, A-8010 Graz, Austria (43-316-873-8303; fax 43-316-810926)

FT-IR PAS
Steps Up to Depth Profiling

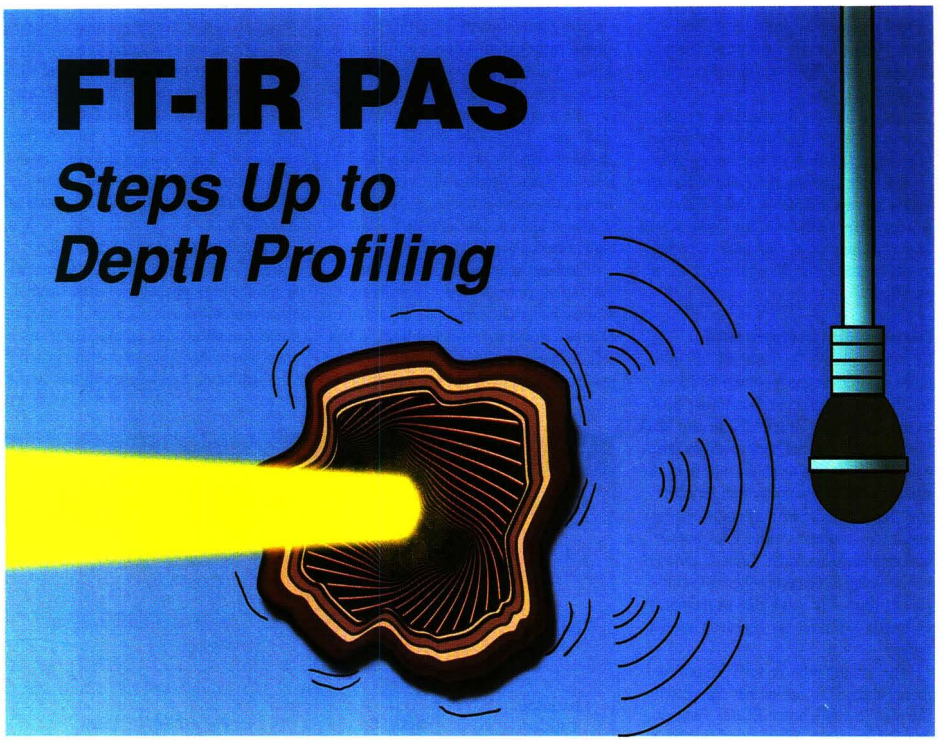

Photoacoustic spectroscopy has become an effective method for nondestructive near-surface analysis of irregular solids

What you can't see, or see through, you can sometimes hear. That's the idea behind photoacoustic spectroscopy (PAS), one of several techniques for acquiring optical spectra while getting around problems such as opacity or sample insolubility. It can be used in any wavelength range, but its most prevalent use is in the IR region of the spectrum, particularly with Fourier transform spectrometers. Although PAS isn't a widely used spectral technique, it holds some advantages over diffuse reflectance (DRIFTS) and attenuated total reflectance (ATR) methods for solid-sample analysis. With new spectrometer capabilities, it should soon be gaining strength as a nondestructive method for process analysis of layered materials.

In the beginning

We know that light absorbed by an object causes it to heat up, but how does it produce sound? If the object passes its thermal energy to a surrounding gas atmosphere in a closed cell, the gas will expand and increase the pressure on the cell walls. A pulsed or modulated light source shining on the object will cause the surrounding gas to respond with pressure pulses. In effect, a sound wave is created whenever the object absorbs light. This photoacoustic effect was first observed by Alexander Graham Bell in the 1880s while he was working on the research that led to the development of the telephone. For a while, Bell even thought the "photophone" might be a more viable instrument than the one he eventually offered.

Although several pioneers explored the use of PAS as early as the 1930s and a Golay PAS cell for gas-phase analyses was available in the 1950s, it was the advent of FT-IR spectroscopy in the 1960s that eventually led to IR's being the most commonly used spectral region for PAS.

In the mid-1970s, researchers' enthusiasm for PAS applications in the UV–vis/near-IR region was running high. It seemed PAS could get a spectrum out of almost any intractable sample: It was nondestructive, required almost no sample preparation, worked for samples that wouldn't dissolve for standard optical spectroscopy, and was unaffected by the optical problems caused by samples that were opaque or irregularly shaped. Several manufacturers, including EG&G Princeton Applied Research, offered dedicated PAS spectrometers for the UV, visible, and near-IR wavelength ranges. However, as the limitations of the technique compared

with others available in these regions became better defined, interest in PAS shifted to the mid-IR. By the mid-1980s, the major use of PAS was for collecting vibrational spectra.

Applications for this method are still growing, and new quantitative capabilities are strengthening its usefulness for solid-sample analysis. *Analytical Chemistry* asked Richard Palmer of Duke University and Peter Griffiths of the University of Idaho for their views on modern developments in analytical PAS equipment and applications.

Commercial instruments

Commercial PAS instruments fall into three categories: gas monitors for industrial hygiene or process monitoring such as those made by Brüel & Kjaer and MSA Instruments, PAS detector modules (also called accessories or cells) that fit in the sample accessory area of an existing spectrometer, and PAS systems consisting of spectrometers with a PAS module included in the package. Table 1, although not intended to be comprehensive, compares features for some PAS instruments currently available for research applications.

The supply picture for PAS instruments in the U.S. market has changed in the past 10 years or so: EG&G Princeton Applied Research, which used to offer a UV–vis/near-IR PAS spectrometer, has discontinued the instrument; Burleigh Instruments and International Crystal Labs have also discontinued their lines of PAS equipment. The current makers of analytical PAS detectors in the United States include MTEC Photoacoustics, headed by John McClelland of Iowa State University/Ames Laboratory, and Bio-Rad's Digilab Division. Perkin Elmer, ATI/Mattson, Bruker, Bomem, and Nicolet each offer FT-IR spectrometers with an MTEC PAS detector as one of the optional accessories.

Signal to noise

According to Palmer, anyone can make a simple PAS cell with a light source, a test tube, and a lapel microphone—an assertion he sometimes demonstrates for his students. However, getting usable data is another matter. "The most important consideration for a PAS cell is the S/N," Griffiths agrees. Solid samples are usually analyzed under a helium atmosphere for better conversion of heat to pressure. Helium is about twice as efficient as air for signal enhancement.

Some commercial PAS units contain an electret (solid dielectric-based) microphone rather than a conventional condenser microphone as a detector because it doesn't require external dc voltage and it can be manufactured in very small sizes. These specialty microphones are available from companies such as Brüel & Kjaer. Whether electret or condenser, the microphones should have sensitivity at least as low as 50 mV/Pa for high performance in FT-IR PAS.

The main sources of noise are absorption signals from the PAS cell walls and window materials, secondary absorption echoes caused by reflected light in the cell, and external sources of acoustic noise or vibrations in the laboratory or spectrometer. Commercial PAS module designs incorporate cell geometries that cut down on internal reflection and partially isolate the system from external vibrations. Rapid-scan FT-IR instruments have some natural Fourier filtering of stray acoustic signals from outside the sample cell, but step-scan and other types of spectrometers may need to be fitted with vibration isolation equipment such as an air table.

The main task of a PAS instrument, however, is differentiating the photoacoustic absorption signal of the sample from other sources of acoustic noise. Most commercial systems use an amplitude- or phase-modulated light source and match the modulation frequency with that of the

Table 1. Summary of representative products

Product	MTEC 200	FTS 60A/896
Company	MTEC Photoacoustics P. O. Box 1095 Ames, IA 50014 515-292-7974	Bio-Rad Digilab Div. 237 Putnam Ave. Cambridge, MA 02139 800-225-1248
Type	PAS detector module	FT-IR spectrometer with PAS module
List price		
Detector	$8500	Part # 099-0741: $8800 MTEC 200: $9000
Spectrometer	NA	$85,500 w/o PAS module
PAS detector	MTEC 200	Part # 099-0741
Max. sample size	10 mm diam., 7 mm h	6 mm diam., 6 mm h
Preamplifier	External	External
Atmosphere	He; desiccator chamber option	He, air; desiccant can be placed under sample cup
Special features	DRIFTS, transmittance, and microsample heads optional; can analyze fibers	Removable sample mount that can be loaded in glove box; shock mount; MTEC 200 recommended for step scanning
Spectrometer		
Modulation	NA	Amplitude (rapid-scan mode), phase (step-scan mode); 10–400 Hz
Scan modes	NA	Rapid, step
Mirror velocity	NA	0.16–8 cm/s
Stepping rate	NA	0.004–800 steps/s
Spectral range (cm^{-1})	NA	42,000–10
Resolution (cm^{-1})	NA	0.25 standard, 0.1 optional
Demodulation and signal processing	NA	Purpose-built demodulator for step-scan mode; interface for commercial lock-in amplifiers; multichannel data acquisition; in-scan co-adding

NA = not applicable

resulting acoustic signal detected by the microphone. The portion of the acoustic signal attributable to the sample thermal expansion from incident light absorption should have a frequency corresponding to that of the modulated light. A lock-in amplifier or other signal demodulator used with the microphone for phase-sensitive detection eliminates noise outside the phase modulation frequency. Filters can suppress acoustic signals that have the wrong frequency, but photoacoustic signals from the cell window material have the same frequency as those from the sample. Residual moisture is also a significant problem, but it can be alleviated by using a dry He atmosphere and placing a desiccator cup under the sample.

FT-IR

PAS can work in any wavelength range, but a high-intensity source and high-throughput optics are required to detect the acoustic signal coming out of the sample cell. Often only a small percentage of the incident light energy is converted to sound. Although the mid-IR region's "fingerprinting" ability makes it particularly useful for PAS, dispersive IR spectrometers produce relatively low light intensity on the sample compared with UV–vis instruments because of the weakness of broadband IR light sources. When commercial interferometers were introduced in the 1960s and 1970s, they provided high enough light intensity to permit PAS in the IR wavelength range for the first time.

Since the introduction of rapid-scanning FT-IR spectrometers, PAS applications in the IR region have developed quickly. "PAS works beautifully with rapid-scan FT-IR for qualitative analyses," says Palmer. "You don't need a chopper for the light source." In rapid-scan FT-IR, as the mirror moves with constant velocity, the modulation frequency varies across the spectrum—light intensity oscillates more slowly at longer wavelengths and more quickly at shorter ones. The signal intensity and the thermal sampling depth (the depth from which the heat can escape to the sample surface before the thermal modulation is damped out) vary inversely with the modulation frequency. Therefore, a rapid-scan FT-IR PAS spec-

Table 1. Summary of representative products (continued)

Product	IFS 66 and 66v	System 2000	Paragon 1000	Magna-IR 550 and 750
Company	Bruker Instruments Manning Park Billerica, MA 01821 508-667-9580	Perkin Elmer 761 Main Ave. Norwalk, CT 06859 203-761-1000	Perkin Elmer 761 Main Ave. Norwalk, CT 06859 203-761-1000	Nicolet Instrument 5225 Verona Rd. Madison, WI 53711 800-356-8088
Type	FT-IR spectrometer without (66) or with (66v) vacuum; equipped with PAS module	FT-IR spectrometer with PAS module	FT-IR spectrometer with integrated electronics for PAS; equipped with PAS module	FT-IR spectrometer with integrated electronics for PAS; equipped with PAS module
List price				
Detector	Not offered as separate module	$12,500–$13,000	$10,000	$9500–$12,000
Spectrometer	IFS 66: $60,000–$90,000 IFS 66v: $90,000–$120,000	$28,000–$38,000	$18,000	$24,000–$35,000
PAS detector	MTEC 200	MTEC 200	MTEC 200	MTEC 200
Max. sample size	10 mm diam., 7 mm h	10 mm diam., 7 mm h	10 mm diam., 7 mm h	10 mm diam., 7 mm h
Preamplifier	External	External	Integrated in system	Integrated in system
Atmosphere	He; desiccator chamber option	He; desiccator chamber option	He; desiccator chamber option	He; desiccator chamber option
Special features	Vacuum bench reduces acoustic noise	DRIFTS, transmittance, and microsampling (e.g., fibers) optional	Modified for use without standard preamplifier or digital filter	DRIFTS, transmittance, and microsample heads optional; can analyze fibers
Spectrometer				
Modulation	Up to seven channels of amplitude or phase modulation; 10–10,000 Hz	Amplitude	Amplitude	Amplitude
Scan modes	Rapid, step	Rapid	Rapid	Rapid
Mirror velocity	0.05–40 cm/s	0.05–5.0 cm/s	0.1–1.5 cm/s	0.15–5.06 cm/s
Stepping rate	0–1000 steps/s	NA	NA	NA
Spectral range (cm^{-1})	45,000–4.7	15,000–20	7800–350	15,800–50
Resolution (cm^{-1})	0.1 maximum	0.3 standard, 0.15 optional	1–16, continuously variable	0.5 standard, 0.1 optional
Demodulation and signal processing	Lock-in amplifier; in-scan co-adding; choice of beam chopper or other modulators; multichannel signal processor	In-scan co-adding	Internal PAS signal channel with preamplifier and digital filter; dedicated analog signal train; in-scan co-adding	Built-in PAS detector preamplifier and cable; in-scan co-adding

NA = not applicable

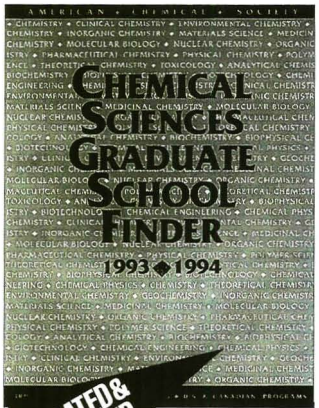

Graduate School... where to go, what to study, how much does it cost? If these are the questions you're asking others, or just yourself, the **Chemical Sciences Graduate School Finder** is the book for you. This concise and easy-to-use guide provides undergraduate chemistry students with the information necessary for selecting a graduate program to suit their needs and goals.

Includes listings from major educational institutions in the United States and Canada offering courses leading to a Master's or Ph.D. degree in chemistry and all allied fields. Provides information on the size and make-up of student population, admission and degree requirements, costs and financial aid, faculty members and their research specialties, and the institution's research facilities and equipment.

Also included is a section on how to apply to graduate school, a checklist of things to do, and perforated pages with preprinted postcards for requesting materials from graduate school.

Contents:
- How to Use This Guide
- Planning for Graduate Work in Chemistry
- Alphabetical List of Schools
- Department Listings
- Fields of Study Index
- Geographic Index
- Fields of Study Table

702 pages (1993) Paperbound
ISBN 0-8412-2739-X — **$49.95**
ACS Student Affiliates — **$17.00**

Order from:
American Chemical Society
Distribution Office, Dept. 74
1155 Sixteenth Street, NW
Washington, DC 20036

Or **CALL TOLL FREE 1-800-227-5558** (in Washington, DC, 202-872-4363) **and use your credit card! FAX:** 202-872-6067

ACS PUBLICATIONS
Essential Resources for the Chemical Sciences

trum reflects the chemical content at varying depths within the sample. However, Palmer says, "As long as you have a homogeneous sample, that's not a problem—you just normalize the spectrum to the PAS spectrum of carbon black."

The "holy grail of PAS"

But what if you want to see differences in composition at different depths in a sample? Light absorbed by solids can penetrate to a depth of ~20 μm (in some materials, up to 100 μm) and still produce a detectable acoustic signal. Recent step-scan design modifications to FT-IR interferometers are now opening the door to depth-specific composition profiling in solids—the "holy grail of PAS," as Richard Crocombe of Bio-Rad's Digilab Division calls it.

"The ability to do depth profiling is the major difference between PAS today and 10 years ago," says Griffiths. Scanning the range of 1–20 μm below the surface, he says, should allow researchers to differentiate between thin layers in a semiconductor or polymer laminate, detect surface oxidation, or characterize the diffusion of plasticizers in a polymer sample.

According to Palmer, depth profiling can also be achieved at a single wavelength in a rapid-scanning instrument by controlling the speed of the interferometer mirror. A series of rapid scans taken at different mirror velocities gives rise to a rough picture of the changes in chemical composition with sample depth, but each scan still represents a range of different depths for different wavelengths. For true depth-specific spectral collection, the modulation frequency of the light source must be made the same at all wavelengths simultaneously.

To do this, spectrometer designers have gone back to the early days of FT-IR and picked up step scanning again—but with much more sophisticated control of the fixed and moving mirrors in the interferometer. At each step, the moving mirror "dithers" sinusoidally about a fixed point at the modulation frequency. Bio-Rad and Bruker Instruments currently market spectrometers with step-scanning capabilities, and Nicolet is also scheduled to introduce a new spectrometer with step scanning.

Palmer says that one of the most important factors for PAS is an appropriate FT-IR spectrometer for the job, and he offers the following advice to prospective buyers. "If you have to buy an inexpensive FT-IR and you have a choice of instruments," he says, "choose the one with the lowest scan speed if it has good control—the PAS signal intensity is inversely related to the scan speed. If you can buy a research-grade instrument, look for one with step scanning and a wide range of stepping rates." Phase modulation that has a wide range of frequencies as well as amplitudes up to at least two times that of the HeNe laser wavelength is also essential for step scanning.

PAS versus DRIFTS

PAS has advantages over IR transmission spectroscopy methods such as specular reflectance, DRIFTS, and ATR because it does not require any particular sample surface characteristics and generally allows samples to be left intact (as long as they fit in the sample cell). DRIFTS is more sensitive than PAS overall, but the spectral bands in PAS are generally less subject to distortion, Palmer says.

For PAS, the plot of signal intensity as a function of sample absorptivity gives a sigmoidal curve. "PAS has a limited linear range," says Palmer, "but there's a considerably larger range in which you could use a calibration curve for useful results before you reach the saturation limit. With DRIFTS, unless the sample absorption is very low, the signal will be warped, and the sample often has to be diluted with KBr. It's my impression that people who want to get quantitative results from DRIFTS need to sample very carefully." He adds that one reason DRIFTS is currently more prevalent than PAS—besides the greater expense of step-scan FT-IR spectrometers for depth-specific PAS—may be that the diffuse reflectance accessory costs a few thousand dollars and a research-grade PAS accessory costs ~ $10,000.

The future

With the prospect of quantitative and nondestructive depth profiling becoming more available commercially, Palmer says, PAS could soon be developing in a variety of new directions. One area of current interest is data analysis. However, although several research groups are actively developing linearization methods for the nonlinear part of the range, no commercial software is yet available for PAS. In addition to its use in industrial applications for solid-sample analysis, says Palmer, depth-specific PAS could also be developed as a new method for GC detection of compounds that absorb very weakly in the IR region of the spectrum.

Deborah Noble

Laboratory Service Center

LABORATORY SERVICE CENTER

(Equipment, Materials, Services, Instruments for Leasing). Maximum space — 4 inches per advertisement. Column width, 2-3/16"; two column width, 4-9/16". Artwork accepted. No combination of directory rates with ROP advertising. Rates based on number of inches used within 12 months from first date of first insertion. Per inch: **1" — $200; 12" — $195; 24" — $190; 36" — $185; 48" — $180.**

ANALYTICAL CHEMISTRY
1599 Post Road East
P.O. Box 231
Westport, CT 06881
203-256-8211/FAX: 203-256-8175

Aluminon • Aniline Sulfate • Brazilin • 2-Chloro-4-Nitrobenzoic Acid
Congo Red • Diethyl & Dimethyl Adipates • Dimethylglyoxime & Na Salt
Disodium Malonate • Histamine Diphosphate • p-Hydroxybenzaldehyde
Hydroxylamine HCl • m-Iodotoluene • Levulinic Acid • Luminol
Maltose • Methyl Acetate • Methylglucamine • 1,10-Phenanthroline
Phenyl Urea • Potassium Biphthalate • Silver Diethyldithiocarbamate
Sodium Pyruvate • Sodium Thioglycolate • Thymolphthalein • Toluidine Blue
Trimethylamine HCl • Triphenylphosphine • Triphenyltetrazolium Chloride

Write for our Products List of over 3,000 chemicals

Tel: 516-273-0900 • TOLL FREE: 800-645-5566 Telefax: 516-273-0858 • Telex: 497-4275

EASTERN CHEMICAL
ADMIRAL SPECIALTY PRODUCTS, INC.
P.O. Box 2500
DEPT. AC
SMITHTOWN, N.Y. 11787

FREE DATA, FAST

To quickly amass data on all of the products you need, consult the Lab Data Service Selection on our *Analytical Chemistry* reader reply card insert.

Index to Advertisers

CIRCLE INQUIRY NO.	ADVERTISERS	PAGE NO.
1	* Chrompack	719A
2	*Sigma-Aldrich Techware	OBC

Directory section, see page 761A.

**See ad in 1994 LabGuide Edition.*

Advertising Management for the American Chemical Society Publications

CENTCOM, LTD.

President
James A. Byrne

Executive Vice President
Benjamin W. Jones

Joseph P. Stenza, *Production Director*

Laurence J. Doyle, *Director of Marketing*

1599 Post Road East
P.O. Box 231
Westport, Connecticut 06881-0231
(Area Code 203) 256-8211
Fax No. 203-256-8175

DIRECTOR, ADVERTISING SALES, LABORATORY PRODUCTS
Bruce E. Poorman

ADVERTISING PRODUCTION MANAGER
Jane F. Gatenby

SALES REPRESENTATIVES

Philadelphia, PA. . . . CENTCOM, LTD., The Meadows, 485 Devon Park Drive, Suite 106, Wayne, PA 19087. Telephone: 610-964-8061, FAX: 610-964-8071

New York/New Jersey . . . Dean A. Baldwin, John F. Raftery, CENTCOM, LTD., Schoolhouse Plaza, 720 King Georges Post Road, Fords, NJ 08863. Telephone: 908-738-8200, FAX: 908-738-6128

Westport, CT./Boston, MA. . . . Dean A. Baldwin, Michael J. Pak, CENTCOM, LTD., 1599 Post Road East, P.O. Box 231, Westport, CT 06881-0231. Telephone: 203-256-8211, FAX: 203-256-8175

Cleveland, OH. . . . Bruce E. Poorman, Dean A. Baldwin, CENTCOM, LTD., 19035 Old Detroit Road, Suite 203. Rocky River, OH 44116. Telephone: 216-331-5151, FAX: 216-331-3432

Chicago, IL. . . . Michael J. Pak, CENTCOM, LTD., 540 Frontage Rd., Northfield, IL. 60093. Telephone: 708-441-6383, FAX: 708-441-6382

Houston, TX./Atlanta, GA. . . . Edward M. Black, CENTCOM, LTD., P.O. Box 820966, Houston, TX 77082-0966. Telephone: 713-493-1560, FAX: 713-493-6673

San Francisco, CA. . . .Paul M. Butts, CENTCOM, LTD., Suite 808, 2672 Bayshore Parkway, Mountain View, CA 94043. Telephone: 415-969-4604, FAX: 415-969-2104

United Kingdom, Scandinavia and Europe (Except: Germany, Switzerland, Austria, France, Italy, Spain) . . . Malcolm Thiele, Technomedia Ltd., Wood Cottage, Shurlock Row, Reading RG10 OQE, Berkshire, England. Telephone: 0734-343302, FAX: 0734-343848

Germany, Switzerland, Austria . . . IMP InterMediaPartners, GmbH, Deutscher Ring 40, 42327 Wuppertall, Germany. Telephone: (0202) 711091, FAX: (0202) 712431

France . . . Gerard Lecoeur, Aidmedia, 31–33 Grand rue de Saint-Rambert, 69009 Lyon, France. Telephone: 78-64-20-37, FAX: 78-83-56-67

Italy, Spain . . . Tess Serranti, Serranti Communications, 43 Van Sant Road, New Hope, PA 18938. Telephone: 610-598-0668, FAX: 610-598-0670

Asia . . . Bruce E. Poorman, CENTCOM, LTD., 19035 Old Detroit Road, Suite 203, Rocky River, OH 44116. Telephone: 216-331-5151, FAX: 216-331-3432

South America . . .Bruce E. Poorman, CENTCOM, LTD., 19035 Old Detroit Road, Suite 203, Rocky River, OH 44116. Telephone: 216-331-5151, FAX: 216-331-3432

ANALYTICAL CHEMISTRY **Information Express**

Get the product data you need fast...

By Phone: Use the reference list below, and contact the companies to fill an immediate need, or...
By Fax: Use the fax form on the opposite page to send a direct written request.

Company	Page	Issue	RSN	Data+	Phone	Fax	Contact
ABC Instruments	712 A	7/1/94	402		800-533-0222	314-449-2988	Shelly Rittgers
Absolute Standards	707 A	7/1/94	3	●	203-468-7407	203-466-3464	Jack Criscio
AccuStandard	713 A	7/1/94	412		203-786-5290	203-786-5287	Michael Bolgar
Aldrich Chemical	OBC	7/1/94	1	●	414-273-3850	414-273-2094	Maryjean Essinger
Alltech Associates	552 A	5/1/94	414	●	708-948-8600	708-948-1078	Laura Inkley
J. T. Baker	672 A	7/1/94	6	●	908-859-2151	908-859-9318	William Broad
Baird Analytical	712 A	7/1/94	406	●	617-276-6163	617-276-6510	Robin Tamulynas
Bodman	713 A	7/1/94	409		800-241-8774	610-459-8036	Kirk Lind
Brinkmann Instruments	676 A	7/1/94	2		800-645-3050	516-334-7506	C. Shevchenko
Burleigh Instruments	641 A	6/1/94	12		716-924-9355	716-924-9072	Brian Samoriski
Camag Scientific	552 A	5/1/94	410	●	800-334-3909	919-343-1834	Jeannie Daab
Chiral Technologies	649 A	6/1/94	8		215-594-2100	215-594-2325	Thomas B. Lewis
Chrompack	719 A	7/15/94	1	●	908-722-8930	908-722-8365	Judy Sparks
Delff Instruments X-ray Diffraction	712 A	7/1/94	405		516-589-2885	516-589-2068	
Dionex	712 A	7/1/94	403	●	800-346-6390	408-739-4398	Nancy Jensen
EG&G Instruments (Princeton)	713 A	7/1/94	411	●	609-530-1000	609-883-7259	Cynthia Nienart
EM Science	713 A	7/1/94	410		800-222-0342		Bruce Hyland
ESA, Inc.	606 A	5/15/94	5		617-275-0100	617-275-5529	K.G. Whitehead
Finnigan MAT	712 A	7/1/94	401		408-433-4800	408-433-4823	Gary Spear
Fisons Instruments	491 A	5/1/94	8–12	●	508-524-1000	508-524-1100	Cathy Schaub
Hamamatsu	639 A	6/1/94	none		800-524-0504	908-231-1218	Robert Wisner
Hewlett Packard	551 A	5/1/94	402	●	415-857-5603	415-857-8228	Doug Forsyth
Hoefer Scientific	663 A	6/1/94	411	●	800-227-4750	415-821-1081	David C. Carter
Horiba Instruments	551 A	5/1/94	405	●	800-446-7422	714-250-0924	Geneen Spence
Isco	624 A	6/1/94	9	●	402-464-0231	402-464-0318	Gary Bakken
Kimble/Kontes	521 A	5/1/94	18	●	609-692-8500	609-692-3242	David Fenili
Lachat Instruments	551 A	5/1/94	404	●	414-358-4200	414-358-4206	Babara Gatford
Labsphere	712 A	7/1/94	407	●	603-927-4266	603-927-4694	Joan A. Beaulieu
Leco	OBC	6/1/94	1		616-983-5531	616-983-4117	W. Stockwell
Macherey Nagel	623 A	6/1/94	5		49-02421-6980	49-02421-62054	
Malvern Instruments	662 A	6/1/94	406	●	508-480-0200	508-460-9692	Mark Bumiller
Matheson Gas Products	560 A	5/15/94	6		215-641-2700	215-641-2714	Kevin McGuffin
Metrohm	620 A	6/1/94	4		41-071-538-585	41-071-538-901	R. Steiner
Micro-Now Instruments	662 A	6/1/94	402	●	708-677-4700	708-677-0394	Clarence Arnow
Midac Corp.	713 A	7/1/94	408		714-660-8558	714-660-9334	Heidi Auth
Millipore	551 A	5/1/94	406	●	508-478-2000	508-478-5839	Kathy Fernandes
Molecular Devices	552 A	5/1/94	407		415-322-4700	415-322-2069	Kim Mulcahey
Nicolet Instrument	511 A	5/1/94	19	●	608-271-3333	608-273-5046	Joni Hansen
NIST	713 A	7/1/94	413	●	301-975-2208	301-926-0416	Standard Reference Materials
Park Scientific	663 A	6/1/94	414	●	408-747-1600	408-747-1601	Lindsey Mitobe
Perkin Elmer	669 A	7/1/94	7–8	●	800-762-4000	203-762-6000	Mary Cooke-Kager
Philips Electronic	662 A	6/1/94	401	●	201-529-3800	201-529-2252	Lisa Schroeder
Rainin Instrument	663 A	6/1/94	410	●	510-654-9142	510-652-8876	C. Stewart
Rigaku/USA	552 A	5/1/94	409	●	508-777-2446	508-777-3594	Alan Robson
RockWare	663 A	6/1/94	409		303-423-5645	303-423-6171	Holly Bidle Reed
Sigma-Aldrich Techware	OBC	7/15/94	2	●	800-231-8327	800-962-9591	J. Russell Gant
SLM-Aminco	681 A	7/1/94	10		217-384-7730	217-384-7744	Don Elmore
Spectra-Tech	712 A	7/1/94	404	●	203-357-7055	203-357-0609	Debbie Esposito
Springer Verlag	622 A	6/1/94	2		212-460-1653	212-533-5587	Raye Hazan
Supelco	IFC	7/1/94	9	●	814-359-3441	814-359-5459	Cathy Gates
Ultra Scientific	663 A	6/1/94	412	●	401-294-9400	401-295-2330	Paul Jennings
Techne	537 A	5/1/94	2		609-452-9275	609-987-8177	P. H. Summers
Technical Manufacturing	552 A	5/1/94	408		508-532-6330	508-531-8682	Dan Foley
Thermo Separation Products	552 A	5/1/94	412	●	510-657-1100	510-490-8182	Marianne Hartfield
TopoMetrix	551 A	5/1/94	401	●	408-982-9700	408-982-9571	Tim Van Slambrouck
Varian	674 A	7/1/94	4–5	●	800-926-3000	713-240-6752	Chris Clark
Waters	618 A	6/1/94	3	●	508-478-2000	508-872-1990	Kathy Fernandes
Wheaton	IFC	6/1/94	6–7	●	609-825-1100	609-825-9035	Frank Norman
Wyatt Technology	611 A	6/1/94	17	●	805-963-5904	805-965-4898	Brian Montgomery

Data+ Column: A bullet indicates that additional product and company information is available in the 1994 *Analytical Chemistry* LabGuide Edition.
RSN: Reader Service Number

Articles

Anal. Chem. **1994,** *66,* 2201–2219

Dynamics and Response of Polymer-Coated Surface Acoustic Wave Devices: Effect of Viscoelastic Properties and Film Resonance

Stephen J. Martin* and Gregory C. Frye

Microsensor Research and Development Department, Sandia National Laboratories, Albuquerque, New Mexico 87185

Stephen D. Senturia

Department of Electrical Engineering and Computer Science, Massachusetts Institute of Technology, Cambridge, Massachusetts 02139

The response of polymer-coated surface acoustic wave (SAW) devices to temperature changes and polymer vapor absorption is examined. A perturbational approach is used to relate velocity and attenuation responses to film translational and strain modes generated by the SAW. Two distinct regimes of film behavior arise, causing different SAW responses. For glassy films, displacement is nearly uniform across the film thickness, varying only in the direction of propagation. A model developed to predict velocity and attenuation in this regime (model 1), reduces to the familiar Tiersten (Wohltjen) equation for purely elastic films. For elastomeric (rubbery) films, inertial effects cause a phase lag to occur across the film for shear displacements. A model to account for these cross-film displacement gradients (model 2) predicts a characteristic resonant response when the film phase shift reaches $n\pi/2$, where n is an odd integer. These model predictions are compared with measured responses from polyisobutylene-coated SAW devices as temperature is varied and during exposure to high vapor concentrations.

Surface acoustic wave (SAW) devices use interdigital transducers photolithographically patterned on the surface of a piezoelectric crystal (Figure 1) to excite and detect surface waves.[1] These waves are excited in a frequency band centered at $f_o = v/d$, where v is the SAW propagation velocity and d is the transducer period. The SAW wavelength Λ generated at f_o matches the transducer period d. SAW devices typically operate in the 30–300-MHz range and use ST-cut[2] quartz substrates for high-temperature stability near room temperature. In the delay-line device configuration,[3] input and output transducers are typically separated by 100–200 wavelengths.

The extreme sensitivity of SAW devices to thin-film properties has been used both (1) to characterize thin film elastic and viscoelastic properties,[4] and (2) to construct gas and vapor sensors.[5] In these applications, a thin film (thickness $h \ll \Lambda$) is coated on the substrate in the region between transducers (Figure 1). If the film is nonconductive, the film may coat the transducers also. Thin-film elastic and viscoelastic properties are studied by using the SAW to deform the film, thereby *probing* its mechanical properties. A chemical sensor results when interaction between the film and a vapor or chemical species modifies the SAW behavior. In both applications, changes in film properties induce two changes in SAW propagation characteristics: velocity and attenuation (rate of amplitude decay).

Since the invention of SAW chemical sensors by Wohltjen,[6] a number of polymer films have been examined as chemically sensitive films[7] or "chemical interfaces". This is due to the

(1) White, R. M.; Volltmer, F. W. *Appl. Phys. Lett.* **1965,** *7,* 314.
(2) The Euler angles for ST-cut quartz are 0°, 132.75°, 0°. SAW velocity in the X-propagation direction is 3.158×10^5 cm/s.

(3) Datta, S. *Surface Acoustic Wave Devices*; Prentice-Hall: Englewood Cliffs, NJ, 1986.
(4) (a) Hickernell, F. S.; Wagers, R. S. *IEEE 1984 Ultrasonics Symposium Proceedings;* IEEE: New York, 1984; pp 253–257. (b) Wagers, R. S. *IEEE 1980 Ultrasonics Symposium Proceedings;* IEEE: New York, 1980; pp 464–469. (c) Ricco, A. J.; Martin, S. J. *Sens. Actuators B* **1993,** *B10* (2), 123–31.
(5) (a) Wohltjen, H.; Dessey, R. *Anal. Chem.* **1979,** *51,* 1458–1464. (b) Wohltjen, H.; Dessey, R. *Anal. Chem.* **1979,** *51,* 1465–1470. (c) Frye, G. C.; Martin, S. J.; Cernosek, R. W.; Pfeifer, K. B.; Anderson, J. S. *IEEE 1991 Ultrasonics Symposium Proceedings*; IEEE: New York, 1991; pp 311–16. (d) Watson, G.; Horton, W.; Staples, E. *IEEE 1992 Ultrasonics Symposium Proceedings*; IEEE Cat. No. 92CH3118–7; IEEE: New York, 1992; pp 269–273. (e) Bowers, W. D.; Chuan, R. L., Duong, T. M. *Rev. Sci. Instrum.* **1991,** *62* (6), 1624–1629. (f) Arn, D.; Amati, D.; Blom, N.; Ehrat, M.; Widmer, H. M. *Sens. Actuators B* **1992,** *8,* 27–31.
(6) Wohltjen, H. U.S. Patent 4,312,228, Jan. 26, 1982.

0003-2700/94/0366-2201$04.50/0
© 1994 American Chemical Society

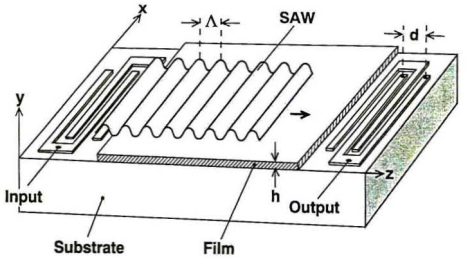

Figure 1. Schematic of a surface acoustic wave (SAW) device with a polymer film coating.

wide range of chemical properties available and the ease of film formation: polymer films can be deposited from solution by spin-casting, air-brushing, or dip-coating; certain ones can also be formed by plasma deposition.[8] As a chemical interface, the film in effect *dissolves* gas-phase species, maintaining a film concentration in equilibrium with the gas-phase concentration. The dissolved species contributes added mass and may, in addition, modify the mechanical properties of the film.

The mechanical properties of a linear, isotropic polymer can be specified by a bulk modulus K and a shear modulus G. Under sinusoidal deformation, these are represented as complex quantities:[9] $K = K' + jK''$ and $G = G' + jG''$. The real parts of K and G represent the component of stress in-phase with strain, giving rise to energy storage in the film (consequently K' and G' are referred to as *storage moduli*); the imaginary parts represent the component of stress 90° out of phase with strain, giving rise to power dissipation in the film (thus, K'' and G'' are called *loss moduli*). An ideal *elastic* film would have $K'' = G'' = 0$.

Polymers exhibit a wide range of viscoelastic properties that depend on the temperature and frequency of measurement. If deformed on a short time scale compared with the time for segmental chain motion τ, strain is accommodated elastically through chain deformations; this is the *glassy* regime, characterized by $G' \cong 10^{10}$ dyn/cm^2 and $G'' \ll G'$. If deformed on a time scale longer than τ, strain is accommodated inelastically by interchain motion; this is the *rubbery* regime, characterized by $G' \leq 10^8$ dyn/cm^2 and G'' comparable to or less than G'. Thus, when probing at a given (angular) frequency ω, the material behaves as glassy if $\omega\tau \gg 1$ and rubbery if $\omega\tau \ll 1$. When $\omega\tau \approx 1$, there is a peak in K'' and G''. Since τ is strongly dependent on temperature, varying temperature can cause this transition from elastic to viscoelastic behavior. The temperature of this transition is the *dynamic glass transition temperature*, T_g. Since this glass transition temperature is defined by $\tau(T_g) = 1/\omega$, the dependence of T_g on measurement frequency is apparent.[10]

There are two quasi-static phenomena associated with the glass transition that are not observable at the high frequencies at which SAW devices operate. These are (1) an increase in specific heat as observed in DSC and (2) an increase in thermal expansion coefficient. The latter has an indirect influence on SAW performance through changes in film thickness. Therefore, it is important to identify the temperature at which these quasi-static effects occur. This temperature is commonly called the "static glass transition temperature," denoted herein as $T_g^{(0)}$, although it must be noted that measurements of $T_g^{(0)}$ are done by scanning methods and, therefore, should be thought of as T_g in the limit of low frequency. $T_g^{(0)}$ and T_g can differ significantly; for example, in the PIB films used here, $T_g^{(0)} = -68$ °C while T_g at 100 MHz is 40 °C.

Although glass transitions have reportedly been observed in the response of polymer-coated SAW devices[11] (including the present authors[12]), this interpretation has been correctly challenged by Grate et al.[13] Changes in the intrinsic polymer properties known to occur at T_g, specifically a rapid decrease in shear storage modulus (G') and a peak in shear loss modulus (G''), have usually been assumed to appear directly as changes in SAW velocity and attenuation.[12] Under this assumption, peaks in attenuation or velocity slope changes with temperature have been used to indicate T_g. However, it will be shown in this paper that velocity and attenuation changes track intrinsic properties only in extremely thin films (defined below). In this limit, attenuation peaks and velocity slope changes do coincide with T_g. For thicker films, however, the acoustic coupling to the film varies strongly with film thickness due to film interference effects. In this case, velocity and attenuation do *not* track changes in the intrinsic properties directly and, therefore, care must be used in inferring glass transitions from SAW velocity and attenuation responses.

SAW velocity and attenuation responses arise from the mechanical interaction that occurs between the SAW and the film overlay. A film that is rigidly bonded to the surface of the piezoelectric substrate undergoes both translation and deformation under the influence of the propagating wave. Translation creates, in effect, mass loading on the SAW device, which decreases the SAW propagation velocity. In addition, the deformation produces energy storage in the film, which results in a change in SAW propagation velocity, and power dissipation in the film, which causes wave attenuation.

(7) (a) Ballantine, D. S.; Wohltjen, H. *Anal. Chem.* **1989**, *61* (11), 704A–715A. (b) Nieuwenhuizen, M. S.; Barendsz, A. W. *Sens. Actuators* **1987**, *11*, 45–62. (c) White, R. M.; Wicher, P. J.; Wenzel, S. W.; Zellers, E. T. *IEEE Trans. UFFC* **1987**, *UFFC-34*, 162–171. (d) Brace, J. G.; Sanfelippo, T. S. *Sens. Actuators* **1988**, *14*, 47–68. (e) Galipeau, D. W.; Feger, C.; Vetelino, J. F.; Lec, R. *IEEE 1990 Ultrasonics Symposium Proceedings;* IEEE: New York, 1990; pp 1087–90. (f) Gizeli, E.; Goddard, N. J.; Lowe, C. R.; Stevenson, A. C. *Sens. Actuators B* **1992**, *B6* (1–3), 131–137. (g) Mizutani, F.; Yoshino, I.; Tamura, M; Yoshida, T. *Koatsu Gasu* **1990**, *27* (5), 339–43. (h) Wenzel, S. W.; White, R. M. *Sens. Actuators A* **1990**, *A21–A23*, 700–703. (i) Katritzky, A. R.; Savage, G. P.; Pilarska, M. *Talanta* **1991**, *38*, 201–204. (j) Chang, S.; Tamiya, E.; Karube, I. *Biosens. Bioelectron.* **1991**, *6*, 9–14. (k) Grate, J. W.; McGill, R. A.; Abraham, M. H. *IEEE 1992 Ultrasonics Symposium Proceedings*; IEEE Cat. No. 92CH3118–7; IEEE: New York, 1992; pp 275–279. (l) Goydan, R.; Reid, R. C.; Tseng, H. S. *Ind. Eng. Chem. Res.* **1989**, *28*, 445–454. (m) Grate, J. W.; Abraham, M. H. *Sens. Actuators B* **1991**, *3*, 85–111. (n) Ballantine, D. S.; Rose, S. L.; Grate, J. W.; Wohltjen, H. *Anal. Chem.* **1986**, *58*, 3058–3066. (o) Carey, W. P.; Kowalski, B. R. *Anal. Chem.* **1986**, *58*, 3077–3084. (p) Rose-Pehrsson, S. L.; Grate, J. W.; Ballantine, D. S.; Jurs, P. C. *Anal. Chem.* **1988**, *60*, 2801–2811. (q) Schmautz, A. *Sens. Actuators B* **1992**, *6*, 38–44.

(8) Sugimoto, I.; Nakamura, M.; Kuwano, H. *Proceedings of Transducers '91*; IEEE: New York, 1991; pp 994–997.

(9) Ferry, J. D. *Viscoelastic Properties of Polymers*, 3rd ed.; Wiley: New York, 1980; Chapter 1.

(10) Lewis, A. F. *Polym. Lett.* **1963**, *1*, 649–654.

(11) (a) Ballantine, D. S.; Wohltjen, H. *Chemical Sens. Microinstrumentation;* ACS Symposium Series 403, American Chemical Society: Washington, DC, 1989; pp 222–236. (b) Wohltjen, H.; Dessey, R. *Anal. Chem.* **1979**, *51*, 1470–1475. (c) Wohltjen, H.; Dessy, R. *Anal. Chem.* **1979**, *51* 1470–1475. (d) Groetsch, J. A.; Dessy, R. E. *J. Appl. Polym. Sci.* **1983**, *28*, 161–178. (e) Caliendo, C.; Fioretto, C.; Socino, G.; Verona, E. *IEEE 1991 Ultrasonics Symposium Proceedings;* IEEE: New York, 1991; pp 387–391.

(12) Martin, S. J.; Frye, G. C. *Appl. Phys. Lett.* **1990**, *57*, 1867–1869.

(13) Grate, J. W.; Wenzel, S. W.; White, R. M. *Anal. Chem.* **1992**, *64*, 413–423.

The wave energy stored and dissipated in the film depends upon the strain modes generated by the SAW in the film. Two distinct regimes of film behavior can be identified. Films that are thin and rigid behave as *acoustically thin*: the entire film moves synchronously with the substrate surface, resulting in uniform displacement across the film thickness. Films that are thick or soft behave as *acoustically thick*: the upper film portions lag behind the film/substrate interface, causing nonuniform displacement across the film thickness. Since the strain modes generated in each regime are different and result in distinct device responses, it is essential to understand the regime of operation for any particular measurement.

Tiersten and Sinha[14] derived a perturbational formula relating SAW velocity to film properties for the case of an acoustically thin, *elastic* film (see eq 6 below). This model has been shown to accurately predict SAW velocity changes arising from metallic,[15] crystalline,[16] or very thin polymer films.[17] Since translation and deformation of a purely elastic film is nondissipative, no film-induced attenuation is predicted by this model.

Wohltjen first applied the Tiersten formula to interpret the response of polymer-coated SAW sensors.[18] Thus, the equation is commonly referred to in SAW sensor literature as the Wohltjen equation. The dominant contribution to the SAW velocity response was assumed to arise from the *mass* of gas or vapor molecules absorbed into the film—the so-called "gravimetric" or "mass loading" response. While providing a good starting point for understanding SAW sensors, recent studies have indicated inadequacies in this model (as applied to polymer films) and called into question the dominance of mass loading in determining the SAW vapor response. For example, significant attenuation responses have been observed during vapor absorption.[12,19] Also, SAW velocity can decrease in some regimes of gas-phase concentration while increasing in others. From thermodynamic arguments, the concentration of absorbed species is expected to increase monotonically with gas-phase concentration. Thus, the nonmonotonic velocity response (i.e., sign change) contradicts the mass loading interpretation.

Several researchers have shown that a nongravimetric response arises from polymer *plasticization*[20] or vapor-induced softening. Grate et al.,[21] comparing SAW responses with chromatographic studies of polymer film absorption, found that the SAW velocity response was four times too large to be accounted for by the mass of absorbed species alone. They proposed "swelling-induced modulus changes" as the origin of the additional velocity change.[22]

The difficulties in reconciling predicted and measured responses arise from the fact that the assumptions underlying the Tiersten model are rarely satisfied by polymer films. First, the *viscoelastic* nature of polymer films causes elastic energy to be both stored and dissipated during film deformation. This results in a significant contribution to SAW attenuation that is neglected in the Tiersten model. Second, the large change in viscoelastic properties undergone by polymers, either due to temperature change or vapor absorption, can cause even films satisfying $h \ll \Lambda$ (the criterion typically applied for invoking the Tiersten model) to behave as *acoustically thick*. This is because the film can be significantly softer than the substrate, resulting in a displacement variation across the film on a scale much smaller than Λ. This violates the assumption of synchronous film motion implicit in the Tiersten model.

In this paper, we investigate the dynamics and response of polymer-coated SAW devices, examining separately the acoustically thin and thick regimes. We begin with a criterion for separating these two regimes and examine the film strain modes that arise in each. A perturbational approach[23] is used to obtain explicit, although approximate, expressions for film-induced velocity and attenuation changes in each regime. In this approach, velocity and attenuation changes caused by the film are related to the surface mechanical impedances (a measure of the difficulty in displacing the film) contributed by the film. These mechanical impedances depend on the film properties and the detailed manner in which the film is translated and deformed by the passing wave. Changes in film viscoelastic properties induced by temperature changes and vapor absorption are expressed in terms of polymer free volume. Incorporating these film property changes into the models yields predictions for velocity and attenuation responses. These predictions are compared with experimental measurements made on polyisobutylene-coated SAW devices operating at 97 MHz. The best agreement is obtained using the acoustically thick model that accounts for cross-film displacement variations.

THEORY

A surface acoustic wave (SAW) in an uncoated substrate is formed by coupled compressional and shear waves propagating together to satisfy the stress-free boundary condition at the surface. Propagation of the SAW in the z-direction results in a displacement $\tilde{\mathbf{u}}$ of particlesfrom their equilibrium position that varies with depth y into the crystal as

$$\tilde{\mathbf{u}}(x,y,z,t) = e^{(j\omega t-\gamma z)}\sum_{i=1}^{3} u_i(y)e^{j\psi_i}\hat{x}_i \qquad (1)$$

where $j = (-1)^{1/2}$; ω is the angular frequency ($2\pi f$); t is time; γ is a complex propagation factor; $u_x(y)$, $u_y(y)$, and $u_z(y)$ represent depth-dependent displacements in the x-, y-, and z-directions (values at the surface are denoted u_{xo}, u_{yo}, and u_{zo}); ψ_i are the relative phases of these components with respect to u_z; $\hat{x}_i$ are unit vectors in the x_i-direction. The amplitude components $u_i(y)$ decay exponentially with distance into the substrate so that most of the wave energy is confined to within one wavelength of the surface. The complex propagation factor in eq 1 is comprised of two components: $\gamma = \alpha + jk$. The

(14) Tiersten, H. F.; Sinha, B. K. *J. Appl. Phys.* **1978**, *49* (1), 87–95.
(15) Skeie, H. *J. Acoust. Soc. Am.* **1970**, *48*, 1098–1109.
(16) Wolkerstorfer, D. C. Methods for Measuring the Acoustic and Optical Properties of Organic Crystals. Ph.D. Thesis, Stanford University, Aug 1971.
(17) (a) Wohltjen, H.; Snow, A. W.; Barger, W. R.; Ballantine, D. S. *IEEE Trans. UFFC* **1987**, *UFFC-34*, 172–178. (b) Grate, J. W.; Klusty, M. *Anal. Chem.* **1991**, *63*, 1719–1727.
(18) Wohltjen, H. *Sens. Actuators* **1984**, *5*, 307.
(19) Frye, G. C.; Martin, S. J. *Sens. Mater.* **1991**, *2*, 187–195.
(20) Ferry, J. D. *Viscoelastic Properties of Polymers*, 3rd ed.; Wiley: New York, 1980, Chapter 17.
(21) Grate, J. W.; Snow, A.; Ballantine, D. S.; Wohltjen, H.; Abraham, M. H.; McGill, R. A.; Sasson, P. *Anal. Chem.* **1988**, *60*, 869–875.
(22) Grate, J. W.; Klusty, M.; McGill, R. A.; Abraham, M. H.; Whiting, G.; Andonian-Haftvan, J. *Anal. Chem.* **1992**, *64*, 610–625.
(23) Auld, B. A. *Acoustic Fields and Waves in Solids*; Wiley: New York, 1973; Vol. II, Ch. 12.

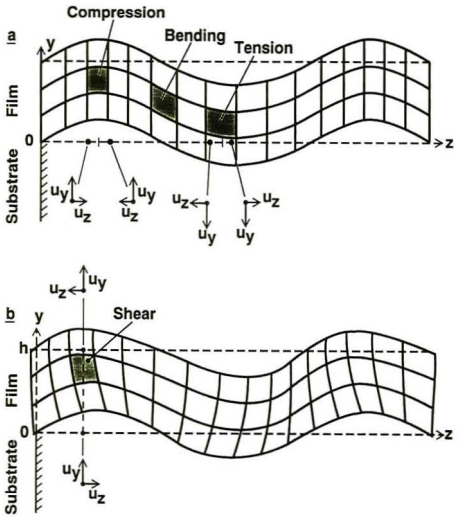

Figure 2. Deformation generated by a SAW (a) in an acoustically thin ($R \ll 1$) film, in which in-plane displacement gradients (due to sinusoidal wave variation) dominate, and (b) in an acoustically thick ($R \geq 1$) film, where cross-film gradients (due to inertial film lag) also arise.

attenuation, α, describes the rate of diminution in wave amplitude with distance; the wavenumber, k_o, describes the oscillatory portion of the wave motion: $k_o = \omega/v_o$, where v_o is the propagation velocity in the uncoated substrate.

Film Strains Induced by a Surface Acoustic Wave. When a thin film ($h \ll \Lambda$) is coated on the SAW substrate, the SAW surface displacements (u_{xo}, u_{yo}, u_{zo}) are unchanged to first order.[23] SAW propagation thus causes a periodic displacement field to be imposed on the lower film surface: u_{xo} lies in the plane of the surface and normal to the direction of propagation, u_{yo} is normal to both the surface and the direction of propagation, while u_{zo} lies in the direction of propagation. This displacement field causes translation of the film and induces strains in the film.

Strain, defined as the symmetric gradient of displacement,[24]

$$S_{ij} = \frac{1}{2}\left(\frac{\partial u_i}{\partial x_j} + \frac{\partial u_j}{\partial x_i}\right) \tag{2}$$

arises whenever there is a spatial variation or *gradient* ($\partial u_i/\partial x_j$) in a displacement component u_i. The surface displacement field has two distinct means of inducing strain in a film overlay: (1) from the in-plane gradients arising *due to the sinusoidal variation in displacement components along the direction of propagation* [the $\exp(-\gamma z)$ term in eq 1] and (2) from surface-normal gradients arising *from inertial lag of the upper film portions* with respect to the "driven" lower film surface.

Figure 2a shows the deformation arising in an acoustically thin film. Displacements u_i are constant across the film thickness, and only gradients *in the plane* of the film arise. The gradient in u_z leads to regions of compression and tension in the film, while the gradient in u_y leads to bending. Figure 2b shows the deformation in an acoustically thick film. Displacement varies not only in the plane of the film but also across the film due to inertial lag of the upper film regions. The deformation in an acoustically thick film arises from a combination of both in-plane and cross-film gradients, with cross-film gradients dominating. As shown in Figure 2b, the gradient in u_z across the film leads to shear deformation of the film. The regimes in which in-plane and cross-film gradients dominate and the corresponding velocity and attenuation changes will be considered below.

The mechanical interaction of the wave with the film results in a perturbation $\Delta\gamma$ of the complex wave propagation factor γ. In normalized form, this is[25]

$$\frac{\Delta\gamma}{k_o} = \frac{\Delta\alpha}{k_o} - j\frac{\Delta v}{v_o} \tag{3}$$

Equation 3 yields two measurable responses: the change in attenuation per wavenumber, $\Delta\alpha/k_o$, and the fractional change in propagation (phase) velocity, $\Delta v/v_o$. Equation 3 also indicates that the attenuation change *divided by wavenumber* is the normalized complement to the commonly measured $\Delta v/v_o$ response.

Criterion for Separating Acoustically Thin and Thick Films. The ratio of film strains generated by cross-film displacement gradients to those generated by in-plane gradients is calculated (appendix B) as

$$R = \frac{Afv_o\rho h}{|G|} \tag{4}$$

where ρ, h, and G are the film density, thickness, and shear modulus, respectively, and A is a substrate-dependent parameter (see Appendix B) having a value of 1.9 for ST-cut quartz. When the film coating is sufficiently thin (small h) and rigid (large $|G|$) in comparison to the oscillation frequency such that $R \ll 1$, in-plane gradients dominate over surface-normal gradients, and the film is *acoustically thin* (Figure 2a). When film properties are such that $R \geq 1$, inertial lag becomes significant so that surface-normal gradients are dominant (Figure 2b), and the film is *acoustically thick*.

Figure 3 shows the variation in R with the magnitude of the film shear modulus for various values of the quantity $fh\rho$ ($v_o \cong 3.2 \times 10^5$ cm/s); $|G|$ is displayed on a reversed logarithmic scale to mimic the way in which polymer properties vary with increasing temperature or vapor absorption. For devices operating at 100 MHz (typical SAW frequency) and coated with films having a density of 1 g/cm^3, the parentheses identify the corresponding film thickness. The curves in Figure 3 indicate that as polymers undergo a glass-to-rubber transition, traversing the G' values along the abscissa from left to right, strains due to in-plane gradients are increasingly dominated by inertially induced cross-film gradients. A 0.1-μm-thick polymer film on a 100-MHz device, for example, behaves as acoustically thin ($R \ll 1$) in the glassy state ($G' \approx 10^{10}$ dyn/cm^2), but behaves as acoustically thick ($R \geq 1$) in the rubbery state ($G' \leq 10^8$ dyn/cm^2). For thinner films, the modulus range over which the film behaves as acoustically thin is wider. However, only films with $h < 20$ nm (at 100 MHz) remain

(24) Auld, B. A. *Acoustic Fields and Waves in Solids*; Wiley: New York, 1973; Vol. II, Chapter 1.

(25) Martin, S. J.; Ricco, A. J. *1991 Ultrasonics Symposium Proceedings*; IEEE: New York, 1989; pp 621–625.

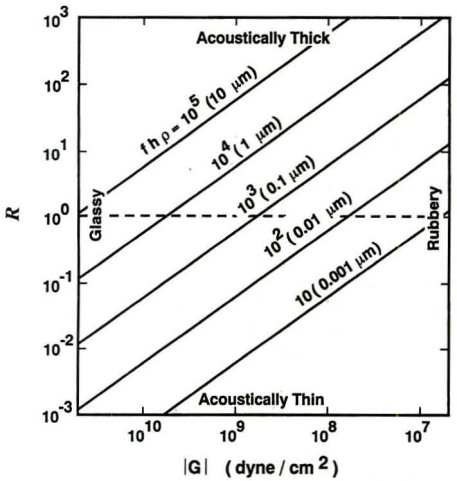

Figure 3. Ratio R of in-plane to cross-film displacement gradients vs $|G|$ at various values of $fh\rho$ (values in parentheses are film thickness for f = 100 MHz and ρ = 1 g/cm³).

thin all the way into the rubbery regime. Polymer films with $h \geq 2$ μm behave as acoustically thick even in the glassy state.

Strain Modes in Acoustically Thin Films. If the film is acoustically thin ($R \ll 1$), then u_x, u_y, and u_z are constant across the film thickness, and only gradients *in the plane* of the film arise. The SAW-induced film deformation can be decomposed into three translations (in the x-, y-, and z-directions) and three strain modes. (Non-zero $\partial u_i/\partial z$ in eq 2 leads to S_{i3} strains.) These strains generate periodic compression, tension, and bending in the film, as shown in Figure 2a, as well as transverse shear (not shown). The strain can be separated into distinct modes generated by each surface displacement component u_{i0}, as shown in Figure 4. Each strain mode arises from interfacial *stresses* imposed on the film by the wave. Since the film is acoustically thin, gradients in the direction of propagation impose stresses T_{i3} (force per area in the ith direction in planes parallel to the direction of propagation—z) on the film. This produces reaction stresses that act on the wave and perturb its propagation velocity and attenuation. An important parameter in determining the contribution of each strain mode in perturbing SAW propagation is the modulus $E^{(i)}$—the ratio of stress to strain associated with each strain mode in Figure 4. These moduli are listed in Table 1 in terms of the intrinsic elastic properties of the film, represented in terms of the Lamé constants (λ, μ) and the bulk and shear moduli (K, G). These sets of moduli are interrelated.[26]

The strain modes generated in an acoustically thin film and the associated moduli $E^{(i)}$ are as follows:

(a) The gradient in $u_x(\partial u_x/\partial z)$ generates a *transverse shear* (a change of angle in each volume element) in the plane of the film, as shown in Figure 4a. The modulus for this shear deformation mode, listed in Table 1, is $E^{(1)} = T_{13}/(2S_{13}) = G$. Thus, this mode probes only the in-plane shear modulus G of the film.

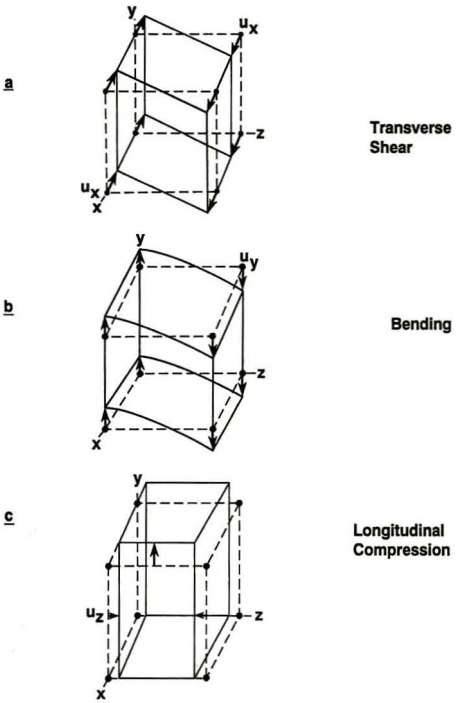

Figure 4. Strain modes generated in an acoustically thin ($R \ll 1$) film due to sinusoidal variation in the direction of propagation of (a) u_x, (b) u_y, and (c) u_z.

Table 1. Moduli Associated with Strain Modes (Figure 4) Generated by SAW in Acoustically Thin Film ($R \ll 1$)

strain mode	displacement gradient	modulus definition	modulus E_i in terms of λ and μ	modulus E_i in terms of K and G
transverse shear	$\partial u_x/\partial z$	$E^{(1)} = T_{13}/(2S_{13})$	μ	G
bending	$\partial u_y/\partial z$	$E^{(2)} = T_{23}/(2S_{23})$	≈ 0	≈ 0
longitudinal compression	$\partial u_z/\partial z$	$E^{(3)} = T_{33}/S_{33}$	$\frac{4\mu(\lambda+\mu)}{\lambda+2\mu}$	$\frac{4G(3K+G)}{3K+4G}$

(b) The gradient in $u_y(\partial u_y/\partial z)$ causes a *bending moment*[27] to be imposed on the film (Figure 4b). If we imagine the film detached from the substrate, it is apparent that it is easier to achieve displacement normal to the film (a bending motion) than in the plane of the film (a stretching motion). The modulus for this bending mode, $E^{(2)} = T_{23}/(2S_{23})$, is proportional to $(h/\Lambda)^2$ and is thus normally *negligible* in comparison with modes a and c. That is, the effect of this strain mode on SAW propagation is not generally observed.

(c) The gradient in $u_z(\partial u_z/\partial z)$ causes *longitudinal tension* (or compression) of the film along the direction of wave propagation (z), as shown in Figure 4c. Since the film is unconstrained in the y-direction, this induces a transverse

(26) Landau, L. D.; Lifshitz, E. M. *Theory of Elasticity*, 3rd ed.; Pergamon: New York, 1986; Chapter 1.

(27) Brekhovskikh, L.; Goncharov, V. *Mechanics of Continua and Wave Dynamics*; Sprinter-Verlag: New York, 1982; Section 3.4.

Table 2. SAW-Film Coupling Parameter c_i and Phase Angles ψ_i for SAW Propagation in X-Direction of ST-Cut Quartz

displacement component	$c_i = v_{io}^2/(4k_oP)$ ($\times 10^{-7}$ cm^2 s g^{-1})	ψ_i (deg)
u_x	0.013	90
u_y	1.421	90
u_z	0.615	0

strain of opposite sign in this direction (the Poisson effect): the film expands (contracts) in the y-direction due to compression (elongation) along the z-direction. No strain occurs along the x-direction since the film is adhered to the substrate surface. Consequently, a plane strain arises from this gradient with an associated elongation modulus $E^{(3)} = T_{33}/S_{33}$, given in Table 1. For soft, elastic solids having $|K| \gg |G|$, $E^{(3)} \approx 4G$. Thus, while this strain mode is tensile (compressive), the ability of the film to contract (expand) in the surface-normal direction yields an elongation modulus $E^{(3)}$ determined largely by the shear modulus G.

SAW Response from Acoustically Thin Films. Changes in SAW propagation velocity and attenuation are determined by the mechanical impedances at the substrate/film interface resulting from film translational and strain modes (see appendix C). The impedance associated with each film *translation* is $j\omega\rho h$ and with each *strain mode* is $-j\omega hE^{(i)}/v_o^2$, where $E^{(i)}$ are taken from Table 1. Thus, from a perturbation analysis (appendix C), the change in SAW propagation arising from acoustically thin films, denoted here as model 1, is

model 1:

$$\frac{\Delta\gamma}{k_o} = \frac{\Delta\alpha}{k_o} - j\frac{\Delta v}{v_o} = j\omega h \sum_{i=1}^{3} c_i\left(\rho - \frac{E^{(i)}}{v_o^2}\right) \qquad (5)$$

where the SAW-film coupling parameter $c_i = v_{io}^2/(4k_oP)$: v_{io} denotes the surface particle velocity (related to surface displacements by $v_{io} = j\omega u_{io}$) in each direction, and P is the SAW power density (power flow per beam width). The c_i parameters, given in Table 2 for X-propagation in the ST-cut of quartz,[28] are determined for SAW propagation in the uncoated substrate and are assumed to be unchanged by the film.[23]

Each displacement component contributes two terms to eq 5: one, proportional to ρ, arises from the *kinetic* energy associated with film translation; another, proportional to $E^{(i)}$, arises from the *potential* energy associated with film strains (modes shown in Figure 4). The kinetic contribution causes a SAW velocity decrease in proportion to film mass per area (ρh)—the mass loading contribution. The relative *kinetic* contribution from each displacement component is proportional to the SAW film coupling parameter c_i. From Table 2, the u_y and u_z displacements make a significant kinetic contribution to SAW propagation, while the u_x contribution is negligible for X-propagation in ST-quartz.

From eq 5, the relative importance of each film *strain* mode in perturbing SAW propagation is determined by the product $c_iE^{(i)}$. We note from Tables 1 and 2 that *only the u_z component has both a significant displacement amplitude (c_3) and associated modulus ($E^{(3)}$) to make a significant elastic contribution to SAW propagation.* Thus, for acoustically thin films, one need consider only the strain mode illustrated in Figure 4c, generating tension and compression in the direction of propagation (with a corresponding expansion and contraction in film thickness) to account for (visco)elastic contributions to velocity and attenuation.

Equating real and imaginary parts of eq 5 yields velocity and attenuation changes resulting from the SAW/film interaction. With *elastic* films, the intrinsic elastic moduli are real, resulting in real $E^{(i)}$ and imaginary $\Delta\gamma/k_o$, so that $\Delta\alpha/k_o = 0$. Substituting the $E^{(i)}$ expressions written in terms of the Lamé constants (λ, μ) from Table 1 into eq 5 yields the Tiersten (Wohltjen) formula[14]

$$\frac{\Delta v}{v_o} = -\omega h\left[c_1\left(\rho - \frac{\mu}{v_o^2}\right) + c_2\rho + c_3\left(\rho - \frac{4\mu}{v_o^2}\frac{\lambda+\mu}{\lambda+2\mu}\right)\right] \qquad (6)$$

which gives the SAW velocity change contributed by an acoustically thin ($R \ll 1$), elastic ($K'' = G'' = 0$) film.

While eq 6 does not apply to *viscoelastic* films, the velocity and attenuation arising from acoustically thin, viscoelastic films can be determined from eq 5 by inserting complex moduli (e.g., K and G) into the $E^{(i)}$ expressions. A simplification can be made in eq 5 by noting that the bulk modulus in soft, elastic solids is typically much larger than the shear modulus ($|K| \gg |G|$), so that $E^{(3)} \approx 4G$. The velocity and attenuation changes arising from an acoustically thin ($R \ll 1$) *viscoelastic* film (written in terms of the commonly reported polymer properties K and G) are then

$$\frac{\Delta v}{v_o} \cong -\omega h\left((c_1 + c_2 + c_3)\rho - \frac{(c_1 + 4c_3)}{v_o^2}G'\right) \qquad (7a)$$

$$\frac{\Delta\alpha}{k_o} \cong \frac{\omega h}{v_o^2}(c_1 + 4c_3)G'' \qquad (7b)$$

where c_1–c_3 are as listed in Table 2. The first point of departure from the Tiersten model is that viscoelastic films cause an *attenuation response* in addition to a velocity response.

Reference to Figure 3 shows that caution must be exercised in applying eqs 5–7 to polymer-coated SAW devices. Even polymer films with $h \ll \Lambda$ have only a limited range (glassy regime plus part of the transition region) in which they actually behave as *acoustically* thin. In the regime where in-plane gradients dominate and eqs 5–7 apply, the SAW response depends in a simple way on the intrinsic polymer shear modulus G: for constant ρ, velocity changes correspond to changes in G' ($\Delta G'$) and attenuation changes reflect changes in G'' ($\Delta G''$). (It should be noted that the *additional* SAW response due to *changes* in film properties is evaluated using eqs 7a and 7b where the terms ρ, G', and G'' are replaced with the change terms $\Delta\rho$, $\Delta G'$, and $\Delta G''$.)

If the glass transition is defined as the temperature corresponding to a maximum in the intrinsic shear loss modulus (G''), then eq 7b indicates that a peak in $\Delta\alpha/k_o$ signals the glass transition at the SAW operating frequency. However, the rapid decrease in G' that accompanies the glass transition

(28) Slobodnik, A. J.; Conway, E. D.; Delmonico, R. T. *Microwave Acoustics Handbook, Vol 1A, Surface Wave Velocities*; National Technical Information Service: Washington, DC, 1973.

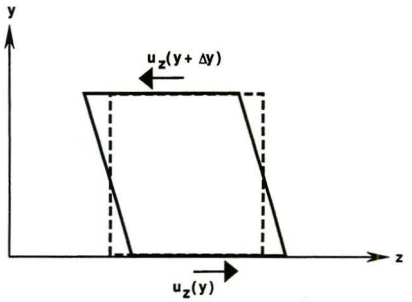

Figure 5. Inertial lag of the upper film region with respect to the lower "driven" surface leads to a cross-film gradient in u_z, generating shear deformation in the film.

causes all but the thinnest ($h < 20$ nm) films to behave as acoustically thick precisely at this point. As will be shown below, acoustically thick films exhibit attenuation peaks at points *not* coincident with the intrinsic loss maximum, making identification of T_g problematical with a high-frequency SAW device.

Strain Modes in Acoustically Thick Films. Neglecting the SAW-induced in-plane gradients for the moment, we focus on a portion of the film that is small in lateral extent compared with the SAW wavelength. As the wave passes a fixed point, the lower surface of the film oscillates laterally in response to the sinusoidal SAW surface displacement (Figure 5). If the film is acoustically thick ($R \geq 1$), the upper portions of the film tend to lag behind the driven substrate/film interface, inducing strains across the thickness of the film. This *inertial deformation* of the film, resulting in nonuniform displacement across the film (i.e., u_i depend on y) leads to nonzero gradients in the direction *normal* to the film surface (i.e., nonzero $\partial u_i/\partial y$) and the generation of S_{i2} strains. Since cross-film gradients arise from inertial deformation, they are strongly dependent upon film properties and operating frequency, as opposed to in-plane gradients that are imposed by wave periodicity. The effect of these cross-film or inertial strains on SAW velocity and attenuation are *not* included in eqs 5–7.

Dynamic Cross-Film Behavior. The displacement in an acoustically thick ($R \geq 1$) film is calculated in appendix D as:

$$\tilde{\mathbf{u}}(y,z,t) = e^{j(\omega t - kz)} \sum_{i=1}^{3} u_{io} e^{j\psi_i} \left(\frac{\cosh[j\beta_i(y-h)]}{\cosh(j\beta_i h)} \right) \hat{x}_i \quad (8a)$$

where

$$\beta_i = \omega \left(\frac{\rho - E^{(i)}/v_o^2}{M_i} \right)^{1/2} \quad (8b)$$

with $M_1 = M_3 = G$, while $M_2 = K$; ψ_i and $E^{(i)}$ values are as given in Tables 1 and 2. The β_i factors in eqs 8 represent propagation constants for waves with polarization direction x_i propagating *across the film* (Figure 6): β_1 and β_3 are associated with shear waves generated by the in-plane surface displacements u_{xo} and u_{zo}, respectively; β_2 is associated with a compressional wave generated by the surface-normal

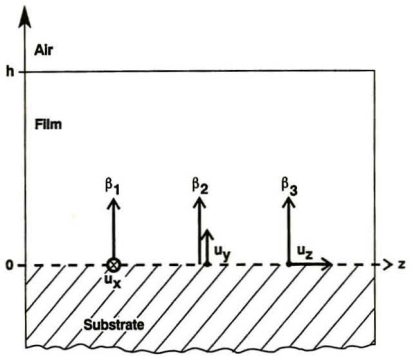

Figure 6. Displacement in the film is a superposition of waves generated at the substrate/film interface by the surface displacements u_i, and radiated across the film with propagation factors β_i: the surface-normal component u_{yo} generates compressional waves while the in-plane components (u_{xo}, u_{zo}) generate shear waves.

displacement u_{yo}. Thus, displacement in the film arises from a *superposition* of waves generated at the substrate/film interface by the surface displacements and radiated into the film (Figure 6).

As indicated in appendix D, the perturbations to SAW velocity and attenuation caused by the film are related to the mechanical impedances experienced by the surface displacement components in deforming the film. The upper film surface reflects the radiated waves downward so that the mechanical impedance seen at the substrate/film interface is dependent upon the phase shift and attenuation undergone by the waves in propagating across the film. Consequently, a distributed model is used for the film in which the impedance at the lower film surface depends upon the nature of the *interference* between the waves generated at the lower film surface and those reflected from the upper (film/air) surface.

Film interference for each polarization (displacement direction x_i) is dependent upon the acoustic phase shift ϕ_i across the film and the attenuation or intrinsic lossiness r_i. The phase shift for each polarization is $\phi_i = \mathrm{Re}\{\beta_i h\}$, where Re{} denotes the real part of the complex expression. For acoustically thick *elastic* films, $\phi_1 \cong \phi_3 \cong \omega h(\rho/G')^{1/2}$ and $\phi_2 \cong \omega h(\rho/K')^{1/2}$.

Since the magnitude of the bulk modulus K remains in the vicinity of 10^{10} dyn/cm^2 in both glassy and rubbery states, ϕ_2 remains small ($<\pi/2$) for typical polymer thicknesses: $h <$ 1 μm. Thus, *polymer films remain acoustically thin with regard to compressive displacement* (u_{yo}) applied to the lower film surface. Consequently, $u_y(y)$ can be regarded as nearly constant across the film so that the surface displacement component u_{yo} simply causes a vertical translation of the film.

Since G' can be as low as 10^7–10^8 dyn/cm^2 in rubbery polymer films, with ϕ_1 and ϕ_3 reaching $\pi/2$ for films as thin as 80 nm (at 100 MHz), *films do not remain acoustically thin with regard to shear displacements* applied to the lower film surface. Since $c_3 \gg c_1$, for an X-propagation SAW in ST-cut quartz, the phase shift ϕ_3 associated with the z-polarized shear wave is the most important in determining the response with acoustically thick films:

$$\phi_3 \equiv \mathrm{Re}\{\beta_3 h\} \cong \frac{\omega h[(a^2 + b^2)^{1/2} + a]^{1/2}}{2^{1/2}|G|} \tag{9}$$

with $a = (\rho G' - 4|G|^2/v_o^2)$ and $b = \rho G''$. Equation 9 allows the critical ϕ_3 phase shift to be calculated in terms of the intrinsic film properties.

The film loss parameter $r_i \equiv -\mathrm{Im}(\beta_i)/\mathrm{Re}(\beta_i)$ describes the intrinsic lossiness of the film as experienced by the x_i-polarized wave. This parameter, a ratio of power dissipation to energy storage, is analogous to a loss tangent, taking on values between 0 and 1 for all viscoelastic materials: $r_i = 0$ for an elastic film and increases toward 1 for purely viscous films. For the z-polarized shear wave

$$r_3 \equiv -\frac{\mathrm{Im}(\beta_3)}{\mathrm{Re}(\beta_3)} \cong \left[\frac{(a^2 + b^2)^{1/2} - a}{(a^2 + b^2)^{1/2} + a}\right]^{1/2} \tag{10}$$

Figure 7 shows the shear displacement profile at the point of maximum substrate surface excursion for various values of the shear wave phase shift ϕ_3 and $r_3 = 0.2$. If the film coating is rigid (e.g., a glassy polymer), $\phi_3 \approx 0$ (curve a) and the entire film moves synchronously with the surface. Since the shear displacement is uniform across the film, no elastic energy is stored or dissipated due to inertial effects. As ϕ_3 increases, the variation in shear displacement across the film increases. In curve b, where $\phi_3 = \pi/4$, the upper film displacement "overshoots" the lower film surface. When the film phase shift reaches $\pi/2$ (curve c), a condition of *film resonance* is reached, causing maximum coupling of acoustic energy from the SAW to the film. As ϕ_3 surpasses $\pi/2$ (curve d), the upper and lower film surfaces go from an in-phase to an out-of-phase condition. This change in film dynamics with ϕ_3 has a profound effect on device response. Similar dynamic behavior occurs with thickness-shear mode resonators coated with polymer films.[29]

SAW Response with Acoustically Thick Films. The dynamic film behavior outlined above influences the coupling of acoustic energy from the SAW into the film and, hence, the propagation velocity and attenuation. The combined influences of in-plane and surface-normal gradients on SAW velocity and attenuation are calculated in appendix D. The resulting perturbational formula for the SAW velocity and attenuation changes, applying to either acoustically thin or thick viscoelastic films, and denoted herein as model 2 is

model 2:

$$\frac{\Delta\gamma}{k_o} = \frac{\Delta\alpha}{k_o} - j\frac{\Delta v}{v_o} = \sum_{i=1}^{3} \frac{c_i\beta_i M_i}{\omega} \tanh(j\beta_i h) \tag{11}$$

Calculating the sum in eq 11 and equating real and imaginary parts determines $\Delta\alpha/k_o$ and $\Delta v/v_o$ explicitly.

Model Predictions. For acoustically thin films, $|\beta_i h| \ll 1$ for $i = 1$, 2, or 3 so that $\tanh(j\beta_i h) \cong j\beta_i h$, resulting in

$$\frac{\beta_i M_i}{\omega} \tanh(j\beta_i h) \rightarrow j\omega h\left(\rho - \frac{E^{(i)}}{v_o^2}\right) \tag{12}$$

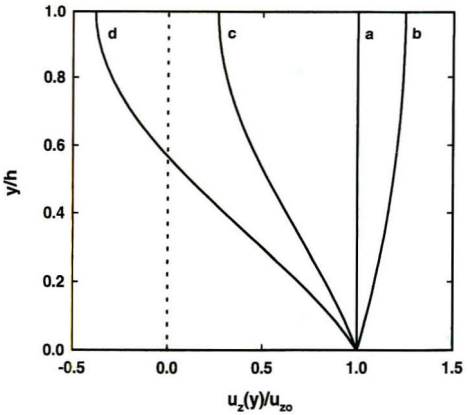

Figure 7. Shear displacement across an acoustically thick ($R \geq 1$) film arising from inertial deformation for ϕ_3 values (a) 0, (b) $\pi/4$, (c) $\pi/2$, and (d) $3\pi/4$.

Thus, for acoustically thin films in which surface-normal gradients vanish, model 2 (eq 11) reduces to model 1 (eq 5), as required.

For acoustically thick, *elastic* films, β_i are real and $\tanh(j\beta_i h) = j\tan(\phi_i)$. In this case, the sum in eq 11 is imaginary, so that $\Delta\alpha/k_o = 0$, as expected. The behavior of $\Delta v/v_o$ is more interesting: when $\phi_i = n\pi/2$ (n = 1, 3, 5, ...), then $\tan(\phi_i)$ "blows up" causing a large negative excursion in $\Delta v/v_o$ for $\phi_i = n\pi/2^-$ and a large positive excursion for $\phi_i = n\pi/2^+$. This is a consequence of *film resonance*, occurring when the shear stresses applied to the lower film surface interfere constructively with those reflected from the upper film surface. Concurrently, the shear particle velocities are interfering destructively, so that the surface mechanical impedance Z_i (the ratio of stress to particle velocity) becomes infinite. Of course, the films of interest in this study are viscoelastic, exhibiting complex β_i; this leads to imperfect interference so that $\Delta v/v_o$ and $\Delta\alpha/k_o$ remain finite. Nonetheless, dramatic responses are observed whenever film resonances are encountered.

As described previously, the compressional wave phase shift $\phi_2 \ll \pi/2$ in all polymer states, so *compressional wave resonances should not be observed.* The surface mechanical impedance experienced by the u_y component reduces to $j\omega\rho h$; thus, only the *mass* of the film is sensed by the surface-normal component.

The shear wave phase shifts ϕ_1 and ϕ_3 may easily reach $\pi/2$ and elicit film resonant responses. Since $c_3 \gg c_1$ when an ST-cut quartz substrate is used, *the z-polarized shear wave resonance dominates the SAW viscoelastic response with an acoustically thick film.* Thus, the effect of shear wave film interference on the SAW response is described by the $\tanh(j\beta_3 h)$ term in eq 11. Figure 8 shows the contributions of this term to SAW velocity and attenuation vs ϕ_3 for several values of the film loss parameter, r_3. The parameter ϕ_3 may be considered a *normalized film thickness.* The SAW velocity decreases linearly with film thickness for $\phi_3 \leq 0.2\pi$ at a rate

(29) Martin, S. J.; Frye, G. C. *1991 Ultrasonics Symposium Proceedings;* IEEE: New York, 1991; pp 393–398.

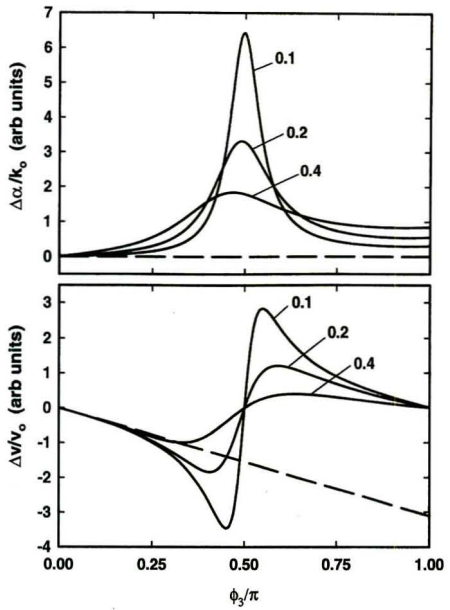

Figure 8. Contributions to SAW velocity and attenuation vs the shear wave phase shift ϕ_3 for several values of the film loss parameter r_3. The dashed line is predicted from the Tiersten[14] (Wohltjen) formula (eq 6).

consistent with the thin-film prediction (dashed line calculated from eq 6, independent of film loss r_3). As ϕ_3 surpasses 0.2π, an *excess* velocity response arises due to shear wave interference effects. Thus, interference affects device response for phase shifts well below $\pi/2$. The size of this excess response varies inversely with the film loss parameter r_3. For $\phi_3 \ll 0.5\pi$, SAW attenuation increases linearly with film thickness and is proportional to G'', as predicted by eq 7b.

In Figure 8, a pronounced response occurs at $\phi_3 = \pi/2$: attenuation goes through a maximum while velocity undergoes an upward transition. These responses are easily confused with the intrinsic relaxation response occurring at the glass transition—a monotonic decrease in G' and a peak in G''. However, a device with an acoustically thin film, whose response tracks these intrinsic film changes, should exhibit a peak in attenuation coincident with a *velocity decrease* (rather than increase). The responses in Figure 8 are due to shear wave interference effects in the film. A shear wave *resonant response* at $\phi_3 = \pi/2$ is most pronounced with low-loss films ($r_3 \ll 1$) and becomes damped as r_3 approaches unity. Off-resonant attenuation increases *proportionally* with film loss, while resonant attenuation is *inversely* dependent upon film loss. In the ideal case of an elastic film, a delta function attenuation response is predicted: attenuation is zero for $\phi_3 \neq \pi/2$, but becomes infinite for $\phi_3 = \pi/2$.

The SAW resonant response predicted vs ϕ_3 can be related to the dynamic film behavior outlined in Figure 7. As ϕ_3 passes $\pi/2$, film motion at the upper surface goes from an in-phase to an out-of-phase condition (with respect to the lower film surface). This coincides with the sigmoidal upward

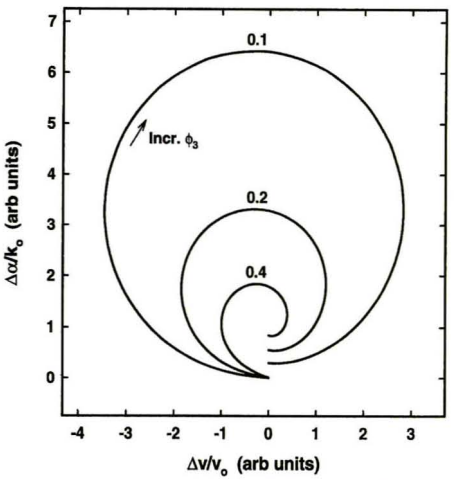

Figure 9. Parametric plot of attenuation changes vs velocity changes as ϕ_3 varies from 0 to π for several values of the film loss parameter r_3.

transition predicted in the SAW velocity response. This phase transition results in a smaller particle excursion in the upper regions of the film, diminishing the kinetic contribution to velocity response. That is, film mass loading is diminished as ϕ_3 exceeds $\pi/2$.

The resonant response at $\phi_3 = \pi/2$ is predicted to recur at $3\pi/2, 5\pi/2$, etc., constituting *harmonics* of the fundamental film resonance. Since the resonance damping varies as $r_3\phi_3$, the harmonic resonant responses become less pronounced. Ballantine[30] has reported observing harmonic film resonances up to $n = 9$; however, results presented in the Results and Discussion section of this paper cast doubt on this interpretation.

Parametric Representation. Frequently, the representation of velocity and attenuation perturbations is simplified by using a parametric representation in which attenuation changes are plotted vs velocity changes (or vice versa) while some independent parameter is varied.[25] Since velocity and attenuation were shown (appendices C and D) to be related to the components of a complex surface mechanical impedance, this representation is equivalent to a Nyquist[31] or Cole-Cole[32] plot in which the imaginary component of impedance is plotted vs the real component (frequency is typically the varying parameter). Figure 9 shows a parametric plot of attenuation vs velocity contributions arising from the $\tanh(j\beta_3 h)$ term of eq 11 as ϕ_3 varies from 0 to π for several values of the film loss parameter r_3. When only ϕ_3 is varied (r_3 fixed), the locus of $(\Delta v/v_o, \Delta\alpha/k_o)$ points generated by film resonance forms a spiral. The curvature and pitch of the spiral are proportional to r_3; a near-circle is formed when r_3 is small. The utility of the parametric plot in comparing data obtained by varying film parameters in different ways is illustrated in the Results and Discussion section.

(30) Ballantine, D. S. *Anal. Chem.* **1992**, *64*, 3069–3076.
(31) Frederick, D. K.; Carlson, A. B. *Linear Systems in Communication and Control*; Wiley: New York, 1971; Chapter 11.
(32) Cole, R. H.; Cole, K. S. *J. Chem. Phys.* **1941**, *9*, 341.

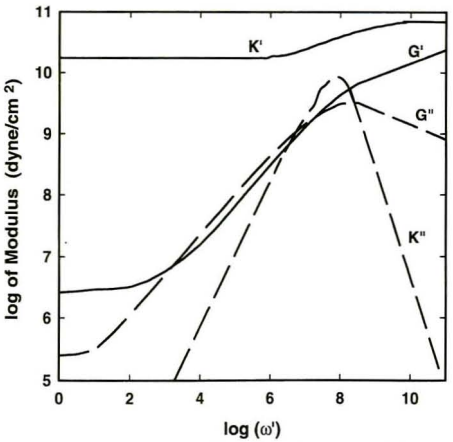

Figure 10. Storage (′) and loss (″) components of the bulk[33] (*K*) and shear[34] (*G*) elastic moduli for polyisobutylene (av molecular weight = 1.56×10^6) vs log(ω′).

Dependence of Film Properties on Temperature and Vapor Absorption. A number of film parameters must be considered in modeling the response of polymer-coated SAW devices to temperature changes or vapor absorption. These include changes in (1) shear modulus G (most important), (2) bulk modulus K, (3) film thickness h, and (4) mass density ρ. In addition, the temperature behavior of the substrate must be included.

Figure 10 illustrates how a typical polymer's viscoelastic properties, i.e., storage and loss components of the bulk[33] and shear[34] moduli, vary with the apparent probe frequency ω' at fixed temperature T_o. At high probe frequencies, the storage components (K', G') are maximum and the polymer is in the glassy state. As ω' decreases, a polymer *relaxation* or *glass transition* is exhibited by the intrinsic elastic properties: K' and G' decrease monotonically, while K'' and G'' go through a maximum. For $\omega' \leq 2$, the polymer is in the rubbery state. The small changes that occur in K' in comparison with G' and the fact that SAW response is inherently less sensitive to K than G in the transition regime result in SAW responses arising largely from changes in G rather than changes in K.

From the time–temperature superposition principle,[35] changes in the viscoelastic properties with temperature or vapor absorption can be expressed as a translation a_T in the polymer relaxation time or the apparent probe frequency ω':

$$\log(\omega') = \log(\omega) + \log(a_T) \tag{13}$$

Thus, the curves of Figure 10 may be considered "master curves" that can be used (vide infra) to describe the moduli as either a function of frequency, temperature, or vapor absorption.

In addition to causing a horizontal translation in ω', temperature changes lead to a slight vertical translation[35] in modulus values due to (1) inherent modulus dependence on absolute temperature and (2) changes in polymer chain density. (Film density is inversely related to film thickness h.) To account for these effects, moduli obtained by translation from reference (h_o, T_o) to (h,T) must be multiplied by the factor $(h_oT)/(hT_o)$.

We now introduce a model in which the shift factor a_T is expressed in terms of a polymer free volume F, analogous to the derivation of the WLF equation,[36] but modified to include the effects of vapor absorption. Free volume is volume *not* occupied by polymer molecules, present as voids of molecular dimension, that enhances polymer chain segmental mobility. The shift factor a_T is given by the generalized Doolittle equation:[37]

$$\log(a_T) = \frac{B}{2.303}\left(\frac{1}{F} - \frac{1}{F_o}\right) \tag{14}$$

where B is a constant (taken as unity); F is the polymer free volume at any temperature or vapor concentration (T, C), while F_o is the free volume of the *pure* ($C = 0$) polymer at some reference temperature (T_o,0). We develop this argument in two steps: first, the effects of temperature in the absence of vapor and, second, the additional effects of plasticization and swelling of the polymer film by the vapor.

Temperature Response. As polymer temperature increases above the "static" glass transition temperature $T_g^{(0)}$, polymer volume expands nearly linearly due to the creation of additional free volume. Due to mechanical constraint in the plane of the film by the substrate, however, volume expansion of the film leads to a combination of increased film thickness and static in-plane compressive stress. The parameter $\xi = 3K'/(3K' + 4G')$, given by Bartley and Dominguez,[38] describes the extent to which free volume addition is converted to changes in film thickness. For rubbery films, $K' \gg G'$, so that $\xi \cong 1$ and film expansion accounts for all free volume addition. For glassy films, $K' \approx G'$, so that $\xi < 1$ and free volume accrual is diminished by generation of in-plane compressive stresses. When operating at temperatures above $T_g^{(0)}$, however, the film is rubbery with regard to static stresses (but may still be in the glassy regime at the SAW frequency). Therefore, setting $\xi \equiv 1$ is reasonable and, as demonstrated below, gives an acceptable fit to the data.

For temperatures above $T_g^{(0)}$, the change in free volume with temperature varies as[20]

$$F = F_o + \alpha_f(T - T_o) \tag{15}$$

where F_o is the free volume at the reference temperature[39] T_o, and α_f is the polymer (volume) thermal expansion coefficient.

Substituting eq 15 into eqs 13 and 14 gives the translation in ω', determining the rate of film softening with temperature. Increases in free volume cause a decrease in ω', leading to changes in K and G determined from the master curves of

(33) Marvin, R. S.; Aldrich, R.; Sack, H. S. *J. Appl. Phys.* **1954**, *25* (10), 1213–1218.
(34) Ferry, J. D. *Viscoelastic Properties of Polymers*, 3rd ed.; Wiley: New York, 1980; Appendix D.
(35) Aklonis, J. J.; MacKnight, W. J. *Introduction to Polymer Viscoelasticity*; Wiley: New York, 1983, Chapter 3.
(36) Williams, M. L.; Landel, R. F.; Ferry, J. D. *J. Am. Chem. Soc.* **1955**, *77*, 3701.
(37) Doolittle, A. K.; Doolittle, D. B. *J. Appl. Phys.* **1959**, *31*, 1164.
(38) Bartley, D. L.; Dominguez, D. D. *Anal. Chem.* **1990**, *62*, 1649–1656.
(39) $F_o = F_g + \alpha_f(T_o - T_g^{(0)})$, where F_g is the free volume at the glass transition temperature $T_g^{(0)}$ with no in-plane stresses.

Figure 10. The most pronounced effect is a glass-to-rubber transition in polymer properties, signaled by a rapid decrease in K' and G'.

The film thickness h changes due to thermal expansion:

$$h(T) = h_o[1 + \alpha_f(T - T_o)] \tag{16}$$

where h_o is the film thickness at the reference temperature T_o. Since the total mass of the film ($h\rho$) is conserved, thermal expansion causes a decrease in film mass density (ρ):

$$\rho(T) = \frac{\rho_o h_o}{h(T)} = \frac{\rho_o}{1 + \alpha_f(T - T_o)} \tag{17}$$

Vapor Response. The absorption of vapor molecules, presumed to be of low molecular weight in comparison with the polymer and molecularly dispersed, causes dilution of the polymer. The diluent molecules lower the effective viscosity and reduce T_g and $T_g^{(0)}$. The effect of the diluent on polymer viscoelastic properties at fixed temperature may be thought to arise from the addition of free volume, in proportion to the volume fraction of diluent:[20]

$$F(T,V_1) = F(T) + \chi V_1 \tag{18}$$

where $F(T)$ is the free volume of the pure polymer (without diluent as in eq 15), χ is an empirically determined plasticizing parameter,[20] and V_1 is the volume fraction of absorbed vapor: $V_1 = CV/(1 + CV)$, where C is the concentration (mol of sorbed vapor/mL of polymer) and V is the specific volume (ml/mol) of absorbed vapor.

The effect of vapor absorption on polymer elastic properties is determined from eqs 13, 14, and 18. As free volume increases with concentration C, the translation factor a_T increases; this leads to a decrease in K and G, according to the master curves of Figure 10.

Film thickness and density vary with the concentration of absorbed species as

$$h(C) = h_o(1 + CV) \tag{19a}$$

$$\rho(C) = \frac{\rho_o + Cm}{1 + CV} \tag{19b}$$

where ρ_o is the pure polymer density (at $C = 0$) and m is the specific mass (g/mol) of the absorbed species.

Combining eqs 14, 15, and 18 gives an equation for the shift factor a_T, analogous to the WLF equation, but including the effects of both temperature changes and vapor absorption:

$$\log(a_T) = -\frac{B}{2.303\,F_o}\left(\frac{\alpha_f(T - T_o) + \chi V_1}{F_o + \alpha_f(T - T_o) + \chi V_1}\right) \tag{20}$$

The free volume treatment above indicates the interchangeability of temperature and vapor absorption in determining film elastic properties.[12,40]

(40) Grate, J. W. *Sensing Glass Transitions in Thin Polymer Films on Acoustic Wave Microsensors;* ASTM Special Technical Publication on Assignment of the Glass Transition; ASTM: Philadelphia, in press.

EXPERIMENTAL SECTION

The experiments consist of measuring the response of polymer-coated SAW devices during temperature changes and during vapor absorption by the polymer.

SAW Devices. The SAW devices used in this study consist of an ST-cut quartz substrate with two photolithographically defined Cr/Au (30/200 nm) transducers separated by a path length (transducer center separation) of 7.2 mm. The transducers each consist of 50 finger-pairs of interdigitated electrodes, with periodicity $\Lambda = 32\ \mu$m (8-μm lines and spaces) for a center frequency of 97 MHz. Devices were bonded into flatpacks; electrical connections were made between flatpack feedthroughs and transducer bonding pads with ultrasonically bonded 75-μm Au wires.

Electronic Instrumentation. Due to the large attenuations encountered in these studies, the two-port oscillator circuit normally used to instrument a SAW sensor would not sustain oscillation over all experimental conditions. Thus, the device was instrumented in a phase–lock–loop configuration: a signal generator (Hewlett-Packard 8656B) input a signal to the input transducer (output terminated in 50Ω) while a vector voltmeter (Hewlett-Packard 8508A) monitored changes in amplitude and phase between input and output ports. A computer monitored these vector voltmeter outputs, controlling the signal generator frequency to maintain constant phase between input and output. Changes in SAW velocity were determined from the changes in frequency required to maintain constant phase. When the coating covers the entire SAW propagation path and the external (electrical) phase shift is small compared with the internal (acoustic) phase shift, then $\Delta f/f_o \cong \Delta v/v_o$. Changes in SAW attenuation $\Delta\alpha$ were determined from the changes in signal amplitude (ΔL, dB) measured between input and output ports: $\Delta\alpha/k_o = \Delta L/(54.6N_\Lambda)$, where k_o is the acoustic wavenumber ($k_o = 2\pi/\Lambda = 1960\ \text{cm}^{-1}$) and N_Λ is the acoustic path length (225 wavelengths).

Polymer Coating. Polyisobutylene (PIB) (Aldrich; MW = 380 000, density 0.92 g/cm^3) coatings were prepared by spin casting at 2000 rpm for 30 s from solutions in chloroform. The solution concentration was varied from 2.0% to 3.5% (by weight) to vary the film thickness of the resulting coatings. Film thickness measurements were attempted by profilometry (Dektak 3030). However, the softness of the films resulted in stylus penetration into the film and erroneously low readings. Therefore, film thicknesses were obtained by measuring changes in transducer center frequency for chilled SAW devices (–10 °C) before and after film deposition. SAW velocity changes were determined from the changes in the transducer center frequency, measured using an HP8751A network analyzer, from which film thickness was estimated. For films chilled into the glassy regime and behaving as acoustically thin, eq 7a relates $\Delta v/v_o$ to film thickness h. Using $G' = 10^{10}$ dyn/cm^2 and $\rho = 0.92$ g/cm^3 for PIB (–10 °C, 97 MHz), mass loading accounts for 88% of the velocity shift, while film elasticity accounts for 12%.

Temperature Measurement. Temperature ramps were obtained by placing the test case containing the SAW device in an environmental chamber whose temperature was under computer control. A dry N_2 purge was maintained over the device during the 4-h temperature ramps.

Vapor Measurement. Vapor isotherms were obtained using a test case with gas inlet and outlet ports and passing a gas stream across the device maintained at constant temperature (20 °C). A computer-controlled vapor test system varied the vapor concentration by varying the relative flow rates of a nitrogen carrier stream saturated with the vapor (by passage through a bubbler) with a nitrogen mix down stream.[41] The vapor partial pressure p was varied from 0 to 97% of the saturation vapor pressure (p_o) at 20 °C and then back to 0 over a 2-h interval.

To determine the concentration of vapor absorbed into the polymer film, an identical PIB film was deposited on a 5-MHz quartz crystal microbalance (QCM, Maxtek Inc., Torrance, CA). The coated QCM was placed in the gas stream with the coated SAW device, and changes in its resonant frequency were monitored during the vapor isotherm. Due to its much lower frequency, the 5-MHz QCM responds as a nearly ideal gravimetric detector for this range of film thicknesses.[29] Thus, changes in resonant frequency indicated the mass of vapor absorbed into the film, from which absorbed vapor concentration was determined.

Calculations. SAW velocity and attenuation responses were calculated from model 1 (eq 5) and model 2 (eq 11), implemented as a computer program for IBM-compatible computers written in HT Basic (TransEra, Provo, UT). This language conveniently handles complex variables and functions of complex variables, e.g., $\tanh(j\beta_i h)$ in eq 11.

RESULTS AND DISCUSSION

Temperature Response. *PIB-Coated SAW Temperature Measurements.* Figure 11 shows velocity and attenuation measurements (points[42]) vs temperature for an uncoated 97-MHz SAW device and one coated with a 0.73-μm PIB film. Velocity and attenuation changes are referenced to values measured at the lowest temperature with the film. As temperature increases, the quartz substrate contributes a slight increase in attenuation and a significant change in wave velocity (velocity varies parabolically with temperature in ST-cut quartz with a turnover temperature of 20 °C[43]). Since the coated device response is due to both the film and the substrate, the *difference* in responses is attributable to the film overlay. Below 80 °C, the film coating causes attenuation to increase and velocity to decrease more rapidly with temperature than for the uncoated device; this is due to changes occurring in the intrinsic polymer properties (G, K, ρ) as well as film swelling (h). At high temperatures, the response exhibits the characteristic signature for a resonance: a peak in attenuation along with a sigmoidal increase in velocity. This response is very similar to that calculated vs ϕ_3 in Figure 8 (for $r_3 = 0.2$), suggesting the shear wave generated by u_z is resonating across the film thickness.

Figure 11 also shows responses calculated from model 1 (dashed line) and model 2 (solid line) using temperature-dependent film parameters and adding in the measured substrate contributions. The components of G and K were determined from the master curves of Figure 10; ω' values

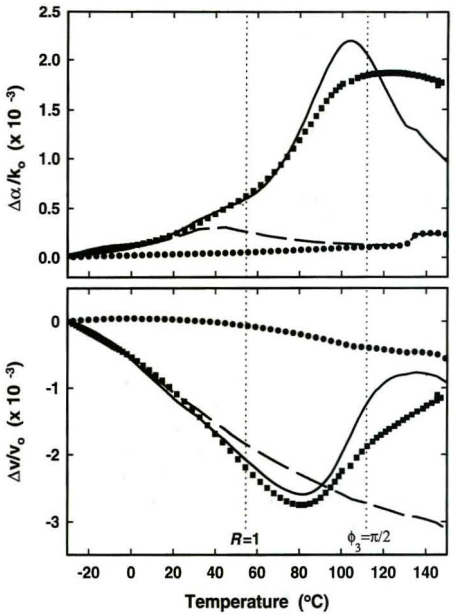

Figure 11. Velocity and attenuation measured (points) and calculated (model 1, dashed lines; model 2, solid lines) vs temperature for a 97-MHz SAW device: (●) uncoated, and (■) coated with a 0.73 μm-thick polyisobutylene film. Vertical lines indicate transition point (R = 1) between acoustically thin and thick regimes, and the center of film resonance ($\phi_3 = \pi/2$).

Table 3. Model Parameters for Polyisobutylene[48]

parameter	value
$T_g^{(0)}$	205 K
T_o	293 K
F_o	0.050
α_f	2.5×10^{-4} (°C)$^{-1}$
ρ_o	0.92 g/cm^3

were determined from eqs 13–15 using the film parameters (T_o, F_o, α_f) given in Table 3. The temperature-dependent film thickness $h(T)$ and density $\rho(T)$ were calculated from eqs 16 and 17 using α_f and ρ_o values from Table 3 and h_o = 0.73 μm. Model 1 accounts for only in-plane displacement gradients (acoustically thin assumption), while model 2 includes both in-plane and cross-film gradients (thin or thick). From eq 4, R = 1 at 55 °C, indicating the transition from acoustically thin (T < 55 °C) to acoustically thick (T > 55 °C) behavior. This transition point is seen to be a good estimate of where model 1 breaks down. In the acoustically thin regime, models 1 and 2 are both valid and adequately fit the attenuation and velocity changes with temperature. The Tiersten[14] formula, eq 6, describes $\Delta v/v_o$ in this regime but does not account for the attenuation observed. The peak in $\Delta\alpha/k_o$ at 40 °C predicted by model 1 and followed by the data below 40 °C is due to a peak in the intrinsic loss modulus G'' (Figure 10).

At temperatures above 55 °C, the film behaves as acoustically thick, and only model 2 is expected to apply. The model 2 predictions (solid lines)—an attenuation peak at 104 °C and the upturn in velocity beginning at 80 °C—are in

(41) Frye, G. C.; Martin, S. J. *Appl. Spectrosc. Rev.* **1991**, *26* (1&2), 73–149.
(42) Only selected data points are shown; data are available from the authors on request.
(43) Morgan, D. P. *Surface-Wave Devices for Signal Processing;* Elsevier: New York, 1985; Section 6.4.

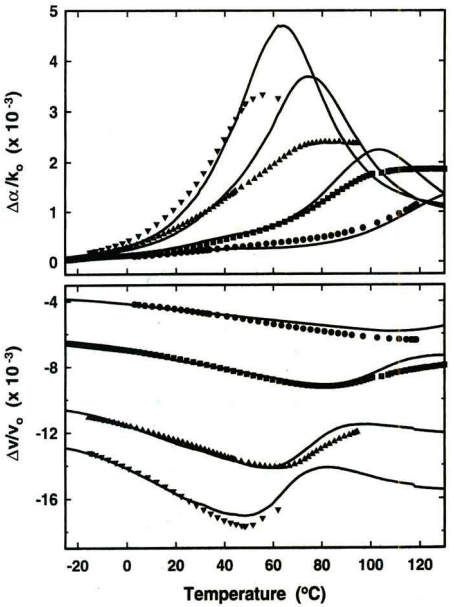

Figure 12. Velocity and attenuation changes measured (points) and calculated (model 2, lines) vs temperature for 97-MHz SAW devices coated with polyisobutylene films of thickness: (●) 0.44, (■) 0.73, (▲) 1.18, and (▼) 1.43 μm.

substantially better agreement with the data than model 1 predictions. The temperature is indicated in Figure 11 at which $\phi_3 = \pi/2$ in the responses calculated from model 2. This marks the center of film resonance: an *inflection* in the sigmoidal velocity response nearly coincident with an attenuation peak. The data and model 2 predictions show that the intrinsic loss peak (G'') at 40 °C is masked by the film resonance centered at 112 °C. Thus, *glass transitions cannot be observed unless the film resonance is far enough removed from the glass transition.* Since G' decreases rapidly near T_g, film resonance tends to occur in the vicinity of T_g unless the product of frequency and film thickness is small enough to ensure that R remains much less than 1. For high-frequency SAW devices, only extremely thin films avoid this problem.

An alternative device, the flexural plate wave (FPW) device,[44] has the same (or greater) inherent sensitivity to film properties, while operating at a much lower frequency. Because of the lower frequency, similar film thicknesses on the two devices result in a much lower R value on the FPW device. For example, measurements on a 1.3-μm PIB film at 5 MHz gave R values below 0.42 even at the maximum temperature of 100 °C. Thus, the T_g at 12 °C could be observed in this case without inducing film resonance.

Film Thickness Effects. Figure 12 shows velocity and attenuation measurements (points) made on 97 MHz SAW devices coated with several thicknesses of PIB. The velocity and attenuation shifts are referenced to the uncoated device.

(44) (a) Wenzel, S. W.; White, R. M. *IEEE Trans. Electron Devices* **1988**, *ED-35*, 735–743. (b) Wenzel, S. W.; White, R. M. *Sens. Actuators A* **1990**, *A21–A23*, 700–703.

Table 4. Estimates of Resonance Temperature and Maximum $\Delta\alpha/k_0$ vs Polyisobutylene Film Thickness for 97-MHz SAW Devices

film thickness (μm)	resonance temp (°C)	max $\Delta\alpha/k_0$ (×10⁻³)
0.44	>120	
0.73	103	2.25
1.18	74	3.75
1.43	64	4.82

Responses calculated from model 2 are also shown (lines) using the temperature-dependent values of G, K, ρ, and h described previously and adding in measured substrate contributions. At a sufficiently low temperature for which $R \ll 1$, the velocity offset is proportional to film thickness—due mainly to mass loading by the film. The attenuation curves in Figure 12 do *not* exhibit a significant offset due to film addition. This is because film-induced attenuation vanishes at low temperatures, due both to a decrease in inertial film strain that occurs as G' and K' increase and to diminished intrinsic polymer lossiness (smaller G'' and K'').

It is significant to note in Figure 12 that the temperature at which attenuation is maximum and velocity makes its sigmoidal excursion varies inversely with film thickness. Table 4 lists the film thicknesses and estimated temperatures where maximum attenuation occurs. These temperatures do *not* coincide with the polymer glass transition temperature T_g of 40 °C (where G'' is maximum) at 97 MHz. This argues strongly that the characteristic responses are *not* due simply to changes in the intrinsic film properties, as Martin and Frye[12] originally proposed to explain data exhibiting trends similar to Figure 12, but are due to thickness-dependent *film resonance effects*. The fact that the resonant temperature depends on film thickness can be understood most easily by considering an elastic film for which $\phi_3 \cong \omega h(\rho/G')^{1/2}$. Since the fundamental film resonance occurs when $\phi_3 = \pi/2$, $G' = \rho(4fh)^2$ at film resonance. For thicker films, resonance occurs at a larger value of G', achieved at a lower temperature. The measured and calculated responses of Figure 12 also indicate that the resonant velocity and attenuation responses increase proportionally with film thickness.

The measured attenuation peaks shown in Figure 12 only attain about two-thirds of the calculated attenuation peak heights. This may be due to nonuniformities in film thickness: calculations indicate that thickness variations diminish resonant film interference, analogous to having a higher r_3 value, leading to a smaller attenuation peak.

Vapor Response. *PIB-Coated SAW Vapor Measurement.* Figure 13 shows velocity and attenuation responses measured (points) vs film concentration as pentane and trichloroethylene were absorbed by a 0.70-μm-thick PIB film. Film concentrations were determined from the mass changes recorded in an identical film on a quartz crystal microbalance (QCM) placed in the same vapor stream. The occurrence of an attenuation peak coincident with an upward sigmoidal velocity change indicates that a shear mode film resonance is occurring. The resonance arises in Figure 13 as vapor molecules plasticize the polymer, decreasing $|G|$ and causing ϕ_3 to pass through $\pi/2$.

The solid lines in Figure 13 are absorption responses calculated from model 2. Tables 3 and 5 list the PIB and

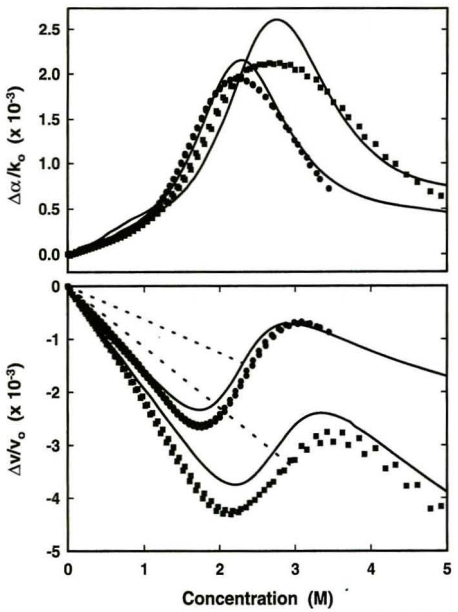

Figure 13. Velocity and attenuation changes measured (points) and calculated (model 2, solid lines; mass loading contribution, eq 21, dashed lines) vs absorbed (●) pentane and (■) trichloroethylene vapor concentrations for a 97-MHz SAW device coated with a 0.70-μm-thick polyisobutylene film. A QCM coated with an identical film was used to measure the mass of absorbed vapor, from which concentration was determined.

Table 5. Model Parameters for Vapors Absorbed by Polyisobutylene

species	mass, m (g/mol)	volume, V (mL/mol)	density, δ (g/cm^3)	χ (°C)
n-pentane	72.2	115.2	0.63	0.083
trichloroethylene	131.4	89.7	1.46	

solvent parameters, respectively, used in eqs 13, 19, and 20 to calculate concentration-dependent values for G, K, ρ, and h. The solvent specific volumes (V) are estimated as $V = m/\delta$, where m is the solvent specific mass and δ is the liquid density.[45] Accounting for changes in film properties arising from vapor absorption yields calculated responses (Figure 13, lines) in reasonable agreement with the measured data. We note that the same plasticizing parameter (χ) was used in calculating both pentane and TCE responses.

At low concentrations, where the film is acoustically thin ($R \ll 1$), a nearly linear $\Delta v/v_0$ response is observed in Figure 13 vs absorbed species concentration. The absorption response may be thought of as a superposition of a mass response (proportional to Cm) and a plasticizing response (determined by CV). The plasticizing response is that shown in Figure 8 and observed during temperature cycling (Figures 11 and 12). The mass response due to vapor absorption (when $R \ll 1$) can be determined from eq 7a, assuming G' and G'' are fixed (no plasticizing effect):

$$\frac{\Delta v}{v_0} = -(c_1 + c_2 + c_3)\omega C m h_0 \qquad (21)$$

The mass contribution to $\Delta v/v_0$ from pentane and trichloroethylene, calculated from eq 21, is shown in Figure 13 as dashed lines. The difference in slope is due to the mass difference (m, Table 5) between species. The mass loading contribution accounts for only 40% of the measured (low concentration) $\Delta v/v_0$ response for pentane and 67% for TCE. The remainder of the response is due to film plasticization by the absorbed vapor molecules. This is consistent with a comparison of SAW and chromatography measurements by Grate[21] that indicated that the mass response was a small fraction (25%) of the total $\Delta v/v_0$ response. As the density (m/V) of absorbed species increases, the larger mass contribution relative to the plasticizing contribution results in eq 21 predicting the total response more accurately (for $R \ll 1$).

At high vapor concentrations, film plasticization due to acquired solvent volume causes the film to behave as acoustically thick. (TCE exhibits greater solubility than pentane: a 97% saturated vapor ambient at 20 °C results in a solvent fraction V_1 of 0.28 for pentane and 0.38 for TCE.) Film resonance occurs when solvent plasticization causes ϕ_3 to reach $\pi/2$. Since this occurs at a fixed value of solvent volume fraction V_1, the larger specific volume V of pentane causes the resonant response to occur at a lower concentration than for trichloroethylene.

Film Thickness Effects. Figure 14 shows velocity and attenuation responses measured vs the partial (gas phase) pressure of n-pentane for SAW devices coated with several different thicknesses of PIB. The response is analogous to that observed as the temperature of a polymer-coated SAW device is increased. The concentration at which resonant responses arise varies inversely with the film thickness, analogous to the response vs temperature shown in Figure 12.

The observation of film resonances has been accentuated in this study by the unusually high vapor concentrations used in the experiments, combined with the unusually low $T_g^{(0)}$ of the polymer examined (polyisobutylene). It should be noted that for many SAW vapor sensors, film resonance effects may not be significant since (1) relatively thin films are used (<100 nm), (2) operating temperature is not as far above $T_g^{(0)}$, and (3) relatively low vapor concentrations are used (trace chemical detection).

Parametric Representation of Data. The parametric representation obtained by plotting attenuation changes vs velocity changes facilitates comparison between data obtained in disparate experiments. Figure 15, for example, shows parametric plots of temperature and vapor data. As the film is softened by either increasing temperature or vapor absorption, loops are formed in the parametric plots. From the calculated parametric responses of Figure 9, in which only ϕ_3 was varied, such loops are indicative of a film resonant response occurring when ϕ_3 goes through $\pi/2$. The loops in Figure 15 are somewhat different from those of Figure 9, however, since increasing temperature or vapor concentration causes an increase in film lossiness (r_3) in addition to increasing ϕ_3.

The locus of points formed in the parametric plots (Figure 15) arises from a combination of plasticizing and mass loading

(45) Weast, R. C.; Astle, M. J.; Beyer, W. H. *CRC Handbook of Chemistry and Physics*; CRC Press: Boca Raton, FL, 1983.

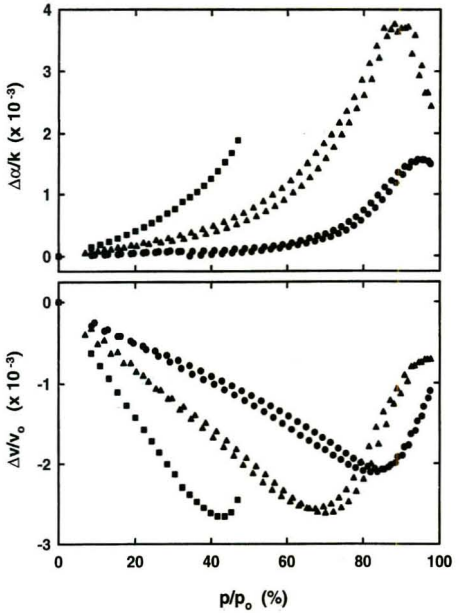

Figure 14. Velocity and attenuation changes measured vs relative ambient vapor pressure (p/p_0) of *n*-pentane with a 97-MHz SAW devices coated with polyisobutylene films of thickness: (●) 0.44, (▲) 0.73, and (■) 1.18 μm.

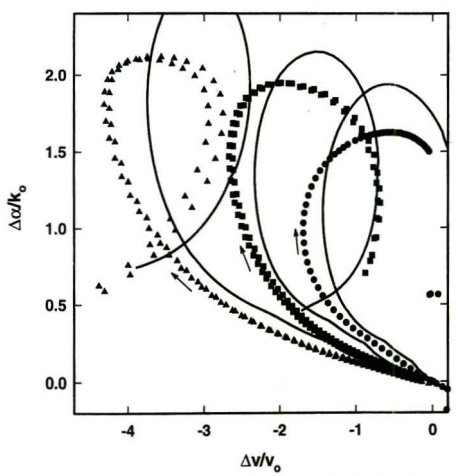

Figure 15. Parametric plots of attenuation vs velocity changes measured (points) and calculated (lines, model 2) as 0.70-μm PIB films were softened by (●) increasing temperature, (■) pentane absorption, and (▲) trichloroethylene absorption. Arrows indicate increasing temperature or solvent concentration.

responses.[12] Film softening causes an increase in ϕ_3 that generates a near-circular or spiral response. Progression around this spiral is dependent upon the free volume accumulated either by thermal expansion or by vapor absorption in the polymer. The mass contributed by solvent absorption causes, in addition, a horizontal *translation of these points toward lower velocity*. Trichloroethylene points are translated more than pentane due to the greater density of this species. The temperature data thus represent a limiting case of vapor data in which the mass of the absorbed species is zero.[12]

Multiple Film Resonances. In our experiments with temperature cycling and vapor absorption in PIB films, only the fundamental ($n = 1$) shear film resonance was observed. Films ranged in thickness from 0.44 to 1.43 μm; the entire resonance was not observed in the thinnest films. Ballantine[30] has reported observing fundamental film resonances at 158 MHz in PIB films only 0.0082 μm thick. For resonance to occur in films of this thickness, G' must reach values as low as 2.5×10^5 dyn/cm^2. The master curves for PIB shown in Figure 10 indicate that this value is inaccessible at any temperature or solvent concentration. In fact, a water layer with viscosity $\eta = 1$ cP exhibits a shear modulus $G' = \omega\eta = 10^7$ dyn/cm^2 at 158 MHz. Thus, resonances should *not* occur in films this thin at 158 MHz. Ballantine also reports observing higher order film resonances (up to ninth order) in PIB. Aside from the fact that the films are much too thin for the resonance condition to be satisfied, calculations indicate that the lossiness r_3 of PIB films in the rubbery regime damps higher order film resonances too highly for them to be observed. These facts indicate that the attenuation peaks and velocity excursions reported by Ballantine are not due to film resonances.

CONCLUSIONS

Typically, polymer films on SAW devices behave as acoustically thin in the glassy regime and thick in the transition and rubbery regimes. The ratio R of in-plane to surface-normal displacement gradients, given by eq 4, indicates the regime of operation. In acoustically thin films, displacement is uniform across the film and varies only in the direction of propagation. In this regime, surface waves probe film viscoelastic properties mainly by imposing longitudinal strains. These cause compression and tension of the film in the direction of propagation, with corresponding expansions and contractions in film thickness. Model 1 (eq 5) gives the velocity and attenuation changes arising from acoustically thin viscoelastic films. [The Tiersten[14] equation (eq 6) is a special case of model 1 that obtains for acoustically thin, elastic films.] When a glass transition occurs in an acoustically thin film, model 1 indicates that an attenuation peak and velocity decrease will coincide with T_g. However, the decrease in shear modulus associated with the glass transition often causes films to behave as acoustically thick. In this regime, attenuation peaks may arise from film resonances and not just intrinsic loss peaks. This is in contrast to FPW devices on which films can behave as acoustically thin in the vicinity of T_g.

In acoustically thick films, inertially induced lag in the film generates cross-film displacement gradients. Model 2 (eq 11) includes the effect of these gradients and approximates $\Delta v/v_0$ and $\Delta\alpha/k_0$ for acoustically thin or thick viscoelastic films. Table 6 summarizes the extreme cases of film strain and the appropriate equations for determining $\Delta v/v_0$ and $\Delta\alpha/k$.

The emergence of film resonances complicates the extraction of T_g, which corresponds to a maximum in the intrinsic modulus G'': the temperature at which attenuation is maximum generally does *not* coincide with the intrinsic

Table 6. Extremes of Film Strain Imposed by SAW on Film Overlay and Appropriate Equations for Calculating Velocity and Attenuation Changes

film condition			appropriate model for $\Delta v/v_o$, $\Delta\alpha/k_o$	
		principal gradient	elastic	viscoelastic
acoustically thin	$R \ll 1$	in-plane	Tiersten (eq 6) model 1 (eqs 5 and 7) model 2 (eq 11)	model 1 (eqs 5 and 7) model 2 (eq 11)
acoustically thick	$R \geq 1$	surface-normal	model 2 (eq 11)	model 2 (eq 11)

modulus maximum but depends critically on film thickness.

In the acoustically thin regime ($R \ll 1$), velocity and attenuation responses arising from vapor absorption are proportional to the species concentration in the film. These responses, previously attributed solely to mass loading, are also due in roughly equal part to polymer plasticization (softening). To obtain SAW velocity changes proportional to absorbed vapor concentration, required if the device is to respond linearly to vapor-phase concentration, it is necessary that the film remain in the acoustically thin regime. The result is a tradeoff, in terms of film thickness, between sensitivity and dynamic range.

When film thickness and absorbed vapor cause R to exceed 1, the film behaves as acoustically thick. Velocity response no longer depends linearly on absorbed vapor concentration. As ϕ_3 approaches $\pi/2$, film resonance occurs and velocity increases with concentration in this regime. This makes the velocity response multivalued: several concentrations lead to the same velocity change. By monitoring both velocity and attenuation responses, the ambiguity in concentration can be resolved.

Film resonances can be used to advantage in constructing "threshold detectors" designed for sensitivity in a specific range of vapor concentrations.[30] Film resonance effects can also be useful in providing large attenuation responses that can be used, along with the velocity response, to provide molecular discrimination and quantitation of isolated species using a single "dual output" SAW sensor.[46]

A parametric plot of attenuation vs velocity changes leads to a distinctive response when film resonance occurs: film softening causes movement around a spiral, while mass loading translates these points toward lower velocity. The result is a characteristic loop in the $\Delta\alpha/k_o$–$\Delta v/v_o$ plane.

ACKNOWLEDGMENT

The authors are grateful to B. L. Wampler of Sandia National Laboratories (SNL) for expert technical assistance and to Dr. T. Schneider and Dr. T. Tanaka of SNL and Dr. Jay Grate of Pacific Northwest Laboratories for helpful technical discussions. This work was performed at SNL and supported by the U. S. Department of Energy under contract No. DE-AC04–94AL85000.

APPENDIX A: SYMBOLS

f_o	synchronous (center) frequency of SAW interdigital transducer
v	SAW propagation (phase) velocity
v_o	SAW propagation velocity in uncoated substrate
d	periodicity of SAW interdigital transducer
Λ	SAW wavelength (along the surface)
j	$(-1)^{1/2}$
i,j	subscripted indices with values 1, 2, or 3, referring to x-, y-, and z-directions, respectively
h	film thickness
h_o	film thickness at reference temperature
T_g	polymer glass transition temperature at f
$T_g^{(0)}$	polymer glass transition temperature at low frequency
α	SAW attenuation: rate of amplitude change with propagation distance
G	complex shear modulus of film ($G = G' + jG''$)
G'	shear storage modulus of film
G''	shear loss modulus of film
K	complex bulk modulus of film ($K = K' + jK''$)
K'	bulk storage modulus of film
K''	bulk loss modulus of film
$\vec{u}$	SAW displacement vector
f	excitation frequency of SAW
ω	angular excitation frequency of SAW ($2\pi f$)
t	time
γ	complex SAW propagation factor ($\gamma = \alpha + jk$)
u_i	SAW displacement in ith direction
u_{io}	displacement in ith direction at substrate surface
v_i	SAW particle velocity in ith direction
v_{io}	particle velocity in ith direction at substrate surface
ψ_i	phase of ith displacement component with respect to u_z
k_o	acoustic wavenumber for SAW in uncoated substrate ($k_o = 2\pi/\Lambda = \omega/v_o$)
$\Delta\gamma/k_o$	change in complex propagation factor per wavenumber
$\Delta\alpha/k_o$	change in attenuation per wavenumber
$\Delta v/v_o$	fractional change in wave velocity
Δf	frequency change of oscillator circuit
κ	fraction of SAW wave path coated with polymer film
S_{ij}	strain tensor: $S_{ij} = 1/2(\partial u_i/\partial x_j + \partial u_j/\partial x_i)$
T_{ij}	stress tensor: force per area in the i-direction on a plane normal to the j-direction
R	ratio of strains generated by cross-film to in-plane displacement gradients
A	substrate-dependent parameter in eq 4 for R
ρ	film mass density
ρ_o	film mass density at reference temperature T_o
λ, μ	Lamé constants for film
ϕ_i	phase shift for ith displacement component across film thickness
β_i	complex propagation factor for displacement u_i propagating across film
$M^{(i)}$	generalized modulus equalling G for $i = 1$ or 3 and K for $i = 2$
$E^{(i)}$	modulus associated with film deformation generated by ith displacement component
r_i	film loss parameter associated with displacement component u_i
$\hat{x}_i$	unit displacement vector in i-direction

(46) Frye, G. C.; Martin, S. J.; Cernosek, R. W.; Pfeifer, K. B.; Anderson, J. S. *1991 Ultrasonics Symposium Proceedings*; IEEE: New York, 1991; pp 311–316.

$\Delta\rho$	change in film mass density
$\Delta G'$	change in shear storage modulus of film
$\Delta G''$	change in shear loss modulus of film
c_i	ratio of particle velocity (squared) at substrate surface to acoustic power flow: $c_i = v_{io}^2/(4k_oP)$
P	SAW acoustic power density (power per beam width)
a, b	film-dependent parameters in ϕ_3 and r_3 expressions (eqs 9 and 10)
n	film resonance harmonic number
Z_i	surface mechanical impedance in ith direction at substrate/film interface
Re	denotes the real part of a complex expression
Im	denotes the imaginary part of a complex expression
ω'	apparent probe frequency of SAW
a_T	shift factor for polymer relaxation or ω' due to temperature change or vapor absorption
F	free volume of polymer at any temperature or vapor concentration
F_o	free volume of pure polymer ($C = 0$) at reference temperature
B	constant in generalized Doolittle equation, taken as unity
ξ	parameter describing extent to which free volume addition swells film
α_f	polymer thermal expansion coefficient
Δh	change in film thickness due to temperature change or vapor absorption
F_g	free volume of polymer at $T_g^{(0)}$
χ	plasticizing parameter for polymer
V_1	volume fraction of absorbed vapor in polymer
C	concentration of absorbed vapor relative to pure polymer
m	specific mass of absorbed vapor
V	specific volume of absorbed vapor
δ	liquid density of vapor
ΔL	change in insertion loss (in decibels)
N_Δ	number of SAW wavelengths separating interdigital transducers (center-to-center)
T	temperature
T_o	reference temperature (film formation temperature)
$\hat{u}(y)$	cross-film displacement vector
$S^{(IP)}$	total strain induced by in-plane (IP) gradients
$S^{(CF)}$	total strain induced by cross-film (CF) gradients
δ_{ij}	Kronecker delta function: equal to 1 when $i = j$ and 0 otherwise

APPENDIX B: RATIO OF FILM STRAINS GENERATED BY SAW-INDUCED CROSS-FILM GRADIENTS TO IN-PLANE GRADIENTS

SAW propagation in the z-direction of a film-coated substrate causes film displacements given by

$$\vec{u} = \hat{u}(y)e^{j(\omega t - kz)} \tag{B1}$$

where y is distance across the film, $\hat{u}(y)$ is the cross-film displacement, ω is the angular frequency($\omega = 2\pi f$), and k is the SAW wavenumber ($k = 2\pi/\Lambda = \omega/v_o$). In-plane gradients arise from harmonic variation in the z-direction, described by the exponential term in eq B1. Cross-film gradients arise from variations in $\hat{u}(y)$ arising from inertial lag of the upper film portions withrespect to the driven lower film surface.

Strains Due to In-Plane Gradients. If we assume that $\hat{u}(y)$ is constant across the film thickness, film strains, $S_{ij} = 1/2(\partial u_i/\partial x_j + \partial u_j/\partial x_i)$, are then generated only by the harmonic variation of $\vec{u}$ in the z-direction:

$$S_{i3} = \frac{1}{2}\frac{\partial u_i}{\partial z} = -\frac{jku_i}{2} \tag{B2}$$

for $i = 1$, 2, or 3. S_{13} and S_{23} are shear strains, and S_{33} is a tensile strain. The magnitude of the total strain induced by in-plane (IP) gradients is

$$S^{(IP)} = \frac{k}{2}(u_{xo}^2 + u_{yo}^2)^{1/2} + ku_{zo} \tag{B3}$$

where the uniform film displacements u_i have been replaced by the displacements at the substrate/film interface, u_{io}.

Strains Due to Cross-Film Gradients. When the lower film surface undergoes SAW-induced displacement, the inertial lag of the upper film portions causes $\hat{u}(y)$ in eq B1 to vary across thefilm. However, shear wave velocity is low enough that gradients of u_x and u_z arise, leading to shear strains in the film. The continuity equation gives

$$\sum_{j=1}^{3}\frac{\partial T_{ij}}{\partial x_j} = \rho\dot{v}_i = -\rho\omega^2 u_i \tag{B4}$$

where particle velocity v_i is $\dot{u}_i = j\omega u_i$, T_{ij} is the stress (force per area in the i-direction on a plane normal to the j-direction), and ρ is film density. Since the upper film surface is stress-free, i.e., $T_{i2}(h) = 0$, we can approximate the derivative in eq B4 as $\partial T_{i2}/\partial x_2 \cong -T_{i2}(0)/h$, where h is film thickness. Then the stresses required at the substrate/film interface to drive the film can be found from eq B4

$$T_{i2}(0) = \rho\omega^2 h u_{io} \tag{B5}$$

for $i = 1$ and 3. The shear strains S_{ij} in the film are related to shear stresses by $T_{ij} = 2GS_{ij}$ (for $i \neq j$), where G is the film's shear modulus. From eq B5, the film shear strains (at the lower film surface) are

$$S_{i2}(0) = \frac{T_{i2}(0)}{2G} = \frac{\rho\omega^2 h u_{io}}{2G} \tag{B6}$$

for $i = 1$ and 3. The magnitude of the total strain induced by inertially generated cross-film (CF) gradients is then

$$S^{(CF)} = \frac{\rho\omega^2 h}{2|G|}(u_{xo}^2 + u_{zo}^2)^{1/2} \tag{B7}$$

The ratio of strain magnitudes induced by cross-film to in-plane gradients is found by combining eqs B3 and B7:

$$R = \frac{S^{(CF)}}{S^{(IP)}} = \left(\frac{(c_1 + c_3)^{1/2}}{(c_1 + c_2)^{1/2} + 2c_3^{1/2}}\right)\frac{\omega v_o \rho h}{|G|} = \frac{Afv_o\rho h}{|G|} \tag{B8}$$

where we have defined $A \equiv 2\pi(c_1 + c_3)^{1/2}/[(c_1 + c_2)^{1/2} + 2c_3^{1/2}]$ and used the definition $c_i = v_{io}^2/(4k_oP) = (\omega u_{io})^2/(4k_oP)$, where v_{io} is the surface particle velocity and P is the SAW acoustic power density (R is independent of P). Taking

c_i values from Table 2, $A \cong 1.9$ for propagation in the X-direction of ST-cut quartz.

APPENDIX C: SAW LOADING BY AN ACOUSTICALLY THIN VISCOELASTIC LAYER

A perturbational method can be applied to approximate the changes in SAW propagation velocity and attenuation contributed by an acoustically thin viscoelastic surface film: changes in the complex propagation factor γ are related to the surface mechanical impedances Z_i experienced by the surface displacement components u_{io} in translating and deforming the film overlay:[23]

$$\frac{\Delta\gamma}{k_o} = \frac{\Delta\alpha}{k_o} - j\frac{\Delta v}{v_o} = \sum_{i=1}^{3} c_i Z_i \qquad \text{(C1)}$$

where c_i are the normalized surface particle velocities (defined in appendix B) and the surface mechanical impedances are[23]

$$Z_i = -\frac{T_{i2}}{v_i}\bigg|_{y=0} \qquad \text{(C2)}$$

where T_{i2} and v_i, evaluated at $y = 0$, denote interfacial stress (defined in appendix B) and particle velocity in the i-direction, respectively. For an isotropic film, the displacement components can be considered independently in calculating Z_i.

For an acoustically thin ($R \ll 1$) film, displacements can be assumed uniform across the film thickness: $u_i = u_{io}$. Applying the continuity equation (eq B4) and assuming uniform wave displacement in the x-direction ($\partial T_{i1}/\partial x_1 = 0$) yields

$$\frac{\partial T_{i2}}{\partial y} + \frac{\partial T_{i3}}{\partial z} = \rho\dot{v}_i \qquad \text{(C3)}$$

for $i = 1$, 2, or 3; ρ is film density. Since wave variations in the x direction are zero, the upper film surface is stress-free so that $T_{i2}(h) = 0$, allowing an approximation for the first term of eq C3:

$$\frac{\partial T_{i2}}{\partial y} \cong -\frac{T_{i2}(0)}{h} \qquad \text{(C4)}$$

We define a deformation modulus relating stress (generated by displacement component x_i) to strain:

$$E^{(i)} = \left(\frac{1+\delta_{i3}}{2}\right)\frac{T_{i3}}{S_{i3}} \qquad \text{(C5)}$$

where $\delta_{i3} = 1$ if $i = 3$ and 0 otherwise. Then we can write the second term of eq C3 as

$$\frac{\partial T_{i3}}{\partial z} = E^{(i)}\frac{\partial^2 u_i}{\partial z^2} \qquad \text{(C6)}$$

Using eqs C4 and C6 in eq C3 yields

$$\frac{T_{i2}(0)}{h} = E^{(i)}\frac{\partial^2 u_i}{\partial z^2} - \rho\ddot{u}_i \qquad \text{(C7)}$$

giving a one-dimensional wave equation in the film overlay. The SAW-supplied stress $T_{i2}^{(0)}$, applied at the lower film surface, acts as a *source* for this wave. Noting from eq B1 that $\ddot{u}_i = (j\omega)^2 u_i$ and $\partial^2 u_i/\partial z^2 = (-jk)^2 u_i = -k^2 u_i$, eq C7 becomes

$$T_{i2}(0) = h(\rho\omega^2 - k^2 E^{(i)})u_{io} \qquad \text{(C8)}$$

Using eq C8 in eq C2 and noting that $v_i = j\omega u_i$ and $v_o = \omega/k$ yields the surface mechanical impedance components

$$Z_i = j\omega h\left(\rho - \frac{E^{(i)}}{v_o^2}\right) \qquad \text{(C9)}$$

where v_o is the unperturbed SAW propagation velocity. The first term of eq C9 is a kinetic contribution, while the second term arises from straining the film overlay.

Substituting eq C9 into eq C1 yields the perturbation in SAW propagation characteristics arising from an acoustically thin ($R \ll 1$) viscoelastic film overlay:

$$\frac{\Delta\gamma}{k_o} = \frac{\Delta\alpha}{k_o} - j\frac{\Delta v}{v_o} = j\omega h\sum_{i=1}^{3} c_i\left(\rho - \frac{E^{(i)}}{v_o^2}\right) \qquad \text{(C10)}$$

with c_i as given in appendix B or Table 2.

We examine a single deformation mode to illustrate the calculation of the deformation moduli $E^{(i)}$ involved in eq C10. Deformation is assumed to be uniform across the film, as shown in Figure 4, consistent with the assumption of acoustic thinness. The compressional modulus $E^{(3)}$, for example, can be related to intrinsic elastic film properties by simultaneously solving the plane-strain relations:[47]

$$T_{33} = \left(K - \frac{2}{3}G\right)(S_{22} + S_{33}) + 2GS_{33} \qquad \text{(C11a)}$$

$$T_{22} = \left(K - \frac{2}{3}G\right)(S_{22} + S_{33}) + 2GS_{22} \qquad \text{(C11b)}$$

where K and G are the bulk and shear moduli, respectively, of the film overlay. Since the upper film surface is stress-free, $T_{22} = 0$, allowing eq C11b to be solved for S_{22}:

$$S_{22} = -\left(\frac{K - \frac{2}{3}G}{K + \frac{4}{3}G}\right)S_{33} \qquad \text{(C12)}$$

Substituting eq C12 into eq C11a yields the compressional modulus defined by eq C5:

$$E^{(3)} = \frac{T_{33}}{S_{33}} = \frac{4G(3K+G)}{3K+4G} \qquad \text{(C13)}$$

The moduli $E^{(1)}$ and $E^{(2)}$ can be derived in a similar manner to produce

$$E^{(1)} = \frac{T_{13}}{2S_{13}} = G \qquad \text{(C14a)}$$

$$E^{(2)} = \frac{T_{23}}{2S_{23}} = \frac{2\pi G(G+3K)}{3(4G+K)}\left(\frac{h}{\Lambda}\right)^2 \qquad \text{(C14b)}$$

where Λ is the SAW wavelength. Typically the modulus $E^{(2)}$ is negligible, due to the $(h/\Lambda)^2$ term, and is taken as zero.

(47) Lai, W. M.; Krempl, E. *Introduction to Continuum Mechanics*; Pergamon: New York, 1974.
(48) Ferry, J. D. *Viscoelastic Properties of Polymers*, 3rd ed.; Wiley: New York, 1989; Chapter 11.

APPENDIX D: SAW LOADING BY AN ACOUSTICALLY THICK VISCOELASTIC LAYER

A perturbational method is applied to approximate the changes in SAW propagation velocity and attenuation contributed by an acoustically thick ($R \geq 1$) viscoelastic film. By considering both in-plane and cross-film displacement gradients, the final result applies to both acoustically thin and thick films. Changes in the complex propagation factor γ are related to the surface mechanical impedances Z_i by eq C1. In calculating the surface mechanical impedances, the SAW surface displacement is resolved into surface-normal and in-plane components; these act as *sources* for radiating waves into the contacting film. A distributed model is used for the film, in which the impedance at the lower film surface depends upon the nature of the interference between the incident waves and those reflected from the upper (film/air) surface.

As in the acoustically thin case (appendix C), the displacement components are considered independently in calculating surface mechanical impedances. Assuming no wave variation in the x-direction, the continuity equation (eq B4) gives

$$\frac{\partial T_{i2}}{\partial y} + \frac{\partial T_{i3}}{\partial z} = \rho \dot{v}_i \tag{D1}$$

for $i = 1, 2,$ or 3. From eq C5, in-plane displacement gradients in the film gives rise to

$$T_{i3} = E^{(i)} \frac{\partial u_i}{\partial z} \tag{D2}$$

with $E^{(i)}$ given by eqs C13 and C14. Cross-film gradients give rise to

$$T_{i2} = M^{(i)} \frac{\partial u_i}{\partial y} \tag{D3}$$

where $M^{(1)} = M^{(3)} = G$, while $M^{(2)} = K$. Substituting eqs D2 and D3 into D1 yields a two-dimensional wave equation for the displacement u_i in the film:

$$M^{(i)} \frac{\partial^2 u_i}{\partial y^2} + E^{(i)} \frac{\partial^2 u_i}{\partial z^2} = \rho \dot{v}_i \tag{D4}$$

Substituting the harmonic solution for the z-propagating wave (eq B1) into eq D4 yields a homogeneous ordinary differential equation for the displacement profile $u_i(y)$ in the film:

$$\frac{d^2 u_i}{dy^2} + \beta_i^2 u_i = 0 \tag{D5a}$$

with

$$\beta_i = \omega \left(\frac{\rho - E^{(i)}/v_o^2}{M^{(i)}} \right)^{1/2} \tag{D5b}$$

where $v_o = \omega/k$ is the unperturbed SAW phase velocity. The solution to eq D5a for $0 \leq y \leq h$ is

$$u_i(y) = Ae^{j\beta_i y} + Be^{-j\beta_i y} \tag{D6}$$

where h is film thickness and A and B are constants. The factors β_i are propagation constants describing wave propagation across the film. For a viscoelastic material, characterized by complex bulk and shear moduli (K and G), β_i are complex.

The constants A and B in eq D6 are determined from the boundary conditions that apply at the upper and lower film surfaces. The first boundary condition stipulates that the displacement at the film/substrate interface be continuous, i.e., $u_i(0^+) = u_{io}$, where $u_i(0^+)$ is the displacement at the lower film surface. Equation D6 gives

$$A + B = u_{io} \tag{D7}$$

The second boundary condition stipulates that the upper film surface (film/air interface) be stress-free: $T_{i2}(h) = 0$. Evaluating eq D3 at $y = h$, with u_z given by eq D6, gives

$$Ae^{j\beta_i h} - Be^{-j\beta_i h} = 0 \tag{D8}$$

Solving eqs D7 and D8 simultaneously determines A and B:

$$A = \frac{u_{io} e^{-j\beta_i h}}{e^{j\beta_i h} + e^{-j\beta_i h}} \tag{D9a}$$

$$B = \frac{u_{io} e^{j\beta_i h}}{e^{j\beta_i h} + e^{-j\beta_i h}} \tag{D9b}$$

Substituting eqs D9a and 9b into D6 determines the displacement profiles $u_i(y)$ across the film:

$$u_i(y) = u_{io} \frac{\cosh[j\beta_i(y - h)]}{\cosh(j\beta_i h)} \tag{D10}$$

for $0 \leq y \leq h$.

The surface mechanical impedance associated with each displacement u_i is given by eq C2. In evaluating this impedance, the interfacial shear stress is found from eq D3, using eq D6 for u_i:

$$T_{i2}(0) = M^{(i)} \frac{\partial u_i}{\partial y}\bigg|_{y=0} = j\beta_i M^{(i)} (A - B) \tag{D11}$$

and the interfacial particle velocity is found from eq D6:

$$v_i(0) = \dot{u}_i(0) = j\omega u_i(0) = j\omega(A + B) \tag{D12}$$

Substituting eqs D11 and D12 into eq C2 and using eq D9 for A and B gives the surface mechanical impedance associated with each displacement u_i:

$$Z_i = -\frac{\beta_i M^{(i)}}{\omega} \left(\frac{A - B}{A + B} \right) = \frac{\beta_i M^{(i)}}{\omega} \tanh(j\beta_i h) \tag{D13}$$

From eq C1, the perturbation in SAW propagation arising from a viscoelastic film is determined from the surface mechanical impedances (eq D13):

$$\frac{\Delta\gamma}{k_o} = \frac{\Delta\alpha}{k_o} - j\frac{\Delta v}{v_o} = \sum_{i=1}^{3} \frac{c_i \beta_i M^{(i)}}{\omega} \tanh(j\beta_i h) \tag{D14}$$

with β_i as given in eq D5b and c_i and $E^{(i)}$ values as given in appendix C and Tables 1 and 2. Equation D14 applies for acoustically thin or thick films (all R values).

Received for review December 6, 1993. Accepted April 19, 1994.[⊗]

[⊗] Abstract published in *Advance ACS Abstracts*, June 1, 1994.

Anal. Chem. **1994,** *66,* 2220–2225

Solvent Extraction–Flow Injection without Phase Separation through the Use of the Differential Flow Velocities within the Segmented Flow

Charles A. Lucy* and Ken K.-C. Yeung

Department of Chemistry, University of Calgary, 2500 University Drive N.W., Calgary, Alberta, Canada T2N 1N4

A simple and robust flow injection extraction system has been developed. The system exploits the wetting film of the organic phase which forms on the walls of the hydrophobic Teflon tubing. This wetting film is stationary and thus reduces the average linear velocity of the organic flow. Any component extracted into the organic phase requires more time to pass through the extraction coil than the unextracted components. Using organic solvents such as hexanol, which have a high viscosity and low interfacial tension, the differential flow velocities can yield a separation in time between unextracted and extracted components. After the separation is complete, methanol addition homogenizes the segmented flow prior to its passage through the flow cell of an absorbance detector. Thus the need for a phase separator has been eliminated. Large aqueous-to-organic phase ratios, high flow rates, and long extraction coils enhance the resolution between the unextracted and extracted components. The active components in motion sickness tablets were determined with an analytical precision of 2.5–4.0% and a throughput of 12 analyses/h.

Since its introduction in 1978,[1,2] solvent extraction–flow injection (SE-FI) has been applied to a wide variety of analytical applications. A 1991 review reported over 100 applications including determinations of metal ions, inorganic anions, surfactants, and drugs in samples ranging from tablets to leachates.[3] However, the same article also stated that "*currently, almost as many phase separators as applications exist.*" This contribution describes a simple and robust SE-FI system not requiring a phase separator.

Typically, SE-FI involves four operations: (i) the injection of the sample into the aqueous phase; (ii) the mixing of immiscible organic and aqueous phases to form a segmented stream; (iii) the distribution of sample components between the two phases; and (iv) the separation of one or both phases for determination. The segmentation[3–6] and extraction[7–9] processes within SE-FI have been extensively studied. The current phase separators fall into one of three classes:[3] (i) those based on differences in the density of the two immiscible phases; (ii) those in which solvent affinities with either hydrophobic or hydrophilic inserts enhance the efficiency of the density phase separators; and (iii) membrane phase separators in which a hydrophobic membrane excludes water and a hydrophilic membrane excludes the organic phase from the stream fed to the detector. The membrane phase separator is currently the preferred methodology. However, there is less than complete satisfaction with the membrane phase separator. The choice of membrane material is a function of flow rate, phase ratio, the physical and chemical nature of the solvents and reagents, the mechanical properties of the material, and the separator design. Furthermore, the presence of surfactants, proteins, and particulate material may alter membrane permeability, necessitating frequent membrane replacement.

A number of alternative FI manifolds have been developed which eliminate the need for phase separation. Most common is the use of "on-tube" detection to directly monitor the analyte contained in the segments within the extraction coil. However, the alternating aqueous/organic nature of the segmented flow results in superimposition of a periodic behavior on the signal.[9–11] Furthermore, the technique requires the construction of custom "on-tube" detector systems. Alternatively, iterative reversal,[12,13] extractive membranes,[14–17] trapped extractants,[18] or zone sampling[19] can be used. However, these techniques either require computer control or monitor only one phase and so are not suitable for many applications.

In this work, the film-forming characteristics of two-phase segmented flow are used to develop a simple and robust SE-FI instrument, one that does not require either a phase separator or on-tube detector and quantifies both extracted and unextracted components from a single injection.

BACKGROUND

In two-phase liquid flow such as that found in the extraction coil, one phase forms a thin wetting film on the walls of the

(1) Karlberg, B.; Thelander, S. *Anal. Chim. Acta* **1978,** *98,* 1–7.
(2) Bergamin, F°. H.; Medeiros, J. X.; Ries, B. F.; Zagatto, E. A. G. *Anal. Chim. Acta* **1978,** *101,* 9–16.
(3) Kubán, V. *Crit. Rev. Anal. Chem.* **1991,** *22,* 477–557.
(4) Cantwell, F. F.; Sweileh, J. A. *Anal. Chem.* **1985,** *57,* 329–331.
(5) Kubán, V.; Ingman, F. *Anal. Chem.* **1990,** *62,* 2026–2032.
(6) Kubán, V.; Danielsson, L.-G.; Ingman, F. *Anal. Chim. Acta* **1991,** *245,* 251–258.
(7) Nord, L.; Bäckström, K.; Danielsson, L.-G.; Ingman, F.; Karlberg, B. *Anal. Chim. Acta* **1987,** *194,* 221–233.
(8) Lucy, C. A.; Cantwell, F. F. *Anal. Chem.* **1989,** *61,* 101–107.
(9) Lucy, C. A.; Cantwell, F. F. *Anal. Chem.* **1989,** *61,* 107–114.
(10) Kubán, V. *Anal. Chim. Acta* **1991,** *248,* 493–499.
(11) Motomizu, S.; Kobayashi, M. *Anal. Chim. Acta* **1992,** *261,* 471–475.
(12) Cañete, F.; Ríos, A.; Luque de Castro, M. D.; Valcárcel, M. *Anal. Chem.* **1988,** *60,* 2354–2357.
(13) Mesa, J. A. G.; Linares, P.; Luque de Castro, M. D; Valcárcel, M. *Anal. Chim. Acta* **1990,** *235,* 441–444.
(14) Sahleström, Y.; Karlberg, B. *Anal. Chim. Acta* **1986,** *179,* 315–323.
(15) Audunsson, G. *Anal. Chem.* **1986,** *58,* 2714–2723.
(16) Gonzalo, E. R.; Pavón, J. L. P.; Ruzicka, J.; Christian, G. D.; Olson, D. C. *Anal. Chim. Acta* **1992,** *259,* 37–44.
(17) Barnes, D. E.; Taylor, M. J. C.; Marshall, G. D.; Van Staden, J. F. *Anal. Chim. Acta* **1993,** *274,* 283–292.
(18) Agudo, M.; Ríos, A.; Valcárcel, M. *Anal. Chem.* **1993,** *65,* 2941–2943.
(19) Lindgren, C. C.; Dasgupta, P. K. *Talanta* **1992,** *39,* 101–111.

0003-2700/94/0366-2220$04.50/0
© 1994 American Chemical Society

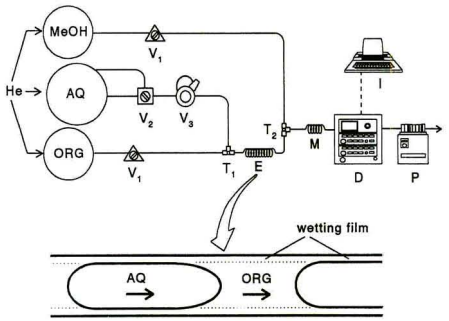

Figure 1. Schematic diagram of the SE-FI manifold based on the differential solvent velocities within the extraction coil. See the Experimental Section for details. The expansion details the features of the segmented flow.

tubing, as shown in the expanded portion of Figure 1. Thus this solvent completely surrounds segments of the other phase.[7,9,20] In hydrophobic tubing such as Teflon, the organic solvent acts as the continuous film-forming phase. The existence of this film, which bridges successive segments of organic solvent, allows transport of solute from one organic segment into adjacent organic segments.[9,20] Thus the presence of the film results in peak dispersion within the extraction coil, with thicker films causing greater dispersion. Therefore the prevailing philosophy in SE-FI has been to minimize the band broadening by using organic solvents that yield thin wetting films.

However, the formation of a wetting film also results in retardation of the organic phase relative to the aqueous phase. Segmented flow within the extraction coil possesses two axial flow velocities. The segments move through the column at a constant velocity, $u_{segment}$. Therefore, the aqueous phase, which does not form a film along the walls of the tubing, will have a linear velocity of

$$u_{aqueous} = u_{segment} \tag{1}$$

Alternatively, the film-forming organic phase is proportioned into both the flowing segments and the stagnant film ($u_{film} = 0$). Thus the organic phase has a velocity of

$$\bar{u}_{organic} = \frac{V_{organic} - V_{film}}{V_{organic}} u_{segment} \tag{2}$$

where $V_{organic}$ is the total volume of the organic phase and V_{film} is the volume of the organic phase in the stagnant film.

Thus, if the film is sufficiently thick, a difference in velocity will develop between the organic and aqueous phase:

$$\frac{\bar{u}_{organic}}{u_{aqueous}} = \frac{V_{organic} - V_{film}}{V_{organic}} \tag{3}$$

This differential velocity enables separation on the basis of time rather than space as has been used in all previous SE-FI systems. After the separation is complete, the two-phase flow is homogenized by the addition of methanol and is passed through the detector cell.

EXPERIMENTAL SECTION

Apparatus. A schematic diagram of the SE-FI manifold used herein is shown in Figure 1. Constant-pressure pumping with helium is used to produce pulseless solvent flow, which can be shut off using valve V_1 (Model 50310, Rheodyne Inc., Cotati, CA).[21] Valve V_2 is a six-position Teflon rotary valve (Model 50110, Rheodyne) which controls the aqueous flow from the multireagent pressure cylinder to the sample injection valve, V_3, and allows selection of various aqueous solutions. The syringe loading sample injector (Model 9125, Rheodyne), V_3, contains a 20-μL Teflon sample loop. Tubing upstream of injection valve V_3 is primarily 1.0-mm i.d., although narrow tubing was added in some experiments to adjust the flow rate. The tubing in the unsegmented flow regions downstream of the injector is 0.5-mm i.d. and is kept as short as possible to minimize band broadening.

The segmentor, T_1, is a 0.73-mm-bore tee-fitting (Part No. 550731, Alltech Associates, Inc., Deerfield, IL) which combines the aqueous and organic solvent streams to produce the segmented flow, which flows through the extraction coil, E, 190 cm of 0.5-mm i.d. coiled (d_{coil} = 5 mm) Teflon tubing. The segmented flow exits the extraction coil and merges with a methanol flow stream at T_2, a 0.51-mm i.d. PEEK tee-fitting (Item No. P-727, Upchurch Scientific, Oak Harbor, WA). To control the methanol, tubings of various lengths and inner diameters are added between the pressure cylinder and T_2. The final mixture flows through the mixing coil, M, a 26.3 cm long 0.8-mm i.d. coiled Teflon tube, to the UV/vis detector, D, (Model 440, Waters Associates, Inc., Milford, MA) which monitors the absorbance at 254 nm. The output signal is transmitted to a digital recording integrator, I (Chromatopac C-R3A, Shimadzu Corp.). Meanwhile, the flow stream exits the detector and passes through a Minipuls variable-speed peristaltic pump, P (Gilson Instruments, Villie-le-Belle, France), before being sent to waste. This pump varies the back pressure and acts as a secondary flow control.[21]

In order to maintain regular segmentation, the extraction coil was washed at the end of each day to remove any surface active agents from the tubing wall. The extraction tube was rinsed successively with concentrated HNO_3, NaOH, and distilled water, washed with methanol, and then allowed to sit overnight in HNO_3.

Reagents. All water used was distilled and deionized (Barnstead Type D4700 NANOpure deionization system). Analytical reagent grade hexanol (Matheson, Coleman and Bell, Norwood, OH) was filtered before use. Aqueous solutions and hexanol were mutually saturated prior to usage. Methanol (B.D.H.) was used as received.

Sample solutions of 1.5 mM *o*-nitrobenzoic acid (B.D.H.) and 4 mM *o*-nitroaniline (Eastman Kodak Co.) were used in studies of the effect of phase ratio, flow velocity, and methanol proportion. The pH's of the standard solutions and aqueous carrier stream were adjusted to 12 with sodium hydroxide (B.D.H.) to ensure extraction of *o*-nitroaniline.

(20) Nord, L.; Karlberg, B. *Anal. Chim. Acta* **1984**, *164*, 233–249.

(21) Fossey, L.; Cantwell, F. F. *Anal. Chem.* **1982**, *54*, 1693–1697.

Pharmaceutical Assay. For the assay of motion sickness tablets, T_1 is replaced by a 0.8-mm-i.d. cross that allows addition of 2 M NaOH in addition to the distilled water carrier stream and the hexanol extractant. The extraction coil, E, was increased to 300 cm of coiled (d_{coil} = 5 mm) 0.5-mm-i.d. Teflon tubing. The assay conditions were 0.123 mL/min of distilled water, 0.039 mL/min of 2 M NaOH, 0.036 mL/min of hexanol, and 1.91 mL/min of methanol.

Each motion sickness tablet contains 50 mg of dimenhydrinate U.S.P. as a 1:1 salt of diphenhydramine and 8-chlorotheophylline. Two tablets were dissolved in 40 mL of water, shaken for 5 min, and then filtered to produce an analytical sample of pH ~7. Standard solutions of dimenhydrinate with concentrations of 2, 3, 4, 5, and 6 mM were prepared by dissolving appropriate quantities of diphenhydramine hydrochloride (Spectrum) and 8-chlorotheophylline (Janssen Chimica) in water and adjusting the pH to 7.

RESULTS AND DISCUSSION

Pentanol–water segmented flow systems have previously been observed to possess thick wetting films. In this work, the organic phase is hexanol: η = 4.578 cP;[22] $\gamma \cong$ 6 dyn/cm (estimated from values for pentanol and octanol).[23] Regular segmentation was routinely achieved using hexanol under a wide variety of experimental conditions provided that the extraction coil had been adequately washed to remove any surface active agents which had accumulated on the tubing walls.

o-Nitrobenzoic acid and *o*-nitroaniline are the model sample components. Both components were injected as an aqueous solution into the pH 12 aqueous carrier stream. *o*-Nitrobenzoic acid is fully deprotonated at pH 12 and therefore remains unextracted. *o*-Nitroaniline is neutral, extracts quantitatively into the organic phase, and is detained by the stagnant organic film. Hence, two individual peaks result for each injection as shown in Figure 2: a sharp peak for the unextracted *o*-nitrobenzoate and a broad peak for the extracted and dispersed *o*-nitroaniline. The variations in the peak resolutions, baseline widths (W_b), and capacity factors (k') of the two analytes were investigated as a function of flow rate, aqueous-to-organic phase ratio, and extraction coil length.

Film Formation. No exact theory exists for film formation in SE-FI systems. Several equations have been used to describe the film thickness, d_{film}, in liquid systems. All of these equations have the general form[3]

$$d_{film} = k d_{tube}\left(\frac{u\eta_c}{\gamma_{org/aq}}\right)^a \qquad (4)$$

where d_{tube} is the inner diameter of the tubing, u is the linear velocity, η_c is the viscosity of the continuous film-forming phase, and $\gamma_{org/aq}$ is the interfacial tension between the organic and aqueous phases. The constants k and a are usually equal to $^1/_2$ or $^2/_3$. Actual measured film thicknesses tend to be smaller than those predicted by eq 4.[9,20] Nevertheless eq 4 indicates

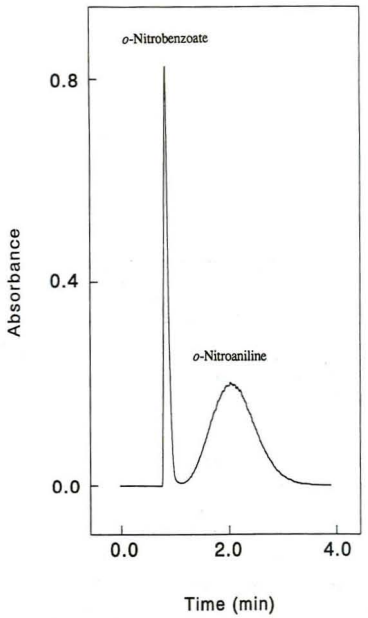

Figure 2. Instrument response for the injection of 1.5 mM *o*-nitrobenzoate and 4.0 mM *o*-nitroaniline. Experimental conditions: aqueous-to-organic phase ratio, 3.13; aqueous segment length, 10.0 mm; organic segment length, 3.2 mm; coil, 190 cm of coiled 0.5-mm i.d. tubing; extraction coil flow rate, 0.47 mL/min; methanol flow rate, 1.68 mL/min.

that thick films result from the use of organic solvents of high viscosity and low interfacial tension.

Flow Rate. From eq 4 it is evident that the film thickness should increase with increased linear velocity. This in turn will cause a greater difference in the aqueous and organic linear velocities (eq 3). Studies of the effect of flow rate were conducted at a constant aqueous-to-organic ratio (5) and constant segment lengths (14.5–15.0 mm for H_2O and 2.8–3.0 mm for hexanol). The *o*-nitrobenzoate remains in the aqueous phase and is used as a measure of $u_{segment}$. The retention time of the extracted *o*-nitroaniline relative to that of the unextracted *o*-nitrobenzoate (t_{org}/t_{aq}) was observed to increase rectilinearly (slope = 0.48 ± 0.02; r^2 = 0.988) over the range of linear velocities studied (1.1–5.3 cm/s). More formally, combining eqs 3 and 4 yields the relationship

$$\frac{t_{aq}}{t_{org}} = 1 - \left[k\pi d_{tube}{}^2\left(\frac{\eta_c}{\gamma}\right)^a\right]u^a \qquad (5)$$

where the terms in the square brackets are constant so long as the extraction coil and solvents are held constant, as in this experiment. Replotting the data as $1 - (t_{aq}/t_{org})$ *vs* linear velocity (not shown) enabled determination of the power term a from eq 3 to be 0.42 (r^2 = 0.999). This is consistent with the general overestimation of film thicknesses by eq 4 when a is assumed to be $^1/_2$ or $^2/_3$.[9,20]

The baseline width in time units for the unextracted *o*-nitrobenzoate decreased as the segmented flow rate in the

(22) *CRC Handbook of Chemistry and Physics*, 73rd ed.; CRC Press, Inc.: Boca Raton, FL, 1992–1993.
(23) *International Critical Tables of Numerical Data: Physics, Chemistry and Technology*, 1st ed.; National Research Council, McGraw-Hill: New York, 1929; Vol. IV.

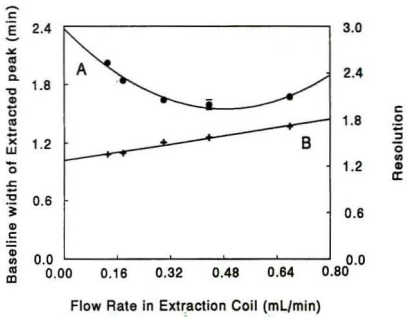

Figure 3. Effect of flow rate on (A) peak width of the extracted components(left *y*-axis) and (B) resolution (right *y*-axis). Experimental conditions: aqueous-to-organic ratio, 5.0; aqueous segment length, 14.5–15.0 mm; organic segment length, 2.8–3.0; extraction coil, 190 cm of coiled 0.5-mm i.d. tubing.

extraction coil increased, as expected for a concentration-based detector. A plot of the *o*-nitrobenzoate baseline peak width versus the reciprocal of the flow rate (not shown) yielded the expected linear relationship (slope = 0.636; intercept = 0.336; r^2 = 0.994).

Figure 3A shows the effect of flow rate in the extraction coil on the extracted *o*-nitroaniline baseline width in time units. The extraction tubing was tightly coiled (d_{coil} = 5 mm) to ensure rapid extraction kinetics.[8] Under such conditions, band broadening due to noninstantaneous extraction are negligible. Thus the observed behavior results from two independent effects. First, the greater linear velocity results in a decrease in the time-based width of the extracted peak, as was observed for the unextracted *o*-nitrobenzoate peak above. This effect is dominant at the lower flow rates in Figure 3. Second, the wetting film thickens as the linear velocity within the extraction coil is increased, as predicted by eq 4. The band broadening which results from the wetting film is described by the nonideal model of Snyder and Alder.[24] This model assumes that no mixing occurs between the organic solvent in the moving segment and the solvent in the wetting film. Solute transfer from the wetting film into the moving organic solvent occurs only via diffusion. The resultant expression for the band broadening, in terms of the variance in segment units, is given by

$$\sigma_{segment}^2 = \frac{LV_{film}^2 d_{tube}^2 u}{36DL_{seg}^2 V_{tube}^2} \quad (6)$$

where L is the tube length, L_{seg} is the segment length, and V_{tube} is the volume of the tube. Under the conditions of this experiment, the only parameter altered is the linear velocity. However, the thickness of the wetting film and thus the film volumes are dependent upon the linear velocity (eq 4) to the power 0.42, as determined above. In summary, the peak variance should depend upon the linear velocity to the power of 1.84 on the basis of the nonideal model. The plot of peak variance in distance units versus the linear velocity displays a power dependence of 1.78 (r^2 = 0.991), indicating that the nonideal model is appropriate for describing the band broadening in this system.

The net effect of the relative velocity and band broadening effects discussed above is a rectilinear increase in the resolution (as defined in chromatography) between the unextracted *o*-nitrobenzoate and the extracted *o*-nitroaniline as the flow rate is increased (Figure 3B; r^2 = 0.988).

Phase Ratio. The influence of the aqueous-to-organic phase ratio on relative retention, band broadening, and resolution was studied at a constant flow rate of 0.16 mL/min in the extraction coil. The linear velocity of the unextracted *o*-nitrobenzoate should be unaffected by the phase ratio and was defined as $u_{segment}$. For an extractable component, such as *o*-nitroaniline, the situation is quite different. The stationary wetting film is present on the walls of the tubing around both the aqueous and organic segments. This is depicted in the insert in Figure 1 and substantiated by the band broadening obeying the nonideal model which assumes no convective mixing between the film and the moving segments. Thus the volume of the wetting film (V_{film}) for a given linear velocity is independent of the phase ratio. However, as the aqueous-to-organic phase ratio increases, the total volume of the organic phase in the extraction coil decreases. Given the constant film volume and the decreasing total organic phase volume, the proportion of the organic phase in the stagnant film must increase as the aqueous-to-organic phase ratio is increased. This has the net effect of decreasing the linear velocity of the organic phase ($u_{organic}$) relative to that of the aqueous phase ($u_{segment}$) as per eq 3. The relative retention of the extracted component should therefore increase with increasing the aqueous-to-organic phase ratio. Indeed the relative retention (t_{org}/t_{aq}) for the extracted *o*-nitroaniline increases rectilinearly (slope = 0.104 ± 0.004; intercept = 0.20 ± 0.04; r^2 = 0.994) with increasing the aqueous-to-organic phase ratio.

Varying the aqueous-to-organic phase ratio also affects the peak widths. The unextracted *o*-nitrobenzoate peak is widest at low aqueous-to-organic phase ratios because the aqueous band is physically broadened by the intervening organic segments. As the aqueous-to-organic phase ratio increases, this broadening decreases asymptotically. Regardless of the conditions, the *o*-nitrobenzoate peak is much narrower than that of the extracted *o*-nitroaniline. Furthermore, the peak width of the extracted *o*-nitroaniline increases linearly as the aqueous-to-organic ratio increases (slope = 0.194; intercept = 0.978; r^2 = 0.999). Again, a greater proportion of the organic phase is in the wetting films when the aqueous-to-organic ratio increases. Thus there will be a greater transfer of solute via these films to adjacent segments.

Figure 4 shows the net result of all of these effects. In this figure the resolution between the extracted and unextracted components is plotted versus the aqueous-to-organic phase ratio. The resolution between the peaks increases with increasing the aqueous-to-organic ratio but with diminishing improvements at the higher aqueous-to-organic phase ratios studied.

Extraction Coil Length. On the basis of chromatographic theory, the retention time of the extracted component should increase linearly with extraction coil length and the peak width should increase with the square root of the coil length. Studies of extraction coils (d_{coil} = 5 mm) from 190 to 600 cm in length

(24) Snyder, L. R.; Alder, H. J. *Anal. Chem.* **1976**, *48*, 1022–1027.

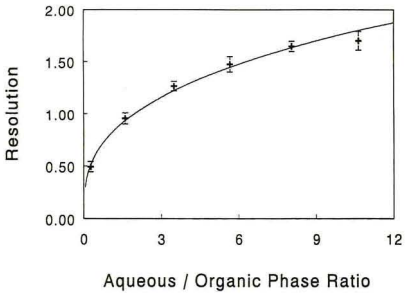

Figure 4. Effect of the aqueous-to-organic phase ratio on the resolution between the extracted and unextracted components. Experimental conditions: coil, 190 cm of coiled 0.5-mm i.d. tubing; extraction coil flow rate, 0.16 mL/min. Uncertainties are the standard deviation (1s) of four replicate injections.

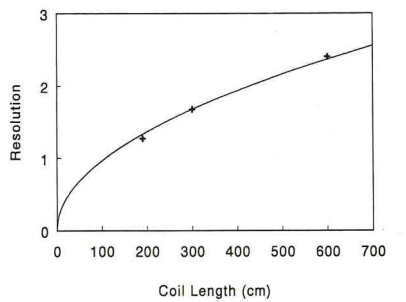

Figure 5. Effect of extraction coil length on the resolution between the unextracted and extracted components (+ denotes experimental points; curve denotes the best fit to the relationship between R_s and $L_{coil}^{1/2}$). Experimental conditions: aqueous-to-organic phase ratio, 4.3; aqueous segment length, 12.0–13.0 mm; organic segment length, 2.8–3.0 mm; flow rate in extraction coil, 0.38 mL/min.

confirmed the linear relationship between the retention time of the extracted component versus the coil length ($r^2 = 0.9996$) and the relationship between the peak width versus the square root of the coil length ($r^2 = 0.988$). As a consequence, the number of theoretical plates increases linearly with extraction coil length ($r^2 = 0.998$), with 75 theoretical plates observed for the extracted component for a 600-cm coil. Figure 5 displays the predicted relationship between resolution and the square root of the extraction coil length. Therefore, the resolution improves with the length of the extraction coil. However, increasing the extraction coil length also decreases the sensitivity.

Methanol Flow Rate. In addition to the aqueous and organic flow rates, the methanol flow also plays an important role in the results obtained. Continuous addition of methanol to the segmented stream homogenizes the two-phase flow for subsequent passage through the detector. Studies assessed the effect of methanol flow on the signal-to-noise ratio at the extracted peak maxima. The aqueous-to-organic phase ratio and segmented flow rate were constant. Figure 6 presents the results of a study on the methanol flow. This curve shows an optimum methanol flow at about 1.2 mL/min. Below this optimum flow of methanol, the signal-to-noise ratio decreases rapidly because of the large noise arising from stream inhomogeniety. On the other hand, high methanol flow rates dilute the solute, thus decreasing the signal intensity.

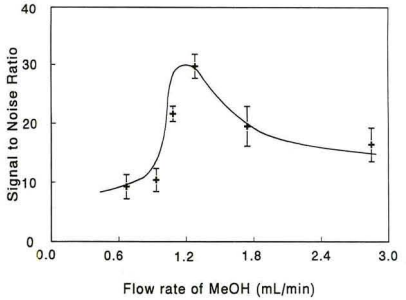

Figure 6. Effect of methanol flow rate on the signal-to-noise ratio of the extracted *o*-nitroaniline peak. Experimental conditions: aqueous-to-organic phase ratio, 4.5; aqueous segment length, 14.5–15.0 mm; organic segment length, 3.0–3.5 mm; total flow rate in extraction coil; 0.32 mL/min. Uncertainties are the standard deviation of three replicate injections.

The data from this study also allow estimation of the band broadening arising within the mixing coil (26.3-cm × 0.8-mm i.d.). The peak broadening from the injection and the extraction coil is independent of the methanol flow rate. However, the broadening occurring in the mixing chamber will be inversely related to the total flow rate, as predicted by the Golay equation.[25] A plot of the peak variance (s^2, measured by the tangent method) for the unextracted *o*-nitrobenzoate versus the total flow rate in the above experiments yielded a straight line (not shown) with a slope of 10 ± 3 s^2 and an intercept corresponding to the combined injection and extraction coil broadening of 7.5 ± 2 s^2. For the optimal methanol flow rate of 1.2 mL/min, the mixing tubing broadening is 7 ± 2 s^2. While this broadening is significant compared to that of the unextracted *o*-nitrobenzoate, it is negligible relative to the band broadening experienced by the extracted *o*-nitroaniline (Figure 2).

Pharmaceutical Assay. To assess the applicability of the SE-FI system discussed above, the technique was applied to the determination of the active components of a motion sickness tablet (8-chlorotheophylline and diphenhydramine). These components are present within the tablet as a 1:1 salt known as dimenhydrinate. Under alkaline conditions, 8-chlorotheophylline does not extract, whereas diphenhydramine extracts readily.[26] However, while their molar concentrations in the sample solution are equal, their absorbances differ radically; 8-chlorotheophylline absorbs about 14 times stronger at 254 nm than diphenhydramine. Thus this sample poses a stringent test of the analytical capability of the SE-FI system based differential migration rates. Upon dissolution in water, dimenhydrinate dissociates into diphenhydramine and 8-chlorotheophylline, both in their ionized form. Such a solution has a pH between 6.8 and 7.3.[27] Standard solutions were prepared by dissolving diphenhydramine hydrochloride and 8-chlorotheophylline in water and adjusting the pH to ~7.

(25) Lucy, C. A.; Glavina, L. L. M.; Cantwell, F. F. *J. Chem. Educ.*, in press.
(26) Fossey, L.; Cantwell, F. F. *Anal. Chem.* **1983**, *55*, 1882–1885.
(27) *The Merck Index. An encyclopedia of chemicals, drugs, and biologicals*, 11th ed.; Merck & Co., Inc.: Rahway, NJ, 1989.

Alkaline conditions are necessary for diphenhydramine to extract into hexanol. However, the deprotonated form of diphenhydramine does not dissolve in water, and precipitation will occur under alkaline sample conditions. Therefore the samples and standards were prepared under neutral conditions, injected into a distilled water carrier stream, and merged with 2 M sodium hydroxide solution at the cross fitting which replaced T_1. A 300-cm extraction coil was used to ensure complete separation of the unextracted 8-chlorotheophylline from the extracted diphenhydramine.

The calibration curves of peak area versus concentration for standards containing 2–6 mM of each standard were linear for 8-chlorotheophylline (slope = 29 750 ± 1 016; $r^2 = 0.9965$) and diphenhydramine (slope = 2290 ± 84; $r^2 = 0.9960$), with intercepts equal to zero (intercept = –260 ± 3274 and –152 ± 268, respectively). Analyses of the motion sickness tablets yielded concentrations of the active ingredients that were in agreement with the label claims, with a precision of 2.5% for 8-chlorotheophylline and 4.0% for diphenhydramine and a throughput of 12 samples/h.

ACKNOWLEDGMENT

The authors are grateful to Dr. Cooper Langford for the use of his peristaltic pump. The constant-pressure cylinders were constructed by the University of Calgary Technical Services. This work was supported by the Natural Science and Engineering Research Council of Canada. Funding provided for K.K.-C.Y. by the Summer Temporary Employment Program sponsored by the province of Alberta is gratefully acknowledged.

Received for review January 5, 1994. Accepted March 30, 1994.®

® Abstract published in *Advance ACS Abstracts*, May 15, 1994.

Anal. Chem. **1994,** *66,* 2226–2231

High-Performance Evolved Gas Analysis System for Catalyst Characterization

P. A. Barnes,* G. M. B. Parkes, and E. L. Charsley

Chemistry Group, Leeds Metropolitan University, Calverley Street, Leeds, LS1 3HE, UK

A new, high-resolution system for analyzing and characterizing materials is described. Based on evolved gas analysis (EGA), it can perform both controlled transformation rate thermal analysis and stepwise isothermal analysis as well as conventional (linear temperature program) EGA. Features include a fast-response furnace, direct temperature measurement, sensitive specific detector, and sophisticated temperature control. The system permits, for the first time, a comparison of the three modes of operation under an identical sample environment. The advantages and limitations of each are illustrated using a sample chosen to model a type of reaction often found in the preparation of catalysts by calcination, the thermal decomposition of hydroxides. It is shown that these methods used with our system have potential advantages in analysis and in the study of complex thermal decomposition processes, by increasing the resolution of consecutive events and providing a more closely controlled sample environment.

In conventional thermal analysis the sample is made to follow a predetermined, usually linear, temperature program while one or more of its properties, e.g., mass loss, energy change, or gas evolution, is measured. To improve resolution and provide better conditions for kinetic studies, a number of workers have developed techniques in which variable heating rates are used.[1-12] These differ from normal thermoanalytical procedures in that the heating rate is not predefined but is altered as a consequence of some change in a monitored parameter of the sample, e.g., in TG it would be the reaction rate as determined from the rate of change of sample mass. As the reaction rate increases the heating rate is decreased, the result being a lowered heating rate through each reaction step. This improves the resolution because of the lower temperature and concentration gradients which exist across the sample under these conditions. The work described in this paper is part of a program to develop new temperature-programmed techniques for characterizing materials and for preparing catalysts with enhanced properties.

Previous Work. In 1962 Paulik and Paulik[1] patented a new approach which they called "quasi-isothermal and quasi-isobaric" thermal analysis. They used a feedback mechanism from a thermobalance to change the heating rate in such a way as to force the sample to react at a constant rate. The partial pressure of the product gas over the sample was also controlled, at approximately 1 atm pressure, by using "convoluted" pans which restricted the escape of product gas from the sample. For reversible dissociation processes, the effect was that the major part of the reaction occurred at a virtually constant temperature, giving rise to the term "quasi-isothermal". A full review of this approach is given in ref 2.

A similar technique, but operating at reduced pressure, was developed independently by Rouquerol[3] who called his method "controlled transformation rate thermal analysis". He utilized a vacuum thermobalance connected to a mass spectrometer via a constriction valve which maintained a fixed pressure of product gas above the sample, thus ensuring a constant reaction rate. Later work by Reading and Rouquerol[4] used infrared detectors, while Stacey[5] used a fluidized bed system, coupled to a katharometer, to investigate the decomposition of boehmite and gibbsite. Real et al.[6] have examined the temperature-programmed oxidation of catalysts using constant reaction rate. Rouquerol has given a detailed review of the technique in a recent paper.[7]

Sorensen[8,9] modified the Pauliks' approach to develop a method called "stepwise isothermal thermal analysis". Instead of a heating rate which changes as the measured sample response varies, Sorensen arranged the apparatus so that the heating rate was switched between zero, when the sample response exceeded an upper preset threshold, and a fixed value, when the response fell below a lower preset threshold. In this approach no attempt is made to keep the reaction rate constant, although it is constrained within limits.

A commercial development, "dynamic rate TGA", which uses a proprietary relationship between the reaction and heating rates, has become available from TA Instruments.[10] Because neither the heating rate nor the reaction rate is kept constant, it has been proposed[11] that this method be called "constrained rate thermal analysis".

There is some confusion in the literature concerning the nomenclature for the above methods. The phrase "constant rate" is somewhat ambiguous as it could refer to the rate of either the reaction or the heating employed. To be absolutely clear in this paper we use the expression "constant reaction rate thermal analysis" (CRRTA) to describe the approach of Rouquerol and the Pauliks. Conventional (linear temperature programmed) evolved gas analysis (EGA) is referred to here as LTP-EGA, and Sorensen's stepwise isothermal thermal analysis method is abbreviated to SITA.

(1) Erden, L.; Paulik, F.; Paulik, J. Hungarian patent 152197, 1962.
(2) Paulik, J.; Paulik, F. *Thermochim. Acta* **1986,** *100,* 23.
(3) Rouquerol, J. *Bull. Soc. Chim. Fr.* **1964,** 31.
(4) Reading, M.; Rouquerol, J. *Thermochim. Acta* **1985,** *85,* 299.
(5) Stacey, M. *Langmuir* **1987,** *3,* 681.
(6) Real, C.; Alcala, M. D.; Criado, J. M. *J. Therm. Anal.* **1992,** *38,* 797.
(7) Rouquerol, J. *Thermochim. Acta* **1989,** *144,* 209.
(8) Sorensen, O. T. *Thermochim. Acta* **1982,** *50,* 263.
(9) Sorensen, O. T. *J. Therm. Anal.* **1992,** *38,* 213.
(10) Gill, P. S.; Sauerbrunn, R.; Crowe, B. S. *J. Therm. Anal.* **1992,** *38,* 255.
(11) Reading, M. In *Thermal Analysis—Techniques and Applications;* Charsley, E. L., Warrington, S. B., Eds.; Royal Society of Chemistry: London, UK, 1992; pp 226–255.
(12) Barnes, P. A.; Parkes, G. M. B., unpublished work.

0003-2700/94/0366-2226$04.50/0
© 1994 American Chemical Society

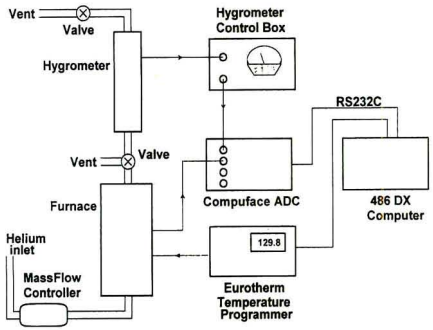

Figure 1. Diagram of the CRRTA and SITA apparatus.

As each variable heating rate technique has its own advantages, the aim of the work described here was to develop a new system which could provide not only conventional LTP-EGA but also CRRTA and SITA, so allowing the operator to select the most appropriate method for the work in hand. Although a specific detector is used in this work, it is equally possible to employ more generally applicable detectors such as a katharometer or mass spectrometer.[12]

EXPERIMENTAL SECTION

Equipment. The apparatus, which is described in detail elsewhere,[13] is illustrated in Figure 1. The evolved gas and temperature signals are processed, and according to the type of thermal analysis experiment in use, the computer instructs the temperature programmer to change the sample temperature or its heating rate appropriately.

The new system has two key features. First, it provides the three types of thermal analysis technique described above. Second, it is designed to minimize the control-loop time constant, which is the time the system takes to adjust the sample temperature in response to an alteration in the reaction rate. The fast response means that good control can be maintained even at high reaction rates. Details of the various components are given below.

Good temperature control, which is essential in CRRTA and SITA measurements, requires a furnace which can be heated and cooled quickly. This is particularly important if run times in CRRTA are to be minimized because this entails operating at high reaction rates, where a rapid furnace response is required to maintain control of the reaction. It is necessary that the system can produce both positive and negative heating rates to obtain true constant reaction rates. The nichrome wound furnace (Stanton Redcroft Model 761) has a maximum operating temperature of 1000 °C. It has a thin ceramic lining and a small swept volume (<7.5 cm^3) and is capable of heating rates of 100 °C min^{-1}. This water-cooled design can be cooled at over 20 °C min^{-1} between 1000 and 100 °C. The furnace has a plate-type thermocouple (type R), on which the sample pan is placed directly, thus ensuring far better temperature measurement than systems where the thermocouple is not in direct contact with the sample pan, as found in most TG instruments.

(13) Barnes, P. A.; Parkes, G. M. B.; Charsley, E. L., in preparation.

The furnace is controlled by a Eurotherm 818P temperature programmer, which is capable of "self-tuning"; i.e., it can alter internal control algorithms to match the particular furnace in use, by optimizing the PID parameters. Any desired temperature or heating rate can be set by means of commands sent from the computer, via an RS232C serial link to the 818P. The EGA detector used is an electrolytic hygrometer (Mark 2) manufactured by Salford Electrical Instruments. As it operates coulometrically, it is intrinsically highly accurate. It is a water-specific device and is very sensitive. It can provide a full-scale response to as little as 10 ppm water vapor in a gas stream. In this application, it is used on the least sensitive setting and with a reduced carrier gas flow rate to avoid overloading the detector. Although scaled in ppm water (by volume), the instrument response is flow-rate dependent and the nominal reading only applies at a flow rate of 100 cm^3 min^{-1}. In this paper, we use a calibration factor which corrects for the different flow rate used and converts the output directly into the rate of evolution of water, expressed in milligrams per minute. This can be related directly to the rate of reaction for the decomposition of the hydroxides. The hygrometer is mounted immediately above the furnace, to keep the swept volume to a minimum, and is connected to it by 15 cm of 3-mm stainless steel tubing which is heated to >100 °C to reduce errors caused by adsorption of water vapor.

Helium is used as a carrier gas because of its good thermal conductivity, which is necessary to minimize the control-loop time constant. An accurate, constant flow of gas is maintained by a Bronkhorst Hi-Tec mass-flow controller.

The output of the hygrometer is sent to the microcomputer via a Comark Compuface 16-bit analog-to-digital-convertor (ADC). This has four thermocouple inputs, four analog inputs, software-selectable voltage ranges, and internal filtering. Connection to the computer is made with a second RS232C serial link.

The apparatus is controlled by a 33 MHz 486DX PC, running a custom-designed program, which controls the temperature programmer, acquires the data, and processes the results. Sophisticated temperature control is used, based on algorithms designed to minimize overshoot, ringing, and response time. The control and data-processing software was written in ANSI C using a C++ compiler (Borland) and provides three principal types of thermal analysis: (a) LTP-EGA, i.e., using conventional preset linear heating rates; (b) CRRTA, i.e., experiments where the temperature is adjusted to keep the rate of reaction constant; (c) SITA, i.e., where the heating rate is switched between a fixed value and zero as the reaction rate crosses preset thresholds.

Depending on the mode selected, the software allows the user to choose and/or record experimental parameters such as maximum and minimum heating rates, various reaction rate threshold values, sample weight and description, data sampling rate, etc. The operational parameters are stored on the computer's hard disk and so may be retrieved later for subsequent examination or printing. During acquisition, data are recorded in real time in ASCII (text) format, which permits it to be reprocessed later, or, alternatively, loaded into a spreadsheet (such as Excel (Microsoft) or the FigP graphics program (Biosoft)) for subsequent analysis and plotting.

Run Conditions. Conventional thermal analysis, using a Stanton Redcroft 625 simultaneous TG-DSC unit was carried out with a helium flow rate of 20 cm^3 min^{-1} and a heating rate of 10 °C min^{-1}. In all the experiments, a sample mass of 5 mg was employed. The LTP-EGA experiments used a heating rate of 10 °C min^{-1}. The CRRTA runs employed maximum and minimum heating rates of ± 10 °C min^{-1} and a target water evolution rate of ca. 3.3 × 10^{-3} mg min^{-1}. SITA was carried out with a heating rate of 10 °C min^{-1}, with the upper and lower reaction thresholds set at ca. 1.8 × 10^{-2} and 3.3 × 10^{-3} mg min^{-1}, respectively. In the CRRTA and SITA experiments, a helium gas flow rate of 20 cm^3 min^{-1} and a hygrometer setting of 3000 ppm were used.

Materials. A suitable material was required to illustrate the different techniques . A mixture was prepared of equal masses of nickel hydroxide (BDH laboratory grade), magnesium hydroxide (BDH laboratory grade), and calcium hydroxide (BDH Analar grade). These decompose, in this order, in single steps, thus providing a good test of resolution.

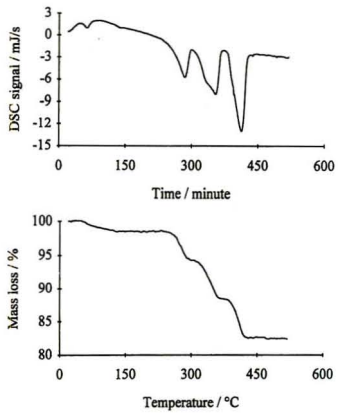

Figure 2. (a, top) DSC curve and (b, bottom) TG curve for the mixed hydroxide sample.

RESULTS AND DISCUSSION

Many catalysts or catalyst supports are prepared by the thermal decomposition of a precursor. For example, high surface area alumina can be made by calcining gibbsite and the ICI methanol catalyst is prepared via the thermal decomposition of an intimate mixture of coprecipitated hydroxy carbonates of copper, aluminium, and zinc. Real catalyst precursors are often complex, and there is a need to characterize and study them by use of techniques which provide much greater detail than is currently possible. The model sample was chosen with this requirement in mind and the system was developed to study the calcination of catalyst precursors, for which the hygrometer is especially suited. Nevertheless, the technique is applicable to any process involving dehydration and can be extended to many other reactions by using alternative detectors.

As has been noted above, other workers have used thermobalances for either CRRTA or SITA and TA Instruments has developed a TG system which performs both techniques, in addition to their dynamic rate measurements.[10] Our system is the first to provide CRRTA and SITA, based on evolved gas analysis. It has some advantages over systems which rely on a thermobalance because it can control individual reactions, simply by changing the detector. For example, we have used a mass spectrometer for CRRTA and SITA to obtain specific information on individual processes.[12]

In thermal analysis, because of the dynamic nature of the temperature and concentration gradients involved, the results obtained from different types of equipment may not be strictly comparable. However, we are able to demonstrate the differences between the various techniques, their advantages and limitations, using an identical sample environment. The results described below illustrate the advantages of CRRTA and SITA, using EGA.

Simultaneous TG-DSC. A conventional simultaneous TG-DSC experiment, Figure 2a,b, was run to provide a reference with which the LTP-EGA, CRRTA, and SITA results could be compared. The results show the three separate hydroxide decompositions, as expected, and an initial small evolution of water vapor, possibly due to the desorption of previously adsorbed moisture from the sample.

Introduction to the LTP-EGA, CRRTA, and SITA Results. To demonstrate these techniques, two figures are shown for each. The first in each series, (a), displays the raw data plotted as the rate of water evolution (in mg min^{-1}) against time. As EGA is used, each reaction gives rise to a peak, analogous to a DSC or DTG signal. In the second plot (b), the EGA signal has been integrated, with respect to time, to give the extent of the reaction, α, on a scale of 0–1, and plotted against temperature. As this is a cumulative function, it is analogous to a TG curve in shape (but inverted, as it represents material detected rather than lost, as in TG).

LTP-EGA. The use of a quantitative detector such as a coulometric hygrometer is a major advantage. Its response depends only on the amount of material evolved and, in this sense, it is similar to TG, although our results show a slightly better signal-to-noise ratio. There is, of course, no baseline shift due to buoyancy as may be found in TG, but a small instrumental drift occurs, arising from the adsorption of evolved water vapor on the walls of the apparatus at one temperature and its subsequent evolution later in the experiment. This effect can be seen, Figure 3a, in the low resolution found in the LTP-EGA results and in the slight baseline drift shown by the difference in signal levels at the start and end of the run. This represents a maximum drift of less than 2% full-scale deflection over a temperature range of 600 °C. Figure 3a shows the rate of evolution of water as a function of time in a conventional LTP-EGA experiment. A key feature is the large variation in reaction rate over each decomposition step. As expected, the peak shapes are very similar to those found using the DSC (Figure 2a). The small initial water evolution at low temperature will be noted. The plot of α against temperature is shown in Figure 3b is similar as the temperature is directly proportional to (elapsed) time because the heating rate is linear. These plots also demonstrate that the resolution of LTP-EGA is not as good that found for DSC (Figure 2a) and TG (Figure 2b), for reasons discussed above.

CRRTA. A relatively high reaction rate target of ca. 3.3 × 10^{-3} mg min^{-1} was selected to minimize the run time. CRRTA is illustrated in Figure 4a, which is more complicated

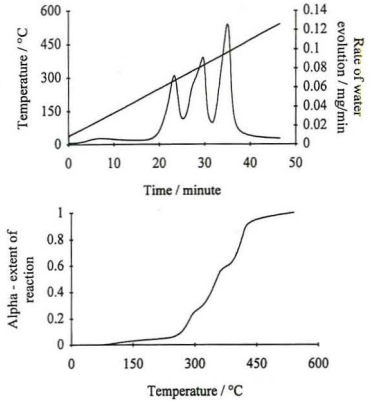

Figure 3. (a, top) LTP-EGA and temperature curves for the mixed hydroxide sample. (b, bottom) Plot of α against temperature for LTP-EGA experiment on the mixed hydroxide sample.

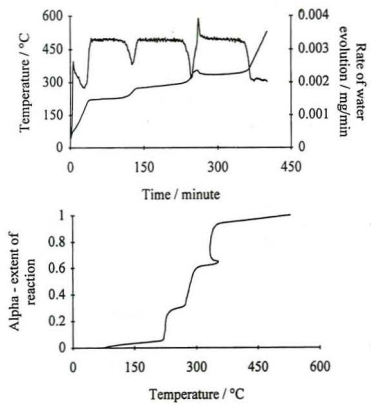

Figure 4. (a, top) CRRTA and temperature curves for the mixed hydroxide sample. (b, bottom) Plot of α against temperature for CRRTA experiment on the mixed hydroxide sample.

than the corresponding LTP-EGA run, Figure 3a. Five processes are revealed. The first, represented by the sharp initial peak, is due to the rapid loss of adsorbed water at low temperatures. This small initial process appears as a transient phenomenon here as it was completed before the reaction rate selected could be achieved.

The three plateaus, which display some noise, represent the thermal events giving rise to the peaks observed in the LTP-EGA experiment. They show that the rate of evolution of water, and hence the rate of reaction, is maintained at a constant value for the duration of the process, apart from small initial and final deviations. Comparison of Figures 4a and 3a show how different the reaction rates are between the two methods. The negative "peaks" found between the plateaus are due to the decrease in the level of water vapor between the three reactions, and the drop in the signal at the end of the run is due to completion of the final decomposition. The temperature required to maintain the reaction rate constant is also shown. It can be seen that during the reactions the temperature rises very slowly and never quite becomes constant.

There is an interesting event at the start of the final reaction, which is shown on both the evolved water and temperature curves as a small, positive peak. This is not an experimental artifact as it is not present in the first two reaction steps. As the previous reaction stops, the hygrometer signal decreases and the heating rate increases as the control system tries to establish the preset reaction rate. At the start of the third main reaction, there is an initial evolution of water vapor and the heating rate starts to decrease as the target reaction rate, which is shown on Figure 4a as the three plateaus, is approached. The rate of reaction then increases rapidly, as indicated by the fast rising edge of the peak on the water trace, and overshoots the target level. At this point, the temperature decreases to establish the preset reaction rate and this is achieved successfully, as demonstrated by the resulting plateau. Analysis of the first two reaction profiles, and the associated temperatures, shows that the effect is not due to a temperature lag between the thermocouple and the sample, but that it is a real phenomenon. It is not the purpose of this paper to provide a detailed interpretation of the event, but two possible alternatives can be outlined. It could be that the main reaction is preceded by a significant nucleation stage[2] which has a larger activation energy or, perhaps, the initial stage involves autocatalysis.

It is interesting to compare the detailed shape of the temperature curves in Figure 4a. The temperature variations required to maintain a constant reaction rate are not the same for the three events, reflecting the different kinetics involved in each.

The advantage of the constant reaction rate method is seen in Figure 4b, which displays the α–temperature curve. Three points become apparent. First, the initial loss of adsorbed water is as clearly demonstrated as in the LTP-EGA diagram (Figure 3a). Second, the consecutive events are much more clearly resolved than on the comparable LTP-EGA figures (Figure 3a,b). The reason can be discerned by examining the temperature traces for the two techniques. While the heating rate in the LTP-EGA run increases linearly, that of the CRRTA experiment is reduced to a very low level during the reaction (Figure 4a), giving rise to the improved resolution expected at low heating rates. Finally, Figure 4b shows the reduction in temperature required to maintain the target rate once the reaction has been initiated for the third event. It is recognized that the appearance of this part of the curve may seem unusual, compared with the results obtained using linear heating rates, but this should not be allowed to detract from its value in revealing the complex nature of the process.

It can be seen that the baseline drift, to which reference was made above, assumes a greater significance in CRRTA (Figure 4a), because the maximum signal which corresponds to the set reaction rate is much lower than in the LTP-EGA run. Fortunately, it has little effect on the shape of the final CRRTA curve (Figure 4b).

SITA. Our implementation of the stepwise-isothermal technique forces each decomposition process to occur at a constant temperature (Figure 5a). In this figure the initial water loss can be clearly seen, followed by the three main reactions, the first two of which produce peaks of an unusual

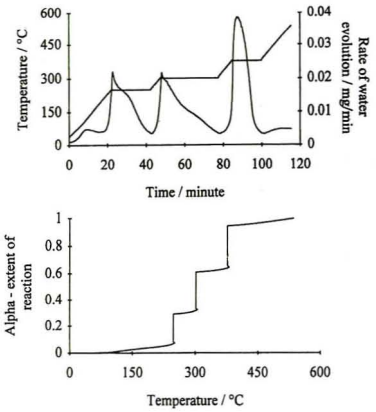

Figure 5. (a, top) SITA and temperature curves for the mixed hydroxide sample. (b, bottom) Plot of α against temperature for SITA experiment on the mixed hydroxide sample.

shape. Figure 5a also highlights the variation in reaction rate, which, though less by a factor of ca. 3 than for the linear heating experiment (Figure 3a), is large when compared with the CRRTA experiment (Figure 4a). Figure 5b shows the plot of α against temperature. This figure shows that the three major events are resolved into sharp steps when the extent of reaction at constant temperature is plotted against temperature. It should be noted that, as the reaction rate is not constant, there will still be variable pressure and concentration gradients across the sample. In practice, the upper and lower threshold levels used to trigger the change in heating rates must be chosen with great care or the resulting curves can display spurious peaks.[14]

The two stages in the third decomposition, revealed in the CRRTA run, are not detected using SITA in the α–temperature plots (Figure 5b). By enforcing a constant temperature, when the extent of reaction is plotted against temperature, any such detail is lost in the resulting vertical line. However, Figure 5a shows the first two main reactions result in very different curve shapes from that found for the third and this is again, we believe, a reflection of the dissimilar kinetics involved.

General Points. A summary of the experiment times and the temperature ranges of the peaks found in DSC, LTP-EGA, CRRTA, and SITA is given in Table 1. In conventional thermal analysis, the duration of the experiment is obviously determined by the heating rate. In CRRTA and SITA, the duration of a run depends on the threshold parameters used, in a complex manner. By choosing a high reaction rate in CRRTA and a high initial threshold in SITA, relatively short run times will be found. Nevertheless, as these techniques rely on using a small and zero heating rate during a reaction, respectively, these experiments will always take more time than conventional thermal analysis, for similar initial heating rates. However, the great increase in resolution provided by CRRTA and SITA outweighs the drawback of extended analysis times in many cases.

(14) Barnes, P. A.; Parkes, G. M. B.; Charsley, E. L., in preparation.

Table 1. Comparison of Times and Temperatures in LTP-EGA[a] and CRRTA[b] and SITA[c]

		temp range of decomp/°C		
expt	duration/min	peak 1	peak 2	peak 3
LTP-EGA	47	240–305	305–376	376–450
CRRTA	420	220–236	273–300	332–341
SITA	120	248	302	377

[a] In the LTP-EGA experiments the peaks overlap so the decomposition temperature range cannot be defined accurately. [b] The temperatures shown for CRRTA are much lower than for the other expeirments as the reaction rate was set at a lower value. [c] In the SITA runs only a single temperature can be given for each event as it an isothermal technique.

The temperatures and temperature ranges of the peaks have no fundamental significance in any of the techniques mentioned as they are dependent on the parameters set in each type of experiment, whether on the heating rate in LTP-EGA, TG, and DSC or the threshold values in CRRTA and SITA. The former effect is well-known, and thermal analysts are used to selecting an appropriate value of heating rate. However, this choice is always empirical, as are the values selected for the various parameters in CRRTA and SITA. With a little experience, it is possible to select these successfully for a given experiment. The results, just as in conventional LTP-EGA, are reproducible provided identical conditions are used and so can be employed equally well for qualitative analysis.

It is usual in many techniques, such as NMR, to routinely display the integrated signal to obtain quantitative information directly from the height of the resulting step function. However, in LTP-EGA, it is often found that consecutive processes are not sufficiently well resolved for this to be useful. The position is very different now that CRRTA and SITA techniques are available, as the start and end of the reactions are very clearly delineated (Figures 4b and 5b). We would expect to see a much wider use of this approach in the future.

CONCLUSIONS

As LTP-EGA, CRRTA, and SITA using evolved gas analysis are available on one system, it is possible to provide a direct comparison of the three methods under identical experimental conditions. Conventional TG and LTP-EGA provide results in the shortest space of time, but suffer from relatively poor resolution. The sample is usually analyzed under conditions far from equilibrium because of the comparatively high heating rates used, so the peak temperatures have no absolute significance. The CRRTA and SITA methods take longer than conventional thermal analysis techniques, by a degree depending on the values of the various parameters used, but have the great advantage of enhanced resolution. CRRTA operates under conditions where the chemical gradients across the sample, due to the diffusion of product gas away from the reaction interface, should be constant. This improves reproducibility and is significant in kinetic studies. One drawback is that the sample temperature may not be constant during a reaction, which is a disadvantage for the latter type of study. On the evidence presented here, SITA produces very high resolution in the temperature domain. In addition, the constant temperature is an advantage in kinetic work, but there must always be some reservations because the

concentration gradient of product gas across the sample will vary with the reaction rate.

The potential of the new system for studying complex reactions of the type often found in the preparation and characterization of catalysts has been demonstrated. The work is now being extended to applying the principles of CRRTA and SITA to temperature-programmed reduction, for which the equipment is ideally suited.

ACKNOWLEDGMENT

The authors thank Dr. M. Reading for his helpful discussions.

Received for review January 4, 1994. Accepted April 21, 1994.[⊗]

[⊗] Abstract published in *Advance ACS Abstracts,* June 1, 1994.

Anal. Chem. **1994,** *66,* 2232–2239

Micellar Catalysis and Product Stabilization in Hydrazone Formation Reactions and Micellar-Modified Determination of Hydrazine and Phenylhydrazine

Anatoly K. Yatsimirsky,* Natalia T. Yatsimirskaya, and Svetlana B. Kashina†

Facultad de Química, Universidad Nacional Autónoma de México (UNAM), México D.F., 04510 México, and Department of Chemistry, Moscow State University, 119899 Moscow, Russia

Kinetics and equilibria of condensation reactions of hydrazine and phenylhydrazine with *p*-(dimethylamino)benzaldehyde in micellar sodium dodecyl sulfate solutions were studied spectrophotometrically. The reaction with hydrazine involves consecutive reversible addition of two aldehyde molecules. The reaction rate under conditions of high excess of aldehyde is determined by the acid-catalyzed attack of aldehyde by hydrazinium cation. The reaction with phenylhydrazine proceeds slower and is characterized by a much smaller equilibrium constant as compared to the reaction with hydrazine. Micelles strongly enhance the observed rate (ca. 10^2 times) and equilibrium (ca. 10^4 times) constants of the reaction with hydrazine and exert more modest (20–30 times) enhancement of the respective parameters of the reaction with phenylhydrazine. The binding constants of reactants and reaction products to surfactant micelles as well as the intrinsic rate constants of the reactions in the micellar pseudophase were calculated from dependencies of observed rate constants and reaction yields on surfactant concentration. Spectrophotometric and kinetic methods of hydrazine determination based on its interaction with *p*-(dimethylamino)benzaldehyde in micellar medium are suggested, which avoid additions of concentrated acids and organic solvents, use ca. 100 times more diluted reagent solution, and can be performed in a shorter time as compared to the traditional procedure.

Aqueous micelle solutions are unique media characterized, in contrast to common mixed aqueous–organic solvents, by a nonuniform distribution of solutes which give rise to modification of their reactivity, spectroscopic, and acid–base properties, extraction, and chromatographic behavior, etc. These effects find numerous applications in analytical chemistry.[1-4] Currently, much attention is attracted to the use of micellar catalysis for improvement of kinetic[5,6] and flow injection[7] methods. Less familiar micellar effects on reaction equilibria (others than shifts of pK_a values of solubilized molecules) have not yet found application in analysis although they can be in principle[8] even stronger than more extensively studied catalytic micellar effects. In particular, they can be used to promote processes strongly reversible in water, e.g., condensation reactions, such as formation of hydrazones, oximes or Schiff bases from carbonyl compounds.

Schiff base and hydrazone formation condensation reactions are widely used for determination of both carbonyl compounds and amines or hydrazines.[9-11] All these reactions are, however, strongly reversible, and sometimes strictly anhydrous conditions are necessary to obtain a close to quantitative yield of the product.[12,13] Another disadvantage is the slow rate of condensation reactions under mild conditions in the absence of specific or general acid catalysts.[14]

Earlier, we observed[15] that micelles of an anionic surfactant sodium dodecyl sulfate (SDS) strongly increase both the rate and the yield of the product of the condensation of benzaldehyde with aniline in aqueous solution. These effects were found to be general for the reactions between arylamines and arylaldehydes and were used for the improvement of spectrophotometric determinations of arylamines with *p*-(dimethylamino)benzaldehyde (DAB) as reagent.[16-18]

Recently, we have found that SDS micelles exert similar effects on the condensation of DAB with hydrophilic hydrazine molecule.[19] This observation opens an opportunity to improve the common method of hydrazine determination in water based on its condensation with two molecules of DAB in strongly acid media.[20-22]

† Moscow State University.

(1) Hinze, W. L. In *Solution Chemistry of Surfactants*; Mittal, K. L., Ed.; Plenum Press: New York, 1979; Vol. 1, pp 79–127.
(2) Hinze, W. L., Armstrong, D. W., Eds. *Ordered Media in Chemical Separations*; ACS Symposium Series; American Chemical Society: Washington, DC, 1987; Vol. 342.
(3) Dorsey, J. G. *Adv. Chromatogr.* **1987,** *27,* 167–214.
(4) McIntire, G. L. *CRC Crit. Rev. Anal. Chem.* **1990,** *21,* 257–278.
(5) Mottola, H. A.; Pérez-Bendito, D. *Anal. Chem.* **1992,** *64,* 407R–428R.
(6) Pérez-Bendito, D.; Rubio, S. *Trends Anal. Chem.* **1993,** *12,* 9–18.
(7) Johnson, B. F.; Malick, R. E.; Ghearing, B.; Dorsey, J. G. *Analyst* **1992,** *117,* 1833–1837.
(8) Berezin, I. V.; Martinek, K.; Yatsimirsky, A. K. *Russ. Chem. Rev.* (*Engl. Transl.*) **1973,** *42,* 787–802.
(9) Siggia, S.; Hanna, J. G. *Quantitative Organic Analysis via Functional Groups*, 4th ed.; Wiley-Interscience: New York, 1979.
(10) Sawicki, E.; Sawicki, C. R. *Aldehydes Photometric Analysis*; Academic Press: London, 1975–1978; Vols. 1–5.
(11) Mázor, L. Methods of Organic Analysis. In *Wilson and Wilson's Comprehensive Analytical Chemistry*; Svehla, G., Ed.; Elsevier: Budapest, 1983; Vol. 15, pp 1–529.
(12) Lopez-Nieves, M.; Wentzell, P. D.; Crouch, S. R. *Anal. Chem.* **1990,** *62,* 304–308.
(13) Lopez-Nieves, M.; Wentzell, P. D.; Crouch, S. R. *Anal. Chim. Acta* **1992,** *258,* 253–258.
(14) Jencks, W. P. *Catalysis in Chemistry and Enzymology*; Dover Publications: New York, 1987.
(15) Martinek, K.; Yatsimirsky, A. K.; Osipov, A. P.; Berezin, I. V. *Tetrahedron* **1973,** *29,* 963–969.
(16) Yatsimirskaya, N. T.; Yatsimirsky, A. K.; Martinek, K.; Berezin, I. V. *Abstr. of Int. Symp. Microchem. Tech.*; Switzerland, 1977; p 216.
(17) Berezin, I. V.; Yasimirskaya, N. T.; Yatsimirsky, A. K.; Martinek, K. *Dokl. Akad. Nauk. SSSR* **1986,** *287,* 643–647.
(18) Krivova, S. B.; Mitiakina, M. G.; Yatsimirskaya, N. T.; Osipov, A. K. *Vestn. Mosk. Univ. Ser. Khim.* **1991,** *32,* 367–372.
(19) Yatsimirsky, A. K.; Krivova, S. B.; Yatsimirskaya, N. T. *Zh. Obsch. Khim.* **1992,** *62,* 916–922; *J. Gen. Chem.* (*Engl. Transl.*) **1992,** *62,* 752–757.
(20) Watt, G. W.; Chrisp, J. D. *Anal. Chem.* **1952,** *24,* 2006–2008.

0003-2700/94/0366-2232$04.50/0
© 1994 American Chemical Society

The purpose of this study is to determine in more detail and to rationalize micellar effects on the reaction between DAB and hydrazine as well as to explore their analytical utility. These effects are of general interest also since they demonstrate the ability of surfactants to accelerate and to enhance the product yield even in reactions with loosely micellar-bound hydrophilic species like the hydrazine molecule. Normally, micellar effects are small for reactions with such reactants and this observation extends the area of applications of micellar media.

The related reaction of DAB with phenylhydrazine in SDS micellar medium was also studied. Determination of this compound with DAB as a reagent under traditional conditions was recently reported.[23] Phenylhydrazine possesses a hydrophobic phenyl group which can enhance considerably the binding of this reactant to micelles as compared to unsubstituted hydrazine. Therefore, a comparative study of micellar effects on reactions with these two molecules can give interesting information concerning the relationship between binding and catalysis in micellar systems.

The condensation of DAB with hydrazine and phenylhydrazine affording azine and phenylhydrazone products, respectively, proceeds according to stoichiometric equations given below

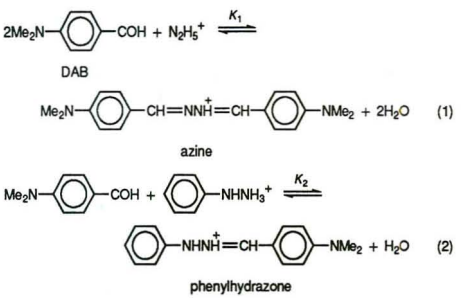

Both reaction products were isolated and their protonated forms proven to have strong absorption maxima in visible region.[24]

Published analytical procedures use 2–4% (0.13–0.26 M) reagent solution in strongly acidic (1–4 M HCl or H_2SO_4) water or alcohol. The final solution is also strongly acidic (0.3–1 M) and contains 0.02 M or higher concentration of DAB and 0–40% of methyl or ethyl alcohol. The reaction time is rather long, ca. 10 min.[20,22]

The use of SDS solution can allow one to avoid extreme conditions of the traditional method as well as to decrease the reaction time. These improvements can facilitate automation of the procedure. It is worth note that attention continues to be attracted to the development of improved methods of hydrazine determination.[25–28]

EXPERIMENTAL SECTION

Reagents. All reagents were analytical-grade commercial products purified when necessary by standard procedures.[29] Distilled water was used for preparation of all solutions.

Procedure. Reactions of DAB with hydrazine and phenylhydrazine were followed spectrophotometrically using a Specord M-40 or a Hitachi 150–20 UV–vis spectrophotometer equipped with a thermostated cell holder. Weekly prepared 2.0×10^{-3} M solutions of hydrazine dihydrochloride and phenylhydrazine hydrochloride (both from Reakhim) in degassed water kept under argon were used as stock solutions. Solutions of DAB (Merck) (0.010 M) were prepared in 96% ethanol or in 0.020 M aqueous SDS (Sigma).

A constant pH was maintained by using 0.010 M acetate–phosphate buffers in an interval of pH 2–6. In more acidic media the desired pH values were obtained by addition of aliquots of standard 1.0 M HCl solution. Since addition of SDS to acid solutions increases the pH even in the presence of buffers[30] the pH values of surfactant solutions were controlled with a glass electrode initially calibrated with HCl solutions of known concentrations and were adjusted to desired values with 1.0 or 0.10 M HCl.

Critical micelle concentrations (cmc's) of SDS were determined kinetically from the reaction rate vs SDS concentration profiles at low SDS concentrations at pH values 2.0 and 1.0. The following results were obtained: at pH 2.0 cmc = 0.0020 M (lit.[30] cmc = 0.00225 M in 0.010 M HCl) and at pH 1.0 cmc = 0.0010 M.

Kinetic and equilibrium measurements normally used 1.0×10^{-5} M and 3.3×10^{-4} M solutions of hydrazine and phenylhydrazine, respectively. In a typical experiment, 3.0 or 2.5 mL of DAB solution containing the desired concentration of SDS at the desired pH value in a 1.0-cm cuvette was placed in the spectrophotometer and equilibrated thermally for 5 min. The hydrazine (15 μL) or phenylhydrazine (500 μL) solution was then added with a micropipet to initiate the respective reaction. All experiments were carried out at 20.0 °C.

All kinetic studies were performed under conditions of a great excess of DAB over hydrazine or phenylhydrazine. The observed pseudo-first-order rate constants were calculated with the method of Guggenheim.[14]

Calculations of observed rate constants and fitting of experimental dependencies to theoretical equations were performed with an IBM AT computer using the SigmaPlot program.

RESULTS AND DISCUSSION

Characterization of Reaction 1 in Micellar Medium. Mixing of hydrazine with an excess of DAB in 0.01–0.02 M SDS solutions at pH < 3.5 results in the formation of a colored product with the absorption maximum at 468 nm. Its molar absorptivity calculated from the limiting value of absorption at [DAB] $\geq 5 \times 10^{-4}$ M and pH 1–2 is $\epsilon_a = 7.5 \times 10^4$ M^{-1} cm^{-1} at 468 nm; for isolated azine in 1 M H_2SO_4 in ethanol $\epsilon = 7.5 \times 10^4$ M^{-1} cm^{-1} at 464 nm.[24] In aqueous solution the

(21) Basson, W. D.; Van Staden, J. F. *Analyst* **1978**, *103*, 998–1006.
(22) *Annual Book of ASTM Standards*; 1991; Vol. 11.01, pp 450–452.
(23) Gutierrez, M. C.; Gomez-Hens, A.; Pérez-Bendito, D. *Anal. Chim. Acta* **1989**, *225*, 115–122.
(24) Masly, L. K.; Umetskaya, M. N.; Tikhomolov, A. A.; Timofeeva, T. N. *Zh. Anal. Khim.* **1983**, *28*, 120–125.
(25) Wang, J.; Naser, N.; Angnes, L.; Wu, H.; Chen, L. *Anal. Chem.* **1992**, *64*, 1285–1288.
(26) Hou, W.; Ji, H.; Wang, E. *Talanta* **1992**, *39*, 45–50.
(27) Ratcliffe, N. M. *Anal. Chim. Acta* **1990**, *239*, 257–262.
(28) Atanasiou-Malaki, E.; Koupparis, M. A. *Talanta* **1989**, *36*, 431–436.
(29) Perrin, D. D.; Armarego, W. L. F.; Perrin, D. R. *Purification of Laboratory Chemicals*; Pergamon Press: Oxford, 1980.
(30) Bunton, C. A.; Wolf, B. *J. Am. Chem. Soc.* **1973**, *95*, 3742–3749.

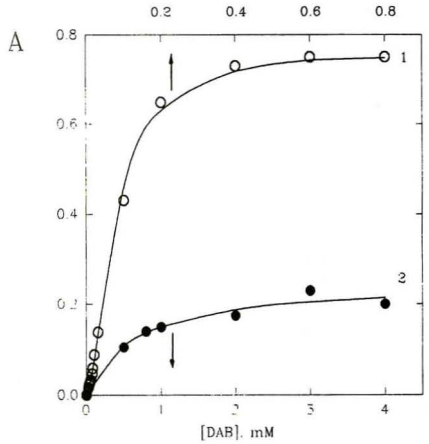

Figure 1. Absorbances of equilibrated solutions of 1.0×10^{-5} M hydrazine, λ 468 nm, pH 1.0 (curve 1) and 1.7×10^{-4} M phenylhydrazine, λ 465 nm, pH 2.0 (curve 2) in 0.020 M and 0.010 M SDS, respectively, vs DAB concentration. The curves are theoretical profiles calculated from eq 5 (curve 1) and the same equation but without the quadratic term and with K_2 instead of K_3 (curve 2) with parameters given in the text and Tables 1 and 2.

azine absorption maximum lies[23] at 452 nm and in 40% aqueous ethanol[20] at 458 nm. Evidently the azine absorption maximum undergoes a red shift on passing from water to less polar solvents. The fact that micellar medium induces more pronounced red shift than ethanol indicates more or less deep penetration of azine molecules into SDS micelles.

Under the same conditions but with an excess of hydrazine over DAB a more wide and less intensive maximum is observed with $\epsilon_h = 2.8 \times 10^4$ M^{-1} cm^{-1} at 468 nm. This spectrum can be ascribed to the hydrazone formed from one hydrazine and one DAB molecule according to eq 3

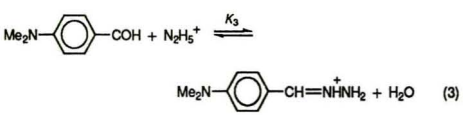

(3)

followed by the second condensation step 4

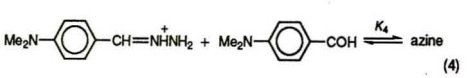

(4)

The existence of an intermediate follows also from the concentration dependence of the absorbance of equilibrated mixtures of hydrazine and DAB, Figure 1, curve 1. Fitting the dependencies of this type obtained at two pH values to the respective theoretical eq 5 gives the equilibrium constants collected in Table 1.

$$\epsilon_{obs} = (\epsilon_h K_3[DAB] + \epsilon_a K_3 K_4[DAB]^2)/(1 + K_3[DAB] + K_3 K_4[DAB]^2) \quad (5)$$

Absorption spectra of azine recorded in the pH interval 1.0–7.8, Figure 2, show the existence of three forms: colorless neutral molecule, monoprotonated form with maximum at 495 nm ($\epsilon = 5.5 \times 10^4$ M^{-1} cm^{-1}), and diprotonated form with maximum at 468 and given above ϵ_a. Evidently, the form actually used for analytical determinations is doubly protonated azine. A routine analysis of pH dependencies of the absorptions at different wavelengths (in the interval 450–500 nm) gives the mean values of $pK_{a1} = 3.35 \pm 0.03$ and $pK_{a2} = 6.76 \pm 0.05$ in 0.020 M SDS. The difference between pK_{a1} and pK_{a2} is surprisingly small, ca. 3.4. The same difference for hydrazine is 8.9. This effect can be explained by delocalization of positive charges on the azine nitrogens due to strong resonance with lone pairs of *p*-(dimethylamino) groups.

Respective pK_a values in aqueous solution are unknown, and one may expect pK_{a1} to be between 0 and 1 since 1 M strong acid is necessary for the complete protonation of azine.[20] Thus, 10^2–10^3 effect of stabilization of doubly protonated azine can be attributed to its incorporation into anionic micelles.

Kinetics of the formation of azine, reaction 1, followed a pseudo-first-order rate law. The dependence of the observed rate constant, k_{obs}, on DAB concentration at pH 1.0 is shown in Figure 3, line 1. As expected for a reversible reaction, this dependence has a positive intercept when extrapolated to zero DAB concentration.

The rate equation derived with a steady-state approximation to the hydrazone intermediate, reaction 3, has the form

$$k_{obs} = (k_{-1}k_{-2} + k_1 k_2[DAB]^2)/(k_{-1} + k_2[DAB]) \quad (6)$$

where the rate constant k_{-1} corresponds to the backward process of step 3 and rate constants k_2 and k_{-2} to the forward and backward processes of step 4. Fitting the results in Figure 3, curve 1, to eq 6 gives $k_2 = 48 \pm 12$ M^{-1} s^{-1}, $k_{-2} = (1.2 \pm 0.4) \times 10^{-3}$ M^{-1} s^{-1}, and $k_2/k_{-2} = K_4 = 4 \times 10^4$ M^{-1} in reasonable agreement with K_4 from the equilibrium study, Table 1.

At high DAB concentrations eq 6 can be presented in a simplified form as eq 7 which corresponds to the linear part

$$k_{obs} = k_1[DAB] \quad (7)$$

of curve 1 in Figure 3 and is indicative of rate-determining forward reaction 3. The respective second-order rate constant k_1 is an apparent parameter which depends on reaction conditions such as SDS concentration and pH. All further discussions are based on values of k_1 which are calculated as slopes of k_{obs} vs [DAB] profiles, like that shown in Figure 3.

Mechanisms of hydrazone formation reactions in the absence of micelles have been studied thoroughly with substituted hydrazines as substrates[14,31,32] (these references contain extensive citation of earlier works). Usually the respective free bases are considered the reacting species. This is not evident for unsubstituted hydrazine, however, since it

(31) Stachissini, A. S.; do Amaral, L. *J. Org. Chem.* **1991**, *56*, 1419–1424.
(32) Somera, N. M.; Stachissini, A. S.; do Amaral, A. T.; do Amaral, L. *J. Chem. Soc., Perkin Trans. 2* **1987**, 1717–1722.

Table 1. Rate and Equilibrium Parameters of Reactions 1 and 2 in Aqueous SDS Solution at 20 °C

reactn	pH	$10^{-3}K_3$[a] (M^{-1})	$10^{-4}K_4$[a] (M^{-1})	k_1[a] (M^{-1} s^{-1})	$k_{1,b}$ (M^{-1} s^{-1})	$k_{H,m}$ (M^{-2} s^{-1})	$k_{H,b}$ (M^{-2} s^{-1})	$10^{-8}K_1$[a,b] (M^{-2})	$10^{-4}K_{1,b}$ (M^{-2})	$10^{-2}K_2$[a] (M^{-1})	$K_{2,b}$ (M^{-1})
1	1.0	2.9 ± 2.1	6.9 ± 0.7	7.5	0.2	0.5 ± 0.1	2.0	2.0	1.0		
1	2.0	6.3 ± 1.4	3.2 ± 0.7	12.0	0.08	1.1 ± 0.4	8.0	2.0	1.0		
2	2.0			2.8	0.1	500 ± 200	7900			6.7 ± 1.4	30

[a] At optimum SDS concentration: 0.020 M for reaction 1 and 0.010 M for reaction 2. [b] $K_1 = K_3K_4$.

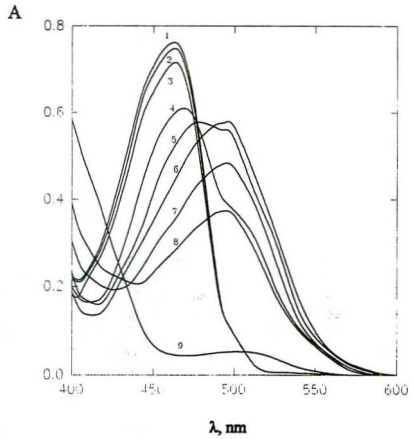

Figure 2. Absorption spectra of 1.0 × 10^{-5} azine in 0.020 M SDS at pH values 1.0 (1), 2.3 (2), 2.7 (3), 3.4 (4), 4.3 (5), 5.2 (6), 6.6 (8), and 7.8 (9).

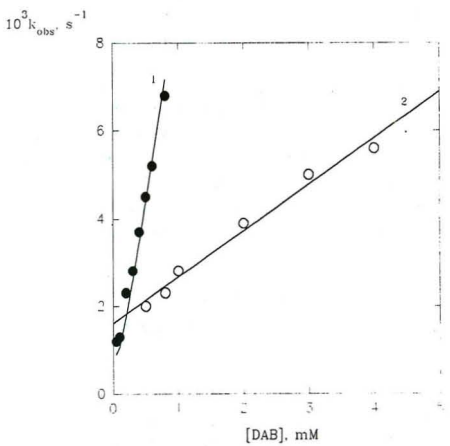

Figure 3. Observed pseudo-first-order rate constants of reactions 1 (curve 1; pH 1.0; 0.02 M SDS) and 2 (line 2; pH 2.0; 0.01 M SDS) vs DAB concentration. Curve 1 is the theoretical profile calculated from eq 6 with parameters given in the text.

is substantially more basic than the usually employed substrates (phenylhydrazine, semicarbazide, etc.) and the concentration of its neutral form in acid solutions can be too small to provide the observed reactivity. To identify the reacting form of hydrazine we studied the pH dependence of k_1 in interval 1 < pH < 4 and found that at pH < 3 the predominant reaction path is a specific acid catalyzed attack of $N_2H_5^+$ cation at DAB with the respective third-order rate constant k_H determined as

$$k_H = k_1/a_{H_3O^+} \quad (8)$$

At pH > 3 a noncatalyzed attack of $N_2H_5^+$ at DAB becomes significant. Values of k_1 pass over an optimum at pH ca. 1.7 and decrease at lower pH probably due to protonation of DAB, $pK_a = 1.61$.[33]

Characterization of Reaction 2 in Micellar Medium. Mixing of phenylhydrazine with an excess of DAB under the same conditions as in the case of hydrazine results in the formation of a colored product with a strong absorbance in UV region and a relatively weak maximum at 465 nm which is associated with the protonated form of the phenylhydrazone product. Dependence of the absorbance at this wavelength on DAB concentration at fixed pH and concentrations of SDS and phenylhydrazine is shown in Figure 1, curve 2. The equilibrium constant K_2 calculated from these results, Table 1, is 1 order of magnitude smaller than K_3 for hydrazine.

The formation of the reaction product followed pseudo-first-order kinetics under conditions of an excess of DAB over phenylhydrazine as in the case of hydrazine. The dependence of k_{obs} on DAB concentration at pH 2 and fixed concentration of SDS is shown in Figure 3, line 2. It follows a simple eq 9for a pseudo-first-order reversible reaction with rate constants

$$k_{obs} = k_1[DAB] + k_{-1} \quad (9)$$

of forward and reversing steps $k_1 = 1.1 \pm 0.1$ M^{-1} s^{-1} and $k_{-1} = (1.6 \pm 0.2) \times 10^3$ s^{-1}, respectively. The ratio of these constants $k_1/k_{-1} = 6.9 \times 10^2$ M^{-1} gives the equilibrium constant which is in a good agreement with that found above from thermodynamic data, K_2, Table 1.

The pH dependence of absorbance at 465 nm at fixed concentrations of components was bell-shaped with a maximum at pH 2.0. The molar absorptivity of phenylhydrazone product at pH 2.0, $\epsilon_{Ph} = (1.5 \pm 0.1) \times 10^3$ M^{-1} cm^{-1}, was found by extrapolation of the absorbance to infinite DAB concentration. In more acid solutions the equilibrium constant becomes so small that no "saturation" of the dependence of absorption vs DAB concentration is observed. This can be due to protonation of DAB molecule. From the part of the dependence at pH > 2 we found $pK_a = 2.7 \pm 0.1$ for the protonated phenylhydrazone product.

The kinetics of condensation of phenylhydrazine with substituted benzaldehydes in the absence of micelles has been studied comprehensively.[31,32] From published data one can

(33) Pal'm, V. A., Ed. *Tables of Rate and Equilibrium Constants of Organic Heterolytic Reactions*; Acad. Sci. USSR VINITI Publ.: Moscow, 1976; Vol. 2(1), p 97.

conclude that the predominant reaction path in acid solutions is the third-order specific acid-catalyzed addition of phenylhydrazine free base to DAB.

Micellar Effects on Reactions 1 and 2. Yields of the products of reactions 1 and 2 in the absence of SDS and pH > 0.5 were very small. Thus, in 20% ethanol (added to increase DAB and product solubility) at [DAB] = 1.0×10^{-3} M the yield of azine was ca. 1% with respect to hydrazine at pH 1.0, and that of phenylhydrazone at [DAB] = 5.0×10^{-3} M and pH 2.0 was less than 1%. The results obtained under these conditions allowed us to obtain only an approximate evaluation of equilibrium and rate parameters in aqueous solution which were used for the purposes of comparison with respective micellar parameters.

A quantitative treatment of micellar effects on rates and equilibria of chemical reactions can be done with the "pseudo-two-phase" theory which is based on the assumption of equilibrium distribution of reactants between balk aqueous and micellar pseudo-phases and simultaneous transformation of reactants in both "phases".[8,34-36] Binding of organic molecules to micelles is usually described as a partition between aqueous and micellar "phases" and that of small hydrophilic ions as an ion exchange with nonreactive micellar counterions tightly bound to the micellar surface layer.

In our case incorporation of DAB and phenylhydrazine into SDS micelles can be described as their partition between two "phases" with partition constants $P_D = [DAB]_m/[DAB]_b$ and $P_{Ph} = [PhNHNH_2]_m/[PhNHNH_2]_b$, respectively. The binding of hydrazinium ions is an exchange of $N_2H_5^+$ with nonreactive counterions (X) in the surface layer of SDS micelles with the equilibrium constant $K_{N/X} = [N_2H_5^+]_m[X]_b/[N_2H_5^+]_b[X]_m$. Strictly speaking, in acid-buffered solutions used in this study, X corresponds to a mixture of nonreactive sodium (both from SDS and buffer) and hydronium cations, but we will not distinguish between these cations here since the ion-exchange constant between H_3O^+ and Na^+ for SDS micelles is close to unity.[37,38]

There are several simplifications in the derivation of final equations. (i) The total concentration of ions in the micellar surface layer is constant and equals[35]

$$[X]_m + [N_2H_5^+]_m = \beta/V_m \qquad (10)$$

where β is the degree of association of micelles with counterions and V_m is the surfactant molar volume. (ii) Concentrations of reactants are much smaller than that of SDS. (iii) The volume fraction of the micellar pseudo-phase is much smaller than unity (this is true when [SDS] < 0.1 M), $[SDS]V_m \ll 1$. (iv) Partition constants of DAB and phenylhydrazine are much higher than unity (this will be proved experimentally).

Equations presented below are derived with these simplifications using general approaches described in refs 8, 34, and 35.

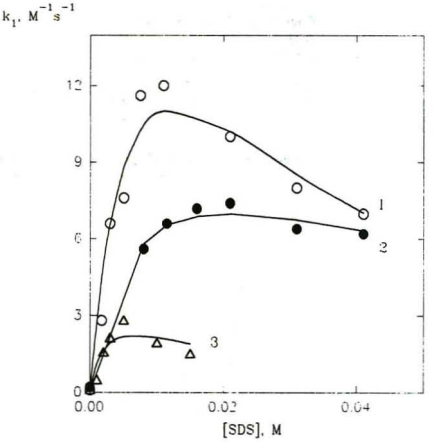

Figure 4. Curves 1 and 2: observed second-order rate constants of reaction 1 vs SDS concentration at pH 2.0 (curve 1) and pH 1.0 (curve 2). The curves are theoretical profiles calculated from eqs 11 and 8 with parameters given in the text and Tables 1 and 2. Curve 3: observed second-order rate constants of reaction 2 vs SDS concentration at pH 2.0. The curve is the theoretical profile calculated from eq 15 with parameters given in the text and Tables 1 and 2.

Micellar Effects on Reaction Kinetics. Figure 4, curves 1 and 2, shows dependencies of observed second-order rate constants k_1 for reaction 1 on SDS concentration at pH 1.0 and 2.0. Qualitatively, these dependencies have typical[8,34-36] forms with maxima. Comparison of the rate constants found in aqueous solution and at optimum SDS concentration (see Table 1) shows observed micellar-induced accelerations to be 150 and 40 times at pH 2.0 and 1.0, respectively.

The above results of the mechanistic study of reaction 1 show that under these conditions the main reaction path is the acid-catalyzed interaction of $N_2H_5^+$ cation with DAB characterized by the rate constant k_H. Therefore, for the quantitative analysis of dependencies in Figure 4 one can apply the theoretical equation for the observed constant k_H which has the form

$$k_H = [k_{H,m}V_m^{-2}K_DK_{N/X}K_{H/X}\beta^2[SDS] + k_{H,b}(\alpha[SDS] + cmc + [B])^2]/[(1 + K_D[SDS])(\alpha[SDS] + cmc + [B])\{(\alpha + \beta K_i)[SDS] + cmc + [B]\}] \qquad (11)$$

where $K_D = P_DV_m$ is an apparent binding constant of DAB to micelles, $\alpha = 1 - \beta$ is the degree of dissociation of micelles, $k_{H,m}$ and $k_{H,b}$ are rate constants in micellar and aqueous "phases" respectively, $K_{H/X}$ is the ion-exchange constant for hydronium ions, and [B] is the concentration of cations from buffer.

To apply eq 11 we used parameters $\alpha = 0.45$ (ref 39), $K_{H/X} = 1$ (refs. 37 and 38), and values of cmc given in the Experimental Section. There is some uncertainty in choosing a proper value of V_m, and reasonable results can be obtained[8,15] with $V_m = 0.35$ M^{-1}. The ion-exchange constant for hydrazonium cation $K_{N/X}$ is unknown, and we used $K_{N/X} = 1$ as an

(34) Quina, F. H.; Chaimovich, H. *J. Phys. Chem.* **1979**, *83*, 1844–1850.
(35) Romsted, L. S. In *Surfactants in Solution*; Lindman, B., Mittal, K. L., Eds.; Plenum Press: New York, 1984; Vol. 2, pp 1015–1068.
(36) Bunton, C. A.; Savelli, G. *Adv. Phys. Org. Chem.* **1986**, *22*, 213–310.
(37) Quina, F. H.; Politi, M. J.; Cuccovia, I. M.; Martins-Franchetti, S. M.; Chaimovich, H. In *Solution Behavior of Surfactants*; Mittal, K. L., Fendler, E. J., Eds.; Plenum Press: New York, 1982; Vol. 2, pp 1125–1136.
(38) Perez-Benito, E.; Rodenas, E. *J. Colloid Interface Sci.* **1990**, *139*, 87–92.
(39) Frahm, J.; Diekmann, S. In *Surfactants in Solution*; Lindman, B.; Mittal, K. L., Eds.; Plenum Press: New York, 1984; Vol. 2, pp 897–914.

Table 2. Binding Constants (M^{-1}) of Reactants and Products of Reactions 1 and 2 to SDS Micelles

	pH	K_D	K_A	K_{Ph}	K_{PhH}	K_P
DAB	1.0	140 ± 30[a]				
	2.0	16 ± 6				
$PhNHNH_2$	2.0			40[b]	350 ± 200[c]	
					290 ± 130[d]	
azine	2.0		$(3.6 \pm 1.6) \times 10^5$			
phenyl-hydrazone	2.0					$(1.8 \pm 0.5) \times 10^4$

[a] Binding constant of protonated DAB. [b] Calculated indirectly. [c] From kinetic data. [d] From equilibrium data.

approximation since for hydrophilic monovalent cations the values of ion-exchange constants vary depending on the cation's nature in a narrow range from 1 to 2.[40]

Fitting of results in Figure 4 to eq 11 together with eq 8 gives rate and equilibrium parameterrs collected in Tables 1 and 2. Comparison of the rate constants in the micellar "phase" with those in water shows the former to be 4–7 times lower than the latter. Evidently, the main source of the observed micellar effect is the concentration of reactants in micelles. In this connection it is noteworthy that hydrazine can interact with DAB in its protonated form which is attracted and concentrated by anionic micelles.

An increase in K_D on passing from pH 2.0 to pH 1.0 is explicable by protonation of DAB since the protonated molecule can interact with anionic SDS micelles more strongly due to additional electrostatic attraction.

Figure 4, curve 3, shows the dependence of k_1 for reaction 2 on SDS concentration at pH 2.0. Observed micellar-induced acceleration of the reaction with phenylhydrazine is 30-fold, Table 1. For a quantitative treatment of this dependence one must use the respective third-order rate constants k_H as in the case of hydrazine. Interrelation between k_1 and k_H is more complicated here, however. In a general form

$$k_H = k_1(1 + a_{H_3O^+}/K_{a,obs})/a_{H_3O^+} \quad (12)$$

where $K_{a,obs}$ is an observed acid dissociation constant of phenylhydrazinium cation. The factor $(1 + a_{H_3O^+}/K_{a,obs})$ is a correction for protonation of phenylhydrazine. At pH 2.0 the ratio $a_{H_3O^+}/K_{a,obs} \gg 1$ and eq 12 takes the form

$$k_H = k_1/K_{a,obs} \quad (13)$$

Treatment of micellar effects on acid–base dissociation constants in terms of the ion-exchange model[40,41] is more complex than needed for this study. A more simple partition model[8,42] gives the following relationship

$$K_{a,obs} = K_{a,b}(1 + K_{Ph}[SDS])/(1 + K_{PhH}[SDS]) \quad (14)$$

where $K_{a,b}$ is the acid dissociation constant in water and K_{ph} and K_{PhH} are the binding constants of neutral and protonated forms of phenylhydrazine, respectively. Using an equation analogous to eq 11 for k_H together with eqs 13 and 14 we obtain

$$k_1 = k_H K_{a,obs} = [k_{H,m}K_D K_{Ph}\beta V_m^{-2}K_{a,b}[SDS] + k_{H,b}(\alpha[SDS] + cmc + [B])]/[(1 + K_D[SDS])(1 + K_{PhH}[SDS])(\alpha[SDS] + cmc + [B])] \quad (15)$$

Fitting of the results in Figure 4 to eq 15 with the previously determined $K_D = 16\ M^{-1}$ (minimization of a function with three unknown parameters gives large errors) gives the parameters $k_{H,m}K_{Ph}K_{a,b}$ and K_{PhH}. To evaluate K_{Ph} one can suppose the ratio K_{PhH}/K_{Ph} to be approximately the same as the ratio of DAB binding constants in protonated (pH 1.0) and neutral (pH 2.0) forms. This allows one to calculate $k_{H,m}$, K_{Ph}, and K_{PhH}, Tables 1 and 2, from experimentally found parameters.

Evidently in this case the micellar medium is unfavorable for the reaction: the third-order rate constant decreases 16 times on passing from aqueous solution to the micellar "phase". This explains the less pronounced micellar effect on the kinetics of reaction 2 as compared to that on reaction 1. On the other hand the "concentration" accelerating effect which is determined by the binding constants of reactants must be approximately the same in both reactions. This indicates that hydrazinium cation and neutral phenylhydrazine have close affinities to SDS micelles. At the same time phenylhydrazine can be localized in a more hydrophobic part of the micelle, and this explains a stronger negative effect of the micellar microenvironment on its reactivity.

Micellar Effects on Reaction Equilibria. Figure 5 shows dependencies of yields (Y, %) of azine and phenylhydrazone on SDS concentration at pH 2.0 and fixed DAB concentrations.

The yield of azine is connected with the observed equilibrium constant as follows

$$Y = 100(K_1[DAB]^2)/(1 + K_1[DAB]^2) \quad (16)$$

where $K_1 = K_3K_4$. The theoretical equation for the observed equilibrium constant of reaction 1 derived in accordance with refs 8 and 35 has the following form

$$K_1 = K_{1,b}\frac{(1 + K_A[SDS])(\alpha[SDS] + cmc + [B])}{(1 + K_D[SDS])^2\{(\alpha + \beta K_{N/X})[SDS] + cmc + [B]\}} \quad (17)$$

where $K_{1,b}$ is the equilibrium constant of reaction 1 in the absence of SDS and K_A is the binding constant of azine. The concentratioon of hydrazone intermediate is neglected in eq

(40) He, Z. M.; O'Connor, P. J.; Romsted, L. S.; Zanette, D. *J. Phys. Chem.* **1989**, *93*, 4219–4226.
(41) Romsted, L. S.; Zanette, D. *J. Phys. Chem.* **1988**, *92*, 4690–4698.
(42) Yatsimirsky, A. K.; Martinek, K., Berezin, I. V. *Tetrahedron* **1971**, *27*, 2855–2868.

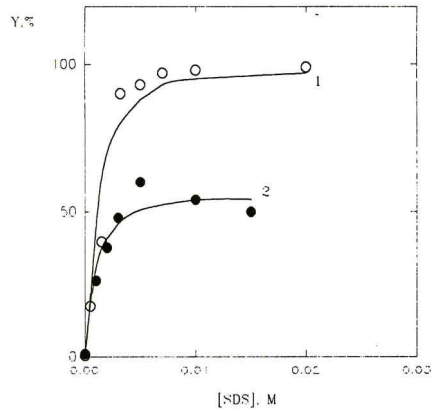

Figure 5. Product yields in reactions 1 (curve 1; 5×10^{-5} M DAB; pH 2.0) and 2 (curve 2; 1×10^{-3} M DAB; pH 2.0) vs SDS concentration. The curves are theoretical profiles calculated from eqs 16 and 17 (curve 1) and eqs 18 and 19 (curve 2) with parameters given in the text and Tables 1 and 2.

16 since under the conditions of Figure 5 its yield is only 6% of the yield of azine, as can be calculated from equilibrium constants K_3 and K_4. It is worth noting that there is a large micellar effect on the equilibrium constant, $K_1/K_{1,b} > 10^4$, Table 1.

Fitting the results in Figure 5, curve 1, to eq 16 with K_1 expressed as eq 17 allowed us to calculate K_A, Table 2. By comparing the binding constants of DAB and azine one can conclude that the micelle-induced shift of the equilibrium originates primarily from much tighter binding of the reaction product as compared with the substrate, $K_A/K_D = 2.1 \times 10^4$. Let us next discuss in more detail the binding constants of reactants and products.

Binding constants for neutral DAB and phenylhydrazine are within the typical range for substituted benzenes.[8,15,43] Their values can be explained by hydrophobic interactions of these molecules with micelles. Azine is the cationic doubly charged species which interacts with SDS micelles both electrostatically and hydrophobically. The contribution of electrostatic interactions to the binding free energy, ΔG_{el}, of a charged species can be evaluated as $\Delta G_{el} = z\Psi_s$, where z is the charge of a species and Ψ_s is the micellar surface potential. For 0.02 M SDS Ψ_s is[44] ca. 100 mV and it gives $\Delta G_{el} = 4.8$ kcal mol^{-1}. This corresponds to a factor of 3×10^3 in the binding constant. The same electrostatic contribution was evaluated above from the observed shift of pK_a of protonated azine as 10^2–10^3. The contribution of hydrophobic interactions can be evaluated as follows. It has been demonstrated[43,45,46] that binding constants of organic molecules to micelles of various surfactants correlate with Hansch hydrophobic parameters π.[47] Parameter π for the p-$C_6H_4NMe_2$ group is[47] 2.3, which corresponds to a factor of 200 in the binding constant K_A due to the presence of such an additional, as compared with DAB, group in the molecule. The combination of both electrostatic and hydrophobic effects can account for the ca. 10^4 times difference between K_A and K_D. This evaluation is of course very rough, but it illustrates that the observed ratio K_A/K_D is quite reasonable.

In the case of phenylhydrazine the yield of phenylhydrazone can be calculated as follows

$$Y = 100(K_2[DAB])/(1 + K_2[DAB]) \qquad (18)$$

with K_2 defined by eq 19

$$K_2 = K_{2,b}(1 + K_P[SDS])/\{(1 + K_D[SDS])(1 + K_{PhH}[SDS])\} \qquad (19)$$

where $K_{2,b}$ is the equilibrium constant of reaction 2 in the absence of SDS and K_P and K_{PhH} are binding constants of phenylhydrazone product and phenylhydrazinium cation.

The micellar effect on the equilibrium constant $K_2/K_{2,b} = 22$, Table 1, is much lower in this case as compared with that in reaction 1. Fitting the data in Figure 5, curve 2, to eq 18 together with eq 19 gives binding constants K_P and K_{PhH}, Table 2. The latter is in good agreement with the same constant found from kinetic results. A smaller value of K_P as compared to K_A seems quite logical since phenylhydrazone is a monocation while azine is a dication. Contributions of hydrophobic interactions are similar for both compounds since values of π for phenyl ($\pi = 1.96$)[47] and p-(dimethylamino)-phenyl (see above) groups differ insignificantly.

Mathematical analysis of eq 17 shows that K_1 for reaction 1 reaches its maximum value at $[SDS]_{opt} \approx 1/K_D = 0.062$ M and the maximum increase in K_1 relative to $K_{1,b}$ is $(K_1/K_{1,b})_{max} \approx K_A/4K_D = 5 \times 10^3$. For reaction 2 from eq 19 we obtain $[SDS]_{opt} \approx 1/(K_D K_{PhH})^{1/2} = 0.014$ M and $(K_2/K_{2,b})_{max} \approx K_P/(K_D^{1/2} + K_{PhH}^{1/2})^2 = 40$. Equilibrium constants for both reactions pass through maxima, but in accordance with these evaluations an optimum equilibrium constant of reaction 2 is observed at lower SDS concentration than that of reaction 1. This explains why the yield vs SDS concentration profile for reaction 2 passes through a maximum while that for reaction 1 does not. Expressions for $(K_1/K_{1,b})_{max}$ and $(K_2/K_{2,b})_{max}$ show that there are two factors responsible for the higher micellar effect on the equilibrium of reaction 1. First, micelles bind the product of this reaction much tighter than that of reaction 2, $K_A \gg K_P$. This produces a stronger decrease in the free energy of products in the case of reaction 1. Second, micelles bind phenylhydrazinium cation tighter than DAB, $K_{PhH} \gg K_D$. Therefore, micelles decrease the free energy of starting compounds of reaction 2 to a greater extent than those of reaction 1. As a result, $\Delta G°$ of reaction 1 decreases in the presence of SDS micelles to a greater extent than $\Delta G°$ of reaction 2.

ANALYTICAL PROCEDURES

Determination of Hydrazine. Results presented in Figures 4 and 5 show that the highest reaction rate and yield of the product are observed at pH 2.0 in 0.01–0.02 M SDS solutions. The preparation of DAB solution and the use of buffers need

(43) Pramauro, E.; Minero, C.; Saini, G.; Graglia, R.; Pelizzetty, E. *Anal. Chim. Acta* **1988**, *212*, 171–176.
(44) James, A. D.; Robinson, B. H. *J. Chem. Soc., Faraday Trans. I* **1978**, *74*, 10–21.
(45) Treiner, C.; Mannebach, M.-H. *J. Colloid Interface Sci.* **1987**, *118*, 243–250.
(46) Valsaraj, K. T.; Thibodeaux, L. J. *Water Res.* **1989**, *23*, 183–189.
(47) Hansch, C.; Leo, A. *Substituent Constants for Correlation Analysis in Chemistry and Bilogy*; Wiley-Interscience: New York, 1979.

some general comments. The efficiency of micellar catalysis is sensitive to the presence of organic cosolvents and inorganic salts. We found that the rate of reaction 1 in the presence of 0.02 M SDS and 5×10^{-4} M DAB at pH 2.0 decreases ca. 15% on addition of a 5% volume of ethanol or duplication of buffer concentration. In view of this, micellar solubilized aqueous rather than alcoholic DAB solution is preferable in this case. To minimize a negative salt effect one can use here a nonbuffered solution containing a known concentration of HCl. It should be noted that SDS micelles behave as a weak electrolyte both with Na^+ and H_3O^+ counterions. This means that acid SDS solutions should have some buffer capacity.

Spectrophotometric Method. The following procedure can be suggested. A known volume of sample or stock hydrazine solution, 1.6 mL of 0.1 M HCl solution, and 1.0 mL of 0.01 M DAB solution in 0.2 M SDS are placed in a 10-mL volumetric flask and diluted with distilled water to 10 mL. After a minimum 5 min the absorbance of solution at 468 nm is measured in a 50-mm cell against the blank. The calibration graph is linear in the range of 0.004–0.1 μg mL^{-1} hydrazine ($r^2 = 0.998$) with a slope 11.7 ± 0.3 μg^{-1} mL and RSD 2.15% for 0.02 μg mL^{-1} hydrazine (11 measurements). The reaction time can be shortened if necessary to 1 min using 0.05 M reagent solution.

Urea, semicarbazide, and ammonia (10 μg mL^{-1} each) tested as possible interfering substances[20] had no effect on the determination of 0.02 μg mL^{-1} hydrazine.

Kinetic Method. The same conditions but with 0.002 M DAB solution in 0.2 M SDS were used. The calibration graph was linear in the range of 0.005–0.5 μg mL^{-1} hydrazine ($r^2 = 0.996$) with a slope of $(2.3 \pm 0.1) \times 10^{-2}$ s^{-1} μg^{-1} mL and RSD of 3.75% for 0.05 μg mL^{-1} hydrazine (11 measurements).

Comparison of characteristics of hydrazine determination in SDS micellar medium with those in classical homogeneous conditions shows the following advantages of the former: (i) no additions of concentrated strong acids and organic cosolvents are necessary, (ii) much more diluted reagent solution can be applied, and (iii) the time of analysis can be shortened considerably.

Determination of Phenylhydrazine. Similar conditions were used for both spectrophotometric and kinetic determinations. The procedure was essentially the same as for spectrophotometric determination of hydrazine. The calibration graph for a spectrophotometric determination was linear in the range of 1–35 μg mL^{-1} phenylhydrazine ($r^2 = 0.997$) with a slope of 0.043 ± 0.001 μg^{-1} mL and RSD of 2.55% for 5 μg mL^{-1} phenylhydrazine (11 measurements) and for kinetic determination in the range of 2–50 μg mL^{-1} hydrazine ($r^2 = 0.996$) with a slope of $(2.7 \pm 0.1) \times 10^{-5}$ s^{-1} μg^{-1} mL and RSD of 2.75% for 5 μg mL^{-1} hydrazine (11 measurements).

The simultaneous determination of hydrazine and phenylhydrazine at the same wavelength can be readily performed since the rates of reactions 1 and 2 differ by 10 times under optimum conditions for hydrazine. It should be noted that DAB is not a suitable reagent for phenylhydrazine due to strong reversibility of condensation and low extinction coefficient of the product although a more sensitive phenylhydrazine determination can be suggested using the absorption below 400 nm. We found in preliminary experiments that much better results can be obtained with other substituted benzaldehydes. Methods of phenylhydrazine determination with the use of micellar media will be presented elsewhere.

ACKNOWLEDGMENT

The work was supported by DGAPA-UNAM, project IN 205393.

Received for review September 2, 1993. Accepted January 11, 1994.*

* Abstract published in *Advance ACS Abstracts,* February 15, 1994.

Anal. Chem. **1994**, *66*, 2240–2244

Biodegradation of Soluble Redox Polymers. 1. (0.017Ferrocene)amylose

Boris B. Gnedenko[†] **and Alexander D. Ryabov**[*,‡]

Department of Chemistry, Moscow State University, 119899 Moscow, Russia, and Division of Chemistry, G. V. Plekhanov Russian Economic Academy, Stremyanny per. 28, 113054 Moscow, Russia

The reaction of amylose with NaH and $FcCH_2NMe_3^+I^-$ in dimethyl sulfoxide brought about a redox-labeled polymer with a *low* degree of modification, viz. 1 ferrocene residue per 60 glucose units. The preparation, (0.017ferrocene)amylose, displays one-electron irreversible behavior at a pyrographite electrode in terms of the Delahay formalism, the formal redox potential $E^{\circ\prime}$ being equal to 0.38 V at pH 6 and 40 °C versus SCE. Specific to amylose enzymes *endo*-depolymerases, which carry out random hydrolysis, accept the labeled amylose providing a significant increase in the peak current on cyclic voltammograms. The absence of potential drifts suggests that the effect is due an increase in the diffusion coefficients of the amylose fragments in the course of enzymatic digestion of (0.017ferrocene)amylose. This proposal was confirmed by the simulation of experimental cyclic voltammograms. Several practical applications of the results of this study for electrochemical assaying the amylolytic activity and evaluation of the mechanisms of the enzymatic catalysis by amylases have been demonstrated.

Chemical and biochemical degradation of polymeric materials,[1–3] often self-assembled via the secondary and tertiary structures, is an urgent challenge to the scientific community encouraged by growing requirements of environmental control.[4,5] Naturally, various approaches, techniques, etc., will contribute to this interdisciplinary area including easy and fast analytical methods controlling the progress of depolymerization reactions. Such features are typical of amperometric biosensors which have recently proved to be extremely competitive as compared with other traditional analytical techniques.[6] Our interests are associated with organometallic electron-transfer carriers,[7,8] and in this paper we present a general approach to follow by cyclic voltammetry a random biodepolymerization of soluble polymer modified with ferrocene residues. Ferrocenes are now widely used as redox modifiers of various polymers[9–11] mostly for electrode coating, but biodegradation of insoluble ferrocene-modified amylose, which was digested by amylases, was only reported by McNeil et al.[12] The enzymatic cleavage provided electrochemically active species responsible for broad traces on cyclic voltammograms. These were much improved for using as an analytical tool by combination with the glucose oxidase amplification.[13] To obtain water-soluble ferrocene-modified amylose with a *low* degree of substitution, we developed a new procedure which is shown in Scheme 1. Amylose is a convenient and promising molecule, since, in addition to its numerous hydroxy groups, it is a polymer with a secondary helical structure[14] and, hence, there was an expectation that, by analogy with the complexation of ferrocenes with cyclodextrins[15–18] and organic molecules with amylose itself,[19,20] bound ferrocene residues could be incorporated into the six to eight-membered inner cavities of amylose and this will decrease their ability to exchange electrons with an electrode. Finally, there is a big family of specific to amylose enzymes which differ in the mechanism of cleavage of the O-1,4-α-glycosidic bonds. One can thus select the pathway of depolymerization, i.e. either endo, when all 1,4-bonds have an equal probability to be cleaved, or exo, when dissociation of terminal residues is highly preferred. We will also present (i) a quantitative rationalization of experimental cyclic voltammograms, (ii) an approach for rapid assay of the amylolytic activity of enzymes and (iii) an easy procedure for preevaluation of either exo or endo mechanism of the enzymatic hydrolysis.

EXPERIMENTAL SECTION

Apparatus. Electrochemical voltammetric measurements were made in a three-electrode thermostated 10-mL cell with pyrographite as a working electrode (surface $A = 1.2 \pm 0.2$ cm^2), a saturated calomel electrode (SCE) (Radiometer), and

† Moscow State University.
‡ G. V. Plekhanov Russian Economic Academy.

(1) Klyosov, A. A. *Biochemistry* **1990**, *29*, 10577–85 (cellulose).
(2) Schoemaker, H. E. *Recl. Trav. Chim. Pays-Bas* **1990**, *109*, 255–72 (lignin).
(3) Evans, J. D.; Sikdar, S. K. *CHEMTECH* **1990**, 38–42 (plastics).
(4) Manahan, S. E. *Environmental Chemistry*, 5th ed.; Lewis Publishers: Chelsea, MI, 1991.
(5) Jones, M. M.; Johnston, D. O.; Netterville, J. T.; Wood, J. L.; Joesten, M. D. *Chemistry and Society*, 5th ed.; Saunder College Publishing: Philadelphia, 1987.
(6) A series of extensive and update reviews demonstrating the recent advantages in this area is summarized in: *Advances in Biosensors*, Turner, A. P. F., Ed.; JAI Press, Inc.: Greenwich, CT, 1992; Vol. 2.
(7) Review: Ryabov, A. D. *Angew. Chem., Int. Ed. Engl.* **1991**, *30*, 931–41.
(8) Ryabov, A. D.; Trushkin, A. M.; Baksheeva, L. I.; Gorbatova, R. K.; Kubrakova, I. V.; Mozhaev, V. V.; Gnedenko, B. B.; Levashov, A. V. *Angew. Chem., Int. Ed. Engl.* **1992**, *31*, 789–90.
(9) Inagaki, T.; Lee, H. S.; Skotheim, T. A.; Okamoto, Y. J. *Chem. Soc., Chem. Commun.* **1989**, 1181–83.
(10) Creasy, K. E.; Shaw, B. R. *Anal. Chem.* **1989**, *61*, 1460–65.
(11) Saji, T.; Hoshino, K.; Ishii, Y.; Goto, M. *J. Am. Chem. Soc.* **1991**, *113*, 450–56.
(12) McNeil, C. J.; Green, M. J.; Hill, H. A. O. Patent GB, Appl. 85/4, 522, 21 Feb 1985; Chem. Abstr. **1988**, *108*, 34501c.
(13) Review: Heller, A. *Acc. Chem. Res.* **1990**, *23*, 128–34.
(14) Kubik, S.; Wulff, G. *Starch/Stärke* **1993**, *45*, 220–25.
(15) Matsue, T.; Evans, D. H.; Osa, T.; Kobayashi, N. *J. Am. Chem. Soc.* **1985**, *107*, 3411–17.
(16) Ryabov, A. D.; Tyapochkin, E. M.; Varfolomeev, S. D.; Karyakin, A. A. *Bioelectrochem. Bioenerg.* **1990**, *24*, 257–62.
(17) Strelets, V. V.; Mamedjarova, I. A.; Nefedova, M. N.; Pysnograeva, N. I.; Pospíšil, L.; Hauzlik, J. *J. Electroanal. Chem.* **1991**, *310*, 179–86.
(18) Isnin, R.; Salam, C.; Kaifer, A. K. *J. Org. Chem.* **1991**, *56*, 35–41.
(19) Wulff, G.; Kubik S. *Makromol. Chem.* **1992**, *193*, 1071–80.
(20) Wulff, G.; Kubik S. *Carbohydr. Res.* **1992**, *237*, 1–10.

0003-2700/94/0366-2240$04.50/0
© 1994 American Chemical Society

Scheme 1

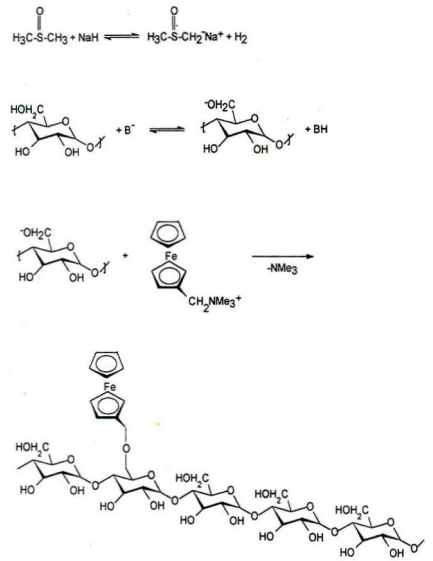

a platinum wire as ancillary electrode. Scans of potential were made by using a potentiostat P-5827M and voltammograms were registered by PDP4–002 and H307 XY recorders. The temperature of the cell was kept constant by circulating water pumped in by a 2219 MULTITEMP II thermostat (LKB). Electronic spectra were recorded on a Beckmann 25 spectrophotometer. The iron content in the labeled amylose was measured by atomic emission with an inductively coupled plasma ICAP-61 spectrometer (TJA Corp.). ^1H and ^{13}C NMR spectra were measured on a CXP 200 Bruker spectrometer in DMSO-d_6 as solvent. Simulations of the cyclic voltammograms were made by a SigmaPlot (Version 4.0) computer program.

Reagents. α-Amylases from porcine pancreas and from human saliva (EC 3.2.1.1) and glucoamylase (exo-1,4-α-glucosidase) from *Aspergillus niger* (EC 3.2.1.3) were Sigma preparations. Amylose from potato (M_n 150 000 g mol^{-1})[21] was purchased from Serva. Samples of resting saliva were used in analyses after 10-fold dilution with 0.1 M acetate buffer (pH 6) containing 15 mM $CaCl_2$. Aliquots (100 μL) were then added into the electrochemical cell. Dimethylsulfoxide, a Merck reagent, was dried over molecular sieves 3A (Ferak). Trimethyl(ferrocenylmethyl)ammonium iodide was prepared by alkylation of ferrocene with (*N,N,N′,N′*-tetramethyldiamino)methane[22] followed by quartenization of [(dimethylamino)methyl]ferrocene formed with iodomethane.[23] Other inorganic salts, mineral acids, phenol, 3,5-dinitrosalycilic acid, and other chemicals used for preparation of the reagents for determination of reducing saccharides[24,25] were Reakhim reagents which were additionally purified in some cases according to the standard procedures.[26]

Preparation of Ferrocene-Modified Amylose. Amylose (2 g) and trimethyl(ferrocenylmethyl)ammonium iodide (0.77 g, 2 mmol) were dissolved in 20 mL of DMSO. On intense stirring (magnetic bar) sodium hydride as a 50% suspension in Nujol (0.24 g, 5.0 mmol) was added to this yellow solution. After violent evolution of dihydrogen the resulting mixture was heated with continued mixing at 100–120 °C for 1 h. The brown-black solution was then cooled to room temperature and the modified amylose was precipitated by addition of a 3–4-fold excess of ethanol (60–80 mL) and washed with 50 mL of ethanol. The slightly colored solid was purified 3 times by dissolving it in 20 mL of DMSO and precipitating with 60–80 mL of ethanol. This was necessary for removal absorbed ferrocene derivatives from amylose. Yield was 1.7 g (80% with respect to amylose).

RESULTS AND DISCUSSION

Synthesis of Soluble (0.017Ferrocene)amylose. The procedure is presented in Scheme 1. Sodium hydride was added to a solution of trimethyl(ferrocenylmethyl)ammonium iodide and amylose in dimethyl sulfoxide (DMSO) to generate a strong base able to deprotonate hydroxy groups of amylose. Subsequent nucleophilic substitution gave rise to a modified polymer which was precipitated by addition of ethanol. The material is poorly soluble in pure water but much better in water–DMSO mixtures. It is slightly colored as a solid, but the solutions in DMSO look yellow-brown and the presence of ferrocene residues can be estimated by conventional UV–vis spectrophotometry at 425 nm where the material has a maximal absorption in 0.1 M acetate buffer, pH 6, in the presence of 10 vol % DMSO at 40 °C (ϵ 0.0175 dm^3 g^{-1} cm^{-1} or 170 dm^3 mol^{-1} cm^{-1} with respect to the concentration of ferrocene residues, vide infra). Our goal was a polymer with a low degree of modification and this was confirmed by the atomic absorption spectrometry. The content of iron attached to amylose was 0.103 mol g^{-1} or, alternatively, 1 ferrocene residue per 60 glucose units (the degree of modification 0.017). Interestingly, a very close value was obtained from the UV-viz measurements using the extinction coefficient for ferrocenecarboxylic acid of 153 dm^3 mol^{-1} cm^{-1} at 446 nm.[27] This limited amount of the conjugated ferrocenes does not change the structure of the polymer in solution as comes from the comparison of the ^1H and ^{13}C NMR spectra of the native[28,29] and modified amylose. Moreover, no ferrocene signals are observed in the proton spectrum giving additional evidence for the low degree of modification. For the same reason it was also impossible to indicate precisely to which of the three hydroxy groups of a glucose unit the methylferrocene moiety was bound. Thus, the binding mode shown in Scheme 1 is one of the possibilities, although the hydroxy group at C6 is usually preferred.[12] The helical structure of (0.017ferrocene)amylose manifests itself in complexation with iodine

(21) Shevel'kova, A. N.; Ryabov, A. D.; Sinitsyn, A. P. *Biokhimia* **1993**, *58*, 928–37.
(22) Osgerby, J. M.; Pauson, P. L. *J. Chem. Soc.* **1958**, 656–60.
(23) Lindsay, J. K.; Hauser, C. R. *J. Org. Chem.* **1957**, *22*, 355–62.
(24) Nelson, N. *J. Biol. Chem.* 1944, *153*, 375–80.
(25) Somogyi, M. *J. Biol. Chem.* **1952**, *195*, 19–23.
(26) Perrin, D. D.; Armarego, W. L. F.; Perrin, D. R. *Purification of Laboratory Chemicals*; Pergamon Press: Oxford, New York, Toronto, Sydney, Paris, Frankfurt, 1980.
(27) Reinehart, Jr., K. L.; Motz, K. L.; Moon, S. *J. Am. Chem. Soc.* **1957**, *79*, 2749–2754.
(28) Dorman, D. E.; Roberts, J. D. *J. Am. Chem. Soc.* **1971**, *93*, 4463–72.
(29) Dais, P.; Perlin, A. S. *Carbohydr. Res.* **1982**, *100*, 103–16.

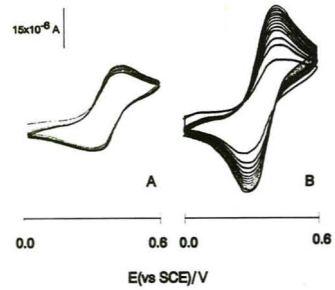

Figure 1. Repetitive cyclic voltammograms of the labeled amylose (10 g dm^{-3}) obtained in the absence (A) and in the presence (B) of α-amylase from porcine pancreas (30 mg dm^{-3} min^{-1}) at a scan rate 0.01 V s^{-1}, 40 °C, pH 6 (0.1 M acetate buffer), and in the presence of 10% DMSO. The time interval between the approaching of anodic peaks was 2 min.

resulting in development of an intense blue color. This observation suggests the principal possibility of incorporation of hydrophobic ferrocene residues into the helical fragments of amylose.

A limited amount of ferrocene moieties brought about only one disadvantage to amylose: common oxidants which are used for assaying the concentration of the reducing saccharides and, thus, the activity of amylases[24,25] were unapplicable for precise quantitative measurements due to oxidation of ferrocene residues. Nevertheless, qualitative experiments using the Somogyi reagent[25] showed that the polymer is still a good substrate for pancreas and salivary α-amylases and glucoamylase.

Electrochemical Properties of (0.017Ferrocene)amylose. Repetitive cyclic voltammograms of the modified amylose dissolved in 0.1 M acetate buffer, pH 6, are presented in Figure 1A. The peak current has only a small tendency to increase on increasing the number of scans. The peak separation was equal to 0.100 V and did not change with time. Such an electrochemical behavior of the redox polymer at the pyrographite electrode can be considered as one-electron and irreversible in terms of the Delahay formalism.[30] Another reason that forces the using of this approach is the fact that the functioning of redox-modified polymers at electrodes might not be necessarily Nernstian. As we will see below, the irreversible behavior of the ferrocene label is advantageous in this case, since, if such, a quantitative theoretical treatment of the data described below simplifies considerably.[31] The one-electron mode implies that only one ferrocene residue is involved in the electron exchange with the electrode provided by the length of the polymer and its low degree of substitution. The formal redox potential (vide infra) of the irreversible oxidation $E^{\circ\prime}$ was equal to 0.38 V at pH 6 and 40 °C versus SCE. The peak current i_p {A} is proportional to the concentration of the conjugate c in the range 1.67–10 g dm^{-3} and the corresponding equation is $10^6 i_p = (2.17 \pm 0.09)c + (0.8 \pm 0.5)$ without correction for background signal. The correlation coefficient r is 0.995. This observation rules out meaningful change in viscosity in the concentration range used.

(30) Delahay, P. *J. Am. Chem. Soc.* **1953**, *75*, 1190–96.
(31) Galus, Z. *Theoretical Basics of Electrochemical Analysis*; Mir Publishers: Moscow, 1974; p 265.

The electrochemical behavior of (0.017ferrocene)amylose changes significantly in the presence of pancreas α-amylase which hydrolyzes O-1,4-α-glycosidic bonds, Figure 1B. An increase in the peak current is bigger, the higher the activity of α-amylase. Other enzymes tested, i.e. salivary α-amylase and glucoamylase, produce similar effects. It should be emphasized that the rates of increase in current were different for the endo- and exo-enzymes of the equal activity. Remarkably, the position of anodic and cathodic maxima, and, hence, the peak separation, does not change with increasing the peak current in all cases. This suggests that the redox label does not change its environment as the depolymerization proceeds, and the increase in current in the presence of depolymerases is not due to the release of ferrocene from the amylose helix. If the increase in current were due to the decomplexation, a drift of the peak potentials should be observed (cf. with the complexation of ferrocenes with cyclodextrins[15–18]). Therefore, the reason for the current increase is likely associated with a change of the molecular weight of the labeled amylose and, hence, of its diffusion coefficient. In the next section, we will show that our electrochemical data can be rationalized in terms of this concept.

Quantitative Treatment of Cyclic Voltammograms. The profile of the anodic wave of a voltammetric curve for an irreversible redox process is given by eq 1,[31,32] where the current

$$i = nFAc_{red}(\pi bD_{red})^{1/2}\chi(bt) \qquad (1)$$

is expressed in μA,[33] $b = [(1 - \alpha)nFv/(RT)]$ {s^{-1}}, D_{red} {cm^2 s^{-1}} and c_{red} {mM} are the diffusion coefficient and concentration of reduced species, respectively, n is the number of electrons transferred, α is the transfer coefficient for a cathodic reaction, v {V s^{-1}} is the scan rate, F is the Faraday constant, A {cm^2} is the electrode surface, and $\chi(bt)$ is the dimensionless current function. If the change in current is only due to depolymerization of (0.017ferrocene)amylose, the growth should arise from an increase in the diffusion coefficient D_{red} which occurs due to random depolymerization of the polymer. If all other characteristics of the electrochemical process are kept constant, it is possible to simulate experimental cyclic voltammograms. The simulation is justified for polymers with a low degree of labeling, since the probability of cleavage of the glycosidic bond in the vicinity of the redox label, which may change the ferrocene environment and, hence, alter the electrochemical properties, is insignificant. This might not be true for a polymer with a bigger amount of redox mediators attached to the polymeric molecule.[12] The diffusion coefficient D_{red} in eq 1 is related to a number-averaged molecular weight of a polymer through the Einstein–Stokes relation 2[34] where r_{red}

$$D_{red} = kT/6\pi\eta r_{red} \qquad (2)$$

{cm} is radius of a spherical particle and η {g cm^{-1} s^{-1}} is the

(32) Bard, A. J.; Faulkner, L. R. *Electrochemical Methods. Fundamentals and Applications*; J. Wiley & Sons: New York, Chichester, Brisbane, Toronto, 1980; pp 222–224.
(33) Yoshida, K. *Electrooxidation in Organic Chemistry. The Role of Cation Radicals as Synthetic Intermediates*; J. Wiley & Sons: New York, Chichester, Brisbane, Toronto, 1984; Chapter 1.
(34) Berezin, I. V.; Klyosov, A. A. *Practical Course of Chemical and Enzymatic Kinetics*; MSU Publishers: Moscow, 1976; p 262.

viscosity of the medium. On assumption that an amylose molecule can be approximated by a sphere of radius r, the latter can be derived from the number-averaged molecular weight of amylose (M_n). The volume (V) of such a molecule is equal to $(^4/_3)\pi r^3$ and alternatively $V = M_n/(\rho N_A)$, where ρ {g cm^{-3}} is the density of amylose and N_A {mol^{-1}} is the Avogadro number. A combination of the two expressions leads to eq 3. Substitution of eq 3 into eq 2 and the resulting

$$r^3 = 3M_n/4\pi\rho N_A \quad (3)$$

one into eq 1 will give a final eq 4 that binds the current with

$$i = 0.29nFAc_{red}\left(\frac{bkT}{\eta}\right)^{1/2}\rho^{1/6}N_A^{1/6}M_n^{-1/6}(\pi)^{1/2}\chi(bt) \quad (4)$$

the number-averaged molecular weight of the labeled amylose. All other parameters in eq 4 can be estimated. In particular, the transfer coefficient for a cathodic reaction α, calculated from the known value of the peak separation $E_{pa} - E_{pc} = 1.857RT/(1 - \alpha)nF$,[35] is equal to 0.5. We assume that the density of the polymer (ρ) and the viscosity of the solution (η) do not change in the course of hydrolysis and are equal to 1.0 g cm^{-3} and 0.01 kg m^{-1} s^{-1}, respectively. The absolute value of the density does not play an important role in this case. It is obvious that it cannot change dramatically on hydrolysis of labeled amylose and the power (1/6) in eq 4 is a guarantee that this term will not affect the current much. The assumption for η is justified because the peak current does not deviate from linearity at the concentrations of the labeled amylose used, vide supra. The numerical values of the function $(\pi)^{1/2}\chi(bt)$ for the given values of α and the peak separation were obtained as described by Nicholson.[36] The dimensionless rate parameter ψ equal to 0.6 was found from the tabulated data. The relation $\psi = k^\circ/(\pi D_{red}a)^{1/2}$ ($a = nFv/RT$) is used for evaluation the electron-transfer rate constant k°.[32] The value of D_{red} for (0.017ferrocene)amylose was estimated from eq 2 (5.9×10^{-7} cm^2 s^{-1}) and k° was then calculated (5×10^{-4} cm s^{-1}). The rate constant is needed for calculation of the formal redox potential $E^{\circ\prime}$ which was equal to 0.382 V versus SCE. When $E^{\circ\prime}$ is known $(\pi)^{1/2}\chi(bt)$ can be obtained. Therefore, if the variation of the number-averaged molecular weight of (0.017ferrocene)amylose is found, a simulation of experimental cyclic voltammograms becomes possible. An agreement between the simulated and the experimental voltammograms would support our mechanistic concept.

The kinetics of random enzymatic hydrolysis of polymeric substrates has been analyzed in the literature.[37-39] Equation 5 gives a time dependence of the number-averaged molecular weight of a polymer in the presence of a depolymerase,[39] where

$$\text{rate} = \frac{d[RS]}{dt} = c\frac{d}{dt}\left(\frac{1}{M_n}\right) \quad (5)$$

(35) Nicholson, R. S.; Chain, I. *Anal. Chem.* **1964**, *36*, 706–23.
(36) Nicholson, R. S. *Anal. Chem.* **1965**, *37*, 1351–55.
(37) Almin, K. E.; Eriksson, K.-E. *Biochim. Biophys. Acta* **1967**, *139*, 238–47.
(38) Almin, K. E.; Eriksson, K.-E.; Petersson, B. *Eur. J. Biochem.* **1975**, *51*, 207–11.
(39) Rabinovich, M. L.; Klyosov, A. A., Berezin, I. V. *Bioorg. Khim.* **1977**, *3*, 405–14.

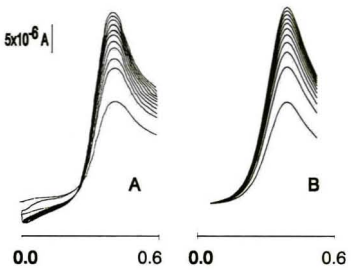

Figure 2. (A) Anodic waves of the cyclic voltammograms obtained during random hydrolysis of (0.017ferrocene)amylose by α-amylase. Conditions are as in Figure 1. (B) Simulated curves for the same experimental conditions calculated on the basis of eq 7. For details, see text.

rate of enzymatic hydrolysis (activity of enzyme) is expressed in {M min^{-1}}, c {g dm^{-3}} is the weight concentration of a polymer which does not change during hydrolysis, M_n {g mol^{-1}} is the number-averaged molecular weight of a polymer, and c/M_n {M} is a current concentration of terminal reducing saccharides (RS). One can integrate eq 5 in the case of the steady-state hydrolysis, i.e. when the rate of enzymatic reaction does not change with time. In fact, we have shown that the rate of enzymatic hydrolysis of amylose (the rate of RS formation {mg dm^{-3}}) is constant over the time of voltammetric experiment (25 min), i.e. $[RS] = [(2.99 \pm 0.05) \times 10^{-2}]t$ ($r = 0.997$) under the conditions given in the caption to Figure 1B. Integration of eq 5 gives

$$\frac{1}{M_n} = \frac{(\text{rate})\,t}{c} + \frac{1}{M_{n0}} \quad (6)$$

where M_{no} and M_n are the initial and current number-averaged molecular weight of a hydrolyzable polymer, respectively. The expression for M_n should be substituted into eq 4, and the current is now a function of time, the activity of enzyme, and the number-averaged molecular weight of the initial amylose preparation, eq 7. The enzymatic activity was determined

$$i = 0.29\,nFAc_{red}\left(\frac{bkT}{\eta}\right)^{1/2}\rho^{1/6}N_A^{1/6} \times \left[\frac{(\text{rate})\,t}{c} + \frac{1}{M_{n0}}\right]^{1/6}\pi^{1/2}\chi(bt) \quad (7)$$

spectrophotometrically by measuring the rate of appearance of the reducing saccharides[24,25] and the resulting value was used in further calculations. The anodic waves of the cyclic voltammograms simulated on the basis of eq 7 are presented in Figure 2B and compared with experimental voltammograms obtained in the presence of the enzyme preparation of equal activity, Figure 2A. The similarity between the two is surprisingly good and, in our opinion, the coincidence is the best proof for our model of the electrochemical response of a limitedly redox-modified polymer that undergoes random hydrolysis.

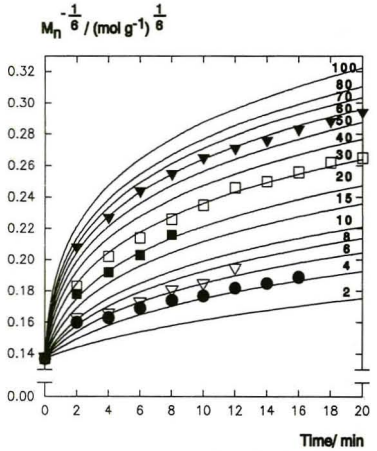

Figure 3. Solid lines are theoretical dependencies of the number-averaged molecular weight of amylose M_n versus time calculated according to eq 6. Numbers above the curves indicate endoamylolytic activity (in mg dm^{-3} min^{-1}). Data were calculated from experimental cyclic voltammograms obtained in the presence of enzyme preparations of different partial activity shown in parentheses and expressed in mg dm^{-3} min^{-1}: ▼, α-amylase from human saliva (60); □, α-amylase from porcine pancreas (30); ■, human saliva of one of us (20); ▽, glucoamylase from *Aspergillus niger* (50); ●, α-amylase from human saliva (4.5).

Applications. Equation 7 shows that the current is a function of the activity of amylase provided other variables are kept constant. Therefore, the "random" activity of amylose depolymerase can easily be assayed as described here. Figure 3 shows how the key parameter $M_n^{-1/6}$ of eq 4 varies with time in the presence of enzyme preparations of different activity (eq 6). Unfortunately, we could not obtain straightforward quantitative information on variation of $M_n^{-1/6}$ with time under exactly the same conditions using, for example, gel chromatography or fluorescence depolarization. However, our data are in agreement with the recent qualitative study of amylase-catalyzed digestion of fluorescein-labeled amylose by fluorescence depolarization.[21] The values of $M_n^{-1/6}$ can alternatively be derived from the experimental cyclic voltammograms using eq 4. A comparison between the theoretical and experimental curves is demonstrated in Figure 3. The proportionality between the current and $M_n^{-1/6}$ might not be that strong in some cases. However, it seems to be quite acceptable when the degree of depolymerization of high molecular weight compound is large provided the digestion is enzymatic, Figure 3. Several enzyme preparations, which carry out random hydrolysis of amylose, were tested and good agreement was observed in all cases. Prior to addition into the electrochemical cell, the enzyme sample was assayed by measuring the rate of formation of reducing saccharides and the value obtained was then compared with that expected from the electrochemical data. Salivary human α-amylase, pancreas α-amylase, as well as a sample of saliva of one of us (B.B.G.) gave a very good coincidence. At the same time glucoamylase from *Aspergillus niger*, which is exo-depolymerase, did show remarkably different behavior, Figure 3. The activity of the sample according to the "reducing saccharides" was equal to 50 mg dm^{-3} min^{-1}, while the value of only 6 mg dm^{-3} min^{-1} was obtained by cyclic voltammetry. In our opinion, this big difference is indicative of the fact that this enzyme cleaves terminal glucose residues, rather than carries out random hydrolysis. Obviously, if a polymer with a low degree of redox modification is depolymerized by exo-enzymes, its bulk electrochemical properties should not change much after dissociation of a few redox-silent terminal units. This is an illustration of advantages of dealing with redox polymers of the low degree of modification.

The amylolytic activity can thus be determined electrochemically using the plots such as Figure 3 in a wide range of enzyme concentrations. The data obtained are in good agreement with the results evaluated by traditional methods. The log–log plot of the enzymatic activity of α-amylase from porcine pancreas determined from the electrochemical measurements A_E {M min^{-1}} versus its concentration in the electrochemical cell {M} is a straight line the analytical form of which is $\log A_E = (1.01 \pm 0.03) \log E - (4.9 \pm 0.1)$ in the range of E (0.02–8.0) × 10^{-8} M with $r = 0.997$.

CONCLUSION

This study has shown a general approach for the investigation of chemical or biochemical random depolymerization of high molecular weight molecules by electrochemical means, cyclic voltammetry, in particular, which is now finding new applications for mechanistic studies of biochemical processes.[40-42] A polymeric substrate must meet several requirements. The degree of its modification by a redox moiety must be low, it should be soluble, and, if a biodegradation is under investigation, the modification should not affect its ability to be accepted by corresponding enzymes-depolymerases.

ACKNOWLEDGMENT

This work was partly supported by Grant 7-192 of the Russian state scientific and technological program "Advanced Methods of Bioengineering". The authors are grateful to Drs. A. N. Shevel'kova and A. P. Sinitsyn for advice concerning catalysis by amylases, Dr. I. E. Nifant'ev for the help in preparation of the labeled amylose, Dr. V. A. Polyakov for recording the NMR spectra, Dr. V. V. Mozhaev for his interest in this work and helpful comments.

Received for review November 2, 1993. Accepted February 18, 1994.®

® Abstract published in *Advance ACS Abstracts*, April 1, 1994.

(40) Bixler, J.; Bakker, G.; McLendon, G. *J. Am. Chem. Soc.* **1992**, *114*, 6938–39.
(41) Bourdillon, C.; Demaille, C.; Moiroux, J.; Savéant, J.-M. *J. Am. Chem. Soc.* **1993**, *115*, 2–10.
(42) Badia, A.; Carlini, R.; Fernandez, A.; Battaglini, F.; Mikkelsen, S. R.; English, A. M. *J. Am. Chem. Soc.* **1993**, *115*, 7053–60.

Anal. Chem. **1994**, *66*, 2245–2249

Metalloporphyrin Derivatives as Neutral Carriers for PVC Membrane Electrodes

De Gao, Jun-Zhong Li, and Ru-Qin Yu*
Department of Chemistry and Chemical Engineering, Hunan University, Changsha, 410082 China

Guo-Dong Zheng
Department of Chemistry, Jilin University, Changchun, 130023 China

The anion-sensitive membrane electrodes based on lipophilic metalloporphyrin derivatives $(FeTPP)_2O$ show similar anti-Hofmeister selectivity sequence: $SCN^- > I^- > ClO_4^- > NO_2^- > Br^- > Cl^- > NO_3^-$. The electrode with an optimum membrane composition has a linear response for SCN^- between 10^{-6} and 10^{-1} mol/L, with a slope of 53.0 mV/*p*-SCN^- (25 °C). The origin of the anti-Hofmeister response characteristics has been discussed in view of the coordination chemistry of the metalloporphyrins. The interaction mechanism between $(FeTPP)_2O$ and SCN^- is studied by UV/vis and IR spectroscopy. The transfer process of SCN^- across the membrane interface is investigated by ac impedance measurements.

Anion membrane electrodes based on classical liquid ion exchangers have the same Hofmeister selectivity sequence: $ClO_4^- > SCN^- > I^- > NO_3^- > Br^- > NO_2^- > Cl^-$. Searching for carriers with the selectivity sequence, which is different from the Hofmeister pattern, is the subject of a series of investigations.[1-12] Among the anti-Hofmeister sensing materials, the vitamin B_{12} derivatives and the metalloporphyrins were supposed to have a certain interaction between the central metal and response anions.[1-8] The alkyl tin compounds show selectivity sequence deviated from the Hofmeister pattern, which is due to the selective extracting ability of these compounds for some anions.[9-11] The lipophilic diquaternary ammonium salt with closely located nitrogen atoms show the anti-Hofmeister character, which is related to the interaction between the sensing material and the anion species to be sensed.[12] In this paper, we report the results of the investigation of oxo bridge iron porphyrin $(FeTPP)_2O$ as a new neutral carrier sensing the thiocyanate ion. The origin of the anti-Hofmeister selectivity sequence observed is discussed; the UV/vis and IR spectra of $(FeTPP)_2O$ interacting with SCN^- as well as the transfer process of SCN^- across the organic/water interface are studied. The preliminary application of the $(FeTPP)_2O$-based membrane electrode for body fluid is investigated.

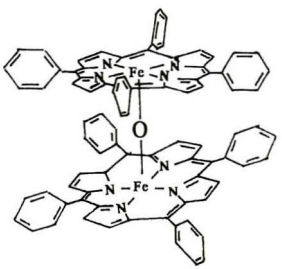

Figure 1. Structure of $(FeTPP)_2O$.

EXPERIMENTAL SECTION

Reagents. Tetraphenyl porphyrin (TPP) was prepared according to the method of Alder et al.[13] Tetraphenyl porphyrinatoiron (FeTPPCl) was synthesized according to the method of Rothemund et al.[14] μ-Oxotetraphenyl porphyrinatoiron $[(FeTPP)_2O]$ was prepared by treating the chloroform solution of FeTPPCl with aqueous NaOH solution for 2 h,[15] and then the organic layer was refined by chromatography using the neutral Al_2O_3 column. The structure of $(FeTPP)_2O$ is shown in Figure 1. Bis(imidazole)-μ-oxotetraphenyl porphyrinatoiron $[(Im)_2(FeTPP)_2O]$ was prepared from $(FeTPP)_2O$ according to the method of Epstein et al.[16] All synthesized ionophores were identified by UV/vis, IR, and elemental analysis. 2-Nitrophenyl octyl ether (*o*-NPOE) was prepared according to the literature method.[17] Tetrahydrofuran (THF), didecyl sebacate (DDS), and dibutyl phthalate (DBP) of pure analytical grade and poly(vinyl chloride) (PVC) of chromatographic grade were purchased from Shanghai Chemical Co. Redistilled deionized water was used throughout.

Apparatus. The potentiometric and pH measurements were carried out on a Model 901 microprocessor Ionalyzer (Orion, Cambridge, MA). Cell assemblies of the following type were

(1) Schulthess, P.; Ammann, D.; Simon, W.; Caderas, C.; Stepanek, R.; Krautler, B. *Helv. Chim. Acta* **1984**, *67*, 1026.
(2) Ammann, D.; Huser, M.; Krauther, B.; Rusterholz, B.; Schultness, P.; Lindemann, B.; Halder, E.; Simon, W. *Helv. Chim. Acta* **1986**, *69*, 849.
(3) Chaniotakis, N. A.; Chasser, A. M.; Meyerhoff, M. E.; Groves, J. T. *Anal. Chem.* **1988**, *60*, 188.
(4) Hodinar, A.; Jyo, A. *Chem. Lett.* **1988**, 993.
(5) Hodinar, A.; Jyo, A. *Anal. Chem.* **1989**, *61*, 1171.
(6) Chang, Q.; Meyerhoff, M. E. *Anal. Chim. Acta* **1988**, *186*, 81.
(7) Chaniotakis, N. A.; Park, S. B.; Meyerhoff, M. E. *Anal. Chem.* **1989**, *61*, 566.
(8) Abe, H.; Kokufuta, E. *Bull. Chem. Soc. Jpn.* **1990**, *63*, 1360.
(9) Glazier, S. A.; Arnold, M. A. *Anal. Chem.* **1988**, *60*, 2540.
(10) Glazier, S. A.; Arnold, M. A. *Anal. Lett.* **1989**, *22*, 1075.
(11) Glazier, S. A.; Arnold, M. A. *Anal. Chem.* **1991**, *63*, 754.
(12) Wotring, V. J.; Johnson, D. M.; Bachas, L. G. *Anal. Chem.* **1990**, *62*, 1506.
(13) Alder, A. D.; Longo, F. R.; Finarelli, J. D. *J. Org. Chem.* **1967**, *32*, 476.
(14) Rothemund, P.; Menotti, A. R. *J. Am. Chem. Soc.* **1948**, *70*, 1808.
(15) Strauss, H.; Pawlik, M. J.; Skowyra, J.; Kennedy, J. R.; Anderson, O. P.; Spartalian, K.; Dye, J. L. *Inorg. Chem.* **1987**, *26*, 724.
(16) Epstein, L. M.; Straub, D. K.; Maricondi, C. *Inorg. Chem.* **1967**, *6*, 1721.
(17) Horning, E. E. *Organic Synthesis*, John Wiley & Sons Inc.: New York, 1955; Collective Vol. 3, p 140.

0003-2700/94/0366-2245$04.50/0
© 1994 American Chemical Society

used:

Hg, Hg_2Cl_2, KCl

(satd.)|sample solution|membrane|0.1 mol/L of KCl|Ag, AgCl

The solution was buffered with 0.01 mol/L of H_3PO_4, and the pH was adjusted with a NaOH solution. The membrane composition was 1% (w/w) ionophore, 33% (w/w) PVC, and 66% (w/w) solvent mediator.

The potentiometric selectivity coefficients, log K_{SCN^-,X^-}^{pot} were obtained by the separate solution method. The solution was buffered with 0.01 mol/L of H_3PO_4 and adjusted to pH 3.01 with a NaOH solution. The single ion activity was calculated by the extended Debye–Huckel equation.

The ac impedance was recorded with a PAR M 368-2 system (EG&G Princeton Applied Research, Princeton, NJ) in 0.01 mol/L of H_3PO_4 solution buffered to pH 3.01; SCN^- concentration ranged from 10^{-6} to 10^{-1} mol/L. The frequency range used was 10^5–10^{-3} Hz (25 °C).

UV/vis and IR Spectra. The chloroform solution of $(FeTPP)_2O$ was treated with aqueous 1.0 mol/L NaSCN solution for 30 min; the organic layer was eliminated in a rotaevaporator. The UV/vis spectra were recorded on a PE λ 17 spectrophotometer (Bodenseewerk Perkin-Elmer & Co. GMBH, D-7770 Ueberlingen, Germany). The IR spectra were recorded on a AQS-20 (Analect Instruments, a Division of Laser Precision Corp.).

The colorimetric experiment was recorded at 457.5 nm based on the $SCN^- - Fe^{3+}$ reaction according to the method of Butts et al.[18]

RESULTS AND DISCUSSION

Selection of Sensing Materials. Because of the specific characteristics of metalloporphyrins, some conditions are important for the incorporation of the ionophores as membrane active components. First, under atmospheric conditions, some metalloporphyrins exposed to air, moisture, or light might cause demetallation or polymerization.[19] For instance, Mo(IV) and Mn(III) porphyrins can polymerize to $(MoOTPP)_2O$ and $(MnTPP)_2O$, respectively, in basic solution.[20,21] When an electrode incorporating MnTPPCl was conditioned in a basic solution, the membrane active component MnTPPCl would convert into $(MnTPP)_2O$. Chaniotakis et al.[3] had reported the potentiometric response characteristics of MnTPPCl as the ionophore, but the real active component might be $(MnTPP)_2O$. Recently, the potentiometric characteristics of binuclear and mononuclear Mn(III) porphyrins were discussed by the coordination chemistry of metalloporphyrins as well as by quantum chemistry in more detail.[22] Anyhow, the stability of membrane active components based on the metalloporphyrins must be considered. As FeTPPCl tends to polymerization, forming stable binuclear $(FeTPP)_2O$, the latter is a favorite candidate to be selected as the electro-active material (vide infra). Due to the instability, up to date, there is no literature reports on electrodes based on FeTPPCl. Secondly, as for vitamin B_{12} derivatives and metalloporphyrins, the coordination or interaction between the carriers and the analyte anions is one of the essential conditions for getting the anti-Hofmeister response pattern; such interaction is determined by the coordination sites in the carrier and the coordination affinity between the ionophore and the analyte anions. In vitamin B_{12} derivatives and metalloporphyrins, a counterion occupies the fifth axial coordination position,[1-8] and the analyte anions can coordinate with the carrier only at the sixth axial coordination site. Introducing more than one coordination position in the carrier molecule would improve the potentiometric response characteristics of the electrodes for anions. $(FeTPP)_2O$ is a very stable binuclear metalloporphyrin and has two coordination sites. Beside the lipophilicity of $(FeTPP)_2O$ which is better than that of the mononuclear metalloporphyrins, it is expected that the electrodes based on $(FeTPP)_2O$ have better potentiometric characteristics.

Table 1. Potentiometric Selectivity Coefficients log K_{SCN^-,X^-}^{pot}[a]

solvent mediator/anions	SCN^-	I^-	ClO_4^-	NO_2^-	Br^-	Cl^-	NO_3^-
DDS	0.00	−2.17	−2.34	−2.73	−2.92	−3.04	−3.70
o-NPOE	0.00	−0.58	−0.30	−1.52	−1.88	−2.02	−1.37
DBP	0.00	−1.30	−0.60	−2.00	−2.50	−2.90	−2.30

[a] Measured by separate solution method.

EMF Response Characteristics and Selectivity. Table 1 summarizes the potentiometric selectivity characteristics of the membranes containing different solvent mediators. The selectivity sequence clearly differs from the classical Hofmeister pattern. This behavior is determined by the characteristics of both the sensing material and the anions. For classical liquid membrane electrodes, the response of the anion is based on the ion-exchange properties between analyte anions and the counterion.[23] The electrostatic interaction plays the dominate role for the transfer of the anion across the organic/water interface. The hydration energy of the analyte anions must be overcome by the electrostatic affinity, and the selectivity sequence is determined by the order of the hydration energy or by the hydrophilicity of the analyte anions. For the ionophores based on vitamin B_{12} derivatives or metalloporphyrins, beside the electrostatic interaction between the central metal and the analyte anions, there is a coordination action between both species. The anion hydration energy is conquered by both electrostatic and coordination forces. As the charges of carriers and analyte anions are fixed, the Hofmeister selectivity sequence of classical liquid membrane electrodes can only be altered, for instance, by the coordination affinity. Taking the anions ClO_4^- and SCN^- as examples, the hydration energy of SCN^- is larger than that of ClO_4^-, when the lipophilic quaternary ammonium salts are used as the sensing materials, the Hofmeister selectivity sequence is realized, and the ClO_4^- preferentially enters the membrane phase. For $(FeTPP)_2O$ membrane, however, beside the electrostatic interaction between the membrane active component and analyte anions,

(18) Butts, W. C.; Kuehneman, M.; Widdowson, G. M. *Clin. Chem.* **1974**, *20*, 1344.
(19) Dolphin, D., Ed. *The Porphyrins*; Academic Press: New York, 1978; Vol. 3A, p 417.
(20) Johnson, J. F.; Scheidt, W. R. *J. Am. Chem. Soc.* **1977**, *99*, 294.
(21) Fleischer, E. B.; Palmer, J. M.; Srivastava, T. S.; Chatterjee, A. *J. Am. Chem. Soc.* **1971**, *93*, 3162.
(22) Gao, D.; Liu, D.; Yu, R. Q.; Zheng, G. D. Submitted to *Sci. China, Ser. B.*
(23) Morf, W. E. *The Principle of Ion-Selective Electrodes and of Membrane Transport*; Elsevier Scientific Publishing Co.: Amsterdam, 1981; p 214.

there are two coordination sites in $(FeTPP)_2O$ at the two sixth axial positions and SCN^- can preferentially coordinate with the ionophore at the two sites, which leads to the selectivity sequence of anion response deviating from the Hofmeister pattern.

In order to verify the hypothesis that the coordination action of membrane active component really plays a main role in the anti-Hofmeister response behavior, the compound bis(imidazole)-μ-oxotetraphenyl porphyrinatoiron [$(Im)_2(FeTPP)_2O$] was synthesized and used to prepare the electrode membrane. Imidazole is one of the strongest electron-donating ligands; its coordination ability toward metalloporphyrins is larger than that of OH^-. As the pH of the solution was adjusted to 8.98, imidazoles occupied the two sixth axial positions, the analyte anions could not coordinate with $(FeTPP)_2O$, and they entered the membrane phase mainly with the aid of electrostatic affinity. The selectivity sequence returned to the classical Hofmeister pattern. When the pH was adjusted to 3.01, the two imidazole molecules combined with H^+ and dissociated from $(FeTPP)_2O$, and the two sixth axial coordination sites became empty and could be coordinated by analyte anions. The selectivity sequence became the anti-Hofmeister one: $SCN^- > I^- > ClO_4^- > NO_2^- > Br^- > Cl^- > NO_3^-$. These results show the importance of the coordination action in altering the selectivity sequence and the possible mechanism of formation of the anti-Hofmeister selectivity sequence.

Effect of pH on Response Characteristics of $(FeTPP)_2O$-Based Membrane Electrodes. Figure 2 shows the effect of pH on response characteristics of $(FeTPP)_2O$-based electrodes. SCN^- and OH^- ions seem to coordinate competitively with $(FeTPP)_2O$. The coordination ability of SCN^- is stronger than that of OH^-. As the concentration of SCN^- is relatively high (10^{-1}–10^{-3} mol/L), the SCN^- ion is the primary analyte ion, and OH^- does not cause remarkable interference for the SCN^- response. The linear response characteristics of the electrode for SCN^- ion are not affected by OH^- substantially. As the concentration of SCN^- is relatively low (10^{-3}–10^{-7} mol/L), with the increase of OH^- concentration, OH^- becomes the primary analyte anion. The potentiometric response characteristics of the electrode for SCN^- are deviated from the linear one, especially at high pH values.

Similar results are obtained for different solvent mediators. For DBP, however, the response characteristics of electrode were not affected by the variation of pH values, although the DBP version showed narrower linear response range. Table 2 shows the response characteristics of $(FeTPP)_2O$-based electrodes for different solvent mediators. Binuclear metalloporphyrins have lower polarity and higher lipophilicity than that of mononuclear metalloporphyrins, so the binuclear metalloporphyrins are more easily solvated in a solvent mediator with lower permitivity than in that with higher permitivity. It is clear that $(FeTPP)_2O$ will have great mobility in the lower permitivity solvents such as DDS than in the other ones. Consequently, the response characteristics are improved by using DDS as a solvent mediator. Although the association constant between the ionophore and the analyte anions is affected by the solvent mediators, the selectivity will change with the solvent mediators.

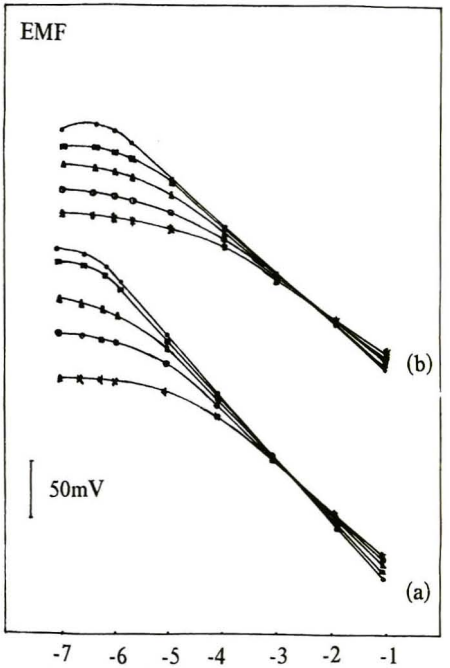

Figure 2. Response characteristics of $(FeTPP)_2O$-based electrodes: (a) DDS; (b) *o*-NPOE; (●) pH 3.01; (■) pH 3.61; (▲) pH 5.08; (○) pH 6.84; (*) pH 8.98. The *x*-axis values are lg a_{SCN^-}.

Table 2. Response Characteristics of $(FeTPP)_2O$-Based Electrodes with Different Solvent Mediators

solvent mediators	DDS	*o*-NPOE	DBP
slope (mV/pSCN$^-$)	53.0	43.0	58.0
linear range (mol/L)	10^{-6}–10^{-1}	10^{-6}–10^{-1}	10^{-4}–10^{-1}
detection limit (mol/L)	3.98×10^{-7}	6.31×10^{-7}	6.31×10^{-5}

Up to now, the best thiocyanate-sensitive electrodes based on metalloporphyrins had been reported by Daunert.[24] The response characteristics of a $(FeTPP)_2O$-based electrode such as the slope, linear range, and detection limit compared favorably with those of Daunert's, which was expected to get application in clinical chemistry.

Interaction Mechanism of $(FeTPP)_2O$ with SCN^-. Although it has been supposed that there is an interaction between metalloporphyrins and anions, the interaction mechanism has not been studied in depth so far. It is interesting to investigate the interaction between $(FeTPP)_2O$ and SCN^- for the elucidation of the potentiometric response mechanism.

Figure 3 shows the UV/vis spectra of $(FeTPP)_2O$ with and without interacting with SCN^-. A summary of electronic absorption spectral data for $(FeTPP)_2O$ and $(FeTPP)_2O$–SCN^- is given in Table 3. Comparing the spectra of $(FeTPP)_2O$ and $(FeTPP)_2O$–SCN^-, one notices that the Soret band of 407.2 nm shifts to 409.2 nm (the precision of the spectrophotometer is of the order of 0.2 nm) with increased

(24) Daunert, S.; Wallace, S.; Florido, A.; Bachas, L. G. *Anal. Chem.* **1991**, *63*, 1676.

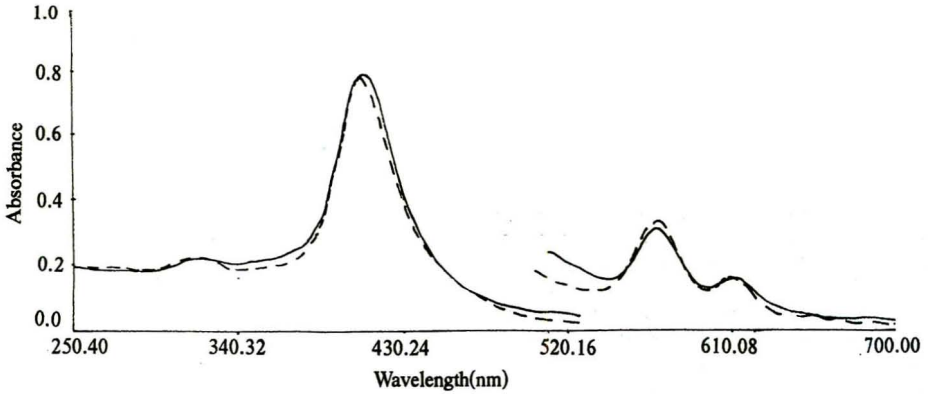

Figure 3. UV/vis spectra ($CHCl_3$ solution): (- - -), $(FeTPP)_2O$; (—), $(FeTPP)_2O(SCN^-)_2$.

Table 3. UV/vis Peaks ($CHCl_3$, nm)

$(FeTPP)_2O$	319.2	407.2	569.6	611.2
$(FeTPP)_2O(SCN^-)_2$	320.4	409.2	570.4	610.8

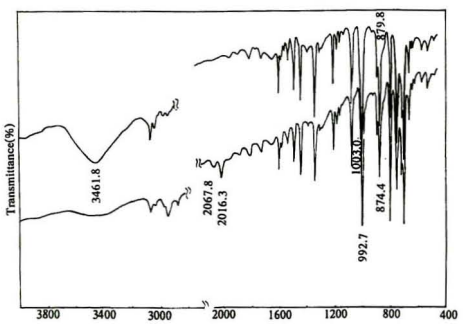

Figure 4. IR spectra (KBr pellets): (a, top) $(FeTPP)_2O$; (b, bottom) $(FeTPP)_2O(SCN^-)_2$. The *x*-axis values are wavenumbers (cm^{-1}).

intensity. This is characteristic for the SCN^- coordination with the central metal.[25] The Soret band reflects the valence state of the central metal. The coordination of SCN^- with the central iron metal leads to the delocalization of the iron d orbitals, which causes the red-shift of the Soret band. Figure 3 also shows that the numbers of the absorption peaks do not change after $(FeTPP)_2O$ is coordinated with SCN^-. This indicates that, after SCN^- is coordinated with the central metal, the symmetry group of $(FeTPP)_2O$–SCN^- agrees with the C_{2v} symmetry group of $(FeTPP)_2O$,[26,27] and two SCN^- anions are coordinated with two central iron atoms in $(FeTPP)_2O$ producing $(FeTPP)_2O(SCN^-)_2$.

Figure 4 shows the IR spectra of $(FeTPP)_2O$ and $(FeTPP)_2O$ interacting with SCN^-. For $(FeTPP)_2O$, the vibrational frequency at 879.5 cm^{-1} is due to the Fe–O bond antisymmetry stretching;[15] 1003.0 cm^{-1} is due to the Fe–N

(25) Jeffrey, H.; Helms, L. W. H.; William, E. H.; David, L. H. *Inorg. Chem.* **1986**, *25*, 2334.
(26) Hoffman, A. B.; Collins, D. M.; Day, V. W.; Fleischer, E. B.; Srivastava, T. S.; Hoard, J. L. *J. Am. Chem. Soc.* **1972**, *94*, 3620.
(27) Dolphin, D., Ed. *The Porphyrins*; Academic Press: New York, 1978; Vol. 3A, p 111.

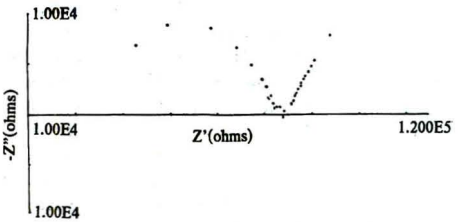

Figure 5. ac impedance spectra of $(FeTPP)_2O$-based electrodes: 0.01 mol/L NaSCN solution, pH 3.01.

characteristic stretching.[28] After $(FeTPP)_2O$ is coordinated with SCN^-, the characteristic vibration of H_2O at 3461.8 cm^{-1} disappears. At the same time, the characteristic vibrational frequencies of SCN^- at 2067.8 and 2016.3 cm^{-1} appear. This indicates that two SCN^- anions occupy the positions of two H_2O and coordinate with the nitrogen atom.[29] The electron delocalization on iron metal reduces the charge density in the vicinity of the Fe atom, which weakens the Fe–O and Fe–N bond strength. The vibrational frequencies of Fe–O and Fe–N shift to 874.4 and 992.7 cm^{-1}, respectively.

The UV/vis and IR spectra confirm that there is a direct interaction between the central metal and the analyte anions.

Transfer Process of SCN^- across Organic/Water Interface. Figure 5 shows the ac impedance spectra of an $(FeTPP)_2O$-based electrode. The ac impedance measurement shows that the bulk resistance decreases with the increasing SCN^- concentration. Negatively charged SCN^- anions coordinate with the neutral carrier $(FeTPP)_2O$ and move across the membrane interface, reducing the membrane impedance. The process is controlled by diffusion.

Preliminary Application for Clinical Chemistry. A chemical test to distinguish smokers and nonsmokers is important in many epidemiologic studies.[18] Experimental results have shown that the urinary thiocyanate concentration is higher for smokers than for nonsmokers, and the assay can be used to detect whether or not a person is smoking. Table 4 lists thiocyanate concentration in human urine measured by the

(28) Boucher, L. J.; Katz, J. J. *J. Am. Chem. Soc.* **1967**, *89*, 1340.
(29) Nakamoto, K. *Infrared and Raman Spectra of Inorganic and Coordination Compounds*, 3rd ed.; John Wiley & Sons Inc.: New York, 1978; p 270.

Table 4. Comparison of SCN^- Concentration in Urine Samples of Smokers and Nonsmokers

sample no.	nonsmokers (mmol/L)		sample no.	smokers (mmol/L)	
	electrode[a]	colorimetric[b]		electrode[a]	colorimetric[b]
1	0.25	0.25	5	0.62	0.63
2	0.18	0.19	6	0.46	0.46
3	0.24	0.25	7	0.68	0.70
4	0.26	0.27	8	0.84	0.85

[a] Urine samples are diluted 10-fold with 0.01 mol/L of H_3PO_4–NaOH solution, pH 3.01. [b] Urine samples are diluted 10-fold according to the method of Butts et al.[18]

$(FeTPP)_2O$-based electrode as well as the colorimetric results for smokers and nonsmokers. As shown in the table, there is a fair correlation between the values obtained by the electrode and the colorimetric methods.

CONCLUSIONS

For plane macrocyclic metallorganic compounds such as vitamin B_{12} derivatives and metalloporphyrins, there is a coordination action between the central metal and the analyte anions. Under certain conditions, the coordination ability determines the selectivity sequence of anions to be sensed. When the $(FeTPP)_2O$ is used as the membrane active component, the response mechanism of electrodes sensing SCN^- is of the following type:

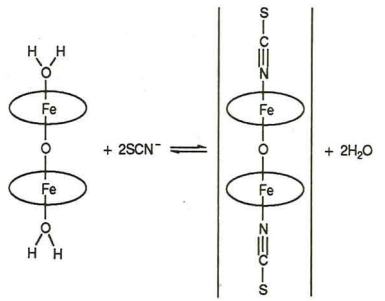

ACKNOWLEDGMENT

The project was supported by the National Natural Science Foundation of China and partially by the Laboratory of Electroanalytical Chemistry, Changchun Institute of Applied Chemistry, Chinese Academy of Science.

Received for review November 10, 1993. Accepted March 28, 1994.[•]

[•] Abstract published in *Advance ACS Abstracts,* May 15, 1994.

Anal. Chem. **1994,** *66,* 2250–2259

Response Mechanism of Polymer Membrane-Based Potentiometric Polyion Sensors

Bin Fu,[†] Eric Bakker,[†] Jong H. Yun,[‡] Victor C. Yang,[‡] and Mark E. Meyerhoff*,[†]

Department of Chemistry and College of Pharmacy, The University of Michigan, Ann Arbor, Michigan 48109

The potentiometric response mechanism of a previously reported polymer membrane-based electrode sensitive to the polyanion heparin is established. Based on transport and extraction studies, the heparin response is attributed to a nonequilibrium change in the phase boundary potential at the sample/membrane interface. While true equilibrium polyion response, obtained for low heparin concentrations only after very long equilibration times (>20 h), yields the expected Nernstian response slope of <1 mV/decade, the observed large and reproducible EMF response to clinically relevant heparin concentrations ($\sim 10^{-7}$ M) during typical measurement periods (2–5 min) is ascribed to a steady-state kinetic process defined by the flux of the polyion both to the surface and into the bulk of the polymer membrane. A model describing this nonequilibrium response is presented. With this model, the uniqueness of the polymer membrane composition (e.g., very low plasticizer content, strictly controlled cationic site concentration, etc.) required to achieve analytically useful heparin response becomes clear. Practical working conditions and limitations of the sensor are discussed. To support the generality of the steady-state model proposed, corresponding EMF response data for a newly developed membrane electrode sensitive to a polycationic protein (protamine) are also presented. It is shown that the protamine-responsive membrane electrode appears to operate via the exact same kinetic mechanism as the heparin sensing system.

Although a large number of polymer membrane-based potentiometric sensors have been applied successfully in clinical chemistry laboratories for the measurement of small ions such as H^+, K^+, Na^+, Ca^{2+}, Cl^-, etc., in undiluted whole blood,[1,2] there are no analogous devices available for direct sensing of important macromolecular ionic species. Recently,[3,4] a specially formulated PVC membrane electrode has been proposed for the detection of heparin, a polyanion (average molecular weight 15 000) which is widely used as an anticoagulant during a variety of clinical procedures (e.g., open heart surgery, kidney dialysis, etc.). Initial studies have clearly demonstrated the utility of this sensor as an indicator electrode to probe the binding interaction of heparin with a variety of biologically important macromolecular species (e.g., low-density lipoprotein, protamine, DNase, etc.) via a classical potentiometric titration method.[5] Additional preliminary studies have suggested that the electrode may also serve as a simple analytical device to monitor relative heparin levels in undiluted whole blood.[4]

The optimum polymer membrane for sensing low levels of heparin is composed of 66 wt % polymer matrix (poly(vinyl chloride); PVC), 32.5 wt % plasticizer (dioctyl sebacate; DOS), and 1.5 wt % ion exchanger (tridodecylmethylammonium chloride; TDMACl), with $TDMA^+$ serving as anion-exchange sites within the organic membrane phase. This membrane composition is unique with respect to its low plasticizer content relative to conventional PVC-based ion-selective electrodes.[6] It has been found previously that this optimized membrane electrode exhibits >40 mV/decade potential change for heparin concentrations in the range of 0.04–0.4 μM (or 0.1–1.0 unit/mL; the conversion factor for heparin concentration is 1 unit/mL = 4×10^{-7} M, assuming an average MW = 15 000) in a background electrolyte solution of 0.12 M NaCl. For such experiments the response times to reach an "apparent" equilibrium EMF change range from 2 to 5 min, depending on the heparin concentration in the test solution (see Figure 4 in ref 3). It is known that lipophilic quaternary ammonium species can bind heparin tightly,[7] suggesting that the $TDMA^+$ in the membrane can selectively extract heparin from the aqueous sample into the organic membrane phase. However, simple *equilibrium* extraction of polyanionic heparin cannot account for the large potentiometric response slope observed. Indeed, the existing theory of ion-selective electrodes would predict <1-mV equilibrium potential change for such a concentration step, since the charge on heparin averages −70/molecule.[8] In addition, other response characteristics of the electrode are not typical for conventional polymer membrane-type ion-selective electrodes; e.g., cylindrical configuration coated wire electrodes exhibit a lower detection limit than planar electrode configurations, and stirring vs nonstirring of the sample solution has a profound influence on the sensor's heparin response (see below).

In this paper, the response mechanism of the heparin sensor is elucidated. It is anticipated that such mechanistic information will lay the foundation for the development of analogous membrane-based devices for sensing other important polyions, either by electrochemical or optical transduction. Indeed, an analogous potentiometric sensor has recently been proposed for sensing protamine,[9] a very important polycationic protein widely used in medicine to neutralize the anticoagulant effect

† Department of Chemistry.
‡ College of Pharmacy.

(1) Yim, H.-S.; Kibbey, C. E.; Ma, S.-C.; Kliza, D. M.; Liu, D.; Park, S.-B.; Torre, C. E.; Meyerhoff, M. E. *Biosens. Bioelectron.* **1993,** *8,* 1.
(2) Oesch, U.; Ammann, D.; Simon, W. *Clin. Chem.* **1986,** *32,* 1448.
(3) Ma, S.-C.; Meyerhoff, M. E.; Yang, V. C. *Anal. Chem.* **1992,** *64,* 694.
(4) Ma, S.-C.; Yang, V. C., Fu, B.; Meyerhoff, M. E. *Anal. Chem.* **1993,** *65,* 2078.
(5) Jong, H. Y.; Ma, S.-C.; Yang, V. C.; Fu, B.; Meyerhoff, M. E. *Electroanalysis* **1993,** *5,* 719.
(6) Craggs, A.; Moody, G. J.; Thomas, J. D. J. *J. Chem. Educ.* **1974,** *51,* 541.
(7) Grant, D.; Long, W. F.; Williamson, F. B. *Biochem. J.* **1992,** *285,* 477.
(8) Casu, B. In *Heparin and Related Polysaccharides, Structure and Activities*; Annals of the New York Academy of Science 556; Ofosu, F. A., et. al., Eds.; The New York Academy of Sciences: New York, 1989.
(9) Jong, H. Y.; Yang, V. C.; Meyerhoff, M. E., *Anal. Biochem.*, submitted.

0003-2700/94/0366-2250$04.50/0
© 1994 American Chemical Society

of heparin (i.e., to reduce the risk of bleeding after heparin therapy). The protamine sensor is prepared with a polymer membrane quite similar in composition to the heparin sensing membrane (low plasticizer content), except that the anion exchanger, $TDMA^+$, is replaced with an appropriate lipophilic cation exchanger, specifically tetrakis(*p*-chlorophenyl)borate.[9]

In the case of the heparin sensing system, we have postulated previously that the observed potentiometric response is due to the interaction of negatively charged heparin with positively charged $TDMA^+$ species on the surface of the membrane. New experimental evidence reported herein now demonstrates clearly that heparin can actually be extracted into the bulk of the membrane and that the potentiometric response is due to a classical phase boundary charge separation that exists for any ion/polyion that can distribute between both the aqueous and organic phases. However, via long-term stability and bulk extraction experiments, it is found that the sensor's membrane is not at full equilibrium when the potentiometric response to heparin is typically recorded (after 2–5 min). Rather, because of the low concentrations of heparin and its slow diffusion in the aqueous test solution, a nonequilibrium steady-state potential develops at the membrane/sample interface during this time frame. An appropriate quasi-steady-state model is developed here that fully explains such a process. The resulting nonthermodynamic yet highly reproducible responses can be used for analytical detection of heparin in its clinically relevant concentration range. The thermodynamic response behavior of the electrode is also examined, both in theory and experimentally. In addition, corresponding kinetic and equilibrium EMF data for the recently developed protamine sensor are presented to demonstrate the general validity of the proposed mechanism for explaining potentiometric polyion response of all appropriately formulated ion-exchange-type polymeric membranes.

EXPERIMENTAL SECTION

Reagents. Tridodecylmethylammonium chloride (TDMAC), potassium tetrakis(*p*-chlorophenyl)borate (KTpClPB), dioctyl sebacate (DOS), *o*-nitrophenyl octyl ether (*o*-NPOE), high molecular weight poly(vinyl chloride) (PVC), and tetrahydrofuran (THF) were purchased from Fluka Chemika-Biochemika (Ronkonkoma, NY). Sodium heparin powder (from porcine intestine mucosa, 169 units/mg) was a product of Hepar Industries, Inc. (Franklin, OH). Fluorescein-labeled heparin was purchased from PolySciences, Inc. (Warrington, PA). Protamine sulfate salt and toluidine blue O dye were obtained from Sigma Chemical Co. (St. Louis, MO). All other reagents were of analytical grade or better. Aqueous solutions were prepared with doubly deionized water.

Membranes Preparation and EMF Measurements. All experiments were performed at ambient temperature (22 °C). The heparin and protamine sensing membranes with different compositions were cast and assembled into a conventional electrode design as described elsewhere.[4,9] Unless otherwise specified, a solution of 15 mM NaCl was used as the internal filling solution for the assembled electrodes. The electrode potential was measured vs a double-junction Ag/AgCl reference electrode from Fisher Scientific (Itasca, IL). Potentials were measured via either a Fisher Scientific Accument pH meter (Model 25) or a Macintosh IIcx computer with a NB-MIO-16× analog/digital input/output board (National Instruments, Austin, TX) and a custom-built electrode interface module controlled by LabView 2 software (National Instruments) as described elsewhere.[10] To record the dynamic response profile of the electrodes, a Fisher Recordall Series 5000 chart recorder was connected to the pH meter. The test solution was constantly stirred with a small magnetic stirrer. To generate different concentrations of heparin or protamine, aliquots of concentrated heparin or protamine stock solution were added to proper background electrolyte (e.g., 0.12 M NaCl) solutions.

Preparation of Coated Wire Electrodes. Copper wires with a length of 6.0 cm and a diameter of 1.3 mm were used for preparing coated wire electrodes. Pretreatment of the wires involved washing with acetone, soaking in acid solution composed of concentrated nitric acid:water = 1:10 for 1 h, extensive rinsing with doubly deionized water, and drying at room temperature. The copper wires thus treated were dip-coated with the respective heparin and protamine membrane casting solutions (200 mg of total ingredients dissolved in 3.0 mL of THF solution). The length of the membrane casting was ~4.0 cm. After dip-coating 10 times, the electrodes were then kept in an oven at 45–50 °C for 6 h. This procedure helps improve the stability and reproducibility of the electrode potential.[11] The electrodes with polymer membrane coatings were soaked in doubly deionized water for ~5 min before use.

Transport Experiments. An in-house dialysis cell was used to carry out the dialysis experiment. A heparin sensing membrane with a thickness of 0.2 mm was placed between the two chambers of the dialysis cell. Two 1.5-mL solutions of 100 units/mL heparin and 2 M NaCl, respectively, were placed into the feed and recipient chambers of the cell. Small magnetic stir bars were used to mix the two solutions. During the dialysis process, fresh heparin was added to the feed solution chamber to compensate for the loss of heparin into the membrane and/or the recipient NaCl solution. After extensive dialysis, the recipient NaCl solution was placed in a dialysis tubing (from Spectrum Medical Industries, Inc., Houston, TX) with a molecular weight cutoff of 3500 and dialyzed against 15 mM NaCl solution for 24 h to remove the high concentration of NaCl electrolyte, which would otherwise interfere with the colorimetric measurement of heparin. The heparin level in the resulting solution was determined spectrophotometrically with toluidine blue O solution to ascertain whether heparin actually is transported through the membrane.[12] An analogous experiment was carried out with fluorescein-labeled heparin. To this end, the fluorescence of the recipient solution was detected to prove the transport of heparin. The fluorescein-labeled heparin was measured with a RF-5000 Schimadzu spectrofluorophotometer using excitation and emission wavelengths of 492 and 513 nm, respectively.

THEORETICAL CONSIDERATIONS

On the basis of preliminary experimental evidence suggesting that heparin may be extracted into the membrane

(10) Telting, M.; Collison, M. E.; Meyerhoff, M. E. *Anal. Chem.* **1994**, *66*, 576.
(11) Covington, A. K.; Whalley, P. D. *J. Chem. Soc., Faraday Trans. 1* **1986**, *82*, 1209.
(12) Jaques, L. B.; Bell, H. J. In *Determination of Heparin*; Glick, D., Ed.; Methods of Biochemical Analysis 7; Interscience Publishers, Inc.: New York, 1959.

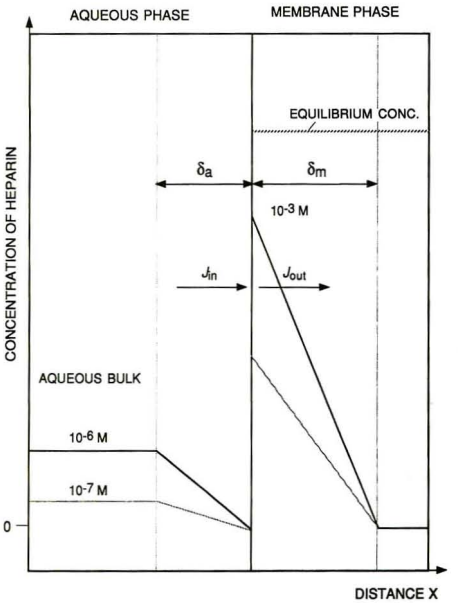

Figure 1. Schematic diagram of the quasi-steady-state model for the potentiometric response of polyanion heparin or polycation protamine sensors: δ_a, δ_m, diffusion layer thickness in the aqueous and membrane phases, respectively; J_{in}, J_{out}, heparin flux from the sample into the interface and from the interface into the bulk of the membrane, respectively.

phase by $TDMA^+$, the observed potentiometric response toward heparin can be ascribed to a change in the phase boundary potential at the membrane/sample interface. There are two possible cases to consider: (a) for high sample concentrations of heparin, or with long equilibrating/conditioning times in the presence of heparin, the initial chloride counterions of the lipophilic anion exchanger (TDMAC) in the membrane phase will be fully displaced by anionic heparin, and the electrode will respond, as classically expected, to heparin in the sample solution with a very low slope (so-called equilibrium or Nernstian response); or (b) for very low concentrations of heparin, and under the assumption that the membrane has been preconditioned in a solution containing only a chloride salt, heparin will not be able to fully displace the initial chloride counterions from the membrane boundary layer within the typical time frame used to measure the cell potentials (e.g., 2–5 min). Instead, the diffusion of heparin from the bulk of the sample solution into the surface membrane layer, and from there, with a much smaller diffusion coefficient, into the bulk of the polymer membrane phase, will lead to a quasi-steady-state nonequilibrium accumulation of heparin at the interface (see Figure 1). While the maximum signal of the sensor will be governed by the equilibrium response, the actual useful working range of the sensor may be quantified via this quasi-steady-state model. In this section, the EMF response function for these two possible cases will be derived mathematically, using heparin as the analyte anion and chloride as the original background counteranion in the sample solution and membrane phase. It should be noted that the equations derived below will also be valid for other important polyionic species (e.g., protamine) after appropriate modification of the respective charge number and sign of the detected polyion as well as the fixed ion-exchange sites in the membrane phase.

Equilibrium Response. To predict, theoretically, the thermodynamic response of the heparin sensor, the following assumptions are made:

(1) The membrane potential is described only by the phase boundary potentials at the inner and outer membrane/solution interfaces. However, since the inner phase boundary potential is fixed by the given internal electrolyte solution, this potential and the diffusion potential within the membrane phase are assumed to be constant.

(2) Activity coefficients in the membrane phase will be assumed to be unity for all ions; therefore, concentrations rather than activities will be used for all species considered to be in the organic membrane phase.

(3) The composition of the inner filling solution of the electrode is constant.

(4) Electroneutrality conditions hold for all phases.

(5) Heparin is assumed to be pure and to have a fixed number of charges.

Assumption 1 is a reasonable approximation and has been shown to hold for liquid membrane-type membrane electrodes.[13] The activity coefficients as mentioned in (2) may be influenced by the membrane composition change such as water uptake, but in a symmetrical arrangement (sensor with internal electrolyte), this effect should take place at the two interfaces equally and the overall influence should be negligible. Assumption 3 will hold under most measurement conditions specified in this paper. Although heparin will eventually migrate to the other side of the membrane, it will not be stripped out into the internal filling solution when 15 mM NaCl is used as the internal electrolyte (see below). Electroneutrality condition 4 is justified, in both aqueous and membrane phases. Assumption 5 is purely for simplicity and certainly not true since it is well-known that commercially available heparin is a highly polydisperse mixture.[8] However, all heparin structures present are polyions, and their general behavior is expected to be similar, albeit not identical.

For a membrane containing a dissociated anion exchanger such as TDMAC, the extraction of heparin into the membrane phase (assuming no strong ion pair formation) may be formulated by the following anion-exchange mechanism:

$$z\mathrm{Cl}_{org}^{-} + \mathrm{Hep}_{aq}^{z-} = z\mathrm{Cl}_{aq}^{-} + \mathrm{Hep}_{org}^{z-} \qquad (1)$$

with the corresponding anion-exchange constant:

$$K_{exch} = \frac{[\mathrm{Hep}^{z-}]}{a_{\mathrm{Hep}}}\left(\frac{a_{\mathrm{Cl}}}{[\mathrm{Cl}^-]}\right)^z = \frac{R_T - [\mathrm{Cl}^-]}{z a_{\mathrm{Hep}}}\left(\frac{a_{\mathrm{Cl}}}{[\mathrm{Cl}^-]}\right)^z \qquad (2)$$

where, $a_{species}$ and brackets ([species]) refer to the activities and concentrations of the corresponding species in the aqueous sample solution and organic membrane phase, respectively; R_T represents the total concentration of ion-exchanger sites, $TDMA^+$, in the membrane phase; and z is the charge of heparin. While the actual ion-exchange process is, in practice, also influenced by ion pair formation in the membrane, this

(13) Cosofret, V. V.; Lindner, E.; Buck, R. P.; Kusy, R. P.; Whitley, J. Q. *Electroanalysis* **1993**, *5*, 725.

effect may shift the extraction equilibrium but does not change the general interpretation of the approach presented here.

Since z is high (on the average, $z = 70$),[8] according to eq 2, even a large heparin sample concentration change will have little influence on the equilibrium concentration of heparin in the membrane. However, a relatively small change in the background anion activity in solution, a_{Cl}, may have a very significant effect on the partitioning of heparin between the two phases. Accordingly, there will be a narrow activity range of chloride over which the concentration of heparin in the membrane changes dramatically. This effect is well-known and has been used previously in liquid/liquid extractions of polyelectrolytes.[14] In the current and previous work with the heparin sensor, this concept is utilized to recondition the electrode membrane after contact with heparinized samples (to return to baseline potential) and for interpreting results of the membrane transport experiments described in the Experimental Section.

The phase boundary potential of a polymer membrane electrode toward chloride as the analyte anion may be described as follows:[15]

$$E_{Cl} = E^0 - \frac{RT}{F} \ln \frac{a_{Cl}}{[Cl^-]} \qquad (3)$$

By inserting eq 2 into eq 3, the phase boundary potential as a function of the heparin sample activity is obtained:

$$E_{Hep} = E^0 - \frac{RT}{zF} \ln K_{exch} - \frac{RT}{zF} \ln \frac{a_{Hep}}{[Hep^{z-}]} \qquad (4)$$

According to eq 4, the slope of the electrode function will be near zero for a membrane fully saturated with heparin ($[Hep^{z-}] = R_T/z$). In practice, however, a potential change is measured after addition of heparin to a sample containing a constant chloride background (e.g., 0.12 M NaCl).[4,5] Under the assumption that a large amount of heparin is extracted, and chloride is completely displaced from the organic phase boundary layer, the expected equilibrium potential change may be formulated by combining eqs 3 and 4 after insertion of the respective electroneutrality conditions:

$$\Delta EMF = \frac{RT}{F} \ln \frac{a_{Cl}}{R_T} - \frac{RT}{zF} \ln \left(\frac{zK_{exch} a_{Hep}}{R_T} \right) \qquad (5)$$

To measure this potential change, it is important that the membrane phase does not contain heparin prior to the experiment. Accordingly, a large and reproducible response toward heparin may be obtained in going from a sample containing the background electrolyte alone to one containing heparin. The magnitude of this response will be determined by the ion-exchange constant (eq 2), by the amount of lipophilic cationic sites in the membrane, and by the chloride activity in the sample. Because of its high valency, the actual amount of heparin in the sample is not expected to influence the final equilibrium response significantly. However, under the working conditions described previously[3-5] (potentials are recorded 2–5 min after samples are added and the heparin concentration is typically less than 4×10^{-7} M), heparin is not yet able to saturate the cationic sites in the organic membrane phase completely, and consequently, an apparent super-Nernstian response slope is obtained. This response is kinetic in nature and is modeled below.

Quasi-Steady-State Response. The quasi-steady-state model relies on the following assumptions:

(1) Under the conditions chosen, heparin completely displaces chloride from the membrane phase when equilibrium is reached.

(2) The rate of the ion-exchange reaction, which takes place in the phase boundary region, is rapid.

(3) Diffusion coefficients are constant for a given phase, and the diffusion coefficients for small ions are much larger than for polyions.

(4) The thickness of the aqueous stagnant layer adjacent to the membrane surface is uniform and constant for a given stirring rate.

Assumption 1 is justified since it has been found that the equilibrium potentials for all sample heparin concentrations of interest are nearly equal, indicating that the original chloride counterion is fully displaced by heparin (i.e., high equilibrium ion-exchange constant for heparin extraction into the membrane phase). For the present evaluation, assumptions 2 and 3 usually hold for ion-exchange-type electrodes.[16] Assumption 4 may be satisfactorily fulfilled in most cases, although the stirring rate and the sample flow were not carefully controlled under the experimental conditions used here. Nonetheless, on the basis of the reproducibility of EMF response data, small changes in convection do not appear to dramatically influence the diffusion layer thickness of the unstirred layer.

We consider a membrane containing an anion exchanger (TDMAC) imposed between a sample solution containing Hep^{z-} and an internal NaCl solution. The transport of ions into the ion-exchange membrane can be controlled or limited by either the membrane or the solution adjacent to the membrane (stagnant Nernst diffusion layer) (see Figure 1). It is well-known that the transport of co-ions into an ion-exchange membrane is almost always controlled by the membrane diffusion.[17] However, for the counterion transport, due to the high ion-exchange constant, the diffusion in the stagnant layer may become the rate-limiting step, depending not only on the membrane but also on conditions within the external solution (concentration, stirring rate, etc.). Helfferich[17] proposed the following equation to evaluate these two processes:

$$L = D_a c_a \delta_m / D_m c_m \delta_a \qquad (6)$$

When $L < 2$, stagnant layer diffusion is the rate-limiting step. Here, δ_m and δ_a are the organic and the aqueous stagnant layer thicknesses, respectively, D_a and D_m are the diffusion coefficients in the solution and membrane phases, and c_a and c_m are the concentrations of the ion in the bulk solution and the outermost region of the membrane phase. To evaluate the rate-limiting step, the membrane thickness d and the limiting equilibrium concentration $c_{m,eq}$ are used here for δ_m and c_m, respectively. If the flux in the stagnant layer is indeed the rate-limiting step, a quasi-steady-state diffusion may be observed at the interface.[18]

(14) Chang, R. *Physical Chemistry with Applications to Biological Systems*; MacMillan: New York, 1981.
(15) Morf, W. E. *The Principles of Ion-Selective Electrode and of Membrane Transport*; Elsevier Science Publishing Co.: New York, 1981.
(16) Morf, W. E.; Lindner, E.; Simon, W. *Anal. Chem.* **1975**, *47*, 1596.
(17) Helfferich, F. *Ion Exchange*; McGraw-Hill Book Co., Inc.: New York, 1962.

The diffusion in a typical planar membrane electrode configuration may be formulated as one dimensional, and thus the flux is described as[19]

$$J = -D\frac{dc}{dx} \tag{7}$$

where x is the coordinate normal to the membrane surface, D is the diffusion coefficient, and c is the concentration. This flux equation holds for the diffusion processes in both the aqueous and membrane phases. For simplicity, we assume that the concentration profiles in each of the two segments are linear, and integration of the flux equations yields

$$J_{in} = D_a\frac{c_{Hep,bulk} - c_{Hep,pb}}{\delta_a} \tag{8}$$

and

$$J_{out} = D_m\frac{[Hep^{z-}] - [Hep^{z-}]_{bulk}}{\delta_m} \tag{9}$$

where J_{in} and J_{out} denote the flux into and out of the membrane surface layer, respectively; $c_{Hep,pb}$ and $[Hep^{z-}]_{bulk}$ represent the concentration of heparin in the boundary layer of the aqueous phase adjacent to the membrane and in the bulk of the membrane, respectively (the first value approaches zero for a high exchange constant); and δ_a and δ_m signify the respective diffusion layer thicknesses (see Figure 1). Equation 9 can be further simplified by assuming that the concentration of heparin in the bulk of the membrane is initially zero. Therefore, at quasi steady state, both fluxes are equal, and for $c_{Hep,pb} \ll c_{Hep,bulk}$ and $[Hep^{z-}]_{bulk} \ll [Hep^{z-}]$, the combination of eqs 8 and 9 gives

$$J_{in} = J_{out} = \frac{D_a c_{Hep,bulk}}{\delta_a} = \frac{D_m[Hep^{z-}]}{\delta_m} \tag{10}$$

and after rearranging

$$[Hep^{z-}] = \frac{D_a\delta_m}{D_m\delta_a}c_{Hep,bulk} \tag{11}$$

In accordance with electroneutrality conditions, the concentration of the original chloride counterion in the membrane phase boundary layer at steady state when heparin is present in the sample solution will be given by

$$[Cl^-] = R_T^+ - z\frac{D_a\delta_m}{D_m\delta_a}c_{Hep,bulk} \tag{12}$$

Interestingly, Hulanicki et al.[20] employed a similar model to quantify the steady-state response of ion-exchange-type membrane electrodes toward monovalent anions. However, they used the empirical Nicolsky–Eisenman equation, which has been shown to be invalid for ions of different valency.[15] The present approach therefore involves the more fundamental phase boundary potential. Accordingly, substitution of eq 12 into eq 3 yields the potential for a sample after contact with heparin:

$$E_{Cl} = E^0 - \frac{RT}{F}\ln\left(\frac{a_{Cl}}{R_T^+ - z(D_a\delta_m/D_m\delta_a)c_{Hep,bulk}}\right) \tag{13}$$

Again, the measured potential change in going from a sample containing chloride only to the same sample after the addition of heparin (at concentration $c_{Hep,bulk}$) may described by the combination of eqs 3 and 13:

$$\Delta EMF = \frac{RT}{F}\ln\left(1 - \frac{z}{R_T^+}\frac{D_a\delta_m}{D_m\delta_a}c_{Hep,bulk}\right) \tag{14}$$

This equation holds if the chloride activity in the aqueous phase boundary layer adjacent to the membrane is equal to the concentration in the bulk sample solution, the membrane does not contain any heparin prior to the measurement, and most importantly, heparin does not displace a large fraction of the total chloride from the outer boundary layer of the membrane phase. In the latter case, the bracketed term in eq 14 approaches 0, and the EMF response function is defined by eq 5, the equilibrium response.

The main factors influencing the quasi-steady-state response are the concentration of heparin in the sample, the site concentration in the membrane, the ratios of the two diffusion coefficients, and the thicknesses of the two stagnant layers. Many of these parameters may be controlled, e.g., by stirring the sample or changing the viscosity and composition of the membrane phase (e.g., via weight percent plasticizer, choice of polymer, etc.). However, the quasi-steady-state response gives no information about the overall maximum response of the sensor, and for this purpose, high concentrations of heparin must be measured for a sufficiently long time period in order to reach a true chemical equilibrium at the membrane/sample interface.

RESULTS AND DISCUSSION

Dynamic Response vs Equilibrium Response. We have reported previously that plasticized PVC membranes, doped with TDMAC, exhibit a large and reproducible potentiometric response toward clinically relevant heparin concentrations. However, the magnitude of the response, particularly toward low levels of heparin, is highly dependent on the polymer membrane composition, not only with respect to the specific quaternary ammonium ion exchanger, but also the fluidity of the polymer film. Specifically, only membranes prepared with 66 wt % PVC, 32.5 wt % DOS, and 1.5 wt % TDMAC exhibit a significant potentiometric response to submicromolar concentrations of heparin in both 0.12 M NaCl solutions and whole blood samples.[4]

To examine whether the observed potential changes for the optimal membrane composition depended on the measurement period, EMF values for the heparin sensor were taken after 5-min (as reported in refs 4 and 5) and after 24-h measurement periods for varying levels of heparin in a 0.12 M NaCl solution. As shown in Figure 2B, we repeatedly find that recording EMF values after 5 min (with stirring), where the potential exhibits an "apparent" equilibrium response, yields bioanalytically useful calibration curves with reproducible potentiometric heparin response over the range of 0.1–

(18) Crank, J.; Park, G. S. *Diffusion in Polymer*; Academic Press: New York, 1968.
(19) Crank, J. *The Mathematics of Diffusion*; Claredon Press: Oxford, England, 1975.
(20) Maj-Zurawska, M.; Sokalski, T.; Hulanicki, A. *Talanta* **1988**, *35*, 281.

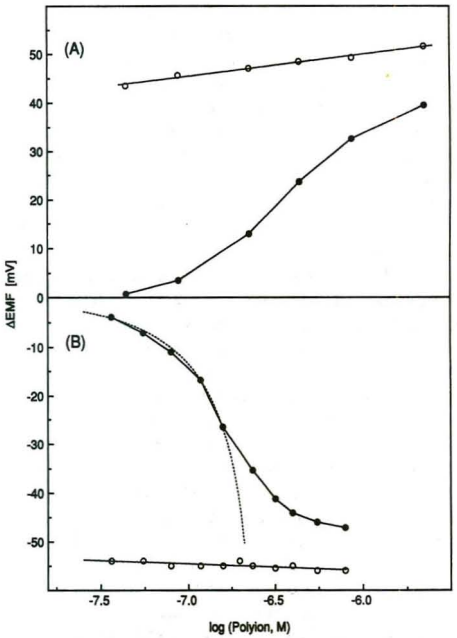

Figure 2. Potentiometric response of protamine (A) and heparin (B) polyion sensors in 0.12 M NaCl solution after different equilibration times: (●) 5 min; (○) 24 h. The membranes were composed of 66 wt % PVC, 32.5 wt % plasticizers, and 1.5 wt % ion exchangers. Dotted line, theoretical curve according to eq 14.

1.0 unit/mL (0.04–0.4 μM). However, if the EMF values are measured after equilibrating the electrode in the given concentrations of heparin for 24 h, little or no useful response to heparin is observed. Under such conditions, the initial chloride counterions of the ion exchanger in the membrane phase boundary layer are completely displaced by heparin and the interface between the organic membrane and the sample solution is at equilibrium. Therefore, according to the equilibrium theory presented above, the electrode should exhibit an ideal response toward heparin with a response slope of about −1 mV/decade. It should be pointed out, however, that the second interface between the membrane and the inner filling solution is assumed to remain unaffected by heparin in the membrane within the entire time frame of the equilibrium measurement. After much longer equilibration times (especially for the low sample heparin concentrations used in these experiments (<5 units/mL)), heparin may eventually reach this other interface and indeed change the overall membrane potential (see below and Figure 7). It can be seen from Figure 2B that the experimental data are in good agreement with that predicted by theory. Therefore, the apparent slope of the analytically useful calibration curve observed when the measurement times are short is obviously due to a kinetic effect. The prerequisite for the quasi-steady-state model is that diffusion in the stagnant layer be the rate-limiting step. In the case of heparin, estimation of L (see eq 6), using a value for D_{aq} of 5×10^{-7} cm^2/s,[21] $D_m = 10^{-9}$ cm^2/s (see below), $\delta_m = 0.003$ cm,[22] $d = 0.03$ cm, and $c_m = 4.5 \times 10^{-4}$ mol kg^{-1}, leads to a value of $L = 1.1 \times 10^7 c_{aq}$.

Obviously, if the concentration of heparin in the sample is less than 2×10^{-7} M, the diffusion in the aqueous stagnant layer will likely be the rate-limiting step during the shorter measurement period. Accordingly, a quasi-steady-state accumulation of heparin at the outer organic phase boundary region will occur under such conditions. To fit the experimental data with eq 14, the site ($TDMA^+$) concentration of 0.032 mol/kg, calculated from the membrane composition, and the ideal response slope of the sensor toward chloride (−59 mV/decade) is used. As shown in Figure 2B, the actual response function agrees reasonably well with the theoretically predicted function for low heparin concentrations. However, at higher heparin concentrations, the experimental points approach the equilibrium potential, indicating that the two models describe, in practice, completely divergent cases.

Figure 2A illustrates analogous EMF data for the newly developed protamine-sensitive membrane electrode.[9] This sensor is realized by incorporating potassium tetrakis-(p-chlorophenyl)borate into a PVC membrane plasticized with 32.5 wt % *o*-NPOE. As shown, just as for the heparin sensing membrane, the EMF function of the protamine sensor exhibits an analytically useful response only when the measurement period is kept relatively short (so-called quasi-steady-state response). After 24 h, the membrane is at equilibrium with the sample solution and the response slope toward protamine is ~4 mV/decade. This thermodynamic response slope seems reasonable considering that the charge on protamine is approximately +20 (based on amino acid composition data determined at the University of Michigan Medical Center).

Effect of Membrane Plasticizer Content on the Sensor Response. The optimum compositions of membranes for both polyanionic heparin and polycationic protamine were selected from a large number of membrane formulations tested.[4,9] The criterion for choosing these compositions was to maximize the observed polyion sensitivity of the sensors. To this end, membranes with much lower plasticizer content, relative to normal ion-selective electrodes, were chosen for both heparin and protamine sensing. To display the effect of plasticizer content, the heparin responses of two different membrane formulations are shown in Figure 3B. As can be seen, nonequilibrium calibration data (measurement time of 5 min) is shifted to lower heparin concentrations when the plasticizer content is reduced (to 32.5 wt %) from that typical in most PVC-type ion-selective membrane electrodes (66 wt %). The exact same effect is seen with the newly developed protamine sensor (see Figure 3A). Qualitatively, the accumulation of heparin or protamine in the boundary layer of the organic membrane depends not only on the diffusion of the polyion in the aqueous Nernst layer but also on the diffusion away from the phase boundary into the bulk of the membrane. The faster heparin or protamine diffuses within the organic phase, the more difficult it is for these species to accumulate in the surface boundary layer of the membrane phase. It has been reported by Oesch and Simon[23] that the diffusion coefficient in the polymer membrane phase may be controlled by varying the relative amount of plasticizer. By decreasing the plasticizer

(21) Barlow, G. H.; Sanderson, N. D.; McNeill, P. D. *Arch. Biochem. Biophys.* **1961**, *94*, 518.
(22) Dinten, O.; Spichiger, U. E.; Chaniotakis, N.; Gehrig, P.; Rusterholz, B.; Morf, W. E.; Simon, W. *Anal. Chem.* **1991**, *63*, 596.
(23) Oesch, U.; Simon, W. *Anal. Chem.* **1980**, *52*, 692.

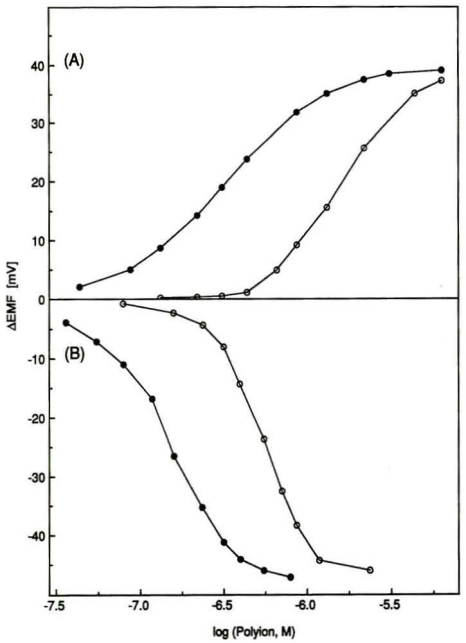

Figure 3. Effect of plasticizer content on the protamine (A) and heparin (B) polyion sensor response in background 0.12 M NaCl solution: (●) 32.5 wt % plasticizer; (○) 66 wt % plasticizer.

content in the membrane, the diffusion of heparin or protamine away from the boundary layer into the bulk of the membrane will be significantly reduced. Hence, a lower detection limit will be achieved when nonequilibrium measurements are made. This fact can also be explained by examining eq 14. For a larger D_m, only higher heparin (or protamine) sample concentrations will lead to the same potential change. Interestingly, the actual membrane selectivity (K_{exch} in eq 2) is not significantly altered by the plasticizer content of the membrane, since the maximum EMF change observed is about the same for the respective heparin and protamine membrane electrodes prepared with the two different weight percents of plasticizers (see Figure 3).

It should be noted that the observed super-Nernstian-type response seen for both heparin and protamine at low concentrations and nonequilibrium measurement times resembles data reported by Hulanicki and Lewandowski[24] for the response of anion-exchanger-based membrane electrodes toward low levels of perchlorate ion. In these early experiments, Hulanicki found that, after conditioning the electrode only in chloride solutions, response to perchlorate and other anions which have high ion-exchange constants for extraction into the membrane was quite super-Nernstian over a very narrow and low concentration range and this unusual response was later modeled using a steady-state approach.[20] Indeed, partly on the basis of such early observations, most workers in this field have always recommended preconditioning of polymer membrane-based electrodes in a solution containing high concentrations of the target analyte ion to obtain Nernstian response over a wide concentration range. On the basis of results for the heparin and protamine sensors, and the theoretical models presented above, one would expect that a similar nonequilibrium steady-state response can also be observed for smaller ions (e.g., perchlorate, etc.) when, at low concentration of such ions, the flux from the sample solution equals the flux into the membrane, a situation that will occur when the electrode is preconditioned in a solution containing relatively high concentrations of an ion that is not the target analyte ion.

Role of Electrode Geometry on Polyion Response Behavior. If the response of the heparin and protamine polyion sensors during practical measurement periods is truly dependent on reaching a quasi steady state of polyion flux up to and into the bulk of the organic membrane phase, then changes in electrode geometry should also influence the EMF response function of the sensors. To test this hypothesis, we examined the response of coated wire-type heparin- and protamine-sensitive electrodes prepared by dip-coating copper wires in the optimal polymer membrane casting solutions useful for detecting each of the polyions. Such coated wire electrodes[25] have been used in certain applications as substitutes for conventional polymer membrane electrode configurations due to their low cost and ease of fabrication. Response characteristics of the coated wire electrodes are usually very similar to the conventional electrode designs, although their long-term performance is inferior, mainly due to an ill-defined boundary potential at the metal/membrane interface.[26]

As shown in parts A and B of Figure 4, both the coated wire heparin and protamine sensors have significantly lower detection limits toward the respective polyions than the corresponding conventional planar membrane electrode designs prepared with the exact same membrane formulations. It is well-known from voltammetry that the mass transfer at a thin wire electrode is subject to cylindrical diffusion except in the vicinity of the tip.[27] Accordingly, in voltammetry, a larger analyte flux for thin cylindrical electrodes than for classical planar electrodes is usually observed.[28] Therefore, for a given sample, the steady-state accumulation of heparin or protamine in the surface layer of the membrane phase is expected to be larger for coated wire electrodes than for the normal planar electrode configuration. It is important, however, to recognize that the expected equilibrium potentiometric response, according to eq 5, does not depend on geometrical factors. That is, only under nonequilibrium or kinetic measurement conditions will the EMF response function be dependent on electrode geometry.

Effect of Ion-Exchanger Site Concentration. It is well-known that for conventional ion-selective membrane electrodes the ionophore concentration in membrane phase does not usually affect the membrane electrode response slope under equilibrium conditions.[15] In contrast, the observed EMF changes for useful polyion membrane electrodes are obtained at quasi steady state, and under such nonequilibrium conditions, the site concentration in the polymer membrane phase

(24) Hulanicki, A.; Lewandowski, R. *Chem. Anal.* **1974**, *19*, 53.

(25) Cattrall, R. W.; Freiser, H. *Anal. Chem.* **1971**, *43*, 1905.
(26) Miyabara, Y.; Simon, W. *Electroanalysis* **1991**, *3*, 287.
(27) Aoki, K.; Honda, K.; Masuda, H. J. *Electroanal. Chem. Interfacial Electrochem.* **1985** *182*, 267.
(28) Murphy, M. M.; O'Dea, J. J.; Osteryoung, J. *Anal. Chem.* **1991**, *63*, 2743.

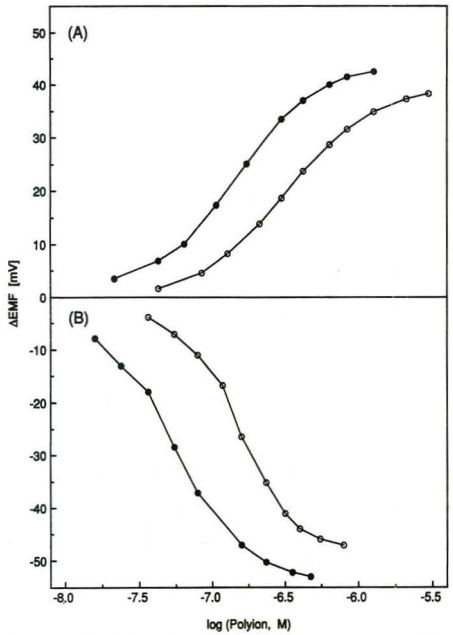

Figure 4. Effect of electrode geometry on the potentiometric protamine (A) and heparin (B) responses in 0.12 M NaCl solutions (membrane compositions were 66 wt % PVC, 32.5 wt % plasticizer, and 1.5 wt % ion exchanger): (●) cylindrically configured coated wire electrode and (○) normal electrode configuration.

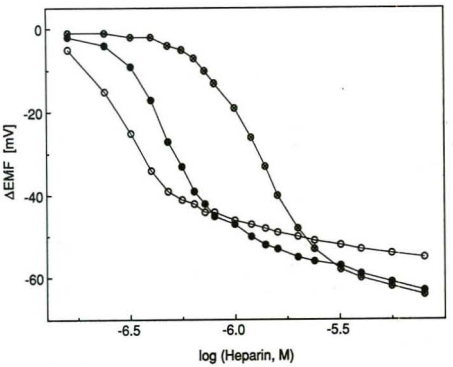

Figure 5. Effect of site concentration in the planar electrode membrane on the heparin response: (○) 2 wt % TDMAC; (●) 4 wt % TDMAC; (⊗) 10.0 wt % TDMAC.

does have a profound effect on the electrode response. Indeed, Figure 5 shows the heparin response of conventional planar membrane electrodes prepared with different membrane concentrations of TDMAC. As can be seen, lower site concentrations in the membrane yield a shift in the nonequilibrium heparin response toward a lower concentration range. This is in agreement with that predicted based on the quasi-steady-state model (eq 14); that is, an increase in the site concentration, R_T, requires a higher sample concentration of heparin to reach the same phase boundary potential (assuming that other parameters do not change). Consequently, the

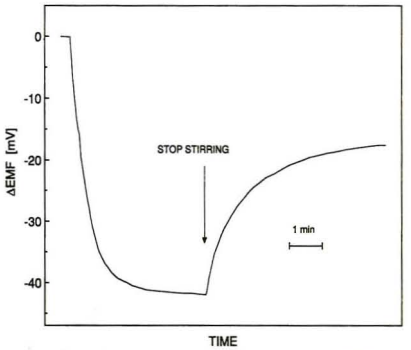

Figure 6. Effect of stirring on the planar heparin sensor's EMF response. The background electrolyte was 0.12 M NaCl; the electrode membrane was composed of 66 wt % PVC, 32.5 wt % DOS, and 1.5 wt % TDMAC; 1.0 units/mL heparin present.

calibration curves for nonequilibrium potentiometric measurements of polyions will shift to a higher concentration range with higher ion-exchanger site concentration in the membrane. The total potential change even under equilibrium conditions will also be affected by the site concentration (see eq 5), with lower R_T yielding less total potentiometric response.

Stirring Effect. It is well-known from fundamental hydrodynamics that convection has a profound influence on the effective thickness of the stagnant aqueous diffusion layer (δ_a).[29] For example, It was found[30] that the stagnant layer thickness at a planar surface is proportional to $V^{-1/3}$, where V (cm/s) is the maximum linear flow velocity. Therefore, it is expected that the stirring rate may affect the quasi-steady-state signal of polyion-sensitive membrane electrodes. As shown in Figure 6 for a conventional heparin-sensitive electrode, a sudden stoppage of sample stirring (via a magnetic stirring bar) causes the EMF signal to revert back and to approach a value closer to the baseline potential. This phenomenon is only observed for low concentrations of heparin. When the potential of the electrode is measured in a solution with a high sample heparin concentration (e.g., 100 units/mL), the electrode response toward heparin is fast and reproducible and is unaffected by the stirring rate of the solution (data not shown).

The observed effects of stirring vs nonstirring are now understood in light of the proposed response mechanism of the heparin- (and protamine-) sensitive electrodes. High heparin concentrations are expected to induce the equilibrium response of the electrode, and no stirring effect would be expected. A sensor in contact with low heparin concentrations will respond as a function of the quasi-steady-state accumulation of heparin in the membrane phase boundary region in contact with the sample solution. In this range, the flux of heparin into the membrane depends on the thickness of the stagnant aqueous layer. After stirring is stopped, the diffusion layer thickness will expand into the bulk of the sample solution, and the flux of polyion to the membrane will decrease. Consequently, this will lead to a smaller steady-state ac-

(29) Levich, V. G. *Physicochemical Hydrodynamics*; Prentice: Englewood Cliffs: NJ, 1962.
(30) Vielstich, W. *Elecktrochem.* **1951**, *57*, 646.

cumulation of heparin and partial return back to the original baseline potential (see eq 14).

Transport Studies. The validity of the quasi-steady-state model described above is highly dependent on the ability of the macromolecular polyions to actually diffuse into the bulk of the ion-exchanger doped polymeric membranes. Thus, one additional study required to further confirm the response mechanism suggested involves determining whether heparin (and/or protamine) can actually be extracted into and diffuse through the optimized membranes used to prepare heparin or protamine sensors. Such processes were investigated for the heparin sensing system via membrane dialysis (or transport) experiments. While, in earlier efforts to assess transport,[4] difficulties were encountered in detecting heparin within the recipient solution, we have now found that the NaCl concentration in that recipient phase has to be kept high, e.g., >1 M, in order to effectively strip the heparin into the aqueous phase (see theoretical section above). In addition, fresh concentrated heparin solution must be added to the feed solution periodically to compensate for the ion-exchange consumption of heparin into the membrane phase. In this way, a reasonable concentration gradient of heparin is maintained to facilitate the diffusion/transport process across the membrane. With these modifications of the experimental conditions, we are now able to detect heparin transported into the recipient solution, both directly by fluorescence (using fluorescein-labeled heparin) and colorimetrically by making use of the metachromatic interaction of heparin with a water-soluble dye, such as toluidine blue O.[12] Since the heparin used in this work is actually a mixture with different molecular weight fragments, explicit quantitative evaluation of the transport process is, however, difficult.

Another means to assess heparin transport through the polymer membrane involves monitoring, over a long time period, the EMF of a conventional electrode configuration in the presence of high sample concentrations of heparin. If heparin can actually diffuse through the membrane and reach the phase boundary between the membrane and inner electrolyte solution (containing 120 mM NaCl as well), then the EMF response of the sensor to heparin should actually begin to reverse in direction (i.e., analogous to adding heparin to the inner reference electrolyte solution). Since it is known that the heparin sensor only exhibits significant potentiometric response (under nonequilibrium conditions) to heparin fragments that are larger than 2500 Da, we can conclude that a significant reversal in the EMF response with time must mean that larger molecular weight fragments of heparin are actually transported through the membrane.

Figure 7 shows the potential vs time profiles for two heparin sensors, one prepared with low plasticizer content (32.5 wt %) and the other with high plasticizer levels (66 wt %). For the two electrodes, the response toward a sample containing 100 units/mL heparin in 0.12 M was monitored for extended time periods. As shown, for both sensors, a point in time occurs in which the EMF value begins to drift back toward the original starting baseline potential (potential without heparin added to sample solution). It is assumed that the potential turning point may be used as an indication of heparin reaching the inner phase boundary of the membrane. If the concentration of heparin in the sample solution is very high (compared to

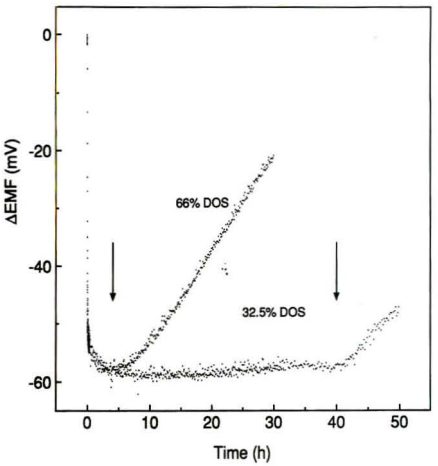

Figure 7. Long-term response profiles of two heparin electrode membranes containing 66 and 32.5 wt % DOS, respectively. The data were collected with a computer-controlled work station (see Experimental Section), which was somewhat noisier than the chart recorder (see Figure 6). The arrows indicate where the electrode potential starts to return back to baseline due to heparin reaching the phase boundary at the membrane/inner filling solution interface.

that used to obtain data in Figure 2) and the outer boundary layer (at sample/membrane interface) is always saturated with heparin, then the time (t) required for heparin to diffuse across the membrane may be used to estimate the diffusion coefficient:[19]

$$d^2 \approx 2D_m t$$

where D_m is the diffusion coefficient of heparin in the membrane phase, t is the time when heparin begins to reach the other side of the membrane, and d is the membrane thickness. Thus, from such experiments, the diffusion coefficients for heparin in 32.5 and 66 wt % DOS plasticized PVC membranes are calculated as 1×10^{-9} and 1.3×10^{-8} cm^2/s, respectively. If all other parameters remain constant, the kinetic EMF response function according to eq 14 is expected to be shifted along the concentration axis by ~1 order of magnitude for the membrane containing the higher levels of DOS plasticizer. This is in good agreement with the actual experimental data shown in Figure 3B.

CONCLUSIONS

We have shown that the observed potentiometric response of ion-exchanger-based polymer membrane electrode toward polyions may be explained via the development of a non-equilibrium, quasi-steady-state change in the phase boundary potential at the membrane/sample interface. Transport experiments clearly indicate that heparin may be extracted into and transported through the polymer membrane, proving that the relatively insensitive equilibrium polyion response can be treated by classical ion-selective membrane theory. Indeed, for long equilibrating times (>24 h for membranes with low plasticizer levels), the response slope toward heparin is found to be very small, i.e., ca. −1 mV/decade. However, for real samples and practical response times of 2–5 min, a

much larger apparent or super-Nernstian response slope for the electrode function is obtained. This behavior is now attributed to a quasi-steady-state accumulation of heparin in the boundary layer of the membrane phase and is akin to the behavior reported by Hulanicki for the low-level perchlorate response of anion-exchanger-based polymer membrane electrodes previously conditioned in solutions containing only chloride ions.[24] Since the flux of heparin from the sample into the membrane phase is small, heparin does not completely displace chloride from the surface of the membrane within the practical time frame of the measurement process. Because this flux is also proportional to the concentration of heparin in the bulk of the sample, an apparent useful slope of the electrode EMF function is obtained. As a result, the influence of the amount of plasticizer, geometric configuration of the electrode, membrane concentration of lipophilic ion exchanger, and stirring rate of the sample solution on the EMF response behavior of the sensor can now be explained semiquantitatively via the proposed steady-state model.

It should be noted that during potentiometric measurement with the polyion sensing membranes, the composition of the sample will be perturbed since the analyte is actually consumed by the membrane. Hence, either a large sample volume or a small membrane surface area must be employed in order to ensure an acceptably small perturbation of the sample composition during the measurement process. Also, since the electrode function relies on an effect which is kinetic in nature, the sensor is expected to measure polyion concentrations rather than activities. However, the assessment of binding constants of polyions to macromolecules as described earlier[5] should be possible if the exchange kinetics of the decomplexation step between the polyion and the other macromolecule are slow. The proposed kinetic model also fully explains the response function of a novel protamine-selective sensor based on a tetraphenylborate-type cation exchanger, indicating that the theory presented is versatile and can be used for understanding the response mechanism of all ion-exchanger-based polymer membranes toward polyions.

ACKNOWLEDGMENT

This work was supported in part by NIH Grants GM-28882 and HL-38353. E.B. gratefully acknowledges financial support from the Swiss National Science Foundation.

Received for review March 2, 1994. Accepted April 29, 1994.[⊕]

[⊕] Abstract published in *Advance ACS Abstracts,* June 1, 1994.

Anal. Chem. **1994,** *66,* 2260–2266

Quantitative Diffuse Reflectance and Diffuse Transmittance Infrared Spectroscopy of Surface-Derivatized Silica Powders

Farnaz Boroumand* and Hubert van den Bergh

Laboratoire d'Etude de la Pollution Atmosphérique et des Sols, Ecole Polytechnique Fédérale de Lausanne, CH-1015 Lausanne, Switzerland

Jacques E. Moser

Institut de Chimie Physique, Ecole Polytechnique Fédérale de Lausanne, CH-1015 Lausanne, Switzerland

Absolute diffuse reflectance and transmittance FT-IR spectra of optically thin layers of surface-derivatized silica powders are measured, using a photopyroelectric detector placed in direct contact with the sample. The role of inhomogeneities in the surface of the powder for quantitative diffuse reflectance and transmittance measurements is examined. It is found to be equally important and nonnegligible for both sampling methods. Diffuse transmittance is shown to be more sensitive to changes of the depth of the layer than diffuse reflectance. The effect of the pressure applied to the sample surface on the scattering coefficient of two types of silica powders of different morphologies is demonstrated. A new analytical procedure based on DRIFT spectrometry is applied to the quantitative study of the influence of the chemical environment of a cyano functional group covalently linked to the silica surface on its molar extinction coefficient.

Diffuse reflectance infrared Fourier transform spectroscopy (DRIFTS) is a well-established method for qualitative analysis. Good quality spectra can be recorded using this technique without extensive sample preparation. The potential of DRIFTS for qualitative measurements was highlighted in a series of papers by Griffiths and co-workers.[1-3] The capability of the method for quantitative measurements was also recognized early on.[1,3-6] However, significant theoretical and practical problems arise when the method is applied for quantitative analysis. Indeed, a very precise sampling method is required in this case. Several hypotheses have to be put forward as well in order to derive various theories describing diffuse reflectance. It has often been found necessary in practice to fix experimental conditions to satisfy these hypotheses so that the appropriate models can be applied.

The effect of several parameters such as particle size,[1] compression procedure,[7,8] mechanical constraint applied on the powder surface,[9,10] angles of incidence and collection,[11,12] and reproducibility of the preparation procedure of the sample and reference mixtures[13] have been discussed in the literature.

The most ubiquitous theory describing the diffuse reflectance phenomenon was developed by Schuster[14] and Kubelka and Munk.[15,16] In this phenomenological model of light absorption and scattering of the powder, the sample is treated as a continuum. A simplified solution of the differential Kubelka–Munk equations is generally used in the literature to relate a chromophore concentration to the intensity of the sample's diffuse reflection:

$$\mathcal{F}(R_\infty) \equiv (1 - R_\infty)^2/2R_\infty = K/S \propto c \qquad (1)$$

In eq 1, R_∞ represents the ratio of the diffuse reflectance of the sample of interest to that of a selected reference sample. K designates an absorption coefficient proportional to the concentration c of the chromophore, and S is the scattering coefficient of the powder.[17]

In such a model, the first assumption made is that the sample thickness d is large enough ($d \rightarrow \infty$) to allow the contribution of light transmission through the layer and the reflection from the background situated behind it to be neglected, i.e., $R \rightarrow R_\infty$. The second assumption requires that both phenomenological parameters K and S are taken to be constant throughout the whole sample volume. The thickness for which the diffuse transmittance is negligible depends on the absorption and scattering coefficients of the powder. In the case of an optically thin sample, i.e., if the thickness of the layer is small compared to the optical penetration depth, or if the absorption and scattering of the light inside the sample are not sufficient, part of the incident light will travel through the whole sample and be transmitted by its back surface. Normally this transmitted light is partially

(1) Fuller, M. P.; Griffiths, P. R. *Anal. Chem.* **1978,** *50,* 1906.
(2) Fuller, M. P.; Griffiths, P. R. *Am. Lab.* **1978,** *10,* 69.
(3) Griffiths, P. R.; Fuller, M. P. In *Advances in Infrared and Raman Spectroscopy*; Hester, R. E., Ed.; Heyden: London, 1982; p 63.
(4) Hamadeh, I. M.; King, D. *J. Catal.* **1984,** *88,* 264.
(5) Fuller, M. P.; Hamadeh, I. M.; Griffiths, P. R.; Lauenhaupt, D. E. *Fuel* **1982,** *61,* 529.
(6) Chalmers, J. M.; Mackenzie, M. W. *Appl. Spectrosc.* **1985,** *39,* 634.
(7) Yeboah, S. A.; Wang, S. H.; Griffiths, P. R. *Appl. Spectrosc.* **1984,** *38,* 259.
(8) Christy, A. A.; Tvedt, J. E.; Karstang, T. V.; Velapoldi, R. A. *Rev. Sci. Instrum.* **1988,** *59,* 423.
(9) Murthy, R. S. S.; Leyden, D. E. *Anal. Chem.* **1986,** *58,* 1228.
(10) Chalmers, J. M.; Mackenzie, M. W. *Advances in Applied Fourier Transform Infrared Spectroscopy*; Wiley: Chichester, 1988.
(11) Brimmer, P. J.; Griffiths, P. R.; Harrick, N. J. *Appl. Spectrosc.* **1986,** *40,* 2581.
(12) Brimmer, P. J.; Griffiths, P. R. *Appl. Spectrosc.* **1987,** *41,* 791.
(13) Hamadeh, I. M.; Griffiths, P. R. *Appl. Spectrosc.* **1987,** *41,* 682.
(14) Schuster, A. *Astrophys. J.* **1905,** *21,* 1.
(15) Kubelka, P. *J. Opt. Soc. Am.* **1948,** *38,* 448.
(16) Kubelka, P.; Munk, F. *Z. Tech. Phys.* **1931,** *12,* 593.
(17) Kortüm, G. *Reflectance Spectroscopy*; Springer: Berlin, 1969; p 12.

0003-2700/94/0366-2260$04.50/0
© 1994 American Chemical Society

absorbed by the sample holder and partially reflected back into the sample. The real diffuse reflectance under these conditions is affected by this background reflection.

Since it is not always possible to achieve an apparent "infinite depth" using a reasonable layer thickness, in particular, in a real nondiluted system, the attempt to measure the diffuse transmittance is very interesting. This measurement provides a supplementary information channel for the determination of parameters of interest, such as the absorption and scattering coefficients. Transmittance measurements have already been performed with partially transparent self-supporting disks using an instrument equipped with an infrared microscope.[18,19]

An original technique of diffuse transmittance infrared Fourier transform spectroscopy (DTIFTS) of loosely packed powders based on a novel photopyroelectric detector has been reported.[20,21] In a recent paper,[22] general hyperbolic solutions of the Kubelka–Munk equation have been adapted to the nonideality of various analyzed systems. To do this, we have taken into account light absorption by the solid substrate, specular reflection, and the possible existence of absorption and scattering coefficients profiles within the depth of the powder layer. The adapted model was applied to relate both the intensity of diffuse reflectance and the diffuse transmittance of a silica powder to the known concentration of a cyano group covalently linked to its surface.

In the present contribution we investigate some of the experimental parameters which influence quantitative diffuse transmittance and reflectance measurements. The effect of the quality of the sample surface in both sampling methods is compared. The effect of the chemical environment on the absorption coefficient of an alkyl-cyano functional group covalently linked to a surface-derivatized silica powder is studied quantitatively.

INSTRUMENTATION AND MATERIALS

A Bomem DA3 Fourier transform infrared (FT-IR) spectrometer was employed to obtain the data presented in this work, in conjunction with a short 25-cm scan tube. The latter was especially designed for the slow mirror velocities inherent in the use of our slow pyroelectric detector that is employed in the diffuse transmittance measurements. A photopyroelectric detector assembly was used both as the sample holder for diffuse reflectance and as a detector for the diffuse transmittance infrared Fourier transform spectroscopy (DTIFTS) developed in our laboratory. The principle and details of the photopyroelectric detector have been reported elsewhere.[23,24] The sample holder/detector used in this work consists of a thin (28-μm) Kynar poly(vinylidene fluoride) (PVDF) film (Pennwalt Corp., Valley Forge, PA), sputter-coated on both sides with ca. 250 nm of Ni–Al alloy layers and inserted in an Inficon microbalance housing.[24] The PVDF photopyroelectric element used for these experiments has an active area of circular cross section with a diameter of 9 mm. To eliminate contributions from light back-reflected by the metalized PVDF surface into the powder, great care was taken to blacken that surface by depositing a layer of carbon soot on it ($\sim$100 μm thick). The sooted surface was checked to generate zero-level signals in the InSb diffuse reflectance detector. The sample holder was mechanically adapted and fitted to the "praying mantis" diffuse reflectance accessory (Harrick Scientific Corp., Ossining, NY, Model IMG 2700 L). Two wire grid KRS-5 polarizers (Harrick Scientific Corp.) were mounted in the analyzing beam of the spectrometer, one just in front of the planar entrance mirror of the accessory and the other after the exit mirror. A low noise, wide bandwidth preamplifier (Ithaco Corp., Ithaca, NY, Model 1201) was used to amplify the photopyroelectric signal to a level compatible with the A/D converter of the spectrometer ($\sim$0.1–10 V). A high-pass first-order electronic filter was added to correct the detector response at low modulation frequencies and to eliminate low frequency noise from the interferogram that affects the reproducibility of the spectral baseline. A second amplifier compensates for the electric signal attenuation due to this filter at different frequencies. Finally, a photopyroelectric signal is delivered to the A/D converter, the amplitude of which does not vary with the modulation frequency by more than 30% between 10 Hz and 1 kHz. DRIFT and DTIFT spectra are obtained sequentially by switching connections from InSb detector and photopyroelectric circuit to the A/D converter, without disturbing the powder between the two measurements. In a typical experiment, a diffuse reflectance spectrum is obtained at a scan speed of 0.5 cm/s, with a resolution of 4 cm^{-1}, by coadding 250 scans. A diffuse transmittance spectrum is typically measured at a scan speed of 0.03 cm/s, with a resolution of 4 cm^{-1}, and by coadding 75 scans. Diffuse reflectance spectra are normalized by the spectrum of a 100% reflecting semiinfinite thickness layer of dry KBr powder. Diffuse transmittance spectra are normalized by the blackbody spectrum of the empty, soot-coated PVDF sample holder/detector. In all cases, the sample compartment of the spectrometer was purged with N_2 to eliminate interference absorption of atmospheric CO_2 and water.

Two kinds of silica powder were employed in this work. The precipitated silica LiChrosorb Si 100 (Merck, Darmstadt, Germany), characterized by a particle diameter ranging from 5 to 10 μm,[25] was dried at 120 °C under vacuum before being used. The fume silica Cab-O-Sil M5 (Cabot Corp., MA) distinguishes by a primary grain diameter of 10–15 Å and a secondary particle size of the agglomerated small particles of the order of 100 Å.[26] This nonporous powder is submitted to consecutive thermal and hydrothermal treatments to obtain a reproducible surface for chemical derivatization.[20,27] Both silica powders are then stored and manipulated in a glovebox under a dry argon atmosphere, at a humidity level not

(18) Fraser, D. J. J.; Griffiths, P. R. *Appl. Spectrosc.* **1990**, *44*, 193.
(19) Fraser, D. J. J.; Griffiths, P. R. *Anal. Chem.* **1990**, *62*, 308.
(20) Boroumand, F. Ph.D. Thesis, Ecole Polytechnique Fédérale de Lausanne, Lausanne, 1991.
(21) Mandelis, A.; Boroumand, F.; van den Bergh, H. *Spectrochim. Acta* **1991**, *47A*, 943.
(22) Boroumand, F.; Moser, J. E.; van den Bergh, H. *Appl. Spectrosc.* **1992**, *46*, 1874.
(23) Coufal, H.; Mandelis, A. *Photoacoustic and Thermal Wave Phenomena in Semiconductors*; North-Holland: New York, 1987; p 149.
(24) Mandelis, A.; Boroumand, F.; Solka, H.; Highfield, J.; van den Bergh, H. *Appl. Spectrosc.* **1990**, *44*, 132.
(25) Unger, K. K. *Porous Silica*; Journal of Chromatography Library Vol. 16; Elsevier: Amesterdam, 1979.
(26) Barby, D. In *Characterization of Powders*; Parfitt, G. D.; Sing, K. S. W., Eds.; Academic Press: London, 1976; p 389.
(27) Gobet, J.; Kováts, E. Sz. *Ads. Sci. Technol.* **1984**, *1*, 77.

exceeding 1 ppm. The specific surface area (S_A) of both silica powders was determined by evaluation of the N_2 adsorption BET isotherm at 77 K. Three independent BET measurements were performed using a Sorptomatic 1900 instrument (Carlo Erba, Milan, Italy) in a relative pressure domain ranging between 0.05 and 0.23. Average values of $S_A = 321 \pm 3 m^2 g^{-1}$ and $S_A = 191 \pm 2 m^2 g^{-1}$ were obtained respectively for the porous LiChrosorb silica and the nonporous Cab-O-Sil.

Hydroxyl groups on the oxide surface can undergo silylation reactions with dimethylaminosilanes. LiChrosorb and Cab-O-Sil powders were chemically treated with two different reagents.[20,28] (5-Cyano-3,3-dimethylpentyl)(dimethylamino)-dimethylsilane (DMP·CN)[29,30] contains a cyano functional group with a relatively sharp characteristic infrared absorption band peaking at ca. 2247 cm^{-1}. (3,3-Dimethylbutyl)(dimethylamino)dimethylsilane (DMB)[29] has approximately the same structure as DMP·CN, but does not carry a cyano chromophore. Potassium bromide (Merck, puriss p.a. grade) powder was finely ground in a Wig-L-Bug mill capsule (Crescent Manufacturing Co., Chicago, IL) and sieved. KBr particles of a diameter of 20 μm or less were then dried for several hours in an oven at 180 °C just before being used as a reflectance standard.

RESULTS AND DISCUSSION

Importance of Surface Homogeneity for Diffuse Reflectance and Transmittance Measurements. The morphology of the top surface of a sample is an important parameter for the reproducibility of diffuse reflectance measurements.[7] The optical or geometrical irregularities at the surface affect the global reflectance and transmittance more than an identical perturbation in the bulk or at the bottom of the sample. To evaluate the uncertainty introduced in the quantitative measurements due to the macroscopic surface imperfections, the spectra are recorded for a sample of derivatized Cab-O-Sil, the surface of which is deliberately deteriorated. The powdered sample placed in the photopyroelectric detector sample holder is submitted to mechanical vibrations of about 100 Hz until a homogeneous 3-mm layer with a horizontal and regular looking surface is attained. The creation of small holes (ca. 10 per cm^2, 0.2 mm in diameter, and 0.2 mm deep) using a needle leads to a decrease of the measured reflectance by about 20–30%. At the same time, diffuse transmittance intensity increases by approximately the same proportion. Such an observation shows that the two analytical channels are equally influenced by the macroscopic state of the sample surface. However, it appears that the quantitative modifications observed are much more important than is predictable for a simple local perturbation of the sample. In the absence of any compression, the thickness of the layer in these conditions remains effectively constant. The systematic decrease of reflectance and the increase of the transmittance intensity therefore suggest a more efficient penetration of light into the bulk of the sample due to a waveguide-like effect. The sensitivity of these quantitative measurements to the surface quality of the analyzed sample hence requires the use of a procedure which ascertains the regularity and the reproducibility of the macroscopic surface of the layer. Two methods have been employed so far with various success:

The first one consists of filling the sample holder with an excess of powder, which is then eliminated by scraping the top of the cup with a spatula. The second one proposed by Yeboah et al.[7] proposes the application of a vertical pressure on the powder surface. These authors showed for their system that such a procedure provides a better reproducibility compared to the spatula method, which is very much dependent on the dexterity of the operator. In the case of pressure application, the result depends essentially on the applied force, the geometry of the initial powder heap, and the achieved compression ratio.

Our experiments have been carried out with 3-mm-thick samples of various mixtures of LiChrosorb powders chemically treated by DMB and DMP·CN aminosilanes, respectively. Four batches of the powder mixture are prepared each time for each of the 10 various concentrations of DMP·CN substituents used. The spatula technique allows a reproducibility of ±3% on the reflectance measurements at a wavenumber $\tilde{\nu} = 2247 cm^{-1}$, which corresponds to the maximum absorption of the cyano group.

To control the applied force on the powder surface, a dynamometric press has been designed in our laboratory. A polished stainless steel piston is operated vertically by a rigid lever on which different brass masses can be hung at various distances from the horizontal axis. The piston is gradually lowered on the sample, on which it can apply a determined pressure during a known period of time. In all except one series of experiments, particularly designed to study the effect of powder compression, the sample cup is filled with a constant excess of silica, and a piston of a diameter larger than that of the cup is used. Since the stroke of the piston is limited by the top of the cup, most of the excess powder is removed, and the pressure is only partially transmitted to the powder. This method minimizes the compression ratio, which is at most 1.05 for the LiChrosorb powder and 1.25 for the less dense and more compressible Cab-O-Sil powder. The reproducibility of the measurements is in this case ±3%, similar to that of the spatula method for the same operator. The pressure application technique is more complex, but its undisputed advantage lies in the possibility of producing optically reproducible surfaces essentially independent of the operator. However in the case of the transmittance measurements, this method cannot be employed with the present experimental configuration. Even a small pressure transmitted to the bottom of the powder is sufficient to modify the sensitive PVDF element, which is also known to display strong piezoelectric properties. This problem prevents the comparison of the sample transmittance intensity with the one corresponding to the empty blackened detector.

The homogenization of thin powdered samples by mechanical vibration is an alternative for the leveling of their surface. The variation recorded for eight independent reflectance and transmittance measurements of a 300-μm-thick layer of a mixture of treated Cab-O-Sil powders is about 6% in both cases. The reproducibility for this preparation method thus appears to be somewhat poorer than that obtained by the pressure application technique used for thicker samples.

(28) Erard, J. F.; Nagy, L.; Kováts, E. Sz. *Colloids Surf.* **1984**, *9*, 109.
(29) Szabó, K.; Ha, N. L.; Schneider, P.; Zeltner, P.; Kováts, E. Sz. *Helv. Chim. Acta* **1984**, *67*, 2128.
(30) Schneider, P.; Cloux, R.; Fóti, K.; Kováts, E. Sz. *Synthesis* **1990**, 1027.

Table 1. Normalized Diffuse Reflectance and Transmittance of KBr Powder Layers of Various Thicknesses [a]

d (cm)	R/R_∞	T/T_0	$R/R_\infty + T/T_0$
0	0	1	1
$0 < d_1 < 0.3$	0.55 ± 0.03	0.42 ± 0.02	0.97 ± 0.05
$0 < d_2 < 0.3$	0.90 ± 0.05	0.13 ± 0.01	1.03 ± 0.06
0.3	1	0	1

[a] The uncertainties on diffuse reflectance and transmittance measurements are estimated at about ±6 and ±5%, respectively.

Normalization of Diffuse Reflectance and Diffuse Transmittance Measurements. The transmittance, T, normalized by the signal obtained with the empty detector is considered to be absolute. The problem is more complex for diffuse reflectance. Only a collection system including an integrating sphere could give an exact indication about the absolute reflectance value R. A quantitative measurement hence implies the normalization of the spectra by using a reference. The choice of this reference is particularly important. The alkali halide salts are well-known for their excellent transmittance in the mid-infrared domain. A thick, totally opaque layer of KBr powder finely ground and carefully dehydrated should display in principle, in the absence of any absorbance, a diffuse reflectance equal to unity. For thinner, partially transparent layers, the conservation of energy implies $R + T = 1$.

In Table 1, the quantitative results obtained for two thin layers of a KBr powder with a particle diameter of less than 20 μm are presented. The values are all taken at $\bar{\nu} = 2247$ cm^{-1}, the wavenumber corresponding to the —C≡N chromophore absorption maximum. The high scattering power of KBr implies a total opacity for a thickness of the layer larger than 2 mm. The reflectance of a 3-mm-thick layer can therefore be used for the normalization of the measurements. The sum of diffuse reflectance and transmittance values reported in Table 1, taking into account the uncertainties, tends to unity, indicating that absolute diffuse reflectance and diffuse transmittance are effectively measured.

Higher Sensitivity of Diffuse Transmittance Channel. In Figure 1, we show as an example two raw spectra obtained by diffuse reflectance FT-IR measurements of both Cab-O-Sil silica powders, treated up to surface saturation by the aminosilanes DMB and DMP-CN, respectively. The narrow and well-defined peak centered at $\bar{\nu} = 2247$ cm^{-1} is easily distinguishable and is characteristic of the nitrile function of the DMP-CN substituent.

A layer thickness of 1.3 mm is not sufficient to ensure the complete opacity of a Cab-O-Sil sample. The light intensity transmitted in a diffuse way can in consequence be measured by the photopyroelectric detector.[21,22] The measured signals are normalized by the spectrum of the soot layer covering the PVDF film placed in the empty container yielding the absolute transmittance of the scattering layer.

Mixtures in different proportions of Cab-O-Sil powders, treated respectively by DMB and DMP-CN, are prepared. The absolute diffuse reflectance and transmittance are measured for different concentrations of the cyano group at $\bar{\nu} = 2247$ cm^{-1} and corrected for light absorption by the oxide substrate, as well as for the Fresnel reflection.[22] The general

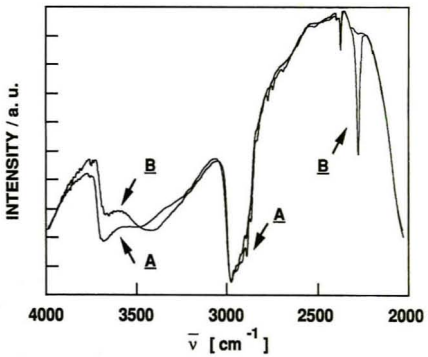

Figure 1. Raw FT-IR diffuse reflectance spectra of a 1.3-mm-thick layer sample of Cab-O-Sil powder, treated up to complete surface coverage by (A) DMB and (B) DMP-CN aminosilane reagents. The spectra are typically obtained at a scan speed of 0.5 cm/s, with a resolution of 4 cm^{-1}, and by accumulation of 250 scans.

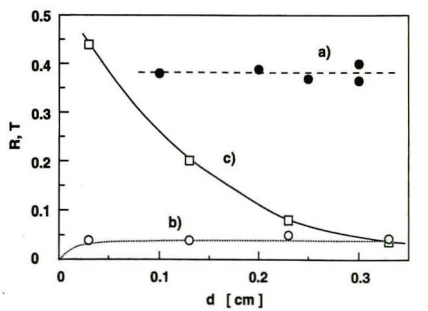

Figure 2. Effect of the depth of the layer d on the absolute diffuse reflectance and transmittance of derivatized LiChrosorb and Cab-O-Sil silica powder samples. Reported values are measured at the maximum of the absorption peak of the CN group at $\bar{\nu} = 2247$ cm^{-1}. (a) Diffuse reflectance of various LiChrosorb silica layers treated up to surface saturation by DMB substituents. (b) Diffuse reflectance of various layers of Cab-O-Sil powder treated by DMP-CN aminosilane. (c) Diffuse transmittance of Cab-O-Sil powder under the same conditions as (b).

hyperbolic solutions of the Kubelka–Munk equation allow the considerations of diffuse reflectance and diffuse transmittance of the sample simultaneously. These solutions are adjusted for both sets of experimental data using a modified Marquardt nonlinear least-squares fitting procedure.[31,32] Results are reported in ref 22. An excellent correlation between the respective transmittance and reflectance measurements is obtained, and the scattering coefficient value at $\bar{\nu} = 2247$ cm^{-1} is determined. In such a case, the absorption coefficient K as well as the scattering coefficient S can be determined simultaneously. Moreover, it was observed that the transmittance channel is more sensitive to concentration variations, therefore this channel can be used advantageously for analysis.

In Figure 2a, we report the reflectance of a LiChrosorb powder derivatized by DMB as a function of the depth of the scattering layer. Results show that the reflectance at the absorption maximum of the CN group does not vary between 1 and 3 mm. No transmittance can be measured for layers

(31) Marquardt, D. W. *Chem. Eng. Prog.* **1959**, *55*, 65.
(32) Marquardt, D. W. *J. Soc. Ind. Appl. Math.* **1963**, *11*, 431.

thicker than 1 mm which have therefore to be considered as pseudoinfinite with $R = R_\infty = 0.38 \pm 0.02$.

For chemically treated Cab-O-Sil powder (Figure 2b), the measured reflectance $R = 0.044 \pm 0.002$ as a function of the depth of the layer between 0.3 and 3.3 mm is much lower than the measured reflectance for LiChrosorb. Even though the scattering power of Cab-O-Sil is smaller than the one characterizing LiChrosorb powder, the reflectance value seems not to change beyond 300 μm depth. Figure 2c shows that the phenomenon is completely different for the transmittance measurements. There is a very important decrease of transmittance from $T = 0.44$ at 0.3 mm to about one-tenth of this value at 3.3 mm. As the reflectance is not affected, such a variation is due to the absorption of the treated silica. This observation shows the higher sensitivity of the transmittance measurements to the absorption of the sample.

A similar conclusion has been drawn from the computer model simulations for the case of a new discontinuous multilayer theory.[21] The transmittance in that case is more sensitive than the reflectance to the number of the particle layers. These observations indicate the necessity of a reconsideration of the total opacity criterion generally used in the literature. Indeed, the fact that there exists a depth beyond which the reflectance no longer increases does not necessary imply the absence of any transmitted light through thicker layers.

Effect of Application of Pressure on Scattering Coefficient of Powder. The application of a mechanical pressure on the surface of the powder can not ascertain a homogeneous density in the depth of the layer. This method is usually employed to level the powder surface and to obtain reproducible surfaces for reflectance measurements. In a recent paper,[22] we have shown that the variation of the scattering coefficient with the depth of the layer can dramatically influence the reflectance value of the layer without necessarily affecting the mean value of this coefficient. In order to separate the effects of applied pressure from those of the apparition of inhomogeneities of the optical properties, such as absorption and scattering coefficients, samples constituted of mixtures of Cab-O-Sil powder with different concentrations of the CN group on their surfaces have been prepared in a particular way: An amount of the powder corresponding to about one tenth of the sample holder volume is compressed using a cylindrical piston penetrating inside the sample holder. A known pressure is applied by a dynamometric press and maintained for 1 min. A same amount of the powder is poured on the top of this first layer and compressed in the same way. Thus, the first sublayer is submitted for a second time to a mechanical pressure. Nevertheless, as the maximum compaction is achieved already at the first compression, the density does not change anymore. This operation is repeated until a 3-mm depth sample constituted of 10 superimposed sublayers is made. Each sublayer is thin enough to consider that absorption and scattering coefficients K and S are effectively constant within the depth of the whole sample.

Three different series of reflectance measurements have been done this way by application of increasing pressures of 5.89×10^6, 1.18×10^7, and 1.05×10^8 Pa. In each case, the density has been determined by weighing the sample holder. The results are presented in Figure 3 and Table 2. The absolute reflectance corrected for the Fresnel reflection[22] increases with increasing pressure up to 1.18×10^7 Pa and decreases by a further increase of pressure up to 1.05×10^8 Pa. For each family of the results, the hyperbolic model of Kubelka[15] is used with success, and one can extract the scattering coefficient S without introduction of any absorption or scattering coefficient profile in the depth of the layer.[22]

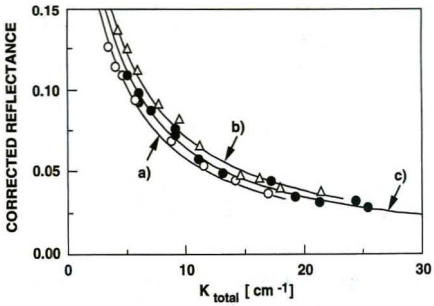

Figure 3. Absolute diffuse reflectance of mixtures in various proportions of both Cab-O-Sil powders treated up to surface coverage by DMB and DMP-CN aminosilanes, respectively. The samples are stacks of 10 thin layers, each of which was compressed under a pressure of (a) 58.9 $\times 10^5$, (b) 117.7 $\times 10^5$, and (c) 1054.5 $\times 10^5$ Pa. Solid curves display the best fit of parameters in Kubelka's equation to the experimental results.

Table 2. Results of Fitting of Scattering Coefficient S in Kubelka's Model to Experimental Data of Figure 3[a]

pressure (10^5 Pa)	ρ (g/L)	S (cm^{-1})
~0	130	1.25
58.9	170	1.30
117.7	220	1.65
1054.5	260	1.47

[a] The mean value in the absence of an applied pressure has been established for the experimental results reported in ref 22, where profiles of scattering and absorbtion coefficients were taken into account.

For the smallest pressure, there is an increase of the compaction density of 40%. By application of further pressures, one obtains a density up to two times higher than the 'natural' density of the powder. The changes in the scattering coefficient follow the variations in the reflectance values. For Cab-O-Sil which is a fluffy powder, this is related to an increase of the number of the scattering centers by unit of volume in the first compaction phase. In a second phase, the number of the interfaces and thus the scattering coefficient decreases.

Griffiths et al.[7] reported an important decrease of the scattering coefficient following application of a pressure on their model systems constituted of dispersed caffeine in potassium chloride. The KCl powder, as well as KBr employed usually as a dilutant, is a compact powder formed by angular particles. A pressure of 6×10^7–10^9 Pa can just rearrange the position of the particles, which will tend to become aligned. Here, in the second phase of the compression of Cab-O-Sil powder, a similar behavior is hence observed.

A similar series of experiments has been carried out with the samples of LiChrosorb (Figure 4). Results are reported in Table 3. For LiChrosorb powder, which has a higher density and a porous morphology, the scattering coefficient increases

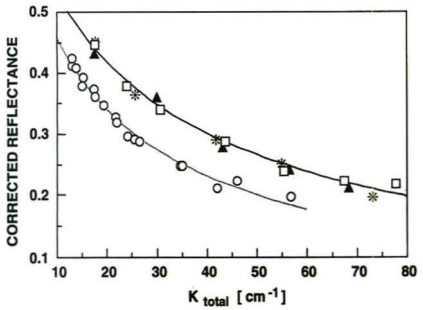

Figure 4. Absolute diffuse reflectance of mixtures in different proportions of both the LiChrosorb silica powders treated up to surface coverage by DMB and DMP·CN aminosilanes, respectively. 3-mm-thick samples are formed by stacking 10 thin layers, each individually compressed under a pressure of 58.9 × 10^5 (–▲–), 117.7 × 10^5 (–✱–), and 1054.5 × 10^5 Pa (–□–). For comparison, values obtained for a noncompressed powder (•••○•••) are also reported. Solid curves represent the best fit of parameters in Kubelka's equation to the experimental results.

Table 3. Results of Fitting of Scattering Coefficient *S* in Kubelka's Model to Experimental Data of Figure 4[a]

pressure (10^5 Pa)	ρ (g/L)	S (cm^{-1})
~0	350–370	26.5
58.9	480	48.1
117.7	500	49.2
1054.5	500	47.0

[a] The mean value in the absence of any applied pressure is reported for comparison.

in the first phase and then remains essentially constant upon further application of pressure. The scattering coefficient S attains a plateau value 48 ± 1 cm^{-1}. A maximum density of about 35% higher than the natural density of the powder is obtained already for the smallest pressure, and hence the compaction does not change by further application of pressure. For a relatively low compression compared to that of Cab-O-Sil, a relatively large increase of about two times of the scattering coefficient is observed. Since the number of optical interfaces inside porous LiChrosorb does not increase by application of a pressure, the coefficient S should not vary. Electron microscopy studies show that the LiChrosorb powder grains might break up under pressure, so one has to be careful in interpreting the scattering coefficient data in this case.

Influence of Chemical Environment of the Functional Group on Its Molar Extinction Coefficient. In order to study the influence of chemical environment of the CN chromophore on its absorption coefficient, two series of the experiment have been carried out. In the first series, two samples of LiChrosorb have been treated up to a maximum surface coverage with DMB and DMP·CN separately. Mixtures with different proportions of the two powders are prepared in order to vary the concentration of the cyano group. In the second series, a sample of LiChrosorb powder is reacted with a mixture of the two aminosilanes. The variation of the concentration of cyano on the same surface is obtained by mixing different proportions of the two aminosilanes before the reaction. In this case, the environment of the cyano group is expected to

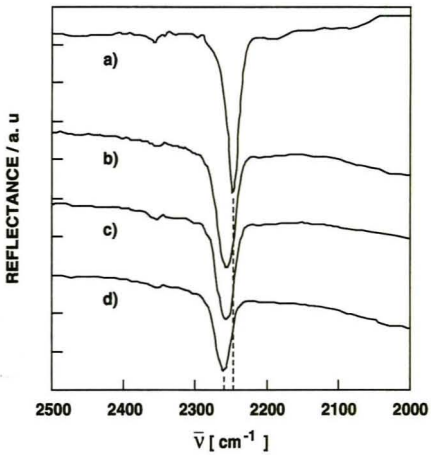

Figure 5. Diffuse reflectance spectra measured for a LiChrosorb silica powder treated by the aminosilane DMP·CN resulting in various fractions of surface coverage: (a) 1.0, (b) 0.71, (c) 0.51, and (d) 0.25. The maximum of the absorption peak is shifted toward the blue as the surface coverage increases. The position of base lines is arbitrary.

depend on the relative rate of coverage of silica by the DMP·CN substituent and on the nature of the other molecules adsorbed on the same surface.

Figure 5 shows four different diffuse reflectance spectra of the LiChrosorb powder, which is partially covered with various concentration of DMP·CN substituents. C, H, and N elementary analyses allow determination in each case of the surface coverage by the siloxy groups. The large IR absorption of hydroxyl groups on the silica surface results in a strongly varying baseline. Quantitative diffuse reflectance analysis of the cyano group is thus impossible in this case. The maximum absorption peak of the cyano group for a total surface coverage is positioned at 2247 cm^{-1}. For the smaller fractions of DMP·CN, one can observe a logical decrease of the band intensity together with a blue shift of the peak. At a quarter of the surface covered with DMP·CN substituents, the maximum of the absorption peak is shifted by 13 cm^{-1} as compared to the completely covered surface. This shift to higher energies may be attributed to the formation of hydrogen bonds CN···OH between the cyano and hydroxyl groups in their environment. Such an effect has been reported for the aliphatic nitrile groups in a protic solvent.[33] Once the silylation reaction is completed with the two aminosilanes simultaneously and saturation of the silica surface is attained, the hydroxyl groups are mostly eliminated, and the above-mentioned effect is no longer expected. The variation of the molar fraction of the DMP·CN substitutents balanced by that of the DMB substitutents does not give rise to any shift of the absorption maximum of the nitrile group, which remains at $\bar{\nu}$ = 2247 cm^{-1}.

Figure 6 shows the absolute diffuse reflectance at $\bar{\nu}$ = 2247 cm^{-1} for the LiChrosorb powder submitted to a reaction with a mixture of both aminosilanes DMB and DMP·CN. The phenomenological absorption coefficient is calculated knowing

(33) Williams, I. *Ind. Eng. Chem.* **1923**, *15*, 154.

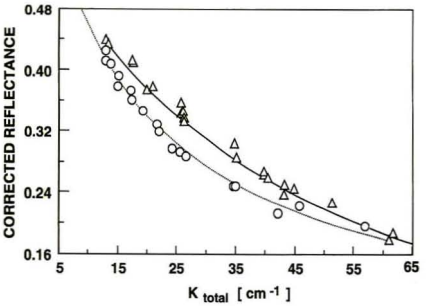

Figure 6. Diffuse reflectance at $\bar{\nu}$ = 2247 cm^{-1} of a LiChrosorb silica powder, treated by a mixture of both aminosilanes DMB and DMP·CN (–Δ–). For comparison, data obtained for mixtures in different proportions of powders treated separately by both aminosilanes DMB and DMP·CN up to surface saturation are also reported (•••O•••).

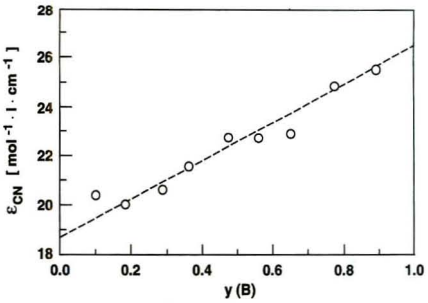

Figure 7. Molar extinction coefficient of the cyano functional group anchored on a LiChrosorb powder treated by a mixture of both aminosilanes DMB and DMP·CN as a function of the various molar fractions $y(B)$ of substituents carrying a CN function.

the molar fraction of DMP·CN and the molar extinction coefficient $\epsilon \cong 27$ L mol^{-1} cm^{-1} determined previously for the CN chromophore.[22] The optical absorption of the silica powder itself has also been taken into account. A quantitative model derived from the hyperbolic solutions of Kubelka for the differential equations of Kubelka–Munk developed in a recent paper is applied to the experimental results. The best Marquardt least-squares adjustment of the results gives a scattering coefficient of S = 39.7 cm^{-1}, which is larger than S = 26.2 cm^{-1} obtained for mixtures of two powders treated up to saturation of their surfaces by both aminosilanes respectively. A first hypothesis put forward to explain this difference is a change in the morphology of the powders used in both cases. No difference is observed in the density of the two powders, nor is any change in the morphology of the grains noticed under the electron microscope. The two groups of results reported in Figure 6 and the two theoretical fits show a good coincidence of the two extreme points $y(B) = 0$ and $y(B) = 1$ where the samples must effectively be nondiscernible. This observation suggests identical scattering coefficients for both sets of samples equal to S = 26.2 cm^{-1}. In these conditions, only an error on the evaluation of the K_{tot} coefficients can explain the difference observed between the scattering coefficients in the two sets of experiments. The molar extinction coefficient of the chromophore can indeed be a function of its molar fraction on the silica mixed treated surface. If this is the case, K_{tot}, which has been calculated using ϵ = 27 L mol^{-1} cm^{-1}, is not correct for the various concentrations, and the difference observed between the two curves is due to the error in the determination of K_{tot}.

The two curves in Figure 6 can be superimposed by identifying at equal reflectance the absorption coefficient to that calculated for the mixture of the powders. Once the real absorption coefficients K are determined, one can obtain the molar extinction coefficient corresponding to each fraction $y(B)$ by using the linear relation

$$K = 2 \ln (10) \epsilon \rho c_m \qquad (2)$$

where ϵ is the chromophore molar extinction coefficient (L mol^{-1} cm^{-1}), ρ is the solid density (g L^{-1}), and c_m is the mass concentration of the substituent carrying the CN group (mol g^{-1}):

$$c_m(B) = \frac{y(B)\Gamma_{tot}}{\frac{1}{S_A} + \Gamma_{tot}[y(B)M_{(B)} + [1 - y(B)]M_{(A)} - \delta]} \qquad (3)$$

In the latter expression, $y(B)$ represents the molar fraction of the substituent containing the CN group, $M(A)$ and $M(B)$ are the molecular weight of the siloxy radical of DMB and DMP·CN, respectively (g mol^{-1}), Γ_{tot} is the total surface concentration of the substitutents (mol m^{-2}), S_A is the specific area of the surface of silica before reaction (m^2 g^{-1}), and δ is a correction factor taking into account the desorbed water and the substitution of one proton during the silylation reaction (g mol^{-1}).[20]

The results of this operation are presented in Figure 7. For a complete surface coverage of silica by DMP·CN substituents, an extinction coefficient of ϵ = 27 L mol^{-1} cm^{-1} is found. This value tends in a linear way to ϵ = 20 L mol^{-1} cm^{-1}, as the molar fraction of the chromophore tends to zero. This phenomena is the result of a change of the environment of the cyano group. For $y(B) = 1$, this implies an important interaction between vicinate nitrile groups. An inductive effect of the nitrogen electronegative group on the electrodefficient carbon of the neighbor group tends to improve the polarization of the triple bond under its mesomer form —C$^+$=N$^-$, which is characterized by a higher absorption. Diluted in the nonpolar DMB substitutent, the chromophore extinction coefficient approaches that of capronitrile in solution in n-dodecane (ϵ = 20 L mol^{-1} cm^{-1}).

ACKNOWLEDGMENT

The authors would like to thank Dr. Roland Cloux for the preparation of the aminosilane reagents and Prof. Andreas Mandelis for fruitful discussions. Financial support of this work has been provided by the Fonds National Suisse de la Recherche Scientifique.

Received for review January 3, 1994. Accepted April 20, 1994.®

® Abstract published in *Advance ACS Abstracts,* May 15, 1994.

Anal. Chem. **1994,** *66,* 2267–2271

In Vivo Percutaneous Absorptiometry by a Laser Photoacoustic Method Using a Novel Open-Ended Cell Combined with Light Guide

Ryuichi Takamoto,[†] Shinya Yamamoto,[†] Ryujiro Namba,[†] Tasuku Takamatsu,[†] Masahiro Matsuoka,[†] and Tsuguo Sawada*[,‡]

Safety & Analytical Research Center, Shiseido Company, Ltd., 1050 Nippa-cho, Kohoku-ku, Yokohama 223, Japan, and Department of Industrial Chemistry, Faculty of Engineering, The University of Tokyo, 7–3-1 Hongo, Bunkyo-ku, Tokyo 113, Japan

A laser photoacoustic (PA) method with high sensitivity and accuracy using a novel open-ended PA cell was developed. This PA cell was constructed by processing the end of a light guide as the sample chamber of the PA cell and by attaching an acoustic pipe which was bent optimally to a right angle at one end. This design minimized the dead volume and provided more measurement flexibility. The PA cell design is based on the principle of a resonance permitting a smaller gas volume in the PA cell than that of Helmholtz resonance. As a result, the new PA cell sensitivity was about 10 times that of a conventional PA cell. The sensitivity and reproducibility for in situ PA measurement of an indomethacin (IDM) ointment introduced in a poly(ethylene glycol) vehicle were excellent over 10 repeated measurements. The signal-to-noise ratio was 46, and the coefficient of variation was not more than 3% for an amount of 2 μg/5 mm i.d. Good linearity was obtained for amounts of 2–120 μg/5 mm i.d. and the correlation coefficient was not less than 0.99. In vivo percutaneous absorptiometry was attempted using 1% IDM ointment. The diffusion coefficient of IDM through the skin measured by this PA method was 6.7 × 10^{-6} cm^2/min. This is of the same order of magnitude as results obtained by the conventional in vitro method using a longitudinal diffusion cell. These results confirmed the effectiveness of this simple newly developed in vivo percutaneous absorptiometry technique, compared with conventional methods such as radioisotopes.

Evaluation of the percutaneous absorption of a substance is very important in development of endemic liniments. Various percutaneous absorptiometry methods have been reported[1–5] including diffusion cell methods and radioisotopes (RI). These cannot be used for humans in vivo because skin is either excised or a radioactive compound is used. Therefore, many investigations have used animal substitutes. However, we need information about percutaneous absorption in humans in vivo. Effective human in vivo measurement using the stripping method has been reported by Rougier et al.,[6,7] but this method damages the skin and causes measurement problems. There are few methods of measuring percutaneous absorption in humans in vivo reliably and easily. The important conditions for human in vivo measurement are safety, accuracy, spee, and simplicity.

Several investigations have reported the photoacoustic (PA) method an effective method.[8–11] The most remarkable point is that the reliability of an open-ended PA cell is influenced by either the surface potential of an in vivo object such as skin or by environmental noise determined by the measurement of signal-to-noise ratios (S/N). Additionally, the PA cell operability must be considered. Several open-ended PA cells have been reported[12–14] for obtaining better S/N values.

We have reported the development of percutaneous absorptiometry using the laser PA method and its usefulness for in vitro and in vivo measurements. This system was combined with a longitudinal diffusion cell used generally for in vitro percutaneous absorptiometry to substantiate its applicability to in vitro measurement.[15] It was actually applied to human in vivo percutaneous absorptiometry[16] to show the potential compared to conventional PA methods.[12–14] This PA system used a laser as the light source, and the laser beam was guided to the open-ended PA cell by an optical fiber. This arrangement minimized the noise level and the detected PA signal had a high S/N. We were able to evaluate the percutaneous absorption of subject drugs by measuring the change in the PA signal with time corresponding to the amount of drug remaining on the skin.

However, when this PA method was tried with many substances, it was apparent that a more sensitive PA device

[†] Shiseido Co., Ltd.
[‡] University of Tokyo.

(1) Bronaugh, R. L.; Stewart, R. F. *J. Pharm. Sci.* **1986,** *75,* 1094–1097.
(2) Southwell, D.; Barry, B. W.; Woodford, R. *Int. J. Pharm.* **1984,** *18,* 299–309.
(3) Tojo, K.; Ghannam, M. M.; Sun, Y.; Chien, Y. W. *J. Controlled Release* **1985,** *1,* 197–203.
(4) Gummer, C. L.; Hinz, R. S.; Maibach, H. I. *Int. J. Pharm.* **1987,** *40,* 101–104.
(5) Guy, R. H.; Carlstrom, E. M.; Bucks, D. A. W.; Hinz, R. S.; Maibach, H. I. *J. Pharm. Sci.* **1986,** *75,* 968–972.
(6) Rougier, A.; Dupuis, D.; Lotte, C.; Roguet, R.; Schaefer, H. *J. Invest. Dermatol.* **1983,** *81,* 275–278.
(7) Rougier, A.; Dupuis, D.; Lotte, C.; Roguet, R.; Wester, R. C.; Maibach, H. I. *Arch. Dermatol. Res.* **1986,** *278,* 465–469.
(8) Rosencwaig, A. *Clin. Chem.* **1982,** *28*(9), 1878–1881.
(9) Rosencwaig, A.; Pines, E. *Biochim. Biophys. Acta* **1977,** *493,* 10–23.
(10) Campbell, S. D.; Yee, S. S.; Afromowitz, M. A. *J. Bioeng.* **1977,** *1,* 185–188.
(11) Campbell, S. D.; Yee, S. S.; Afromowitz, M. A. *IEEE Trans. Biomed. Eng.* **1979,** *BME-26*(4), 220–227.
(12) Poulet, P.; Chambron, J. *J. Photoacoust.* **1983,** *1,* 329–346.
(13) Kolmel, K; Sennhenn, B.; Giese, K. *J. Soc. Cosmet. Chem.* **1986,** *37,* 375–385.
(14) Giese, K.; Nicolaus, A.; Sennhenn, B.; Kolmel, K. *Can. J. Phys.* **1986,** *64,* 1139–1142.
(15) Takamoto, R.; Namba, R.; Nakata, O.; Sawada, T. *Anal. Chem.* **1990,** *62,* 674–677
(16) Takamoto, R.; Namba, R.; Matsuoka, M.; Sawada, T. *Anal. Chem.* **1992,** *64,* 2661–2663.

0003-2700/94/0366-2267$04.50/0
© 1994 American Chemical Society

was required. This was necessary because we used a light source oscillating in the ultraviolet (UV) wavelength region because many drugs generally absorb light at wavelengths of 200–300 nm. In this case, the most significant problem is related to the safety of skin irradiated with UV light. Use of visible laser light causes no problem because the maximum permissible exposure (MPE) values for human skin are clearly known. However, the MPE values for human skin irradiated by UV light wavelengths (less than 290 nm) are not clearly known because these wavelengths do not reach the earth's surface and experimental data have rarely been reported. Accordingly, the intensity of the light applied to the skin sample must be as low as possible. Under this condition, we must be able to detect a small change in the PA signal when the substance penetrates the skin.

We tried to develop an open-ended PA cell with a higher sensitivity than that of the conventional PA cell.[16] We know that reducing the total gas volume of the PA cell produces higher sensitivity, within limits.[17] We designed a PA cell on this basis by determining parameters such as the sample chamber, the microphone chamber, and length and cross-sectional area of the acoustic pipe. However, designs based on the conventional open-ended PA cell[12–14,16] increased the total gas volume more than necessary, causing a drop in sensitivity. We needed a design that did not increase the gas volume and minimized the dead volume. In addition, most conventional open-ended PA cells are based on the Helmholtz resonance theory[18] to amplify the PA signal. The Helmholtz resonance frequency, f_R, is given by

$$f_R = (cd/4p)[(V_{MC} + V_{SC})/(V_{MC}V_{SC}(L + 0.85d))]^{1/2} \quad (1)$$

where c is the speed of sound in the coupling gas, V_{SC} and V_{MC} are the volumes of the sample and microphone chambers, respectively, and d is the diameter of the sample/microphone acoustic coupling tube of length, L, connecting V_{SC} and V_{MC}. The Helmholtz resonance theory requires a certain volume in both the sample and microphone chambers. This means that minimizing the total gas volume in the PA cell has limits. V_{SC} is required to transform heat from the sample into sound, but V_{MC} increases the total gas volume of the PA cell as a result.

Four points occurred in developing a new open-ended PA cell: (1) use resonance theory for causing resonance with no V_{MC}; (2) minimize the influence of skin surface potential and environmental noise (less than 100 Hz); (3) minimize the dead volume of the PA cell; (4) miniaturize the PA cell for easy measurement. We developed a novel open-ended PA cell on the basis of these concepts.

A bundle-type guide was used to guide the UV light from the light source to the PA cell to provide more flexibility during measurement. To minimize the dead volume of the cell, the end of the light guide was used as a cell by attaching an acoustic pipe to the end of the light guide. This PA cell is hardly affected by light scattering in the sample chamber. This design was expected to provide better sensitivity and more accurate measurements than obtained with a conventional PA cell.[16] In vivo absorptiometry was attempted using a 1% indomethacin (IDM) ointment applied to a hairless mouse. The propriety and effectiveness of this PA method was investigated by comparing the results obtained with this PA method with those from the diffusion cell method for typical percutaneous absorptiometry.

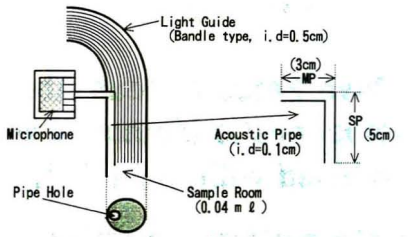

Figure 1. Diagram of a novel open-ended PA cell combined with the light guide.

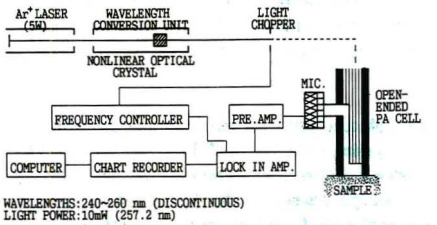

Figure 2. Diagram of laser PA system using the open-ended cell.

EXPERIMENTAL SECTION

Figure 1 shows the construction of the novel open-ended PA cell combined with light guide. A bundle-type guide (Asahi Glass Corp., 5 mm diameter × 1 m length), which can transmit more than 85% of the UV light, was used to provide more measurement flexibility and to minimize the dead volume of the cell. The open-ended PA cell uses the end of the light guide as the sample chamber (stainless steel) by attaching an acoustic pipe (β-brass) bent at a right angle inside the end of the light guide. A microphone (Primo, MP-10) was threaded to the acoustic pipe to control its length and to eliminate the volume of the microphone chamber. The volume and width of the air layer in the sample chamber are 0.04 cm^3 and 0.2 cm, respectively. This volume is about 40% of that of the conventional PA cell.[16] Figure 2 shows an in vivo percutaneous absorptiometry system using the open-ended PA cell combined with the light guide. UV light with a CW of 257 nm was used as the light source and was obtained by oscillating a multiple Ar^+ laser beam (Spectra Physics, Model-2020) at 5 W and using a β-BaB_2O_4 (BBO) crystal wavelength conversion unit (Ascal Corp., UVA-4), which can be microadjusted optically. The UV laser beam was modulated at 2.2 kHz (the resonance frequency of the PA cell) using a light chopper (NF Corp.). The optical path was very easily adjusted because the PA cell was combined with the light guide. The output intensity of the light source was set to 3 mW by the light guide. The PA signal detected by the PA cell was analyzed using a lock-in amplifier (NF Corp, 5610A), recorded using a chart recorder (Rika Denki Kogyo, NP-0393) and calculated using a computer (Nippon Denki Corp., VX).

(17) Aamodt, L. C.; Murphy, J. C.; Parker, J. G. *J. Appl. Phys.* **1976**, *47*, 64–68.
(18) Thompson, M. M.; Palmer, R. A. *Anal. Chem.* **1988**, *60*, 1027–1032.

Indomethacin ($C_{19}H_{16}ClNO_4$, Wako Pure Chemical, reagent class; for biochemistry), which absorbs light at a wavelength of 257 nm, was used as the model sample. The IDM ointment was prepared using poly(ethylene glycol) (PEG) as the vehicle, and the mixture was heated (80 °C). A hairless mouse was used as the subject animal.

First, the sensitivity of this new PA cell was optimized. In vivo percutaneous absorptiometry was then applied to the hairless mouse.

RESULTS AND DISCUSSION

Resonance Theory of a New PA Cell and Determination of Total Length of Acoustic Pipe. We attempted to clarify the resonance mechanism of this PA cell designed to minimize total cell volume. The total length of the acoustic pipe is L (SP + MP), and the coordinates x are given along the axis of the acoustic pipe. When the sample chamber–acoustic pipe interface is defined as $x = 0$, the sound field in this PA cell is equivalent to that of a diaphragm vibrating at $U_0 \sin(\omega t)$ at $x = 0$ and the point ($x = L$) is closed by the microphone, where U_0 is the initial particle velocity, ω is the angular frequency, and t is time. Since the wavelength of the sound generated in the PA cell is much longer than the inner diameter of the acoustic pipe, only a plane wave progressing along the axis of the acoustic pipe occurs in the air of the PA cell. This sound field is analyzed below. Since the sound is reflected by the microphone, the stationary wave (the sound pressure amplitude (P_r) of the reflective sound is equal to that (P_i) of the incident sound) is generated in the acoustic pipe. In addition, at the point of $x = L$ (P_r is in phase of P_i), the sound pressure amplitude (P) of the stationary wave becomes maximum ($2P_i$) and the particle velocity becomes minimum (0). Accordingly, the distribution $P(t,x)$ of the sound pressure of the stationary wave in the acoustic pipe is expressed as

$$P(t,x) = 2P_i \cos[(kx - (\varphi_{0i} - \varphi_{0r})/2] \sin[\omega t + (\varphi_{0i} + \varphi_{0r})/2] \quad (2)$$

where k is the phase constant, φ_{0i} is the initial phase of the incident sound, and φ_{0r} is the initial phase of the reflective sound. Since P is equal to $2P_i$ at $x = L$, we can write

$$\varphi_{0i} - \varphi_{0r} = 2kL - 4n\pi \quad (n = 0, 1, 2, \ldots) \quad (3)$$

Equation 2 then becomes

$$P(t,x) = 2P_i \cos[k(L - x)] \sin(\omega t + \varphi_{0i} - kL) \quad (4)$$

By the same treatment, the distribution $U(t,x)$ of the particle velocity of the stationary wave in the acoustic pipe is given by

$$U(t,x) = (2P_i/\rho_c) \sin[k(L - x)] \cos(\omega t + \varphi_{0i} - kL) \quad (5)$$

where ρ_c is the specific acoustic resistance. Since eq 4 becomes $U_0 \sin(\omega t)$ at $x = 0$, it can be shown that

$$U_0 \sin(\omega t) = (2P_i/\rho_c) \sin(kL) \cos(\omega t + \varphi_{0i} - kL) \quad (6)$$

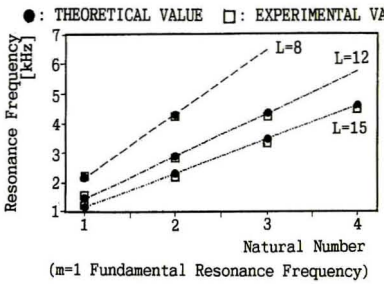

Figure 3. Theoretical treatment of the resonance frequency caused by changing the total length of the acoustic pipe.

The conditions for forming eq 6 are given by

$$\varphi_{0i} = kL + (2n + 1)\pi/2 \quad (n = 1, 2, 3, \ldots) \quad (7)$$

$$2P_i/(\rho_c) = U_0/[\sin(kL) \sin(2n + 1)\pi/2] \quad (8)$$

Consequently, the distribution of the sound pressure and the particle velocity are expressed as

$$P(t,x) = \rho_c U_0/[\sin(kL)] \cos[k(L - x)] \cos(\omega t + \pi) \quad (9)$$

$$U(t,x) = U_0/[\sin(kL)] \sin[k(L - x)] \sin(\omega t) \quad (10)$$

As obtained from eqs 9 and 10, the conditions for creating resonance in the PA cell are given by

$$kL = m\pi \quad (11)$$

$$L = m\lambda/2 \quad (12)$$

where m is the natural number and λ is the wavelength of the sound generated in the PA cell. Therefore, the resonance wavelength (λ_R) and the resonance frequency (f_R) are determined by

$$\lambda_R = 2L/m \quad (13)$$

$$f_R = m(V_s/2L) \quad (14)$$

where V_s is the sound velocity of about 340 m/s at room temperature (15 °C). The $m = 1$ resonance is the fundamental one. From eqs 13 and 14, it is clear that this resonance type is equal to the open-pipe resonance when a sound pressure was given at $x = 0$.

We examined this resonance theory. As shown in Figure 3, the resonance frequencies measured when the total length of the acoustic pipe was changed were in good agreement with those calculated from the resonance theory (eq 14). Consequently, it is obvious that the resonance frequency of this new PA cell is determined by the total length of the acoustic pipe. The total length of the acoustic pipe connecting the sample chamber and the microphone is set to 8 cm, giving a resonance of about 2 kHz, which is hardly affected by skin pulsation and environmental noise. In addition, the resonance can be adjusted by changing the length of the acoustic pipe.

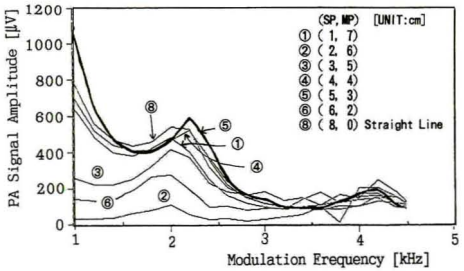

Figure 4. Comparison of the PA signal amplitude with change in the length of SP and MP (SP + MP = 8 cm).

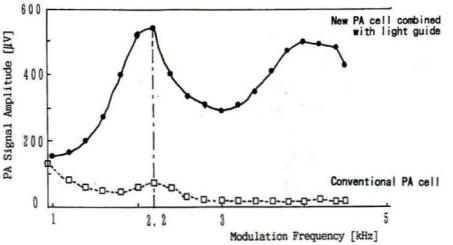

Figure 5. Comparison of the sensitivity of the new PA cell and the conventional PA cell utilizing the Helmholtz resonance theory.

Determination of the Bend Point of an Acoustic Pipe. The acoustic pipe attachment to the PA cell was optimized. We investigated the frequency characteristics of the PA signal amplitude by changing the bend point (SP) of the acoustic pipe so that the total length was 8 cm at the right angle. This bending angle test was carried out only at two points with angles of both 0° (straight) and 90°, with no other angles between 0° and 90°, because we judged that the sound behaves similarly to a straight line when the bend angle is smaller and closer to a right angle when the bend angle is bigger. Figure 4 shows the results. The resonance frequency was kept constant at about 2.2 kHz; the PA signal amplitude at the resonance frequency was largest when SP was equal to 5 cm. From this result, we decided that the acoustic pipe should be bent at a right angle with sides of 5 (SP) and 3 cm (MP) in length. The changes in the PA signal amplitude accompanying changes in the length of SP seem to be caused by a very complex interaction such as the relationship between the wavelength (16 cm at room temperature, obtained from eq 13) at a frequency of 2.2 kHz and the sound reflection from the bend of the acoustic pipe. This result gave a structure for a PA cell producing a resonance effect much greater than the PA cell (SP = 8), previously reported.[16] The total length of the acoustic pipe can be changed by adding a threaded pipe 3 cm long (MP) to the acoustic pipe. This is effective for depth-profiling analysis performed by changing the measurement frequency. When the length of MP is changed, the changes in the resonance frequency conform to eq 14. The lower the used frequency, the bigger the amplitudes of both the PA signal and noise. When considering that an S/N of more than 5 was obtained for in vivo skin measurement, resonance frequency adjustment is effective over the range of about 800–5000 Hz. This method could be used very effectively in depth-profiling analysis.

Sensitivity and Reproducibility of a Novel Open-Ended PA Cell Combined with a Light Guide. The sensitivity of the newly developed PA cell was studied by comparing it with the conventional and Helmholtz resonance type PA cell.[16] Black rubber was used as the PA measurement sample. The Ar^+ laser beam (wavelength 488 nm) used as the light source was modulated with the light chopper at 2.2 kHz. The output intensity of the light source was adjusted to 3 mW. The characteristics of the PA signal of the new PA cell based on a specific measurement frequency were compared with those of the Helmholtz resonance PA cell. As shown in Figure 5, two resonance peaks were found at about 2.2 and 4.0 kHz. The intensities of these peaks were about 7 and 26 times, respectively, larger than that for the conventional PA cell. In the new PA cell, the peak intensity of the harmonics generated at about 4.0 kHz is very close to that of the fundamental vibration generated at 2.2 kHz. This suggests that the resonance mechanism of this new PA cell is different from that of Helmholtz resonance and that this resonance is better suited to surface analysis than Helmholtz resonance. In addition, the difference between each resonance curve is based on the different resonance types. The Q value (sharpness of resonance curve) obtained from this PA cell is sharper than that of the conventional PA cell (Helmholtz resonance type). From these results, the sensitivity of the new PA cell is approximately 10 times greater than that of the conventional PA cell.

The detection accuracy of PA measurement of IDM was investigated using a UV laser PA system. IDM ointments of concentrations of 0.2% and 1.0% were applied to quartz plates at thicknesses of 100 mm and were used as samples for determining the PA measurement reproducibility. Excellent sensitivity and reproducibility were obtained over 10 repeated measurements; the S/N was 46 and the coefficient of variation (CV) was not more than 3%. Calibration curves were obtained for PA measurements under the same conditions. The PA signal of the novel open-ended PA cell had excellent linearity, with a correlation coefficient of 0.996 for the IDM range (2–24 μg/5 mm i.d.) applied to the skin at in vivo measurement. In addition, a good linear correlation coefficient of 0.99 was obtained for IDM amounts (2–120 μg/5 mm i.d.) extending the measurement range. The novel open-ended PA cell is effective for in vivo percutaneous absorptiometry using this PA measurement system. When the S/N obtained from IDM ointment on the quartz plate is compared with that of the same sample on in vivo skin, the former is lower than the latter. This is because the gas seal of the PA cell on quartz is worse than on skin because the quartz plate is very hard and inelastic. Hence, although factors such as the skin surface potential or environmental noise decrease the S/N in measurement of in vivo skin, this PA cell is hardly affected. This means that the S/N and accuracy of in vivo skin measurement is better than that of the quartz plate. Consequently, the open-ended PA cell combined with the light guide is extremely useful for in vivo percutaneous absorptiometry.

Measurement of In Vivo Percutaneous Absorption. A series of in vivo percutaneous absorptiometries using the new open-ended PA cell was performed using 1% IDM ointment applied to a hairless mouse. Measurements were made every 5 min

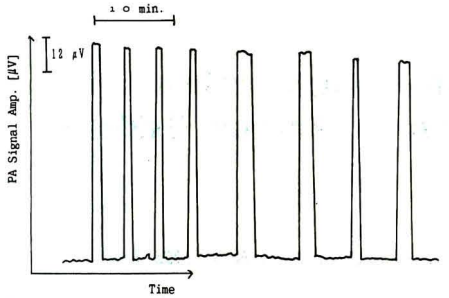

Figure 6. Raw data of the in vivo measurement of percutaneous absorption in the hairless mouse.

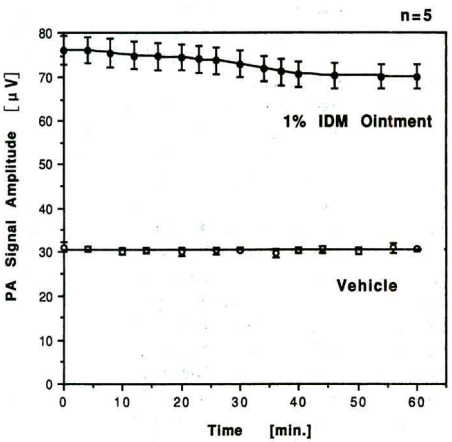

Figure 7. PA signal versus time when measuring hairless mouse in vivo percutaneous absorption.

to avoid accelerated percutaneous absorption as a result of heating by the UV laser beam. The measurement time of 15 s, or half the best measuring time yet, was reduced by the improved S/N. This was very effective in minimizing damage to in vivo skin as much possible. The obtained S/N was about 40 (Figure 6). Figure 7 shows the results of five repeats. When the PA signals obtained by applying only the PEG vehicle were compared with those of the 1% IDM ointment measured under the same conditions, the former was nearly constant with time, while the latter indicated a 5% reduction in the initial PA signal after 60 min. It was confirmed that the reduction of the PA signal is not due to chemical changes in or destruction of the IDM by irradiation. The change in the PA signal is thought to reflect the percutaneous absorption of IDM. We then tried to obtain the diffusion coefficient of IDM across the skin of a hairless mouse in vivo by observing the time constant of the decrease in the PA signal.[11] Since the decrease in the concentration of the IDM was essentially exponential, the time constant was obtained by plotting logarithmic PA signals with time. In addition, from the theory of diffusion of substances across membranes of finite width, it was found that the time constant, τ, of such processes is expressed as

$$\tau = 4L^2/\pi^2 D \quad (15)$$

where L is the width of the membrane and D is the diffusion coefficient of the substance in a given medium. This principle was applied to the results in Figure 6. A time constant of 607 min was obtained with a correlation coefficient of 0.948; the diffusion coefficient was calculated to be 6.7×10^{-6} cm/min for a skin thickness of 0.1 cm. This value is of the same order (3.5×10^{-6} cm^2/min) as that obtained by the conventional in vitro method using the longitudinal diffusion cell.

These results confirmed the effectiveness of this newly developed in vivo percutaneous absorptiometry technique, which is simpler than other methods such as RI. Additionally, this UV laser PA method using a novel open-ended cell may be applicable to in vivo human percutaneous absorptiometry, because we know from experience that the S/N of in vivo human skin is about 5 times better than that of in vivo animal skin. Humans can consciously control their skin pulsation but animals cannot, so a PA signal with a larger S/N is required for animals. The better performance of the developed PA system is clearly demonstrated by the results of PA measurement for a hairless mouse in vivo.

CONCLUSIONS

A novel in vivo percutaneous absorptiometry system using an open-ended PA cell combined with a light guide was developed. The sensitivity of this system was nearly 1 order of magnitude better than that of the conventional open-ended PA cell.[16]

A 1% IDM ointment was applied to hairless mice, and the in vivo percutaneous absorption was measured. A reasonable diffusion coefficient was obtained from the PA signal related to percutaneous absorption of IDM. This result confirmed the feasibility of in vivo percutaneous absorptiometry using this PA method.

Application to in vivo human skin must be safe, the total UV energy received at the skin was less than 40 mJ, and no ill effects were observed on the skin of hairless mice. Applying this energy to human skin in vivo seems to be safe but final confirmation is required. Experiments to confirm safety for human skin are under way.

This newly developed open-ended PA cell has other advantages. Depthwise analysis is possible by changing the length of the acoustic pipe. In addition, the open-ended PA cell can be used as a closed cell by mounting a sample holder made of quartz on the end of the light guide (the sample chamber of the open-ended cell). Consequently, this PA system will be easier to use with higher sensitivity and greater accuracy.

Received for review July 21, 1993. Accepted April 20, 1994.*

* Abstract published in *Advance ACS Abstracts,* June 1, 1994.

Anal. Chem. **1994,** *66,* 2272–2278

Laser-Induced Photofragmentation/Photoionization Spectrometry: A Method for Detecting Ambient Oxides of Nitrogen

J. B. Simeonsson,[†,‡] G. W. Lemire,[†,§] and R. C. Sausa*

U.S. Army Research Laboratory, AMSRL-WT-PC, Aberdeen Proving Ground, Maryland 21005-5066

Laser-induced photofragmentation/photoionization (PF/PI) spectrometry has been used to detect trace ambient concentrations of NO, NO_2, HNO_3, and CH_3NO_2. The method uses a single laser operating near 226 nm to both fragment the parent molecule and photoionize the resultant NO fragment by a (1 + 1) resonance-enhanced multiphoton ionization (REMPI) process via its $A^2\Sigma^+ \leftarrow X^2\Pi$ (0,0) band. Ion detection is accomplished by using a pair of miniature electrodes. Use of a single laser and optogalvanic ion detection greatly simplifies the instrumental requirements of the method and allows for real time, in situ monitoring of the above-mentioned compound under ambient conditions. Analytical merits of the technique have been evaluated as a function of the sampling pressure and detection electrode voltage. Limits of detection (LODs) determined for NO, NO_2, HNO_3, and CH_3NO_2 are 1, 22, 5, and 220 ppbv, respectively, using 10 μJ of pulse energy and an integration time of 10 s. Results of the study indicate that PF/PI spectrometry enables a simple instrument design to be used for sensitive measurements of these compounds. The high sensitivity is a reflection of the high efficiency of each of the photofragmentation and photoionization processes employed. The ability to use low fluences has the added benefit of suppressing nonresonant multiphoton ionization background signals. Sensitivities demonstrated for species in this study suggest that the technique has excellent potential for measurements of NO_x (NO + NO_2) and NO_y, the concentration of total reactive odd nitrogen compounds.

The development of real-time, laser-based sensitive monitors of pollutants in the atmosphere (e.g., automobile exhaust, waste products of incineration) has been of great interest in recent years. (See refs 1–7 and references cited therein for a partial list of representative studies.) Of importance is the detection and monitoring of atmospheric nitrogen oxide compounds because of their key roles in atmospheric reaction cycles, such as the production of acid rain and photochemical smog, and the regulation of species such as OH and ozone in the atmosphere.[8–10] Precise measurements of NO_x (NO, NO_2) and NO_y, the sum concentration of NO, NO_2, HNO_3, HNO_2, NO_3, N_2O_5, HO_2NO_2, organic nitrates (e.g., PAN, PPN) and other nitrocompounds, are crucial if a comprehensive understanding of the processes that determine the tropospheric levels of these compounds is to be achieved.

Presently, the measurement of NO, NO_2, and other nitrogen oxide compounds at background and polluted levels (pptv to ppbv) remains an important analytical challenge.[11,12] For NO, the most common method of detection is by chemiluminescent reaction (CL) with O_3. The reaction produces electronically excited NO_2* whose emission intensity is proportional to the initial concentration of NO. Other measurement methods include long path absorption and differential absorption LIDAR (DIAL).[13] For NO_2, the EPA standard method for measurement is also by CL with ozone; however, prior to measurement, NO_2 must be quantitatively converted to NO by catalytic or photolytic means.[11] An alternate method is based on a different chemiluminescence reaction in which NO_2 reacts directly with a luminol solution (CL-luminol) at a wetted surface.[11] Other methods include tunable diode laser absorption spectrometry (TDLAS),[14] differential optical absorption spectrometry (DOAS),[15] optoacoustic spectrometry,[16] denuder methods, and wet chemical methods. Methods for detecting HNO_3 are generally limited to filtration techniques employing wet chemical and chromatographic detection of the filtrate,[11,17] denuder techniques, and optical absorption spectrometries. The sensitivity of the above-mentioned methods for detecting nitrogen oxide compounds in the atmosphere usually requires that the signal be integrated over time or distance, resulting in a loss of temporal or spatial resolution. Furthermore, the selectivity of these methods is often insufficient to prevent interference effects for low-level determinations.

Laser photoionization (LPI) spectroscopy was proposed as a method for detecting atmospheric pollutants as early as

† NRC/ARL Postdoctoral Research Associate.

‡ Present address: Department of Chemistry, University of Iowa, Iowa City, IA 52242.

§ Present address: U.S. Army Dugway Proving Ground, Joint Contact Point Directorate, Dugway, UT 84022-5000.

(1) Lemire, G. W.; Simeonsson, J. B.; Sausa, R. C. *Anal. Chem.* **1993,** *65,* 529.
(2) Simeonsson, J. B.; Lemire, G. W.; Sausa, R. C. *Appl. Spectrosc.* **1993,** *47,* 1907.
(3) Cool, T. A.; Williams, B. A. *J. Combust. Sci. Technol.* **1992,** *82,* 67.
(4) Halpern, J. B.; Jackson, W. M.; McCrary, V. *Appl. Opt.* **1979,** *18* (5), 590.
(5) Jeffries, J. B.; Raiche, G. A.; Jusinski, L. E. *Appl. Phys. B* **1992,** *55,* 76.
(6) Zhu, J.; Lustig, D.; Sofer, I.; Lubman, D. M. *Anal. Chem.* **1990,** *62,* 2225.
(7) Syage, J.; Pollard, J. E.; Cohen, R. B. *Appl. Opt.* **1987,** *26* (17), 3516.
(8) Singh, H. B. *Environ. Sci. Technol.* **1987,** *21* (4), 320.
(9) Logan, J. A. *J. Geophys. Res.* **1983,** *88* (C15), 10785.
(10) Seinfeld, J. H. *Atmospheric Chemistry and Physics of Air Pollution*; Wiley and Sons: New York, 1986; pp 3–22, 157–164.
(11) Sickles, J. E. In *Gaseous Pollutants*; Nriagu, N. O., Ed.; Wiley and Sons: New York, 1992; pp 51–128.
(12) *Assessment of Techniques for Measuring Tropospheric N_xO_y*; NASA Conference Publication No. 2292; NASA: 1983.
(13) Edner, H.; Sunesson, A.; Svanberg, S. *Opt. Lett.* **1988,** *13* (9), 704.
(14) Schiff, H. I.; Hastie, D. R.; Mackay, G. I.; Iguchi, T.; Ridley, B. A. *Environ. Sci. Technol.* **1983,** *17* (8), 352A.
(15) Plane, J. M. C.; Nien, C.-F. *Rev. Sci. Instrum.* **1992,** *63* (3), 1867.
(16) Fried, A. *Appl. Spectrosc.* **1982,** *36,* 562–565.
(17) LeBel, P. J.; Huebert, B. J.; Schiff, H. I.; Vay, S. A.; VanBramer, S. E.; Hastie, D. R. *J. Geophys. Res.* **1990,** *95* (D7), 10199.

This article not subject to U.S. Copyright. Published 1994 by the American Chemical Society

1979. Briefly, the results of selected representative studies are as follows. Brophy and Rettner first demonstrated the feasibility of the approach by using two-photon ionization to detect trace levels (ppmv) of aniline in air.[18] High sensitivity was also demonstrated by Frueholz et al., who used two-photon ionization to detect naphthalene vapor at densities less than $10^7/cm^3$.[19] Cool and Williams have recently demonstrated the detection of chlorinated ethylenes using resonance-enhanced multiphoton ionization (REMPI) with time-of-flight mass spectrometry (TOFMS).[20,21] Using this technique, they detected C_2Cl_4 at the 240 ppb level in a mixture prepared from automobile exhaust and a set of chlorinated hydrocarbons chosen as potential interferences. Recent studies by Lubman and co-workers[6] reveal that a resonance two-photon ionization (R2PI) at 266 nm can be used to detect trace levels (ppb) of substituted nitrobenzenes at atmospheric pressures by soft ionization with a minimum amount of fragmentation.

REMPI with TOFMS has also been employed by Syage and co-workers for the sensitive detection of atmospheric constituents.[7] The studies were conducted using air expansions for a variety of organophosphonates and organosulfides. Detection limits as low as 300 ppt were reported for dimethyl sulfide using (2 + 1) REMPI near 391 nm corresponding to a resonance enhancement through the vibrationless level of the 3p Rydberg state at 195.31 nm. More recent studies in our laboratory have shown that molecular beam sampling with TOF spectrometry can be used to detect NO (8 ppb) at atmospheric pressures by (1 + 1) REMPI via its $A^2\Sigma^+ \leftarrow X^2\Pi$ (0,0) band near 226 nm.[1] The above-mentioned examples reveal that the sensitivity of LPI is high and that it can be employed for detecting trace pollutants in various environments. However, a potential problem of LPI is that moderate to high laser intensities are required for the method to be analytically useful. This can result in the generation of intolerable background signals due to nonresonant ionization processes.

An alternate method to LPI for monitoring trace atmospheric constituents is laser photofragmentation with subsequent fragment detection. This method is particularly useful for fragile molecules such as NO_2 and HNO_3, which easily dissociate upon the absorption of UV–visible radiation or for molecules that lack absorption features in the UV–visible. Recently, a laser photofragmentation-fluorescence (LPFF) technique has been used to determine atmospheric levels of HNO_3 in situ.[22,23] An ArF laser served as the excitation/photolysis source while emission of the excited $OH(A^2\Sigma^+)$ fragment was monitored near 308 nm. By simultaneously measuring the HNO_3 with LPFF and conventional filter methods, an intercomparison of the two approaches demonstrated that LPFF provides good agreement with the filter methods. It has nearly the same sensitivity, yet allows significantly faster response times (nominal 75% reduction in integration times). Sandholm and co-workers have reported on a photofragmentation/laser-induced fluorescence (PF/LIF) technique using a two-color excitation scheme for the detection of NO_2[24] and NO.[24,25] The measurement of NO_2 was accomplished by the photofragmentation of NO_2 at 355 nm via a XeF excimer laser, and the resultant NO fragment was then quantitatively detected using two-photon LIF via the $A^2\Sigma^+ \leftarrow X^2\Pi$ (0,0) and $D^2\Sigma^+ \leftarrow A^2\Sigma^+$ (0,0) bands near 226 nm and 1.1 μm, respectively. The fluorescence signal resulting from $D^2\Sigma^+ \rightarrow X^2\Pi$ transitions was monitored in the 187–220 nm region. Limits of detection (S/N = 2) of 10 pptv for NO_2 (6 min of integration time) and 3.5 pptv for NO (2 min of integration time) were reported.

Recent studies in our laboratory have shown that an approach which combines laser-induced photofragmentation with LPI, photofragmentation/photoionization (PF/PI), can be used to detect NO and nitro-containing vapors with both high sensitivity and selectivity.[1,2] In one study, a single laser was employed to both fragment the parent molecule and photoionize the resultant characteristic NO fragment by a (1 + 1) REMPI process via its $A^2\Sigma^+ \leftarrow X^2\Pi$ (0,0) band near 226 nm.[1] The technique employed molecular beam sampling with time-of-flight mass spectrometric detection of the ions. At 226 nm, NO^+ ions were generated from a variety of nitro compounds and were produced almost to the exclusion of any other ions such that the use of mass spectrometric detection was virtually unnecessary. By virtue of the selectivity and efficiency of the PF/PI mechanism employed, it was possible to achieve high sensitivities with relatively low laser pulse energies (<100 μJ). For this reason, it was believed that the photofragmentation approach could be extended and applied equally to detecting trace levels of NO_x and NO_y at atmospheric pressures with nonselective ion detection. More recently, we have reported results of studies employing a PF/PI approach with nonselective ion detection for measuring ambient NO, NO_2, and HNO_3 under atmospheric conditions.[26] Similar studies of NO/NO_2 have been performed by Ledingham and co-workers.[27]

In this paper, we report further studies of a PF/PI spectrometry technique used to measure trace levels of NO, NO_2, HNO_3, and CH_3NO_2 under ambient conditions. Measurements are performed at pressures ranging from 5 to 760 Torr with total (integrated) optogalvanic ion detection. The technique employs one laser to both photofragment the precursor molecule and ionize the characteristic NO fragment by a (1 + 1) REMPI process via its $A^2\Sigma^+ \leftarrow X^2\Pi$ (0,0) transition near 226 nm. Due to the high efficiency of photofragmentation and photoionization processes at 226 nm, only 10 μJ of pulse energies are required to achieve high sensitivity measurements for the compound studied. The use of total ion detection and a single laser in the PF/PI approach minimizes the complexity of the instrumentation and makes the current approach a feasible alternative to conventional methods. Evaluations of the sensitivity, selectivity, and signal-to-noise characteristics have been performed. Results of this

(18) Brophy, J. H.; Rettner, C. T. *Opt. Lett.* **1979**, *4* (10), 337.
(19) Frueholz, R.; Wessel, J.; Wheatley, E. *Anal. Chem.* **1980**, *52*, 281.
(20) Cool, T. A.; Williams, B. A. *Hazard. Waste Hazard. Mater.* **1990**, *7*, 21.
(21) Williams, B. A.; Cool, T. A.; Rohlfing, C. M. *J. Chem. Phys.* **1990**, *93*, 1521.
(22) Papenbrock, Th.; Stuhl, F. *J. Atmos. Chem.* **1990**, *10*, 451.
(23) Papenbrock, Th.; Stuhl, F.; Müller, K. P.; Rudolph, J. *J. Atmos. Chem.* **1992**, *15*, 369.
(24) Sandholm, S. T.; Bradshaw, J. D.; Dorris, K. S.; Rodgers, M. O.; Davis, D. D. *J. Geophys. Res.* **1990**, *95*, 10155.
(25) Bradshaw, J. D.; Rodgers, M. O.; Sandholm, S. T.; KeSheng, S.; Davis, D. D. *J. Geophys. Res.* **1985**, *90*, 12861.
(26) Simeonsson, J. B.; Lemire, G. W.; Sausa, R. C. *Proceedings of the 1993 SPIE/Air and Waste Management Association International Symposium on Optical Sensing for Environmental Monitoring*; SPIE: Bellingham, WA, 1994; in press.
(27) Clark, A.; Deas, R. M.; Kosmidis, C.; Ledingham, K. W. D.; Marshall, A.; Sander, J.; Singhal, R. P. *Proceedings of Sensors 2: Technology, Systems, and Applications*; 1993; in press.

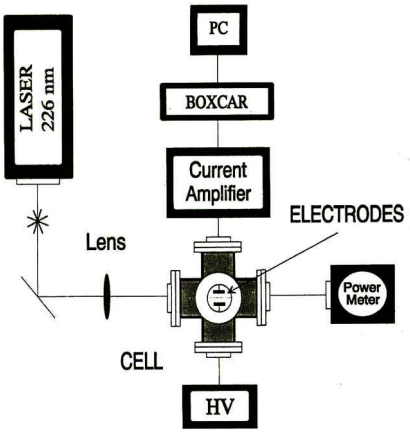

Figure 1. Diagram of experimental apparatus.

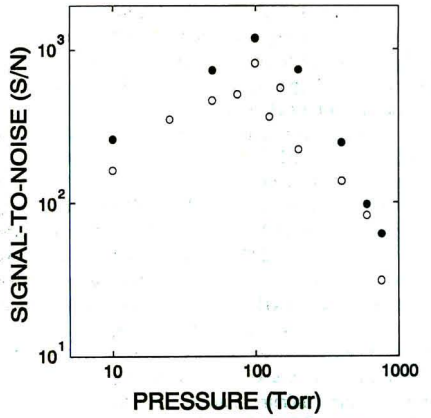

Figure 2. Plot of the signal-to-noise ratio (SNR) as a function of the measurement cell pressure for NO (filled circles) and NO_2 (open circles). Experimental conditions given in text.

study are compared to those reported previously using similar photofragmentation LIF techniques.

EXPERIMENTAL SECTION

Figure 1 is a diagram of the experimental apparatus used to perform the PF/PI studies. An excimer-pumped dye laser system with frequency doubling (Lumonics, HYPER EX-400, HYPER DYE-300, and HYPER TRAK-1000) was used to provide tunable UV radiation in the region of 224–228 nm (coumarin 450). The line width for wavelengths obtained by frequency doubling is approximately 0.11 cm^{-1} (fwhm). The pulse energies were nominally 10–100 μJ and were monitored between measurements using a Joulemeter (Molectron Detector Inc., J4-05). The laser was operated at 10 Hz, and the output was directed using prisms to the photolysis/ionization sampling cell. Focusing of the laser was accomplished using a 250-mm lens (suprasil) external to the cell.

The photolysis cell consisted of a six-arm stainless steel cross with arm diameters of 4 cm. Quartz windows mounted on the cell provided optical access to the center of the cell where two planar electrodes served as ion/electron detectors. The electrodes were laboratory constructed from stainless steel square sheets, each approximately 1.5 cm^2 in area, and were separated by 0.63 cm. Collection voltages ranged from 0 to 800 V. The laser beam passed between the electrodes and was focused in the center of the electrode length to optimize ion/electron collection. The beam waist in the focal region is estimated to be 90 μm in diameter resulting in a maximum fluence of 10^8 W/cm^2. An estimation of the effective volume probed by the laser is approximately 10^{-5} cm^3 (equal to 2-mm path length and 6×10^{-5} cm^2 focal area).

NO and NO_2 samples were prepared by serial dilution of NO or NO_2 in air or N_2 (Matheson, >99.999%). Nitromethane (Mallinckrodt, spectroscopic grade) and nitric acid, 70 wt % aqueous solution (Fisher, ASC grade), were sampled at their room temperature vapor pressures as trace species in buffer gases (air, N_2). HNO_3 comprises approximately 42% of the total vapor pressure above such a solution.[28] Samples were flowed through the photolysis cell to prevent accumulation of photolysis products. Sample flows were nominally 500 cm^3/min. The photolysis cell volume was estimated to be 350 cm^3.

Signals from the detection electrodes were amplified using a current amplifier (Keithley 427, gain 10^5–10^7 V/A, time constant 0.01 ms) and then sampled by a boxcar averager with a gate of 15 μs. The amplifier was connected as close as possible to the collection electrode output to minimize radio frequency pickup along the signal cable. The signals were viewed in real time on a 125-MHz digital oscilloscope (LeCroy 9400). The boxcar output was acquired by a personal computer for storage and subsequent data analysis. Signals were integrated for 10 s at 10 Hz with 100 shot averaging. The background noise was evaluated off resonance at 224.17 nm and was taken to be the standard deviation (σ) of 16 independent measurements. The minimum noise measured was 150 μV (referred to the boxcar input), which corresponds to 15 pA or approximately 1400 electrons/pulse for a 15-μs gate width and a 10^7 gain on the current-to-voltage amplifier. The limiting noise in this study is due to fluctuations in the nonresonant ionization background present in all the measurements.

RESULTS AND DISCUSSION

To optimize the experimental conditions and to assess the analytical utility of the PF/PI technique, parametric studies of the signal-to-noise ratio (SNR) were performed. The measurement of cell pressure is an important experimental parameter that was studied for the following reasons: (1) the collisional dynamics affect the photofragmentation efficiency yielding ground-state NO, (2) collisional ionization processes may determine both the production of electrons and NO ions, and (3) collisional broadening of the spectral features degrades the spectral resolution. Spectral resolution is improved at lower pressures, but only at the cost of a corresponding reduction in sample density.

Shown in Figure 2 is a plot of the SNR for NO and NO_2 (both approximately 6 ppmv) as a function of the cell pressure.

(28) *Chemical Engineers' Handbook*, 5th ed.; McGraw-Hill: New York, 1973.

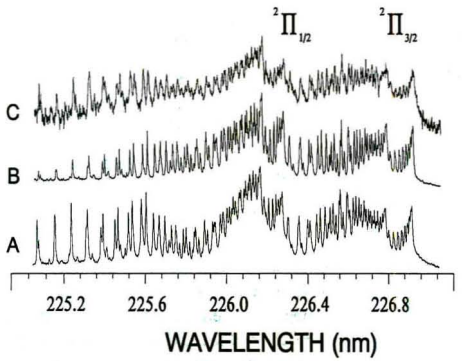

Figure 3. Ionization spectrum of 6 ppmv of NO at 100 Torr (A). Ionization spectra of NO produced by the 226-nm photolysis of 6 ppm of NO_2 at 100 (B) and 760 Torr (C).

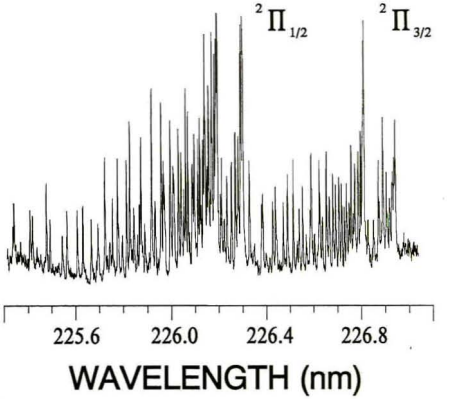

Figure 4. Ionization spectrum of NO generated by the photolysis of trace HNO_3 at 100 Torr.

It is important to note that the sample density changes with respect to the pressure; thus, the plot represents the SNR for a fixed mixing ratio of gases (initially at 1 atm) over the pressure range indicated. Experimental conditions for these measurements were laser pulse energies of 10 μJ at 226 nm and a collection electrode voltage of 150 V. The plot shows that the optimum pressure is approximately 100 Torr for both NO and NO_2. It appears that, at this pressure, the favorable effects of reduced collisions and a lower background signal are balanced by dilution of the sample and loss of signal with further decreases in the pressure.

Figure 3 shows the ionization spectra for NO at 100 Torr and for NO_2 at 100 and 760 Torr, respectively. The concentrations of NO and NO_2 are approximately 6 ppmv, and the collection electrode voltage is 150 V. A comparison of the ionization spectra for NO and NO_2 at 100 Torr shows that the spectral features are very similar and, in fact, correspond directly to the $A^2\Sigma^+ \leftarrow X^2\Pi$ (0,0) band of NO. The two bandheads displayed in the spectra arise from the $^2\Pi_{1/2}$ and $^2\Pi_{3/2}$ spin-orbit components of the NO ground electronic state. The NO_2 spectrum demonstrates the utility of the PF/PI approach for detecting NO_2 by monitoring the ionization of the NO photofragment. It is observed that the spectral resolution at 100 Torr is sufficient to differentiate individual rotational lines in the spectra. Ionization spectra for other nitro compounds such as nitromethane and HNO_3 exhibit nearly identical spectral features in the region of 225–227.25 nm, as illustrated in Figure 4 which shows the spectrum for HNO_3.

The analytical selectivity of the present technique is solely reliant on the spectral selectivity of the laser, as ion detection in the approach is nonselective. Therefore, it is crucial that the technique possess sufficient spectral resolution such that characteristic spectral features of the NO fragment can be identified unequivocally. As shown in Figures 3 and 4, the vast majority of the rotational features are resolved to the baseline, confirming their identification. An ionization spectrum of air over the same region shows minimal background ionization above the noise. The ionization spectra collectively demonstrate both the spectral selectivity and the feasibility of the PF/PI approach for ambient measurements.

The selectivity is demonstrated by (1) the high spectral resolution available in the $A^2\Sigma^+ \leftarrow X^2\Pi$ (0,0) band at 100 Torr and (2) the high efficiency of the PF/PI approach at only modest pulse energies (10 μJ), which minimizes nonresonant multiphoton ionization interferences. Nonspecific ionization interferences resulting from broad absorptions are possible, but are unlikely for atmospheric constituents at these wavelengths. Moreover, if they exist, they will not exhibit the rotational structure observed for NO. Most ionization interferences can thus be accounted for simply by scanning the laser wavelength and by measuring the signal on and off resonance.

Another study was performed to determine the relationship of the SNR to the collection electrode voltage. At a given pressure, the measured noise was little affected by changes in the voltage, and the SNR was primarily determined by the signal magnitude. The SNR as a function of the electrode voltage (0–800 V) was measured for NO at 5, 100, and 760 Torr and for NO_2 at 100 Torr using laser pulse energies of 10 μJ near 226 nm. At low voltages (0–250 V), the SNR increases linearly to a maximum value at 400 V, beyond which no improvement is realized. The plateau is indicative of saturation in the charge collection. Although the trend is the same at 5 Torr, it was not possible to raise the electrode voltage above 270 V due to instabilities and potential breakdown between the electrodes. It is noted that optimum conditions (i.e., voltage, pressure) determined in this study depend on experimental parameters characteristic of the instrumentation and conditions utilized. Due to the multiphoton nature of the PF/PI approach, it is anticipated that changes in the experimental parameters (e.g., laser pulse energy, laser focusing characteristics, or electrode spacing) could result in different optimum conditions.

Once the optimum conditions were established, analytical sensitivities were determined for NO, NO_2, HNO_3, and CH_3-NO_2. Conditions for these determinations were 10 μJ of laser pulse energy at 226.29 nm (P_{11} branch, $J'' = 9.5$–11.5), 100 Torr total pressure, and 400 V on the detection electrodes. Limits of detection (LODs), reported as the concentration equivalent to 3σ, are given in Table 1 for the above-mentioned

Table 1. Limits of Detection (in ppbv) and Absolute Number of Molecules Detected for Signal-to-Noise Ratio of 3

	PF/PI[a]	MB/PF/PI[b]	PF/LIF
NO	1 (3.3×10^4)	8 (2000)	0.05[c]/0.005[d] (6.9×10^9/1×10^8)
NO_2	22 (7.3×10^5)	240 (6×10^4)	0.015[e] (3.1×10^8)
HNO_3	5 (1.2×10^5)		0.03[f] (7.5×10^8)
CH_3NO_2	220 (7.3×10^6)	1000 (2.5×10^5)	2.0[g,h] (1.6×10^8)

[a] This work; assuming $V = 10^{-5}$ cm^3. [b] Ref 1; assume $V = 5 \times 10^{-5}$ cm^3. [c] Ref 29; $V = 0.18$ cm^3. [d] Ref 25; $V = 1.2$ cm^3. [e] Ref 24; $V = 1.2$ cm^3. [f] Ref 23; $V = 0.45$ cm^3. [g] Ref 30; $V = 0.0375$ cm^3. [h] Not sampled from atmosphere; equivalent mixing ratio assuming measurement at 100 Torr, final density of 4.2×10^9/cm^3 and s/n = 3.

compounds. In addition to the current PF/PI results, LODs are given for the same compounds using the PF/PI technique with molecular beam sampling and TOFMS ion detection (MB/PF/PI) from ref 1 and for a variety of PF/LIF techniques. Also shown in Table 1 are values (given in parentheses) corresponding to the number of analyte molecules estimated to be in the laser probe volume at the LOD. Comparison of concentration LODs as well as absolute numbers of molecules detected gives an indication of the detection capability of the PF/PI technique relative to the PF/LIF techniques. Using 10^{-5} cm^3 as an estimate of the probe volume, a LOD of 1 ppbv for NO corresponds to 3×10^9 molecules/cm^3 or 30 000 NO molecules probed by the laser per pulse. Assuming 100% ionization and detection efficiency of the probed molecules, a detection limit of 1 ppbv is within 1 order of magnitude of the detection limit determined by the noise (15 pA equal to 1400 electrons/pulse). This estimate of the absolute number of molecules detected is also within an order of magnitude of the minimum detectable concentration predicted using expressions given by Winefordner and Rutledge.[29] The linear dynamic range (LDR) of the technique extends from the LOD up to 10 ppmv for NO.

A comparison of the PF/PI results in Table 1 with MB/PF/PI indicates a nearly 1 order of magnitude increase in sensitivity. Although the sample density is much higher in the PF/PI measurement cell than in the molecular beam, collisional effects reduce the efficiency of signal production. Consequently, only a moderate increase in overall sensitivity is realized. The PF/PI apparatus does represent a considerable improvement over the molecular beam system, however, in terms of instrumental complexity and expense.

Shown in the last column of Table 1 are LODs for PF/LIF measurements of NO, NO_2, HNO_3, and CH_3NO_2. The PF/LIF measurements of NO and NO_2 both employ laser excitation of the $A^2\Sigma^+ \leftarrow X^2\Pi$ transition of NO at 226 nm as the first excitation step,[24,25,30] the same as is employed in the present studies. The HNO_3 measurements were performed using an ArF laser as the excitation/photolysis source.[22,23] Emission of the photolysis product OH is observed near 308 nm corresponding to the $A^2\Sigma^+ \rightarrow X^2\Pi_i$ transition and is used to quantitate HNO_3. Measurements of CH_3NO_2 were also performed using an ArF excimer laser as the excitation source with CH photofragment emission ($A^2\Delta \rightarrow X^2\Pi$) observed at 431 nm.[31] As seen in Table 1, the LODs for the various PF/LIF techniques are well into the parts per trillion by volume for NO, NO_2, and HNO_3 while the PF/PI results are in the low parts per billion by volume. The higher sensitivities for PF/LIF are probably a consequence of longer integration times, which range from minutes for NO and NO_2 to 1 h for HNO_3. Longer integration periods enhance the ultimate sensitivity of the PF/LIF method, although the relationship of the enhancement to the integration period cannot be accounted for directly. The integration time for each of the PF/PI results in the present work is 10 s.

NO and NO_2. Two different LODs are shown in Table 1 for the PF/LIF detection of NO. The first LOD corresponds to one-color excited fluorescence of NO,[30] while the second corresponds to two-color excited fluorescence (first at 226 nm followed by 1.1 μm).[24,25] Two-color excitation followed by emission detection at 187 nm results in at least an order of magnitude improvement relative to the one-color result. Both results are reported here for completeness; however, it is most appropriate in this study to compare the one-color PF/LIF to the PF/PI as the PF/PI only employs one-color excitation. A direct comparison of the two results indicates that the sensitivities are nearly within an order of magnitude despite a considerable difference in integration periods. For similar integration times, the sensitivities are likely to be more similar.

Due to the similarity of the approaches, it is worthwhile to compare the relative merits of PF/LIF and PF/PI for NO and NO_2. Both methods are capable of high sensitivity (ppbv to sub-ppbv) and both have high spectral selectivity, although the selectivity of the PF/LIF approach is somewhat higher as the detection step provides an additional degree of selectivity. Since the PF/PI technique employs total ion detection, analyte selectivity is determined solely by the laser excitation/ionization processes.

As presented in this study, the PF/PI technique is easier to implement than comparable PF/LIF techniques as it only requires a single laser for simultaneous measurement of NO, NO_2, and other nitro compounds. By comparison, the PF/LIF techniques of refs 24 and 25 require two and three lasers for measurements of NO and NO_2, respectively. Furthermore, the arrangement of the PF/PI laser beam and detection apparatus (i.e., focusing the laser between two electrodes) is considerably less complex than the alignment of two spatially and temporally coincidental laser beams in the viewing region of multiple photomultiplier tubes, as is required for PF/LIF. In short, instrumental cost and simplicity are important advantages of the current PF/PI technique.

An important fundamental distinction between PF/LIF and PF/PI methods is the difference in detection efficiencies. First, it is possible in ionization methods to collect practically 100% of the produced charges with each laser pulse (i.e., detection efficiencies approaching 1). This is demonstrated by the measured signals that are consistent with near-unity

(29) Winefordner, J. D.; Rutledge, M. *Appl. Spectrosc.* **1985**, *39*, 377.
(30) Bradshaw, J. D.; Rodgers, M. O.; Davis, D. D. *Appl. Opt.* **1982**, *21* (14), 2493.
(31) Schendel, J.; Hohmann, R.; Wehry, E. L. *Appl. Spectrosc.* **1987**, *41* (4), 640.

collection/detection efficiency using an estimated probe volume of 10^{-5} cm^3. In LIF, the fluorescence photons are emitted isotropically and detection efficiencies are nominally 10^{-4}. The difference in detection efficiencies of the two approaches is clearly evident when comparing the absolute numbers of molecules detected at the LOD (see Table 1). Approximately 10^4 NO molecules are required for the PF/PI technique, whereas 10^8 NO molecules are required for the two-color (PF/LIF) technique, a difference of about 4 orders of magnitude. Normalized to the same concentration, the difference is approximately 6 orders of magnitude. Furthermore, collisional quenching and/or reactions of electronically excited NO with atmospheric gases are more prominent in LIF than ionization methods. The radiative lifetime of NO-($A^2\Sigma^+$), approximately 200 ns, is much longer than the time required for photon absorption of this state leading to ionization, typically picoseconds. Above the ionization threshold, ionization occurs typically in the subpicosecond time scale. For these reasons, it is believed that the PF/PI approach has great analytical potential and could prove to be superior to PF/LIF for rapid measurements of nitrogen oxides at the parts per trillion by volume level.

Presently, the NO and NO_2 PF/LIF techniques possess an important advantage over the PF/PI approach. By employing two-step excitation and fluorescence detection at 187 nm, Bradshaw and co-workers have reportedly achieved signal-limited (SL) measurement conditions in their determinations of NO and NO_2 for measurement times of up to 5 min.[24,25] In essence, SL operation means that there are so few (or no) background counts over the measurement period such that the sensitivity is limited by the photon statistics of signal counts. This is an attribute which enhances the ultimate sensitivity of the method, since under SL conditions the LOD improves linearly with the integration period. Under more typical shot noise-limited conditions, the LOD improves with only the square root of the integration period. The present PF/PI technique is not signal limited due to detectable background ionization signals. A more careful study of the limiting noises is required to determine whether SL conditions are achievable by the PF/PI method.

HNO_3. Using PF/PI, the LOD for HNO_3 is 5 ppbv. This compares favorably with those of NO and NO_2 at 1 and 22 ppbv, respectively. These results indicate that the 226 nm photolysis of HNO_3 yielding ground-state NO is more efficient than that of NO_2. The excitation of NO_2 at 226 nm corresponding to the $\tilde{B}(^2B_2) \leftarrow \tilde{X}(^2A_1)$ transition results in predissociation into NO($X^2\Pi$) and O(^{1}D) (see ref 1 and references cited therein). For HNO_3, the UV photolysis is generally understood to occur by way of the following reaction

$$HNO_3 \xrightarrow{h\nu} NO_2 + OH \qquad (1)$$

with a quantum efficiency approaching unity in the wavelength range of 200–315 nm.[32] Subsequent photodissociation of ground-state NO_2 at 226 nm would then yield NO($X^2\Pi$). However, this two-step mechanism is not consistent with our results, which show that the sensitivity for HNO_3 is significantly higher than that for NO_2. If this mechanism was responsible for the production of NO, then the sensitivity of HNO_3 would be at best equal to or less than that for NO_2.

In a recent study on the 248-nm photolysis of HNO_3 in a flow tube using flash kinetic spectroscopy, Schiffman and co-workers[33] concluded that other photodissociative pathways are energetically possible for wavelengths less than 250 nm in addition to reaction 1. These pathways are represented by the following reactions:

$$HNO_3 \xrightarrow[<239\ nm]{h\nu} NO(X^2\Pi) + OH(X^2\Pi) + O(^3P) \qquad (2)$$

$$HNO_3 \xrightarrow[<245\ nm]{h\nu} HONO + O(^1D) \qquad (3)$$

The HONO intermediate has absorption features in the range of 185–270 nm and can further fragment to yield NO and OH. Kenner and co-workers have invoked reaction 3 to explain the production of NO($X^2\Pi$) and OH($A^2\Sigma^+$) from the 193-nm photolysis of HNO_3 by way of the HONO intermediate.[34] Energetically, reaction 2 and the two-photon mechanism proposed by Kenner et al. are accessible with 226-nm radiation via the 260-nm band of HNO_3[35] assigned as a n–π^* transition localized on the nitro group.[36] This suggests that the high sensitivity of the PF/PI approach may be due to the direct formation of NO via reaction 2 and/or the production and subsequent photolysis of the HONO intermediate rather than reaction 1 followed by the predissociation of NO_2. These two mechanisms are consistent with our results. However, other mechanisms, particularly those that involve electronically excited species, cannot be ruled out.

NO_y. The concentration of total reactive odd nitrogen, NO_y, is a quantity that is necessary to establish primary contributors to the total atmospheric nitrogen budget of a given region.[37] NO_y measurements are currently performed using a chemiluminescence (CL) instrument as is used to measure NO or NO_2.[11,37] The PF/PI method is an excellent candidate for NO_y determinations as it is highly sensitive to NO and can photolytically generate NO from a variety of NO_y. Furthermore, it is not sensitive to the chemical interferents (i.e., NH_3, HCN, and sulfur and chlorine species) that are problematic when using catalytic converters with CL detection.[11] Unlike CL, zeroing in the PF/PI method is accomplished easily by tuning the laser to a nonresonance wavelength. With refinement of the current technique, it is projected that PF/PI (possibly combined with a photolytic converter) would be capable of detecting NO_y at the parts per trillion by volume level with rapid (s) response times.

N_2O. Nitrous oxide, which is not a constituent of NO_y, is the most abundant nitrogen oxide compound in the troposphere and is an important greenhouse gas. Although it is relatively inert in the troposphere, N_2O is readily photolyzed in the stratosphere and becomes a major source of NO_x.[8] It was

(32) Johnston, H. S.; Chang, S.-G.; Whitten, G. *J. Phys. Chem.* **1974**, *78*, 1.

(33) Schiffman, A.; Nelson, D. D., Jr.; Nesbitt, D. J. *J. Chem. Phys.* **1993**, *98* (9), 6935.

(34) Kenner, R. D.; Rohrer, F.; Papenbrock, Th.; Stuhl, F. *J. Phys. Chem.* **1986**, *90*, 1294.

(35) Johnston, H.; Grahm, R. *J. Phys. Chem.* **1973**, *77*, 62.

(36) Harris, L. E. *J. Chem. Phys.* **1973**, *58*, 5615.

(37) Fahey, D. W.; Hübler, G.; Parrish, D. D.; Williams, E. J.; Norton, R. B.; Ridley, B. A.; Singh, H. B.; Liu, S. C.; Fehsenfeld, F. C. *J. Geophys. Res.* **1986**, *91* (D9), 9781.

therefore of interest whether the PF/PI technique employing 226-nm radiation is sensitive to N_2O, as this would present a major chemical interference for trace detection of NO_x and NO_y. While nitrous oxide absorbs at 226 nm, absorption in this region primarily results in the products $N_2 + O$,[38,39] with much lesser production of NO + N. Attempts in this study to detect NO^+ ions from even highly concentrated samples of N_2O in air were unsuccessful using the PF/PI approach, indicating that N_2O will not be an interference at typical tropospheric levels.

CONCLUSIONS

The analytical utility of the PF/PI technique has been demonstrated for trace level determinations of NO, NO_2, HNO_3, and nitromethane in air. The technique employs direct atmospheric sampling and total ion detection in a simple cell. By using a single laser operating at 226 nm, successive photofragmentations and a (1 + 1) photoionization process can be performed with only 10 μJ of laser pulse energy due to the highly favorable nature of the individual processes at this wavelength. Limits of detection in the low parts per billion by volume range have been achieved for all four compounds with instrumental response times of 10 s, making the PF/PI method competitive with standard methods of NO/NO_2 detection (i.e., CL methods). It is anticipated that sub parts per billion by volume sensitivities can readily be attained with refinements of the current apparatus. The PF/PI technique is ideally suited to determinations of NO_x. It is also projected that the technique can be adapted for rapid and sensitive determinations of NO_y. With steady improvements in the size, cost, and performance of tunable lasers (especially solid state), the PF/PI approach is certain to become an attractive alternative to CL and other standard methods presently used for measurements of nitrogen oxides.

ACKNOWLEDGMENT

This work was supported by the ARL Independent Laboratory Innovative Research Program. Purchase of equipment through the Productivity Capital Investment Program (R.C.S.) and support from the NRC Postdoctoral Research Program (J.B.S. and G.W.L.) are gratefully acknowledged.

Received for review January 10, 1994. Accepted March 28, 1994.*

* Abstract published in *Advance ACS Abstracts*, May 15, 1994.

(38) Herzberg, G. *Molecular Spectra and Molecular Structure III. Electronic Spectra and Electronic Structure of Polyatomic Molecules*; Van Nostrand Reinhold Co.: New York, 1966; pp 505–507, 595–596.

(39) Sponer, H.; Bonner, L. G. *J. Chem. Phys.* **1940**, *8*, 33.

Anal. Chem. **1994,** *66,* 2279–2284

Particle- and Vapor-Phase Contributions to Metallic Impurities in Electronic-Grade Chlorine

Tracey Jacksier,* Richard Udischas, and Hwa-Chi Wang
Air Liquide, Chicago Research Center, Countryside, Illinois 60525

Ramon M. Barnes
Department of Chemistry, Lederle Graduate Research Center, University of Massachusetts, Box 34510, Amherst, Massachusetts 01003-4510

Techniques are described to quantify both the particulate and vapor phase impurities in electronic-grade chlorine. A particle counter was used in tandem with the sealed inductively coupled plasma system to establish particle size, particle concentration, and elemental composition of impurities present in a chlorine gas stream. The total particle volume (deduced from particle counts) and the total impurity emission were correlated. Al, C, Ca, and Sn were present in both particle and vapor phases, while Ti was present solely as particles. More than 65% of elemental impurities occur as particles with 35% as volatile impurities. Carbon accounts for 80% of these volatile impurities (or 21% of the total impurity content).

Electronic specialty gases (ESGs), such as chlorine, play a significant role in the production of integrated circuits of very large scale integration (VLSI), particularly for chemical vapor deposition (CVD) and reactive ion etching (RIE). The purity of ESGs influences the yield and reliability of devices produced. For example, the electrical performance of semiconductor films can be affected by metallic contamination on the wafers during processing.[1] Despite the importance of metal contaminants, their determination in corrosive gases is limited by the analysis techniques. Trapping particles from gases with microfilters and subsequent analysis of the trapped particles[2] and hydrolysis methods[3] are the primary analysis approaches. The particle composition in anhydrous hydrogen chlorine (HCl) has been investigated by passing large volumes of HCl through a membrane filter with subsequent analysis of the filter by graphite furnace atomic absorption spectroscopy (GFAAS).[2] However, the gaseous contributions to the total impurity content are undetermined.[4] Hydrolysis methods for chlorine parallel hydrolysis techniques for HCl. However, owing to the limited solubility of gaseous chlorine in water,[5] hydrolysis products may not represent the impurities present because they pass unreacted through the aqueous trap. In addition, both filtration and hydrolysis techniques are indirect methods, time consuming, and prone to contamination.

A direct field usable technique to monitor metallic impurities in ESGs is needed. Particle counting technology in ESGs, recently developed[6] and implemented at Air Liquide, represents a viable approach. However, the partition of metallic impurities between vapor and particulate phases must be known for particle counting to reflect the total impurity concentration in the gas accurately. Comparison of particle counts with metallic impurities was attempted with conventional techniques.[7] However, the correlation was inconclusive, probably due to the limitation of the experimental design that required off-line metal analyses. In addition, the noise background level of the particle counter employed was high.

To examine the complexity of particle- and vapor-phase impurity analysis, two independent real-time analyses were applied in this study: a sealed inductively coupled plasma (SICP) and a laser-based particle counter. A pure, low-flow atmospheric pressure chlorine discharge in the SICP can be formed and has been applied to the impurity analysis of chlorine.[8-10] Additionally, optical particle counters have been widely used to determine particle concentration and size distribution from gas streams.[11-13] The general operating principle of the particle counter involves passing a particle-laden gas stream into a sensing volume illuminated by a laser and detecting the scattered light by a photodetector. Particle concentration is deduced from the frequency of the above-noise pulses, while the size distribution is determined from the intensity distribution with a set of predetermined calibration data.

The ability to measure particle size distributions is important to many industries. However, the field of microcontamination does not share these measurement needs. Differential size distribution data are less important than the cumulative concentration totals at sizes above a threshold value where chip failure will occur.[14] Therefore, in microelectronics success hinges on the ability to count the total particles present rather than their distribution. However, since

(1) Cooper, D. W. *Aerosol Sci. Technol.* **1986,** *5,* 287.
(2) Faix, W. G.; Schramm, W.; Vix, F.; Weichbrod, G.; Hendelmann, R. *Fresenius Z. Anal. Chem.* **1988,** *329,* 847.
(3) Bridenne, M.; Carre, M.; Coffre, E.; Marot, Y.; Simondet, F. Presented at the 1992 Winter Conference on Plasma Spectrochemistry, San Diego, CA, January 1992; poster WP35.
(4) Schram, J. *Fresenius Z. Anal. Chem.* **1992,** *343,* 727.
(5) *Handbook of Chemistry and Physics,* 61st ed.; Weast, R. C., Ed.; Chemical Rubber Co.: Cleveland, OH, 1980.
(6) Wang, H-C.; Udischas, R. *Solid State Technol.,* in press.
(7) Flaherty, E. T.; Johns, L.; Amato, A. F. *Solid State Technol.* **1992,** *1,* S1.
(8) Jacksier, T.; Barnes, R. M. Presented at the Pittsburgh Conference and Exposition, Chicago, IL, 1994; paper 1186.
(9) Jacksier, T.; Barnes, R. M. *Spectrochim. Acta, Part B,* in press.
(10) Jacksier, T.; Barnes, R. M. *Appl. Spectrosc.* **1994,** *48,* 382.
(11) Wang, H.-C.; Doddi, G.; Jurick, B.; Nishikawa, Y. *Microcontamination* **1993,** *4,* 25.
(12) Hardy, T. K.; Christman, D. D.; Shay, R. H. *Solid State Technol.* **1988,** *10,* 83.
(13) Wang, H.-C.; Wen, H. Y.; Kasper, G. *Solid State Technol.* **1989,** *5,* 155.
(14) Knollenberg, R.; Veal, D. L. *J. Inst. Environ. Sci.* **1992,** *3,* 64.

0003-2700/94/0366-2279$04.50/0
© 1994 American Chemical Society

correlation between emission and particles is desired, it is necessary to convert particle counts into volume of particles. It is possible to convert particle counts into total particle volume by assuming the particles are spherical and the geometric diameter is the same as the optical equivalent diameter ($^4/_3\pi r^3$).

Particle counting in inert gases is part of the continuous quality control today in the semiconductor industry owing to the availability of particle counters with low noise, accurate sizing, and high counting efficiency.[15] Particle counting in specialty gases has required additional consideration of material compatibility and flow control.[16] These two techniques operated in tandem yield both emission signals and particle number (particle volume) and size distribution of the same sample. Preliminary results for impurity contributions to electronic-grade chlorine are given.

EXPERIMENTAL SECTION

Sealed Inductively Coupled Plasma. An enclosed plasma developed as an analytical spectrochemical source for the analysis of toxic and reactive gases[17–19] exhibits advantages that suggest its suitability for the analysis of chlorine. Low chlorine flow rates (<100 mL/min) limit sample consumption without dilution. No sample preparation is required because chlorine is a gas at room temperature; therefore, the possibilities for external contamination are eliminated.

The discharge is formed with a plasma gas and sample enclosed inside a quartz container. In this arrangement the discharge is initiated in pure argon under flowing conditions, and chlorine (Electronic Grade, Carbon Steel Cylinder, Air Liquide, Walnut Creek, CA) is added to the argon stream. The argon flow is slowly decreased until the chlorine concentration is approximately 50%. After the plasma stabilizes (approximately 30 s), the argon flow is stopped and a chlorine plasma forms at atmospheric pressure. A minimum of 800 W (at 40.68 MHz) is required to maintain the chlorine discharge. Techniques developed for the analytical applications of the SICPs have been described elsewhere,[18,19] and the direct analysis of chlorine in the SICP is underway.[8,9]

The chlorine discharge was maintained at 40.68 MHz (Model HFS 5000D, 0–5 kW, RF Plasma Products, Marlton, NJ) and 1.0-kW foward power, by using a 65-mm, quartz, SICP container.[20] Details of experimental equipment and operation were reported previously.[18,19]

Particle Counter. A particle counter (Particle Measuring Systems, Boulder, CO) was used in this study (Table 1). The wetted portions of the counter are made from stainless steel, glass, and a Kalrez o-ring. Therefore, gases compatible with these materials can be measured with this sensor. Additionally, the optimal flow rate through the detector at atmospheric pressure is 20 mL/min.

Gas entering the particle counter passes through a glass capillary where a laser diode beam (780 nm) crosses orthogonally. Both the light scattered by the glass capillary and particles in the flowing gas are detected by a photodiode. There are three types of background for this counter: electronic, light scattering from the surface of the glass capillary, and particles generated by the sampling system. Obtaining a low background is important to ensure that detected particles are from the gases to be sampled and not particles generated within the whole sampling system.[13] A transient signal is observed for the particles as they travel with the gas through the laser beam. The transient signal is measured above a constant background signal. This restricts the detection limit of the particle diameter to approximately 0.2 μm.

Table 1. Particle Counter Instrumental Components

particle counter	Particle Measuring Systems, Model CGS-200
size range	>0.2 μm
channel thresholds	0.20, 0.25, 0.30, 0.35, 0.40, 0.45, 0.50, 0.55, 0.60, 0.70, 0.80, 0.90, 1.0, 1.5, 2.0, 3.0
optical design	passive, glass capillary
laser source	laser diode, 780 nm
environment	inert or reactive gases up to 207 bar
spectrometer	μLPS

The counter background noise is less than 1 particle/standard cubic foot (<35/m³) at 0.2 μm (the smallest particle size channel).[6] The equivalent background noise in mass concentration, assuming spherical particles and a density of 10 g/cm³, is approximately 1 part in 10^{15} or 1 ppq. The low detection limit coupled with the ease of operation and low cost makes particle counters an excellent instrument for monitoring metallic impurities.

Gas Handling System. A gas handling system designed to allow introduction of chlorine into the argon stream (Figure 1) has been described elsewhere.[9,18,19] To examine the effect of particle generation by valve wear or the gas system surface losses, a tee was installed before the particle counter to bypass the in-line 0.01-μm particle filter (ceramic gas filter, Model 6112-V4MM, Fastek, Rochester, NY) through mass flow controller F5 and valve V14. A segment of 316L electropolished stainless steel tubing was used to connect the particle counter with the SICP, and the total gas volume from the particle counter was introduced into the SICP. The gas handling system, including the filter bypass, was purged for 24 h to remove entrained air. Before experimental measurements, 10 mL/min chlorine was passed through the filter for no less than 6 h to condition it.

Experimental Design. The contribution and composition of particles generated from a chlorine cylinder, regulator, and gas handling system valves were evaluated by monitoring total generated particle counts (as the sum of all 16 particle size channels, Table 1) and the emission spectrum between 200 and 400 nm as the chlorine cylinder or gas distribution system was mechanically shocked. A total of five experiments were conducted with mechanical shocking. Three of the experiments were performed without the chlorine gas regulator and the remainder with the regulator in place. Owing to the low cylinder pressure of pure chlorine (5.9 bar), the cylinder regulator can be safely removed without leakage from the mass flow controller (leakage occurs at pressures greater than

(15) Wang, H.-C.; Wen, H. Y.; Kasper, G. Proceedings of Institute of Environmental Science, 1989 Technical Meeting, Anaheim, CA, 1989; paper 419.
(16) Wang, H.-C.; Udischas, R. Microcontamination 1993 Conference Proceedings, San Jose, CA, 1993; p 465.
(17) Jahl, M. J.; Jacksier, T.; Barnes, R. M. *J. Anal. At. Spectrom.* **1992**, *7*, 653.
(18) Jacksier, T.; Barnes, R. M. *J. Anal. At. Spectrom.* **1992**, *7*, 839.
(19) Jahl, M. J.; Barnes, R. M. *J. Anal. At. Spectrom.* **1992**, *7*, 833.
(20) Jacksier, T.; Barnes, R. M. *Spectrochim. Acta* **1993**, *48B*, 944.

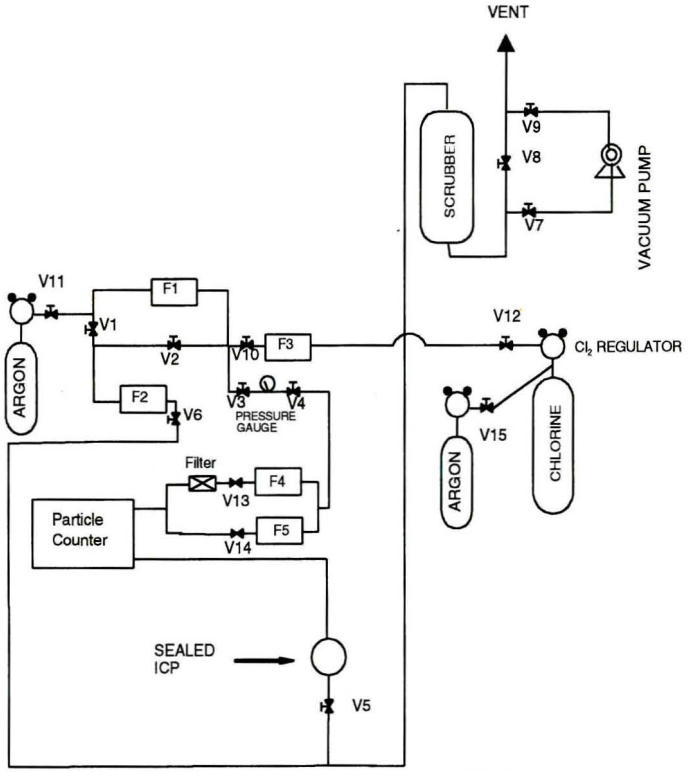

Figure 1. Gas handling system for the introduction of chlorine and argon into the sealed ICP. F1–F5 are mass flow controllers; V1–V14 are shut-off valves. Filtered chlorine gas flow is introduced into the plasma through F4. An unfiltered gas flow into the plasma is introduced through F5. All tubing is 316L electropolished stainless steel.

6.9 bar). The mass flow controller serves as a pressure regulator for these experiments.

A vapor-phase blank was also acquired by purging the gas handling system at 100 mL/min total gas flow for 8 h through an in-line 0.01-μm particle filter before obtaining particle or emission data. No chlorine pressure regulator was employed.

Particles originating from the chlorine cylinder were obtained by mechanically shocking the cylinder.[11] The particle contribution resulting from the gas handling system valves (Figure 1, valves V4 and V10) was recorded when the valves were operated vigorously. For all cases, when the transient particle concentration reached a maximum value, the flow of chlorine through the particle counter and the SICP was stopped (Figure 1). Since the analyte emission signal is stable in the no-flow SICP for no less than 60 min,[18] the emission spectrum could be recorded between 200 and 400 nm without loss of analyte emission intensity. Qualitative identification of the spectrum established the emitting species.

Caution: Chlorine is a poisonous gas with a threshold limit value of 1 ppm. Chlorine should be handled with appropriate safety precautions and only by persons trained in the use and handling of corrosive gases.

The gas handling system is pressurized with argon and leak tested (GOW-MAC leak detector, Model 2-1, GOW-MAC Instrument Co., Bridgewater, NJ) prior to the introduction of chlorine. The gas handling system is continuously purged with argon when not in use to eliminate accumulated gases and oxygen from the system. All gases introduced into the system are passed through a scrubber to remove any reactive compounds.

RESULTS AND DISCUSSION

The emission spectrum of the vapor-phase impurity blank is illustrated in Figure 2a. The prominent spectral feature is the Cl_2 emission continuum. Element atomic emission lines are superimposed. Elements identified in the vapor-phase blank include Al, C, Ca, Cu, and Sn (Table 2). Since the induction coil is in contact with the discharge container wall, copper from the induction coil is believed to diffuse through the quartz container and thereby produce significant emission.[18,19]

The effects on the emission spectra for valve operation and mechanical cylinder shocking are demonstrated in Figure 2b. Compared to the chlorine blank in Figure 2a, Al, Ca, and Sn emission intensities increased. Additionally, emission from titanium at 334.941, 336.121, and 337.280 nm is observed with component agitation.

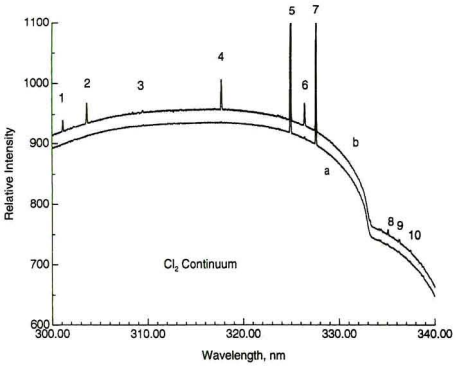

Figure 2. Emission spectra of a 100% chlorine plasma between 300 and 340 nm at 1.0 kW in a 65-mm discharge container with no gas flow. Wavelengths and elements identified include the following: (1) 300.914 nm, Sn I; (2) 303.412 nm, Sn I; (3) 309.280 nm, Al I; (4) 317.505 nm, Sn I; (5) 324.754 nm, Cu I; (6) 326.396 nm, Sn I; (7) 327.396 nm, Cu I; (8) 334.941 nm, Ti II; (9) 336.121 nm, Ti II; (10) 337.280 nm, Ti II. (a) No cylinder regulator and 0.01 μm in-line filter. Only copper and tin emission lines are observed. Spectrum obtained after an 8-h filtered purge; (b) no in-line filter illustrating Al, Cu, Sn, and Ti emission lines. Particles generated by shocking the cylinder.

Table 2. Prominent Emission Line Wavelengths for Impurity Identification in Chlorine

element	wavelength, nm
Al I	396.86
C I	247.86
Ca II	393.37
Cu I	324.75
Sn I	284.00
Ti II	334.94

The molecular spectrum, extending to approximately 343 nm having a maximum at 307 nm in all emission spectra, has been attributed to chlorine emission continua. The maximum at 330 nm has been characterized as the dissociation of normal chlorine atoms.[10]

When the volume of particles observed for each experiment was plotted against the sum of the net intensities for the major wavelength (Table 2) for each element observed (total impurity emission), a correlation with $r^2 = 0.9616$ was observed (Figure 3). This correlation indicates a direct relationship between particles and their total composition. Since no particles were generated during the filtered experiment, data for this experiment were excluded because a comparison between different levels of particles was desired.

To evaluate the relationship between individual elements and total particle volume, the emission intensity for each element was plotted against the total particle volume (Figures 4 and 5). Calcium, tin, and titanium emission intensities do not appear to correlate with the total particle volume. A factor of 2 decrease in emission for calcium and increase for tin were observed for similar particle volume values (5.73×10^{-10} and 1.78×10^{-9} mL, respectively). Titanium emission decreased slightly as the total particle volume increased from 4.23×10^{-10} to 2.4×10^{-9} mL. Carbon emission is unchanged with particle volume, suggesting that the most likely form of carbon in chlorine is CO_2. Aluminum emission was increased with increasing particle counts, indicating that aluminum

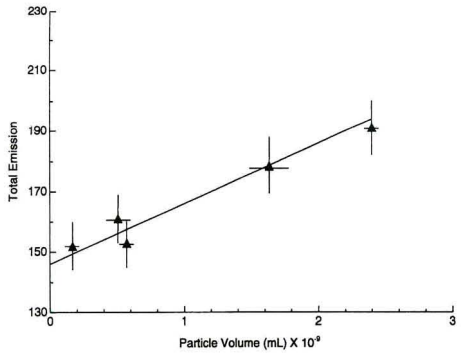

Figure 3. Correlation of total particle volume to total net emission. The total emission represents the sum of the net signal intensities for the major wavelength for each element observed.

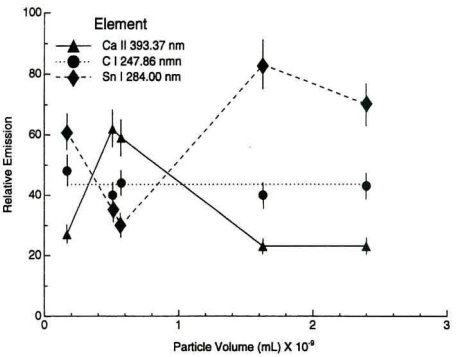

Figure 4. Correlation of total particle volume to net element emission signals for calcium II 393.37 nm (▲), carbon I 247.86 nm (●), and tin I 284.00 nm (▲).

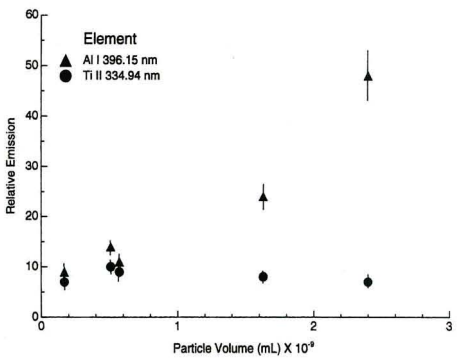

Figure 5. Correlation of total particle volume to net element emission signals for aluminum I 396.15 nm (▲) and titanium II 334.94 nm (●).

particles were liberated from the cylinder and gas distribution stream. These data suggest that the particle composition is not homogeneous.

Calcium and tin emission signals do, however, depend on the presence of the chlorine regulator at the chlorine cylinder (Figure 6). With the chlorine regulator in the gas system, both the Ca and Sn emission signals were statistically

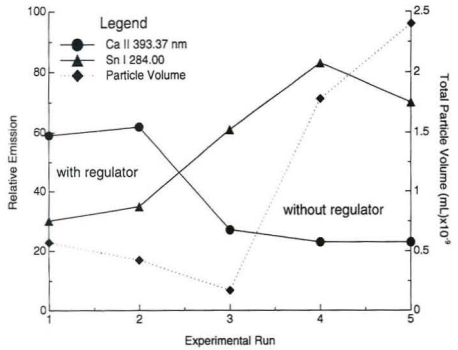

Figure 6. Component correlation to Ca (●) and Sn (▲) emission signals with and without chlorine regulator compared with the total particle volume (◆).

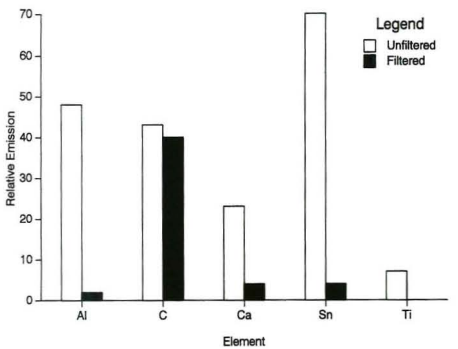

Figure 7. Effect of particle filtration on relative emission illustrating the presence of a vapor-phase impurity component to the total impurity content.

unchanged when the volume of particle increased from 4.23×10^{-10} to 5.73×10^{-10} mL (experiments 1 and 2). Without the regulator, the tin emission signal increased and the calcium signal decreased significantly compared to the regulated stream. A nonproportional increase in emission intensity was observed with increased particle volume. This may be due, in part, to the inability to agitate the system repeatedly to release identical particles for both size and distribution consistently. The interaction of the chlorine with the gas regulator must be evaluated as a source of impurities.

Only the total particle volume was used in these experiments, and the contribution of individual elements to the overall particle size distribution is unknown. The absence of correlation, therefore, indicates that the element in question does not appear uniformly in all particle size channels. Further study of the impurity–particle relationship will be undertaken taking the size distribution into account. This requires knowledge of the mass fraction of each element and the corresponding particle size channels.

The vapor-phase impurity component was obtained by comparing emission intensities for filtered (vapor-phase blank) and unfiltered chlorine (Figure 7). This comparison reveals a significant decrease in emission for Al, Ca, and Sn and the absence of Ti. Carbon emission was statistically unchanged with volume of particles. Assuming that the total impurity content (particle and vapor phases) can be obtained from emission data, the total vapor-phase impurity contribution can be determined. The sum of the net emission intensities for the major wavelength for each element observed was obtained for both the vapor-phase blank and the unfiltered sample (containing both vapor-phase and particulate impurities). The sums of the relative emission intensities for the filtered and unfiltered chlorine samples were 50 and 191, respectively (Figure 7). Assuming that the contributions to the vapor-phase impurities were similar in both experiments, the vapor-phase contribution to the unfiltered sample was determined to be 35% ($50/(191 - 50) \times 100$). The carbon contribution to the vapor-phase impurity content was determined to be 80% (21% of the total impurity contribution).

CONCLUSIONS

The feasibility of the application of the SICP and particle counter for impurity analysis for both vapor and particle phases has been demonstrated. The low gas flow rate through the particle counter (20 mL/min) permits direct introduction of gas into the SICP. The SICP emission signals and particle counter revealed a correlation between total particle volume and net impurity emission. A correlation between aluminum emission and total particle counts was also observed. Calcium and tin impurity emissions were related to the presence of the regulator. Calcium is a common ambient impurity and may have been introduced during connection of the regulator to the cylinder. This would explain the decrease in calcium emission without the regulator. Tin is a component in 316L stainless steel and therefore present at the valve of the cylinder. It is reasonable to expect that particles will be generated by the cylinder valve and that these particles would be trapped by the regulator. Therefore, when the regulator is removed it would be expected to show greater emission of tin.

Titanium was present only in particulate form. Since no correlation with titanium, calcium, and tin appeared with particle generation, different types of particles may be released during cylinder shocking and valve operation. These particles may vary in size and/or composition.

Metal impurities in chlorine occur in both volatile (as volatile chlorides) and particulate forms; this confirms comments by Schram.[4] Our experiments illustrate that more than 65% of detected elemental impurities occur in particles with 35% as volatile impurities. Carbon was determined to account for 80% of these volatile impurities (or 21% of the total impurity content in the unfiltered chlorine sample). Furthermore, variation of the partition of impurities between vapor and particle phases for various elements indicates the need to establish a particle–metal correlation for each element. A correlation for other ESGs also needs to be established. These experiments do not indicate whether the impurities result from an interaction of the chlorine gas with the cylinder, or with the cylinder valve, or are present in the chlorine. Further experimentation is necessary comparing cylinder valves and the cylinders.

ACKNOWLEDGMENT

This research was funded by Air Liquide. Experiments were carried out at the University of Massachusetts. This work was presented, in part, at the Twentieth Annual Meeting of the Federation of Analytical Chemistry and Spectroscopy Societies, Detroit, MI, October 1993, as paper 727. The authors acknowledge Greg Jursich for helpful discussions during this work and for his help in the preparation of the manuscript.

Received for review February 4, 1994. Accepted May 1, 1994.[•]

[•] Abstract published in *Advance ACS Abstracts,* June 1, 1994.

Anal. Chem. **1994,** *66,* 2285–2292

Electrospray-Condensation Particle Counter: A Molecule-Counting LC Detector for Macromolecules

Kenneth C. Lewis, Daniel M. Dohmeier,† and James W. Jorgenson*
Department of Chemistry, University of North Carolina at Chapel Hill, Venable Hall, CB 3290, Chapel Hill, North Carolina 27599-3290

Stanley L. Kaufman, Fahimeh Zarrin, and Frank D. Dorman
TSI Incorporated, P.O. Box 64394, St. Paul, Minnesota 55164

A new detector for macromolecular separations is described. The detector counts individual macromolecules (molecular weights greater than about 10 000) and reports counts per second. The chromatographic effluent is electrosprayed, neutralized, and swept to the detector by a stream of air. The detector is a condensation particle counter that detects individual particles by light scattering from droplets condensed on the particles. When used as the detector for a size exclusion separation of proteins, the detector has a linear range of 4 orders of magnitude with detection limits as low as 0.1 μg/mL. The detector can be directly interfaced (no makeup flow) with effluent flows as low as 10 nL/min. A Monte Carlo model based on size measurements of the electrosprayed droplets correctly predicts the observed detector behavior.

The lack of a sensitive universal detector for large molecules in capillary separations has hindered the development of capillary liquid chromatography. Although smaller molecules such as peptides can undergo derivatization and be detected by laser-induced fluorescence, larger biopolymers cannot be quantitatively tagged in a consistent manner.[1] Tagging reactions often produce multiple products that give rise to multiple peaks in the chromatogram. Therefore, the standard method for detecting biopolymers is UV absorption. While UV absorption offers reasonable detection limits when the path length is 1 cm, detection limits are rather poor for capillary separations where the path length is often the diameter of the capillary. The limitation of UV absorbance is particularly evident for those compounds that are poor UV absorbers. For these reasons, a truly universal detector with high sensitivity at flow rates under 100 nL/min is greatly desired.

The detection of single nanometer-sized particles in the gas phase is well-known in aerosol science, but until now no effort has been successful at transferring particles in that size range from a liquid suspension to aerosol form. Particles formed by the residue from salt solutions have been detected by light scattering after undergoing a condensation growth process,[2] but a condensation particle counter (CPC) has never been used to count single molecules. The electrospray condensation particle counter (ES-CPC) described below counts single macromolecules and can be used as a detector for any liquid separation technique that maintains a flow of liquid greater than about 10 nL/min.

The microcolumn outlet is connected to an electrospray needle, and the effluent is electrosprayed to produce dry particles. Signal is generated by the presence of single analyte molecules (particles) in the gas phase, and background results from gas-phase particles containing only nonvolatile residue from the mobile phase. Both analyte and background particles are neutralized by a static charge neutralizer. The resulting particles are swept by a stream of air to the CPC, where the individual particles are counted. The CPC can detect any particle greater than 3 nm in diameter. This detection limit translates to approximately 10 000 Da. Therefore any molecule larger than this limit can be detected.[3,4] This size threshold is nearly independent of the particle material.[5,6] Thus for example it would be expected that, for equivalent number concentrations of proteins, carbohydrates, and polystyrene, equivalent counts (signal intensities) would be produced.

EXPERIMENTAL SECTION

Electrospray Supplies. Fused-silica capillary was purchased from Polymicro Technologies (Phoenix, AZ). Hydrofluoric acid was purchased from Fisher Scientific (Raleigh, NC). Teflon tubing with an inner diameter of 0.010 in. and an outer diameter of $^1/_{16}$ in. was purchased from Alltech (Deerfield, IL). Breathing-quality compressed air and sulfur hexafluoride were purchased from National Welders Supply (Raleigh, NC).

Reagents. Protein standards were purchased from Sigma Chemical Co. (St. Louis, MO). Buffer reagents were purchased from Fisher Scientific. All chemicals were used as received.

The buffer used for all separations reported was 10 mM ammonium acetate adjusted to pH 8.0 with ammonium hydroxide. The buffer solution was made with deionized water purified with a Barnstead Nanopure system (Boston, MA).

† Present address: Rohm & Haas Research Laboratories, 727 Norristown Rd., P.O. Box 904, Springhouse, PA 19477-0904.

(1) Zhao, J. Y.; Waldron, K. C.; Miller, J.; Zhang, J. Z.; Harke H.; Dovichi, N. J. *J. Chromatogr.* **1992,** *608,* 239–242.
(2) Allen, L. B.; Koropchak, J. A. *Anal. Chem.* **1993,** *65,* 841–844.
(3) Zarrin, F.; Kaufman, S. L.; Dorman, F. D. Method and Apparatus for Determining Concentration of Macromolecules and Colloids in a Liquid Sample. U.S. Patent 5,076,097, 1991.
(4) Kaufman, S. L.; Zarrin, F.; Dorman, F. D. Electrospray Apparatus for Producing Uniform Submicrometer Droplets. U.S. Patent 5,247,842, 1993.
(5) Metayer, Y.; Madelaine, G. In *Atmosperhric Pollution 1980, Proceedings of the 14th International Colloquium,* Paris, 5–8 May 1980; Benarie, M. M., Ed.; Studies in Environmental Science 8; Elsevier: Amsterdam, 1980.
(6) Bartz, H.; Fissan, H.; Helsper, C.; Kousaka, Y.; Okuyama, K.; Fukushima, N.; Keady, P. B.; Kerrigan, S.; Fruin, S. A.; McMurry, P. H.; Pui, D. Y. H.; Stolzenburg, M. R. *J. Aerosol Sci.* **1985,** *16,* 443.

0003-2700/94/0366-2285$04.50/0
© 1994 American Chemical Society

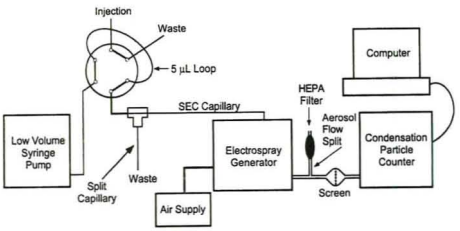

Figure 1. Overall schematic of the SEC separation and detection system. Figures 2–4 show detailed parts of the overall setup.

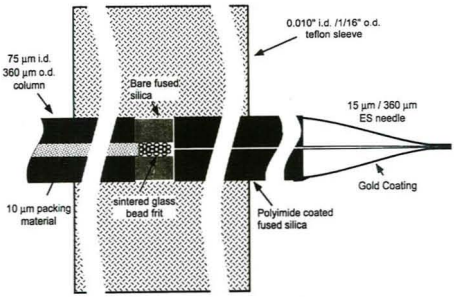

Figure 2. Union between the SEC column and electrospray needle, shown to scale.

Sample Preparation. Solutions and mixtures were made from protein standards of thyroglobulin (THYRO), chicken egg albumin (OVA), and horse heart myoglobin (MYO) in the ammonium acetate buffer. The mixtures were centrifuged at 16,000*g* for 2 min to remove any undissolved particulate matter. After centrifugation the supernatants were drawn off and stored at 4 °C.

Column Packing Procedure. Separations were performed on a size exclusion microcolumn. A fused-silica capillary with a nominal inner diameter of 75 µm, an outer diameter of 360 µm, and a length of 30 cm was slurry packed in our laboratory with 10-µm, spherical, HEMA 1000 particles (Alltech). The packing procedure has been described previously[7] and was modified slightly in the fritting process.[8]

Instrumentation. Figure 1 is a schematic of the entire instrumental setup.

Chromatographic System. The chromatographic injection system operates on the principle of a dynamic split. A 4-cm section of 0.030-in. PEEK tubing connects the injection valve to the splitter tee. The capillary column passes completely through the tee and is sleeved inside of the 0.030-in. PEEK tubing. The end of the column extends as far as possible into the valve. The majority of liquid flows between the outer wall of the capillary column and the inner wall of the 0.030-in. PEEK tubing until it reaches the splitter tee where it goes to waste. A 5.0-µL loop on a six-port injection valve (Valco Instruments) is filled with sample solution. The valve is then rotated to inject the sample on the column. At this point the sample is divided between the column and the flow splitter. Because the flow through the splitter is 30 µL/min and the flow through the capillary is 52 nL/min, almost all of the sample goes to waste. Only a small fraction of the 5.0 µL (approximately 8.6 nL) is actually injected onto the column. Flow rates were determined by immersing the outlet end of the capillary into mineral oil and allowing a drop to form. The diameter of the drop (and therefore the volume) was determined under a microscope fitted with a calibrated reticule.[9] A column flow of 52 nL/min was chosen from the studied range of 10–200 nL/min because it was the best compromise between speed and resolution.

Fabrication of the MicroElectrospray (µES) Needle. Dohmeier and Jorgenson have described the fabrication of an electrospray needle from fused-silica capillary (µES needle).[10,11] A major advantage of µES needles over conventional electrospray (ES) needles (as used, for example, in an electrospray mass spectrometer interface) is their ability to spray aqueous solutions over the flow range of 20–200 nL/min. Therefore, µES needles can be interfaced directly onto capillary columns without a makeup flow. Figure 2 is a detailed drawing of a µES needle attached to a capillary column.

To fabricate the µES needle a piece of fused-silica capillary, usually 15-µm i.d., 360-µm o.d., and 20 cm long, is placed in a capillary pulling machine (W-P Instruments Inc.) and heated with a butane/nitrous oxide microtorch (Radio Shack Inc.) until the capillary pulls apart. This procedure burns the polyimide off the end of the resulting capillary, and the capillary is sealed at the terminus. The sealed end is cut from the capillary with a sapphire scribe (Supelco) yielding a terminal inner diameter of approximately 9 µm and an outer diameter near 150 µm. The unmodified end of the capillary is then attached via a Teflon tubing union[12] to a capillary of larger bore (50–150 µm i.d.). Filtered deionized water is pumped through the capillary at approximately 500 nL/min. The modified tip of the needle is immersed approximately 2 mm in a stirred solution of 48% hydrofluoric acid. Water flow is necessary to prevent the HF from flaring the inner diameter of the capillary tip into a "trumpet bell" shape. The tip is etched in the HF for 40 min and then disconnected from the etching apparatus. At this point the tip of the needle will have an inner diameter of 9 µm and an outer diameter less than 20 µm. With the aid of a microscope, the tip is trimmed using the sapphire scribe, to an outer diameter between 20 and 40 µm. It is essential that the tip be flat, with no rough or sharp edges, which might lower the onset potential for a corona discharge when the tip is in operation.

The final preparation steps are coating the tips with chromium and gold. The needles are mounted on a microscope slide with about 3 cm of each tip extending over the edge of the slide. Because every exposed surface inside the evaporator bell jar will be coated with gold, all but the overhanging 3 cm is covered with aluminum foil to limit gold deposition to the tip of the needle. The slides are positioned parallel to the base plate in an evaporative coating machine. A total of 30 nm of chromium is deposited on the tip, and then 100 nm of gold

(7) Kennedy, R. T.; Jorgenson, J. W. *J. Microcolumn Sep.* **1990**, *2*, 120.
(8) Hoyt, A. M., Jr.; Beale, S. C.; Larmann, J. P., Jr.; Jorgenson, J. W. *J. Microcolumn Sep.* **1993**, *5*, 325–330.
(9) Kennedy, R. T.; Jorgenson, J. W. *Anal. Chem* **1988**, *60*, 1521–1524.
(10) Dohmeier, D. M.; Jorgenson, J. W. Microelectrospray Method and Apparatus. U.S. Patent 5,115,131, 1992.
(11) Dohmeier, D. M. Ph.D. Dissertation, University of North Carolina, Chapel Hill, NC, 1991.
(12) Lemmo, A. V.; Jorgenson, J. W. *Anal. Chem.* **1993**, *65*, 1576–1581.

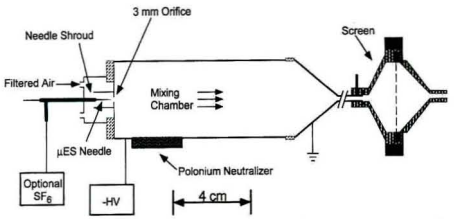

Figure 3. Electrospray chamber and diffusion screen shown to approximate scale. The mixing chamber has a 1.5-in. i.d.

is deposited on the tip. The tips are turned over, and the other side is coated in the same manner. After coating, the tips are ready for use.

Electrospray Chamber and Screen. Figure 3 shows a schematic view of the electrospray chamber, the screen between the electrospray chamber, and the detector (CPC). The μES needle is at ground while the orifice and body of the electrospray chamber are at negative high voltage. A polonium-210 (α emitter) static eliminator with an activity of 5.0 mC (NRD Inc., Grand Island, NY) creates a weak bipolar plasma in the mixing chamber to neutralize the charge of the electrosprayed droplets. Without the polonium source the highly positively charged particles are attracted to the negatively charged walls of the electrospray chamber and never reach the detector. The electrosprayed particles are swept to the detector by 2.0 L/min filtered air.

A provision is made to sheath the electrospray needle with a small flow of gas such as sulfur hexafluoride.[13] The gas is introduced inside the needle shroud and exits at the end of the shroud about 1.5 mm above the end of the electrospray needle. An SF_6 flow of approximately 20 mL/min increases the potential range for electrospray by 500–1000 V before the onset of corona. To be more specific, electrospray onset is usually at 1.8 kV with corona onset at 2.6 kV. With the addition of SF_6 electrospray is onset at 1.8 kV but a corona discharge is not observed until the potential is greater than 3.4 kV. However, it was determined that SF_6 is only beneficial to the final detector signal-to-noise ratio when one tries to electrospray at liquid flow rates greater than 60 nL/min. For all of the SEC work presented here, SF_6 is not used.

When the effluent is sprayed at lower macromolecule concentrations, the droplet volumes are small enough so that most droplets are "empty," i.e., contain no macromolecules but only water with dissolved buffers and any impurities. Under these conditions, some droplets contain one macromolecule, and a negligible few contain more than one. This is analyzed in greater detail below. The volatile portion of each droplet (water, ammonia, acetic acid) evaporates quickly. The droplets containing macromolecules thus produce a dried macromolecule aerosol, while the "empty" droplets produce smaller residue particles of any nonvolatile dissolved material. The macromolecule aerosol component is to be detected, while the residue of "empty" droplets constitute an interfering background. To remove this background selectively, a single 3.81-cm-diameter, 600-mesh screen (Model 376060 particle

(13) Ikonomou, M. G.; Blades, A. T.; Kebarle, P. *J. Am. Soc. Mass Spectrom.* **1991**, *2*, 497–505.

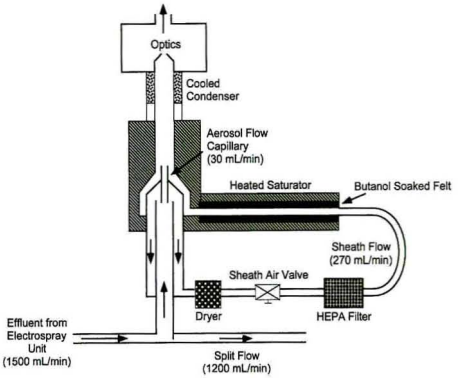

Figure 4. Schematic diagram of the CPC flow path.

size selector, TSI Inc., St. Paul, MN) is introduced into the flow path. The screen wire is 20 μm in diameter and the openings are 20 μm. The smaller size and consequent larger diffusion coefficient of the residue particles make them more likely than the macromolecules to reach the screen wire and be trapped.[3,14,15]

Condensation Particle Counter. A Model 3025 condensation particle counter (CPC) (TSI Inc, St. Paul, MN) is used as the detector for this system. Figure 4 is a schematic of the CPC. Only a general overview of the instrument is given here while detailed information about the detector can be found elsewhere.[16–18] Of the 2.0 L/min air passing through the electrospray chamber, only 1.5 L/min enters the detector. The remaining 0.5 L/min is shunted to waste via a high-efficiency particle aerosol (HEPA) filter which keeps room-air particles from being entrained in the flow. Of the 1.5 L/min analyte/air mixture entering the detector, 1.2 L/min is used to provide a sufficiently fast flow to limit particle diffusion to tubing walls and is vented to waste inside the instrument. Of the remaining 300 mL/min in the detector, 270 mL/min is split off, dried, filtered in a HEPA filter to remove all particulate matter, and passed through a heated saturator where it is saturated with butanol vapor. Only 30 mL/min of analyte/air mixture remains and is inspected in the CPC. The analyte/air mixture passes through the aerosol flow capillary and is combined in a sheath-flow geometry with the 270 mL/min air saturated with butanol vapor. The net sheathed flow stream of 300 mL/min passes through a cooled condenser where butanol condenses on the analyte particles and the nucleated drops grow to micrometer size. All particles above the threshold size grow to the same size droplet. This threshold size is determined by the Kelvin diameter of butanol droplets at the given butanol supersaturation ratio and is practically independent of the nature of the particle.[5,6] The droplets then pass through the optics chamber where they are detected by light scattering and recorded as discrete particle "counts".

(14) Cheng, Y. S.; Yeh, H. C. *J. Aerosol Sci.* **1980**, *11*, 313–320.
(15) Hinds, W. C. *Aerosol Technology: Properties, Behavior, and Measurement of Airborne Particles*; Wiley: New York, 1982; pp 148–150.
(16) Agarwal, J. K.; Sem, G. J. *J. Aerosol Sci.* **1980**, *11*, 343–357.
(17) Kesten, J.; Reineking, A.; Porstendorfer, *J. Aerosol Sci.* **1991**, *15*, 107–111.
(18) Stolzenburg, M. R.; McMurry, P. H. *AEROSOLS: Formation and Reactivity*; 2nd International Aerosol Conference, Berlin; Pergamon Journals Ltd.: Oxford, Great Britain, 1986; pp 786–789.

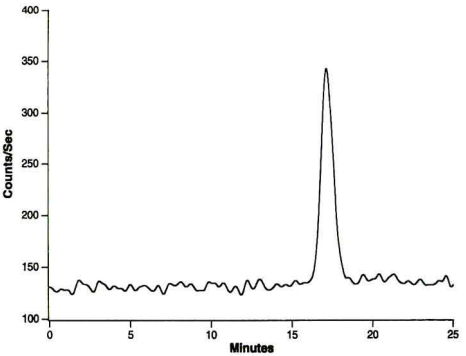

Figure 5. Myoglobin sample (1 μg/mL) analyzed on a SEC column with ES-CPC detection. The chromatogram has been filtered with a low-pass Butterworth no phase frequency filter with a frequency cutoff of 0.03 Hz and an order of 4.

Table 1. Detection Limit for Proteins

sample	molarity injected ($\times 10^{-9}$)	concn injected (μg/mL)	moles injected ($\times 10^{-17}$)	grams injected ($\times 10^{-12}$)	molecules injected ($\times 10^{6}$)
THYRO	1	1	1	9	8
OVA	2	0.1	2	0.9	10
MYO	20	0.3	20	3	90

Instrument Control and Data Analysis. An IBM-compatible personal computer is used to control the condensation particle counter. Software written in-house with Quick C for Windows (Microsoft Corp., Redmond, WA) provides control over data acquisition while Excel (Microsoft Corp.) and LabView (National Instruments, Austin, TX) are used for data processing.

RESULTS

To best evaluate the performance of this detection system for biological macromolecules, a variety of protein standards were chosen. Thyroglobulin (THYRO), ovalbumin (OVA), and myoglobin (MYO) were chosen for their wide range of molecular weight with some consideration of their chromatographic behavior. The molecular masses of THYRO, OVA, and MYO are approximately 669, 40, and 17 kDa, respectively. Calibration curves were generated for these three proteins by analyzing each one individually with blank runs between sample runs to eliminate the possibility of sample carryover. Typical sample concentrations were 1000, 300, 100, 30, 10, and 3 μg/mL, providing evenly spaced points on a log–log calibration plot. These solutions were prepared by serial dilution from stock solutions. The chromatographic peak, and any tail associated with it, was integrated to determine the actual number of particles seen by the CPC. Figure 5 is an example of a chromatogram used in the determination of a calibration curve for myoglobin. The chromatogram exhibits the typical baseline and peak shape seen when a protein is analyzed on a size exclusion column.

Table 1 gives the detection limits for these three proteins with a signal-to-noise ratio of 3. The upper detection limit before saturation of the CPC is 3000 μg/mL for THYRO, 1000 μg/mL for OVA, and 3000 μg/mL for MYO. Table 2 contains the coefficients and range for a log–log calibration curve for each of the three proteins. The equation is log(total counts) = intercept + [log(μg/mL) × slope]. The slope of 1 illustrates that this detection system has a linear response over 4 orders of magnitude for OVA and MYO and the dynamic range for THYRO is almost as large, while a correlation coefficient near 1 indicates a good fit to the data. Figure 6 shows theoretical and experimental calibration curves for MYO and will be discussed in detail later.

Table 2. Calibration Curve Coefficients

sample	slope	intercept	corr coeff	range (μg/mL)
THYRO	1.04	3.57	0.993	1–3000
OVA	1.00	3.97	0.994	0.1–1000
MYO	1.00	3.79	0.990	0.3–3000

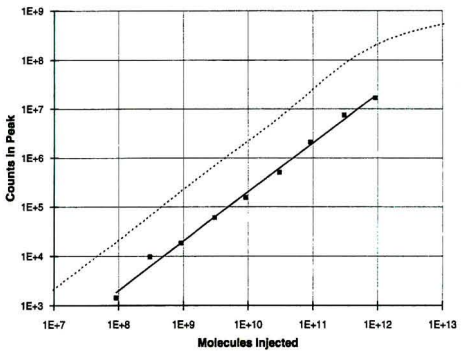

Figure 6. Integrated peak area (molecules detected) versus macromolecules injected, from the model (dashed line) and from the SEC experiments (points and solid line). See text for discussion.

A comparison was made between a Linear Instruments Model 200 variable-wavelength UV/visible detector outfitted with an on-column capillary flow cell (Linear Instruments, Reno, NV) and the ES-CPC. A piece of fused silica capillary with an inner diameter of 50 μm was joined to the end of the separation capillary in the same manner as the electrospray needle. UV detection was done on the 50-μm open capillary. The UV detector was set at a wavelength of 214 nm with a sensitivity of 0.5 milliabsorbance units full scale and a rise time of 1 s. Figure 7 is a direct comparison between the two detectors. The significant enhancement in detection limit offered by the ES-CPC is obvious. The flow rate in Figure 7 was 217 nL/min compared to 52 nL/min for all of the calibration runs. At this higher flow rate the background increases from 130 (as seen in Figure 5) to 500 counts/s. Operation at the highest possible sensitivity causes significant drift in the UV runs. The range used is 1–2 orders of magnitude more sensitive than conventional operating parameters. The drift is not due to insufficient warmup time as the detector had overnight to warm prior to use.

DISCUSSION

Linearity and Single-Molecule Detection. Because the CPC is capable of counting discrete particles in the size range of the individual macromolecules, the observed linearity of the calibration curves over such a wide range of concentrations suggests the validity of the simple picture of single-molecule

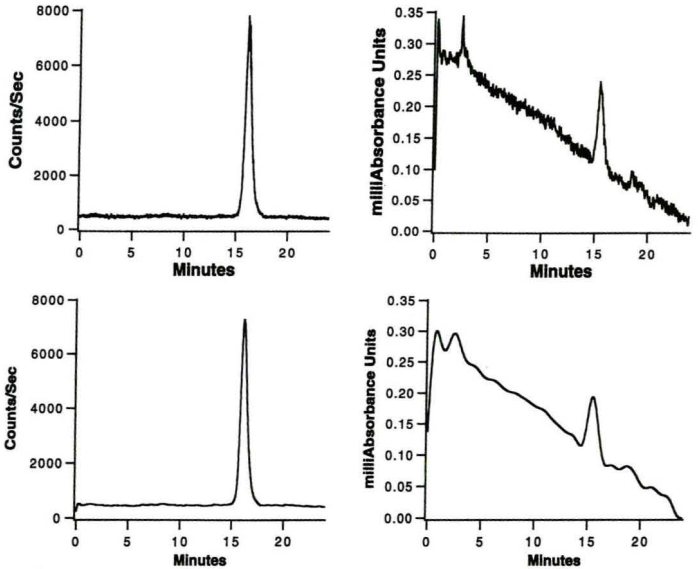

Figure 7. SEC of 20 μg/mL ovalbumin on a 150 μm i.d. × 61 cm HEMA packed column with a flow rate of 217 nL/min. The left chromatograms were obtained by CPC detection while the two on the right were obtained by UV detection. The top chromatograms are unfiltered and the bottom chromatograms are filtered the same as for Figure 5. The injection method used for these runs required a momentary stop in flow before and after the injection. The spikes seen at the beginning of the UV run are a direct result of a stop in flow.

detection presented in the introduction. The number of macromolecules per droplet is governed by Poisson statistics. At low concentrations, most of the droplets are "empty". The number of droplets containing exactly one macromolecule tracks linearly with the macromolecule concentration, and the number of droplets containing more than one macromolecule is negligible. As concentration increases, according to this picture, the portion of droplets containing more than one macromolecule increases, at first quadratically. Such droplets dry to macromolecule aggregates, which the CPC registers as one count for the entire aggregate. Thus, in this simple picture the slope of the response decreases as the concentration becomes significantly greater than one molecule per droplet volume.

This picture assumes a sharp detection threshold (above the size of empty-droplet residues and below the size of single-molecule droplet residues) and a monodisperse electrosprayed droplet distribution. The CPC threshold is very sharp, but the added diffusion screen modifies the overall response probability so that its initial rise is approximately quadratic with particle diameter. This makes it possible that the observed linearity is in part due to a compensating effect whereby the absence of particles due to aggregation is offset by the increased overall detection probability with aggregate size. Furthermore, although the size of the electrosprayed droplets was known to be small, their detailed size distribution was not firmly established at the outset of the SEC experiments. Thus, although the expected and observed linearity is consistent with the ES-CPC detector counting discrete analyte molecules, as opposed to aggregates of molecules, it does not alone justify the claim of single-molecule detection.

Droplet Size Distribution. In order to investigate this issue, we determined the electrosprayed droplet size distribution experimentally and used it as the basis for a Monte Carlo model of the complete ES-CPC detector. To the SEC buffer we added a known concentration of sucrose and used a simple syringe pump to electrospray this solution at the same flow rate and current as in the SEC work. The droplet size distribution was obtained from the electrical-mobility size distribution of the dried aerosol particles and the known sucrose concentration.

The electrical-mobility size distribution of the dry residue was measured using a scanning mobility particle sizing system (SMPS; TSI Model 3934U) in the scanning method described by Wang and Flagan.[19] In this method, the aerosol is first brought into charge equilibrium.[20] It then enters a continuous-flow differential mobility analyzer[21] (DMA; TSI Model 3071) which allows aerosol particles within a scannable narrow band of electrical mobilities to pass through. A CPC (TSI Model 3025A-S) detects the residue particles and also controls the scanning of the DMA, an IBM PC-compatible computer is used for data acquisition and analysis. By use of the known flows, the SMPS software converts CPC counts to aerosol particle concentration, at the same time making corrections for the known equilibrium charge distribution.[19,20]

Figure 8 shows a typical measured SMPS size distribution for particles from the electrosprayed sucrose solution. The small lobe on the large-diameter side of the main peak (seen in Figure 8) appeared consistently. Without further analysis, this lobe is believed to be due to multiples from diffusive coagulation of the aerosol.[15] The distributions were fitted by least squares to a log-normal distribution function, excluding

(19) Wang, S. C.; Flagan, R. C. *Aerosol Sci. Technol.* **1990**, *13*, 230.
(20) Fuchs, N. A.; *Geofis. Pura Appl.* **1963**, *56*, 185.
(21) Knutson, E. O.; Whitby, K. T. *J. Aerosol Sci.* **1975**, *6*, 443. Knutson, E. O.; Whitby, K. T. *J. Aerosol Sci.* **1975**, *6*, 453.

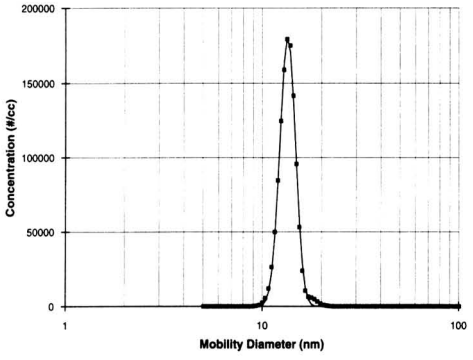

Figure 8. Measured size distribution of dried residue particles for 0.1% (v/v) sucrose solution in SEC buffer electrosprayed at 50 nL/min. The fitted log-normal distribution has zero baseline and excludes the shoulder at 19 nm. See text for details.

the "doublet lobe" just to the right of the peak in Figure 8. The coefficient of determination (r^2) in the fits in every case exceeded 0.99. Due to the narrowness of the peak, equally good fits could have been obtained using a normal distribution. Under electrospray conditions where larger droplets were formed, the log-normal distribution generally produced a better fit[22] than the normal distribution. Unlike the normal distribution, the log-normal distribution does not imply negative diameters. It contains a larger proportion of large droplets than the normal distribution and is thus a "worst case" for the concerns prompting these measurements. For these reasons, the model used only the results from fitting to a log-normal distribution.

The count median electrical-mobility diameter for the sucrose residue averaged 13.4 nm over 12 runs, and the natural logarithm of geometric standard deviation[15] $\ln(\sigma_g)$ averaged 0.094. The sucrose concentration was 0.1% (v/v). If the dry residue particles and droplets were both spherical, their diameters scaled as the cube roots of their volumes. Accordingly, we assumed that the primary droplet distribution was also log-normal, with median diameter 13.4 nm/$[0.1\%)^{1/3}]$ = 134 nm and $\ln(\sigma_g)$ = 0.094 (σ_g is dimensionless and scale-invariant[15]). This method of drop size determination has been tested over a range of sucrose concentrations from 2.5 ppm to 10% and the cube-root-law scaling was found to hold extremely well.

ES-CPC Detector Model. "Droplets" were "generated and processed" by a Monte Carlo method as follows. For each droplet, a primary diameter was picked from pseudorandom log-normal deviates[22] having median 134 nm and $\ln(\sigma_g)$ = 0.094. The expected mean number of molecules was calculated, for droplets of this diameter, from the product of the droplet volume and the molecular concentration. The actual number of molecules in the droplet was then drawn from pseudorandom Poisson deviates[22] having this mean value. The total volume of the dry residue particle was calculated from the sum of volumes of the macromolecule(s) (if any) and nonvolatile dissolved material. Then the diameter of the residue particle was calculated under the simplifying assumption that it was spherical.

(22) Press, W. H.; Flannery, B. P.; Teukolsky, S. A.; Vetterling, W. T. *Numerical Recipes in Pascal*; Cambridge University Press: New York, 1989; Chapter 7.

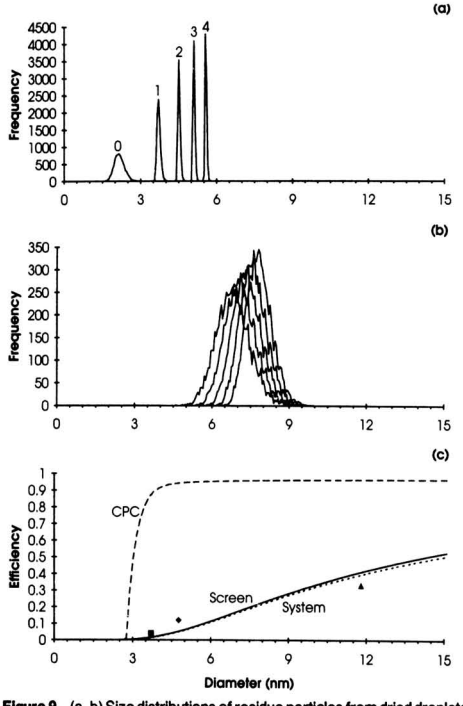

Figure 9. (a, b) Size distributions of residue particles from dried droplets containing 0–4 MYO molecules with (a) 4 or (b) 128 ppm (v/v) dissolved nonvolatile material. Any roughness in the plots is due to the limited number of simulated particles. (c) Screen penetration probability, CPC detection probability, and their product as a function of particle diameter over the same range. In (c) the measured values of screen penetration are shown for the three molecules studied, assuming the dried residue particles to have specific gravity of MYO, 1.34 (square); OVA 1.30 (diamond); THYRO 1.30 (triangle), and assuming a 4 ppm (v/v) nonvolatile solute contribution to the particle size.

As an example, size distributions from our model for residue particles with 0, 1, 2, 3, and 4 MYO molecules are shown in Figure 9 at low and high concentrations of nonvolatiles. For sufficiently low nonvolatile solute levels (Figure 9a), the size distributions of the residues from single-macromolecule droplets are resolved from those of "empty" droplets. For high levels of nonvolatile solutes (Figure 9b), these size distributions become unresolved. Therefore, to achieve single-molecule detection by this method, nonvolatile materials in the buffer must be kept to a minimum.

The probability of detection for a given size aerosol particle is the product of the screen penetration probability and the CPC detection probability. We used the screen penetration formula of Cheng and Yeh[14] and the semiempirical CPC response formula of Kesten et al.[17] to calculate these quantities and thus the detection probability for the dried droplet residue (Figure 9c). For each residue particle in the model, a uniformly distributed random deviate on [0, 1] was generated; if its value was less than the detection probability, the droplet was scored as "detected", otherwise as "not detected". In this manner we could fully simulate according to primary droplet

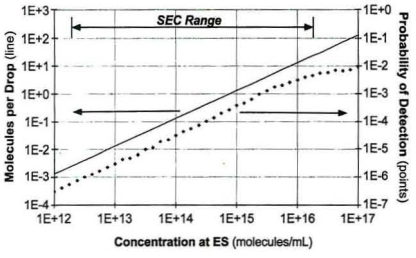

Figure 10. Points: probability of detection of the residue from a randomly chosen electrosprayed droplet versus MYO concentration *in the eluting peak*. The Monte Carlo model results have been multiplied by a factor of 0.015, the fraction of the aerosol inspected. Line: mean number of molecules per droplet from the model. Range line indicates the concentration range of MYO studied in the SEC work, calculated from the injections by assuming Gaussian peaks and no losses in the liquid phase. The model assumed 4 ppm (v/v) of nonvolatile salts.

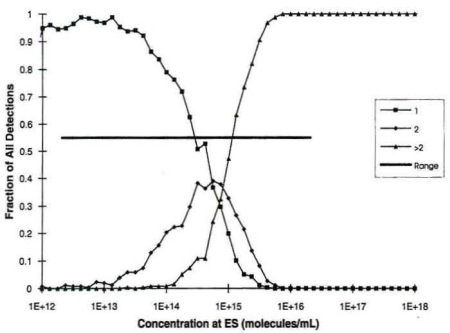

Figure 11. Fraction of simulated detections arising from droplets containing 0, 1, 2, and more than 2 MYO molecules. The bold horizontal line shows the range of MYO concentrations in the SEC work. The roughness is due to the limited number of particles simulated.

size, dry particle size, and detection probability what the expected response should be for any given particle generated by the electrospray.

For each set of conditions (molecular concentration, etc.) considered, we generated and processed droplets in this manner until a total of 256 detections was recorded. The number of detections and nondetections of droplets containing 0, 1, 2, and more than 2 macromolecules, and the number of droplets generated, were also recorded.

The number concentration of MYO was the highest of those in the SEC work reported; therefore, MYO is a "worst case" for the concerns prompting the model calculations. Thus the discussion here focuses on the MYO simulation results. The OVA and THYRO cases involved lower molecular concentrations, and these larger molecules are better resolved from the empty-droplet residues. In fact, THYRO never reaches multiple molecules per drop and OVA crosses this threshold only for the uppermost point on the calibration curve. The model results for OVA and THYRO did not lead to any new conclusions.

The number of detections in this model, per droplet generated, multiplied by a factor of 0.015 to account for the ratio of inspected aerosol to total electrospray air flow, is shown in Figure 10 as a function of the macromolecule concentration for MYO at low (4 ppm) nonvolatile solute levels. The mean number of molecules per droplet from the model is also shown. The range of concentrations in the SEC work, from the highest peak concentration to S/N = 3, is indicated by the bold horizontal line on the figure. The peak concentration was calculated from the parameters of the injection and the observed elution peak width, assuming Gaussian peaks but neglecting any loss of macromolecules while in the liquid phase. The linearity of the response, which holds as expected when the mean number of molecules per droplet was less than unity, was shown by the model to extend well into the region where the mean number of molecules per droplet was greater than unity, confirming the existence of a compensating mechanism in the response of the detector with diffusion screen. As will be seen below, integration to obtain total peak area extended the linear region somewhat further.

Figure 11 shows the fraction of detections, according to the model, arising from droplets containing 1, 2, and more than 2 MYO molecules. The range of MYO concentrations in the SEC work, calculated as in Figure 10, is also shown. Single-molecule detection dominates from the limit of detection up to about 10^{15} MYO molecules/mL.

The concentration of analyte molecules is higher at the center of the eluting peak and lower in the wings. Figure 10 shows how the detector overall response declines at high concentrations. To make a direct comparison with the experimental values of SEC peak area versus molecules injected, we fitted an interpolation function to the Monte Carlo results to represent the concentration response shown in Figure 10 and calculated the integral of the response to Gaussian peaks of fwhm = 0.8 min (the experimental value found at low concentration) in the macromolecule concentration of the eluting stream. Figure 6 shows the results. The use of peak area extends the linear response beyond that found for concentration (or peak height) to include the entire range of the experiments. The SEC linearity data are also shown in the figure. The agreement of the slopes is excellent, but the results show losses unaccounted for in the model.

Detection Efficiency and Losses. The model accounts for losses due to the following: (1) the fraction of aerosol flow inspected by the CPC (1.5%); (2) the theoretical diffusion screen penetration; (3) the literature values for the CPC detection probability. When the losses included in the model are taken together, the maximum detection probability is 5.2×10^{-3} for THYRO, 6.3×10^{-4} for OVA, and 2.2×10^{-4} for MYO. Nonetheless, even after allowing for all of the losses implicit in the model, a majority of the injected protein is unaccounted for. Only 1 in 4 THYRO molecules injected can be accounted for, while the corresponding ratio is 1 in 9 for OVA and 1 in 11 for MYO (the difference between the model line and calibration line in Figure 6). The unaccounted for losses increase when the measured screen penetrations are used instead of the theoretical. Penetration of the proteins through the screen was determined experimentally to be 33% for THYRO, 12% for OVA, and 4.0% for MYO. These values are represented by symbols in Figure 9c. The trend and order of magnitude are as predicted, though the absolute values do not agree with the theoretical screen penetration for spheres. In view of experimental uncertainty, this disagreement is not surprising. If instead of the theoretical diffusion screen

penetration, we use the empirical values listed above, the ratios of expected signal to experimental signal becomes, respectively, 1 in 3.2 (THYRO), 1 in 21 (OVA), and 1 in 27 (MYO).

These unaccounted for and size-dependent losses may arise from several sources. First, the positively charged electrosprayed effluent must pass, assisted by the air flow, through an orifice at the negative bias of the mixing chamber. Nonquantitative experiments on similar apparatus, in which fluorescein dye solution was electrosprayed, showed that a significant amount of dye was collected on the orifice plate. This is probably the most significant loss mechanism. Losses here would be mobility dependent and, therefore, size dependent, which would agree with higher losses for smaller proteins. Another possible loss of signal could come from incomplete neutralization of the charge on the analyte aerosol. If the α emitter does not fully equilibrate the charge carried by the electrospraygenerated aerosol, some particles will be lost to the walls of the electrospray chamber or to the walls of the connecting tubing. Third, there are several unions and tees in the connecting tubing that create turbulent flow paths for the air carrying the analyte to the CPC. If the analyte comes in close proximity to a wall, it will be retained by adsorption to the wall. Lastly, a probable contribution to signal loss is adsorption to the column and stationary phase. Work in the Jorgenson laboratory has shown adsorption to be a serious problem when CZE of proteins is attempted with this mobile phase. While the column surface-to-volume ratio is lower with SEC and would not pose as severe a problem as with CZE, the packing material has an enormous surface area which cannot be ignored as having possible adsorption sites. These four major loss mechanisms, passage through the orifice, charge, adsorption to connecting tubing, and adsorption to the column, combine to reduce the transmission of analyte to the CPC.

In order to truly evaluate the capabilities of this detector principle, the chromatographic system should be modified to assure there is no loss of sample before the electrospray. An obvious sample loss is the dilution by 2 L/min air and the fact that only 30 mL/min is sampled. It would be ideal to sample 100% of the electrospray effluent, but this will require a major revision of the CPC. To solve the other problems it will be necessary to improve the ES-CPC unit to minimize the loss between the electrospray needle and the condenser inside the CPC, perhaps in part by minimizing the length of connecting tubing. The diffusion screen might be eliminated by changing the temperatures of the CPC saturator and condenser. By shortening connections, increasing neutralizer power, and isolating losses, it should be possible to significantly increase the signal throughput from the electrospray to the CPC. Because the CPC is counting single molecules, the ultimate theoretical detection limit is 1 molecule injected. Although it is not presently possible to envision a detection limit of a few molecules injected for an aqueous salt-based system because of background arising from nonvolatile residue, many ways are available to increase the efficiency of the detection system. As shown by the model and confirmed by experience, it is important to avoid *nonvolatile* salts in the buffer above the ppm range. As this work has shown, volatile salts may be used; a change from ammonium acetate to triethylamine, ammonium carbonate, ammonium hydroxide, or acetic acid does not produce a noticeable change in background.

The only significant problem encountered thus far occurred with the use of silica-based columns. An attempt was made to use Zorbax GF450 as a SEC stationary phase since it has proven to be an efficient size exclusion phase for proteins.[12] Even though the silica has a diol silane coating, enough nonvolatile residue was produced to yield 25 times the normal background. This test was not conclusive, yet it indicates more work must be performed before a silica-based packing support can be used for an aqueous SEC separation with the ES-CPC detector.

The ES-CPC is also promising as a detector for other separation modes. The flow rates through the electrospray needle are comparable with those in capillary zone electrophoresis. In fact, preliminary results using a 15-μm-i.d. CZE capillary show a decrease in background and an over 1 order of magnitude increase in peak height relative to the results reported for SEC. The exact capability of the ES-CPC is currently being determined for CZE. Another promising application for the ES-CPC is the analysis of synthetic polymers. The lack of salt and the lower surface tension of traditional mobile phases used for synthetic polymers, such as tetrahydrofuran, should yield background and detection limits significantly below those observed for biopolymers. We are currently investigating the potential application of ES-CPC to the analysis of both nonpolar and polar synthetic polymers.

ACKNOWLEDGMENT

We thank Alltech for the donation of the HEMA 1000 packing material and Rockland Technologies for the donation of the Zorbax GF450 packing material. Support for this work was provided by the National Institutes of Health under Grant GM-39515.

Received for review October 13, 1993. Accepted April 21, 1994.•

• Abstract published in *Advance ACS Abstracts,* June 1, 1994.

Anal. Chem. **1994,** *66,* 2293–2301

Elucidation of Species in Alcohol–Water Mixtures Using Near-IR Spectroscopy and Multivariate Statistics

M. Kathleen Alam*,† and James B. Callis

Center for Process Analytical Chemistry, Department of Chemistry, B-10, University of Washington, Seattle, Washington 98195

High precision near-infrared spectroscopy in the wavelength region 1100–1800 nm was used to provide data on the intermolecular interactions of alcohols and water. This data can be used to further refine alcohol/water composition diagrams as an aid to understanding gradient elution in reversed-phase chromatography using an alcohol/water mixture as a mobile-phase system. The spectral data were analyzed using multivariate model-based regression. Within the approximation of the ideal associated solution model, a lower limit on the number of alcohol/water complexes was determined. Additionally, the spectra, stoichiometry, and equilibrium constants governing the interrelationships of the pure species and their complexes were obtained. The spectroscopic data were consistent with four species in the alcohol/water composition diagrams. While a 1:1 alcohol/water complex is observed at high alcohol concentrations, a complex involving a higher number of waters becomes important at low alcohol concentration. This latter species may explain the unusual elution behavior patterns obtained when using low alcohol concentrations in reversed-phase chromatography.

Condensed-phase mixtures and blends seldom behave ideally. Due to intercomponent interactions and complex formation, the properties of mixtures are found to depend nonlinearly on the amounts of added components. In reversed-phase chromatography, the behavior of the mobile-phase mixture is of particular importance, since the distribution of a solute between stationary and mobile phases determines a solute's retention time. For normal-phase (nonpolar mobile-phase) systems, there are several theories that attempt to describe the distribution of a solute in each phase.[1,2] These theories have not always been adequate for reversed-phase (polar mobile-phase) systems. Katz et al.[3] extended earlier distribution theories to reversed-phase systems by treating the mobile phase, such as methanol–water, as a ternary system composed of unassociated water, unassociated methanol, and a 1:1 complex of methanol and water. In later work, Katz and co-workers[4] noted that, during gradient elution of water and methanol on reversed-phase chromatography columns, the elution characteristics of certain solutes do not vary linearly with the nominal concentrations of water and methanol. Using the volume of mixing and the index of refraction measurements, an equilibrium constant for the complexation of water and methanol was derived.[4] The distribution of certain solutes between the mobile and stationary phases was found to be dependent on the concentration of the methanol that was unassociated with water.

While the above work provides an ample demonstration of the utility for investigating complexation behavior in mixtures, additional information on the nature of the complexes is desirable. In this paper, we apply vibrational spectroscopy and multivariate statistical analysis to this task. Infrared and near-infrared absorption spectroscopies have been used to elucidate the numbers and types of molecular complexes,

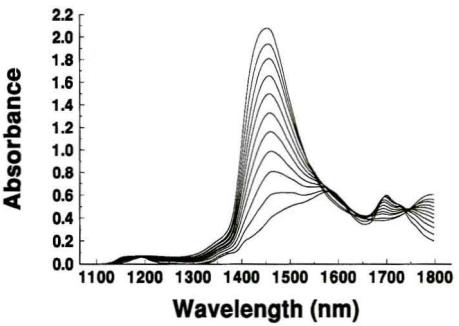

Figure 1. Absorbance spectra, 1100–1800 nm, illustrating water and alcohol mixtures. Eleven spectra from each set of mixtures are shown from the methanol data set. The band at 1450 nm increases with increasing water concentration, while bands between 1600 and 1750 nm increase with increasing alcohol concentration.

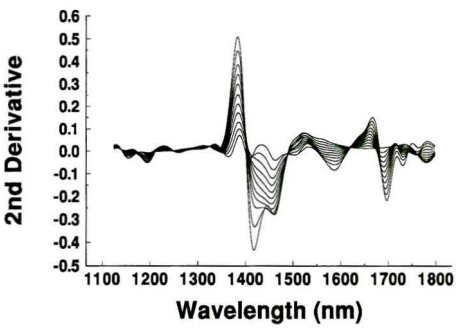

Figure 2. Second derivative transformations of methanol/water spectra. Eleven transformed spectra from the set are shown. Bands between 1600 and 1750 nm are distinctly different for each alcohol.

† Present address: Sandia National Laboratories, Dept. 1823, MS 0343, Albuquerque, NM 87185.

(1) Snyder, L. R.; Poppe, H. *J. Chromatogr.* **1980,** *184,* 363–416.
(2) Scott, R. P. W. *J. Chromatogr.* **1976,** *122,* 35–53.
(3) Katz, E. D.; Ogan, K.; Scott, R. P. W. *J. Chromatogr.* **1986,** *352,* 67–90.
(4) Katz, E. D.; Lochmüller, C. H.; Scott, R. P. W. *Anal. Chem.* **1989,** *61,* 349–355.

0003-2700/94/0366-2293$04.50/0
© 1994 American Chemical Society

especially when hydrogen bonding is involved.[5-7] Yet, the lack of resolution in the data often prevents unambiguous recovery of the spectra associated with the different species. In principle, using multivariate techniques, it is possible to overcome resolution limitations and extract information concerning the number of the spectrally different complexes. Of particular value in infrared/equilibria experiments are the approaches of evolving factor analysis[8] and model-based regression.[9-11]

In this work, the above methods are employed to study near-infrared spectra of alcohol and water mixtures over a wide range of concentrations. Using evolving factor analysis and examining the loadings and scores from principal components analysis, the number of spectroscopically distinguishable species is determined. The stoichiometric nature of the complexes is determined using model-based regression. For the methanol and water solutions studied, we find not only the 1:1 complex proposed by Katz et al.[4] but also a species involving a greater number of waters as well. This complex appears at low methanol concentrations and arises from the disruption of hydrogen bonding between bulk water molecules caused by the hydrophobic alkyl portion of the alcohol. Experimental data show that longer chain alcohols cause a greater change in bulk water hydrogen bonding. The results of these studies are used to explain the elution behavior of water/methanol gradients.

EXPERIMENTAL SECTION

Methanol, ethanol, 2-propanol, and 1-propanol were reagent grade, obtained from J. T. Baker. Water was distilled in-house. Quantitative mixtures of alcohol and water were prepared by weight using grade-A volumetric flasks. Alcohol concentration was varied from 0 to 100%, in approximately 5% steps, for a total of 20–21 solutions per alcohol. Near-infrared absorbance spectra were collected using a NIRSystems (formerly Pacific Scientific) 6250 scanning spectrometer over the wavelength range of 1100–2500 nm to acquire a total of 700 data points. Data analysis was limited to 1100–1800 nm to avoid the 1900-nm water band, whose high absorbance values were greatly distorted by stray light. Solutions were placed in a quartz cuvette with a path length of 1.6 mm. All spectra were referenced to an empty cuvette. Temperature remained constant to 1 °C throughout the experiment. Spectra were the result of averaging 64 scans, with the total collection time being approximately 30 s (~2 scans/s). The NIRSystems software package,[12] running on an IBM AT-compatible computer, was used for calculating second derivative transformations of the spectra using a segment size of 20 nm and a gap size of 20 nm. Data were then transferred to mainframe systems for further analysis. Fitting routines were developed on a VAX/VMS system running under VMS version 4.7 using the computing environment MATLAB.[13] Modules for singular value decomposition, Newton–Raphson root-finding, and Nelder–Meade simplex were used as supplied by MATLAB. Some polynomial expressions were simplified using the SOLVE routine available in the interactive package MACSYMA, run on a UNIX platform.

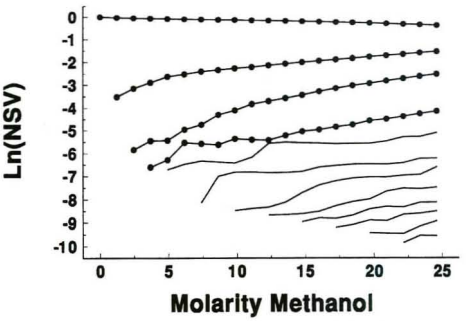

Figure 3. Evolving factor analysis of the second derivative methanol spectral data. Shown is the natural logarithm of normalized singular values [ln(NSV) versus alcohol concentration (M). Noise is estimated to appear at ln(NSV) ≈ −7. Using this plot, rank was estimated to be 4 or 5.

THEORY

Associative Models. Many models have been used to describe alcohol/water behavior in terms of properties such as partial molar volume. At infinite dilution, Monte Carlo calculations have been used to infer structure and thermodynamic properties. For finite dilutions systems, two approaches are often taken. Mathematical approaches, such as the Kirkwood–Buff integral, and power series expansions based on the McMillan–Mayer theory have been used to approximate the data. For alcohol/water mixtures, these approaches have not always been satisfactory due to the large number of parameters required and the lack of physical significance of those parameters.[14] The second approach considers the solution as a chemical system of associated and unassociated molecules in equilibrium. In a further simplification, only a small number of species are considered, and activity effects are neglected. Known as the ideal associated solution model, this model proves satisfactory for finite dilution mixtures because it focuses on the solute–solvent interactions. For the present study, two chemical models based on the ideal associated solution, a single association model[4] and a double association model,[15] were examined and are described below.

Single Association Model. The single association model proposed by Katz and co-workers[4] is depicted in eq 1

$$ROH + H_2O \rightleftharpoons ROH(H_2O) \qquad (1)$$

where R represents the alkyl group and $ROH(H_2O)$ represents the hydrogen-bonded alcohol/water complex. The equilibrium

(5) Falk, M.; Hartman, K. A., Jr.; Lord, R. C. *J. Am. Chem. Soc.* **1963**, *85*, 387–394.
(6) Kobayashi, M.; Matsushita, R. *J. Phys. Chem.* **1990**, *94*, 2789–2784.
(7) Li, Y.-S.; Jeng, M.-L. H. *J. Chem. Educ.* **1988**, *65*, 920–922.
(8) Cartwright, H. *J. Chemom.* **1987**, *1*, 111–120.
(9) Sylvestre, E. A.; Lawton, W. H.; Maggio, M. S. *Technometrics* **1974**, *16*, 353–368.
(10) Shrager, R. I. *Siam J. Alg. Disc Methods* **1984**, *5*, 351–358.
(11) Frans, S. D.; Harris, J. M. *Anal. Chem.* **1985**, *57*, 1728–1721.
(12) Pacific Scientific Co. Gardener/Neotec Instrument Division Multilinear Regression Analysis, Silver Springs, MD, 1987.
(13) The Mathworks Inc. PRO-MATLAB for VAX/VMS Computers, Sherborn, MA, 1989.
(14) Roux, A. H.; Desnoyers, J. E. *Proc. Indian Acad. Sci.* **1987**, *98*, 435–451.
(15) Dethlefsen, C.; Sorensen, P. G.; Hvidt, A. *J. Solution Chem.* **1984**, *13*, 191–203.

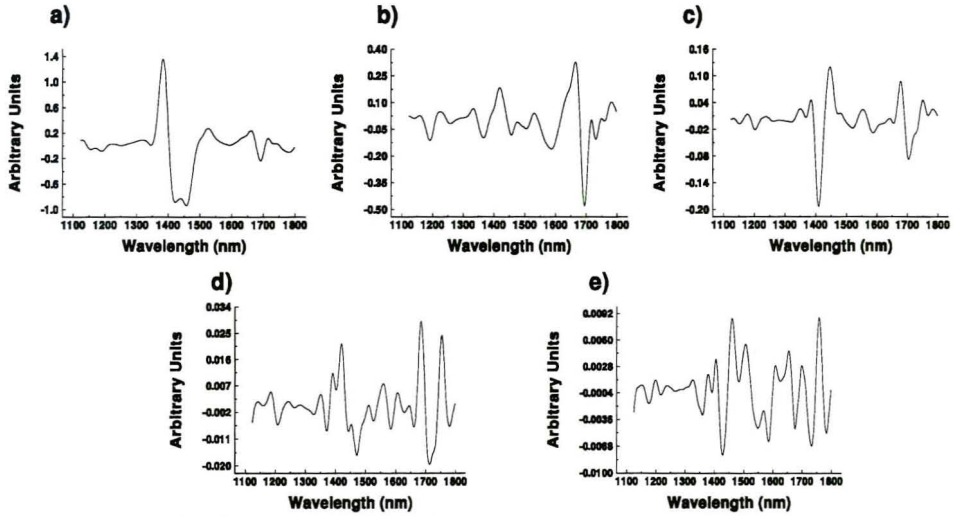

Figure 4. Loadings from principal components analysis of second derivative spectral data from methanol (a) loading 1, (b) loading 2, (c) loading 3, (d) loading 4, and (e) loading 5. All loadings appear to contain information.

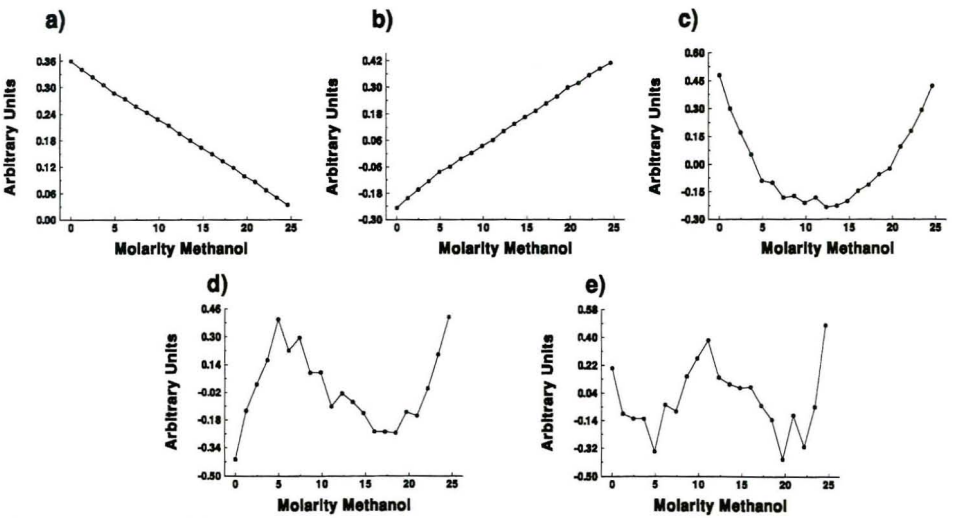

Figure 5. Scores from principal components analysis of second derivative data from methanol: (a) vector 1, (b) vector 2, (c) vector 3, (d) vector 4, and (e) vector 5. While all scores vectors appear to be non random, vector 5 was not reproducible for a repeat data set, thus rank was estimated to be 4.

constant κ is given by

$$\kappa = \frac{\chi_{(alc)(H_2O)}}{\chi_{(alc)}\chi_{(H_2O)}} \tag{2}$$

where concentrations have been expressed in mole fraction. The mass balance equations for this system are

$$\chi^{\circ}_{(alc)} = \chi_{(alc)} + \chi_{(alc)(H_2O)} \tag{3}$$

and

$$\chi^{\circ}_{(H_2O)} = \chi_{(H_2O)} + \chi_{(alc)(H_2O)} \tag{4}$$

where $\chi^{\circ}_{(alc)}$ is the original added mole fraction of alcohol, $\chi^{\circ}_{(H_2O)}$ is the original added mole fraction of water, $\chi_{(alc)}$ is the resultant mole fraction of alcohol, $\chi_{(H_2O)}$ is the resultant mole fraction of water, and $\chi_{(alc)(H_2O)}$ is the resultant mole fraction of the 1:1 complex. The mole fraction of each species can then be expressed in terms of κ, $\chi^{\circ}_{(alc)}$, and $\chi^{\circ}_{(H_2O)}$. Solving

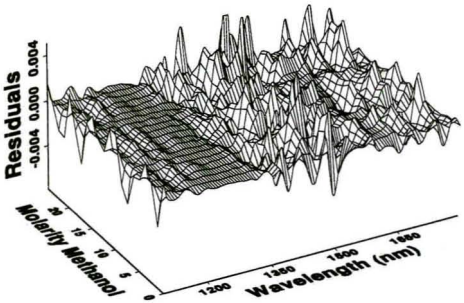

Figure 6. Residuals remaining after removal of the first four eigenvectors from the second derivative methanol spectral matrix. The residuals were sufficiently random enough to warrant reduction to rank 4.

for a positive concentration of the $\chi_{(alc)(H_2O)}$ complex using eqs 2–4 gives

$$\chi_{(alc)(H_2O)} = \frac{(\kappa\overset{\circ}{\chi}_{(alc)} + \kappa\overset{\circ}{\chi}_{(H_2O)} + 1) + ((\kappa\overset{\circ}{\chi}_{(alc)} + \kappa\overset{\circ}{\chi}_{(H_2O)} + 1)^2 - 4\overset{\circ}{\chi}_{(alc)}\overset{\circ}{\chi}_{(H_2O)}\kappa^2)^{1/2}}{2\kappa} \quad (5)$$

Once the solution for the mole fraction of the 1:1 complex is obtained, the free alcohol and free water are easily solved for using eqs 3 and 4.

Double Association Model. A double association model for alcohol/water systems,[15] which describes hydrophobic and hydrophilic equilibria, was also examined. One interaction occurs between the hydrophobic end of the alcohol molecule and the bulk water (see eq 6). The other association involves the hydrogen bonding of water with the hydroxyl end of the alcohol molecule and results in an equation identical to eq 1.

$$ROH + \eta H_2O \rightleftharpoons (ROH)(H_2O)_\eta \quad (6)$$

This model is an extension of the single association model, with the addition of the hydrophobic interaction. The mass balance equations and equilibrium constants for the double equilibrium association model are

$$\overset{\circ}{\chi}_{(alc)} = \chi_{(alc)} + \chi_{(alc)(H_2O)_\eta} + \chi_{(alc)(H_2O)} \quad (7)$$

$$\overset{\circ}{\chi}_{(H_2O)} = \chi_{(H_2O)} + \eta\chi_{(alc)(H_2O)_\eta} + \chi_{(alc)(H_2O)}$$

$$\kappa_1 = \frac{\chi_{(alc)(H_2O)_\eta}}{\chi_{(alc)}\chi^{\eta}_{(H_2O)}} \quad (8)$$

$$\kappa_2 = \frac{\chi_{(alc)(H_2O)}}{\chi_{(alc)}\chi_{(H_2O)}}$$

A polynomial expression with variable $\chi_{(H_2O)}$ and constants $\overset{\circ}{\chi}_{(alc)}$, $\overset{\circ}{\chi}_{(H_2O)}$, κ_1, and κ_2 was derived using the SOLVE routine in MACSYMA:

$$0 = \kappa_1\chi^{\eta+1}_{(H_2O)} + (\eta\kappa_1\overset{\circ}{\chi}_{(alc)} - \kappa_2\overset{\circ}{\chi}_{(H_2O)})\chi^{\eta}_{(H_2O)} + \kappa_2\chi^{2}_{(H_2O)} + (1 + \kappa_2\overset{\circ}{\chi}_{(alc)} - \kappa_2\overset{\circ}{\chi}_{(H_2O)})\chi_{(H_2O)} - \chi_{(H_2O)} \quad (9)$$

Roots of this polynomial were estimated using the Newton–Raphson method.

Evolving Factor Analysis. Evolving factor analysis not only allows an estimation of rank but also provides visual

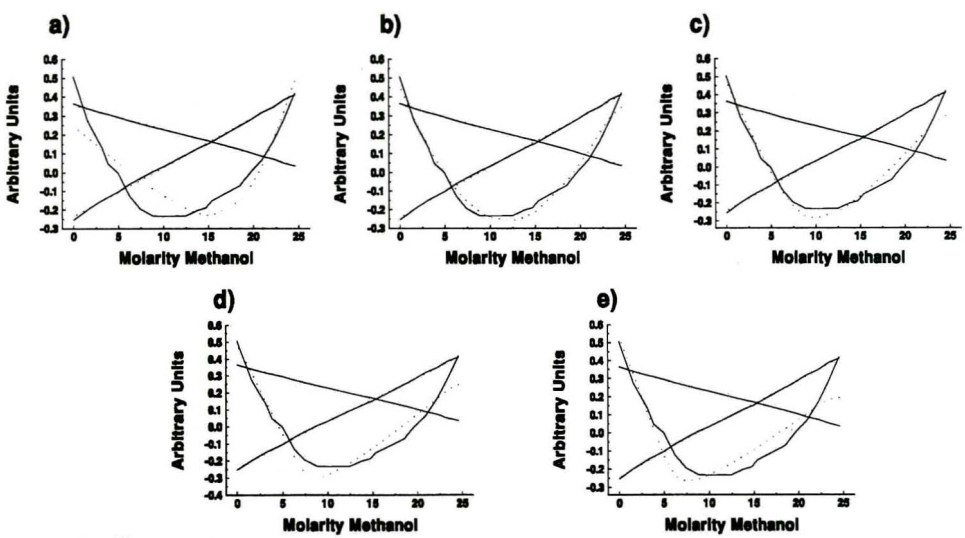

Figure 7. Fit to $\bar{V}$ matrix for single association model,[4] for varying numbers ofwater molecules: one alcohol and (a) one water, (b) two water, (c) three water, (d) four water, and (e) five water molecules. The solid line (–) represents the first three vectors of $\bar{V}$ while the dotted line (···) represents the first three vectors of $\hat{V}$. The fit to the third vector was not satisfactory for all alcohol complexes.

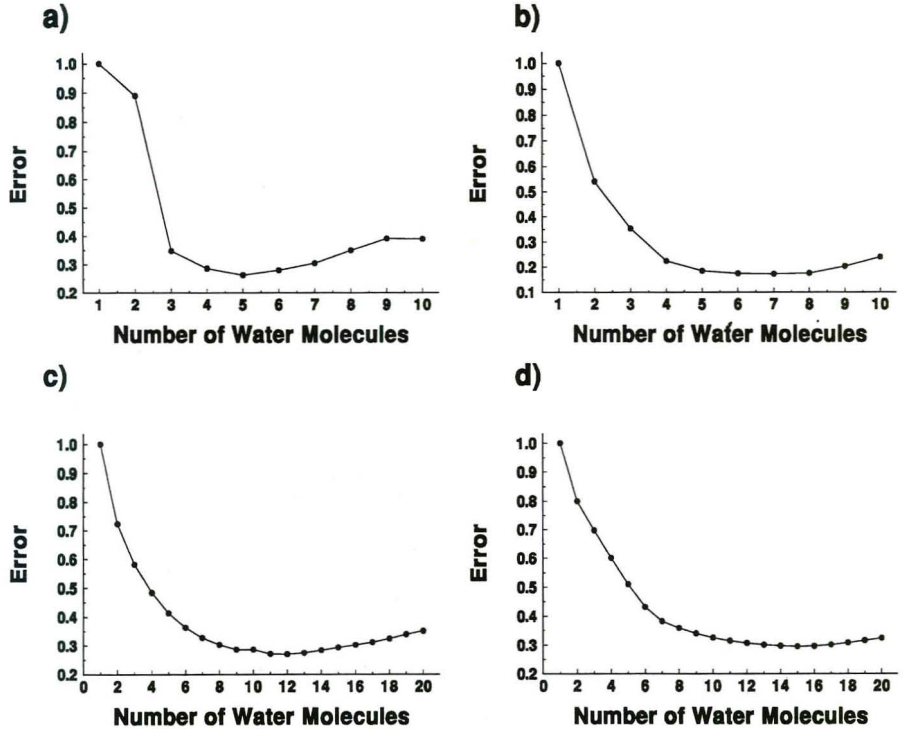

Figure 8. Minima in error function plotted versus the number of waters (η) for the double association model: (a) methanol, (b) ethanol, (c) 2-propanol, and (d) 1-propanol.

interpretation of the progression of a titration. The detailed procedure of evolving factor analysis has been described previously.[8] Briefly, steps include ordering the spectra according to alcohol concentration. Next, successive sets of data are created by appending spectra to the previous set, such that the first set consists of spectrum 1, the second set of spectra 1 and 2, and so on. Normalized singular values are then determined for each set and plotted versus alcohol concentration.

Iterative Modeling. Model-based regression[9] was used to interpret the spectroscopic data in terms of the two associative models. Given the spectra from a set of mixtures made from known components and proportions, the problem is to determine the number of species involved (original components and their associations) and the molar extinction coefficients of each; i.e., given a spectral data matrix, **R**, with dimensions m by p, determine the equilibrium constants, κ, a concentration matrix, **C**, dimensions m by a, and matrix of pure component spectra, **S**, dimensions a by p. Indices m, p, and a represent the number of samples, the number of digitized spectral points collected and the number of distinguishable, independently varying components, respectively. The spectral data matrix is represented as the product of the concentration matrix and the matrix of pure component spectra:

$$\mathbf{R} = \mathbf{CS} + \mathbf{E} \tag{10}$$

where **E** is an m by p error matrix.

The spectral data matrix, **R**, is then rank reduced to eliminate noise in the data and decrease calculation time[11] and is represented in terms of its singular value decomposition:

$$\bar{\mathbf{R}} = \bar{\mathbf{V}}\bar{\mathbf{\Sigma}}\bar{\mathbf{U}}^{\mathrm{T}} \tag{11}$$

where bars represent the rank reduced matrices. Rank reduction is carried out by evolving factor analysis and/or by examination of scores and loadings for their noise content. $\bar{\mathbf{U}}$ is a p by a dimension matrix of eigenvectors from $\mathbf{R}^{\mathrm{T}}\mathbf{R}$, and $\bar{\mathbf{V}}$ is an m by a dimension matrix of the eigenvectors of $\mathbf{R}\mathbf{R}^{\mathrm{T}}$. The diagonal a by a matrix, $\mathbf{\Sigma}$, contains the corresponding singular values.

The matrix $\bar{\mathbf{V}}$ contains information regarding the concentration variations of the system. A rotation matrix, **H**, can be estimated that transforms **C** into $\bar{\mathbf{V}}$:

$$\bar{\mathbf{V}} = \mathbf{CH} \tag{12}$$

The least-squares estimate of **H** is given by

$$\hat{\mathbf{H}} = (\mathbf{C}^{\mathrm{T}}\mathbf{C})^{-1}\mathbf{C}^{\mathrm{T}}\bar{\mathbf{V}} \tag{13}$$

where **C** is originally estimated with an initial guess for κ. The estimated rotation matrix can then be used to calculate an estimate of $\bar{\mathbf{V}}$:

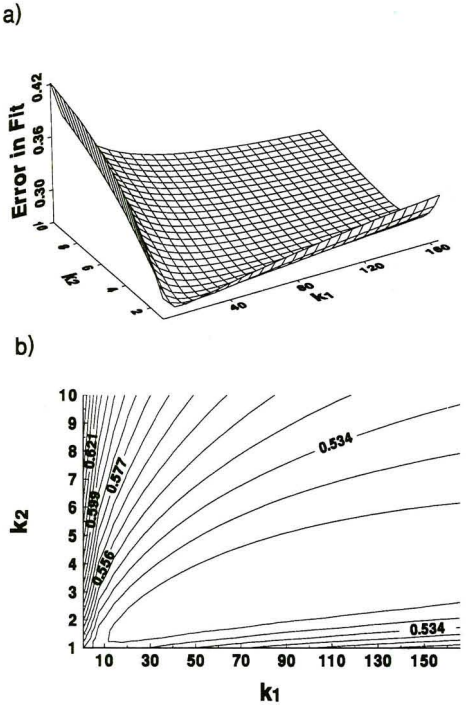

Figure 9. (a) Three-dimensional plot of the error function (eq 15) from methanol using the double association model, for $\eta = 5$. (b) Two-dimensional contour of the same data. Square root of the error is plotted versus the equilibrium constants κ_1 and κ_2. Note the long curved valley.

$$\hat{\mathbf{V}} = \mathbf{C}\hat{\mathbf{H}} \tag{14}$$

The estimate $\hat{\mathbf{V}}$ is compared to $\bar{\mathbf{V}}$ and the error

$$\|\hat{\mathbf{V}} - \bar{\mathbf{V}}\| \tag{15}$$

is minimized iteratively, by altering values of κ, computing new concentration matrices, and new estimates of $\hat{\mathbf{H}}$. Once the optimum estimates of $\hat{\mathbf{H}}$ and κ are calculated, the corresponding estimate of $\hat{\mathbf{S}}$, estimates of the pure spectral components, can be found by replacing $\bar{\mathbf{V}}$ in eq 11 with $\mathbf{C}\hat{\mathbf{H}}$:

$$\hat{\mathbf{R}} = \mathbf{C}\hat{\mathbf{H}}\bar{\Sigma}\bar{\mathbf{U}} = \mathbf{C}\hat{\mathbf{S}} \tag{16}$$

Factoring out the concentration dependence provides an estimate of the pure component spectra. The error in κ is estimated by adding varying amounts of noise to the spectral data and calculating new estimates of κ.

RESULTS AND DISCUSSION

Spectroscopy. Figure 1 shows the spectra of methanol in water over the wavelength range of 1100–1800 nm. Ethanol, 1-propanol, and 2-propanol spectra are provided in the supplementary material (Figure a1–a3). The concentration of alcohol ranges from 0 to 100% alcohol. Bands from water and alcohol are evident in the spectra. At 1420 nm is a water combination band, assigned to $\upsilon_1 + \upsilon_3$, where υ_1 refers to the symmetric stretching mode of water and υ_3 refers to the antisymmetric stretching mode of water.[16] The first overtone of the C-H stretches from the methyl groups are present at 1698 and 1705 nm. In the spectra from the higher order alcohols, the first overtone of the C-H stretches from the methylene groups are visible at 1725 and 1765 nm. The first overtone (2υ) of the O-H stretch from the alcohol is at 1400 nm.[17] Bands at 1515 and 1530 nm are thought to arise from combination bands of OH fundamental stretching modes at 2750 nm and CH fundamental stretching modes at 3370 and 3480 nm, respectively.[18,19] Second derivative transforms of the data were used for further data analysis to alleviate baseline effects and to aid in the separation of spectral features.[20] The transformed data from the spectra of methanol and water are shown in Figure 2. The transformed data from ethanol, 1-propanol, and 2-propanol are provided in the supplementary material (Figure b1–b3).

Determination of Rank. Evolving factor analysis (EFA) was performed on the four second derivative data sets. Results from the methanol data set are shown in Figure 3. Supplemental Figure c1–c3 shows the results from the higher order alcohols. Simulated data, with added Gaussian-distributed random noise on the order of that expected under experimental conditions, suggested that the normalized singular values (NSV) from noise appear on EFA plots at $\ln(\text{NSV}) \approx -7$. However, reproducibility studies have shown that long-term drift limits consideration of singular values to those with $\ln(\text{NSV}) > (-5)$. Using this value as a guideline suggests that experimental data contain four, possibly five, significant eigenvectors. As a further indication of rank, the first five loading and score vectors for each alcohol were examined (Figures 4 and 5 show loadings and scores from the methanol data set, respectively). While the first five loading vectors all appear to contain information, the fifth score vector is not reproduced when compared to scores determined on an additional data set. Finally, the residual matrix left after the removal of four eigenvectors was examined for all the alcohol mixtures to determine if nonrandom variance was present. Figure 6 shows the residuals from the methanol data set. Residuals from the higher order alcohols are shown in the supplementary material (Figure d1–d3). Although it is apparent that the data could be interpreted with higher rank, the variances remaining after the removal of four eigenvectors is small. In addition, there was sufficient lack of reproducibility in the fifth and higher eigenvectors to warrant reduction to rank four. As experimental conditions improve, it may prove valuable to include more vectors in the basis set.

Iterative Modeling. *Single Association Model.* Using the nominal concentrations of water and alcohol, a three-component concentration matrix was calculated iteratively by adjusting κ to minimize the error between the first three vectors of $\bar{\mathbf{V}}$ and the estimate $\hat{\mathbf{V}}$. Figure 7a shows the resulting fit to $\bar{\mathbf{V}}$ recovered from the methanol data set. Fits to this model were unsatisfactory. The behavior of the third concentration eigenvector was not satisfactorily predicted by a 1:1 association model. Associations of 2:1, 3:1, 4:1, and 5:1

(16) Buijs, K.; Choppin, G. R. *J. Chem. Phys.* **1963**, *39*, 2035–2041.
(17) Wheeler, O. H. *Chem. Rev.* **1959**, *59*, 629–666.
(18) Fletcher, A. N.; Heller, C. A. *J. Phys. Chem.* **1968**, *72*, 1839–1841.
(19) Kaye, W. *Spectrochim. Acta* **1954**, *6*, 257–287.
(20) Weyer, L. G. *J. Appl. Poly. Sci.* **1986**, *31*, 2417–2431.

Table 1. Results of Fitting Procedure Using Double Association Model with Second Derivative Spectral Data from Four Alcohol Data Sets Studied

	methanol	ethanol	2-propanol	1-propanol
no. of waters surrounding hydrophobic portion	5	7	11	14
κ_1, hydrophobic	78 ± 1.2	0.403 ± 0.007	8.06 ± 0.08	3.87 ± 0.035
κ_2, hydrophilic	2.86 ± 0.02	0.127 ± 0.0025	0.185 ± 0.0025	0.075 ± 0.001

water/methanol were evaluated as well, following similar arguments made in eqs 1–5 for the 1:1 complex. As Figure 7a–d shows, no single association complex fully explains the third eigenvector nor reduces the residuals to the level of the known random noise in the spectral data.

Double Association Model. To assess the viability of the double association model, various integer values of η were tried for each data set until a minimum in the error matrix of eq 15 was achieved. Significant differences in fit were observed for different values of η in each of the alcohol mixtures investigated. Figure 8 shows plots of the least-squares error versus the value of η, showing shallow but reproducible minima. Variation of κ_1 and κ_2 within a given value of η did not produce fits significantly different from one another. Thus, any meaning attached to a particular set of equilibrium constants may be suspect. This is evident in Figure 9a,b, in which the error in the fit for the methanol/water system ($\eta = 5$) is plotted versus combinations of the equilibrium constants surrounding the simplex minimum. Notable is the lack of a deep minimum well in the surface. The long curved valley in the contour plot indicates parameter interdependence.

Table 1 summarizes the results from the fitting procedure for the double association model for all the alcohols studied. As expected, the value of η increases with the size of the hydrophobic portion of the molecules, i.e., solvent cages form around the alkane group. Consistent with this idea is the finding that η is larger for 2-propanol than for 1-propanol reflecting the greater bulk of the branched propanol group.

The values of κ derived have associated with them uncertainties not described by the standard error appearing in the table. Instead, the uncertainties arise from parameter interdependencies as noted above. Prior to discussing the recovered κ, the composition diagrams and recovered spectra will be presented in order to provide a clear understanding of the estimated κ's.

Figure 10 shows the composition profiles recovered for the methanol data set. Composition profiles for the other alcohols are provided in supplemental Figure e1–e3. For clarity, each species has been normalized to its maximum concentration. Also shown is an experimental concentration profile, **Q**, calculated as

$$\mathbf{Q} = (\hat{\mathbf{H}}^T\hat{\mathbf{H}})^{-1}\hat{\mathbf{H}}^T\bar{\mathbf{V}} \qquad (17)$$

Evident in Figure 10 is that the $(ROH)(H_2O)_\eta$ species is more prevalent at lower alcohol concentrations, while at higher alcohol concentrations the $(ROH)(H_2O)$ complex dominates. While solution studies and index of refraction studies readily detect the $(ROH)(H_2O)$ species, very fine intervals of partial molar volume must be employed to detect the $(ROH)(H_2O)_\eta$ species using such techniques. Classical textbook treatments of partial molar quantities often give a plot of partial molar volume, taken at fine intervals, versus composition for the select alcohol/water systems.[21] These graphs show a marked deviation of partial molar volume at low mole fractions of alcohol. Such treatments corroborate the results of the current spectroscopic study.

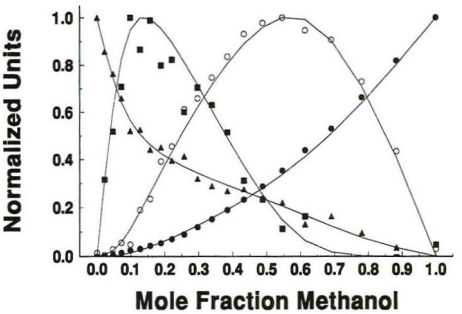

Figure 10. Scaled concentration profiles for methanol data recovered from iterative fit. The solid line (–) represents the results from the iterative fit while, the estimated experimental concentration matrix, **Q**, is shown as symbols: (▲) represents pure water, (●) represents pure alcohol, (■) represents $(ROH)(H_2O)_\eta$, and (O) represents $(ROH)(H_2O)$.

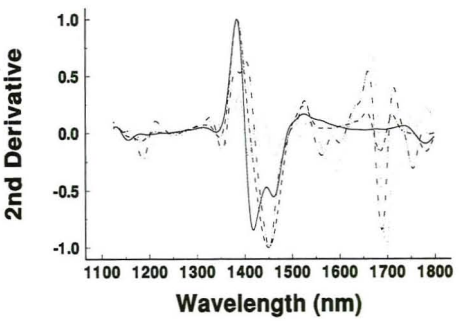

Figure 11. Recovered second derivative spectra for methanol data from iterative fit procedure using double association model. Spectra have been scaled for clarity. The solid line (–) represents the recovered water spectrum, the dotted line (···) represents the recovered alcohol spectrum, the dot–dash line (· – ·) represents the 1:1 species, and the dash–dot line (– ··· –) represents the n:1 species.

Recovered second derivative spectra for the methanol data set are presented in Figure 11. Recovered spectra for ethanol, 2-propanol, and 1-propanol are provided in supplemental Figure f1–f3. Spectra have been normalized for clarity. The estimated $(ROH)(H_2O)_\eta$ spectrum contains several interesting features. The hydroxyl band from water at 1450 nm of the associated species is red-shifted relative to bulk water, suggesting an increase in the hydrogen bonding of water molecules and, thus, an increase in water structure around the nonpolar solute.

(21) Atkins, P. W. *Physical Chemistry;* W.H. Freeman and Co.: San Francisco, 1982.

The effect of solutes on water structure has been a matter of debate.[22] In a paper discussing seemingly contradictory data, which have been gathered from nonpolar solutes, Muller[23] iteratively fit existing thermochemical data to obtain distinctive bond-breaking enthalpies and entropies for the hydration shell molecules, finding energy values larger than in bulk water. His data suggest that, although there are fewer hydrogen bonds for the hydration shell molecules than for bulk molecules, the hydrogen bonds of the associated water appear to have stronger bonding energies, thus accounting for both the "structure making" and "structure breaking" explanations previously offered.

Also noticeable in the spectra of the $(ROH)(H_2O)_\eta$ complex in Figure 11 is that the carbon–hydrogen overtone at 1680 nm is blue-shifted from that of the pure alcohol, suggesting that the C-H bond in the hydrated alcohols is effected by the high dielectric constant of the water molecules.

As previously noted, the objective of this analysis was to extract estimates of η, κ_1, κ_2, and the extinction coefficients of the two complexes $(ROH)(H_2O)_\eta$ and $(ROH)(H_2O)$ from the set of spectra **R**. Given an overdetermined set of data, such that there are more data points than parameters to be determined, the parameters can be extracted uniquely using a maximum likelihood estimate by the method of least squares. However, when parameters to be determined are dependent on each other, they cannot be separated uniquely. For a two-parameter system, this interaction can be readily illustrated by plotting contour maps of the sums of squares of error versus values of the parameters. Figure 9b shows such a plot for κ_1 and κ_2 derived for the methanol/water system. As previously noted, there is a long curved valley in the contour plot where the fit error is essentially constant. Thus, a high κ_1/low κ_2 interpretation is as probable as a low κ_1/high κ_2 interpretation.

At the same time, the values of the κ's and the extinction coefficients are not independent. Thus, the product of κ_1 and the extinction coefficient of the alc(H_2O) complex is very certain, but the values of the separate parameters are highly dependent. In a separate study,[24] it has been shown that, when the low κ/high extinction coefficient solution is examined, the spectra of the complexes have maximal overlap with the spectra of the pure constituents. Conversely, for the high κ/low extinction coefficient interpretation, the spectra have minimal overlap with the spectra of the pure constituents.

The uncertainty in the present experiments is particularly large because the data sets are coarse in their composition variation. Nevertheless, the uncertainties in the parameters do not detract from the conclusion that at least a four-component basis set is needed to describe the behavior of the alcohol/water system.

CONCLUSIONS

The above findings have important implications for the explanation of nonlinear solute retention in reversed-phase liquid chromatography. Investigators have found that for partially or completely ionized polar compounds the relationship between capacity factor and methanol concentration is nonlinear in nature.[25] Previously, this nonlinear behavior has been described in terms of hydrophilic repulsion of the solute by the solvent at low solvent modifier (alcohol) concentration and silanophilic interaction at high modifier concentrations.[26] Mathematically, retention becomes a quadratic function of modifier concentration. An alternate theory proposed by Katz et al.[4] suggested that the ternary nature of the modifier–water system was responsible for the nonlinear behavior. In particular, for the methanol/water system, the third component is assigned to a 1:1 methanol/water associate. This has recently been supported by T_1 data collected from ^2H NMR studies.[27] It was shown in the Katz study that the retention of several polar solutes was controlled almost exclusively by the methanol not associated with the water.

The present spectroscopic study also predicts the presence of a 1:1 hydrogen bonded methanol/water species (hydrophilic), as well as a larger, associated complex involving the hydrophobic end of the alcohol. While the effect of the hydrophilic species occurs at high methanol concentrations, the larger hydrophobic methanol complex may be involved in nonlinear retention behavior at low methanol concentrations. Organic modifiers, such as alcohols, are known to preferentially adsorb to stationary phases in reversed-phase columns, thus effecting retention. At 20% (~0.1 mole fraction), the adsorption of methanol onto a hydrophobic stationary phase, as measured by distribution isotherms, reaches a maximum.[26] This adsorption phenomena corresponds roughly to the concentration maximum of the large methanol associated species seen in the present study and may provide an explanation for the phenomena and, thus, retention behavior.

In the field of solution structure elucidation, the present results also have consequences. In particular, consider the estimates of the number of water molecules surrounding the hydrophobic portions of the solute. Data from Monte Carlo simulations[28] show that approximately 20 molecules of water are needed to enclose the methyl group of methanol. Yet our spectroscopic data indicate a 5:1 stoichiometry is involved. This conflict may be resolved by considering that the Monte Carlo simulation represents the system at infinite dilution. In this region, a hydrophobic cage of 20 water molecules is a sensible number. However, at higher concentrations, the water molecules become insufficient to surround the methanols in an independent fashion. Thus the water "walls" become shared to two or more methanols. Finally, at the ratio water/methanol of 5:1, the system is saturated. Any further addition of methanol cannot be accommodated by hydrophobic solvation (cage formation), and the entire structure breaks down. It now converts to one where methyl–methyl contacts become important contributors to the overall structure. Thus, the spectroscopic data measures a rather different supramolecular complex (a methanol/water associate) than the Monte Carlo simulation (isolated hydrophobic cage).

The present data is also consistent with the "new view of hydrophobic effects", in which the formation of "more

(22) Hertz, H. G. *Agnew. Chem., Int. Ed. Engl.* **1970**, *9*, 124–138.
(23) Muller, N. *J. Solution Chem.* **1988**, *17*, 661–673.
(24) Thompson, C.; Alam, M. K.; Callis, J. B. Unpublished results.
(25) El Tayar, N.; Van De Waterbeemd, V.; Testa, B. *J. Chromatogr.* **1985**, *320*, 293–304.
(26) Reymond, D.; Chung, G. N.; Mayer, J. M.; Testa, B. *J. Chromatogr.* **1987**, *391*, 97–109.
(27) Bliesner, D. M.; Sentell, K. B. *Anal. Chem.* **1993**, *65*, 1819–1826.
(28) Jorgensen, W. L.; Gao, J.; Ravimohan, C. *J. Phys. Chem.* **1985**, *89*, 3470–3473.
(29) Muller, N. *Acc. Chem. Res.* **1990**, *23*, 23–28.

structured" water is involved in the formation of cages[29] around hydrophobic groups. The NIR spectra of the alc$(H_2O)_n$ complexes reported here are characterized by shifts of the hydroxyl bond frequency to lower energy, a sign of a stronger hydrogen bond. At the same time, there is evidence of a number of non-hydrogen-bonded water molecules associated with the complex.

The use of ideal solution theory represents a gross oversimplification of the actual situation. However, the present data are not of sufficient quality to justify a more complex model. Instrumentation and methodology are currently being developed to improve long-term stability. This may lead to a more definitive estimate of the dimension of a linear basis set needed to describe the methanol/water systems.

ACKNOWLEDGMENT

The authors would like to acknowledge Dr. Michael Schurr whose insight proved invaluable and Dr. Randy J. Pell for his help with the modeling technique. M.K.A. would like to thank Dr. D. Haaland for his useful comments and Dr. T. M. Alam for his critical evaluation of the manuscript. Research support was provided by CPAC, Guggenheim Foundation (J.B.C.), and Fulbright Commission (J.B.C.). This work was partially supported by the United States Department of Energy, under Contract DE-AC04-94AL85000.

SUPPLEMENTARY MATERIAL AVAILABLE

Ethanol, 1-propanol, and 2-propanol spectra (Figure a1–a3); the transformed data from ethanol, 1-propanol, and 2-propanol (Figure b1–b3); results from higher order alcohols (Figure c1–c3); residuals from higher order alcohols (Figure d1–d3); composition profiles for other alcohols (Figure e1–e3); recovered spectra for ethanol, 1-propanol, and 2-propanol (Figure f1–f3) (7 pages). Ordering information is given on any current masthead page.

Received for review September 20, 1993. Accepted March 28, 1994.[•]

[•] Abstract published in *Advance ACS Abstracts,* May 15, 1994.

Anal. Chem. **1994**, *66*, 2302–2312

Investigation of Molecular Weight and Terminal Group Effects on the Time-of-Flight Secondary Ion Mass Spectra of Polyglycols

Lucinda R. Hittle, Diane E. Altland, Andrew Proctor, and David M. Hercules*
Department of Chemistry, University of Pittsburgh, Pittsburgh, Pennsylvania 15260

A series of poly(ethylene glycol) (PEG) and poly(propylene glycol) (PPG) samples ranging in molecular weights from 400 to 100 000 Da were characterized by time-of-flight secondary ion mass spectrometry. Molecular weight values from the oligomer distributions in the spectra were determined and compared to those obtained by conventional methods. The fragmentation patterns of the polyglycols were examined and can be explained by mechanisms involving simple chain scissions. The predominant fragmentation mechanisms involve scission of the C–O bonds, similar to fragmentation pathways observed for aliphatic ethers in other types of mass spectrometry. The relative fragment intensities of the clusters in the PEG and PPG fragment patterns were examined as a function of sample molecular weight. Although no dramatic changes in relative intensity were observed for the PEGs, the PPG fragment patterns were found to change with the molecular weight of the polymer. A series of poly(ethylene glycols) containing different terminal groups were also examined to determine the effect of the terminal group on fragmentation. In general, the major peak series observed in the spectra of small diacrylate-, dimethacrylate-, dipalmitate-, and distearate-terminated PEGs correspond to either oligomers or single cleavage of the PEG chain. Peaks resulting from cleavage within the terminal group or cleavage of the terminal group from the PEG chain were generally not observed for MW <4000. The terminal groups in high molecular weight PEGs can be qualitatively identified on the basis of the fine structure of clusters within the main chain fragment patterns. In addition, it was determined that PEG distearate was actually terminated with a mixture of palmitate and stearate groups.

Mass spectrometric analyses of polymers have grown exponentially in the past decade. Perhaps the most universally analyzed polymers are the polyglycols, which have been studied by a host of mass spectrometric techniques. Polyglycols are an industrially important class of polymers used in the pharmaceutical and cosmetic industries as lubricants, fillers, and matrices for drug transport systems. Studies of the molecular weight distributions of poly(ethylene glycols) and poly(propylene glycols) have been conducted using laser desorption,[1–5] field desorption,[6–8] electrohydrodynamic,[9] and fast atom bombardment mass spectrometries.[10] Fenn and co-workers have examined several poly(ethylene glycols) with molecular weights ranging from 200 to 5 million Da using electrospray mass spectrometry.[11,12] They found that individual poly(ethylene glycol) oligomers may carry multiple charges, with up to 8000 charges on a 5-million-Da molecular weight sample. Tandem mass spectrometry has been used by Lattimer and co-workers to elucidate the fragmentation mechanisms of low molecular weight polyglycols.[13–15] Poly(ethylene glycol) samples have also been analyzed by other types of mass spectrometry, such as thermospray,[16] spontaneous desorption,[17] supercritical fluid chromatography,[18–20] and liquid chromatography[21] mass spectrometries. The primary purpose of these analyses was to demonstrate the general utility of the technique for a range of sample types rather than to study specific polymers in detail. The high resolution possible with Fourier transform ion cyclotron resonance (FTICR) instruments has been shown for poly(ethylene glycols) of molecular weights up to 8000 Da by Ijames and Wilkins.[22] FTICR MS has also been used to investigate mass discrimination effects,[23] proton affinity, and collision-induced decomposition of polyglycols.[24]

Time-of-flight secondary ion mass spectrometry (TOF-SIMS) has previously been used to study the fragmentation mechanisms of poly(styrenes),[25] polyurethanes,[26,27] perflu-

(1) Mattern, D. E.; Hercules, D. M. *Anal. Chem.* **1985**, *57*, 2041–2046.
(2) Cotter, R. J.; Honovich, J. P.; Olthoff, J. K.; Lattimer, R. P. *Macromolecules* **1986**, *19*, 2996–3001.
(3) Ijames, C. F.; Wilkins, C. L. *J. Am. Chem. Soc.* **1988**, *110*, 2688–2689.
(4) Brown, R. S.; Weil, D. A.; Wilkins, C. W. *Macromolecules* **1986**, *19*, 1255–1260.
(5) Bahr, U.; Deppe, A.; Karas, M.; Hillenkamp, F.; Giessmann, U. *Anal. Chem.* **1992**, *64*, 2866–2869.
(6) Chait, B. T.; Shpungin, J.; Field, F. H. *Int. J. Mass Spectrom. Ion Processes* **1984**, *58*, 121–137.
(7) Lattimer, R. P.; Hansen, G. E. *Macromolecules* **1981**, *14*, 776–780.
(8) Neumann, G. M.; Cullis, P. G.; Derrick, P. J. *Z. Naturforsch., A: Phys. Sci.* **1980**, *35A* (10), 1090–7.
(9) Lai, S.-T. F.; Chan, K. W.; Cook, K. D. *Macromolecules* **1980**, *13*, 953–956.
(10) Seraglia, R.; Traldi, P.; Mendichi, R.; Sartore, L.; Schiavon, O.; Veronese, F. M. *Anal. Chim. Acta* **1992**, *262*, 277–283.
(11) Wong, S. F.; Meng, C. K.; Fenn, J. B. *J. Phys. Chem.* **1988**, *92*, 546–550.
(12) Nohmi, T.; Jenn, J. B. *J. Phys. Chem.* **1992**, *114*, 3241–3246.
(13) Lattimer, R. P.; Munster, H.; Budzikiewicz, H. *Int. J. Mass Spectrom. Ion Processes* **1989**, *90* (2), 119–129.
(14) Lattimer, R. P. *Proceedings of the 40th Conference on Mass Spectrometry and Allied Topics*, Washington, DC; ASMS: East Lansing, 1992; pp 281–282.
(15) Lattimer, R. P. *J. Am. Soc. Mass Spectrom.* **1992**, *3*, 225–234.
(16) Fink, S. W.; Freas, R. B. *Anal. Chem.* **1989**, *61*, 2050–2054.
(17) Salehpour, M.; Hunt, J. E. *Int. J. Mass Spectrom. Ion Processes* **1988**, *85* (1), 99–115.
(18) Matsumoto, K.; Tsuge, S.; Hirata, Y. *Shitsuryo Bunseki* **1987**, *35* (1), 15–22.
(19) Cousin, J.; Arpino, P. J. *J. Chromatogr.* **1986**, *398*, 125–141.
(20) Kalinoski, H. T.; Udseth, H. R.; Wright, B. W.; Smith, R. D. *J. Chromatogr.* **1987**, *400*, 307–316.
(21) Lai, S.-T. *J. Chromatogr.* **1986**, *363*, 444–447.
(22) Ijames, C. F.; Wilkins, C. L. *J. Am. Chem. Soc.* **1988**, *110*, 2688–2689.
(23) Hogan, J. D.; Laude, D. A. *Anal. Chem.* **1992**, *64*, 763–769.
(24) Lin, H.-Y.; Rockwood, A.; Munson, M. S. B.; Ridge, D. P. *Anal. Chem.* **1993**, *65*, 2119–2124.
(25) Chiarelli, P. M.; Bletsos, I. V.; Hercules, D. M.; Feld, H.; Leute, A.; Benninghoven, A. *Macromolecules* **1992**, *25*, 6970–6976.
(26) Bletsos, I. V.; Hercules, D. M.; van Leyen, D.; Benninghoven, A.; Karakatsanis, C. G.; Rieck, J. N. *Macromolecules* **1990**, *23*, 4157–4163.

0003-2700/94/0366-2302$04.50/0
© 1994 American Chemical Society

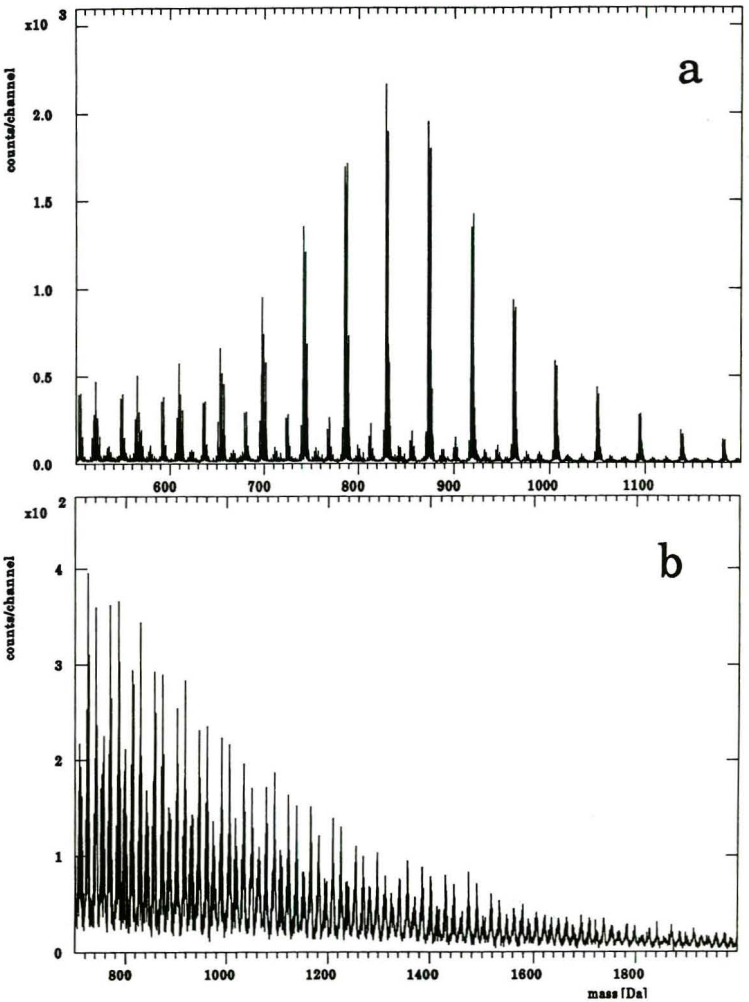

Figure 1. TOF-SIMS poly(ethylene glycol) spectra. Molecular weight: (a) 800 and (b)100 000.

orinated polyethers,[28] polymethacrylates,[29] polyacrylates,[30] and poly(butadienes).[31] Previous TOF-SIMS studies of polyglycols have focused on cationization efficiencies from various substrates[32] and comparison of ion yields with those from plasma desorption mass spectrometry.[33] The purpose of this study is to characterize a series of polyglycols ranging in molecular weights from 400 to 100 000 Da to determine the fragmentation mechanisms responsible for ion formation. The fragmentation mechanisms of poly(ethylene glycols) and poly(propylene glycols) will also be compared. Since the chemical structure of these two polymers differs only by a methyl group, differences in the fragment patterns of these polymers can be related to the presence of the pendant methyl groups. A series of poly(ethylene glycols) containing different terminal groups were also examined to determine the effect of the terminal group on fragmentation.

(27) Bletsos, I. V.; Hercules, D. M.; van Leyen, D.; Benninghoven, A.; Karakatsanis, C. G.; Rieck, J. N. *Anal. Chem.* **1989**, *61*, 2142–2149.
(28) Bletsos, I. V.; Hercules, D. M.; Fowler, D.; van Leyen, D.; Benninghoven, A. *Anal. Chem.* **1990**, *62*, 1275–1284.
(29) Zimmerman, P. A.; Hercules, D. M. *Anal. Chem.* **1993**, *65* (8), 983–991.
(30) Zimmerman, P. A.; Hercules, D. M. *Anal. Chim. Acta*, in press.
(31) Hittle, L. R.; Hercules, D. M. *SIA, Surf. Interface Anal.*, in press.
(32) van Leyen, D.; Deimel, M.; Hagenhoff, B.; Benninghoven, A. *Secondary Ion Mass Spectrometry (SIMS VII)*; Benninghoven, A., Ed.; Wiley-Interscience: Chichester, 1989.
(33) Feld, H.; Leute, A.; Zurmuehlen, R.; Benninghoven, A. *Anal. Chem.* **1991**, *63* (9), 903–910.

EXPERIMENTAL SECTION

TOF-SIMS. *Instrumentation.* The instrument used in these studies was a time-of-flight secondary ion mass spectrometer, TOF-SIMS III, designed and manufactured by Ion-Tof GmbH, Münster, Germany. This instrument was designed for analysis of biomolecules on the pico- and femtomole level,

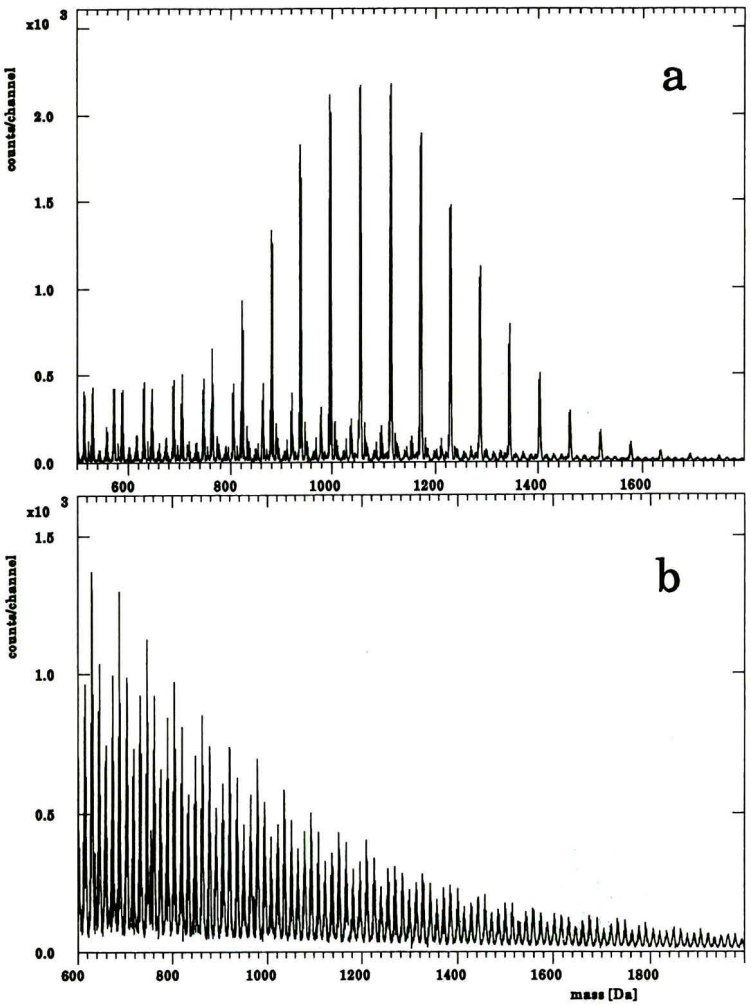

Figure 2. TOF-SIMS poly(propylene glycol) spectra. Molecular weight: (a) 1000 and (b) 100 000.

but it has also been used for analysis of semiconductors and polymers.[34] The TOF-SIMS III is a compact modular design comprising a custom-built pulsed primary Ar^+ ion source, a high-resolution first-order reflectron time-of-flight analyzer, and a pulsed charge neutralization system for analysis of insulating materials. The TOF-SIMS has been described in more complete detail elsewhere.[35,36]

The primary ion gun consists of a standard electron impact argon ion source combined with a pulsed 90° deflector for beam chopping and primary ion mass separation followed by an axial buncher for pulse compression. The resultant mass-separated primary ion bunches have a typical pulse length of about 1 ns and a variable spot diameter between 5 and 50 μm.

Secondary ions generated by a primary ion pulse on the target surface are extracted and accelerated to an energy of 3 keV. In the following 2-m flight path, an Einzel lens and reflectron optics are integrated for focusing the secondary ion beam and for energy compensation, respectively. To achieve high detection efficiency, in particular for molecular ions in the high-mass range, the ions are postaccelerated to 10 keV, where they are then detected by a channel plate–scintillator–photomultiplier combination.

The data collection system consists of a time-to-digital converter, a fast buffer memory, and an accumulating memory board. The spectra are accumulated in the single ion counting mode with a maximum of 256 stops/pulse, a time resolution of 1.25 ns/channel, and a total time range of 320 μs. The cycle time was set at 200 μs, allowing investigation of ions from 1 to 4000 Da. The base pressure of the main chamber of the instrument was typically 3×10^{-8} Pa, and the operating

(34) Niehuis, E. *Secondary Ion Mass Spectroscopy* (*SIMS VII*); Benninghoven, A., Ed.; Wiley-Interscience: Chichester, 1989; pp 299–304.
(35) Niehuis, E.; Heller, T.; Feld, H.; Benninghoven, A. *J. Vac. Sci. Technol., A* **1987**, *5* (4), 1243–1246.
(36) Niehuis, E.; van Veltzen, P. N. T.; Lub, J.; Heller, T.; Benninghoven, A. *SIA, Surf. Interface Anal.* **1989**, *14*, 135–142.

Table 1. Poly(ethylene glycol) Molecular Weight Determinations

	TOF-SIMS			GPC		
nominal MW[b]	M_n	M_w	M_w/M_n	M_n	M_w	M_w/M_n
200	358	362	1.01			
600	549	571	1.04			
1500	741	787	1.06	1076	1374	1.28
8000	*a*	*a*		12 860	13 560	1.05
20 000	*a*	*a*		30 830	29 810	1.03

[a] Fragment patterns, not oligomer distributions, observed. [b] As listed by manufacturer.

Table 2. Poly(propylene glycol) Molecular Weight Determinations

TOF-SIMS			GPC			
M_n	M_w	M_w/M_n	M_n	M_w	M_w/M_n	OH[a,b]
651	677	1.04	440[b]	470[b]	1.07	430
1004	1037	1.03	877	1142	1.30	1040
1962	1997	1.02	2074	2327	1.12	2040
2935	2849	1.03	2697	3200	1.19	2840

[a] Hydroxyl number determination (M_n). [b] Supplied by manufacturer.

pressure was approximately 1×10^{-6} Pa, with a pressure of 4×10^{-4} Pa in the primary ion source. During the analysis, the target was bombarded by a 10-keV Ar^+ beam with an average pulsed primary ion current of 0.5–1.0 pA for a total collection time of 200 s. The total primary ion current density was less than 10^{13} ions/cm^2 (static SIMS). Typical resolution ($m/\Delta m$) was 8000 at m/z = 1000.

Sample Preparation. A series of poly(ethylene glycol) (PEG) and poly(propylene glycol) (PPG) polymers ranging in molecular weights from 450 to 100 000 Da were examined. Hydroxy-terminated poly(ethylene glycol) molecular weight standards, PEG dimethacrylate 200, 400, and 1000, PEG diacrylate 400 and 4000, and PEG distearate 600 and 6000 were purchased from Polysciences, Inc. (Warrington, PA). The PPG samples were purchased from Scientific Polymer Products (Ontario, NY). The samples were prepared for analysis by dissolving the polymer in methanol or tetrahydrofuran. Typical solution concentrations were 10^{-3} M with respect to the repeat unit; 1–5 μL of the sample was deposited onto a silver target with an area of about 12 mm^2. The silver had been etched in nitric acid (20 vol %) and rinsed with deionized water and methanol.

Gel Permeation Chromatography. GPC measurements were carried out in THF at 35 °C at a flow rate of 0.35 mL/min maintained by a Perkin-Elmer series 100 pump. The GPC instrument was equipped with two Phenomenex narrow-bore GPC columns, a Waters 410 differential refractometer detector, and a Waters 745 data module. Calibration was performed using poly(styrene) standards from Waters; typical sample concentration was 25 mg/mL.

Nuclear Magnetic Resonance. Number-average molecular weights (M_n) were determined by end group NMR analysis using a Bruker AM-500 instrument at 125 MHz (^{13}C). Samples were prepared for analysis by dissolving in D_2O at a concentration of 100–200 mg/mL. The spectra were taken under a long delay time (40 s) without nuclear Overhauser enhancement (NOE). The intensity of the signal from the carbon atoms in the repeat unit divided by a factor corresponding to the number of equivalent carbon atoms is ratioed to the intensity due to the chain-end carbon atom. This number is then multiplied by the mass of the repeat unit, and the masses of the end groups (methacrylate, acrylate, or stearate groups) are added. This procedure gives an estimate of the number-average molecular weight of the oligomers within the polymer sample.

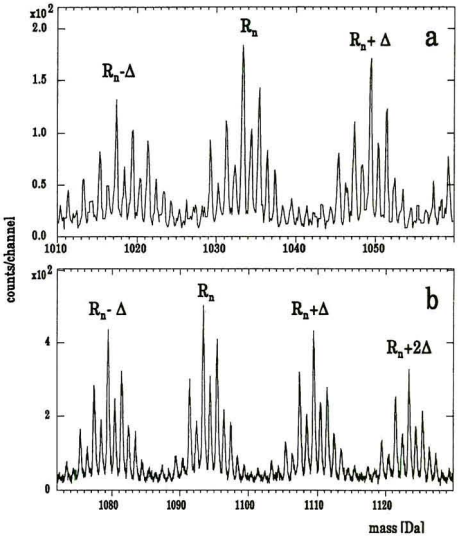

Figure 3. Typical fragment patterns for 100 000 molecular weight (a) poly(ethylene glycol) and (b) poly(propylene glycol).

RESULTS AND DISCUSSION

Hydroxyl-Terminated Polyglycols. *Survey Spectra.* In general, it is possible to detect oligomers from polyglycols with molecular weights up to ca. 5000 Da. Main chain fragments in the mass range from 500 to 3000 Da are observed for samples with molecular weights above 5000 Da. Figures 1 and 2 show typical oligomer distributions for low molecular weight PEGs and PPGs (Figures 1a and 2a, respectively) and main chain fragment patterns for high molecular weight samples (Figures 1b and 2b). The oligomer distributions can be used to calculate the number-average (M_n) and weight-average (M_w) molecular weights. The results are shown in Tables 1 and 2; the values from TOF-SIMS are comparable to those from GPC for the PPG samples.

Unfortunately, the results of the two techniques for the PEG samples can only be compared for a single sample since TOF-SIMS spectra of PEG 8000 and 20 000 show fragment patterns but no oligomer distributions. GPC results for low molecular weight samples (<1000 Da) could not be obtained due to the limited resolution of the instrument at low masses. Although oligomers with higher molecular weights (up to 10 000 Da) have been detected in the TOF-SIMS spectra of poly(styrenes)[37] and poly(dimethylsiloxanes),[38] fragmentation

(37) van Leyen, D.; Hagenhoff, B.; Niehuis, E.; Benninghoven, A.; Bletsos, I. V.; Hercules, D. M. *J. Vac Sci. Technol., A* **1989**, *A7*, 1790.
(38) Hagenhoff, B.; Benninghoven, A.; Barthel, H.; Zoller, W. *Anal. Chem.* **1991**, *63* (21), 2466–2469.

Scheme 1

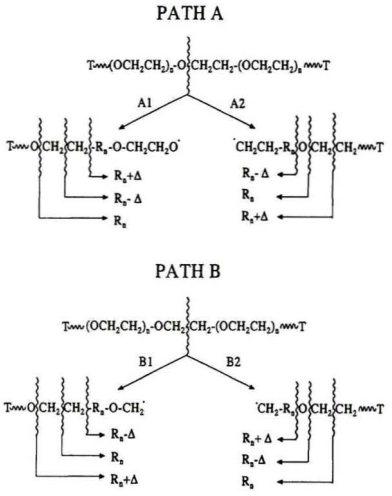

rather than desorption of intact oligomers is the dominant mechanism of ion formation for medium to high molecular weight polyglycols (>5000 Da). Hindered desorption of oligomers may be caused by a variety of factors such as polymer conformation (linear versus entangled) and binding interactions of the ether groups with the silver substrate. For polyglycols, it is doubtful that cationization efficiencies limit the transformation probabilities of the oligomers, considering the ease of attachment of many types of cations to PEG.[39]

Fragmentation in Polyglycols. The following terminology will be used to describe the TOF-SIMS spectra: *fragment* will refer to a segment from a polymer chain; *cluster* will refer to a group of peaks for a mass range of ca. 5 Da corresponding to a particular ion; *pattern* will refer to a repeating sequence of clusters in the TOF-SIMS spectrum. The term Δ will refer to the spacing between methylene (CH_n) or oxygen groups (approximately 12–16 Da), and R_n will refer to a fragment containing an integral number (n) of repeat units. Δ is used rather than a numerical value due to the presence of species with varying numbers of unsaturations which contribute to a cluster. The terms R_n, $R_n + \Delta$, $R_n - \Delta$, and $R_n + 2\Delta$ are used to generalize the structural formulas of main chain fragments within a pattern. It is understood that these types of fragments may result from different oligomers. A more extensive description of this nomenclature, and of the general mechanisms of ion formation in SIMS, is contained in ref 25.

Details of a typical fragmentation pattern for PEG and PPG are shown in Figure 3.. Clusters approximately 14–16 mass units apart can be seen for the fragments R_n, $R_n + \Delta$, and $R_n - \Delta$. An additional $R_n + 2\Delta$ cluster appears in the PPG fragment pattern in Figure 3b. As is shown in Figures 1b and 2b, the fragment pattern begins at ca. 500 Da and repeats up to ca. 3000 Da. Each cluster within the fragmentation patterns contains several peaks, due in part to contribution from ^{13}C and the two Ag isotopes. All of the main chain fragments described in the following schemes, and observed in TOF-SIMS spectra, were silver cationized. Since silver was used as a sample substrate, Ag cationization was universal for all types of fragments larger than one or two monomer units. Some sodium cationization was observed for low molecular weight oligomers but did not contribute significantly to the observed fragment patterns.

The fragment patterns which appear in the TOF-SIMS spectra of polymers can be largely explained by simple statistical chain fracture. The formalism for interpretation of these fragmentation pathways has been previously described in detail.[25] Scheme 1 shows two possible pathways for simple statistical chain fracture of PEG. Path A indicates cleavage of the C–O bond which would produce two fragments shown by A1 and A2. These two radical fragments can undergo further chain scission to produce R_n, $R_n + \Delta$, and $R_n - \Delta$ fragments. Fragmentation at the C–C bond within the repeat unit, shown by paths B1 and B2, will also ultimately produce R_n, $R_n + \Delta$, and $R_n - \Delta$ fragments. If no chemical effects are considered, both paths will produce the same fragments with equivalent intensities; i.e., the ratio of R_n:$R_n + \Delta$:$R_n - \Delta$ should

Scheme 2

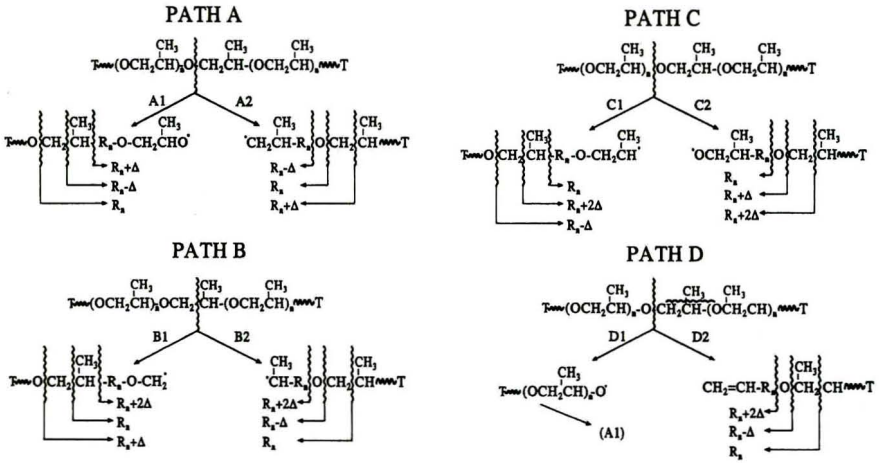

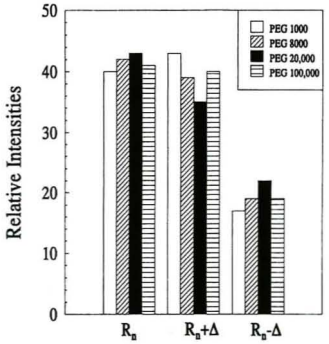

Figure 4. Relative intensities of fragment clusters for different poly(ethylene glycol) molecular weights.

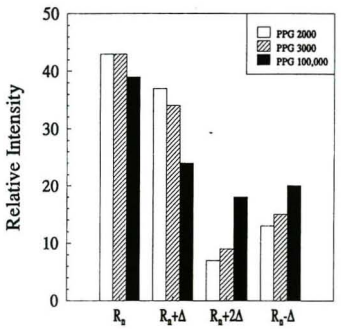

Figure 5. Relative intensities of fragment clusters for different poly(propylene glycol) molecular weights.

be 1:1:1. However, the actual intensities are 40:35:20 or approximately 2:2:1. So, simple statistical chain fracture, with no consideration of chemical effects, does not sufficiently account for the results. If scission of the C–O bond is preferred over C–C bond cleavage, then path A should show higher probability than path B. If C–O bond scission is also preferred in the second step, different relative intensities should result from paths A1 and A2 (also B1 and B2). By adjusting the ratios of the various pathways, it is possible to arrive at a set of coefficients (A11 and B11, etc.) which approximate the observed relative intensities. However, such treatment is questionable because all pathways generate the same three fragments, making a unique solution impossible. Preferential C–O cleavage may be partially explained by the slightly lower bond energy of C–O compared to that of the C–C bond which is ca. 78–85 versus 80–90 kcal/mol, respectively.[43] Cleavage of the C–O bond also predominates in electron ionization mass spectrometry of aliphatic ethers, where a larger tendency

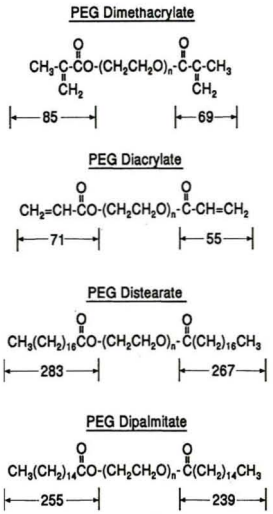

Figure 6. Structures of diacrylate-, dimethacrylate-, distearate-, and dipalmitate-terminated poly(ethylene glycols).

for charge-site cleavage occurs.[44] Similarly, chemical ionization mass spectrometric studies have shown fragmentation mechanisms for crown ethers where protonation of the oxygen is followed by α-cleavage.[45] Although it is not clear whether Ag^+ cationization occurs before or after fragmentation of the polymer chain, it is possible that attachment of the Ag^+ to the oxygen groups within the polymer may precede α-cleavage, similar to CI mechanisms. Although the free radical chain scissions proposed for TOF-SIMS fragmentation differ from those in EI or CI, similar chemical effects may occur.

Similar fragmentation mechanisms can be proposed for the PPGs and are shown in Scheme 2. Scission of the C–O bond within the repeat unit will produce two different initial fragments, depending on whether the O–CH_2 bond (paths A1 and A2) or the O–CH bond (paths C1 and C2) is broken. Path B corresponds to fracture of the C–C bond. Subsequent fragmentation of the primary radicals will yield different combinations of the four possible fragments. Another possible mechanism, shown in path D, is scission of a pendant methyl group to produce a radical which then undergoes α-scission to produce a neutral (D2) and another radical fragment (D1), which is identical to the radical formed in path A1. The neutral fragment produced in path D2 can also undergo further fragmentation to produce R_n, $R_n - \Delta$, and $R_n + 2\Delta$ fragments. As for the PEGs, more quantitative interpretation is not possible.

In order to determine if the fragmentation pattern will change as a function of polymer size, a range of molecular weights of PEGs and PPGs were analyzed. The relative intensities of the major fragment clusters were calculated for PEGs and PPGs. These intensities were normalized by dividing the peak area of a given cluster by the sum of the

(39) Llenes, C. F.; O'Malley, R. M. *Rapid Commun. Mass Spectrom.* **1992**, *6* (9), 564–570.
(40) Zimmerman, P. A.; Hercules, D. M. Unpublished results.
(41) Odian, G. *Principles of Polymerization*; John Wiley and Sons: New York, 1981; pp 514–517.
(42) Schule, U.; Pallix, J. B.; Becker, C. H. *J. Vac. Sci. Technol., A* **1988**, *6* (3), 936–940.
(43) *Gas Phase Ion and Neutral Thermochemistry*; American Chemical Society and the American Institute of Physics for the National Bureau of Standards: New York, 1988.
(44) McLafferty, F. W. *Interpretation of Mass Spectra*; University Science Books: Mill Valley, CA, 1980; pp 209–210.
(45) van Gaever, F.; Van de Sande, C. C.; Bucquoye, M.; Goethals, E. J. *Org. Mass Spectrom.* **1978**, *13* (8), 486–488.

Table 3. Terminated Poly(ethylene glycol) Molecular Weight Determinations

			TOF-SIMS			GPC		
	nominal MW[b]	NMR M_n	M_n	M_w	M_w/M_n	M_n	M_w	M_w/M_n
dimethacrylate 200	354	350	409	412	1.01			
dimethacrylate 400	554	532	526	543	1.03			
dimethacrylate 1000	1154	1100	1105	1122	1.02			
diacrylate 4000	4126	3884	*a*	*a*		3330	4680	1.41
distearate 600	1150	3308	*a*	*a*		870	1740	1.99
distearate 6000	6550	11 887	*a*	*a*		9890	13 780	1.39

[a] Fragment patterns, not oligomer distributions, observed. [b] As listed by manufacturer.

peak areas of the clusters in a pattern. The relative intensities of these fragment clusters are shown in Figures 4 and 5. In general, the relative intensities within the fragmentation patterns of the PEGs were the same regardless of molecular weight. However, the relative intensities of the fragments resulting from cleavage within the PPG repeat unit (such as $R_n + 2\Delta$ and $R_n - \Delta$) increased with increasing PPG molecular weight. The contribution of pendant groups within the polymer repeat unit may play an important role in fragmentation of high molecular weight polymers. Similar results have been obtained for poly(methyl methacrylate) where the relative intensities of fragment clusters also change as a function of molecular weight.[40] Unfortunately, only a qualitative comparison between low molecular weight (<5000 Da) and high molecular weight (>100 000 Da) PPGs is possible, due to the unavailability of medium size PPGs. Anionic polymerization, used to synthesize PPGs with narrow molecular weight distributions, can produce samples with molecular weights up to only 5000 Da, due to side reactions.[41] However, semiquantitative determination of PPG molecular weight by

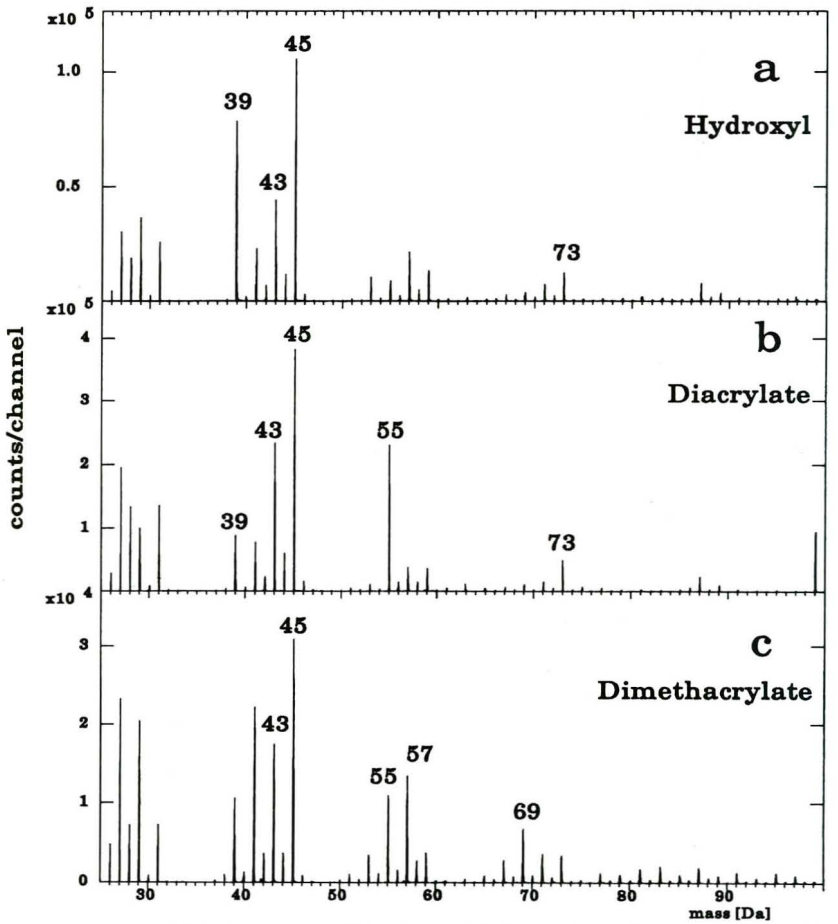

Figure 7. Mass region from 20 to 100 Da for (a) hydroxyl-, (b) diacrylate-, and (c) dimethacrylate-terminated poly(ethylene glycols).

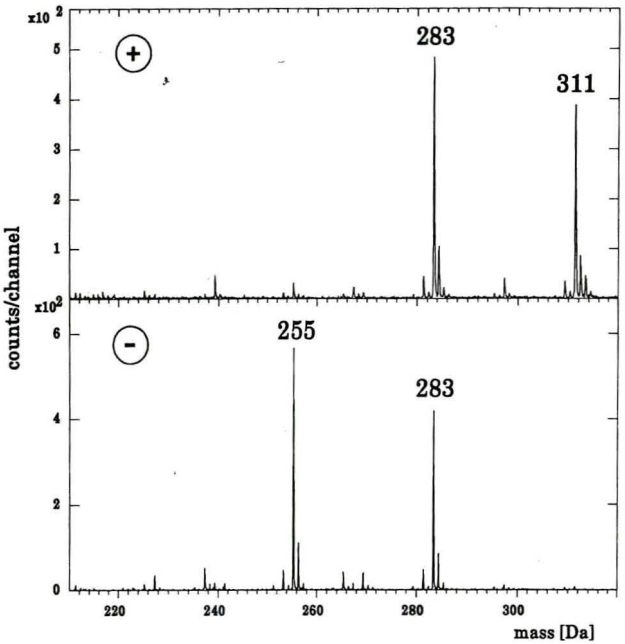

Figure 8. Positive- and negative-ion spectra from 200 to 325 Da for PEG distearate, molecular weight 600.

calculation of the relative cluster intensities may be possible for high molecular weight samples, for which oligomer distributions are not observed.

Dimethacrylate-, Diacrylate-, and Distearate-Terminated Poly(ethylene glycols). *Molecular Weight Determinations.* Poly(ethylene glycols) are frequently used in copolymer manufacturing as chain extenders or cross-linking agents. The properties of the copolymer, and the ease with which cross-linking is achieved, can be altered by changing the terminal groups. In this study, the TOF-SIMS spectra of six PEGs terminated with acrylate, methacrylate, or stearate groups were examined to determine the extent of fragmentation of the terminal group from the polymer chain and the effect of the terminal group on main chain fragmentation pathways. The structures of the terminated polymers are shown in Figure 6. Although the polymer is terminated at both ends with the same substance, the mass of the terminal group depends on whether it is attached to the C or O of the $(CH_2CH_2O)_n$ repeat unit. For example, when the polyglycol is reacted with acrylic acid, one end of the chain will contain a $CH_2{=}CHCOO$ group (71 Da) and the other end will contain a $CH_2{=}CHCO$ group (55 Da).

The molecular weights of these samples were first determined by ^1H or ^{13}C NMR and gel permeation chromatography (GPC); results are listed in Table 3. If the TOF-SIMS spectrum did not contain an oligomer distribution, GPC and NMR analyses were conducted to verify the nominal sample molecular weight listed by the manufacturer. In general, reasonable agreement was seen between the expected molecular weights and those determined by NMR and GPC, with the exception of PEG Distearate 600 and 6000. The accuracy of the GPC results may be affected by changes in the hydrodynamic volume of the polymer by addition of the long hydrocarbon chain stearate groups. However, as will be discussed in a subsequent section, the distearate samples were synthesized with a mixture of starting materials, and this is partially reflected in the molecular weight values observed by NMR and GPC.

Low-Mass Spectra. One method of identification for the terminal group in these polymers is to examine the low mass region (<500 Da) of the spectra. Figure 7 shows the mass region from 20 to 100 Da for hydroxyl-, diacrylate-, and dimethacrylate-terminated PEGs. Each spectrum contains an identifying PEG peak at 45 Da which corresponds to the monomeric fragment $CH_2CH_2OH^+$. The PEG diacrylate spectrum contains an intense peak at 55 Da, which corresponds to $COCH{=}CH_2$ from the acrylate group. Similarly, the PEG dimethacrylate spectrum contains an intense peak at 69 Da corresponding to the methacrylate group. The PEG diacrylate and dimethacrylate spectra do not include peaks for the oxygen-containing counterparts at 71 ($CH_2{=}CHCOO^+$) and 85 Da ($CH_2C(CH_3)COO^+$), which indicates that cleavage of the terminal group occurs primarily at the C–O bond α to the carbonyl within these terminal groups. Logically, positive charge would be more easily located on the carbon of the carbonyl group rather than the neighboring oxygen.

Although the mass region from 1 to 200 Da for PEG distearate does not differ significantly from the hydroxyl-terminated PEG, characteristic peaks for the stearate group are observed from 200 to 350 Da in both the positive- and negative-ion mode spectra, as is shown in Figure 8. In the positive-ion mode, intense peaks are observed at 283 and 311

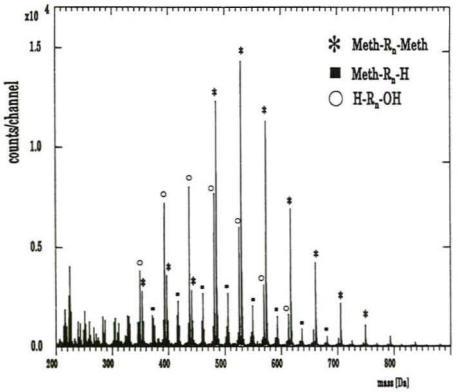

Figure 9. TOF-SIMS spectrum of PEG dimethacrylate, molecular weight 400. Major peak series: (*) Meth-R_n-Meth, (■) Meth-R_n-H, and (O) H-R_n-OH.

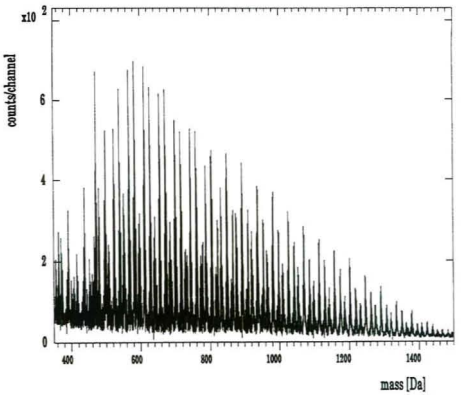

Figure 10. TOF-SIMS spectrum from 400 to 1500 Da for PEG distearate, molecular weight 600.

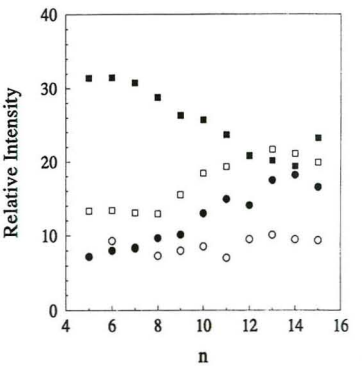

Figure 11. Relative intensities of major peak series in PEG distearate, molecular weight 600, as a function of pattern number (n). Key: (■) R_n + 283 + H, (□) R_n + 283 + 239, (●) (R_n + 255 + 239, and (O) R_n + 267 + 283.

Da, whereas the negative-ion peaks occur at 255 and 283 Da. The ratios of peak intensities of these two sets of peaks (255/283 in the negative and 283/311 in the positive) are approximately the same, which indicates a possible relationship between the two sets. Commercially, PEG distearate is manufactured using natural product grade stearic acid, which contains significant amounts of palmitic acid, $CH_3(CH_2)_{14}$-COOH. The negative-ion mode peaks can be assigned to the $(M - H)^-$ ions from palmitic (255 Da) and stearic acid (283 Da), and the peaks at 283 and 311 Da in the positive mode can be assigned to the palmitate and stearate groups plus an additional C_2H_4 group resulting from cleavage at the C–O bond within the neighboring PEG repeat unit. Similar results in the positive-ion laser desorption spectra of PEG monostearate have been reported by Becker and co-workers, where the primary fragments occurred at 256 and 284 Da.[42] Although the peak at 256 Da was proposed to result from loss of the carbonyl group along with rearrangement of an oxygen from stearic acid, it is more likely the $(M + H)^+$ ion for palmitic acid.

Oligomer Distributions. It was possible to obtain spectra of the oligomer distributions for the lower molecular weight PEG dimethacrylate and distearate samples. For PEG dimethacrylate 200, sodium-cationized oligomers were observed from ca. 400 to 500 Da. Some concern has been previously expressed that low molecular weight polymers (<500 Da) may be pumped away under the high-vacuum conditions of the TOF-SIMS, thereby skewing the observed oligomer distribution toward higher mass oligomers. Fortunately, no such problems were encountered. For PEG dimethacrylate 400, two series of peaks were observed in addition to cationized oligomers, as shown in Figure 9. The most intense peaks are the dimethacrylate oligomer peaks (*) (Meth-R_n-Meth), but monomethacrylate-terminated PEGs (■) (Meth-R_n-H) as well as hydroxyl-terminated PEGs (O) also appear as major series of peaks within the spectrum. Since singly methacrylate-terminated PEGs are observed, the hydroxyl-terminated PEGs are probably the unreacted polymer which was not successfully terminated with the methacrylate groups. The spectrum of PEG dimethacrylate 1000 also showed dimethacrylate-terminated oligomer peaks (results not shown). Unlike the hydroxyl-terminated PEG 1000 shown in Figure 1a, significant fragmentation of the terminal groups occurred, producing a characteristic fragment pattern from 350 to 900 Da. The presence of the methacrylate terminal groups has a definite effect on the preferred ion formation pathway, promoting fragmentation rather than oligomer desorption.

In contrast to the PEG dimethacrylate spectra, the spectrum of PEG distearate 600, shown in Figure 10, exhibits much more complex fragmentation patterns. The peak series can be divided into two groups: (1) single stearate- or palmitate-terminated fragments and (2) oligomers (diterminated species). Between 400 and 1000 Da, the most intense peaks can be assigned to monostearate-terminated PEG, including R_n + 268 (a 267-stearate terminal group plus H) or R_n + 284 (283 + H), as well as monopalmitate-terminated PEG at R_n + 256 (255 + H). The reader is encouraged to refer to the structures shown in Figure 6. Above 1000 Da, the spectrum is dominated by oligomer ion peaks resulting from distearate (R_n + 267 + 283), dipalmitate (R_n + 255 + 239), or stearate and palmitate ((R_n + 267 + 255) or (R_n + 283 + 239) = R_n

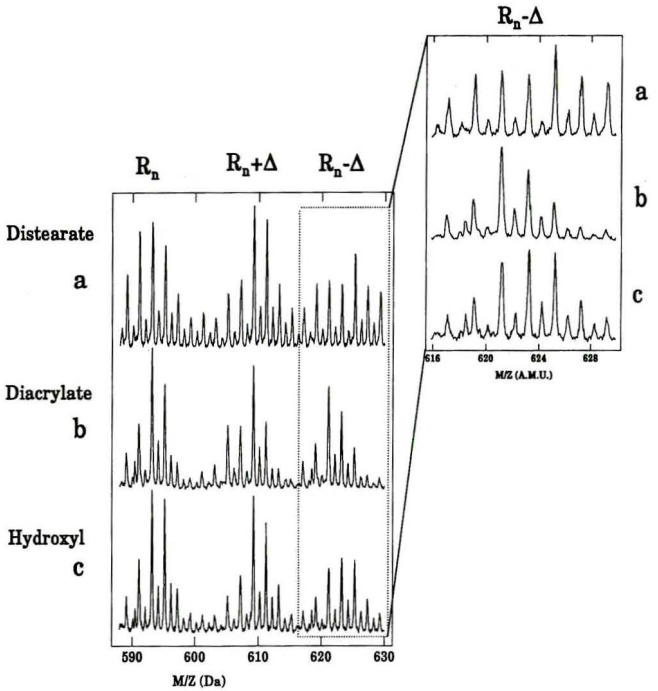

Figure 12. Typical fragment patterns for (a) distearate-, (b) diacrylate-, (c) hydroxyl-terminated, high molecular weight PEGs.

+ 522) termination. The relative intensities of four of these fragment series were calculated as a function of the number of repeat units (n) and are shown in Figure 11. Comparison of the relative intensities aids in distinguishing between several series in a complex spectrum. For example, the R_n + 284 series, which would result from single termination by the stearate group or from fragmentation of a distearate-terminated PEG, decreases with increasing n, similar to the trends observed for main chain fragments. The oligomeric species ((R_n + 255 + 239) and (R_n + 522)) increase gradually with increasing n and most probably follow a Gaussian curve similar to the oligomer distributions observed for hydroxyl-terminated PEGs. Thus, the major peak series corresponding to ions which result from oligomers or from fragmentation of the chain can be identified and distinguished in a very complex spectrum containing several series of peaks.

Fragment Patterns for High Molecular Weight Terminated PEGs. Although the general appearance of the spectra of high molecular weight PEGs terminated with acrylate and stearate groups is very similar to that of the hydroxyl-terminated samples, examination of the fine structure permits qualitative identification of the terminal groups. Figure 12 shows a fragment pattern for PEG distearate 6000, PEG diacrylate 4000, and hydroxy-terminated PEG 8000. Despite the fact that the fragment patterns of all three samples contain the same R_n, R_n + Δ, and R_n – Δ clusters, the intensities of peaks within the clusters vary for differently terminated PEG samples. For example, the R_n – Δ cluster, which is enlarged in the figure, shows several additional peaks for the PEG distearate sample. It is not possible to exactly identify the structure of the peaks within the clusters, but the identity of the terminal group clearly influences the spectral patterns which are observed. Three possible explanations for this behavior can be proposed. First, the terminal group may direct the fragmentation mechanism in some fashion, particularly if a cyclization step is involved, as has been proposed for poly(styrenes).[25] The resultant fragments would have a preferred number of double bonds or carbonyl functionalities. An alternative explanation is that the additional peaks result from single cleavage of the polymer chain along with hydrogen abstraction at that same site rather than two separate cleavages of the chain. This mechanism would produce singly terminated main chain fragments. Finally, these "extra" peaks might result from cleavage of the main chain and cleavage within a terminal group. However, since the number of repeat units in the main chain is so much greater than the number of terminal groups, this would not be statistically preferred for the diacrylate- or dimethacrylate-terminated PEGs. For the distearate-terminated PEGs, the stearate group is large enough that, even for a molecular weight of ca. 10 000 Da, it would still contribute 5% of the total weight of the polymer.

CONCLUSIONS

The fragmentation patterns of the polyglycols were examined and can be explained by mechanisms involving simple chain scissions. The predominant fragmentation mechanisms involve scission of the C–O bonds, similar to fragmentation pathways observed for aliphatic ethers in other

types of mass spectrometry. The relative fragment intensities of the clusters in the PEG and PPG fragment patterns were examined as a function of sample molecular weight. Although no dramatic changes in relative intensity were observed for the PEGs, the PPG fragment patterns were found to change with molecular weight of the polymer. The pendant methyl groups within the PPG repeat unit must play an influential role in fragmentation. Molecular weight determinations of PPGs may be possible from comparison of the relative cluster intensities in the fragment patterns.

In general, the major peak series observed in the spectra of small diacrylate-, dimethacrylate-, dipalmitate-, and distearate-terminated PEGs correspond to either oligomers or single cleavage of the PEG chain. Peaks resulting from cleavage within the terminal group or cleavage of the terminal group from the PEG chain were generally not observed for MW <4000. The terminal groups in high molecular weight PEGs can be qualitatively identified on the basis of the fine structure of clusters within the main chain fragment patterns. In addition, it was determined that PEG distearate was actually terminated with a mixture of palmitate and stearate groups. TOF-SIMS is a useful tool for both structural elucidation and detection of impurities or mixtures in polymer samples.

ACKNOWLEDGMENT

This work was supported by the National Science Foundation (Grant CHE-9022135). L.R.H. thanks Dow Chemical Co. for a graduate fellowship. The authors also thank Kathy Kuhar for her assistance with the GPC experiments and Fu-Tyan Lin for conducting the NMR analyses.

Received for review November 4, 1993. Accepted April 22, 1994.[⊗]

[⊗] Abstract published in *Advance ACS Abstracts,* June 1, 1994.

Anal. Chem. **1994,** *66,* 2313–2317

MS/MS and MS/MS/MS Analyses in a Multisector Time-of-Flight Mass Spectrometer

Toru Sakurai, Hiroyuki Ito, and Takekiyo Matsuo*

Department of Physics, Faculty of Science, Osaka University, Toyonaka, Osaka 560, Japan

The principles of MS/MS and MS/MS/MS analyses using a multisector TOF mass spectrometer are studied. The theoretical investigations and experimental results are reported. Product ion spectra are obtained by measuring the total flight time and the kinetic energy of the products without any additional separation process, any coincidence techniques, or any special timing circuits. MS/MS and MS/MS/MS product ion spectra from mercury/cesium complex cluster ions, Hg_nCs^+, are obtained and metastable decay and sequential decay of the cluster can be directly observed.

Time-of-flight (TOF) mass spectrometry, in combination with matrix-assisted laser desorption, is now widely used as a tool for the analysis of biomolecules and has recently been the subject of two extensive reviews.[1,2] There are two principle merits of TOF mass analyzers: (i) a theoretically unlimited mass range because any heavy ions reach the ion detector after the relevant time interval and (ii) a very high sensitivity because no scanning is necessary and all the ions generated in the ion source are used in the subsequent analysis.

Tandem mass spectrometry (MS/MS), in association with dissociation of precursor ions, has been widely used for structural elucidation of molecules.[3] In the field of TOF mass spectrometry, MS/MS capability has been sought for reasons in addition to those outlined above, and in order to achieve this aim, several approaches have been proposed.

Linear tandem TOF analyzers have been proposed by Schey et al.[4,5] to investigate the products produced by surface-induced dissociation. In collision-induced dissociation, linear tandem TOF analyzers with floating collision cells have been developed by Jardine et al.[6] When ion reflectrons are used in conjunction with TOF mass analysis, the flight times of the product ions are dependent on their masses when the floating cell is not used, because the ions passing through the ion-mirror field have modified trajectories according their kinetic energies. The flight times of product ions are a function of the physical nature of the reflector device, but there are no general relationships between the mass of product ion and the associated flight time. In order to overcome this fundamental obstacle, a number of special techniques have been proposed. Standing et al.[7,8] used an additional detector behind the ion reflector to detect neutral fragments produced in the decomposition process. When a neutral species is detected at this detector, it is assumed that an associated ion will have been formed from the dissociation of the precursor ion into a product ion and a neutral species. Haberland et al.[9] and Bhaskar and Klimcak[10] used the TOF instrument to investigate the fragmentation processes of cluster ions. Spengler et al.[11] have observed the metastable decay of peptides in matrix-assisted laser-desorption ion production. Cornish and Cotter[12] have developed a tandem reflectron for MS/MS analysis in which the first reflectron separates precursor ions and mass-selected ions are collisionally activated using a pulsed gas injection into the collision chamber at an appropriate time interval. Subsequent analysis of the resultant product ions is performed using the second reflectron. Strobel et al.[13] have proposed a hybrid instrument with a magnetic sector mass spectrometer where the TOF analyzer is used as MS-2 in order to increase the sensitivity in the detection of products.

Stults et al.[14] have postulated the use of a sector magnet-TOF instrument in which MS/MS measurements are performed using momentum analysis in the magnet and TOF measurements for velocity analysis. Pinkston et al.[15] have taken TOF MS/MS measurements incorporating kinetic energy analysis using an electric sector analyzer.

In the present paper, we report MS/MS and MS/MS/MS analyses using a multisector TOF mass spectrometer comprised of four electric sector analyzers.[16,17] We can operate the four sectors in such way that MS/MS and MS/MS/MS analyses can be executed. The theoretical investigations and experimental results are reported.

THEORY

Our TOF mass spectrometer is comprised of four toroidal electric sector analyzers (ESAs) with 269° deflection,[17] as

(1) Cotter, R. J. *Anal. Chem.* **1992,** *64,* 1027A.
(2) Hillenkamp, F.; Karas, M.; Beavis, R. C.; Chait, B. T. *Anal. Chem.* **1991,** *63,* 1193A.
(3) McLafferty, F. W., Ed. *Tandem Mass Spectrometry (MS/MS)*; Wiley: New York, 1983.
(4) Schey, K. L.; Cooks, R. G.; Grix, R.; Wollnik, H. *Int. J. Mass Spectrom. Ion Processes* **1987,** *77,* 49.
(5) Schey, K. L.; Cooks, R. G.; Kraft, A.; Grix, R.; Wollnik, H. *Int. J. Mass Spectrom. Ion Processes* **1987,** *94,* 1.
(6) Jardine, D. R.; Morgan, J.; Alderdice, D. S.; Derrick, P. J. *Org. Mass Spectrom.* **1992,** *27,* 1077.
(7) Lafortune, F.; Ens, W.; Hruska, F. E.; Sadana, K. L.; Standing, K. G.; Westmore, J. B. *Int. J. Mass Spectrom. Ion Processes* **1987,** *78,* 179.
(8) Tang, X.-J.; Ens, W.; Standing, K. G.; Westmore, J. B. *Anal. Chem.* **1988,** *60,* 1791.
(9) Haberland, H.; Kornmeier, H.; Ludewigt, C.; Risch, A.; Schmidt, M. *Rev. Sci. Instrum.* **1991,** *62,* 2621.
(10) Bhaskar, N. D.; Klimcak, C. M. *Int. J. Mass Spectrom. Ion Processes* **1992,** *113,* 13.
(11) Spengler, B.; Kirsch, D.; Kaufmann, R. *Rapid Commun. Mass Spectrom.* **1991,** *5,* 198.
(12) Cornish, T. J.; Cotter, R. J. *Anal. Chem.* **1993,** *65,* 1045.
(13) Strobel, F. H.; Solouki, T.; White, M. A.; Russel, D. H. *J. Am. Soc. Mass Spectrom.* **1990,** *2,* 91.
(14) Stults, J. T.; Enke, C. G.; Holland, J. F. *Anal. Chem.* **1983,** *55,* 1323.
(15) Pinkston, J. D.; Rabb, M.; Watson, J. T.; Allison, J. *Rev. Sci. Instrum.* **1986,** *57,* 583.
(16) Sakurai, T.; Matsuo, T.; Matsuda, H. *Int. J. Mass Spectrom. Ion Processes* **1985,** *63,* 273.
(17) Sakurai, T.; Fujita, Y.; Matsuo, T.; Matsuda, H.; Katakuse, I.; Miseki, K. *Int. J. Mass Spectrom. Ion Processes* **1985,** *66,* 283.

0003-2700/94/0366-2313$04.50/0
© 1994 American Chemical Society

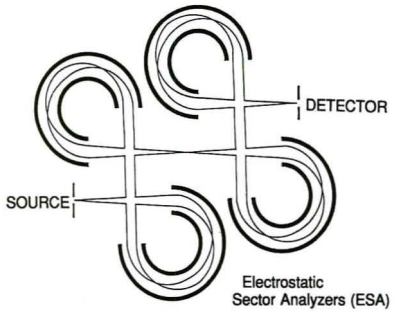

Figure 1. Schematic representation of the four-sector TOF mass spectrometer.

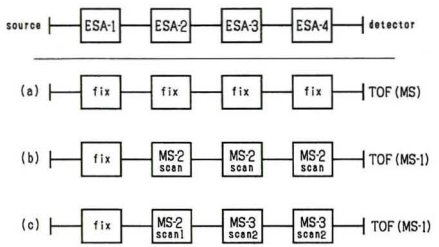

Figure 2. Schematic representation of the functionality of a multisector TOF-mass spectrometer. The first row indicates the configuration of the instrument. (a) MS analysis: The symbol "fix" means the applied voltage of ESA is fixed for the appropriate acceleration energy. (b) MS/MS analysis: The mass of the precursor ion is determined by using the time-of-flight as MS-1. The mass of the product ions is determined by scanning the appropriate ESA (MS-2). (c) MS/MS/MS analysis: First-generation product ion spectra can be obtained by scanning MS-2 (scan 1), and second-generation product ion spectra can be obtained by scanning MS-3 (scan 2).

shown in Figure 1. The principle operations for MS, MS/MS, and MS/MS/MS analyses using the multisector instrument are schematically delineated in Figure 2. The configuration of the instrument is represented in the first row of Figure 2. The functions and roles of the ESAs in MS, MS/MS, and MS/MS/MS analyses are shown in the lower part and are explained in detail below.

MS Analysis. Detailed discussions about the multiple focusing feature of the mass spectrometer were given in previous paper;[16] we here simply explain the outline. The flight time, T_0, of an ion mass, m_0, is inversely proportional to its velocity, v_0. The mass may then be determined from the flight time:

$$T_0 = \frac{L}{v_0} = \left(\frac{m_0 L^2}{2U_0}\right)^{1/2} \tag{1}$$

where L is the distance between the source and the detector and U_0 is the translational energy of the ion accelerated from the source.

For considering the mass resolution of a TOF system, the time difference between the flight time of an arbitrary particle and that of the reference particle is important. The time difference, Δt, and the spatial deviations, Δx, Δy, at the detector position are given to a first-order approximation:

$$\Delta t = T_x x_0 + T_\alpha \alpha_0 + T_\delta \delta + \Delta t_0$$

$$\Delta x = X_x x_0 + X_\alpha \alpha_0 + X_\delta \delta$$

$$\Delta y = Y_y y_0 + Y_\beta \beta_0 \tag{2}$$

where Δt_0 is the duration of the ion source operation, x_0 and y_0 are the initial spatial deviations, α_0 and β_0 are initial incidence angles to the x and y axes, respectively, and δ is the relative velocity deviation.

The mass resolution may be expressed as a half of the temporal resolution:

$$m_0/\Delta m = T_0/2\Delta t \tag{3}$$

In order to improve the mass resolution, therefore, a long flight path and a short time deviation are preferable. We require a triple isochronous focusing condition, $T_x = 0$, $T_\alpha = 0$, $T_\delta = 0$, to minimize the time deviation. Also, in order to increase the ion transmission efficiency of the instrument, two-dimensional stigmatic focusing and velocity spatial focusing conditions $X_\alpha = 0$, $X_\delta = 0$, $Y_\beta = 0$, are also required. The 6-fold multiple-focusing condition (triple isochronous and triple spatial focusing) can be achieved in a TOF mass spectrometer using four toroidal electric sectors. The system has good characteristics in terms of both ion-optical features possessing small higher order aberrations and a practical geometric size. TOF mass spectra may be obtained when a constant voltage is applied to the ESAs.

MS/MS Analysis. In MS/MS analysis, by using a magnetic sector instrument of reverse geometry, the mass of a product ion may be determined from the ion kinetic energy spectrum (MIKES)[18,19] generated by scanning the applied voltage to the electric sector. In our TOF mass spectrometer, product ion spectra are generated in a way similar to MIKES by scanning the voltage on the electric sectors. There are four electric sectors in this instrument; thus, we can choose one of four positions as the place of decomposition: (i) immediately after the ion source, (ii) between first and second sectors, (iii) between second and third sectors, and (iv) between third and fourth sectors.

Figure 2b illustrates the principle of MS/MS analysis utilizing decomposition between the first and second sectors. If we consider the decomposition of a precursor ion of mass m_1, yielding a product ion of mass m_2, then the kinetic energy, U_2, and velocity, v_2, of the product ion are given as

$$U_2 = (m_2/m_1)U_0 - \Delta U$$

$$v_2 = v_1 - \Delta v \tag{4}$$

where U_0 is the acceleration energy, v_1 is the velocity of the precursor ion, and ΔU and Δv are, respectively, energy and velocity shift in the decompositio process. Because Δv is usually

(18) Russell, D. H.; Smith, D. H.; Warmack, R. J.; Bertram, L. K. *Int. J. Mass Spectrom. Ion Phys.* **1980**, *35*, 381.
(19) Wachs, T.; Bente, P. F., III; McLafferty, F. W. *Int. J. Mass Spectrom. Ion Phys.* **1972**, *9*, 333.

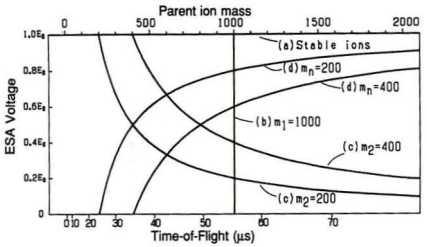

Figure 3. Relationships between the TOF and the applied voltage of ESA for obtaining the MS/MS spectra; (a) shows the relationship for a TOF spectrum of stable ions, (b) indicates the relationship for a product ion spectrum of a defined precursor m_1 (m_1 = 1000 in this example), (c) indicates the relationship for a precursor ion spectrum of a defined product m_2 (m_2 = 200 and 400 in this example), and (d) indicates the relationship for the constant neutral loss spectrum of m_n (m_n = 200 and 400 in the examples illustrated).

much smaller than v_1, the velocity of the product ion is considered to be equal to that of the precursor in a first-order approximation. The mass of the precursor ion, m_1, can be identified from the total flight time, T. The total flight time is the time it takes for the ion to travel from the ion source to the detector, regardless of the place of decomposition, and it may be expressed as

$$T = \frac{L}{v_2} = \frac{L}{v_1} = \left(\frac{m_1 L^2}{2U_0}\right)^{1/2} \tag{5}$$

However, mass of the product ion cannot be determined from the total flight time, T, because the flight time of the product after decomposition is independent of its mass, m_2. We know that the kinetic energy of the product ion, U_2, is related to the mass of the ion, m_2, as shown in eq 4. By using an electric sector analyzer, we can analyze the energy of the product; thus the mass m_2 may be calculated.

There are three MS/MS scan modes: (i) product ion scanning, (ii) precursor ion scanning, and (iii) constant neutral loss scanning. In order to realize the scan modes, the following relationships between the total flight time, T, and the voltage applied to electric sectors, E, should be satisfied, the relations are drawn as lines b–d in Figure 3.

(i) Product Ion Scanning. In obtaining a product ion spectrum derived from a defined precursor of mass m_1, the mass of products, m_2, may be calculated from eq 4 as

$$m_2 = (E/E_0)m_1 \tag{6}$$

where E is the applied ESA voltage and E_0 is the ESA voltage corresponding to the acceleration energy. The total flight time, T, is independent on E for any product and is given in eq 5. The relation is indicated by line b in Figure 3.

(ii) Precursor Ion Scanning. In obtaining a precursor ion spectrum for a defined product ion of mass m_2, the mass of precursors, m_1, may be calculated as

$$m_1 = (E_0/E)m_2 \tag{7}$$

the relationship between the total flight time and the ESA voltage for the product m_2 is given as

$$T = \left(\frac{E_0}{E}\frac{m_2 L^2}{2U_0}\right)^{1/2} \tag{8}$$

which is shown as line c in Figure 3.

(iii) Constant Neutral Loss Scanning. In obtaining a spectrum for a constant neutral loss of mass m_n ($= m_1 - m_2$). The mass of the precursor, m_1, and the product, m_2, may be calculated:

$$m_1 = \frac{E_0}{E_0 - E}m_n$$

$$m_2 = \frac{E}{E_0 - E}m_n \tag{9}$$

the relationship between T and E for the neutral m_n (line d in Figure 3) is

$$T = \left(\frac{E_0}{E_0 - E}\frac{m_n L^2}{2U_0}\right)^{1/2} \tag{10}$$

When TOF spectra are measured by scanning the applied voltage on ESA, three-dimensional data (T, E, ion intensity) are obtained. The above three scanning modes may then be realized by plotting the data along the three lines in Figure 3. The MS/MS analysis of a sample mixture may be simultaneously performed without a preseparation process.

MS/MS/MS and MS^n Analyses. If we consider the sequential decompositions of an ion in its flight from the ion source to the detector, the kinetic energy and velocity of the products are given in eq 4. The function of the ESAs for MS/MS/MS analysis is shown schematically in Figure 2c, and in this case, the position of the first decomposition is chosen as being between the first and second ESAs. A second decomposition, from a first-generation product to a second-generation product, is assumed to occur between the second and third electric sectors. The voltage applied to the second ESA (MS-2) should be set to pass ions of the kinetic energy of the first-generation products, and the voltage applied to the third and fourth ESAs (MS-3) should be set to pass ions of the kinetic energy of the second-generation product ions. The mass of the precursor ion can be determined by the total flight time (MS-1). The sequential product ion spectra from a defined precursor and a defined first-generation product can be obtained by scanning MS-3. Reaction intermediate scanning for a defined precursor subsequently decomposing to a defined second-generation product can be performed by scanning MS-2.

The TOF mass spectrometer has four electric sectors, and the principles behind MS^4 and MS^5 analyses for sequential decompositions can easily be envisaged, being a natural extension of the MS/MS/MS analysis. The mass of the precursor ion is again determined from the total flight time (MS-1), and ESA-1, ESA-2, ESA-3, and ESA-4 act as MS-2, MS-3, MS-4, and MS-5, respectively.

EXPERIMENTAL SECTION

The multisector mass spectrometer consists of four toroidal electric sector analyzers with 269° deflection,[17] and a

schematic representation of the instrument is shown in Figure 1. The total flight path is 1.73 m, and the diameter of the vacuum chamber is 0.41 m. A 20-keV Cs^+ (Antek 160-250B) secondary ion source was used for generation of ions from the sample of interest. The pressure of the primary ion source housing was maintained at 4×10^{-5} Pa. A pulse generator (Hewlett-Packard 214B or Avtech AVL-C) was used for pulsed operation of the ion source. The applied pulse width was variable from 18 ns to 1 μs at 4 kHz. The acceleration energy of the secondary ions was 5 keV, and the applied voltage for the electric sectors was ±800 V. The energy bandpass of the ESAs was ±1%. The pressure in the analyzing region was maintained at 8×10^{-5} Pa, and no collision gas was introduced. A conventional Be/Cu electron multiplier (Hamamatsu Photonics R667) was used for ion detection. Flight time measurement was performed with a time-to-analog converter (Ortec 467). TOF mass spectra were obtained with pulse height analysis mode of a multichannel analyzer (Canberra 35 plus). Mass calibration was performed using cesium iodide. In the MS/MS and MS/MS/MS measurement, the voltage for the ESAs was scanned using a sweep adapter (Takasago AP-4KS) in 10–800 s for a scan. The time-to-analog converter was used as a single-channel analyzer with a certain time window. MS/MS and MS/MS/MS spectra were obtained with the multichannel scaling mode of the multichannel analyzer. The accuracy of mass determination had an error of 0.05%.

Metastable decay of mercury/cesium complex cluster ions was measured to demonstrate MS/MS and MS/MS/MS analyses. Sample mercury was purchased from Kanto Chemical Co. We had previously analyzed mercury/cesium complex clusters using a grand-scale magnetic-sector-type mass spectrometer[20,21] since in order to investigate the stability of the clusters, it is important to compare distribution pattern and the metastable decays obtained by using two distinct mass-measuring methods.

RESULTS AND DISCUSSION

MS Analysis. By applying the appropriate voltage to the ESAs, according to the acceleration energy, TOF mass spectra of stable ions can be obtained. The mass spectrum of mercury/cesium complex clusters, Hg_nCs^+, is shown in Figure 4. A partial spectrum for the Hg_4Cs^+ cluster is expanded in the inset to the figure. A mass resolution of 1500 (fwhm) is obtained and each of the isotopes is clearly resolved. In the present TOF mass spectrometer triple isochronous focusing is achieved, such that ions having an initial energy spread could be detected at the same time. The duration of the ion source operation was 18 ns and the flight time of Hg_4Cs^+ was 54.8 μs in this measurement. The calculated mass resolution is expected to be 1520, and we can see that the calculated and experimental mass resolution coincide reasonably. Discontinuities in the relative abundance of the clusters causing the stability of the cluster structure are clearly seen in this spectrum. The number of mercury atoms in the clusters at such discontinuities is called the "magic" number. The magic

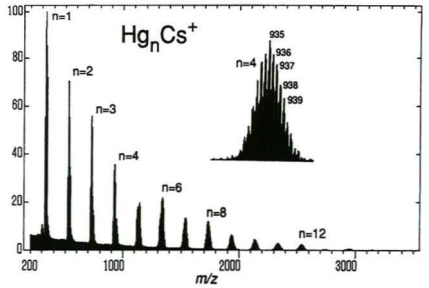

Figure 4. Mass spectrum of mercury/cesium complex cluster, Hg_nCs^+. Background is not subtracted.

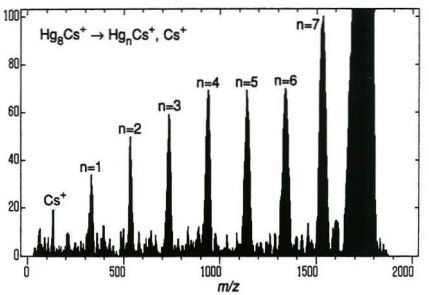

Figure 5. Product ion spectrum derived from the mercury/cesium complex cluster Hg_8Cs^+ (m/z = 1738). The product ions are Cs^+ and Hg_nCs^+. Smooth background is subtracted.

numbers observed in this experiment, n = 4, 6, 8, 12, 14, 18, 22, and 25, are identical to the results obtained using a magnetic sector instrument.[20]

MS/MS Analysis. MS/MS spectra can be obtained by scanning the applied voltage of one or more of the ESAs, as described above. Figure 5 shows the product ion spectrum generated from the Hg_8Cs^+ precursor ion. The mass of the precursor ion is 1738 u and its flight time is 74.7 μs. In this experiment, the applied voltage of the first sector was fixed to ±800 V to eliminate stray ions with differing energies. The applied voltages to the second, third, and fourth electric sectors (MS-2) were scanned simultaneously such that metastable decay between the first and second electric sectors could be detected. The probability of metastable decay of the cluster is very small; thus, the intensity of the product ions was very low. In order to detect the product ions effectively, the duration of ion source operation was extended to 700 ns at 4 kHz, and the ESA scan was 400 s. The width of the time gate for ion detection was also 700 ns around the flight time of the precursor, 74.7 μs; thereby the theoretical mass resolution was 50. The acquired spectral peaks were broadened by this time width, and individual separation of the naturally occurring isotopes was lost. The product ions were determined as Cs^+ and Hg_nCs^+. Ions of pure mercury Hg_n^+ were not observed.

There are two important requirements for an MS/MS instrument: (i) the selectivity of precursor ions and (ii) the resolution obtainable for the product ions.

The mass separation of precursor ions is executed in the time domain in accordance with the total flight times. To a

(20) Sakurai, T.; Ito, H.; Matsuo, T.; Katakuse, I. *Rapid Commun. Mass Spectrom.* **1991**, *5*, 437.
(21) Ito, H.; Sakurai, T.; Matsuo, T.; Ichihara, T.; Katakuse, I. *Phys. Rev. B* **1993**, *48*, 4741.

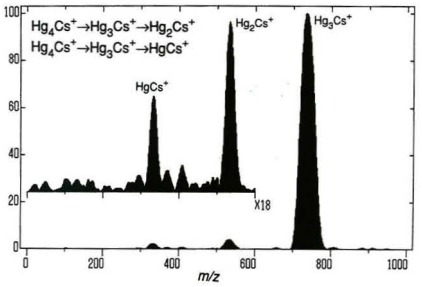

Figure 6. Second-generation product ion spectrum generated from a precursor Hg_4Cs^+ (m/z = 935) and a first-generation product Hg_3Cs^+ (m/z = 735). The second-generation product ions are $HgCs^+$ (m/z = 333) and Hg_2Cs^+ (m/z = 534). Smooth background is subtracted.

first-order approximation, the velocity spread, Δv, given in eq 4, has been neglected. However, in an actual decomposition process, relatively large velocity shifts are often observed. In a TOF instrument without velocity isochronous focusing at the decomposition position, the total flight time depends on the velocity shift; thus, the separation ability decreases. In our TOF mass spectrometer, velocity focusing is achieved in the second, third, and fourth field-free regions; hence the flight time of the product ions can be uniformly focused even if a velocity shift occurs. Precursor ion separation is higher than in the case without velocity focusing capability.

In the case of MIKES using a magnetic sector mass spectrometer, the mass resolution of the product ions is limited to the energy resolution as $U_2/\Delta U$, where U_2 is the energy of the product ion and ΔU is the energy spread in the decomposition. The mass resolution is poor, especially in the lower mass region, because the energy U_2 is small. However, in MS/MS analysis using a sector-TOF instrument, the mass resolution may be improved, even for product ions formed with large energy spreads. When the energy shift exists, the electric sector cannot separate ions of different mass with the same energy. But since the velocity of the product ions is also shifted, as in eq 4, then the flight times will differ. By measuring both the applied voltage and the flight time, it is therefore possible to resolve product ions that have been formed with a large energy shift. When we use the time window, Δt, for obtaining a product ion spectrum, the mass resolution of the spectrum is given as $T/2\Delta t$, and the mass resolution of the product ion spectrum is theoretically constant for the whole mass range. Such a situation is clearly illustrated in Figure 5.

MS/MS/MS Analysis. A sequential product ion spectrum can be obtained by scanning of MS-3, as shown schematically in Figure 2c. Figure 6 shows the spectrum obtained for the second-generation product from $Hg_4Cs^+ \rightarrow Hg_3Cs^+ \rightarrow$ products. In this experiment, the pulse duration of the ion source was increased to 1.0 μs at 4 kHz and scan speed was 800 s, in order to effectively detect the sequential decay of the cluster. The mass resolution of each stage of precursor/product selection was 25, with the extreme width of the peaks being a result of the relatively long ion source pulse. The first decay from the precursor to the first-generation product occurred between the first and second sectors as

$$Hg_4Cs^+ \rightarrow Hg_3Cs^+$$

The ion Hg_3Cs^+ in the MS/MS/MS spectrum is the first-generation product passed through MS-3. The second-generation product ions of Hg_2Cs^+ and $HgCs^+$ are clearly seen in this spectrum, the result of from the metastable decays:

$$Hg_4Cs^+ \rightarrow Hg_3Cs^+ \rightarrow Hg_2Cs^+$$

$$Hg_4Cs^+ \rightarrow Hg_3Cs^+ \rightarrow HgCs^+$$

Approximately 5% of the first-generation product ions decayed to second-generation products between the second and third sectors. The flight time between the sectors was 7.2 μs; thus the half-life of the first-generation product ions Hg_3Cs^+ is of the order of 10 μs.

CONCLUSION

We have proposed the principles of MS/MS and MS/MS/MS analyses using a multisector TOF mass spectrometer. Product ion spectra can be obtained by measuring the total flight time and the kinetic energy of the products without any additional separation process, any coincidence techniques, or any special timing circuits.

We have obtained MS/MS and MS/MS/MS product ion spectra from mercury/cesium complex cluster ions, Hg_nCs^+, and have observed the size distribution of the clusters and found clusters with magic numbers of n = 4, 6, 8, 12, 14, 18, 22, and 25. The magic numbers are identical with those obtained using a magnetic-sector mass spectrometer with a similar ion source. We detected metastable decay and sequential decay of the cluster. The mass resolution of the product ion spectra acquired was relatively low because the pulse duration of the ion source was selected to be long in order to generate sufficient ions for effective detection of metastable decay. This technique can be applicable to practical requirements in combination with a short pulsed intense ion source and collision cells in the appropriate field-free regions to effect useful fragmentation.

ACKNOWLEDGMENT

The authors thank Professors H. Matsuda, I. Katakuse, and R. Arakawa (Osaka University) and Dr. M. Morris (National Research Council, CANADA) for their valuable discussions.

Received for review February 4, 1994. Accepted May 4, 1994.®

® Abstract published in *Advance ACS Abstracts,* June 1, 1994.

Anal. Chem. **1994,** *66,* 2318–2329

Spontaneous Injection in Microcolumn Separations

Harvey A. Fishman, Nabeel M. Amudi, Thomas T. Lee,† Richard H. Scheller,‡ and Richard N. Zare*

Department of Chemistry, Stanford University, Stanford, California 94305

The phenomenon of spontaneous (ubiquitous) injection in microcolumn separations has been characterized to improve quantitative precision for ultramicrosampling and to enhance separation efficiency. By combining fluorescence imaging, video microscopy, and measurements from capillary electrophoresis, we demonstrate that spontaneous injection is caused primarily by an interfacial pressure difference formed at the inlet of the capillary. This complex injection mechanism has been modeled with some simple assumptions based on fluid dynamics. In particular, studies showed that extraneous injection is reduced up to 12-fold by etching the capillary inlet or by using a thin-walled capillary. Variations by a factor of 2 in the injection length can result from delays between sample introduction and reinsertion into the inlet vial if the timing is not controlled precisely. Evidence is presented that evaporation of buffer from the inlet can reduce the injection length by more than 1 order of magnitude.

Microchannel separation techniques, such as capillary electrophoresis (CE) and open tubular liquid chromatography, are especialy well-suited for chemical analysis in small volumes.[1] The ability to perform subnanoliter injections[1-3] offers many opportunities for chemically profiling complex samples in cellular biochemistry and biotechnology. Examples include the analysis of single cells, subcellular organelles, and vesicles.[1-8] The use of narrow injection plugs also significantly improves separation efficiency and resolution.[9-11] Indeed, the importance of performing small injections has been recognized, and several approaches for ultramicrosample injection and manipulation have been demonstrated including CE on a chip,[12,13] electrophoresis across a gap,[14,15] specialized micro-injection techniques,[16-19] and on-column microreactions.[20,21]

Simply touching the capillary to the sample solution, however, has long been recognized to cause an extraneous injection that accounts for the nonzero intercept when calibrating injection volumes in CE[9-11,22,23] and in electrokinetic chromatography.[24] As sample volumes decrease further, reducing this type of injection error becomes critical. Even for routine analysis, capillary electrophoresis has suffered from poor reproducibility,[25-28] and improvements in quantitative precision and accuracy are needed. Grushka and McCormick[9] were the first to report on this extraneous injection, a phenomenon they called "ubiquitous injection". They found that ubiquitous injection could start as soon as the capillary made contact with the sample. After the capillary was removed, the sample had penetrated ~700 μm into the capillary, corresponding to an approximate volume of 3 nL for a 75-μm-i.d. capillary. Furthermore, they reported that the process of sample penetration showed no correlation to the interval of time the capillary was in contact with the sample. Other studies[27,29] established that this extraneous injection would lead to errors in calibration and quantitation for which compensation is difficult even with internal standards. In addition to degrading quantitation, this extraneous injection can severely reduce separation efficiency.[9-11]

Dose and Guiochon[27,29] discussed an inherent difficulty in quantitative CE injections, namely, that the injection zone boundaries are defined by interfaces between miscible solutions that spontaneously lead to dispersion. They argued that diffusion might play the dominant role in extraneous injection. Using computer simulations, they showed that the concentration gradient at the inlet caused a rapid net flow of the sample into or out of the capillary. In addition, as a filled capillary touches a liquid surface, the surface tension is broken and the resultant convective mixing can contribute to extraneous injection of the sample.[30] Although these arguments based

† Current Address: Gilead Sciences, Foster City, CA 94404.
‡ Howard Hughes Medical Institute, Department of Molecular and Cellular Physiology, Stanford University, Stanford, CA 94305.

(1) Kennedy, R. T.; Oates, M. D.; Cooper, B. R.; Nickerson, B.; Jorgenson, J. W. *Science* **1989**, *246*, 57–63.
(2) Olefirowicz, T. M.; Ewing, A. G. *Anal. Chem.* **1990**, *62*, 1872–1876.
(3) Ewing, A. G.; Wallingford, R. A.; Olefirowicz, T. M. *Anal. Chem.* **1989**, *61*, 292A–303A.
(4) Lee, T. T.; Yeung, E. S. *Anal. Chem.* **1992**, *64*, 3045–3051.
(5) Hogan, B.; Yeung, E. S. *Anal. Chem.* **1992**, *64*, 2841–2845.
(6) Cooper, B. R.; Jankowski, J. A.; Leszczyszyn, D. J.; Wightman, R. M.; Jorgenson, J. W. *Anal. Chem.* **1992**, *64*, 691–694.
(7) Sweedler, J. V.; Shear, J. B.; Fishman, H. A.; Zare, R. N.; Scheller, R. H. *Proc. SPIE-Int. Soc. Opt. Eng.* **1992**, *1439*, 27–33.
(8) Sweedler, J. V.; Fuller, R.; Tracht, S.; Timperman, A.; Toma, V.; Khatib, K. *J. Microcolumn Sep.* **1993**, *5*, 403–412.
(9) Grushka, E. M.; McCormick, R. M. *J. Chromatogr.* **1989**, *471*, 421–428.
(10) Huang, X.; Coleman, W. F.; Zare, R. N. *J. Chromatogr.* **1989**, *480*, 95–110.
(11) Schwartz, H. E.; Melera, M.; Brownlee, R. G. *J. Chromatogr.* **1989**, *480*, 129–139.
(12) Harrison, D. J.; Fluri, K.; Seiler, K.; Fan, Z.; Effenhauser, C. S.; Manz, A. *Science* **1993**, *261*, 895–897.
(13) Effenhauser, C. S. Manz, A.; Widmer, H. M. *Anal. Chem.* **1993**, *65*, 2637–2642.
(14) Kuhr, W. G.; Licklider, L.; Amankwa, L. *Anal. Chem.* **1993**, *65*, 277–282.
(15) Amankwa, L.; Kuhr, W. G. *Anal. Chem.* **1993**, *65*, 2693–2697.
(16) Linhares, M. C.; Kissinger, P. T. *Anal. Chem.* **1991**, *63*, 2076–2078.
(17) Kennedy, R. T.; Jorgenson, J. W. *Anal. Chem.* **1988**, *60*, 1521–1524.
(18) Wallingford, R. A.; Ewing, A. G. *Anal. Chem.* **1988**, *60*, 1972–1975.
(19) Wallingford, R. A.; Ewing, A. G. *Anal. Chem.* **1987**, *59*, 678–681.
(20) Fishman, H. A.; Shear, J. B.; Sweedler, J. V.; Zare, R. N.; Scheller, R. H. The Pittsburgh Conference on Analytical Chemistry and Applied Spectroscopy, March 9–12, New Orleans, LA, 1992; Abstract 300.
(21) Harmon, B. J.; Patterson, D. H.; Regnier, F. E. *Anal. Chem.* **1993**, *65*, 2655–2662.
(22) Rose, D. J., Jr.; Jorgenson, J. W. *Anal. Chem.* **1988**, *60*, 642–648.
(23) Honda, S.; Iwase, S.; Fujiwara, S. *J. Chromatogr.* **1987**, *404*, 313–320.
(24) Bruin, G. J. M.; Tock, P. P. H.; Kraak, J. C.; Poppe, H. *J. Chromatogr.* **1990**, *517*, 557–572.
(25) Li, S. F. Y. *Capillary Electrophoresis*; Elsevier: London, 1992.
(26) Weinberger, R. *Practical Capillary Electrophoresis*; Academic Press: Boston, MA, 1993.
(27) Dose, E. V.; Guiochon, G. *Anal. Chem.* **1992**, *64*, 123–128.
(28) Lookabaugh, M.; Biswas, M.; Krull, I. S. *J. Chromatogr.* **1991**, *549*, 357–366.
(29) Dose, E. V.; Guiochon, G. *Anal. Chem.* **1991**, *63*, 1063–1072.
(30) Bird, R. B.; Stewart, W. E.; Lightfoot, E. N. *Transport Phenomena*; Wiley: New York, 1960.

0003-2700/94/0366-2318$04.50/0
© 1994 American Chemical Society

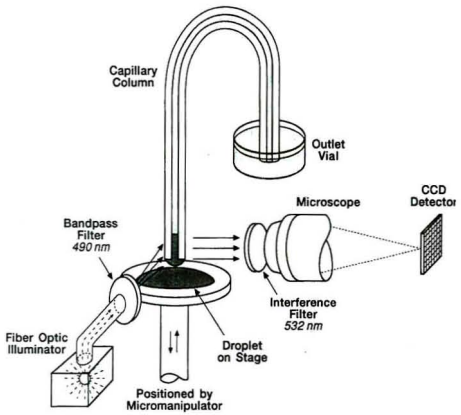

Figure 1. Fluorescence imaging system used to visualize and quantitate directly spontaneous extraneous injection. A video-speed CCD camera was reversibly interchanged with a low-noise, scientific-grade CCD camera. Objects are not drawn to scale. A 10-μL drop was injected onto the stage for all experiments.

on diffusion and convection can partially explain how sample enters the capillary, additional factors must contribute to account for the observed amount and speed of injection.[9–11,23,24] Several additional explanations have been offered, but the dominant mechanism responsible for this spontaneous (ubiquitous) injection remains unresolved and a matter of some concern to the CE research community.

In this work, we characterize a predominant mechanism of spontaneous extraneous injection in capillary electrophoresis. Using a fluorescence imaging system equipped with a scientific-grade charge-coupled device (CCD), video microscopy, and quantitative measurements from capillary electrophoresis, we demonstrate that extraneous injection originates primarily from the formation of an interfacial pressure difference across a droplet at the inlet of the capillary upon removal from the sample reservoir. Sample is introduced into the capillary by a process known in the chemical engineering community as *spontaneous fluid displacement*.[31] Because penetration is time dependent, transfer times that differ between sample introduction and reinsertion into the inlet vial can result in reproducibility errors. In addition, we also identify that the vapor pressure surrounding the capillary during the transfer delay may significantly affect the injection process and lead to a massive loss of running buffer, which causes sample compression in the entrance of the column. We demonstrate the deleterious nature of both spontaneous fluid displacement and sample compression to injections in capillary electrophoresis and offer practical methods for controlling these effects.

EXPERIMENTAL SECTION

Imaging System. Figure 1 shows the imaging system used to visualize and quantitate extraneous injection plugs. The inlet end of a fused silica capillary column (25 × 348, 50 × 345, 75-μm i.d. × 345-μm o.d.) (Polymicro Technologies, Phoenix, AZ) was cleaved by first scoring the polyimide coating with a ceramic cleaving square (Polymicro Technologies) and then carefully bending the capillary to fracture it. With care, this procedure consistently produced a nearly flat surface (as observed under a stereomicroscope) with an angle of ~87 ± 3° with respect to the capillary wall. A 5-mm section of the polyimide coating at the inlet end was removed with a Bunsen burner flame. The capillary was then fixed in position and imaged by a stereomicroscope (SMZ-2T, Nikon, Tokyo, Japan). For the qualitative visualization experiments, images were taken with a CCD video camera (Sony) and recorded with a VHS video recorder (Panasonic). A fiber-optic bundle (Cole-Palmer, Niles, IL) was directed into the microscope's built-in optics to provide Koehlerlike illumination. For displaying images on film, the video recorder was stopped (paused) and photographs were taken of the video screen (Sony Trinitron) using a Nikon 35-mm camera (Model N80085).

For the fluorescence imaging studies, a liquid-nitrogen-cooled (–126 °C), scientific-grade CCD camera (Photometrics, Tucson, AZ) equipped with a 512 × 512 CCD chip (PM512, Photometrics) was used for imaging. The CCD was controlled by IPLab software (Signal Analytics, Vienna, VA) using a photometrics NU-200 camera controller board, CC200 camera controller, and PS200 power supply module. The fiber-optic bundle directly illuminated the capillary with broad-band excitation that was sent through a 490-nm bandpass filter (BG-7, Schott Glass Technologies, Duryea, PA). Fluorescence from the capillary was collected from the microscope optics (32× magnification), which had a 532-nm interference filter (Oriel, Stratford, CT) mounted on its front. The CCD was positioned at the focal plane of the stereomicroscope. A chamber was built around a small platform that holds the sample solution. The chamber was made from a standard plastic cuvette (1-cm path length) that was inverted and the open end sealed to a piece of Plexiglas. A small hole (slightly larger than the capillary) was drilled into the top of the chamber so that the capillary could enter for the purpose of making injections.

Sample solution was injected onto the small platform inside the chamber. For experiments performed in a saturated environment, the chamber was filled with water to the level of the platform to provide a water-vapor-saturated environment. For experiments performed in ambient conditions, an identical chamber was made with the top completely open to the atmosphere, and the humidity of the air in the chamber (Palo Alto, CA) ranged from ~40 to 65%. Each chamber was mounted on a Plexiglas plank raised and lowered by a micromanipulator (Prior, England). To prevent inadvertent hydrodynamic injection, each capillary was positioned so that the meniscus in the outlet reservoir would be 2–3 mm above the meniscus of the sample solution. Moreover, the capillary was in contact with the sample no longer than 5 s.

CCD Image Processing. CCD images were collected by a Macintosh IIci computer using the IPLab spectrum software. The capillary inlet was imaged onto a region of the CCD that had a width ranging from 20 to 60 (2 × 2 binned pixels) and a length from 200 to 400 (2 × 2 pixels). Because the magnification was slightly different for each capillary inner diameter, the pixel geometry read out by the CCD varied to accommodate the different image dimensions. These pixel

(31) Marmur, A. In *Modern Approaches to Wettability: Theory and Applications*; Schrader, M. E., Loeb, G., Eds.; Plenum: New York, 1992; pp 327–356.

geometries were read out with exposure times between 0.1 and 0.5 s and a gain setting of 1.0. Collection rates were between 0.75 and 1.7 Hz for entire snapshots. Image dimensions were estimated by using the known premeasured outer diameter of the capillary as an internal calibration. Images of the capillaries had similar cross-sectional profiles. From these images we could estimate the position of the edge of the outer capillary wall with an uncertainty of 3 pixels, thus making the internal calibration distances accurate to within 6 pixels (final injection lengths ranged between 50 and 165 pixels). The front end of the capillary was identified by a bright spot that appeared at the front end of all capillaries before and after the fluorescein solution entered the column. The fluorescence response from the channel of the capillary filled with a homogeneous solution of fluorescein was roughly uniform and varied linearly with the concentrations used in these studies.

To determine spontaneous extraneous injection lengths, a plot of the fluorescence intensity along the length of the capillary channel was obtained. First, pixels across the width of the channel were averaged. This averaging resulted in a single intensity value for each point along the length of the column, thus resulting in a one-dimensional image slice down the capillary. These slices were converted to one-dimensional text file arrays and then analyzed on the Macintosh IIci using programs written in Igor (WaveMetrics, Lake Oswego, OR). Plots of the image slice showed the concentration profile along the length of the injection plug. The front end of the concentration profile for an injection plug is defined by an error function.[32,33] To quantitate the length of the injection, the front end of the injection profile was defined as the point where the intensity had decreased by 50% of the maximum (the inflection point). The maximum intensity level was determined by taking the average intensity along a segment of the uniformly filled portion of the capillary, just prior to the injection front. For all curves, the 50% point compared favorably with the actual calculated inflection point and was used because it was easier to obtain. By use of the 50% point for the leading edge, injection lengths were normalized for each image. Thus, comparisons between the kinetics of injection penetration for each run with a particular capillary inner diameter were internally consistent and averaged out any nonuniformity in illumination or fluorescence intensity. For these reasons, flat-field correction of the data was not performed. Although no dark-current subtractions on the CCD images were made, baseline subtractions were carried out on the intensity profiles along the column length. To more easily compare the amount of injection for different capillary inner diameters, the length of the injection plug was converted to an effective cylinder with a given volume. Calculation of the volume in this manner with the assumption of a homogenous solution provided a reasonable estimate of the amount of sample. The penetration kinetics are obtained by plotting this effective volume against time. For these penetration curves, we have chosen the time point immediately before a sharp increase in penetration kinetics as the starting time for spontaneous injection.

CE Detection System. Separations were performed using a home-built CE system with an absorbance detector (Isco CV4, RI). The detector wavelength was set at 340 nm with a time contant of 0.2 s. The voltage control has been described elsewhere.[34] The inlet of the capillary was manually transferred from the sample solution to the inlet reservoir. As in the CCD imaging studies, injections were made from a 10-μL droplet on a patform surrounded by the cuvette chamber. A larger hole in the top of the chamber was used to facilitate the manual transfers. In addition to filling the chamber to the level of the platform with water, a saturated environment for the CE experiments was ensured by positioning the capillary just above the sample droplet after solution breakup. The capillary was in contact with the sample no longer than 5 s. Timing for the transfer was accomplished using either a stopwatch or an alarm timer. During the injection, the sample solution was held 1–2 mm below the level of the outlet reservoir to prevent inadvertent hydrodynamic injection. Similarly, to prevent loss of the sample from inadvertent hydrodynamic outflow when the capillary was reinserted into the inlet buffer reservoir, the outlet reservoir was held 1–2 mm below the inlet. A delay of ~10 s occurred between reinserting the capillary into the inlet vial and applying the voltage across the capillary. Data were collected with a 486 computer (Adisys, Santa Clara, CA) using Lab Calc data acquisition software and a Chrom-1AT data acquisition board (Galactics, NH). Peak areas were determined using the Lab Calc software algorithm. Analyte bands that travel past the detector at different velocities give different peak areas. Hence, only analyte bands that had migration times within 5% of each other were used in this analysis. Random noise spikes in electropherograms were removed for clarity of presentation.

Chemicals and Reagents. All solutions were repared from a Millipore water filter system (Milli-Q Plus/UV, Milli-RO 6 Plus, Waters, Bedford, MA). A 15 mM phosphate buffer, pH 8.9 (Mallinckrodt, San Francisco, CA), was used for all studies. For CE runs, the buffer was filtered through 0.2-μm pore size syringe filters. Imaging studies were carried out using a 0.4 mM 2′,7′-dichlorofluorescein solution dissolved in 15 mM, pH 8.9 phosphate buffer. Stock solutions of N_ϵ-dansyl-L-lysine, N_α-dansyl-L-tryptophan, and dansyl-L-alanine (Sigma Chemical Co., St. Louis, MO) prepared in the phosphate running buffer were stored in the refrigerator and serially diluted as needed before use.

Capillary Treatments. All capillaries were conditioned with 0.1 M sodium hydroxide (Mallinckrodt) prior to use, and buffer was then electrophoresed through the column for 1 h. For some studies, the outer surface of the capillary was silanized by holding an air-filled column in a solution of dimethyldichlorosilane in toluene (silanization solution from Supelco, Bellefonte, PA) for 30 min. Afterward, the column was purged with nitrogen and air-dried for several minutes. The outer diameter of some capillaries was chemically etched with 0.1 M hydrofluoric acid (Sigma) for 2.5 h. Because hydrofluoric acid is extremely harmful upon skin contact, thick gloves and protective clothing must be worn when it is handled, and the vapors must not be inhaled. To maintain a constant inside diameter, the other end of the column was

(32) Crank, J. *The Mathematics of Diffusion*; Clarendon Press: Oxford, UK, 1956.
(33) Giddings, J. C. *Unified Separation Science*; Wiley: New York, 1991.
(34) Sweedler, J. V.; Shear, J. B.; Fishman, H. A.; Zare, R. N.; Scheller, R. H. *Anal. Chem.* **1991**, *63*, 496–502.

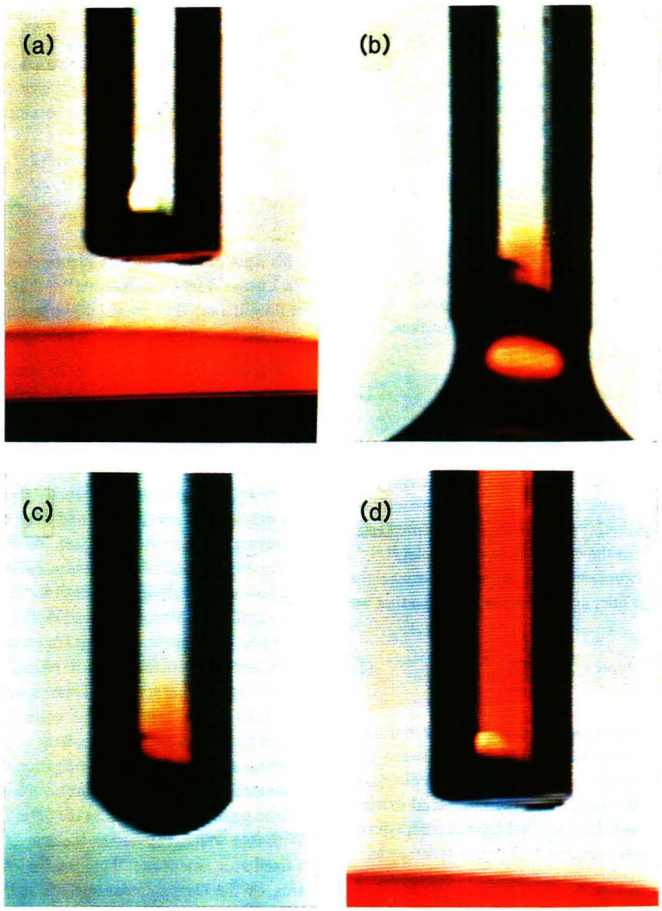

Figure 2. Video images showing the inlet end of a 75-μm-i.d., 343-μm-o.d. capillary with polyimide removed. Capillary (a) prior to sample contact, (b) contact with the sample immediately before solution breakage, (c) 34 ms after leaving solution, and (d) ~10 s after leaving solution. The orange solution below the capillary inlet is 2′,7′-dichlorofluorescein dissolved in 15 mM, pH 8.9 phosphate buffer.

attached to a pressure-regulated nitrogen tank, thereby creating a constant flow of nitrogen through the column to prevent the acid from entering the inside of the column. The capillary was rinsed with water before use.

To maintain uniform wetting on the outside surface of the capillary (i.e., to reproduce the surface conditions), excess water droplets were removed from the outside of the capillary before each run. For the CCD imaging experiments, this removal was accomplished by slowly withdrawing the analyte solution from contact with the capillary. For CE runs, water drops that adhered to the outside capillary surface were removed by lightly drawing the edge of a cover slip across the surface. Only runs with no noticeable surface spreading after sample contact were used in these studies.

THEORY

A video microscope imaging system reveals an unexpected mechanism for spontaneous extraneous injection. Parts a–d of Figure 2 show images of the inlet of a fused silica capillary (75-μm i.d., 343-μm o.d.) as it enters and leaves a solution of fluorescein dissolved in the running buffer. Upon contact with the surface (Figure 2b), the solution immediately wets the sides of the capillary and spreads upward until the interfacial energy between the water and the glass are balanced.[35] As the solution is slowly lowered below the capillary inlet, the solution forms a quasicylinder of liquid that eventually becomes unstable toward the necking (Rayleigh instability[36,37] and collapses into two segments. One segment of the collapsed cylinder forms a droplet that adheres to the end of the capillary (Figure 2c), and the rest falls back into the bulk of the solution. Spontaneously, the droplet penetrates into the capillary, and within a few seconds, the entire droplet

(35) Hunter, R. J. *Foundations of Colloid Science*; Clarendon Press: Oxford, UK, 1987; Vol. 1, pp 272–299.
(36) Rayleigh, Lord. *Proc. London Math. Soc.* **1878**, *10*, 4–13.
(37) Rumscheidt, F. D.; Mason, S. G. *J. Colloid Interface Sci.* **1962**, *17*, 260–269.

has entered into the capillary and displaced the buffer present (Figure 2d). This type of capillary penetration from a limited reservoir has been termed *spontaneous liquid–liquid displacement* or *spontaneous fluid displacement* by Marmur.[31]

Interfacial pressure difference across the curved droplet drives the penetration process. As originally noted by Young[38] and Laplace[39] around the turn of the 19th century, the pressure difference, Δp, across a curved surface is given by the following:

$$\Delta p = \gamma\left(\frac{1}{R_1} + \frac{1}{R_2}\right) \tag{1}$$

where γ is the surface tension of the solution and R_1 and R_2 are the principal radii of curvature of the droplet. If the meniscus is approximated by a hemispherical surface, then the pressure difference becomes

$$\Delta p = 2\gamma/R \tag{2}$$

The droplet maintains the curved shape to minimize the surface area.[40] As long as an inward pressure exists at the entrance of the capillary, penetration occurs. The equilibrium condition is one in which a counteracting pressure opposes the interfacial pressure difference from the curvature of the droplet;[31,41–43] in the case of CE, this counterpressure can arise from a height difference between the inlet and outlet reservoirs, so that we have

$$2\gamma/R + \rho g h = 0 \tag{3}$$

where ρ is the density of the solution, g is the gravitational acceleration, and h is the height difference between the reservoirs. From Marmur's results,[31,43] we can predict (and later will show) that the force from the interfacial driving pressure can be much greater than that formed from typical height differences between reservoirs. This pressure may have interesting ramifications for injections in small-bore capillaries (2 and 5 μm).

Flow kinetics for capillary penetration have been described in detail by several authors.[44–46] Lucas[44] and Washburn[45] first developed a quasi-steady-state theoretical approach for capillary penetration that was based on fully developed laminar flow of a Newtonian liquid with negligible inertia effects. They combined the pressure difference across the curved interface with known flow dynamics in a capillary. The total fluid flux of the solution in a capillary is given by the Hagen–Poiseuille equation:[33]

$$\frac{dV}{dt} = \frac{\pi \Delta p r^4}{8 \eta L} \tag{4}$$

where dV/dt is the flux (volume per unit time), Δp is the pressure difference, r is the radius of the inside of the capillary, L is the length of the capillary, and η is the viscosity of the solution. By substituting eq 3 into eq 4, a differential equation for the flow kinetics into a capillary caused by a pressure difference across the droplet is obtained:

$$\frac{2\gamma}{R} - \rho g h - \frac{dV}{dt}\frac{8\eta L}{\pi r^4} = 0 \tag{5}$$

This equation is essentially identical to the general form of the Lucas–Washburn equation[44,45] that describes the kinetics of flow in a capillary in which the pressure difference results from the curved meniscus in classic capillary rise experiments.

Equation 5 allows us to make some general predictions about what types of flow kinetics occur provided we know how the curvature of the meniscus varies in time. In one possible mechanism, the droplet surface can be thought of as a portion of a sphere with the ends attached to the outside of a thin-walled capillary. As the fluid is forced into the capillary, the droplet surface flattens, and accordingly, the radius of curvature of the droplet increases. As the radius of curvature increases, the interfacial pressure difference decreases, and the flow velocity slows down until the droplet penetrates into the capillary. Marmur[31] describes a different geometric situation, in which the droplet is attached at the inner capillary walls, and instead of flattening, it reduces its volume by forming smaller and smaller spheres. This scenario creates an opposite dynamics of flow, namely, one in which the radius of curvature continually decreases, thus leading to greater pressure differences and an increasing penetration velocity. Equation 5 assumes that the droplet is a portion of a sphere that maintains a fixed point of attachment at the outer edge of the capillary. With thin-walled capillaries, the droplet can easily maintain a fixed attachment site; there is a limited amount of surface area on the front annular surface at the capillary inlet to which the droplet can adhere.

In practice, many factors can modify the interfacial energy of the curved meniscus and must be taken into account when the actual interfacial pressure difference at the capillary entrance is modeled. The surface morphology, especially how well the capillary is cleaved, and the wettability of the capillary surface are extremely important. Cohen and Grushka[47] have studied the influence of the shape of the inlet on the observed efficiencies in capillary separations, and they found that straight-edge capillaries are superior to slanted ones. Surface roughness can cause contact angle hysteresis[31] and result in deviations from a spherical droplet surface. In general, any factor that affects the apparent contact angle between the droplet and the capillary surface or the point of attachment can significantly affect the shape and amount of the droplet present at the entrance. With 360-μm-o.d. capillaries, the annular front surface area is significant. Video observations demonstrate that the droplet attaches at the outer edge of the annulus immediately after solution breakage. As the droplet

(38) Young, T. *Philos. Trans. R. Soc. London* **1805**, *95*, 65–87.
(39) Laplace, P. S. de M.; *Supplement au dixieme livre du traite de mecanique celeste*; 1806; Bowditch, N. Translated and annotated; Boston, 1829–1839, 4 vols. Reprinted, Chelsea: New York, 1966.
(40) Adamson, A. W. *Physical Chemistry of Surfaces*, 5th Ed.; Wiley: New York, 1990.
(41) Marmur, A. *J. Colloid Interface Sci.* **1988**, *122*, 209–219.
(42) Marmur, A. *J. Colloid Interface Sci.* **1989**, *130*, 288–289.
(43) Marmur, A. *Chem. Eng. Sci.* **1989**, *44*, 1511–1517.
(44) Lucas, R. *Kolloid Z.* **1918**, *23*, 15–22.
(45) Washburn, E. W. *Phys. Rev.* **1921**, *17*, 273–283.
(46) Szekely, J.; Neumann, A. W.; Chuang, Y. K. *J. Colloid Interface Sci.* **1971**, *35*, 273–278.
(47) Cohen, N.; Grushka, E. *J. Chromatogr.*, in preparation.

penetrates into the capillary, the contact line for the droplet may move toward the inner walls and affect the interfacial pressure difference. In addition, any surface spreading onto the outside walls of the capillary would act to increase the radius of curvature of the meniscus and relax the interfacial energies. For example, when a capillary is cleaved with the front surface edge more rounded and less defined, solution may more easily spread along the outside surface.

Differences in the process where the solution necks and breaks apart to form the droplet at the end of the capillary may also contribute to variability in amount injected.[48] One factor that may affect the breakup of the necking solution and hence the amount of droplet formed on the end is the radius of curvature of the sample solution into which the capillary is inserted. Moreover, the speed at which the capillary leaves the sample solution may affect how much liquid forms at the entrance. For rapid removal, we observed that the droplet formation is not localized to just the front surface of the capillary but instead pours over the edge and spreads along the outside surface of the capillary.

RESULTS AND DISCUSSION

Generality of Mechanism. We tested several different experimental conditions to confirm the generality of this mechanism for spontaneous injection. This penetration process occurred with 75-, 50-, and 25-μm-i.d. capillaries ($\sim$345-μm o.d.) with and without the polyimide coating removed. These video experiments were performed with the fluorescein solution dissolved in the same buffer as in the filled column. Qualitatively, we found the same mechanism of injection for the case in which the fluorescein was dissolved in different buffers and at different pHs (pH 8.7 phosphate, pH 9.3 borate, and pH 12 phosphate buffers). Furthermore, the spontaneous injection effect was found to occur with other dyes (bromophenol blue and rhodamine). In 50 trial experiments, we observed that the amount of fluorescein injected simply upon contact with the solution comprised only a small fraction (less than 10%) of the overall amount injected after the capillary was removed entirely from the sample. This reproducible observation is inconsistent with initial reports by Grushka and McCormick,[9] who observed that the sample could penetrate as much as 700 μm upon contact. Spontaneous injection resulted when the capillary was removed from both a small sample reservoir (10-μL droplet on a slide) having a small radius of curvature and from a large sample reservoir (1-mL vial) having a large radius of curvature.

For the capillaries we studied, spontaneous fluid displacement of the droplet was the dominant contribution to extraneous injection. Because many factors can affect the spontaneous injection, we have chosen to study the behavior using a set of capillary conditions that were reproducible in surface flatness, surface wettability, removal speed, and size of the sample solution reservoir (see Experimental Section). Even with some differences in cleave angle and surface roughness (as observed under the microscope), the obtained conditions are sufficiently reproducible to give similar injection amounts (within approximately 10–20%) with different capillary cuts. Although variations in surface conditions from capillary to capillary or differences in the radius of curvature of the sample solution may affect injection amounts, the mechanism of spontaneous fluid displacement is general enough that important trends and conclusions can be derived from investigating more quantitatively a single set of reproducible conditions such as those chosen in this work.

(48) Fishman, H. A.; Scheller, R. H.; Zare, R. N., submitted to *J. Chromatogr.* symposium volume for the 6th International Symposium on High Performance Capillary Electrophoresis.

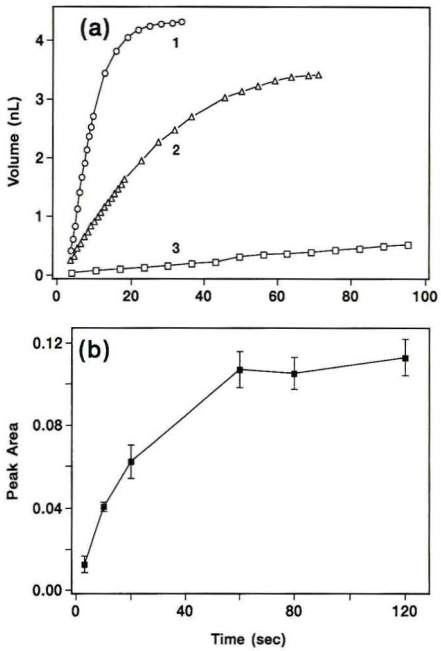

Figure 3. (a) Kinetic curves for spontaneous capillary penetration. The capillary is surrounded by a vapor-saturated environment. Each curve shows the volume of the injection plug as a function of time. Injection plugs were quantitated directly from images taken by a scientific-grade CCD camera. Shown are penetration curves for (1) 75-μm-i.d., 343-μm-o.d. capillary; (2) 50-μm-i.d., 345-μm-o.d. capillary; and (3) 25-μm-i.d., 348-μm-o.d. capillary. Statistics for the injection length after leveling off (mean $\pm 1\sigma$): 132 $\pm$ 2.6 pixels (n = 3), 7.4 μm/pixel (75-μm-i.d. capillary); 165 $\pm$ 5 pixels (n = 3), 9.9 μm/pixel (50-μm-i.d. capillary); 132 $\pm$ 3.5 pixels (n = 2), 13.9 μm/pixel (25-μm-i.d. capillary). The sample consisted of 0.4 mM 2′,7′-dichlorofluorescein dissolved in 15 mM pH 8.9 phosphate buffer; the column length was $\sim$58 cm for each case and was filled with 15 mM, pH 8.9 phosphate buffer. (b) Peak area for dansylated lysine as a function of transfer time. (Analysis is from electropherograms of spontaneous injection of a mixture of the three dansylated amino acids described in Figure 4.) Capillaries were surrounded by a vapor-saturated atmosphere during the transfer. Each point represents the mean peak area for a particular transfer time. Error bars represent 1σ (n = 3).

Penetration Kinetics in Saturated Atmosphere. The kinetics of sample penetration into the capillary were quantitatively imaged using a charge-coupled device. To decouple the effects of evaporation on the droplet, the inlet was contained in a water-vapor-saturated compartment. Shown in Figure 3a are curves quantifying the effective volume of the spontaneous injection as a function of time *after* removal the capillary from the sample solution. Representative penetration curves for 75-, 50-, and 25-μm-i.d., $\sim$345-μm-o.d. capillaries are plotted. As predicted by eq 5, the velocities decreased with

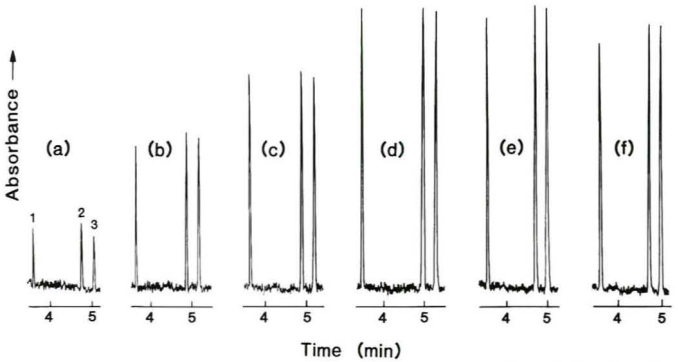

Figure 4. Effect of varying the time between transferring the capillary inlet from the sample solution and reinserting it in the inlet reservoir. The capillary was transferred in a vapor-saturated atmosphere. Each electropherogram shows a separation of ~0.5 mM (1) dansyllysine, (2) dansyltryptophan, and (3) dansylalanine. The different electropherograms correspond to the following transfer times: (a) 2, (b) 10, (c) 20, (d) 60, (e) 80, and (f) 120 s. The mean and standard deviations for each set of delay times are shown in Figure 3b. Separation capillary, 75 μm i.d. × 62 cm (27 cm to detector); buffer, 15 mM phosphate, pH 8.9; 16kV voltage.

smaller inner diameter and the penetration velocity eventually leveled off; this result is consistent with the increasing radius of curvature as the droplet flattens and goes into the capillary. We numerically evaluated eq 5 and compared these numerically predicted penetration curves (not shown) with the penetration curves from the CCD imaging. Although qualitatively similar, the simulated curves exhibited faster penetration kinetics than the experimental findings; this discrepancy suggested that interfacial energy was dissipated under our experimental conditions. According to the measurements obtained by the CCD for the 75-μm-i.d. capillary, the length injected approached 1 mm, an amount that corresponds to a volume of roughly 4 nL of injected material. This amount of material can represent almost half of typical injections in CE. Moreover, these penetration curves show that penetration can be a problem even with smaller capillaries, but the kinetics are markedly slower. This finding suggests that diffusional or convective mixing contributions to spontaneous extraneous injection may become more important as the transfer time and capillary inner diameter decreases. For longer delay times, however, penetration clearly dominates extraneous injection by diffusion or convective mixing.

The ability to form images of the injection kinetics with the CCD and video microscopy provides valuable information about what occurs before the separation voltage is applied. Direct measurements of the peaks resulting from spontaneous injection in actual capillary electrophoresis separations are crucial, however. By recognizing that extraneous injection results from spontaneous fluid displacement, a time-dependent process, the idea becomes apparent that differential delay time *after* withdrawing the capillary from the sample and reinserting it into the inlet solution can substantially affect the amount of the sample droplet that penetrates into the capillary. Figure 3b illustrates the effect of differential delay time on peak area. Each point is the average peak area from a separation of dansylated lysine resulting from a different transfer time, and the error bars represent one standard deviation. The curve shown is for a 50-μm-i.d., 345-μm-o.d. capillary and is qualitatively similar to the shape of the penetration kinetics as determined by CCD imaging.

Figure 4 shows a sequence of electropherograms of three dansylated amino acids. Each group of three peaks results from a single spontaneous extraneous injection. The only difference between them is the length of time between transferring the capillary inlet out of the sample solution and reinserting it into the buffer reservoir. Figure 4 demonstrates that varying the delay time can significantly affect the resulting spontaneous injection peak. The separation shown for each time delay is a representative run of the mean peak area for several identical injections. Mechanistically, once the capillary enters the solution, a curved meniscus no longer gives rise to a spontaneous penetration from a pressure difference; any remaining sample at the entrance will have either diffused away or become washed away by the movement of the capillary through the inlet buffer. The main result from Figures 3 and 4 is that, by inadvertently changing the delay interval, the injection contribution from spontaneous fluid displacement can change by more than 1 order of magnitude.

The amount of injection upon contact with the sample is controlled by diffusion[27] and convection[30] and other possible reported mechanisms that can result in the mixing of the sample with the buffer.[40,48] In the experiments with the 75-μm-i.d. capillaries, less than 10% of the entire possible ubiquitous injection occurs before the capillary is removed from the sample solution, which amounts to an initial length of ~100 μm and a volume of ~0.4 nL. These results are consistent with the simulations performed by Dose and Guiochon,[27] in which they predicted that 10% of a 1-mm plug penetrates into the column in the first 2 s after presentation of a sample that has a slightly higher diffusion coefficient than that of fluorescein. Note that in these experiments the sample solution was dissolved in the same buffer as in the filled capillary. Under these conditions, the length of injected sample upon contact with the sample never reached 700 μm, as reported previously.[9]

Penetration Kinetics in Ambient Atmosphere. In CE the capillary may not be surrounded by an environment saturated with water vapor. A similar set of penetration kinetics for capillaries held in an ambient atmosphere was quantitatively imaged using the CCD system. The experimental conditions are identical to those for the saturated environment except

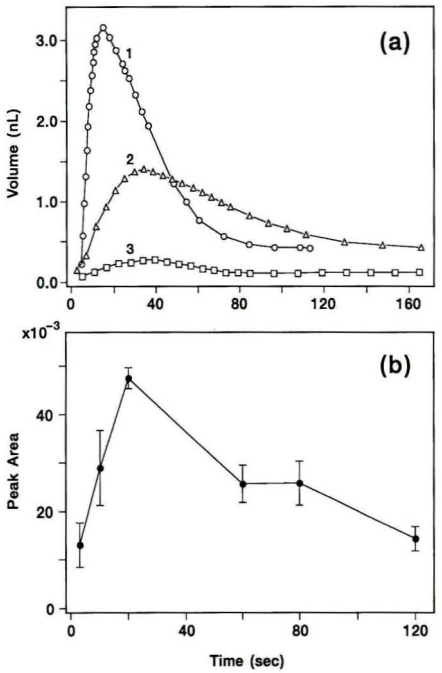

Figure 5. (a) Kinetic curves for spontaneous capillary penetration. The capillary is surrounded by an ambient environment. Each curve shows the volume of the injection plus as a function of time. Injection plugs were quantitated directly from images taken by a scientific-grade CCD camera. Shown are prenetration curves for (1) 75-μm-i.d., 343-μm-o.d. capillary; (2) 50-μm-i.d., 345-μm-o.d. capillary; and (3) 25-μm-i.d., 348-μm-o.d. capillary. Statistics for the maximum injection (mean $\pm 1\sigma$): 93 $\pm$ 3 pixels (n = 3), 7.6 μm/pixel (75-μm-i.d. capillary); 68 $\pm$ 6 pixels (n = 3), 10.1 μm/pixel (50-μm-i.d. capillary); 47 $\pm$ 9 pixels (n = 3), 13.9 μm/pixel (25-μm-i.d. capillary). All other conditions the same as in Figure 3. (b) Peak area for dansylated lysine as a function of varying the transfer time. (Analysis is from electropherograms of spontaneous injection of a mixture of the three dansylated amino acids described in Figure 4.) Capillaries were surrounded by an ambient atmosphere during the transfer. Each point represents the mean peak area for a particular transfer time. Error bars represent 1σ (n = 3).

that the capillary is exposed to ambient air. Shown in Figure 5a are representative examples of penetration curves for spontaneous injection in 75-, 50-, and 25-μm-i.d. capillaries. As in the experiments with the saturated environment, a similar penetration process takes place at early times, but two significant and interesting differences are evident. First, the length of injection reaches a maximum and then becomes smaller in time. This surprising result shows that the injection plug slowly compresses into the entrace of the column, and the effect can be observed directly with video microscopy. In addition, the video images show that as the fluorescein plug retreats toward the inlet, it appears to become darker. Although direct video observation suggests that the sample is becoming concentrated in the inlet end, more rigorous experiments are needed to quantitate and elucidate the mechanism. Second, the maximum length of injection at the peak is lower than it is in a saturated atmosphere. A likely explanation is that the droplet volume is being reduced by evaporation during the injection.

Several different control experiments suggest that evaporation of the buffer is what affects the injection length. By positioning sample solution at different distances from the inlet of the capillary after injection, the effective vapor pressure surrounding the capillary and droplet is made to vary. At distances very close to the inlet, the vapor pressure is high and falls off as the distance is increased. We find that the amount of injected volume increases when the capillary is closer to the surface of the sample solution after injection. Moreover, under these conditions, the degree the sample is compressed is minimized. Thus by holding the capillary directly above the solution, we could obtain penetration curves similar to those in the vapor-saturated chamber. In addition, if evaporation were occurring, a presure difference would be created, and consequently, the outlet buffer would be drawn into the capillary. To test this idea, the outlet capillary end was imaged during the delay time. When the inlet end was held in ambient conditions, fluorescein in the outlet vial entered and filled the entire end of the imaged part of the capillary. The same test was performed with the inlet held in a saturated chamber. Only a negligible amount of the fluorescein was observed to enter, as expected by diffusion.

Figure 5b illustrates the effect of differential delay time on peak area when the capillary is held in an ambient atmosphere. Again, each point is the average peak area that results from a separation of dansylated lysine resulting from a different transfer time. As was evidenced by direct CCD imaging, the trend in the peak area shows that the injection volume grows in size, reaches a maximum, and then decreases as a function of delay time. Similarly, Figure 6 shows a series of electropherograms of three dansylated amino acids, each differing only in the delay time between withdrawing the capillary and reinserting it into the inlet buffer reservoir. A similar trend in peak height is apparent.

To summarize the results, Figure 7 directly compares spontaneous injection between saturated and ambient conditions and between CCD imaging and peak area analysis. Figure 7a compares the length of injection (converted to a volume) meaured with the CCD, and Figure 7b compares peak areas using 50-μm-i.d., 345-μm-o.d. capillaries. These results show that variations in the vapor pressure of water surrounding the capillary can lead to injection lengths that differ by more than 1 order of magnitude if care is not taken to prevent buffer loss from the front end of the capillary. As in the saturated environment, differing transfer times also lead to errors in peak quantitation. Thus, exposure to ambient air adds an extra level of complexity to that of the two competing effects, spontaneous penetration and buffer loss (sample compression).

It is interesting that the trends in peak area are remarkably similar to the penetration curves as measured from direct CCD imaging of the plug length. If the sample were simply becoming concentrated in the end of the column, then the peak areas would increase and level off as in the experiments performed in the saturated atmosphere; furthermore, peak heights would be expected to increase at each delay time. In contrast, the decreasing peak areas and heights show that considerable sample loss occurs during some stage of the injection process under ambient conditions.

Several mechanisms for sample loss as a function of reinserting the capillary into the inlet solution have been

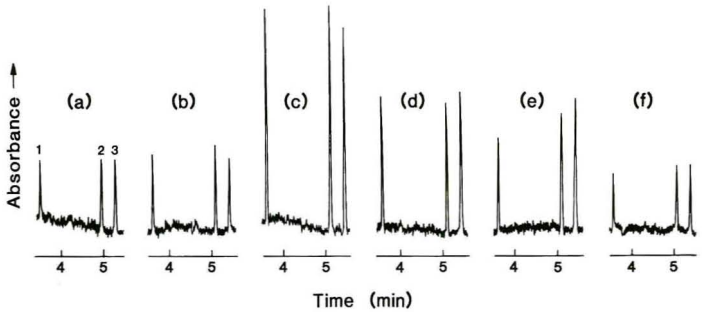

Figure 6. Effect of varying the time between transferring the capillary inlet from the sample solution and reinserting it in the inlet reservoir. The capillary was transferred in ambient atmosphere. Each electropherogram shows a separation of ~0.5 mM (1) dansyllysine, (2) dansyltryptophan, and (3) dansylalanine. The different electropherograms correspond to the following transfer times: (a) 2, (b) 10, (c) 20, (d) 60, (e) 80, and (f) 120 s. The mean and standard deviation for each set of delay times are shown in Figure 5b.

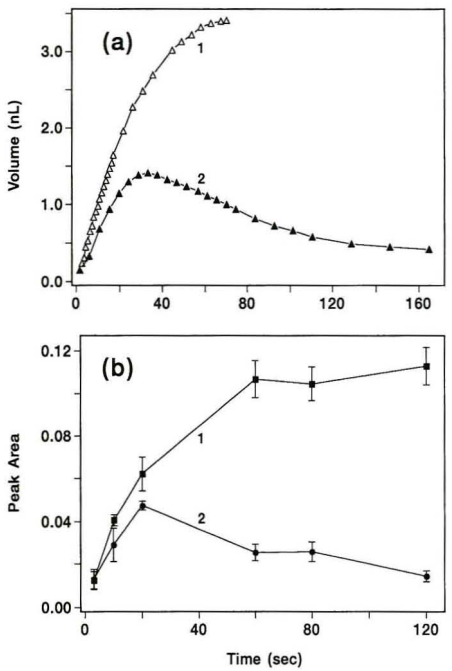

Figure 7. Comparison between spontaneous extraneous injection for delay times in (1) saturated and (2) ambient atmosphere. Shown are (a) injection lengths as determined by CCD measurements and (b) peak areas from CE separations. Both sets of curves are for a 50-μm-i.d., 345-μm-o.d. fused silica capillary. Conditions are identical to those in Figures 3–6.

thoroughly discussed by Dose and Guiochon.[27] One scenario is that as the column is reinserted into the solution, rapid outward diffusion occurs. From these results, we can predict that if the sample were actually concentrated at the entrance, then the concentration profile would be steeper in the saturated conditions, thus causing an even greater loss from the column. Another scenario is that sample simply flows out the column by inadvertent flow. Although inadvertent hydrodynamic outflow may have occurred in these experiments, it is less likely because care was taken in positioning the inlet and outlet reservoirs. Other potential mechanisms based on convective outflow[30] or Marangoni mixing[40,48] are possible, and precedence is found in the literature for them. The salient message is that when the capillary is transferred in ambient air, compression of the injection plug occurs at long delay times and loss of sample can result. This conclusion further emphasizes the need to control such factors as inadvertent hydrodynamic flow and outward diffusion by reducing the delay times between reinserting the capillary into the inlet reservoir and applying the voltage.

The consequences of the sample plug's becoming compressed into the end of the capillary are serious when longer than normal delay times occur. We have been exploring the possibility of performing chemical derivatization in the entrance of the column.[20] In some instances, the derivatization reaction is allowed to proceed for several minutes. Allowing the capillary to be exposed to air be problematic in that variable amounts of sample can be lost from the column when it is replaced in the inlet solution. Furthermore, this effect should be taken into account in experiments in which the capillary is manipulated for direct cellular sampling or for microinjection onto the column—scenarios that may require longer than usual delay times. Finally, in working with minute samples, such as single synaptic vesicles that have volumes of attoliters or less, extreme care must be taken after the sample is injected onto the column to avoid loss.

Effect of Delay Time on Gravity Injections. The magnitude of the effect of spontaneous capillary penetration on actual injections in CE depends on the length of the injection. Obviously, the volume of the extraneous injection makes up a larger fraction of a narrow zone than it does of a broader one. Figure 8 is a demonstration of the effect of spontaneous capillary penetration for two different transfer times on a 4-s gravity injection during which the sample is elevated 3.8 cm above the outlet. The capillary is held directly above the sample droplet so that it is in a nearly saturated environment. The peaks shown are representative of several runs for each delay time. The average peak area increases by a factor of 2 when the delay time changes from 1 to 10 s. Such a variation in peak area would lead to poor quantitative accuracy and precison. A typical injection penetration curve (Figure 3) shows fast kinetics in the initial portion of the curve and slower penetration velocities as the curve levels off. If the delay time

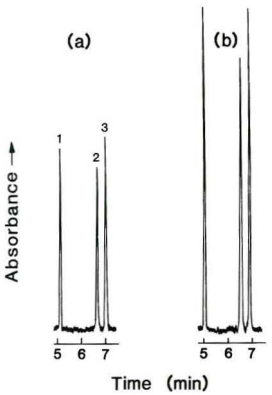

Figure 8. Effect of spontaneous capillary displacement on a 4-s gravity injection. The sample is held 3.8 cm above the outlet solution. Shown are electropherograms of ~0.5 mM (1) dansyllysine, (2) dansyltryptophan, and (3) dansylalanine that differ only in the transfer time between injecting the sample and reinserting the capillary in the inlet reservoir. Transfer times are (a) 1 s and (b) 10 s. Several runs were performed, and the electropherogram shown is representative of the mean peak area for the dansylated lysine peak. Peak area statistics (mean $\pm 1\sigma$): 0.29 ± 0.01 (n = 3), 1-s transfer delay; 0.15 ± 0.02 (n = 3), 10-s transfer delay. Separation capillary, 75-μm i.d. × 62 cm (27 cm to detector); buffer, 15 mM phosphate, pH 8.9; 16kV voltage.

is increased such that it merely extends further into the slow portion of the penetration curve, only a minimal additional contribution from spontaneous fluid displacement on the gravity injection results. When a similar experiment is performed under ambient conditions, however, investigation by CCD imaging and peak area analysis reveals that long delay times (>60 s) result in a significant reduction in injection length and loss in peak area. For shorter delay times (<20 s), a variation in peak area analogous to that found under saturated conditions is predicted from findings shown in Figures 5 and 6. Results from gravity injections carried out in both saturated and ambient environments suggest that reproducibility for small injections can be improved by maintaining constant delay time after each injection.

Minimizing Spontaneous Injection. Our results indicate that a main contribution to the extraneous injection in 75-, 50-, and 25-μm-i.d., ~345-μm-o.d. capillaries is from spontaneous fluid displacement. Consequently, several approaches for dramatically minimizing this extraneous injection are now possible. Minimizing the volume of the droplet, lowering the interfacial pressure difference by decreasing the curved surface, or providing a counteracting back pressure all act to decrease penetration. As indicated in eq 5, when the outlet reservoir is raised above the inlet reservoir, a back pressure, $\rho g h$, from the gravitational weight of the water results in slowing the penetration process. In fact, we found that by raising the outlet by 18 cm, no detectable injection was observed, either during initial contact or after the capillary was removed from the sample. In addition, we found that introducing a 1-cm height difference minimized penetration of sample during the initial contact. This result is in contrast to previous findings[9] that even in the presence of a 5-cm height difference, significant injection occurred upon initial contact with the sample.

Another approach is to reduce the droplet volume by reducing the outer diameter of the capillary. Because the droplet spans entirely across the end surface of the capillary, the size of the droplet is defined by the morphology (and size) of the outer diameter of the capillary. Any reductions in the outer diameter will significantly minimize the size of the droplet that forms. Figure 9 illustrates the effect of etching the outer diameter of the capillary to ~110–120 μm with hydrofluoric acid. These video images show a reduction in the amount of sample penetration after the etched capillary is removed from the solution. The slightly jagged end of the etched capillary may have helped in reducing the effective surface for droplet attachment. As evidenced, most of the injection occurred during the initial contact. Representative separations comparing untreated and etched capillaries are shown in Figure 10. A reduction in the amount of spontaneous extraneous injection by as much as ~12-fold can be achieved by etching the capillary. In each set of runs, the time delay before the etched capillary is reinserted into the inlet vial is 10 s. By minimizing the formation of a curved meniscus at the inlet end of the capillary, there should be comparatively no dependence on the delay time. Indeed, Figure 11 shows little difference in amount injected by changing the delay from 2 to 10 s for an etched capillary. Alternatively, to show that a reduction in injection length can be achieved with a smoother, less jagged surface, we tested well-cleaved, thin-walled capillaries that maintain the same inner diameter but have smaller outer diameters. From video and CCD imaging data, a reduction by ~7-fold in the length of spontaneous injection was found with commercially available thin-walled capillaries (131-μm o.d., 52-μm i.d.). These data suggest that the use of etched capillaries or thin-walled capillaries will improve reproducibility and separation efficiencies.

As discussed earlier, methods that change the wettability of the surface can also affect the degree of extraneous penetration by affecting the volume of the droplet reservoir that adheres to the end surface. One approach is to make the outside surface of the capillary more hydrophobic, which makes it more difficult for the solution to wet to the surface and can reduce the droplet size. Some silanized capillaries did result in a slight reduction of peak areas (~2-fold) for the spontaneous injection, and this conclusion was qualitatively confirmed by observing a smaller droplet at the end of the capillary with video imaging. We found it difficult, however, to make reproducible reduced droplet volumes with the silanization procedure used in these studies. The other possibility is to lower the apparent contact angle by adding surfactant to the sample, which has the effect of increasing surface wetting by inducing greater spreading onto the sides of the capillaries, as described by Adamson.[40] Again, the reservoir volume is reduced but from a different mechanism, that of the droplet spreading onto the outside surface of the capillary. As an example, we found spreading to occur when sodium dodecyl sulfate (SDS) (Life Technologies Inc., Gaithersburg, MD) was added to the sample (solution was 50% in SDS). In general, it is important to understand the surface wettability with respect to both the sample and buffer solution for controlling spontaneous injection.

(49) Ruckenstein, E.; Suciu, D. G.; Smigelschi, O. In *Modern Approaches to Wettability: Theory and Applications*; Schrader, M. E., Loeb, G., Eds.; Plenum: New York, 1992; pp 379–422.

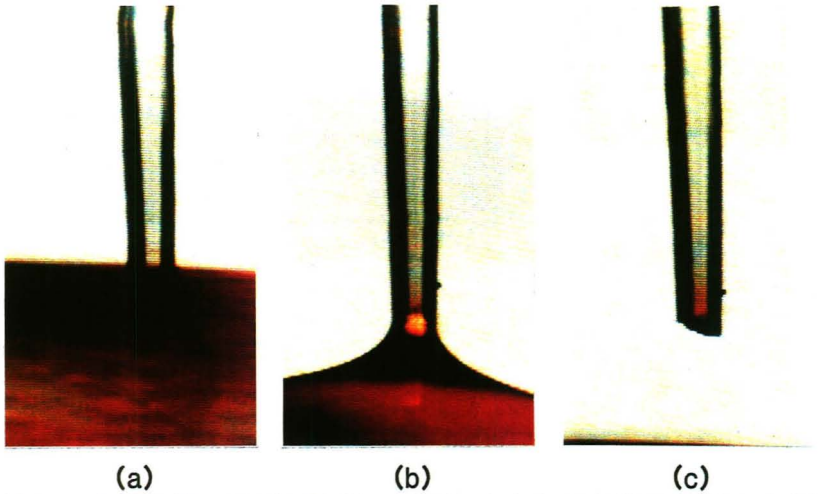

Figure 9. Video images showing the inlet end of a 75-μm-i.d., 343-μm-o.d. capillary that has been etched down to ~130-μm o.d. with hydrofluoric acid (0.1 M) and then silanated: (a) insertion into solution, (b) contact with sample immediately before solution breakage, and (c) ~10 s after leaving solution.

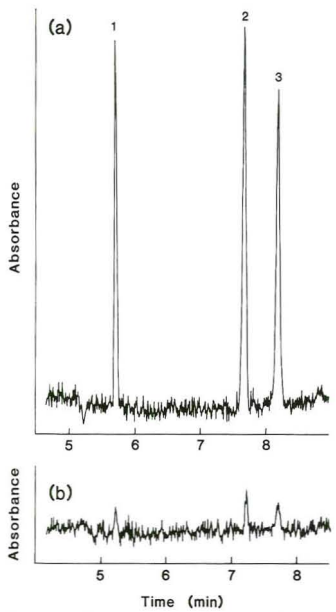

Figure 10. Electropherogram comparing spontaneous extraneous injection in an (a) untreated and (b) etched capillary. Separation of ~0.5 mM (1) dansyllysine, (2) dansyltryptophan, and (3) dansylalanine. Separation capillary, 75 μm i.d. × 62 cm (27 cm to detector); buffer, 15 mM phosphate, pH 8.9.

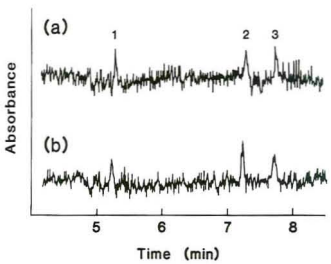

Figure 11. Comparison of different delay times between injection and reinsertion into the inlet vial for etched column: (a) 2- and (b) 10-s delay before reinsertion. All conditions are the same as in Figure 10.

CONCLUSION

We have identified that spontaneous fluid displacement resulting from an interfacial pressure difference is a main cause for extraneous injection in 25-, 50-, and 75-μm-i.d., ~345-μm-o.d. fused silica capillaries. By characterizing this mechanism, we have discovered new parameters that must be controlled to achieve small injections in a quantitative manner. These parameters include precise timing between withdrawing the capillary from the sample and reinserting it into the inlet reservoir, constant vapor pressure surrounding the capillary during the transfer time, and reproducible surface wettability and morphology of the capillary walls at the inlet. Consideration of these results is essential when claims are made for high-sensitivity mass analysis, particularly in 360-μm-o.d. and larger capillaries. Extreme care must be taken with long delay times to prevent significant loss of buffer from the end of the column and compression of the sample. Because this effect can lead to sample losses, it is important to consider for applications such as on-column derivatization[20] and single-cell analysis. Finally, we have developed several methods to minimize spontaneous injection including etching the outer diameter of the capillary inlet, using a thin-walled capillary, and manipulating the wettability of the surface at the inlet. Whichever strategy is implemented, the reduction in the extraneous injection should lead to better separation efficiency and to more precise quantitation for ultramicrosampling in capillary electrophoresis.

ACKNOWLEDGMENT

We thank Professor George M. Homsy of the Stanford University Chemical Engineering Department and Professor Jonathan V. Sweedler of the University of Illinois Chemistry Department for many useful discussions and advice. We are also grateful to Rajeev Dadoo, Jason B. Shear, and Robert Guettler for many helpful comments on the manuscript. H.A.F. is a W. R. Grace Fellow. This work was supported by Beckman Instruments, Inc. and the National Institutes of Mental Health (Grant NIH 5RO1 MH45423-03).

Received for review December 21, 1993. Accepted March 25, 1994.[⊗]

[⊗] Abstract published in *Advance ACS Abstracts,* May 15, 1994.

Anal. Chem. **1994,** *66,* 2330–2335

Class-Selective Collisionally Activated Dissociation/ Ion–Molecule Reactions of 4-Quinolone Antibiotics

Armando Colorado and Jennifer Brodbelt*

Department of Chemistry and Biochemistry, University of Texas, Austin, Texas 78712

A new combination of collisionally activated dissociation and ion–molecule reactions in a quadrupole ion trap mass spectrometer is developed for the class-selective determination of 4-quinolones, an important group of antibiotics. In this method, collisionally activated dissociation is used to promote dehydration of each protonated quinolone, and the resulting dehydrated fragment ion undergoes an addition reaction with an auxiliary reagent. The auxiliary reagents, including acetone, acetic anhydride, and *n*-propylamine, have structures that specifically allow formation of a cyclic adduct with the analyte ion. This sequential process is characteristic of a class of analyte molecules that have adjacent carboxylic acid and ketone functional groups anchored on a rigid ring and undergo facile, efficient dehydration.

Applications of tandem mass spectrometry[1] have grown tremendously over the past decade with the increasing complexity and variety of analytical problems. Chemical ionization (CI)[2] and collisionally activated dissociation (CAD)[3] are typically used as complementary techniques, in which CI is used to protonate the analyte or generate new adducts, with CAD used to provide confirmatory structural identification. The use of ion–molecule reactions to selectively derivatize molecules in the gas phase has also proved to be particularly useful as an auxiliary structurally specific tool.[4–9] In many types of analysis, the primary objective is to develop a means of uniquely distinguishing a whole class of compounds, perhaps in the presence of interferences from a complex matrix and contamination by undesirable isobars, rather than to design a method selective for each individual analyte. Conventional CI in conjunction with CAD is a powerful technique for structural elucidation of most organic compounds but may not provide the necessary class selectivity. With a reversal of the traditional method of combining ion–molecule reactions with CAD, a new approach to uniting these two techniques provides an excellent protocol for class analysis, as described in this report. CAD may be used to generate analyte-related fragment ions that subsequently and selectively interact with a reactive gas, even when the intact molecular ions are nonreactive with the auxiliary reagent. The present study describes the development of this technique as a means to identify a large class of antibiotics, the quinolones[10] (see Figure 1).

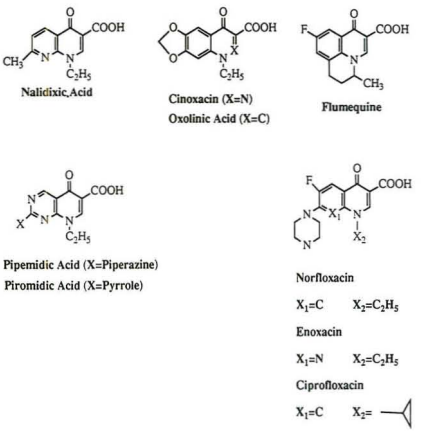

Figure 1. Structures of the quinolones.

The history of the 4-quinolones begins with the serendipitous discovery of nalidixic acid during chloroquine synthesis in the early 1960's.[11] Nalidixic acid offered sufficient activity against Gram-negative bacteria to treat urinary tract infections. In the early 1980's, new *fluoro*quinolones, such as enoxacin, ciprofloxacin, norfloxacin, and flumequine, were introduced. The main difference between the classical quinolones and the fluoroquinolones is that the latter group contains a fluorine atom at the C-6 position and a piperazinyl (or piperazine derivative) group at the C-7 position (Figure 1). Structure–activity relationship studies show that the fluorine atom enhances DNA gyrase complex binding and cell penetration.[10] Additionally, the introduction of a piperazine unit increases antibacterial potency far greater than those compounds not having one. These antibiotics are broad spectrum agents that are active against 37 different kinds of bacteria. They have been used clinically for urinary tract infections, bacterial prostatitis, sexually transmitted diseases, gastrointestinal infections, respiratory tract infections, bone and joint infec-

(1) Busch, K. L.; Glish, G. L.; McLuckey, S. A. *Mass Spectrometry/Mass Spectrometry: Techniques and Applications of Tandem Mass Spectrometry*; VCH Publishers, New York, 1988.
(2) Harrison, A. G. *Chemical Ionization Mass Spectrometry*; CRC Press, Boca Raton, FL, 1983.
(3) Levsen, K.; Schwarz, H. *Mass Spectrom. Rev.* **1983**, *2*, 77.
(4) Vairamani, M.; Rajeev, M. S.; Rao, G. K. V. *Org. Mass Spectrom.* **1992**, *27*, 57–58.
(5) Gross, M. L.; Lin, P.-H.; Franklin, S. J. *Anal. Chem.* **1972**, *44*, 974.
(6) Bjarnason, A.; Taylor, J. W.; Kinsinger, J. A.; Cody, R. B.; Weil, D. A. *Anal. Chem.* **1989**, *61*, 1889.
(7) Heath, T. G.; Allison, J.; Watson, J. T. *J. Am. Soc. Mass Spectrom.* **1991**, *2*, 270.
(8) Brodbelt, J.; Liou, C.-C.; Donovan, T. *Anal. Chem.* **1991**, *63*, 1205–1209.
(9) (a) Pachuta, R. R.; Kenttamaa, H. I.; Cooks, R. G.; Zennie, T. M.; Ping, C.; Chang, C.-J.; Cassady, J. M. *Org. Mass Spectrom.* **1988**, *23*, 10. (b) Cole, M. J.; Enke, C. G. *J. Am. Soc. Mass Spectrom.* **1991**, *2*, 470.
(10) Chu, D. T. W.; Fernandes, P. B. *Antimicrobial Agents and Chemotherapy.* **1989**, *33*, 131–135.
(11) Norris, S.; Mandell, G. In *The Quinolones*; Andriole, V. T., Ed.; Hardcourt Brace Jovanovich: New York, 1988; p 1.

0003-2700/94/0366-2330$04.50/0
© 1994 American Chemical Society

tions, skin and soft tissue infections, and other related infections.[12] Previous methods used for the analysis of quinolones include HPLC/MS,[13,14] NMR,[15] and GC/MS.[16] A general class-specific method for the determination of these compounds continues to be a formidable challenge because the various quinolone structures have vastly different substituents that greatly alter their individual characteristic properties. As shown in this report, a simple method of joining collisionally activated dissociation with ion–molecule reactions provides one means for this type of class-specific analysis.

EXPERIMENTAL SECTION

All experiments were performed in a Finnigan ITMS operated in the mass-selective instability mode.[17] Samples were introduced via a heated solids probe inlet to 2×10^{-6} Torr. All chemical ionization reagents were introduced through a leak valve to a pressure of $(0.5–1.5) \times 10^{-5}$ Torr. Helium was also admitted into the chamber to 1 mTorr. Ion–molecule reaction times ranged between 50 and 400 ms. The trap temperature was held at 120 °C. For mass-selective isolation, a DC voltage was applied to the ring electrode in combination with an appropriate rf voltage. For the experiments in which protonated quinolones were isolated prior to collisional activation in the presence of auxiliary reagents, the quinolones were ionized by self-chemical ionization, via ion–molecule reactions between neutral quinolone molecules and molecular or fragment ions of the quinolones initially formed by electron ionization in the trap. For collisional activation dissociation experiments, typical tickle voltages used were between 700 and 1200 mV. Also, an activation time of 5–25 ms and a q value of 0.4 were used.

All quinolones were obtained from Sigma Chemical and used without further purification. Dimethyl ether (DME) was obtained from MG Industries, vinyl methyl ether was obtained from Matheson Gas Co., and isobutane was obtained from Liquid Carbonic Inc. All other compounds were obtained from Aldrich Chemical Co.

RESULTS AND DISCUSSION

Chemical Ionization with Novel Reagents. In this first section, the reactions of quinolones with an array of novel chemical ionization reagents are described. The reagents, including dimethyl ether, acetone, allyl alcohol, acetic anhydride, 2-(trimethylsilyl)ethanol, propylamine, and *d,l*-2-aminopropanol, were chosen because of their reactive functional groups. Some of these have been used for selective chemical ionization applications previously.[8,18–28] For the present study, the reactions were performed primarily to examine the extent and selectivity of ion–molecule reactions of the *neutral* quinolones with an array of reagent *ions*.

Table 1. CAD of Protonated Quinolones: Fragment Ions, Percentages, and Proposed Neutral Losses

quinolone (mol wt)	fragment ions (%)		neutral losses
enoxacin			
320	232 (25)	−89	$-(H_2O + C_2H_4 + C_2H_5N)$
	303 (75)	−18	$-H_2O$
norfloxacin			
319	254 (10)	−66	$-(H_2O + 28 + HF)$
	282 (25)	−38	$-(H_2O + HF)$
	302 (65)	−18	$-H_2O$
ciprofloxacin			
331	230 (15)	−102	$-(H_2O + 2CO + C_2H_4)$
	314 (85)	−18	$-H_2O$
oxolinic acid			
261	244 (100)	−18	$-H_2O$
cinoxacin			
262	161 (5)	−102	$-(H_2O + 2CO + C_2H_4)$
	189 (20)	−72	$-(H_2O + CO + 28)$
	217 (15)	−46	$-(H_2O + 28)$
	245 (60)	−18	$-H_2O$
piromidic acid	243 (20)	−46	$-(H_2O + 28)$
288	271 (80)	−18	$-H_2O$
pipemidic acid	215 (20)	−89	$-(H_2O + C_2H_4 + C_2H_5N)$
303	286 (80)	−18	$-H_2O$
nalidixic acid	159 (35)	−74	$-(H_2O + CO + 28)$
232	187 (25)	−46	$-(H_2O + 28)$
	215 (40)	−18	$-H_2O$
flumequine			
261	244 (100)	−18	$-H_2O$

In general, the different CI reagents do not show structurally specific reactions with the array of quinolones. For example, the two major reactive ions formed upon DME ionization are the protonated species (47^+) and the methoxymethylene cation (45^+). These DME reagent ions result in formation of $[M + H]^+$, $[M + CH_3OCH_2]^+$, and $[M + CH_3]^+$ products upon reaction with each quinolone, but these reactions are nonspecific for the class of quinolones. Chemical ionization with acetone, allyl alcohol, and acetic anhydride results only in protonation of the quinolones. Evidently, proton transfer is kinetically favored relative to any other reaction, such as acetylation. Chemical ionization with 2-aminopropanol, 2-(trimethylsilyl)ethanol, and propylamine reagent ions results in a more extensive array of product ions, including some simple addition adducts such as $(M + (CH)_3Si)+$ for reactions with (trimethylsilyl)ethanol ions. With propylamine CI, the products $(M + NH_3)+$ and $(M + H +$ propylamine$)+$ are observed, but not exclusively or universally for the whole series of quinolones. From these preliminary studies, selective CI proves to be largely unpromising for specifically targeting the class of quinolones.

Collisionally Activated Dissociation of Protonated Quinolones. CAD spectra were acquired for each protonated quinolone in order to evaluate the additional structural information provided by the fragmentation patterns (see Table 1). As a characteristic example, the CAD spectrum of protonated nalidixic acid is shown in Figure 2. Collisional

(12) Hooper, D. C.; Wolfson, J. S. *N. Engl. J. Med.* **1991**, *324*, 384–393.
(13) Horie, M.; et al. *J. Liq. Chromatogr.* **1993**, *16*, 1463.
(14) Cepa, S. P.; Hill, P.; Buko, A. M. *Biomed. Mass Spectrom.* **1992**, *21*, 176.
(15) Tugnait, M.; et al. In *Bioanalytical Approaches for Drugs*; Reid, E., Wilson, I. D., Eds.; Royal Society of Chemistry: Cambridge, 1992; p 291.
(16) Takatsuki, K. *J. Chromatogr.* **1991**, *538*, 259.
(17) March, R. E.; Hughes, R. J. *Quadrupole Storage Mass Spectrometry*; Wiley-Interscience: New York, 1989.
(18) Keough, T. *Anal. Chem.* **1982**, *54*, 2540–2547.
(19) Wang, S.; et al. *Anal. Chem.* **1985**, *57*, 2283–2286.
(20) Dua, S.; Bowie, J. H.; Hayes, R. N. *Rapid Commun. Mass Spectrom.* **1993**, *7*, 336–338.
(21) Eberlin, M. N.; Majumdar, T. K.; Cooks, R. G. *J. Am. Chem. Soc.* **1992**, *114*, 2884–2896.
(22) Odiorne, T. J.; Harvey, D. J.; Vouros, P. *J. Phys. Chem.* **1972**, *76*, 3217–3220.
(23) Orlando, R.; et al. *Org. Mass Spectrom.* **1987**, *22*, 597–605.
(24) Dzidic, I. *J. Am. Chem. Soc.* **1972**, *94*, 8333–8335.
(25) Wilson, M. S.; McCloskey, J. A. *J. Am. Chem. Soc.* **1975**, *97*, 3436–3444.
(26) Bankova, V. S.; Mollova, N. N.; Popov, S. S. *Org. Mass Spectrom.* **1986**, *21*, 109–116.
(27) Reiner, E. J.; Poirier, R.; Peterson, M. R.; Csizmadia, R. G.; Harrison, A. G. *Can. J. Chem.* **1986**, *64*, 1652–1660.
(28) Bowen, D. V.; Field, F. H. *Org. Mass Spectrom.* **1974**, *9*, 195–203.

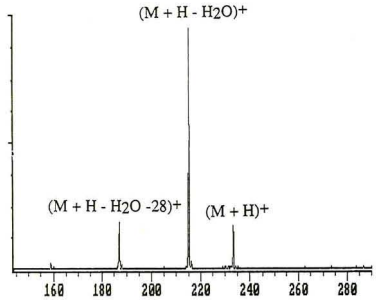

Figure 2. CAD spectrum of protonated nalidixic acid.

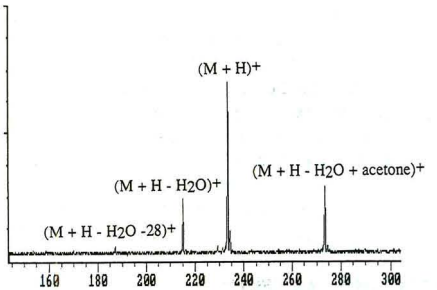

Figure 3. CAD spectrum of protonated nalidixic in the presence of acetone.

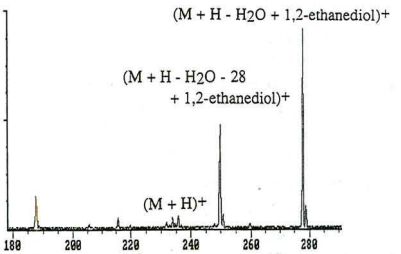

Figure 4. CAD spectrum of protonated nalidixic acid in the presence of 1,2-ethanediol.

activation of the protonated quinolone antibiotics indicates that dehydration is the predominant fragmentation pathway. Because of the highly stable bicyclic aromatic structures of these compounds, very few other competing fragmentation pathways are observed. As shown in Table 1, many of the dissociation routes involve dehydration in conjunction with elimination of one or more units of CO or C_2H_4. For example, loss of 46 amu (H_2O + 28 Da) is observed for protonated cinoxacin, piromidic acid, and nalidixic acid. MS/MS/MS experiments performed on the dehydrated fragment ion for each quinolone indicates that all of the fragments listed in Table 1 can be directly produced from further activation of the dehydrated precursor. The latter result supports the idea that dehydration is a characteristic and facile process for all of the quinolones, thus suggesting that this reaction may be incorporated into the design of a class-selective analytical scheme.

CAD of Protonated Quinolones in the Presence of Reactive Gases. Collisional activation dissociation was performed on each protonated quinolone in the presence of a variety of different auxiliary reagent gases (see Tables 2 and 3). The auxiliary reagent gases, including dimethyl ether, acetone, allyl alcohol, acetic anhydride, 2-(trimethylsilyl)ethanol, propylamine, 2-aminopropanol, ethylene oxide, anisole, cyclohexanone, isobutane, and 1,2-ethanediol, possessed an array of sizes and functional groups. Depending on the structure of the reagent gas, the $[M + H]^+$ quinolone ion rapidly dissociates after collisional activation to form a highly reactive $[M + H - H_2O]^+$ ion, which then subsequently interacts with the auxiliary reagent to generate an interesting array of new products. For example, activation of protonated nalidixic acid in the presence of acetone results in the formation of an adduct ion assigned as $(M + H - H_2O + \text{acetone})^+$ (see Figure 3). This unusual occurrence is presumably linked to the extreme reactivity of the dehydrated nalidixic acid ions in the presence of a special reagent. In contrast, with dimethyl ether as an auxiliary reagent, protonated nalidixic acid mainly dissociates into its dehydrated form, with no further reaction (refer to Figure 2).

Activation of the other protonated quinolones exhibits behavior similar to that observed for protonated nalidixic acid. In each case, the dehydrated species is the base peak upon CAD in the presence of dimethyl ether but constitutes only 5–10% of the ion current upon CAD in the presence of acetone. Again, the $[M + H - 18 + \text{acetone}]^+$ product is the dominant ion. The results described here show that each neutral quinolone or protonated intact quinolone does not form any stable adduct with the acetone reagent; on the other hand, the *dehydrated* quinolone ion reacts very efficiently with neutral acetone. Because acetone, but not dimethyl ether, promotes formation of the adduct ions, there appears to be some structural requirements of the auxiliary reagent, as described later. Cyclohexanone, another carbonyl-containing reagent, and *n*-propylamine are two other auxiliary reagents that also promote formation of the addition adducts with the dehydrated fragment ions.

Activation of the protonated quinolones in the presence of allyl alcohol or 1,2-ethanediol yields results similar to those found for CAD in the presence of acetone, except that all of the dehydration-related fragment ions of the quinolones may undergo addition to the auxiliary alcohol neutrals. For allyl alcohol in particular, no dehydration fragment ions survive without spontaneous attachment of the alcohol, even at relatively short reaction times. An example of this general type of behavior is shown in Figure 4 for CAD of protonated nalidixic acid in the presence of 1,2-ethanediol. As shown, both the dehydration fragment and the fragment attributed to loss of H_2O in conjunction with 28 Da undergo attachment to 1,2-ethanediol. The fact that all the dehydration-related fragment ions undergo adduct formation to some extent may be due to the especially favorable hydrogen-bonding capabilities of the alcohol reagents, resulting in stabilized ion–molecule complexes and reaction rates faster than those found between acetone and the dehydrated quinolone. Additionally, the tiny peak observed at m/z 259 in Figure 4 is assigned as $(M + H - H_2O + 1,2\text{-ethanediol} - H_2O)^+$. The appearance of this product suggests that the newly formed adduct has some excess energy which catalyzes the subsequent low-energy dehydration.

Table 2. CAD and Ion–Molecule Reactions in the Presence of Auxiliary Reagents

quinolone (mol wt)	product ion (% ion current) acetone	allyl alcohol	acetic anhydride	2-TMS-ethanol	propylamine	2-aminopropanol
norfloxacin						
319	302 (10)	*340 (5)*	302 (35)	*372 (40)*	*361 (100)*	*359 (55)*
	360 (90)	*360 (95)*	*362 (15)*	*392 (60)*		*377 (45)*
			404 (50)			
ciprofloxacin						
331	230 (10)	*372 (100)*	230 (15)	230 (45)	*373 (100)*	*371 (55)*
	314 (10)		314 (25)	*404 (55)*		*389 (45)*
	372 (80)		*374 (15)*			
			416 (45)			
enoxacin						
320	303 (20)	*361 (100)*	232 (20)	*393 (90)*	*362 (100)*	*360 (55)*
	361 (80)		303 (25)	*421 (55)*		*378 (45)*
			363 (20)			
			405 (35)			
cinoxacin						
262	161 (10)	161 (10)	*305 (100)*	161 (15)	*304 (100)*	161 (5)
	189 (25)	189 (15)		189 (15)		189 (5)
	217 (15)	245 (10)		217 (20)		217 (5)
	245 (10)	*275 (15)*		*335 (50)*		*302 (80)*
	303 (40)	*303 (50)*				*320 (5)*
oxolinic acid						
261	244 (30)	*274 (20)*	244 (20)	244 (10)	*286 (5)*	*301 (70)*
	302 (70)	*302 (80)*	*304 (55)*	*334 (90)*	*303 (95)*	*319 (30)*
			346 (25)			
pipemidic acid						
303	286 (20)	*343 (100)*	215 (15)	215 (45)	*345 (100)*	*343 (75)*
	343 (80)		286 (20)	*376 (55)*		*361 (25)*
			346 (45)			
			388 (20)			
piromidic acid						
288	243 (25)	243 (15)	243 (40)	*361 (100)*	*330 (100)*	*328 (70)*
	271 (20)	*301 (50)*	271 (40)			*346 (30)*
	329 (55)	*329 (35)*	*331 (2)*			
			373 (18)			
nalidixic acid						
232	187 (15)	187 (10)	159 (10)	*305 (100)*	*257 (10)*	*272 (99)*
	215 (55)	215 (5)	187 (35)		*274 (90)*	*290 (1)*
	273 (30)	*245 (15)*	215 (30)			
		273 (70)	*275 (25)*			

Table 3. Summary of Adduct Formation for CAD with Auxiliary Reagents

reagent	adducts observed
acetone	$(M + H - H_2O + \text{acetone})^+$
allyl alcohol	$(M + H - H_2O + \text{allyl alcohol})^+$
acetic anhydride	$(M + H - H_2O + \text{acetic anhydride})^+$
	$(M + H - H_2O + \text{acetic anhydride} - CH_2{=}CO)^+$
cyclohexanone	$(M + H - H_2O + \text{cyclohexanone})^+$
1,2-ethanediol	$(M + H - H_2O + \text{1,2-ethanediol})^+$
	$(M + H - H_2O + \text{1,2-ethanediol} - H_2O)^+$[a]
2-(trimethylsilyl)-ethanol	$(M + H - H_2O + \text{2-TMS-ethanol} - 28)^+$
propylamine	$(M + H - H_2O + \text{propylamine})^+$
2-aminopropanol	$(M + H - H_2O + \text{2-aminopropanol})^+$
	$(M + H - H_2O + \text{2-aminopropanol} - H_2O)^+$[a]

[a] Observed to some extent for the various quinolones.

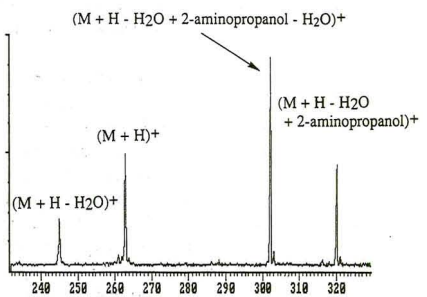

Figure 5. CAD spectrum of protonated oxolinic acid in the presence of 2-aminopropanol.

Protonated 1,2-ethanediol undergoes facile dehydration after collisional activation, and thus we speculate that the second dehydration step of the $(M + H - H_2O + \text{1,2-ethanediol})^+$ quinolone ion involves the 1,2-ethanediol portion.

Adduct formation was also observed upon activation of the protonated quinolones in the presence of acetic anhydride. Upon activation, two new adducts are formed: $[M + H - 18 + \text{acetic anhydride}]^+$ and $[M + H - 18 + \text{acetic anhydride} - 42]^+$. The loss of 42 amu is presumably due to elimination of ketene from the acetic anhydride portion of the adduct, because acetic anhydride molecular ions are known to dissociate by elimination of ketene. With 2-aminopropanol as the reactive gas, attachment of neutral 2-aminopropanol to the dehydrated analyte occurs, and then this complex may lose water to produce an ion, $[M + H - 18 + \text{2-aminopropanol} - H_2O]^+$. An example of this type of behavior is shown in Figure 5 for CAD of protonated oxolinic acid. The loss of H_2O is known to be the most facile fragmentation pathway of protonated 2-aminopropanol.[29] When 2-aminopropanol or acetic anhydride is used as an auxiliary reagent, the fact that some of the adducts undergo subsequent dissociation

(29) Eichmann, E. S.; Brodbelt, J. S. *Org. Mass Spectrom.* **1993**, *28*, 665.

indicates that there is excess internal energy from the initial activation/addition reactions of the quinolones which is dissipated through further fragmentation of the intact adduct ion. Moreover, these secondary fragmentations must involve some rearrangement of the adduct ion, such as hydrogen migrations, in order for the pathways to be rationalized.

Another reagent that promotes rather unusual secondary reactions is 2-(trimethylsilyl)ethanol. After activation of each protonated quinolone, the resulting dehydrated fragment ion undergoes a rapid reaction with neutral 2-(trimethylsilyl)-ethanol to generate the unusual product labeled as $(M + H - H_2O + 2\text{-(trimethylsilyl)ethanol} - 28)^+$. Isolation and collisional activation of the new product causes it to dissociate to $(M + H - H_2O)^+$, thus suggesting that the auxiliary reagent is actually undergoing the elimination of 28 Da, not the quinolone substrate. To rationalize this behavior, we speculate that the hydroxyl end of the 2-TMS-ethanol molecule attaches to the acylium ion portion of the dehydrated quinolone substrate, and then the excess energy of the collision complex causes an intramolecular rearrangement and elimination of ethylene from the (trimethylsilyl)ethanol portion of the adduct (see mechanism shown in Figure 7). This reaction would leave the trimethylsilyl unit attached directly to an oxygen atom.

Isolation of the $(M + H - H_2O)^+$ quinolone ions, followed by a reaction period with each auxiliary reagent, also results in efficient formation of the adduct ions. Thus, the reactions of the dehydrated ions with the reagent appear to be spontaneous exothermic processes, and it is the first dehydration step that represents the reaction barrier that prevents any adduct formation from the intact protonated quinolones.

Other reagents that were found to be nonreactive included vinyl methyl ether, anisole, ethylene oxide, and isobutane. As discussed later, these four reagents lack the appropriate structural features needed to assist in formation and stabilization of the adducts.

CAD and Reactions of Model Compounds. In order to provide evidence for the mechanism and specificity of the intriguing addition reactions of the $[M + H - H_2O]^+$ ions, studies of model compounds were performed to reveal insight into the reactive region of the quinolones and offer support that the carboxylic acid/ketone interaction provides a valuable means for uniquely identifying the quinolone class. In this section, six model compounds having functional groups similar to those of the quinolones are characterized utilizing the auxiliary reagents described earlier. The six model compounds studied are cyclohexanone, benzoic acid, propionic acid, 3-oxoglutaric acid, and coumarin-3-carboxylic acid, and ethyl-2-cyclohexanone carboxylate (Figure 6). The key to the first five models is that they all dehydrate upon activation of the protonated molecules. Thus, each follows the characteristic first reaction step noted for the activated protonated quinolones. The sixth model undergoes facile loss of ethanol after protonation and activation, resulting in formation of the 2-cyclohexanonyl acylium ion. The main objective was to evaluate the influence of different functional groups on promoting the various unusual products formed during the CAD experiments of the $[M + H]^+$ ions.

As noted, upon collisionally activated dissociation of the first five models, the protonated models predominantly undergo

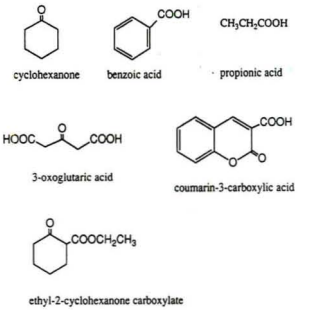

Figure 6. Structures of six model compounds.

dehydration. Then the CAD spectra were reexamined in the presence of neutral auxiliary reagent gases. For example, the fragmentation patterns of protonated cyclohexanone, propionic acid, 3-oxoglutaric acid, and benzoic acid in the presence of allyl alcohol, acetone, acetic anhydride, and 3-propylamine were analogous to those found in the absence of the auxiliary reagents, and no new adducts were observed. CAD of protonated coumarin-3-carboxylic acid in the presence of the auxiliary reagents, however, resulted in adduct formation similar to that of the quinolones. For instance, in the presence of allyl alcohol, the most abundant peak in the spectrum was the attachment of neutral allyl alcohol to the dehydrated coumarin-3-carboxylic acid ion. In the presence of acetic anhydride, coumarin-3-carboxylic acid produced a new ion corresponding to $[M + H - 18 + \text{acetic anhydride} - 42]^+$, again a behavior analogous to that of the quinolone class. CAD of protonated coumarin-3-carboxylic acid in the presence of propylamine results in $[M + H - 18 + \text{propylamine}]^+$. Likewise, dehydrated coumarin-3-carboxylic acid reacts with neutral 2-aminopropanol to form $[M + H - 18 + \text{2-aminopropanol}]^+$ and $[M + H - 18 + \text{2-aminopropanol} - H_2O]^+$.

The sixth model, ethyl-2-cyclohexanone carboxylate, was chosen to represent a substrate that possessed the neighboring carbonyl groups positioned on a saturated ring system, in contrast to the coumarin-3-carboxylic acid model in which the two carbonyl groups are fixed on a more rigid, partially unsaturated ring. The sixth model does not undergo the characteristic addition reactions with the auxiliary reagents after protonation and activation. This result suggests that the rigidity of the ring system may also play a role in correctly anchoring the two carbonyl substituents in order to promote the secondary reactions.

In summary, of all the model compounds chosen, only coumarin-3-carboxylic acid undergoes adduct formation after dehydration. The failure of the other models to react may be rationalized in several ways. The interaction of two functional groups, such as the proximity of the ketone–carboxylic acid functional groups, may be important for any attachment to the dehydrated species. Thus, it appears that the carboxylic acid or ketone group alone is insufficient to promote the characteristic addition reaction. Even more importantly, the flexible oxoglutaric acid which has two acid groups and a nearby ketone and the ethyl-2-cyclohexanone carboxylate are perhaps too floppy to allow stabilization of the adduct, or they may favor other intramolecular interactions rather than adduct

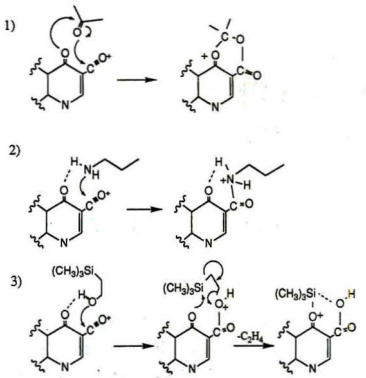

Figure 7. Proposed reaction pathways for adduct formation.

formation. For example, activation of protonated glutaric acid may promote formation of a dehydrated fragment ion which stabilizes via intramolecular cyclization, thus disfavoring interaction with any auxiliary reagent. Four of the models have acidic groups and dehydrate readily, but it is not until the ketone and carboxylic acid functional groups are nearby and fixed in a fairly rigid positioning (as for coumarin-3-carboxylic acid) that the same adducts found in the quinolone CAD spectra are produced. Thus, we speculate that the ability of the analyte to undergo facile dehydration and also to have close interaction of two oxygenated groups is *critical* for formation of the new products.

Figure 7 shows possible reaction mechanisms between the auxiliary reagent gases and the dehydrated ions. In the figure, the dehydrated species shown is not a complete quinolone but a reasonable model of the active region. In the first reaction, neutral acetone and the dehydrated species associate to generate a stable six-membered ring. Of the gases utilized in this study, acetone and acetic anhydride may follow this first reaction pathway. The other gases such as propylamine, 1,2-ethanediol, and 2-aminopropanol which are capable of hydrogen bonding may follow the second pathway, in which a six-membered ring stabilized by hydrogen bonds is formed. Allyl alcohol may follow both reaction schemes since it contains an olefin functional group and an alcohol substituent which is capable of hydrogen bonding. 2-(Trimethylsilyl)ethanol also promotes an unusual secondary process in which 28 Da is eliminated, and a mechanism which accounts for this reaction is also shown. The loss of 28 Da occurs by an intramolecular rearrangement in which ethylene is eliminated. Dimethyl ether, ethylene oxide, anisole, vinyl methyl ether, and isobutane do not react with the dehydrated species, presumably due to their inability to form a ring system. For example, the oxygen atom in the DME molecule could attack the positively charged carbonyl carbon of the quinolone. However, the ketone substituent cannot form a favorable bond with the saturated carbon atom in DME; thus, instead the typical CAD fragmentation channels of the quinolone ions prevail.

CONCLUSIONS

This study has illustrated a new and promising application of ion–molecule reactions. Secondary ion–molecule reactions stemming from the CAD experiments showed that CAD fragment ions (i.e. dehydrated quinolones) may react selectively with auxiliary reagent molecules. These reactions are characteristic of a particular active region in the quinolone analyte and only seem to occur when stable cyclized adducts can be formed. The results obtained for the six model compounds thus show how influential the position and interaction of the functional groups can be for promoting adduct formation. Ultimately, this use of ion–molecule reactions proves valuable as a structurally selective target probe of the quinolone class and can also be used to form new higher mass products that can be moved to regions of lower noise or interferences in a mass spectrum. Additionally, if there are two isobaric components in a mixture, only the component with the correct active region would undergo the multistep reaction and thus be shifted to a new mass, allowing it to be analyzed or quantitated distinctly from the other component. Knowledge gained from these sets of experiments can be applied to developing class-selective methods for other biological molecules, such as aminoglycoside antibiotics or penicillins.

ACKNOWLEDGMENT

This research was supported by grants from NSF (CHE-9122699), the Welch Foundation (F1155), NIH (R01-GM46723-01), and ACS-PRF (25485-AC5). J.B. acknowledges The Camille and Henry Dreyfus Teacher-Scholar Awards Program, the Alfred P. Sloan Research Fellow Program, and the NSF-NYI program (CHE-9357422).

Received for review December 16, 1993. Accepted April 22, 1994.[•]

[•] Abstract published in *Advance ACS Abstracts,* June 1, 1994.

Anal. Chem. **1994,** *66,* 2336–2347

Factors Controlling Precision and Accuracy in Isotope-Ratio-Monitoring Mass Spectrometry

Dawn A. Merritt[†] **and J. M. Hayes***

Biogeochemical Laboratories, Departments of Chemistry and of Geological Sciences, Geology Building, Indiana University, Bloomington, Indiana 47405-1403

The performance of systems in which picomole quantities of sample are mixed with a carrier gas and passed through an isotope-ratio mass spectrometer system was examined experimentally and theoretically. Two different mass spectrometers were used, both having electron-impact ion sources and Faraday cup collector systems. One had an accelerating potential of 10 kV and accepted 0.2 mL of He/min, producing, under those conditions, a maximum efficiency of 1 CO_2 molecular ion collected per 700 molecules introduced. Comparable figures for the second instrument were 3 kV, 0.5 mL of He/min, and 14 000 molecules/ion. Signal pathways were adjusted so that response times were <200 ms. Sample-related ion currents appeared as peaks with widths of 3–30 s. Isotope ratios were determined by comparison to signals produced by standard gases. In spite of rapid variations in signals, observed levels of performance were within a factor of 2 of shot-noise limits. For the 10-kV instrument, sample requirements for standard deviations of 0.1 and 0.5‰ were 45 and 1.7 pmol, respectively. Comparable requirements for the 3-kV instrument were 900 and 36 pmol. Drifts in instrumental characteristics were adequately neutralized when standards were observed at 20-min intervals. For the 10-kV instrument, computed isotopic compositions were independent of sample size and signal strength over the ranges examined. Nonlinearities of <0.04‰/V were observed for the 3-kV system. Procedures for observation and subtraction of background ion currents were examined experimentally and theoretically. For sample/background ratios varying from >10 to 0.3, precision is expected and observed to decrease approximately 2-fold and to depend only weakly on the precision with which background ion currents have been measured.

It has been conventional, when abundances of the stable isotopes of hydrogen, carbon, nitrogen, oxygen, and sulfur are to be determined with a precision of 1 in 10^3 or better, to integrate ion currents resulting from the admission of H_2, CO_2, N_2, O_2, SO_2, or SF_6 to the ion source of a mass spectrometer. Specialized inlet systems allowing this are designed to avoid isotopic fractionation[1] and to allow close comparison of isotopic abundances in two[2] or more[3] gases delivered to the ion source at closely matched and carefully stabilized rates. Even when these inlet systems are miniaturized, however, sample amounts on the order of 0.1 μmol are required to reach minimal operating pressures.[4] Dilution of samples with inert gases further reduces sample requirements but exacerbates problems associated with operation of the inlets.[5] Although the actual integration of ion currents seldom requires more than 60 s and consumes at most a few nanomoles of sample (the remainder of the gas serving merely to pressurize the inlet system), completion of more than 12 analyses/h is unusual and examination of submicromole samples actually requires more time because gas transfers are slower.

"Isotope-ratio monitoring" (irm) refers to a potentially large range of techniques in which conventional inlet systems are avoided. Widely varying ion currents are accepted and all of the sample is utilized. Analysis times can drop from tens of minutes to tens of seconds and subnanomole samples can be accommodated. The strategy has thus far been applied to continuous observation of gas chromatographic effluents following combustion[6–9] or other postcolumn reactions, but can be extended to any procedure in which the sample can be packaged as a zone within a carrier gas stream.

The utility of isotope-ratio-monitoring GC/MS procedures has already been established through a variety of successful applications,[10,11] but reports of those have provided few details about the technique itself and have not systematically considered more general aspects of isotope-ratio monitoring. Accordingly, we describe here procedures for collection of data; subtraction of background ion currents, including those derived from combustion of gas chromatographic column bleed; and manipulation of data. Attainable levels of precision are examined for two different isotope-ratio mass spectrometers, one with a conventional ion source operating at an accelerating potential of 3 kV and the other with a high-sensitivity source operating at an accelerating potential of 10 kV.

EXPERIMENTAL SECTION

Instrumentation. *Mass Spectrometers.* Isotopic abundances in CO_2 were measured using Delta-S and 252 isotope-

[†] Present address: Environmental Chemistry Laboratory, DowElanco, Box 68955, Indianapolis, IN 46268-1053.

(1) Halsted, R. E.; Nier, A. O. C. *Rev. Sci. Instrum.* **1950,** *21,* 1019–1021.
(2) McKinney, C. R.; McCrea, J. M.; Epstein, S.; Allen, H. A.; Urey, H. C. *Rev. Sci. Instrum.* **1950,** *21,* 724–730.
(3) Schoeller, D. A.; Peterson, D. W.; Hayes, J. M. *Anal. Chem.* **1983,** *55,* 827–832.
(4) Bridger, N. I.; Craig, R. D.; Sercombe, J. S. F. *Adv. Mass Spectrom.* **1974,** *6,* 365–375.
(5) Schoeller, D. A.; Hayes, J. M. *Anal. Chem.* **1975,** *47,* 408–415.
(6) Sano, M.; Yotsui, Y.; Abe, H.; Sasaki, S. *Biomed. Mass Spectrom.* **1976,** *3,* 1–3.
(7) Matthews, D. E.; Hayes, J. M. *Anal. Chem.* **1978,** *50,* 1465–1473.
(8) Barrie, A.; Bricout, J.; Koziet, J. *Biomed. Environ. Mass Spectrom.* **1984,** *11,* 583–588.
(9) Hayes, J. M.; Freeman, K. H.; Popp, B. N.; Hoham, C. H. *Org. Geochem.* **1990,** *16,* 1115–1128.
(10) Freeman, K. H.; Hayes, J. M.; Trendel, J.-M.; Albrecht, P. *Nature* **1990,** *343,* 254–256.
(11) Jasper, J. P.; Hayes, J. M. *Nature* **1990,** *347,* 462.

0003-2700/94/0366-2336$04.50/0
© 1994 American Chemical Society

ratio mass spectrometers (Finnigan MAT, Bremen, Germany). Ions were generated by electron impact (70 eV). The ion-source regions were differentially pumped so that pressures of 3×10^{-6} and 7.5×10^{-7} Torr were maintained in the ion source and analyzer regions. Accelerating potentials were 3 (Delta-S) or 10 kV (252). Ion currents at masses 44, 45, and 46 were simultaneously collected by Faraday cups connected to feedback electrometers. The feedback resistors were nominally 300 MΩ (m/z 44), 30 GΩ (m/z 45), and 100 GΩ (m/z 46). A 1-nA current at m/z 44 therefore produced a 0.3-V signal.

Signals were converted to frequencies at a rate of 2000 Hz/V, and pulses were counted in order to effect analog-to-digital conversion. Two sets of counters were employed together with a secondary oscillator. For each channel, one counter (the *nonius*, from the German for vernier) accumulated pulses from the secondary oscillator while the other accumulated signal pulses. For each integration interval, the nonius was triggered *on* on the rising edge of the first signal pulse and *off* on the rising edge of the first signal pulse after the nominal counting time had ended. Although nominal integration intervals were operator selectable (62.5, 125, 250 ms..., 8 s), actual times required to collect an integral number of counts varied slightly and were given by n/f where n is the number of nonius counts and f is the frequency of the oscillator (4.2 MHz). In turn, the precise count rate for the signal was given by

$$F_S = S/(n/f) \quad (1)$$

where F_S is the count rate and S is the number of signal pulses.

Electrometer Offsets and Time Constants. A small offset current was added to the ion current at the summing point of each electrometer. In the absence of any ion current, resulting signals were 90–110 (m/z 44), 110–130 (m/z 45), and 140–160 mV (m/z 46). The resulting signal ratios approximated those obtained from CO_2 with natural abundances of ^{13}C, ^{17}O, and ^{18}O. The nominal time constants calculated from specifications citing capacitance values of 470, 5, and 2 pF for the m/z 44, 45, and 46 electrometers were 0.14, 0.15, and 0.20 s, respectively. The actual time constants depend also on circuit components beyond the electrometer feedback loops and on stray capacitance in the collector system. Response times can be altered by adjustment of a capacitance feedback circuit. Use of this feature to optimize performance is described in a later section of this report.

Gas-Flow Pathways. For the experiments described here, (i) CO_2 was introduced *via* conventional, viscous-flow capillary leaks while a constant flow of helium carrier gas entered the ion source or (ii) CO_2 was injected directly into the carrier gas stream. As shown in Figure 1, the gas chromatographic column was connected to an injection valve with an internal 1-μL sample volume (Valco Instruments, Houston, TX). The flow rate of carrier gas (0.5–1.0 mL of He/min) was set using an adjustable flow controller (Porter Instrument, Hatfield, PA). Both Ultra-1 (50-m length, 0.32-mm i.d., 0.52-μm film thickness; Hewlett Packard, Avondale, PA) and Poraplot Q (25-m length, 0.32-mm i.d., 10-μm particle layer, 1-m particle trap; Chrompack, Raritan, NJ) columns were employed. For these investigations, the function of the columns was not

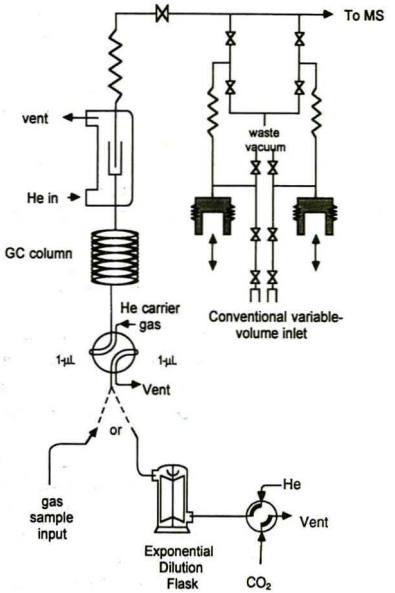

Figure 1. Schematic view of gas inlets. Adjustment of variable volumes regulated pressures upstream from capillary leaks (represented here as resistors) through which, by manipulation of switching valves, steady flows of gas were sent either to waste vacuum or to the mass spectrometer. A third capillary accepted a portion of the effluent of a chromatographic column. At the inlet of the column, a four-port sampling valve with internal, 1-μL sampling volumes was connected either to a steadily flowing gas stream with constant composition or to the effluent of an exponential dilution flask. The flask was initially filled with CO_2 and then purged with He.

purification of CO_2 but, instead, broadening of the 100-ms CO_2 spikes introduced by the valve so that smoothly varying sample pressure vs time profiles with widths of 10–20 s were obtained.

The rate of admission of gas to the mass spectrometer was controlled by a capillary leak. The capillary (0.11 mm-i.d. deactivated silica) was inserted approximately 1 cm into the end of a transfer line exiting the column. This junction was housed within a 10-cm length of 6-mm-o.d. Pyrex tubing. A constant flow of dry helium (2 mL/min) passed through that tube at all times so that this unit acted as an open split. Connections were made using $^1/_4$–$^1/_{16}$-in. reducing-tee unions with graphitized-vespel ferrules (SGE, Austin, TX). At its low-pressure end, the flow from the inlet capillary entered an on–off valve through a $^1/_4$–$^1/_{16}$-in. Swagelok reducing union, and the valve was connected to the ion source housing through a $^1/_4$-in. Swagelok union. The length of the restrictor capillary was adjusted such that the pressure in the ion source was $(2–4) \times 10^{-6}$ Torr and the flow of carrier gas entering the mass spectrometer was approximately 0.2 (10-kV instrument) or 0.5 mL/min (3-kV instrument).

Experimental Procedure. All high-precision isotopic analyses are based on comparisons of ion current ratios between "standards", substances for which isotopic compositions are accurately known, and "samples", materials for which the isotopic composition is to be determined. Supplies of standards

are usually plentiful, but sample quantities may be sharply limited. In recognition of this, procedures for handling of standards and samples commonly differ, and that distinction was preserved in these investigations even though the "samples" were in all cases standard materials that were being used to test instrumental performance.

Introduction of Isotopic Standards. Carbon dioxide (Coleman grade; Air Products, Allentown, PA) was introduced via either of the variable-volume inlets of the mass spectrometer. Under control of the switching valves (Figure 1), CO_2 flowed from the variable volumes through a capillary leak to the ion source. To introduce an isotopic standard during an analysis, CO_2 from the inlet was admitted to the ion source for 15–20 s. The valves were operated either manually via a touch-screen controller or by computer control.

Introduction of Samples. Samples of CO_2 for which the isotopic compositions were to be determined were admitted either from a variable-volume inlet or by injecting CO_2 directly into the carrier gas stream. In either case, a constant flow of carrier gas entered the mass spectrometer. When injected samples of constant size were desired, a 1:5 mixture of CO_2 and helium (v/v) was used with the 3-kV instrument (the 1-μL sampling volume thus yielding 6.7 nmol of CO_2); 0.66% CO_2 in helium (v/v) was used with the more sensitive instrument (1 μL → 0.3 nmol of CO_2). Alternatively, the effluent of an exponential dilution flask (EDF[12]) was sampled.

The arrangement of the EDF is shown in Figure 1. At any time during the course of an experiment, the concentration of CO_2 in the effluent from the flask was given by

$$C_t = C_0 e^{-tF/V} \tag{2}$$

where C_t is the concentration at time t, C_0 is the concentration at $t = 0$, F is the flow rate of diluent gas (commonly 14 mL of He/min), and V is the volume of the flask (365 mL). If the gas initially present in the EDF was pure CO_2, samples as large as 40 nmol were obtained by use of the 1-μL sampling volume. Extension of t (eq 2) allowed convenient production and introduction of samples as small as 10^{-13} mol of CO_2.

Introduction of Background CO_2. To simulate conditions of irmGC/MS analyses at high column temperatures, a second stream of CO_2 was sometimes admitted simultaneously to the mass spectrometer to mimic the presence of background derived from the combustion of column bleed. This gas was either added directly into the ion source from the variable-volume inlet or mixed into the carrier gas stream using an exponential dilution flask. Background levels increased either continuously or incrementally, and they approximated levels typical in irmGC/MS (m/z 44 ion currents of 0–7 and 0–2 nA for the 10- and 3-kV instruments, respectively).

Determination of Ionization Efficiency. When CO_2 was injected directly into the carrier gas stream, ionization efficiency (E, ions/molecule) was calculated by comparing the collected charge to the number of molecules introduced:

$$E = A/mR_f q_e N_A \tag{3}$$

where A is the area of the m/z 44 peak (V·s); m is the sample size (mol of CO_2); R_f is the resistance of the feedback resistor in the electrometer amplifier for m/z 44 (3×10^8 Ω); q_e is the electronic charge, 1.6×10^{-19} C/ion; and N_A is Avogadro's number.

When CO_2 was introduced from the variable-volume inlet, the rate at which sample molecules entered the ion source was determined using a capacitance micromanometer (MKS Instruments, Burlington, MA) to monitor the pressure within the inlet. The ionization efficiency was then given by

$$E = {}^{44}VP_i\Delta t/m_i R_f q_e N_A \Delta P \tag{4}$$

where $\Delta P/\Delta t$ is the rate of decrease of pressure (Torr/s), ${}^{44}V$ is the mass-44 signal (V), and P_i is the initial pressure (Torr) after introduction of a sample with initial size m_i (mol) into the inlet system. For the 10- and 3-kV instruments, values of m_i were commonly 52–55 and 205–207 μmol, respectively. Accordingly, with allowance for the differing split ratios, nearly constant fluxes of 0.21 and 0.45 nmol of CO_2/s entered the ion source and produced mass-44 signals of 4 and 0.4 V, respectively.

Calculations and Presentation of Results. Ratios of sample-derived ion currents and isotopes are denoted by R. A left superscript indicates the mass or isotope in the numerator. The most abundant related species always appears in the denominator. For example, ${}^{17}R \equiv {}^{17}O/{}^{16}O$ and ${}^{45}R \equiv ({}^{13}CO_2 + {}^{12}C{}^{17}O{}^{16}O)/{}^{12}C{}^{16}O_2$. Isotope ratios were calculated using the method described by Santrock, Studley, and Hayes[13] and are reported in terms of δ values in units of parts per thousand, or per mil (‰):

$$\delta^{13}C_{PDB} \equiv 10^3[({}^{13}R/{}^{13}R_{PDB}) - 1] \tag{5}$$

where ${}^{13}R$ is the isotope ratio for the sample and ${}^{13}R_{pdb}$ is the accepted isotope ratio for the PeeDee Belemnite primary standard.[14]

The mass spectrometer and data acquisition events were controlled by a computer with a 80386 CPU and a 20-MHz clock speed (Deskpro 386/20e; Compaq, Inc., Houston, TX). Data points corresponding to integrated ion currents were collected at approximately 0.25-s intervals, with the precise counting period defined by the independent time base (nonius oscillator) described earlier.

Peak Definition. Digital records were scanned to distinguish signals derived from sample injections. "Peaks" corresponding to inputs of CO_2 were recognized by use of adjustable thresholds for slope and amplitude. For each point in the mass-44 record, the local slope (mV/s) was calculated using an unweighted, five-point linear regression. The first point within a peak was that at which the value exceeded the starting slope threshold. The last point was that at which the slope dropped below a user-defined ending slope threshold. The retention time for each peak was defined as the time corresponding to the peak maximum. Peaks for which the maximum height was less than a chosen amplitude threshold were ignored.

(12) Lovelock, J. E. *Nature* **1971**, *230*, 379–380.

(13) Santrock, J.; Studley, S. A.; Hayes, J. M. *Anal. Chem.* **1985**, *57*, 1444–1448.

(14) Bakke, E. L.; Beaty, D. W.; Hayes, J. M. *Geol. Soc. Am. Abstr. Prog.* **1991**, *23*, A150.

Background Subtraction. The signal corresponding to each mass has multiple components:

$$i_t = i_s + i_b \quad (6)$$

$$i_b = i_e + i_i + i_r + i_l \quad (7)$$

where i refers to ion current (or, in the case of some background components, *apparent* ion current) and the subscripts are defined as follows: t, total; s, sample-related; b, background; e, electronic offset; i, impurities in carrier gas stream; r, residual gases in ion source; and l, air leaks. In most cases, background ion currents were measured collectively for each mass—the individual components were not treated separately. Although more sophisticated algorithms are available within the software, backgrounds for the peaks examined in this work were defined by averaging separately for each mass the total ion current at the five points immediately preceding each peak.

Manual Editing of Peak Files. When desired, the starting point, ending point, and background levels for any peak can be defined manually. To facilitate this, the mass chromatograms at m/z 44, 45, and 46 and the time-dependent 45/44 ratio are displayed on an expanded time base. Tick marks on the traces indicate the software-selected starting and ending points for each peak. When new, manually chosen points are specified, the software-selected points are not overwritten. Instead, an additional "peak" (i.e., the original peak, redefined) is added to the file. Isotope ratios are then reported for both software- and operator-defined peaks so that the effects of the manual adjustment can be studied.

Calibration of δ Scale. Peaks corresponding to isotopic standards were identified by the operator and their $\delta^{13}C_{pdb}$ and $\delta^{18}O_{smow}$ values specified. Corresponding isotope ratios and ion current ratios were then calculated.[13] Values of δ for peaks other than isotopic standards were calculated by use of procedures outlined by Ricci et al.[15] For sample peaks which occurred between standard peaks, drifts in instrumental characteristics were corrected by linear interpolation. For peaks which occurred before the first standard and after the last standard, the correction was determined by linear extrapolation of the correction defined by the first or last pair of adjacent standards.

RESULTS AND DISCUSSION

Recorded Signals. *Samples Introduced from the Variable-Volume Reservoirs.* As shown in Figure 2, signals responded rapidly when the switching valves were manipulated to mix CO_2 (flowing from the variable-volume reservoir) with He flowing through the inlet capillary shown in Figure 1. All signals quickly returned to baseline values after the switching valves were returned to their original positions. Because the rates of flow of CO_2 from the variable-volume reservoirs were constant, the peaks approximated square waves.

The appearances of the 46/44 and 45/44 ratio traces are dependent not only on the signals produced by the sample but also on the magnitudes of the background signals at each collector. In the present case, the background for each signal consisted almost entirely of electronic offset currents applied to the summing point of the electrometer for each collector.

(15) Ricci, M. P.; Merritt, D. A.; Freeman, K. H.; Hayes, J. M. *Org. Geochem.*, in press.

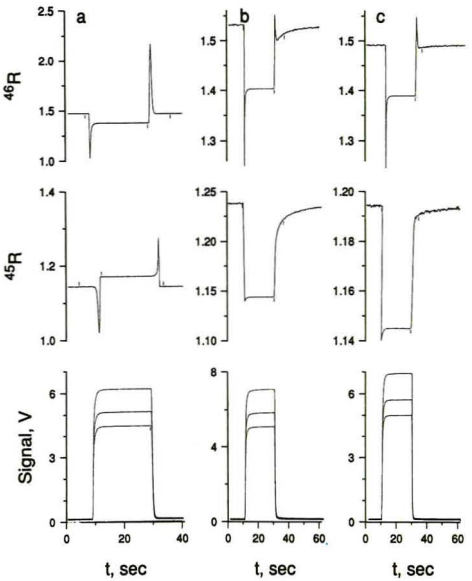

Figure 2. Recordings of the signals produced when CO_2 was admitted to the ion source via the conventional inlet system for the 10-kV instrument. Upper plots display the ion current ratios 46/44 (^{46}R) and 45/44 (^{45}R) and lower plots display the total signals at each collector (highest signal mass 46, lowest mass 44). Both a and b represent the same gas sample, but the mass-45 offset current is slightly higher in the second case, thus changing the background value of ^{45}R. More importantly, optimal matching of the mass-44 and -45 time constants (and minimization of the mass-46 time constant) also greatly reduced transients on the ratio trace in (b) relative to those observed in (a). In (c), an increase in the gas dynamic conductance of the ion source also reduced the tailing on the ^{45}R trace relative to that seen in (b). Note that the ^{45}R scales are progressively expanded in (b) and (c).

These guard against the appearance of negative voltages at the input of the voltage-to-frequency conversion system and provide helpful control over the appearance of the output. Signals observed in the absence of ion current are large enough that they are not exceptionally noisy, and in turn, noise on the signal ratios is limited. If offset currents were not applied, the ratio signals would be well defined only in the presence of ion currents, the displays would be cluttered with distracting noise, and the complexity of data processing would be increased.

In Figure 2a, the offset currents were chosen such that the background signal ratio (^{45}R) was smaller than that characteristic of the sample. As a result, ^{45}R increased when the sample was admitted. In contrast, a different adjustment of the offset currents yielded a higher background ratio at the time Figure 2b was recorded. The introduction of the sample was thus recorded in terms of an decrease in ^{45}R. Of principal interest, however, is the appearance of prominent transients in the ^{45}R and ^{46}R traces shown in Figure 2a.

Transient Signals. Switching of gas inputs—an inescapable operation in isotopic gas analysis—will inevitably produce abrupt changes in the density and composition of gas within the ion source. The subsequent response of the system will be modulated not only by finite time constants within the

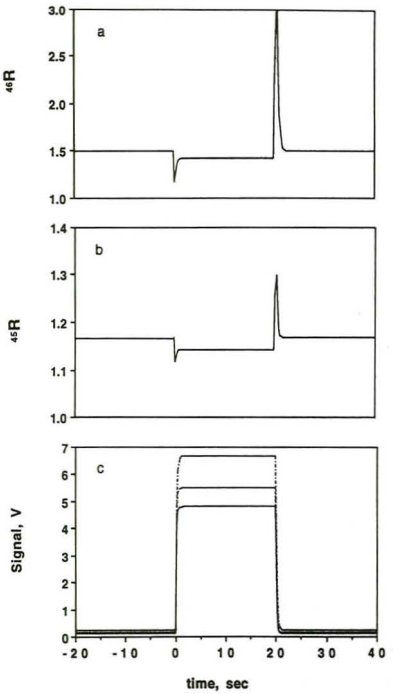

Figure 3. Mathematical modeling of ion current traces and ratio traces. Electronic time constants that were measured for the 10-kV instrument were used to construct ion current and ratio traces assuming ideal *RC* behavior.

signal-processing pathways but also by physical processes such as the growth and decay of space charges within the ion source and sorption and desorption of molecules at surfaces along the sample-transfer pathway. For example, the ion current recordings in Figure 2 (the voltage signals, not the calculated ratios) indicate only small deviations from a perfect square wave. Effects are exaggerated, however, when ratios are considered. At that point, any mismatch between time constants or any differential sorption–desorption phenomena will produce significant transients in computed ratios. Since perfect elimination of such phenomena is impossible, systems for the acquisition and processing of data must be tolerant of them.

An idealized view of electronic effects is shown in Figure 3, which depicts calculated ion currents and ion current ratios rather than actual recordings. In this case, transients expected from mismatched time constants have been modeled by assumption of perfect *RC* behavior. Time constants assigned to the mass-44, -45, and -46 signals were 170, 180, and 300 ms, respectively, and the effects on square waves of realistic amplitude were determined by calculation of instantaneous signals and ratios as a function of time. The resulting wave forms are similar to those in Figure 2a but not identical, in spite of the fact that the assigned time constants match those measured prior to the recording of the data in Figure 2a. It follows that (as is likely) the actual signal pathways do not display ideal *RC* behavior and/or that nonelectronic effects are present.

Resolution and minimization of electronic effects are demonstrated in the sequence of recordings shown in Figure 2. In part b of the figure, adjustment of the time constant of the mass-45 amplifier allowed nearly complete elimination of overshoot on the ^{45}R trace. Because the time constant on the higher resistance mass-46 amplifier had already been minimized, elimination of transients on the ^{46}R trace would have required lengthening the mass-44 time constant and consequent degradation of the response time of the overall system. Accordingly, the presence of overshoot in the ^{46}R record, which is involved only indirectly in the calculation of carbon isotopic abundances, was accepted. The third set of recordings (Figure 2c) indicates the effect of maximizing the gas dynamic conductance of the ion source and thus confirms the presence of nonelectronic effects. The return of the ^{45}R trace to the background level occurs significantly more promptly when the "window" in the ion source is opened to the greatest possible extent. The "window" is an externally adjustable shutter provided by the manufacturer and is intended to allow optimization of ion source sensitivity and sample change-over times when the mass spectrometer is operated with a conventional dual inlet. Under the conditions employed here (notably the high throughput of He), maximum sensitivity was obtained when the window was opened to 25% of maximum. However, as shown by the tailing ^{45}R trace in Figure 2b, the temporal response is degraded. When the window was fully closed, sensitivity was *decreased* by 5–10% and tailing was only slightly worse than that shown in Figure 2b. With the window was opened to 50% of maximum, temporal response was greatly improved (Figure 2c) but sensitivity was also only 50% of maximum. Further increases in source conductance did not improve temporal performance but did result in further losses of sensitivity and were thus avoided. The ^{45}R signal shown in Figure 2b is consistent with an expected effect, namely, the removal of $^{12}C^{16}O_2$ from the ion source more rapidly than $^{13}C^{16}O_2$ and $^{12}C^{17}O^{16}O$.

Measurement of Isotopic Abundances. In isotope-ratio-monitoring measurements, ion currents are integrated as samples of interest pass through the ion source. Integration intervals may be brief—only a few seconds. Sample pressures and resulting signal levels may vary widely. Observations of standards may be infrequent. Questions then arise concerning methods for selection and definition of integration intervals, attainable levels of precision and accuracy, and optimization of procedures. These can be addressed by examination of system performance as procedures are varied, but it is useful first to consider an absolute standard of performance, namely, the "shot-noise limit". This refers to the precision that would be obtained if the ion beam itself were the only significant noise source,[16] with all transducers, amplifiers, and other components of the signal pathway being completely free of noise. It represents a level of performance that can be improved only by redesign of the measurement so that more ions are observed or collected.

Calculation of the shot-noise limit is based entirely on the statistics of ion collection. For the precision-controlling ratio in the present work, $R = {}^{45}i/{}^{44}i$, the standard deviation will

(16) Peterson, D. W.; Hayes, J. M. In *Contemporary Topics in Analytical and Clinical Chemistry*; Hercules, D. M., Hieftje, G. M., Eds.; Plenum Publishing: New York, 1978; Vol. 3, pp 217–252.

be given by

$$\sigma_R^2 = (\partial R/\partial {}^{45}i)^2\sigma_{45}^2 + (\partial R/\partial {}^{44}i)^2\sigma_{44}^2 \quad (8)$$

where σ_{45} and σ_{44} are the standard deviations of the ion currents. Evaluating the derivatives, we can write

$$\sigma_R^2 = R^2[(\sigma_{45}/{}^{45}i)^2 + (\sigma_{44}/{}^{44}i)^2] \quad (9)$$

For any ion current, $i = Nq_e/t$, where N is the number of ions collected in a time interval, t. Since, at the shot-noise limit, the variance in N is N, it follows that $(\sigma_i/i)^2$ is $1/N$ and that

$$(\sigma_R/R)^2 = (1/{}^{45}N) + (1/{}^{44}N) \quad (10)$$

Recalling that $R = {}^{45}i/{}^{44}i = {}^{45}N/{}^{44}N$, this expression can be rewritten in terms only of ${}^{44}N$:

$$(\sigma_R/R)^2 = (1/{}^{44}N)[(1 + R)/R] \quad (11)$$

The sensitivity of the mass spectrometer can be described in terms of the number of molecular ions received at the collector per molecule introduced to the ion source. If this factor is termed the efficiency and assigned the symbol E, we can write

$${}^{44}N = EmN_A/(1 + R) \quad (12)$$

where m is the number of moles of sample gas introduced and N_A is Avogadro's number. It follows that

$$(\sigma_R/R)^2 = (1 + R)^2/EmN_AR \quad (13)$$

Considering the definition of δ, we can write that

$$\sigma_\delta^2 = (\partial\delta/\partial R_{sample})^2\sigma_{Rsample}^2 + (\partial\delta/\partial R_{standard})^2\sigma_{Rstandard}^2 \quad (14)$$

where, in practice, values of R_{sample} and $R_{standard}$ are essentially equal, differing only in the third or fourth significant figure. The expression can thus be rewritten in terms of a single R value. If R_{sample} and $R_{standard}$ have been determined with equal precision, the two terms on the right of eq 14 are equal, and evaluating the derivatives, we obtain an expression for the maximum attainable (i.e., shot-noise limited) performance:

$$\sigma_\delta^2 = 2 \times 10^6\,(\sigma_R/R)^2 = 2 \times 10^6(1 + R)^2/EmN_AR \quad (15)$$

where σ_δ is the standard deviation characteristic of the distribution of observations of δ, and R is the ion current ratio characteristic of the gas being analyzed (approximately 0.011 for 45/44 in the mass spectrum of CO_2). In this expression, the product EmN_A is simply the number of mass-44 ions collected. That quantity is also given by ${}^{44}it/q_e$, where ${}^{44}i$ is the mass-44 ion current, t is the integration time, and q_e is the electronic charge. The value of ${}^{44}i$ is in turn given by ${}^{44}V/R_f$, where ${}^{44}V$ is the mass-44 signal and R_f is the feedback resistance of the mass-44 electrometer. Substituting $q_e = 1.6 \times 10^{-19}$ C, $R_f = 3 \times 10^8\ \Omega$, and $R = 0.011$, a simplified expression for the shot-noise-limited precision as a function of the integrated signal (A, V·s) is obtained:

$$\sigma_\delta^2 = 0.00892/{}^{44}A \quad (16)$$

For instances in which the integrated ion currents for the sample and standard have not been equal, this expression becomes

$$\sigma_\delta^2 = 0.00446(1/{}^{44}A_{sample} + 1/{}^{44}A_{standard}) \quad (17)$$

Definition of Integration Intervals. Addition of the sample to the stream of gas flowing through the ion source produces a sharp rise in ion current, and as outlined in the Experimental Section, the data system can be programmed to define the beginning of a sample zone in terms of an operator-selected slope threshold.[15] The default used in the present work was 1.0 mV/s (equivalent to 30 fmol·C·s^{-2}). The end of a sample zone, or "peak", was defined in terms of the decreasing negative slope as the ion current returned to baseline values, the operator-selected threshold in this case being –1.0 mV/s. On average, integrated ion current ratios determined within these automatically selected limits differed by less than 0.01‰ from those resulting from manually selected limits placed arbitrarily before the beginning and after the end of sample zones. The precision of δ values from automatically defined peaks is always superior to that obtained with manually selected limits of integration,[15] except where manual techniques allow removal of artifacts, as with transients at the borders of square peaks.

Stability. In conventional, dual-inlet procedures, each integration of sample ion currents is immediately preceded and/or followed by an equivalent observation of ion currents derived from an isotopic standard. In isotope-ratio-monitoring procedures, observations of samples and standards may be separated by a considerable interval. In order to examine limitations imposed by instabilities in components and operating conditions, experiments were performed in which ion current ratios from a single gas sample were observed repeatedly. An early observation in the series was arbitrarily taken as "the standard", and all subsequent observations were treated as unknown samples. Any sample vs standard differences which then appeared indicated the occurrence of drifts that, in real measurements, would degrade the accuracy of computed isotope ratios unless multiple standards were distributed throughout the run in order to allow recognition of and correction for such drifts.

Results from two sets of observations using the 10-kV instrument are summarized in Figure 4. In the first case (Figure 4a), gas samples were repeatedly introduced in the absence of carrier gas. The background pressure in the ion source was 10^{-8} Torr and the pressure during sample introduction was 2×10^{-7} Torr. The sample introduction rate for these measurements was 0.45 nmol of CO_2/s. The resulting signal level (mass 44) was 4.8 V, and integration of ion currents for 15 s was thus expected to produce—at the shot-noise limit—a population of δ values with a mean of zero and a standard deviation of 0.011‰. In fact, as shown by the minimal variations in the lines tracking the variations in the *apparent* δ value, the drift rate was only 0.00038‰/min and the scatter of δ values around the central trend corresponded to a standard deviation of 0.017‰. The two runs indicated are typical and were separated in time by 6 months. For many applications, the indicated stability is great enough that observation of a single standard could provide calibration for isotopic analyses over a period of more than 1 h. As shown in Figure 4b, drift rates up to 10-fold higher were encountered when a stream of helium carrier gas (0.2 mL/min, indicated

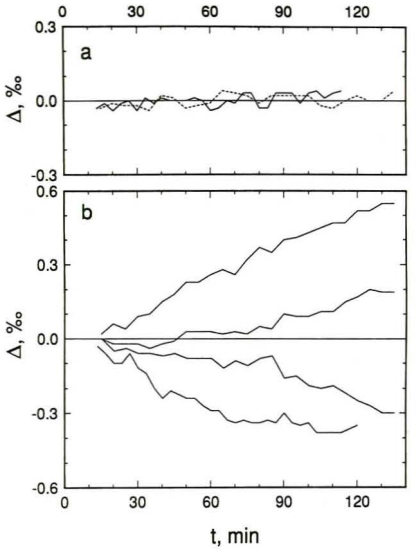

Figure 4. Results of repeated analyses of a single sample using the 10-kV instrument. Each line represents a continuous series of observations; except as noted, conditions were not varied and the lines differ due only to random fluctuations in drift. If the characteristics of the ion source and analyzer were perfectly constant, i.e., if drift were absent, all observations would scatter around the zero line with no long-term trends. (a) Samples (0.45 nmol of CO_2/s, 15 s, shot-noise-limited σ = 0.011‰, intervals between observations 185 or 285 s) admitted in the absence of carrier gas, $P_{source} = 2 \times 10^{-7}$ Torr. (b) same as (a) except for presence of carrier gas, 0.2 mL of He/min, indicated $P_{source} = 3 \times 10^{-6}$ Torr.

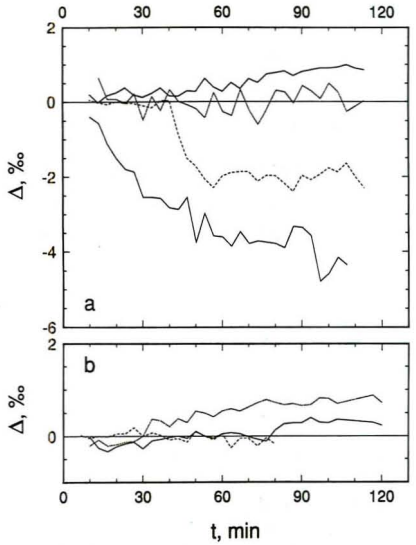

Figure 5. Results of repeated analyses of a single sample using the 3-kV instrument, as for Figure 4 except 0.86 nmol of CO_2/s, 15 s, shot-noise limited σ = 0.027‰, interval between observations = 185 s. (a) $P_{source} = 2 \times 10^{-7}$ Torr. (b) He carrier gas, 0.5 mL/min, indicated $P_{source} = 3 \times 10^{-6}$ Torr.

source pressure 3×10^{-6} Torr) was admitted to the ion source. The four lines shown summarize results of four typical runs and correspond to drift rates as high as 0.005‰/min. The cause of these drifts is not easy to identify. Their origin is clearly not electronic (if electronic, they ought also to have affected the runs depicted in Figure 4a), but the "obvious" idea that some varying background component is present in the He carrier gas must be set aside when it is recalled that the zero baseline for integration of ion currents is automatically reset at the beginning of each integration interval (see Experimental Section). It follows that the drift is associated with some variation in properties or performance of the ion source or analyzer system. Conceivably, a slightly unstable mass discrimination is associated with the presence of the He plasma in the source.

The 3-kV instrument was less stable, both with and without carrier gas in the ion source (Figure 5). Because nonstandard, prototype amplifiers are employed on that system, this low performance indicates nothing about characteristics of instruments that may be in use elsewhere. There are, however, two broader elements of significance. First, the drift in the presence of carrier gas is not markedly worse than that in the 10-kV instrument. The different ion source design in the 3-kV instrument is therefore not associated with any significantly different level of unstable mass discrimination if, indeed, that is the cause of the drifts seen in Figure 4b. Second, however severe these instabilities may appear, they have not hindered the very successful use of this instrument in numerous isotope-ratio-monitoring GCMS analyses (e.g., refs 10 and 11).

Table 1. Precision of Isotopic Measurements vs Frequency of Introduction of Standards

MS[a]	flow rate (mL of He/min)	t,[b] h	n[c]	representative max drift rate, ‰/min	σ_δ-(snl)[d] ‰	σ_δ-(obsd)[e] ‰	max time between standardizations, h: $\sigma_{obs} \leq 3\sigma_{snl}$	max time between standardizations, h: $\sigma_\delta \leq 0.1$‰
1	0	4.5	56	0.00050	0.011	0.017	>4.5	>4.5
1	0.2	9.0	112	±0.0045	0.011	0.021	1.5	>2.3
2	0	7.0	123	±0.085	0.026	0.29	0.3	
2	0.5	5.5	86	±0.015	0.027	0.090	1–1.5	0.3–0.5

[a] Mass spectrometer: (1) 10-kV MAT 252; (2) 3-kV Delta-S. [b] Total time represented by all observations of stability. [c] Number of discrete measurements of δ represented by all observations of stability. [d] Standard deviation that would be observed if system operated at shot–noise limit (eq 16). [e] Standard deviation observed for measurements of δ calibrated as described by Ricci et al.[16] Since this procedure recognizes and applies corrections for drift, this value reflects the scatter of points around the trends shown in Figures 5 and 6.

Drift characteristics and the observations on which they are based on summarized in Table 1. The significance of the tabulated "representative maximum drift rates" can be inferred by comparing the data shown in Figures 4 and 5 with the numerical entries in Table 1; the tabulated drift rates provide a quantitative indication of the differences between the instruments and operating conditions noted. The practical effects of these instabilities depend on the nature of the drifts (e.g., if drifts were perfectly linear, their effects could be neutralized by use of only two standards, one at the beginning of an analytical run and one at the end). The columns headed "maximum time between standardizations" are based on long-term experience. For example, the accuracy of applied

Table 2. Sensitivity and Precision of Isotope-Ratio-Monitoring Analyses

MS[a]	flow rate (mL of He/min)	sample [CO_2] (nmol)	peak[b]	signal (V·s)	1/E^c (molecule/ion)	σ_δ (‰)	n^a	std signal (V·s)	σ_δ-(snl)[d] (‰)
1	0	1.8	SW, 9	19	2800	0.025	5	19	0.022
1	0	4.7	SW, 11	46	2900	0.017	5	46	0.014
1	0.2	2.0	SW, 10	20	2900	0.016	5	20	0.021
1	0.2	4.0	SW, 10	40	2800	0.016	5	40	0.015
1	0.2	0.060	G, 14	2.2	790	0.061	5	48	0.046
1	0.2	0.17	G, 22	6.9	710	0.047	4	25	0.029
1	0.2	0.29	G, 31	14	610	0.042	5	40	0.021
1	0.4	0.29	G, 20	3.6	2300	0.082	4	42	0.037
2	0	8.6	SW, 15	13	19000	0.28	6	13	0.018
2	0.5	8.6	SW, 15	11	24000	0.058	6	11	0.019
2	0.5	0.2	G, 12	0.5	12000	0.16	4	23	0.095
2	0.5	1.0	G, 17	2.1	14000	0.079	4	15	0.049
2	0.5	5.0	G, 23	9.5	15000	0.039	4	16	0.027
2	0.5	10	G, 29	21	14000	0.031	4	16	0.022
2	0.5	35	G, 42	40	25000	0.013	3	18	0.019

[a] As in Table 1. [b] SW, square wave; G, Gaussian; width in seconds. [c] Calculated using eq 3. [d] Calculated using eq 17.

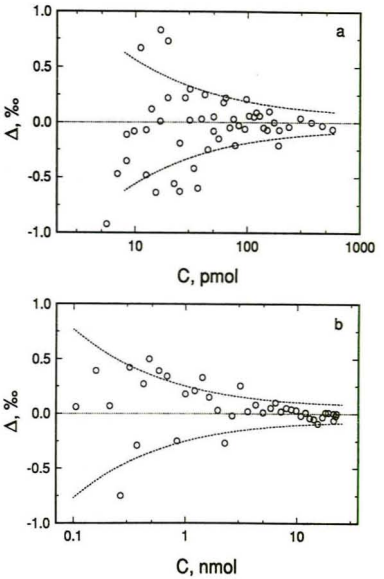

Figure 6. Results of repeated analyses of samples of varying size prepared by exponential dilution. For a system displaying a complete absence of systematic errors related to sample size, points would scatter around the zero lines within boundaries like those indicated. Here, in both graphs, the envelopes have been placed at $\pm 5\sigma$ (shot-noise limits calculated using eq 17). For performance *at* the shot-noise limit, 99% of points would lie within $\pm 2.5\sigma$. (a) 10-kV instrument, $^{44}A_{standard}$ = 25 V·s. The observation that the $\pm 5\sigma$ envelope encloses results for samples larger than 50 pmol indicates that the system operated within a factor of 2 of theoretical maximum performance in that sample range. (b) 3-kV instrument, $^{44}A_{standard}$ = 23 V·s. Note differing horizontal axes.

measurements has routinely been monitored by repeated analyses of mixtures containing a homologous series of *n*-alkanes with known isotopic compositions. Only three or four isotopic standards have been employed in chromatographic runs covering approximately 100 min, yet root-mean-square errors in δ values assigned to the *n*-alkanes have seldom exceeded 0.2‰ and are commonly as low as 0.05–0.10‰.

Sensitivity and Precision. When standards are introduced frequently enough to neutralize effects of drift, the performance of this technique will be limited by instrument sensitivity and sample size. Results of trial analyses are summarized in Table 2, in which efficiencies of ionization and transmission are listed and observed standard deviations are compared to shot-noise limits. For the 3-kV system, approximately 15 000 molecules were required for each molecular ion collected under irm conditions. For Gaussian peaks containing from 200 to 35 000 pmol of CO_2, the observed standard deviation exceeded the shot-noise limit by a factor of 1.7 or less. For the 10-kV instrument under irm conditions, optimal tuning yielded sensitivity 20× higher than that observed with the 3-kV system. The observed efficiency of ionization and transmission is equal to that specified by the manufacturer for operation of the instrument under high-vacuum conditions. If the same tuning was used in the absence of carrier gas, efficiency decreased 4-fold. The observed precision under irm conditions fell short of the shot-noise limit by an average factor of 1.8. The failure of both instruments to achieve theoretical maximum levels of performance must indicate that not all noise sources have been eliminated, but the closeness of the approach to theoretical maxima is notable. For the 10-kV instrument, the observed standard deviation was still well below 0.1‰ even for samples as small as 60 pmol of CO_2.

Dynamic Range. Samples with widely varying sizes were prepared using the exponential dilution system described in the Experimental Section. Standards isotopically identical to the samples were admitted at 20-min intervals using the variable-volume inlets of the mass spectrometers. Any deviation of observed values of δ from 0‰ represents effects of noise or systematic error. Results are graphically summarized in parts a (10-kV instrument) and b (3-kV instrument) of Figure 6.

For the 10-kV instrument, there is no evidence for any systematic trend to positive or negative deviations at high or low sample sizes and thus, no evidence for any consequential nonlinearity in overall performance. For samples larger than 50 pmol of CO_2, virtually all observations fall within the indicated $\pm 5\sigma$ envelope (where σ is the shot-noise limit calculated by use of eq 17). Since 99% of all observations would be expected to fall within $\pm 2.5\sigma$ if shot noise were the *only* noise source, these observations are consistent with those above, demonstrating that actual performance of the system falls short of the theoretical maximum by roughly a factor of 2 in the sample range indicated. For smaller samples, decreased precision is observed, possibly because the handling and processing of such small quantities of gas is itself a significant noise source.

For the 3-kV instrument (Figure 6b, note change in range of sample size axis), values of δ tend slightly to drift to positive values at small sample sizes. Expressed in terms of the mass-44 signal maximum, this nonlinearity amounts to 0.03–0.04‰/V. Relative to the shot-noise limits, the precision indicated by the data in Figure 6b, in which the envelope is placed at

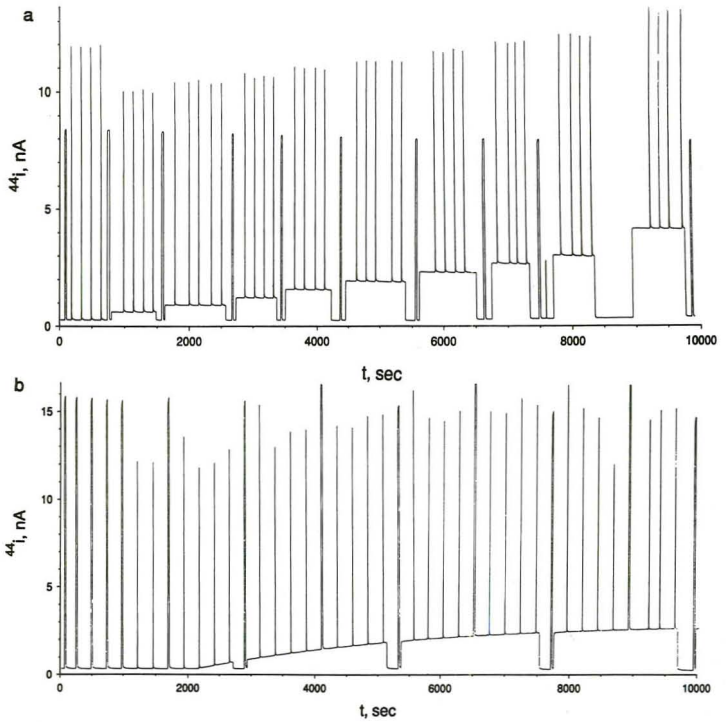

Figure 7. Representative ion current recordings (m/z 44) for sample peaks introduced to the 10-kV instrument together with varying amounts of "background" CO_2. In (a) peaks of CO_2 admitted using the 1-μL sampling valve were superposed on constant levels of background CO_2 admitted from the variable-volume inlet of the mass spectrometer. At intervals, the flow of "background" CO_2 was interrupted and a wider peak of standard CO_2 was admitted from the alternate reservoir of the variable-volume inlet (see Figure 1). In (b) the exponential dilution flask, initially filled with pure He, was placed in the carrier gas supply line for the chromatographic column and then purged with 284 ppm CO_2 in He. As a result, the concentration of CO_2 in the carrier gas asymptotically approached 284 ppm, a trend that roughly duplicated the rise in CO_2 levels associated with increasing column bleed rates. Peaks of CO_2 were again injected by use of the sampling valve, and the flow from the open split was diverted intermittently to allow introduction of standards against zero background.

$\pm 5\sigma$, is marginally lower than that obtained in the experiments summarized in Table 2.

A useful summary can be cast in terms of sample sizes required to obtain standard deviations of 0.1 and 0.5‰, assuming that both instruments fall short of theoretical maximum performance by a factor of approximately 2. For the 10-kV instrument, with a 60 V·s standard and $E = 1/700$ ions per molecule, 45 pmol of CO_2 will be required to obtain $\sigma_\delta = 0.1$‰. For the 3-kV system, with a 45 V·s standard and $E = 1/14\,000$ ions per molecule, the sample requirements for standard deviations of 0.1 and 0.5‰ would be 900 and 35 pmol of CO_2, respectively.

Evaluation of Procedures for Background Correction. Particularly in gas chromatographic applications of isotope-ratio-monitoring techniques, where peaks of CO_2 derived from the combustion of chromatographically separated substances are likely to be superposed on substantial fluxes of CO_2 derived from the combustion of column bleed, corrections for contributions from background ion currents are critical if accurate results are to be obtained. Moreover, any imprecision in the background corrections will propagate and increase uncertainties in calculated values of δ. To test the procedures employed here, experiments have been performed in which additional, "background" CO_2 was deliberately added to the gas stream carrying the sample. The accuracy of the results and effects on precision were then examined.

Ion current traces representative of data collected using the 10-kV instrument are shown in Figure 7. In the first experiment, sample peaks had Gaussian profiles and background levels of CO_2 were increased incrementally (Figure 7a). Corresponding deviations of observed δ values from correct results are summarized graphically in Figure 8a, which includes data not only from the run shown in Figure 7a but also from additional runs in which sample size and the isotopic difference between "sample" and "background" CO_2 were varied. In neither of these cases or in similar experiments in which an exponential dilution system was used to produce a smoothly rising background (Figures 7b and 8b) was any evidence observed indicating the presence of systematic errors related to the background corrections.

During two tests of background corrections using the 3-kV instrument, sample CO_2 was introduced in the carrier gas stream (Gaussian profiles). Ion current traces were similar to those shown in Figure 7b. As shown by data in Figure 8c,

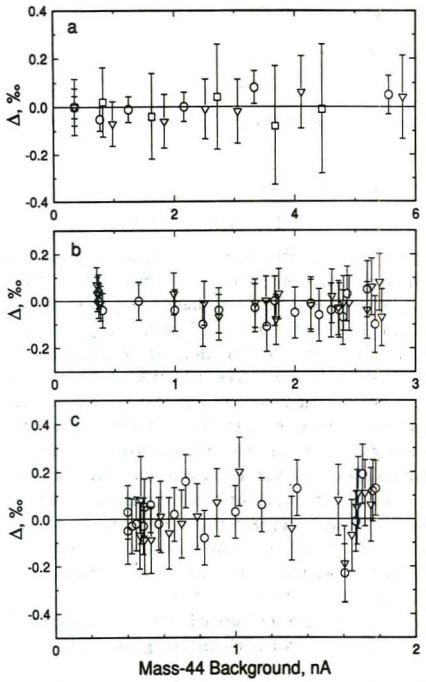

Figure 8. (a) Summary of isotopic results obtained in experiments like those depicted in Figure 7a. For each peak, the difference between the observed and expected δ value is plotted as a function of background signal level. Error bars are $\pm 2\sigma$ (shot-noise limit) as calculated using eq 27. Lengths of error bars vary because quantities of CO_2 (both sample and standard) varied. In addition, isotopic differences between sample and "background" CO_2 varied. The open circles represent 13.8 V·s samples (290 pmol) depleted in ^{13}C by 34‰ relative to the background; standards, 40 V·s. The open triangles represent 4.8 V·s samples (120 pmol) with an isotopic composition equal to that of the background; standards, 31 V·s. The open squares represent 2.2 V·s samples (60 pmol) enriched in ^{13}C by 19‰ relative to the background; standards, 48 V·s. (b) Results of experiments like that shown in Figure 7b. Error bars, $\pm 2\sigma$. Both series of points represent 5.0 V·s samples (120 pmol). Open circles: CO_2 enriched in ^{13}C by 19‰ relative to the background; standards 52 V·s. Open triangles: CO_2 depleted in ^{13}C by 16‰ relative to the background; standards 38 V·s. (c) Results of background-corrected analyses of standard *n*-alkanes combusted on line,[9] with the resulting CO_2 being led to the ion source of the 3-kV instrument. In this case, the error bars have been lengthened to $\pm 4\sigma$ in order to regularly intercept the $\Delta = 0$ line, indicating that the process of combustion is itself a significant source of noise. Open circles: 7–24 V·s samples (4–12 nmol of CO_2); standards, 11.6 V·s. Open triangles: 4–16 V·s samples (2–8 nmol of CO_2); standards, 9.9 V·s. Samples were depleted in ^{13}C by 0–10‰ relative to the background.

there is no significant change in δ values as a function of the magnitude or isotopic composition of background CO_2 relative to the sample.

Effects on Precision. Table 3 summarizes results of trials in which 60- and 170-pmol samples were repeatedly analyzed in the presence of varying backgrounds. The 10-kV system was used, and a small sample size was chosen to allow sample/background ratios to reach low levels representative of the worst cases encountered in applied analyses. To further duplicate conditions encountered in practical work, times devoted to observation of background levels were minimized, being held to 1 s, maximum, or as little as 250 ms. The latter

Table 3. Effect of Background Correction on Precision

sample pmol of CO_2	bkgd[a] (V)	t_b[b] (s)	n	sample background area	sample background ampl[c]	Δ[d] (‰)	σ_δ (‰) obsd	σ_δ (‰) eq 27
60	0.096	1.0	4	4.2	11	0.02	0.089	0.049
60	0.096	0.25	4	4.2	11	0.14	0.098	0.049
60	0.214	1.0	5	1.9	4.9	0.00	0.061	0.054
60	0.331	1.0	4	1.1	3.2	–0.07	0.078	0.059
60	0.480	1.0	4	0.76	2.2	0.00	0.11	0.064
60	0.480	0.25	4	0.76	2.2	–0.01	0.13	0.068
60	0.697	1.0	4	0.49	1.5	–0.01	0.13	0.070
60	0.878	1.0	4	0.39	1.2	0.07	0.16	0.076
60	1.119	1.0	3	0.28	0.9	0.00	0.20	0.082
60	1.119	0.25	3	0.28	0.9	0.02	0.22	0.095
170	0.099	1.0	4	4.6	29	0.02	0.047	0.028
170	0.202	1.0	3	2.2	14	–0.01	0.11	0.031
170	0.291	1.0	5	1.6	9.8	0.03	0.073	0.033
170	0.387	1.0	4	1.2	7.4	0.00	0.052	0.034
170	0.489	1.0	4	0.93	5.8	0.02	0.10	0.036
170	0.595	1.0	5	0.76	4.8	0.00	0.086	0.038
170	0.712	1.0	4	0.64	4.0	0.01	0.10	0.040
170	0.815	1.0	4	0.56	3.5	0.04	0.16	0.042
170	0.906	1.0	4	0.50	3.1	0.00	0.17	0.044
170	1.238	1.0	3	0.37	2.3	0.21	0.15	0.048

[a] Background signal measured at m/z 44 (V). [b] Interval of time for measurement of background signals. [c] Ampl, amplitude corresponding to peak maximum for m/z 44 peak trace. [d] $\Delta = \delta_{obsd} - \delta_{true}$.

condition corresponds to situations in which background levels are based on a single integration interval. This minimizes the precision of background measurement and thus maximizes chances for propagation of random errors. It might, however, still provide the best estimate of background levels when observations on either side of a minimum point clearly trend to higher values and thus indicate the presence of nonbackground components.

The first entry in Table 3 represents observations made with *no* background CO_2 added to the sample stream. The "background signal" is, nevertheless, correctly represented as 96 mV, this nonzero level representing the offset current described in the Experimental Section. If the presence of this offset is ignored and the shot-noise limit for analysis of the 60-pmol sample in the absence of any background computed (eq 17), the result is $\sigma_\delta = 0.046$‰. As shown in Table 3, the observed standard deviation was—as expected based on the results summarized in the preceding section—about 2-fold worse, 0.089 or 0.098‰, depending on the time spent observing the background. Subsequent entries in the table show, remarkably, that, as background levels were increased so that sample/background ratios dropped as low at 0.28, observed standard deviations increased by only a factor of about 2. Two questions arise: (i) Is noise associated with the correction for the offset currents responsible for the failure to achieve maximum performance? (ii) Can the relationship between precision and background levels be adequately modeled?

When an ion current comprised of sample and background components is integrated so that a total number of ions, N_Σ, is observed, we can write

$$N_\Sigma = N + N_b \tag{18}$$

where N represents the sample-derived component and N_b represents the sum of all background components (nonsample CO_2, ion currents from other residual gases in the ion source, and pseudo ion currents such as the electronic offsets applied

to the summing points of the electrometers). The arithmetic of the required correction is trivial, $N = N_\Sigma - N_b$, but consideration of the propagation of errors is not. *If* variations in N_Σ and N_b were independent, it would be correct to take a conventional approach, writing

$$\sigma_N^2 = (\sigma N/\partial N_\Sigma)^2 \sigma_{N\Sigma}^2 + (\partial N/\partial N_b)^2 \sigma_{Nb}^2 \quad (19)$$

where $\sigma_{N\Sigma}$ and σ_{Nb} represent, respectively, the standard deviations of N_Σ and N_b. However, N_Σ and N_b are strongly covariant. N_b contributes directly to N_Σ, and any increase in N_b tends very strongly to produce an increase in N_Σ.

We have therefore approached this problem in terms of the analysis of variance, starting from the expression

$$\sigma_{N\Sigma}^2 = \sigma_N^2 + \sigma_{Nb}^2 \quad (20)$$

At the shot-noise limit, each of these variances is equal to its related variable, thus $\sigma_{N\Sigma}^2 = N_\Sigma$, $\sigma_N^2 = N$, and $\sigma_{Nb}^2 = N_b$. Equation 20 is thus equivalent to eq 18 and it might be concluded that application of the background correction imposes *no* penalty on the precision with which N can be measured. Indeed, this would be true *if* the measurement of the background were based on observation of N_b ions, that is, a number of background ions equal to the number underlying the sample-derived signal. For a sample-related peak with width, w (i.e., some period of time), this would require that the background be observed in a sample-free interval *also* having width w. In practice, however (see Experimental Section), the estimate of N_b is usually based on observation of the background during a small time interval immediately preceding the peak, and it is advantageous to minimize that interval in order to allow more time for observation of sample-related signals. Moreover, in a typical chromatogram, it can be difficult to *find* sample-free intervals, and minimization of the time required for observation of background signals is desirable for that reason. If the background level is observed for some time interval t_b, we can write

$$N_b = n_b w/t_b \quad (21)$$

where n_b is the number of ions collected in the interval t_b. The corrected signal level is then given by

$$N = N_\Sigma - n_b w/t_b \quad (22)$$

and we recognize that, even though the total variance in the integrated signal must still be given by N_Σ, the variance associated with the background correction is less than N_b by a factor t_b/w. By difference, the variance associated with the corrected signal level is thus

$$\sigma_N^2 = \sigma_{N\Sigma}^2 - \sigma nb^2 = N + (1 - t_b/w)N_b \quad (23)$$

where the additional term, $(1 - t_b/w)N_b$, represents the contribution of the background correction to the uncertainty in N.

Resultant uncertainties in R can be derived from an expression analogous to eq 10:

$$(\sigma_R/R)^2 = (\sigma_{45N}/{}^{45}N)^2 + (\sigma_{44N}/{}^{44}N)^2 \quad (24)$$

Rearranging eq 23 in terms of measured quantities, we can write

$$N + (1 - t_b/w)N_b = N + N_b - n_b = N_\Sigma - N_b \quad (25)$$

From which it follows that

$$(\sigma_R/R)^2 = ({}^{45}N_\Sigma - {}^{45}n_b)/({}^{45}N_\Sigma - {}^{45}n_b w/t_b)^2 + ({}^{44}N_\Sigma - {}^{44}n_b)/({}^{44}N_\Sigma - {}^{44}n_b w/t_b)^2 \quad (26)$$

For cases in which ${}^{45}n_b/{}^{44}n_b \approx {}^{45}N/{}^{44}N$, an equation analogous to eq 17 is then

$$\sigma_\delta^2 = 0.00446\{[(A_\Sigma - a_b)/(A_\Sigma - wa_b/t_b)^2]_{sample} + [(A_\Sigma - a_b)/(A_\Sigma - wa_b/t_b)^2]_{standard}\} \quad (27)$$

where A_Σ and a_b are the integrated total and background (i.e., during t_b) signals (V·s) for mass 44. Unlike errors predicted by eq 19, which would increase dramatically as A_Σ/a_b ratios declined, those predicted by eq 27 increase only moderately. Specifically, for the cases listed in Table 3, expected standard deviations double, from 0.049 to 0.095‰. In answer to the first question posed above, we find that, when background signals are minimal, expected levels of performance do not differ significantly from those predicted by eq 17. Correction for offset currents is thus not the noise source responsible for the 2-fold degradation of performance relative to theoretical maxima. Second, it appears that the error model developed here does correctly represent the effects of background correction on precision. The increases in *observed* standard deviations are proportional to those predicted by eq 27, indicating that the model correctly predicts the degradation associated with decreased signal/background ratios.

CONCLUSION

In spite of the contrast with operating conditions used in conventional isotopic analyses, isotope-ratio-monitoring techniques are capable of providing high performance. For many applications, the advantages of speed and the ability to deal with samples $10^5\times$ smaller than those required by conventional techniques will be crucial. To a great degree, isotope-ratio monitoring combines the speed and convenience of GC/MS or flow injection analysis with the accuracy and precision of conventional isotope-ratio mass spectrometery.

Key factors in performance identified and investigated here include characteristics of the signal pathway, which should minimize the appearance of artifactual features in recorded ion currents and, in particular, ion current ratios; the stability of instrumental performance, in which characteristics of mass discrimination in the ion source, analyzer, and collector system should change slowly enough that observations of standards can be infrequent; and sensitivity, since the efficiency with which ions are produced, transmitted, and collected determines the precision attainable. Here, two instruments were compared. That with the higher accelerating potential and greater efficiency was superior in all respects, but results obtained using the less sensitive instrument would be fully satisfactory for many applications.

The treatment of propagation of errors associated with background-corrected signals developed here is, to our knowledge, novel. The correspondence between actual and predicted results is excellent and attests to the validity of the approach taken. Since integration of background-corrected signals is a common feature of many modern techniques, this discussion may be of broad interest. An analyst seeking to

apply a background correction often confronts a choice between making a brief observation of background signals during a rare, sample-free interval or making a more extensive background measurement that might be corrupted by intrusion of some sample-related signals. Because it avoids any nonbackground signals but is brief, the first option is more accurate but less precise than the second. Observations reported here show clearly that the cost in precision is small and that the first option should thus commonly be preferred.

ACKNOWLEDGMENT

We are indebted to Katherine H. Freeman, Margaret P. Ricci, and Stephen A. Studley for valuable discussions and technical assistance. We thank W. Brand and K. Habfast of Finnigan MAT for their continuing interest and scientific collaboration. We also thank Finnigan MAT for making available the MAT 252 and Chevron Petroleum Technology Co. and MAT for supporting purchase of the Delta S and development of irmGC/MS. Partial support of personnel costs associated with this work has come from NASA (NAGW-1940) and from a GE Fellowship awarded to D.A.M.

Received for review December 8, 1993. Accepted April 22, 1994.[⊗]

[⊗] Abstract published in *Advance ACS Abstracts,* June 1, 1994.

Anal. Chem. **1994,** *66,* 2348–2355

Electrospray Ionization Ion Mobility Spectrometry

Doug Wittmer
Millipore Corporation, Waters Chromatography Division, 34 Maple Street, Milford, Massachusetts 01757

Yong Hong Chen, Brian K. Luckenbill, and Herbert H. Hill, Jr.*
Department of Chemistry, Washington State University, Pullman, Washington 99164–4630

An improved electrospray ionization source for ion mobility spectrometry was developed by making three salient modifications to the electrospray needle. First, the needle was removed from the ion drift region, reducing neutralization of charged drops and ions on the walls of the ion mobility drift tube. Second, the tip of the spray needle was electrically insulated, extending the voltage range with which a stable electrospray could be achieved. Third, the needle was cooled, eliminating problems associated with solvent volatilization in the spray needle. Ion mobility spectra of cytochrome *c* and Triton X-100 were compared with those obtained by electrospray ionization mass spectrometry. While direct mass/charge comparison with ion mobility was not possible, similar electrospray ion patterns between the IMS and MS data suggest that the electrospray ionization source for IMS behaved in a manner consistent with that of other electrospray ionization sources. In addition, mass assignments of IMS ion peaks, made by matching patterns from mass spectra, fit well with those expected from IMS theory.

The inherent high resolution of capillary electrophoresis (CE) and microbore liquid chromatography (MLC) along with ease of sample preparation has made high-performance liquid-phase separation (HPLPS) the method of choice for many analytical applications. For the most part, however, detection of samples in the liquid phase has been limited to those analytes which absorb or fluoresce in the UV and visible regions of the spectrum. For compounds which absorb poorly, additional sample cleanup or derivatization procedures are required. Thus, development of a simple and dependable detection method for non-UV-absorbing compounds in solution would significantly expand the analytical applications for HPLPS.

In gas chromatography, ionization methods have provided a basis for universal detection. Most of these methods, however, rely on the selective ionization of analytes in the presence of the mobile phase and, with the exception of mass spectrometry, have not been successfully interfaced to HPLPS methods because of solvent interferences. Ion mobility spectrometry (IMS) is a technique for detecting ions in the gas phase which are separated on the basis of differences in cross sectional area. Since most analytes in HPLPS give rise to ions of larger cross section than those of the solvent, IMS would seem a logical choice as an alternative detection method. Furthermore, the feasibility of IMS-based detection for HPLPS has already been demonstrated[1] using an electrospray nebulizer as an ionization source.

Electrospray ionization ion mobility spectrometry (ESI-IMS) was first described in 1972 by Gieniec et al.,[2] who modified a Plasma Chromatograph manufactured by Franklin GNO Corp. (West Palm Beach, FL). In their design, the normal sample entrance and the ^{63}Ni ion source were removed from the commercial instrument and replaced with an electrospray chamber. Liquid samples were introduced into the enclosed glass spray chamber by a syringe pump via a Teflon tube connected to a 27-gauge hypodermic needle. The spray chamber was separated from the ion drift tube by a brass plate containing a large orifice for the bath gas and ions to enter the drift region. Electrospray was developed by applying a potential between the needle tip and the brass plate. The bath gas was introduced into the spray chamber at the rear of the needle. According to the authors, this heated gas flow served to help evaporate the droplets and to sweep the ions downstream through the orifice in the brass plate. Unfortunately, all of the solvent was swept toward the ion drift region and apparently contaminated this region, decreasing both sensitivity and resolution in the spectrometer.

Smith and co-workers have reported the ESI-IMS spectra for cytochrome *c*[3] and lysozyme.[4] These spectra, obtained at low temperatures (25–90 °C), were similar in resolution, shape, and drift time to those first reported by Gieniec et al.[2] The peaks drifted at relatively long drift times (>50 ms), and only one broad peak (peak width at half-height of about 25 ms) was observed for each compound. An obvious concern with respect to these spectra was presented by Fernandez de la Mora.[5] "... ESI mass spectrum (of cytochrome *c*) generally contains between 15 and 20 charges. Should not then the mobility spectrum contain also six peaks at least for cytochrome *c*?"

Improvement in both sensitivity and resolution was reported by Shumate and Hill by incorporating an electrospray needle directly into a unidirectional flow ion mobility spectrometer.[6] While this design worked well for low molecular weight compounds, high molecular weight, nonvolatile compounds were not detected. In addition, enclosure of the needle in the stainless steel drift tube made it difficult to achieve electrospray conditions, and the most stable operation of the detector

(1) Hill, H. H., Jr.; Siems, W. F.; St. Louis, R. H.; McMinn, D. G. *Anal. Chem.* **1990**, *21*(5), A362.
(2) Gieniec, J.; Cox, H. L., Jr.; Teer, D.; Dole, M. *Abstracts, 20th Annual Conference on MS and Allied Topics*, Dallas, TX, 1972, 276.
(3) Smith, R. D.; Loo, J. A.; Loo, R. R. O.; Busman, M.; Udseth, H. R. *Mass Spectrom. Rev.* **1991**, *10*, 359–451.
(4) Smith, R. D.; Loo, J. A.; Loo, R. R. O.; Udseth, H. R. *Mass Spectrom. Rev.* **1992**, *11*, 434–443.
(5) Fernandaz de la Mora, J. *Mass Spectrom. Rev.* **1992**, *11*, 431–434.
(6) Shumate, C. B.; Hill, H. H., Jr. *Anal. Chem.* **1989**, *61*(6), 601.

0003-2700/94/0366-2348$04.50/0
© 1994 American Chemical Society

occurred when a corona discharge was visible at the tip of the spray needle. Nevertheless, with this "coronaspray" ionization ion mobility spectrometer (CSI-IMS), a wide variety of compounds could be detected from solution with good sensitivity. Subsequently, potential applications of IMS as a detector for liquid chromatography,[7] as a detector for capillary electrophoretic methods,[8] and as an on-line liquid-stream process sensor were reported.[9]

Although initial investigations of the IMS as a detection method for liquid samples were encouraging, lack of response for high molecular weight compounds indicated that the spray source was not behaving in a manner analogous to that observed when electrospray sources were used with mass spectrometry.

Our experience, coupled with that reported by others, led us to further investigations of ESI-IMS for the purpose of identifying the cause of these differences between data observed with ESI-IMS and those expected from ESI-MS. The overall objective was to design an IMS with predictable response characteristics and which could be used for detection after HPLPS.

EXPERIMENTAL SECTION

Two ion mobility spectrometers were used in these investigations: The first was identified as a coronaspray ion mobility spectrometer (CSI-IMS) since it was primarily operated in that mode. The second was identified as the electrospray ionization ion mobility spectrometer (ESI-IMS) and was the design developed as a result of information gained from experiments with the CSI-IMS instrument. The drift tubes of both spectrometers were based on the standard stacked ring configuration used by a variety of commercial instruments. A series of stainless steel rings alternating with a series of insulator rings were assembled to produce the atmospheric pressure ion drift tube. The insulating rings served to isolate the stainless steel rings from one another while the stainless steel rings, called guard rings, were connected by a series of matched megaohm resistors. Applying a high voltage to the first ring of the tube generated a uniform electric field in the center of the tube, directing the coronasprayed or electrosprayed ions down the tube to a terminal Faraday plate where current was collected and measured.

The CSI-IMS. This spectrometer was designed by Shumate[10] and constructed under consignment by ScienTech, Inc. (Pullman, WA). A schematic diagram of the spectrometer is shown in Figure 1. Guard rings in this design had an internal diameter of 2.5 cm and were 0.8 cm in width. Teflon insulators, fitted around each ring, served to isolate the guard rings from the aluminum housing as well as from each other. The oven was constructed from a 10 in. long temperature-controlled aluminum cylinder. Figure 1a provides a view of the entire drift tube assembly which was located inside the aluminum oven, and Figure 1b shows a cut-away schematic of the

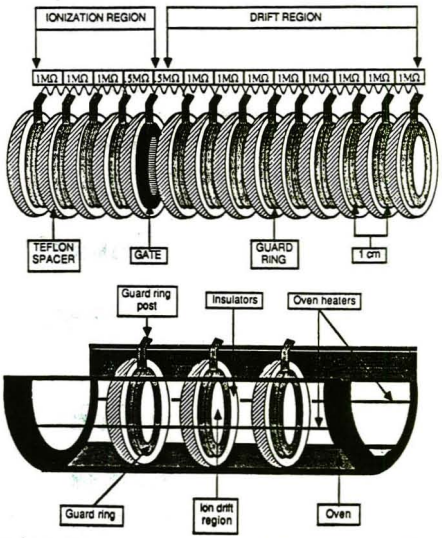

Figure 1. Cut-away design of the ion mobility spectrometer showing the guard ring and ion gate assembly (a, top) and the aluminum housing which served as the IMS oven (b, bottom).

aluminum oven with only three guard rings. In operation, all of the guard rings shown in Figure 1a were inserted into the aluminum oven.

Electronic components of the spectrometer included an IMS controller, a current amplifier, a data acquisition/control system, an interface box, and a temperature controller. The IMS controller was a custom-built device containing electrospray high-voltage supplies (Model 02–150P, Bertan Associates, Inc., Hicksville, NY), drift field high-voltage supplies, and a "gate driver". The electrospray high-voltage supply provided both positive and negative voltage which could be varied up to 15 000 V. The drift field supply provided positive and negative voltages which were variable up to 5000 V.

The coronaspray needle was modified from the design given in refs 6 and 7 and is shown in Figure 2. It consisted of a 316 stainless steel union with ferrules and compression screws (Waters Division of Millipore, Milford, MA). A commercially available 25-gauge polished needle (P/N 80726, Hamilton, Reno, NV) was cut to a length of approximately 1.3 in. The cut end of the needle was inserted into a Teflon sleeve ($^1/_{16}$ in. o.d. 0.006 in. i.d.) and pushed through a loosened compression screw and ferrule in the steel union. The compression screw was tightened and the entire assembly inserted into a Teflon housing which was clamped to a ring stand. The polished needle tip protruded 0.05 in. inside the first of two stainless steel drift tube rings. The spray assembly was fed by a prototype dual syringe micropump via a 3-ft length of PEEK tubing ($^1/_{16}$ in. o.d., 0.006 in. i.d.).

For solvent spray experiments, the first guard ring was biased at +250 V and the second guard ring was at ground as shown in Figure 2a. Solvents evaluated were water, methanol, acetonitrile, tetrahydrofuran, isopropyl alcohol, ethyl acetate, methylene chloride, toluene, hexane, and isooc-

(7) McMinn, D. G.; Kinzer, J. A.; Shumate, C. B.; Siems, W. F.; Hill, H. H., Jr. *J. Microcolumn Sep.* **1990**, *2*, 188–192.
(8) Hallen, R. W.; Shumate, C. B.; Siems, W. F.; Tsuda, T.; Hill, H. H., Jr. *J. Chromatogr.* **1989**, *480*, 233–245.
(9) Shumate, C. B.; Hill, H. H., Jr. *Electrospray Ion Mobility Spectrometry—Its Potential as a Liquid-Stream Process Sensor* In Pollution Prevention in Industrial Processes—The Role of Process Analytical Chemistry; Breen, J. J., Dellarco, M. J., Eds.; American Chemical Society: Washington, DC, 1992.
(10) Shumate, C. B. An Electrospray Nebulization/Ionization Interface for Liquid Introduction into an Ion Mobility Spectrometer. Ph.D. Thesis, Washington State University, 1989.

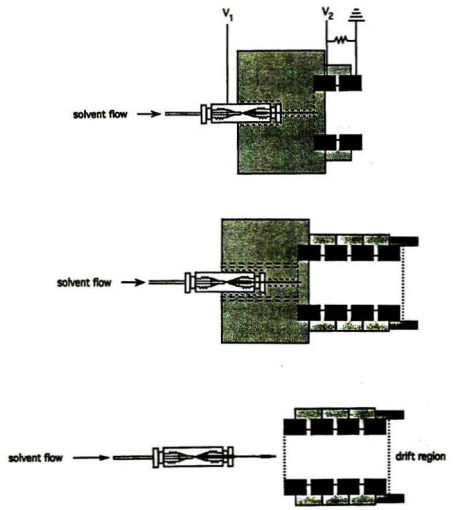

Figure 2. Schematic diagrams of spray ionization sources. (a, top) Design used in solvent spray experiments. Needle: 25-gauge polished SS, noninsulated. Solvent flow rate: 10 μL/min. Voltages: 5–6 kV on needle; 250 V on first guard ring; second guard ring at ground. Temperature: ambient. (b, middle) Design used in coronaspray experiments. Needle: uninsulated 25-gauge polished stainless steel inserted into IMS tube. Solvent flow rate: 10 μL/min. IMS nitrogen drift gas flow rate: 800 mL/min. Voltages: 5–6 kV on needle; 2–3 kV on first drift ring, generating a drift field of 200–300 V/cm in the IMS tube. Temperature: 60–80 °C. (c, bottom) Open design of electrospray IMS. In this design the needle is located in the ambient temperature of laboratory air and outside the ion drift field. The focusing screen shown in this design served to direct the electrosprayed ions down the center of the ion drift region.

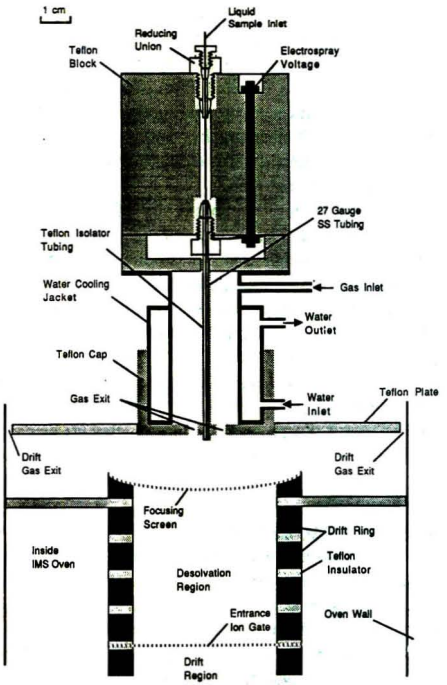

Figure 3. Closed design of the electrospray ion mobility spectrometer showing a cooled electrospray needle, insulated electrospray needle, and spray focusing screen.

tane in addition to several mixtures typical of HPLC mobile phases. In each case, flow rates were adjusted to 10 μL/min.

For coronaspray experiments, the IMS was interfaced to the Teflon spray assembly as shown in Figure 2b. The spray assembly was identical to that shown in Figure 2a to which a guard ring stack, shutter grid, and collector assembly were added to form a typical IMS drift tube as shown in Figure 1a. Four $^1/_8$-in. holes were drilled in the Teflon block which housed the needle assembly, allowing the drift gas to exit the tube. An injector (Rheodyne 7000, Rheodyne, Cotati, CA) with 20-μL loop was installed between the pump and the needle, leaving 3 ft of PEEK tubing between the needle and injector. The drift tube field strength was set at 200–300 V/cm. The drift gas was nitrogen with a flow rate of 800 mL/min. The drift tube temperature was set at 60 or 80 °C. Needle voltage was established for each set of drift tube conditions by the following procedure: The IMS was turned on, and spectral scans were monitored with no solvent flow to the needle. Needle voltage was initially set to equal that of the first guard ring and was successively increased until reactant ion spectra were observed, indicating a corona discharge at the needle tip.[6] Solvent flow rate was then set at 8 μL/min, and samples were injected. The solvent used for this study was 50% methanol/water.

With the same drift tube described above, the coronaspray source was modified as shown in Figure 2c to produce a stable electrospray. The needle assembly described above was removed from the Teflon housing and directly attached to a ring stand with an insulated clamp. A grid consisting of nickel mesh was fused to the first guard ring of the drift tube to direct ionizd spray into the tube. Finally, a double-layer Teflon sleeve, fabricated from shrink-tubing, was slipped onto the needle tip. In operation, the insulated tip was placed outside of the drift tube, $^1/_8$–$^1/_4$ in. from the focusing grid. Conditions for experiments, unless otherwise specified, were as follows: drift mode, positive; drift gas, nitrogen at 800 mL/min; pressure, barometric; desolvation region, 4 cm; drift region, 10 cm; field strength, 310 V/cm; drift temperature, 167 °C; pulse width, 0.5 ms; gain, 10^9 V/amp; scan time, 50 ms; scans averaged, 50 or 100.

The ESI-IMS. A schematic diagram of this instrument is shown in Figure 3. As with the IMS described previously, the ion drift tube was constructed from stacked stainless steel rings, separated by Teflon insulators, and electrically connected by a series of megaohm resistors. This configuration provided a uniform electric field inside the drift region. The inside diameter of the tube was 4.22 cm, and the outside diameter was 5.71 cm. All of the characteristics required for stable electrospray described for the previous design were incorporated into the closed design. First, the spray needle was removed from the drift tube of the spectrometer, minimizing the electrical field strength between the needle and the drift tube wall. Second, a focusing screen was added to the first guard ring of the drift tube, directing the sprayed ions into the desolvation region of the ion drift tube. And third, the

27-gauge SS spray needle was insulated with 0.4 mm i.d. Teflon tubing with a wall thickness of 0.2 mm.

The salient difference between this design and the one described above was that the spray needle was completely enclosed in the spectrometer, eliminating contamination from laboratory air and stabilizing the temperature inside the drift tube. As a result of enclosing the needle in the spectrometer, the spray needle had to be externally cooled in order to avoid volatilization of the liquid stream in the needle. When the liquid stream vaporized before it reached the tip of the needle, the spectra became unstable. As shown in the figure, external cooling was applied to the needle via a water-cooled/air-cooled jacket. The entire assembly consisted of a water chamber surrounding an air chamber which housed the insulated spray needle.

The electronics of the electrospray IMS included a high-voltage supply for the spray needle, a high-voltage supply for the drift field, a temperature controller for the IMS oven, a gate driver under software control, and a current amplifier to amplify the ion signal. The spray voltage was supplied by two high-voltage supplies, one for positive and one for negative. Both were Model 602B–200P (Bertan Associates, Inc. Hicksville, NY) with a maximum potential of 20 000 V. Typically, 10 000 V was applied to the needle for generating the electrospray. The drift field potential was provided by a single 5000-V high-voltage supply (Model PMT-50 A, Bertan Assoc. Inc., Hicksville, NY). The current limit of the power supply was 0.5 mA. At the total drift tube resistance of about 16 MΩ, only about 0.31 mA was flowing through the resistor chain connecting the guard rings.

The gate driver was controlled by a CACTUS PC/XT computer (Cactus Computer Co., Moscow, ID). The computer was equipped with a Burr-Brown PCI-20000 data acquisition/control system (Burr-Brown Corp., Tucson, AZ) which included a high-performance carrier (PCI-20041C carrier with DMA capability, plugged into the I/O channel of the computer), a high-speed A/D module (PCI-20019M), a counter timer (PCI-20007M), and PCI-200021S high-speed and DMA software. The high-speed A/D module (12-bit dynamic range, 54-kHz maximum sampling rate) was used to measure 0–1 voltage of the electrometer output and convert this analog signal to a digital one. The counter–timer module of the Burr–Brown board, controlled entirely by lab-designed software, provided timing for digitization and gates.

The solvent used throughout this portion of the investigation was a mixture of water, methanol, and acetic acid in a volume ratio of 47.5/47.5/5. The liquid was pumped to the electrospray needle by a dual piston syringe pump (Microgradient System, BrownLee Labs, Applied Biosystems, Santa Clara, CA). The syringe pump provided pulseless flow at low flow rates (1–10 μL/min.). The injector (C6W, Valco Instruments Co., Houston, TX) was a six-port valve with 6-μL external injection volume. A 100 μm i.d. and 200 μm o.d. deactivated vitreous silica tubing (J&W Scientific, Folsom, CA) of aproximately 1 m in length was used as a transfer line. One end of the tubing was connected to the pump through a $^1/_{16}$–$^1/_{32}$-in. zero dead volume internal reducer (1ZR1.5T, Valco Instru. Co. Inc.). The other end of the transfer line was inserted through the 27-gauge stainless steel electrospray needle. A $^1/_{16}$–$^1/_{32}$-in. zero dead volume internal reducer (1ZR1.5T, Valco Instr. Co. Inc.) was used to hold the transfer line, so that the exit of the fused silica transfer line was recessed about 1 mm from the end of the electrospray needle.

Electrospray Ionization Mass Spectrometry. A previously characterized lab-made mass spectrometer with an electrospray interface was used to obtain mass spectra.[11] For these studies, however, there was no grid between the needle and the inlet nozzle, and the needle was maintained at a constant positive voltage rather than pulsed as was described in ref 11. Mass spectra were acquired using a Quadstar (Balzers) data system. Resulting data files were converted to ASCII format and further reduced using Microsoft Excel (Microsoft). Finished spectra were generated using Deltagraph (Deltapoint).

Computer Simulation. Computer modeling of the electric fields generated by the application of bias voltages was accomplished using the MacSimion (Montech PTY, Ltd., Clayto, Victoria, Australia) ion trajectory simulation program performed on an Apple Macintosh personal computer (Apple Computer, Cupertino, CA). Although the program was designed to calculate and display ion trajectories in a vacuum, the program module also calculated the electrical fields and displayed equipotential contours imposed by the IMS geometry. With the electric fields accurately represented, the electrostatic forces experienced by the ions were described. Ion trajectories under atmospheric conditions are orthogonal to equipotential contour lines of the electric fields.

RESULTS AND DISCUSSION

As stated in the introduction, the objective of these investigations was to identify problems associated with CSI-IMS with the final goal of constructing a stable electrospray ionization source for IMS which behaved in a manner consistent with electrospray ionization sources commonly used in mass spectrometry.

Initial experiments served to standardize hardware and operating conditions, comparing results with those achieved previously. The first experiments were performed without the drift tube in order to observe the spray and evaluate the spray of several solvents. Through the use of the configuration shown in Figure 2a, several solvents were sprayed. These experiments permitted visual inspection of the needle tip, as well as the spray plume generated under field conditions similar to that of a stacked ring IMS drift tube. For each solvent, needle voltage was successively increased until a typical plume was observed, characterized by the appearance of the "Taylor cone" at the needle tip. When voltage was increased beyond that of the Taylor cone formation, this single cone disappeared and several smaller jets could be observed. Most of the spray generated in this experimental configuration collided with one or both of the rings. At 5–6 kV, a corona electrical discharge was clearly visible at the needle tip. Solvents investigated in this study included water, methanol, acetonitrile, tetrahydrofuran, isopropyl alcohol, ethyl acetate, methylene chloride, toluene, hexane, and isooctane. Results of the test indicated that dry hexane and isooctane were not amenable to electrospray. A spray for dry toluene was

(11) Tomany, M.; Wittmer, D.; Gabeler, S.; Jarrell, A. *Design and Performance Characteristics of a Particle Beam Interface and an Electrospray Interface*: Proceedings of the 40th ASMS Conference on Mass Spectrometry and Allied Topics; Washington, DC, May 31–June 5, 1992.

Table 1. Spectral Detection Limits of CSI-IMS for Selected Compounds Using the Signal Averaging Mode

compd	class	MW	pg/μL	pmol/μL
methiocarb	pesticide	225	600	2.7
tributylamine	industrial	185	1.2	0.006
streptomycin sulfate	antibiotic	1457	1600	1.1
phenylalanine	amino acid	165	300	1.8

observed but only at voltages well into the corona regime. However, when a solvent of higher dielectric such as methanol, acetonitrile, or THF was added in a proportion of 5% (v/v) to any of these, the mixture readily electrosprayed at voltages somewhat higher (0.5–1 kV) than that required for the pure modifier. All other solvents produced electrospray within the range of 2–3 kV. Stability of the electrospray plume varied from solvent to solvent at a given voltage. It generally appeared that plume stability increased with volatility and polarity of the solvent, and decreased with viscosity. A stable spray could be obtained by adjusting the needle voltage.

Initial investigations spraying into the ion mobility spectrometer were conducted using the configuration shown in Figure 2b. In this configuration, IMS spectra for several compounds were obtained and good sensitivities observed. Examples of detection limits for several compounds are given in Table 1. With this method, detection of amines looked particularly promising. Thus a series of amines were evaluated, and all provided good IMS response although K_0 values did not match those in the literature. Other problems associated with this design were also encountered. At low temperatures, stable spectra were obtained for low molecular weight compounds. When a homologous series of organic acids successively were observed, the signal decreased drastically for hexanoic acid, and no signal was observed for heptanoic acid. A signal for heptanoic acid was observed at higher (80 °C) temperature and appeared to be the result of well-resolved clusters. At temperatures greater than 80 °C, the reactant ion peak became unstable, presumably as a result of outgassing or boiling of the solvent in the needle. Several small changes were made to the hardware, each with an increase in performance, but the problems inherent at low drift tube temperatures proved too troublesome to continue.

Results of computer-simulated studies of the CSI-IMS design are shown in Figure 4. Equipotential lines at 250-V intervals were drawn inside the drift tube. The collecting electrode, located below the aperture grid at the bottom of the figure, was at ground potential. The aperture grid served to shield the collection from inductive effects of the ion cloud as it migrated down the drift tube toward the collector. Just above the aperture grid was a relatively steep electrical gradient which focused the ions to the collecting electrode. In the main portion of the drift tube, the field gradient was found to be relatively smooth with a simulated field of 250 V/cm. Above the ion entrance gate, equipotential lines indicated that ions were directed toward the walls of the detector. This simulation, coupled with results found using the spray configuration in Figure 2a, indicated that when the needle was located inside the drift tube, sensitivity was lost due to neutralization of ions on the guard rings of the spectrometer.

In order to focus ions into the center of the ion drift region where the field was uniform and to avoid problems associated

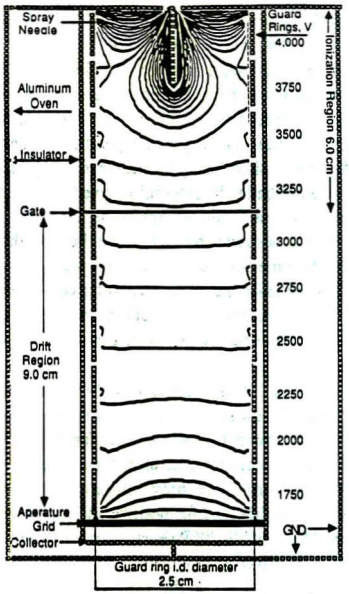

Figure 4. Computer simulation of coronaspray ion mobility spectrometer showing the contour profile of the equipotential field lines. Each equipotential field line in the figure represents a potential drop of 250 V. Note the circular nature of the equipotential lines near the spray needle. Since ions travel perpendicular to field lines, most were directed radially to guard rings instead of longitudinally to the center of the drift tube.

with heating the needle, the needle assembly was removed from the drift tube as shown in Figure 3c. A grid consisting of nickel mesh was fused to the first guard ring to direct the spray into the drift tube. With the needle removed from the drift tube, temperature of the drift gas could be increased to about 170 °C, permitting efficient desolvation of the spray drops prior to reaching the ion entrance gate. In addition, the needle remained cool, avoiding buildup of nonvolatile material at the needle tip.

Because the needle was located outside of the drift tube, the ion spray could be observed. Under these conditions a corona discharge could be seen similar to that observed in the experiments described for Figure 3a. Insulating the tip of the spray needle with Teflon tubing eliminated visual observation of the corona discharge. With the insulated needle, there was less tendency for arcing from the needle tip to the ring or grid, allowing a higher field strength to be generated at the origin of the plume, either by moving the insulated spray tip closer to the grid or by increasing needle voltage. With increasing needle voltage, it was found that the maximum flow rate at which a stable plume and spectra were obtained had increased from a typical 6–8 μL/min to a typical 16 μL/min. Minimum flow remained 1 μL/min, the limit of the pump.

Under this configuration, electric current from both a noninsulated and an insualted needle was monitored and recorded as a function of voltage with no solvent flow passing through the needles. Results of this experiment are shown in Figure 5a. With the noninsulated steel needle, onset of the corona discharge could be clearly seen as a sharp increase in

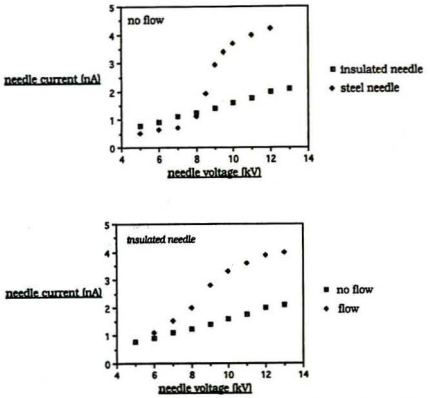

Figure 5. Electrospray needle current. (a, top) Comparison of total ion current from insulated and noninsulated needles. (b, bottom) Comparison of total ion current from an insulated needle with and without solvent flow. These data illustrate the fact that the insulated needle increases the potential range in which a stable electrospray can be obtained.

Table 2. Reduced Ion Mobilities (K_0) of Organic Amines from ESI-IMS Compared with ^{63}Ni Source Literature Values

amine	MW	K_0[a] (ESI)	K_0 (NOR)	K_0 (^{63}Ni)
ammonia	17	1.86	1.97	3.02
methylamine	31	1.75	1.85	2.65
n-butylamine	73	1.86	1.97	1.98
triethylamine	101	1.85	1.96	1.95
lutidine	107	1.84	1.95	1.95
isoquinoline	129	1.73	1.83	1.85
dibutylamine	129	1.59	1.68	1.64
tributylamine	185	1.36	1.44	1.38
tetrabutylammonium	242	1.19	1.26	
tetrapentylammonium	298	1.03	1.09	
tetraheptylammonium	410	0.81	0.86	
tetraoctadecylammonium	916	0.44	0.47	

[a] $K_0 = (d^2/Vt)(P/760)(273/T)$ where d is the drift distance, V is the potential across the drift distance, t is the ion drift time, P is the pressure in Torr, and T is the temperature of the drift region in degrees Kelvin.

needle current around 8–10 kV. While a small current was observed for the insulated needle, no sharp increase in current was noted in this region, indicating that background ionization from the corona was significantly reduced with the insulated needle. Figure 5b compared the needle current observed for 8 μL/min of solvent (50% methanol/water) flowing through the insulated needle with that observed for the no solvent flow condition. In similar experiments reported in ref 6, it was found that, with a noninsulated needle located inside the drift tube, the region in which solvent flow enhanced current over the no flow condition was quite limited. Thus the primary advantage of the insulated needle was to provide an increased range of needle voltage and flow rate over which true electrospray ionization spectra could be obtained.

To investigate the extent of desolvation with this design, a series of amines were electrosprayed into the ion mobility spectrometer and their K_0 values calculated. Inadequate desolvation resulted in ions of lower than expected mobilities. As shown in Table 2, most K_0 values compared well with those obtained by Karpas[12] using a conventional ^{63}Ni ionization source. This was especially true when K_0 values were

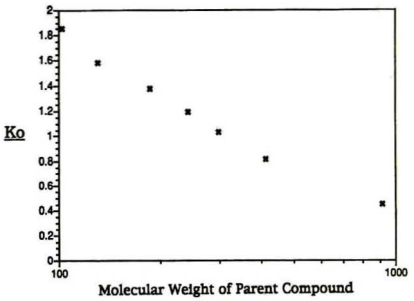

Figure 6. Log MW vs ion mobility constants (K_0) for quaternary and tertiary amines. Data were obtained with ESI-IMS configuration shown in Figure 2c. Data plotted are shown in Table 2, demonstrating that tetraalkylammonium ions apparently do not dissociate during soft electrospray ionization.

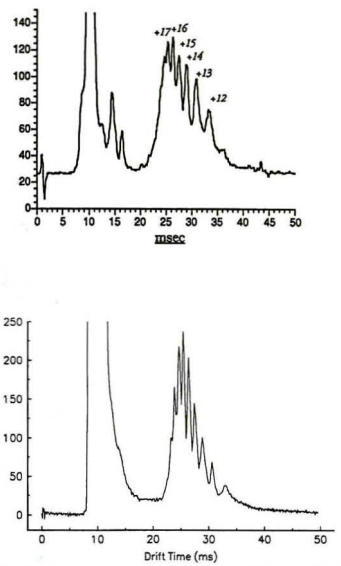

Figure 7. Electrospray ionization ion mobility spectrometry of cytochrome *c*. (a, top) Open electrospray design and (b, bottom) closed electrospray design. By comparison with ESI-MS spectra in Figure 9, this figure illustrates the first example of multiply charged ions separated by IMS.

normalized to 1.95, the K_0 value for lutidine. The exceptions were those of low molecular weight, which appeared in the region of the background solvent (reactant ion) peak. With regard to organic amines, electrospray ionization did have at least one distinct advantage over the ^{63}Ni source. The K_0 values of quaternary amines have been reported as difficult to measure, presumably due to dissociation in the IMS cell. This appeared not to be the case with this electrospray configuration. Figure 6 shows a relatively smooth curve when log MW was plotted as a function of K_0 for quaternary and tertiary amines together.

Figure 7a and Figure 8a are ion mobility spectra of high molecular weight compounds. Detection of these compounds

(12) Karpas, Z. *Anal. Chem.* **1989**, *61*, 684.

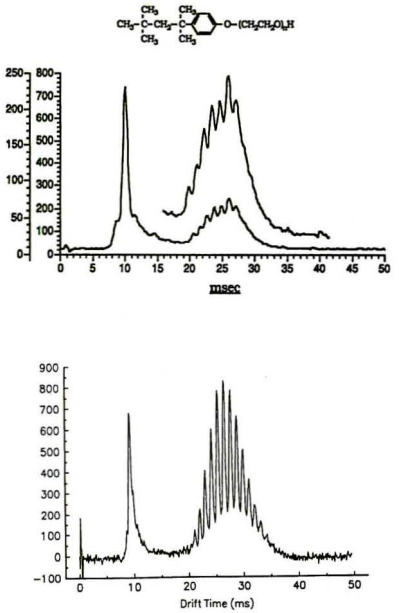

Figure 8. Electrospray ionization ion mobility spectrometry of Triton X-100. (a, top) Open electrospray design and (b, bottom) closed electrospray design. By comparison with the ESI-MS data presented in Figure 9, this figure represents singly charged ions of Triton X-100 oligomers. Note that the IMS resolution is sufficient to separate one gas-phase ion oligomer from the next. Each oligomer ion peak is separated by 44 mass units.

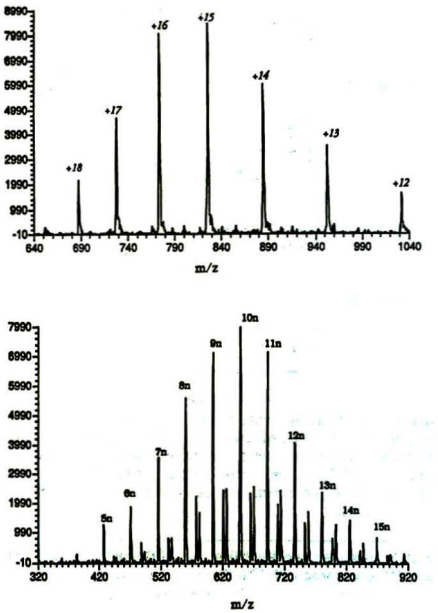

Figure 9. Electrospray ionization mass spectrometry. (a, top) Cytochrome *c* and (b, bottom) Triton X-100. Both spectra are similar to those reported for other ESI-MS systems and were used to make the mass/charge assignments in Figures 7 and 8.

was not possible with CSI-IMS. Figure 7a is an ESI-IMS spectrum of a protein, cytochrome *c*, and Figure 8a is the ESI-IMS spectrum of a polymer, Triton X-100. Both spectra produced a response for ions drifting from about 20 ms to about 35 ms. In each case, some resolution of individual ion peaks can be observed.

Figures 7b and 8b show ESI-IMS for the same compounds with the closed design shown in Figure 3. This instrument differed from the prototype in that the electrospray needle assembly was sealed from the laboratory atmosphere and the internal diameters of the guard rings were increased from 2.5 to 4.22 cm. To prevent volatilization of the solvent in the spray needle, the needle assembly was water cooled. Advantages of the sealed configuration were that the temperature in the drift region of the spectrometer remained uniform throughout the desolvation and drift region and contaminants from the laboratory air were excluded from the ionization region. Spectra obtained with the sealed source appeared to exhibit both higher sensitivity and higher IMS resolution.

Figure 9a,b shows ESI-MS spectra of cytochrome *c* and Triton X-100. For cytochrome *c*, seven ions were observed, corresponding to multiple charged ions containing +12 to +18 charges. Multiple charged ions are characteristic of ESI-MS of proteins which have a number of basic sites. Comparing the MS spectrum with the IMS spectra, it is possible to speculate that the multiple peaks observed in the IMS spectrum were also due to multiple charged ion species. If this is true, it is the first time that multiple charged peaks have been reported in IMS.

The ESI-MS spectrum of Triton X-100 was of singly charged ions corresponding to 11 different oligomers ranging in degree of polymerization (n) from 5 to 15. In the IMS spectrum using the open needle design, a total of seven ion peaks were detected and with the closed design 14 peaks were observed. In both cases the patterns of IMS spectra were similar to those obtained by ESI-MS.

CONCLUSIONS

True electrospray ion mobility spectrometry has been achieved. To achieve electrospray conditions, three important problems which occurred in previous designs of ion spray ion mobility spectrometers were identified and corrected. The problems were the following: (1) background contribution and dissociative ionization from corona discharge, (2) reduced response due to ion collection on the walls of the drift tube, and (3) prespray precipitation of nonvolatile compounds in the needle due to solvent volatilization. In addition, volatilization of the solvent in the needle prior to spraying led to unstable spray due to bubbles of vapor sputtering from the tip of the needle. Thus, successful operation of IMS in the electrospray ionization regime requires three specific design modifications of the spray needle from that reported in previous studies:

First, ion contribution of corona discharge to the overall current of IMS can be eliminated by enclosing the needle in a nonconductive (e.g. Teflon) sleeve. Under these conditions, ions are only produced as a result of electrospraying a solvent. When no solvent flow is present through the needle, no ions in the IMS will be observed.

Second, when a spray needle is inserted into the drift region of the IMS, electric field lines are produced such that trajectories of the electrosprayed ions are toward the walls of the drift tube, reducing the current directed down the tube. Creating the spray outside of the dirft region and adding a focusing screen which is positioned across the entrance to the ion drift region and a few centimeters in front of the tip of the spray needle directs the electrosprayed ions into the center region of the drift tube. With this modification, more of the ions reach the ion drift region and the sensitivity of the instrument is substantially enhanced.

Finally, desolvation of the sprayed ions requires elevated temperatures of the drift gas to evaporate solvent from the ionized spray drops as they migrate down the drift tube and before they reach the first ion gate of the spectrometer. When the electrospray source is incorporated as an integral part of the instrument in a closed design, heat transfer from the drift gas to the needle is sufficient to volatilize the solvent in the needle prior to electrospray. To prevent solvent volatilization in the spray needle, the needle must be cooled.

With a cooled and electrically insulated ion spray needle, and with the electrosprayed drops focused into the desolvation region of the IMS, stable and well-resolved response ions for nonvolatile high molecular weight compounds can be achieved. Moreover, the ion patterns produced with this electrospray IMS were similar to those observed in electrospray mass spectrometry, indicating that the response and behavior of an electrospray ionization source for IMS can be predicted from mass spectral data. Although optimized sensitivity studies were not conducted in this investigation, estimates made from these studies predict that the detection limit for IMS response will be similar to or less than that achieved for most optical detection methods. Thus, the electrospray IMS appears to offer a viable complementary detection method for liquid chromatography and capillary electrophoresis. Further investigations of this design with respect to liquid-phase detection are currently being conducted.

ACKNOWLEDGMENT

The authors express their gratitude to Andy Jarrell, Steve Gabeler, and Mike Tomany for their assistance in these studies. Initial data included in this paper were first reported by D. P. Wittmer at the 1992 Workshop on Ion Mobility Spectrometry held in Mescalaro, NM, June 1992.

Received for review December 21, 1993. Accepted April 11, 1994.[⊗]

[⊗] Abstract published in *Advance ACS Abstracts,* May 15, 1994.

Anal. Chem. **1994,** *66,* 2356–2361

Determination of Nanogram Levels of Peptide Drug in Rabbit and Human Plasma Using High-Performance Liquid Chromatography Coupled with Electrospray Ionization Mass Spectrometry

J. Crowther,* V. Adusumalli, T. Mukherjee, K. Jordan, P. Abuaf, N. Corkum, G. Goldstein, and J. Tolan†
Immunobiology Research Institute, Annandale, New Jersey 08801

High-performance liquid chromatography (HPLC) coupled to mass spectrometry (MS) using an electrospray ionization (ESI) interface provides a sensitive method for the quantitative analysis of peptide drugs in complex biological matrixes. ESI HPLC–MS was applied to the analysis of a pentapeptide drug (IRI-514) in rabbit and human plasma. Prior to analysis, the plasma samples were prepared using protein precipitation followed by solid-phase extraction. The lower limit of quantitation using selected ion monitoring was determined to be 2 ng/mL, when 8 mL of human plasma spiked with 1–40 ng/mL was extracted. Rabbit plasma (1 mL) samples spiked with 10–40 000 ng of authentic drug/mL gave a linear response when a deuterated peptide analog was employed as an internal standard. A commercial ESI interface was modified to permit higher flow rates (10–20 μL/min) to enter the mass spectrometer source. The revised interface provided a 10-fold increase in sensitivities and permitted the use of standard HPLC columns (2.0-mm i.d.) and HPLC instrumentation. ESI HPLC–MS analysis was automated to provide unattended, precise, and sensitive detection of small peptides in both human and rabbit plasma. Using this methodology, a toxicokinetic study of intravenously administered IRI-514 at three dose levels indicated that the area under the curve values were dose proportional.

Electrospray ionization (ESI) mass spectrometry (MS) has been used extensively recently for the characterization of small proteins[1–5] and peptides.[6–8] In addition to qualitative studies, this technique can be adapted to the quantitative determination of low levels of peptide due to the inherent high sensitivity of ESI MS. By interfacing high-performance liquid chromatography (HPLC) directly to ESI MS instrumentation, trace levels of peptide drug can be measured in relatively complex samples such as plasma, serum, and urine.[9–11]

Fouda et al.[12] reported excellent sensitivities for the quantitative LC–MS analysis of a renin inhibitor in serum. This derivatized hydrophobic dipeptide was analyzed by use of a heated nebulizer interface. Peptides which are larger or more hydrophilic, however, are more readily analyzed using ESI MS.

ESI LC–MS for the analysis of peptide drug in plasma provides an accurate, sensitive, and reproducible technique, features that are necessary for the determination of low levels of peptide in bioavailability and toxicokinetic studies.[13] Previous approaches to peptide analysis in plasma at these low levels involved derivitization followed by quantitation of the fluorescent derivative, but these methods suffered from endogenous interferences and reproducibility problems.[14] Radiochemical techniques[15] lack sufficient sensitivities in addition to the inconvenience of synthesis and handling of radiolabeled drug.

When peptide drugs are dosed orally, highly specific and particularly sensitive methodology must be used, since oral peptide formulations are known to have limited bioavailability,[16–18] which results in low levels of the drug in plasma. Natural peptides are quickly degraded through acid and enzymatic hydrolysis in the stomach and gut, obviating the absorption of effective quantities of drug into the circulatory system. To improve absorption, peptide analogs resistant to enzymatic and acid hydrolysis may be synthesized. IRI-514 (Ac-Arg-Pro-Asp-Pro-Phe-NH_2), a pentapeptide

† Current address/Affiliation: Affymax Pharmaceuticals, 3410 Central Expressway, Santa Clara, CA 95051.

(1) Bruins, A. P.; Covey, T. R.; Henion, J. D. *Anal. Chem.* **1987,** *59,* 2642–2646.
(2) Fenn, J. B.; Mann, M.; Meng, C. K.; Wong, S. F.; Whitehouse, C. M. *Science* **1989,** *246,* 64–71.
(3) Loo, J. A.; Udseth, H. R.; Smith, R. D. *Anal. Biochem.* **1989,** *179,* 404–412.
(4) Feng, R.; Konishi, Y. *Anal. Chem.* **1992,** *64,* 2090–2095.
(5) Gallagher, R. T.; Chapman, J. R.; Barton, E. C. *Proceeding of the 39th ASMS Conference on Mass Spectrometry and Allied Topics,* Nashville, TN, 1991; Elsevier: New York, 1991; pp 244–243.
(6) Chait, B. T.; Kent, S. B. H. *Science* **1992,** *257,* 1885–1884.
(7) Guzzetta, A. W.; Basa, L. J.; Hancock, W. S.; Keyt, B. A.; Bennett, W. F. *Anal. Chem.* **1993,** *65,* 2953–2962.
(8) Scindler, P. A.; Van Dorsselaer, A.; Falick, A. M. *Anal. Biochem.* **1993,** *213,* 256–263.
(9) Schneider, R. L.; Cole, M. J.; Fouda, H. G. *Proceedings of the 41st ASMS Conference on Mass Spectrometry and Applied Topics,* San Francisco, CA, May 31–June 4, 1993; p 53.
(10) LeBlanc, M. D.; Quilliam, M. A.; Bailey, M. R.; North, D. H. *Proceedings of the 41st Conference on Mass Spectrometry and Applied Topics,* San Francisco, CA, May 31–June 4, 1999; p 837.
(11) Kaye, B.; Clark, M. W. H.; Cussans, N. J.; Macrae, P. V.; Stopher, D. A. *Biol. Mass Spectrom.* **1992,** *21,* 585–589.
(12) Fouda, H.; Nocerini, M.; Schneider, R.; Gedutis, C. *J. Am. Soc. Mass Spectrom.* **1991,** *2,* 164–167.
(13) Peck, C. C.; Barr, W. H.; Benet, L. Z.; Collins, J.; Desjardins, R. E.; Furst, D. E.; Harter, J. G.; Levy, G.; Ludden, T.; Rodman, J. H.; Sanathanan, L.; Schentag, J. J.; Shah, V. P.; Sheiner, L. B.; Skelly, J. P.; Stanski, D. R.; Temple, R. J.; Viswanathan, C. T.; Weissinger, J.; Yacobi, Av. *Clin. Pharmacol. Ther.* **1992,** *51,* 465–473.
(14) Newcomb, R. *LC-GC* **1993,** *10* (1), 34–39.
(15) Digenis, G. A.; Sadefer, E. P.; Parr, A. F.; Beihn, R. M.; McClain, C.; Scheinthal, B. M.; Ghebre-Sellasie, I.; Lyer, U.; Nesbitt, R. U.; Randinitis, E. *J. Clin. Pharmacol.* **1990,** *30,* 621.
(16) Wood, J. M.; Criscione, L.; de Gasparo, M.; Buhlmayer, P.; Rueger, H.; Stanton, J. L.; Jupp, R. A.; Kay, J. *J. Cardiovasc. Pharmacol.* **1989,** *14,* 221–226.
(17) Lee, V. H. L. In *Peptides, a Target for New Drug Development;* Bloom, S.R., Burnstock, G., Eds.; IBC Technical Services: London, 1991; pp 120–134.
(18) Kompella, U. B.; Lee, V. H. L. In *Peptides and Protein Drug Delivery;* Lee, V. H. L., Ed.; Marcel Dekker: New York, 1991; pp 391–486.

0003-2700/94/0366-2356$04.50/0
© 1994 American Chemical Society

undergoing evaluation in the treatment of anxiety and depression, was found to be stable in several in vitro enzymatic models (pepsin, carboxypeptidase, prolidase) and in 0.1 M HCl.

ESI HPLC–MS was used to analyze plasma samples to determine the concentration of this peptide analog following oral dosing. Present methodology and its application for the assay of IRI-514 in rabbit and human plasma is presented. Samples of rabbit plasma were collected following the intravenous administration of IRI-514 to determine the toxicokinetics of the drug. Similarly, samples of human plasma were analyzed to estimate the bioavailability and dose proportionality of IRI-514 upon oral administration. Prior to analysis, the plasma samples were processed using protein precipitation followed by solid-phase extraction (SPE) to remove high molecular weight contaminants and particulates. Significant modification of commercial ESI MS instrumentation was necessary to provide the required sensitivities and system reliability. The concentration ranges studied for the rabbit and human plasma using SPE-ESI-HPLC–MS were 10–40 000 ng/mL and 2–40 ng/mL, respectively.

ESI HPLC–MS is ideally suited for the target analysis of peptides and proteins in complex biological matrixes due to the ability of the mass spectrometer to selectively monitor only specified molecular weights corresponding to the peptides of interest. The mass spectrometer thus serves as a very sensitive HPLC detector with tunable selectivity. The analysis of plasma samples, in particular, provides a means to determine a drug's bioavailability despite low plasma levels, which is useful in comparing various dosage forms, in comparing routes of administration, and in correlating plasma levels with pharmacodynamic results.

EXPERIMENTAL SECTION

Materials, Reagents, and Peptide Standards. HPLC grade acetonitrile and methanol were obtained from Burdick and Jackson (Muskegon, MI). Trifluoroacetic acid (HPLC spectro grade) was obtained from Pierce Chemical Co., Rockford, IL. ACS grade ammonium formate and formic acid were purchased from Eastman Kodak, Rochester, NY. HPLC grade water was obtained using a Millipore (Super 2) water purification system (Milford, MA).

Phosphate-buffered saline (PBS) used in standard dilutions was purchased through Sigma Chemical Co., St. Louis, MO, and prepared according to the manufacturer's specifications. Supelclean LC-18 SPE cartridges of 3- and 8-mL capacity were used with disposable flow control valve liners in a Visiprep DL manifold (Supelco, Inc., Bellefonte, PA). Blank rabbit and human plasma were obtained to use as controls.

IRI-514 was synthesized by Bachem (Bubendorf, Switzerland) as the citrate salt. The deuterated analog, IRI-514-d_5 (Ac-Arg-Pro-Asp-Pro-d_5-Phe-NH_2), was synthesized as the acetate salt at IRI using solid-phase synthesis and *t*-BOC synthesis strategies. The deuterated phenylalanine (MSD isotopes, Toronto, ON, Canada) was tested by separate ESI HPLC–MS experiments to determine the isomeric purity (98%+ D_5 and no detectable D_0) prior to synthesis to ensure that no undeuterated IRI-514 was present in the internal standard.

Preparation of Standards. The internal standard (IS) solution, 2.0 μg/mL, was prepared by dissolving 1.2 mg of IRI-514-d_5, equivalent to 1.0 mg of the peptide (peptide content determined by amino acid analysis), in 500 mL of water. The stock solution A of IRI-514, 100.0 μg/mL, was prepared by dissolving 14.0 mg of IRI-514, equivalent to 10.0 mg of the peptide, in 100 mL of HPLC grade water. The stock solution B of IRI-514, 1.0 μg/mL, was prepared by diluting 1.0 mL of stock solution A to 100 mL with HPLC grade water.

IRI-514 standards were prepared in both water and blank rabbit and human plasma by spiking with an appropriate volume of the IRI-514 stock solutions A and B.

An 8-mL aliquot of plasma was spiked with 100 μL of a 2000 ng/mL solution of deuterated IRI-514 (Phe-d_5) to serve as an internal standard.

Pretreatment of Plasma Samples. Prior to ESI HPLC–MS analysis, plasma samples were pretreated to "desalt" the sample and remove both very hydrophilic and hydrophobic impurities. Internal standard, preferably a deuterated analog of the peptide drug, was first added to the plasma samples. The internal standard served both to compensate for the recovery of drug from plasma and to reduce the variability in the sensitivity of the electrospray process run to run. Samples were then pretreated to precipitate proteins and extracted using reversed-phase SPE cartridges to remove excess salts and interfering substances. Upon removal of the elution solvent, the dried residue was dissolved in 0.5 mL of HPLC mobile phase. IRI-514 was concentrated 2–16-fold during pretreatment.

Solid-Phase Extraction of Rabbit Plasma Samples and Standards. Briefly, 0.100 mL of a 2.0 μg/mL IS solution and 2 mL of acetonitrile were added to 1.0 mL of each IRI-514 spiked rabbit plasma. The sample was vortexed for 1 min and centrifuged at 3000 rpm for 15 min at 4 °C. The supernatant obtained was evaporated and dried under nitrogen at room temperature. Before use, the SPE C_{18} cartridges from a single lot were preequilibrated by washing sequentially with 3.0 mL each of 100% acetonitrile, 75% (v/v) acetonitrile in water, 50% (v/v) acetonitrile in water, 25% (v/v) acetonitrile in water, 100% water, and finally 5.0 mL of 0.1% (v/v) TFA in water. The dried acetonitrile extract was redissolved in 1.0 mL of PBS by vortex mixing for 1 min and applied to the resin bed of a 3-mL capacity preequilibrated SPE cartridge for IRI-514 extraction. The cartridges were initially eluted with 3.0 mL of 0.1% TFA and then with 3.0 mL of 3% acetonitrile in 0.1% TFA to wash impurities from the column. Finally, IRI-514 was eluted from the cartridges with 3.0 mL of 30% acetonitrile in 0.1% TFA. For the elution of IRI-514 from the cartridges, many compositions of acetonitrile in 1% TFA aqueous solution were tried, and the final elution solvent mixture for SPE, 30% acetonitrile in 1% TFA solution, was found to be optimal for the acceptable recovery of IRI-514 and IS, while coelution of plasma interferences was avoided.

Solid-Phase Extraction of Human Plasma Samples and Standards. In the same manner, 8.0 mL of IRI-514 spiked human plasma standards or actual samples had 0.100 mL of IS added prior to precipitation with 13 mL of acetonitrile, and the resultant mixture was processed as described above. The dried residue was redissolved in 3.0 mL of PBS and further processed using a 6-mL-capacity preequilibrated SPE cartridge

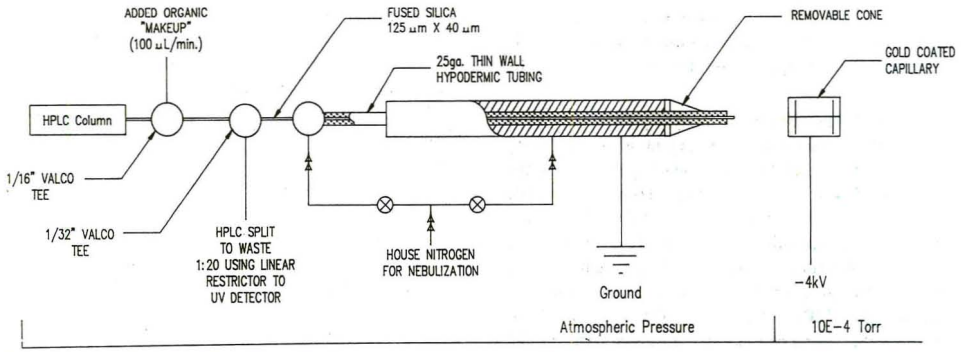

Figure 1. Schematic of ESI HPLC–MS modifications.

as described above. The solvent mixtures used for the 1-mL method, as described above, were also applied to this 8.0-mL method, however, at higher volumes (5.0 mL).

Concentration of Extracts Prior to ESI HPLC–MS Analysis. The eluents were brought to dryness in a Savant (Farmingdale, NY) Speed-Vac under vacuum. Each residue was redissolved in 0.500 mL of the mobile phase and vortexed. The solution was transferred to autosampler vials. Standards and samples were processed similarly.

Instrumentation. *HPLC.* The HPLC consisted of a Waters (Milford, MA) 717 autosampler (temperature controlled at 10 °C), a 600MS pump, and a 486 detector. An Applied Biosystems 400 HPLC pump was used to deliver additional methanol postcolumn. All Waters equipment was controlled and UV data recorded using the Waters 860 data system.

Isocratic analysis of samples was performed using a mobile phase consisting of 1% (v/v) methanol, 20% acetonitrile in 10 mM ammonium formate pH adjusted to 5.2 with 1% formic acid. A YMC reversed-phase (Wilmington, NC) Basic HPLC column (5-µm silica, 2.0 mm × 250 mm) was used throughout all experiments. The flow rate was 0.25 mL/min and the detector set at 220 nm. A 30 µL aliquot of each sample was injected onto the HPLC column using the autosampler; run time was set at 15 min. Since many samples (45–96) were often analyzed in a single run, the autosampler was programmed to chill the samples and limit sample degradation.

MS. The mass spectrometer was a Nermag R1010C with an Analytica of Branford (Branford, CT) electrospray interface modified for nebulization and a postcolumn split flow. Instrument control and data analysis was accomplished using Spect420 software modified (Mass Evolutions, Houston, TX) to permit unattended and multiple sample analyses using a Waters autosampler. The resolution was optimized using a software-controlled and updated microprocessor board (Mass Evolutions). The instrument's ion optics were adjusted to maximize sensitivity at approximately monthly intervals by infusion of a 100 µM solution of IRI-514 dissolved in mobile phase. The mass spectrometer was programmed to monitor ions m/z 672 (IRI-514) and 677 (IRI-514-d_5 internal standard) with a total cycle time of 3 s (dwell time of 1.5 s). Since the HPLC effluent into the source was at ground potential, a –3.3-kV potential was applied to the interfaces's 600 µm-i.d. capillary tube to provide electrospray conditions.

Two 1010 L/min capacity rotary pumps (No. D045, Galileo, East Granby, CT) were used to evacuate the electrospray chamber, and two additional pumps were used to provide rough pumping for the instrument diffusion pumps.

ESI Source Modification. The inlet to the Analytica source was modified to accept the 0.25 mL/min flow rates which were compatible with the chromatographic column diameter (2.0 mm) used in this study. Smaller diameter columns (<1.5 mm) were found to be less robust and the required low flow rates limited the use of commercial autosamplers due to extracolumn band spreading. As shown in Figure 1, effluent from the HPLC column was mixed with a 100 µL/min "makeup flow" of methanol–HPLC mobile phase (90:10) to add additional volatility to the mobile phase to improve droplet desolvation.[19] The flow rate was then split using a $^1/_{32}$-in. tee (Valco, Houston, TX) and a 0.007 in. × 25 cm $^1/_{16}$-in. PEEK linear restrictor which was connected to the HPLC UV detector. Approximately one-twentieth of the flow (18 µL/min) entered a 40 µm i.d. × 125 µm o.d. fused silica capillary (Polymicro Technologies, Phoenix, AZ) at ground potential. Thin-walled stainless steel hypodermic tubing (25 g, 0.12-in. i.d.) was obtained from Small Parts (Miami Lakes, FL). Assorted valves and tubing used to provide nebulization of the electrospray were purchased from Alltech Associates (Deerfield, IL).

Due to careful sample pretreatment and an in-line HPLC column, this system typically analyzed samples continuously for several months without clogging of the fine tubing. Thin-walled hypodermic tubing surrounding the fused silica tubing permitted coaxial nitrogen gas (90 mL/min) to provide nebulization assistance to the desolvation of the electrospray droplet. The tip of this hypodermic tubing was electropolished to both deburr the tubing and reduce its diameter so the removable cone (supplied in the Analytica interface) fit easily over the tube. A separate supply of nitrogen (15 mL/min) flowed between the tube and the cone. Best electrospray conditions were obtained when the fused silica capillary extended a few millimeters beyond both the hypodermic tubing and the cone. Nitrogen at 185 °C flowed (250 mL/min) countercurrent to the electrospray to further assist in desolvation of the droplets.

(19) Kebarle, P.; Tang, L. *Anal. Chem.* **1993**, *65*, 972A–986A.

Further sensitivity was gained by using a 600-μm-i.d. gold-coated glass capillary instead of the 500-μm-i.d. capillary originally supplied with the interface. Additional rough pumping was necessary (2 × 1010 L/min) to maintain suitable analyzer vacuum with the larger diameter capillary.

Data Processing. Concentrations of IRI-514 in the unknown samples were determined from concentration and peak area data for the standards and the internal standard using a commercial least-squares linear regression analysis program, TableCurve (Version 2.1, Jandel Scientific, Corte Madera, CA) and a commercial spreadsheet, EXCEL program (Version 4.0, Microsoft Co., Redmond, WA). Statistical analysis[20] was performed to evaluate the assay precision using relative standard deviation (RSD), accuracy using root mean error (RME) and overall performance using total error (TE).

RESULTS AND DISCUSSION

Analysis by ESI HPLC–MS. The extracted samples were analyzed by HPLC coupled to an ESI-MS instrument. A commercial ESI interface was modified to reduce extracolumn chromatographic band broadening while coaxial nebulization enabled increased flow rates into the ESI interface. This modification permitted higher flow rates (10-20 μL/min as opposed to 1–2 μL/min)) to enter the electrospray source. Higher flow rates reduced the postcolumn split (with HPLC flow rates of 250 μL/min) from 200:1 to 20:1, resulting in a 8–10-fold increase in sensitivities. Furthermore, since electrospray sensitivities were greatly reduced by highly aqueous mobile phases, organic modifier was added postcolumn to maintain the total organic content in mobile phase entering the source above 30%.

These modifications of the ESI HPLC–MS provided a rugged and reliable system. The use of a HPLC autosampler and modification of the mass spectrometer data system hardware to provide a contact closure start signal enabled unattended operation. This system typically ran 65+ samples (test samples, controls, standards) per day, five days a week. Calibration of the mass axis was monitored daily through analysis of a "system suitability" mixture of peptides. The only routine maintenance, other than vacuum system upkeep, was the occasional replacement (1–2/month) of the 600-μm-i.d. capillary when signal deteriorated.

Electrospray mass spectra of IRI-514 and IRI-514-d_5 at the experimental conditions display predominant $(M + 1)^+$ ions. Therefore, ions m/z 672 (IRI-514) and 677 (IRI-514-d_5) were monitored in all experiments.

Calibration Curve of the ESI HPLC–MS System. Prior to the analysis of each day's unknown study samples, standard curves (Figure 2) were generated using spiked plasma samples which followed sample pretreatment procedures similar to actual study samples. Calibration curves were linear (R^2 ~0.999) over a very large dynamic range (10–40 000 ng/mL). Detection limits (S/N ~5:1) were found to be 10 ng/mL.

Similarly, the calibration plot for IRI-514 spiked in human plasma was linear (r^2 = 0.99) over the concentration range studied, 2–40 ng/mL (Figure 3). The 8.0-mL human plasma sample, compared to the 1.0-mL rabbit plasma sample, improved detection limits for the method to 2 ng/mL.

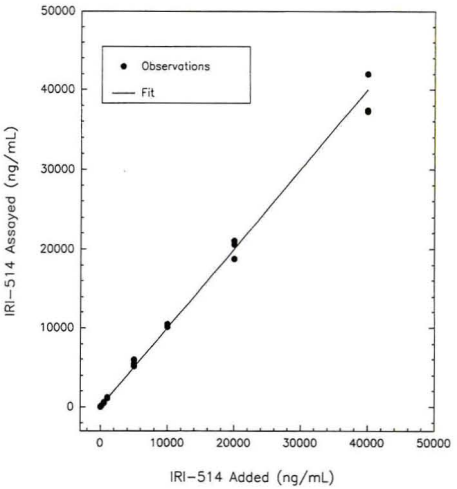

Figure 2. Assay linearity for the range 10–40 000 ng/mL IRI-514 spiked in 1.0 mL of rabbit plasma.

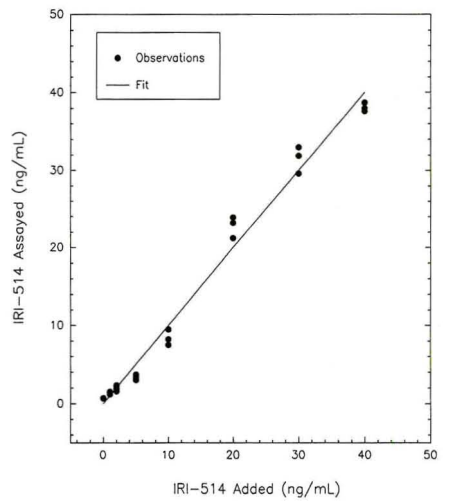

Figure 3. Assay linearity for the range 2–40 ng/mL IRI-514 spiked in 8.0 mL of human plasma.

Recoveries of IRI-514 in Spiked Plasma. Recoveries of IRI-514 and IS from the spiked plasma were assessed by comparing their absolute peak areas after extraction from plasma standards with those peak areas measured in the solvent (water) standards. The relative recovery of IRI-514 and IS from rabbit and human plasma processed through SPE cartridges was consistently above 70%.

Analysis of Samples. Figure 4 shows two typical mass chromatograms for rabbit plasma containing 0 and 100 ng/mL of IRI-514; both samples contain 200 ng/mL IS. Analysis of blank plasma samples revealed no detectable levels of background peaks at the mass of either the analyte or IS.

(20) McFarren, E. F.; Lishka, R. J.; Parker, J. H. *Anal. Chem.* **1970**, *42*, 358–361.

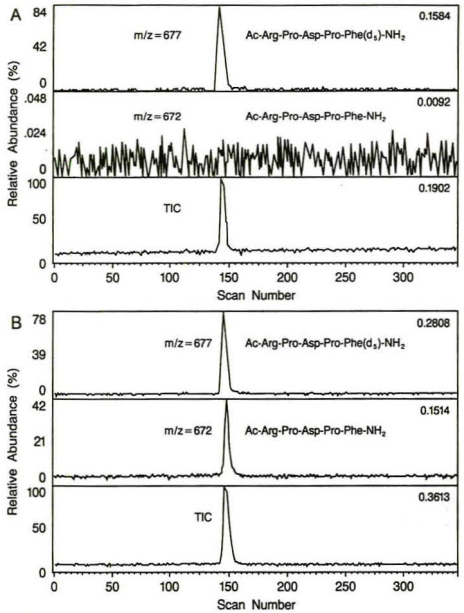

Figure 4. Extracted ion chromatogram of rabbit plasma containing (A) zero and (B) 100 ng/mL IRI-514, each with 200 ng of the internal standard IRI-514-d_5.

Table 1. Within-Day Precision, Accuracy, and Total Error for IRI-514 in Rabbit Plasma[a,b]

IRI-514 added to rabbit plasma (ng/mL)	assayed IRI-514 (ng/mL)	RSD (%)	TE (%)
0	0	na	na
10	10	20.0	40.0
50	54	5.3	20.2
100	110	9.0	29.4
500	537	4.3	16.5
1000	1130	2.6	18.8
5000	5490	7.3	25.9
10000	10324	1.8	7.0
20000	20124	5.8	12.4
40000	38882	6.9	16.2

[a] Samples (n = 3) analyzed in triplicate on a single day. [b] na, not applicable; RSD, relative standard deviation; TE, total error.

Samples were analyzed along with appropriate blanks and controls to monitor the performance of the system throughout a "run". At least 500 samples have been assayed per HPLC column without significant increases in column back pressure or loss in column performance.

Assay Precision, Accuracy, and Total Performance. The 1.0-mL method was developed in order to quantitate IRI-514 in plasma samples from a toxicokinetic study in rabbits. The within-day assay statistics calculated for the triplicate analyses of each IRI-514 standard prepared in rabbit plasma and analyzed on the same day (n = 3) are presented in Table 1. The precision varied from 1.8% to 20.0% and the total error varied from 7.0% to 40.0%. The lower limit of quantitation (LOQ) for this method was set at the lowest concentration, yielding a total error of less than 50%. Based on this criterion, the LOQ for IRI-514 was set at 10 ng/mL of IRI-514 in rabbit plasma and the corresponding upper limit of quantitation was 40 000 ng/mL. The within-day assay statistics indicate that the method for quantitation of IRI-514 in 1.0 mL of rabbit plasma is accurate and reproducible.

Table 2. Within-Day Precision, Accuracy, and Total Error for IRI-514 in Human Plasma[a,b]

IRI-514 added to human plasma (ng/mL)	assayed IRI-514 (ng/mL)	RSD (%)	TE (%)
0	0.7	na	na
1	1.3	11.5	63.9
2	1.9	15.8	33.9
5	3.4	12.0	48.8
10	8.4	9.5	31.7
20	22.7	6.6	28.4
30	31.4	4.2	13.4
40	38.2	1.5	7.3

[a] Samples (n = 3) analyzed in triplicate on a single day by the same analyst. [b] na, not applicable; RSD, relative standard deviation; TE, total error.

Table 3. Between-Day Precision, Accuracy, and Total Error for IRI-514 in Human Plasma[a,b]

IRI-514 added to human plasma (ng/mL)	assayed IRI-514 (ng/mL)	RSD (%)	TE (%)
0	0.7	na	na
1	1.7	29.3	153.9
2	2.3	18.2	55.9
5	4.1	16.9	45.9
10	8.9	11.6	31.5
20	20.2	10.7	22.7
30	29.1	7.2	17.0
40	40.9	5.6	13.6

[a] Samples (n = 9) analyzed in triplicate on three different days. [b] na, not applicable; RSD, relative standard deviation; TE, total error.

The 8.0-mL method was developed for quantitation of IRI-514 in plasma samples from drug bioavailability studies in man. The within-day assay statistics calculated for the triplicate analyses of each IRI-514 standard prepared in human plasma and analyzed on the same day (n = 3) are presented in Table 2. The precision varied from 1.5% to 15.8% and the total error varied from 7.3% to 63.9%. The lower LOQ for this method was set at the lowest concentration, yielding a total error of less than 50%. Based on this criterion, the LOQ for IRI-514 was set at 2 ng of IRI-514/mL in human plasma and the corresponding upper limit of quantitation was 40 ng/mL. The between-day assay statistics calculated for the triplicate analyses of each standard prepared in 8.0 mL of human plasma and analyzed on three separate days (n = 9) are presented in Table 3. The precision varied from 5.6% to 18.2% and the total error varied from 13.6% to 55.9% over the 2–40 ng/mL range. The within-day and between-day assay statistics indicate that the method for quantitation of IRI-514 in human is accurate and reproducible.

Toxicokinetic and Bioavailabililty Findings. Application of the 1.0 mL method with 10 ng/mL LOQ was demonstrated by measuring IRI-514 concentrations in plasma samples from a IRI-514 toxicokinetic study in rabbits (Figure 5). In that study, the pentapeptide was administered by a 10-min intravenous infusion to rabbits at 1.0, 10.0, and 100.0 mg/kg and blood samples were collected over a 24-h period during and after drug administration. The area under the concen-

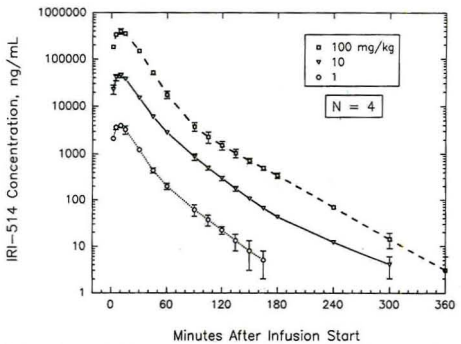

Figure 5. Mean plasma concentrations of IRI-514 during and after single intravenous infusion in rabbits.

Table 4. Bioavailability[a]

(a) In Rabbits Following a Single Intravenous Infusion dose (mg/kg)	AUC (±SD) (ng/mL × min) $n = 4$
1	106 534
10	1 240 867
100	11 101 962

(b) In Humans Following a Single Oral Dose total dose (mg)	AUC[b] (ng/mL × min) $n = 4$
300	7.9
600	20.2
900	54.2

[a] Determined by area under the curve (AUC). [b] AUC for the mean concentration versus time data.

tration versus time curve (AUC) values for the three intravenous administrations was proportional to the respective doses of IRI-514 (Table 4a).

The 8.0-mL method with a LOQ of 2 ng/mL, was applied to the determination of IRI-514 in plasma samples from a Phase I human safety and tolerance study after a single oral administration at 150, 300, 600, or 900 mg (Figure 6) to fasted male subjects. The AUC values are presented in Table 4b. The AUC value for a 150-mg dose was not calculated since plasma concentrations of IRI-514 following the dose were below the limit of quantitation. These results clearly demonstrated that this SPE-ESI-HPLC–MS method permits rapid, accurate, and sensitive quantitation of the pentapeptide in plasma samples following either intravenous or oral administration in rabbit and human pharmacokinetic studies.

CONCLUSIONS

A procedure for the sensitive and accurate determination of low levels of peptides in plasma was developed which is easily automated for routine use. ESI HPLC–MS has proven to be a powerful and flexible tool for sensitive quantitative analysis, using a deuterated analog of the drug as an internal

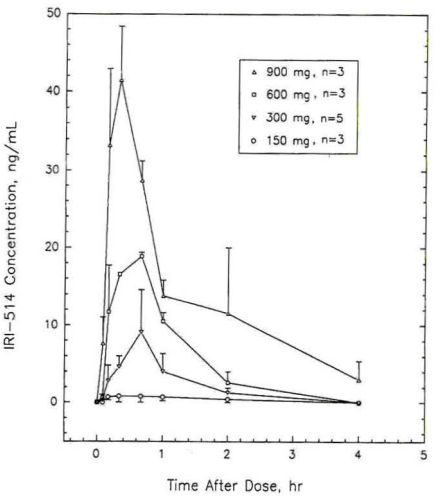

Figure 6. Mean plasma IRI-514 concentrations in fasted male human volunteers following single oral administration at various dosages.

standard. This procedure analyzes complex samples with sensitivity and specificity superior to what is usually observed with conventional UV and fluorescent detectors, without problematic derivatization techniques.

Modifications were made to the commercial electrospray interface to permit use of standard HPLC columns and instrumentation. The instrument ran continuously (over 65 samples/day), with the exception of occasional replacement of the 600-μm-i.d. capillary used in the interface and periodic (monthly) vacuum system maintenance.

This procedure was applied to the analysis of IRI-514 in human and rabbit plasma samples to determine the bioavailability of an oral administration of the pentapeptide and the toxicokinetics of the drug following intravenous injection.

Other IRI developmental peptides have also been successfully analyzed in plasma and other biological fluids of various species. While ESI HPLC–MS measurement of each new peptide analog's concentration is relatively straightforward, each peptide drug and each new matrix requires optimization.

ACKNOWLEDGMENT

We thank Ponniah Shenbagamurthi for synthesis of the deuterated IRI-514 standards used in this work, David Goodlett for his review of the manuscript, and Ben Gerberville for his assistance in technical drawings.

Received for review January 3, 1994. Accepted April 22, 1994.[•]

[•] Abstract published in *Advance ACS Abstracts,* June 1, 1994.

Anal. Chem. **1994,** *66,* 2362–2368

Quantitative Measurement of Cyclosporin A in Blood by Time-of-Flight Mass Spectrometry

David C. Muddiman, Arkady I. Gusev, Andrew Proctor, and David M. Hercules*
Department of Chemistry, University of Pittsburgh, Pittsburgh, Pennsylvania 15260

Raman Venkataramanan
Department of Pharmaceutical Sciences, University of Pittsburgh, Pittsburgh, Pennsylvania 15213

Warren Diven
Department of Pathology, University of Pittsburgh, Pittsburgh, Pennsylvania 15213

Analytical methods have been developed for the detection and quantification of cyclosporin A (CsA) in blood using time-of-flight secondary-ion mass spectrometry (TOF-SIMS) and matrix-assisted laser desorption/ionization time-of-flight mass spectrometry (MALDI/TOF-MS). Linear calibration curves were obtained for both methods in the range 25–2000 ng/mL in whole blood. The limit of detection (LOD) and limit of quantification (LOQ) were determined to be 7 and 23 ng/mL, respectively, for the TOF-SIMS method; the LOD and LOQ were 10 and 33 ng/mL, respectively, for the MALDI/TOF-MS method. Coefficients of variation ranged from 3 to 5% for the TOF-SIMS method and from 4 to 8% for the MALDI/TOF-MS method. Blood samples were also analyzed by a nonspecific method, fluorescence polarization immunoassay (FPIA), and by a specific method, high-performance liquid chromatography (HPLC). The TOF-MS results are in good agreement with the HPLC results, but not with the FPIA results. The TOF-MS methods can also provide information about CsA metabolites.

The recent success in organ transplantation can be primarily attributed to the development of immunosuppressive agents such as cyclosporin A (CsA). CsA was first discovered during the 1970s.[1] The narrow therapeutic index and the large inter- and intraindividual variation in the pharmacokinetics of CsA necessitates routine therapeutic monitoring for optimizing drug therapy. Whole blood has been recommended as the biological fluid of choice for monitoring CsA concentrations and for pharmacokinetic studies due to the temperature-dependent distribution of CsA between red blood cells and plasma.[2] Several analytical methods have been reported for measuring CsA concentrations in whole blood. Methods such as fluorescence polarization immunoassay (FPIA),[3] radioimmunoassay (RIA),[4] and enzyme-linked immunosorbent assay(ELISA)[5] are rapid, less expensive, and easier to use than HPLC but are nonspecific and simultaneously measure some of the metabolites of CsA.[4]

High-performance liquid chromatography (HPLC)[6] is the standard method due to its ability to specifically measure only the parent CsA. Time-of-flight secondary-ion mass spectrometry (TOF-SIMS) and matrix-assisted laser desorption/ionization time-of-flight mass spectrometry (MALDI/TOF-MS) have proven to be sensitive as well as selective techniques and should prove to be valuable tools in therapeutic drug monitoring.[7,8] TOF-SIMS has been used for quantification of CsA in ethanol solutions and in spiked blood samples;[9,10] this technique is capable of detecting nonvolatile and thermally labile molecules in the femtomole range.[11] Typically, TOF-SIMS has offered qualitative information about biopolymers[12] and synthetic polymers[13] with only limited quantitative work conducted to date. Quantitative analysis of molecular species by SIMS requires the use of internal standards for two reasons. First, the ionization probability of sputtered molecular species strongly depends on the chemical environment of the molecule on the specially prepared surface. This environment is hard to control, but can be compensated for by simultaneously depositing an internal standard having similar properties. Second, the extraction efficiencies of biological compounds from the matrices in which they reside (such as blood) are not constant from sample to sample. Addition of an internal standard with an extraction efficiency similar to the analyte of interest prior to extraction compensates

(1) Borel, J. F.; Feurer, C.; Gubler, H. U.; Stahelin, H. *Agents Actions* **1976,** *6,* 468.
(2) Ptachcinski, R. J.; Burckart, G.; Venkataramanan, R. *J. Clin. Pharmacol.* **1986,** *26,* 358.
(3) Wang, P. P.; Simpson, E.; Meucci, V.; Morrison, M.; Lunetta, S.; Zajac, M.; Boeckx, R. *Clin. Biochem.* **1991,** *24,* 55.
(4) Burckart, G.; Starzl, T.; Williams, L.; Sanghvi, A.; Gartner, C., Jr.; Venkataramanan, R.; Zitelli, B.; Malatack, J.; Urbach, A.; Diven, W.; Ptachcinski, R.; Shaw, B.; Iwatsuki, S. *Transplant. Proc.* **1985,** *17* (1), 1172.
(5) Kobayashi, M.; Tamura, K.; Katayama, N.; Nakamura, K.; Nagase, K.; Hane, T.; Tutumi, M.; Niwa, M.; Tanaka, H.; Iwasaki, K.; Kohsaka, M. *Transplant. Proc.* **1991,** *23,* 2725.
(6) McBride, J. H.; Kim, S. S.; Rodgerson, D. O.; Reyes, A. F.; Ota, M. K. *Clin. Chem.* **1992,** *38,* 2300.
(7) Hercules, D. M. *J. Mol. Struct.* **1993,** *292,* 49.
(8) Hillenkamp, F.; Karas, M.; Beavis, R.; Chait, B. *Anal. Chem.* **1991,** *63,* 1193A.
(9) Meyer, K.; Hagenhoff, B.; Deimel, M.; Benninghoven, A. *Org. Mass Spectrom.* **1992,** *27,* 1148.
(10) Hagenhoff, B.; Kock, R.; Deimel, M.; Benninghoven, A.; Bauch, H.-J. In *Secondary Ion Mass Spectrometry: Proceedings of the Eighth International Conference (SIMS VIII)*; Benninghoven, A., Janssen, K. T. F., Tumpner, J., Werner, H. W., Eds.; John Wiley & Sons: Chichester, England, 1992; p 831.
(11) Benninghoven, A.; Musche, H.; Wunsche, C. *Proceedings of the Seventh International Conference on Secondary Ion Mass Spectrometry (SIMS VII)*; J. Wiley: Chichester, England, 1990; p 293.
(12) Poppe-Schriemer, N.; Binding, D. R.; Ens, W.; Mayer, F.; Standing, K. G.; Tang, X.; Westmore, J. B. *Int. J. Mass Spectrom. Ion Processes* **1991,** *111,* 301.
(13) Bletsos, I. V.; Hercules, D. M.; vanLeyen, D.; Benninghoven, A. *Macromolecules* **1987,** *20,* 407.

0003-2700/94/0366-2362$04.50/0
© 1994 American Chemical Society

for the sample-to-sample variation in extraction. In the present study cyclosporin D (CsD), an analog of CsA which does not exhibit immunosuppressive activity, was used as an internal standard.[9,10]

Another technique which has been used for quantification of CsA was MALDI/TOF-MS. The MALDI method was introduced in 1987 by Karas and Hillenkamp and has become a powerful tool for obtaining mass spectra of high molecular weight biomolecules.[14] Analysis of proteins mixtures,[15,16] oligosacharides,[17] oligonucleotides,[18] enzymatic protein digests,[19,20] underivatized DNA oligomers,[21] and tryptic maps of recombinant human growth hormone and human tissue plasminogen activator[22] have previously been investigated by the MALDI/TOF-MS method. Most applications of the method have involved determination of molecular weight; detection of unfragmented parent ions with molecular masses over 200 kDa has been achieved.[23] The application of MALDI for quantitative analysis has been demonstrated only recently.[24-26]

In the present study, we compare quantitative measurement of CsA using TOF-SIMS and/or MALDI/TOF-MS. The results are compared to those obtained using HPLC (a specific assay for CsA) and FPIA (a nonspecific assay for CsA).

EXPERIMENTAL SECTION

Reagents and Materials. Cyclosporins A and D were obtained from Sandoz Corp. Diethyl ether (purified grade) and HPLC grade methanol were obtained from Fisher Scientific. HPLC grade hexane (85% *n*-hexane) was obtained from Baker. 2,5-Dihydroxybenzoic acid (DHB) was obtained from Sigma Chemical Co.

Instrumentation. *FPIA.* This assay was performed according to the procedure described in the text supplied by Abbott Laboratories.[27]

HPLC. Samples were reconstituted with mobile phase prior to injection onto a 15-cm, 5-μm, C_{18} column (Supelco, Bellefonte, PA) heated to 70 °C. The mobile phase was acetonitrile/water (68:32) delivered at 1.5 mL/min. Column eluents were monitored at 214 nm using an ultraviolet detector (Model 441; Waters Associates, Milford, MA). The retention time was 8.3 min for CsA and 11.2 min for CsD. All samples and standards were assayed in duplicate. For HPLC analysis, 140 μL was injected onto the column.

TOF-SIMS. A time-of-flight secondary-ion mass spectrometer, TOF-SIMS III, manufactured by Ion-Tof GmbH, Münster, Germany, was used in this study. This instrument was designed for analysis of biomolecules at the pico- and femtomole level and has also been used for the analysis of semiconductors and polymers.[28] The TOF-SIMS III incorporates a pulsed Ar^+ ion source, a high-resolution first-order reflectron time-of-flight analyzer, and a pulsed charge-neutralization system for analysis of insulating materials. The TOF-SIMS has been described in more detail elsewhere;[29,30] however, a brief overview is presented below.

The primary ion source consists of a standard electron impact argon ion source combined with a 90° deflector for beam chopping and primary ion mass separation, followed by an axial buncher for pulse compression. The resultant mass-separated ion pulses have a typical pulse length less than 1 ns and a variable spot diameter between 5 and 50 μm.

Secondary ions generated by a primary ion pulse on the target surface are extracted and accelerated to an energy of 3 keV. In the following 1.87-m flight path, an Einzel lens and reflectron optics are integrated for focusing the secondary ion beam and for energy compensation, respectively. The ions were postaccelerated to 10 keV, where they were then detected by a channel plate/scintillator/photomultiplier combination.

The spectra are accumulated in the single-ion counting mode with a maximum of 256 stops/ion pulse, a time resolution of 1.25 ns/channel, and a total time range of 320 μs. The repetition rate was set at 200 μs allowing investigation of ions from 1 to 4000 Da.

The TOF-SIMS III incorporates several sample holders that can accommodate up to 24 different samples; however, the sample holder used for these experiments could hold 10 targets. The different targets are accessed using a high-precision *XYZ* manipulator.

During analysis the target was bombarded by a 10-keV Ar^+ beam with an average pulsed primary ion current of 0.5–1.0 pA for a total collection time of 300 s. The total primary ion dose during data acquisition was less than 10^{13} ions/cm^2 (static SIMS). Typical resolution ($M/\Delta M$) at m/z = 1000 is 8000 (fwhm).

For TOF-SIMS analysis, a 3-μL aliquot of the reconstituted residue was deposited onto a silver target with an area of about 150 mm^2. The silver had been previously etched in nitric acid (20 vol %) and rinsed with deionized water and methanol.

Processing of data included mass calibration and measuring the analyte and the internal standard peak areas. The peak areas were determined using the $(M + {}^{107}Ag)^+$ peak of each component with the integral determined by the fwhm using a linear background.

MALDI/TOF-MS. The TOF-MS employed in these investigations was a modified LAMMA 1000 (Leybold-Heraeus GmbH) mass spectrometer. The modification

(14) Karas, M.; Hillenkamp, F. *Anal. Chem.* **1988**, *60*, 2299.
(15) Hillenkamp, F.; Karas, M.; Beavis, R.; Chait, B. *Anal. Chem.* **1991**, *63*, 1193.
(16) Beavis, R.; Chait, B. *Proc. Natl. Acad. Sci. U.S.A.* **1990**, *87*, 6873.
(17) Stahl, B.; Steup, M.; Karas, M.; Hillenkamp, F. *Anal. Chem.* **1991**, *63*, 1463.
(18) Wu, K.; Steding, A.; Becker, C. H. *Rapid Commun. Mass Spectrom.* **1992**, *6*, 365.
(19) Schar, M.; Bornsen, K. O.; Gassman, E. *Rapid Commun. Mass Spectrom.* **1991**, *5*, 319.
(20) Juhasz, P.; Papayannopoulous, I. A.; Zeng, Ch.; Papov, V.; Biemann, K. *Proceedings of the 40th ASMS Conference on Mass Spectrometry and Allied Topics*, Washington, DC, American Society for Mass Spectrometry: Santa Fe, NM, 1992; p 1813.
(21) Kuang, J. W.; Stending, A.; Becker, C. H. *Rapid Commun. Mass Spectrom.* **1993**, *7*, 142.
(22) Billeci, T. M.; Stults, J. T. *Anal. Chem.* **1993**, *65*, 1709.
(23) Juhasz, P.; Costello, C. E.; Biemann, K. *J. Am. Soc. Mass Spectrom.* **1993**, *4*, 399.
(24) Gusev, A. I.; Wilkinson, W. R.; Proctor, A.; Hercules, D. M. *Applied Spectrosc.* **1993**, *47*, 8.
(25) Nelson, R. W.; McLean, M. A.; Vestal, M. L. *Proceedings of the 40th ASMS Conference on Mass Spectrometry and Allied Topics*, Washington, DC, American Society for Mass Spectrometry:Santa Fe, NM, 1992; p 1919.
(26) Farmer, T. B.; Caprioli, R. M. *Presented at the 41st ASMS Conference on Mass Spectrometry and Allied Topics*, San Francisco, May 30–June 4, 1993; Paper TbP 70.
(27) Abbott Laboratories, One Abbott Park Rd., Abbott Park, IL 60064.
(28) Niehuis, E. *Secondary-ion Mass Spectroscopy (SIMS VII)*; Benninghoven, A., Ed.; Wiley-Interscience: Chichester, England, 1989; pp 299–304.
(29) Niehuis, E.; Heller, T.; Feld, H.; Benninghoven, A. *J. Vac. Sci. Technol. A* **1987**, *5*, 1243.
(30) Niehuis, E.; van Veltzen, P. N. T.; Lub, J.; Heller, T.; Benninghoven, A. *Surf. Interface Anal.* **1989**, *14*, 135.

involved replacement of the laser, from a Nd–YAG to a N_2 laser (VSL 337 ND; Laser Science Inc., Boston, MA) emitting at 337 nm. Laser irradiance was approximately 5.0×10^7 W/cm^2. Typical mass resolution of the system is 400 (fwhm) at $m/z = 1000$.

The ions created at the surface were accelerated to 4 kV and space focused using an Einzel lens. To increase detection efficiency, the ions were postaccelerated to 10 keV onto a discrete dynode type secondary electron multiplier (SEM). The signal from the SEM was amplified and collected in a recording system consisting of two 200-MHz, 8 × 32 kbyte channel transient recorders (TR 8828 B, MM8103A, LeCroy Inc.). To expand the dynamic range of the system, the signal was split and differentially amplified before being fed into the transient recorders.

Spectra were collected over several sections of the sample to compensate for sample heterogeneities arising from the crystallization process. Up to 120 shots were averaged due to lack of shot-to-shot reproducibility. For these measurements, the laser beam was defocused to 200 × 150 μm; defocusing was behind the focal plane.

The pressure in the sample chamber was $(1–2) \times 10^{-4}$ and 2×10^{-5} Pa in the TOF chamber. The instrument contains an *XYZ* manipulator which is used to precisely control the place the laser interacts with the sample. Up to 30 samples can be incorporated into the instrument at any given time.

Data collection and subsequent analysis were carried out on an IBM PC-compatible running under DOS with software which was written in-house (GOOGLY). Processing of the mass spectra included the following steps: acquisition, mass calibration, smoothing of the spectra, curve fitting, and subsequent measurement of the intensities of the analyte and internal standard. To increase the accuracy of the peak intensity measurements, we applied a linear background to avoid problems connected with metastable decay and additional noise.

DHB was used at a concentration of 20 mg/mL in a 9:1 water/ethanol solution. A 4–8-μL aliquot of the reconstituted extract was combined 1:1 with the matrix solution and mixed either by vortexing or in an ultrasonic bath. A 1-μL aliquot of this mixture was deposited on a polished stainless steel substrate and dried in a high-purity N_2 stream. Typically, $1:10^3–1:10^5$ analyte/matrix molar ratios were used.

Sample Preparation. *Blood Sample Preparation.* One milliliter of whole blood was placed in a 30-mL test tube and the internal standard, CsD (625 ng/mL), was added as a methanol solution (50 μL). The same stock solution of internal standard was used in all of the investigations. The mixture was vortexed for 3 min, and 2 mL of distilled water and 14 mL of ether were added. The mixture was then shaken for 15 min in a shaker (Eberbach and Son Inc.). Samples were centrifuged for 5 min at 2500 rpm. The ether layer was then transferred into a 15-mL conical bottom centrifuge tube and evaporated to dryness using a Savant SpeedVac System (Model SC110). The residue was redissolved in 2 mL of MeOH, and 1 mL of 25 mM HCl was added along with 7 mL of hexane. This mixture was then shaken for 5 min and centrifuged for 5 min. The hexane layer was then aspirated off and discarded. An additional 7 mL of hexane was added to the remaining components, shaken for 5 min, then centrifuged for 5 min. The hexane layer was aspirated off and then 1 mL of 25 mM NaOH was added to the tube along with 7 mL of ether. This mixture was then shaken for 10 min and then centrifuged for 5 min. The ether layer was then transferred to a conical bottom centrifuge tube and evaporated to dryness. The residue was reconstituted in 150 μL of MeOH just before analysis.

Standard Curve Preparation. The standard curve was prepared using whole blood blanks and methanol solutions of CsA and CsD; nine samples with different CsA concentrations (0, 25, 50, 100, 250, 500, 1000, 1375, and 2000 ng/mL) were used. The standard samples were then prepared for analysis following the procedure described above, starting with addition of the internal standard.

Standard Sample Preparation. To measure the accuracy and precision of the TOF-MS analysis, 10 samples were prepared using blank whole blood; 5 contained 150 ng/mL CsA and 5 contained 1.5 μg/mL CsA. In addition to these 10 samples, 3 other samples with CsA concentrations of 1375, 1000, and 500 ng/mL were prepared to correct for any changes in the standard curve. All 13 samples contained 625 ng/mL CsD as an internal standard. The accuracy of both TOF-MS methods was determined by use of the mean concentrations which was determined from the five samples for each concentration. The accuracy is reported as the relative error (RE). RE is the absolute error expressed relative to the size of the measured quantity. The precision of both TOF-MS methods was determined by use of the five samples for each concentration; it is expressed as the coefficient of variation (CV). CV is the standard deviation expressed as a percentage of the mean.

Transplant Patient Samples. Whole blood samples from five transplant patients receiving CsA were obtained from the University of Pittsburgh Medical Center (UPMC). Patient samples were analyzed to document the capability of the TOF-MS methods to measure CsA in the presence of its metabolites and other medication administered to transplant patients. Samples from transplant patients were processed by use of the extraction procedure described above. In addition, three more standard samples were prepared as described in the standard sample preparation section to make slope corrections for the standard curve. Samples 1, 2, 4, and 5 were from patients who received heart transplants and sample 3 was from a lung transplant patient.

RESULTS AND DISCUSSION

Standard Curve. *TOF-SIMS.* Figure 1 shows the molecular structures of CsA (1202 Da) and CsD (1216 Da), the only difference being the nature of the R group. Figure 2 shows the positive secondary-ion mass spectrum of a blood extract containing 100 ng/mL CsA and 625 ng/mL CsD obtained from an etched silver substrate. The dominant peaks are due to CsA and CsD cationized with Ag. The weaker peaks in the spectrum are due to protonated CsA and CsD; both components are cationized with Na. Note that the high resolution of the TOF-SIMS allows the isotopic distributions of the peaks to be resolved.

The limit of detection (LOD) and limit of quantification (LOQ) were calculated from the signal-to-noise ratio (S/N) for CsA. The LOD and LOQ were defined as 3 and 10 times the S/N ratio, respectively. The LOD for CsA was determined

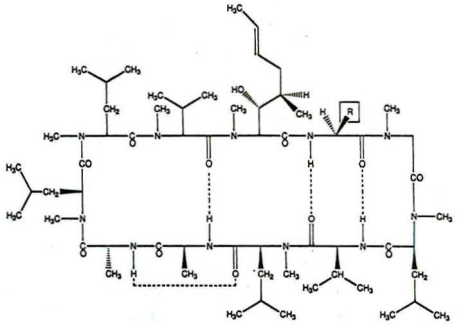

Cyclosporin A: R = -CH_2-CH_3
Cyclosporin D: R = -$CH(CH_3)_2$

Figure 1. Molecular structures of cyclosporins A and D.

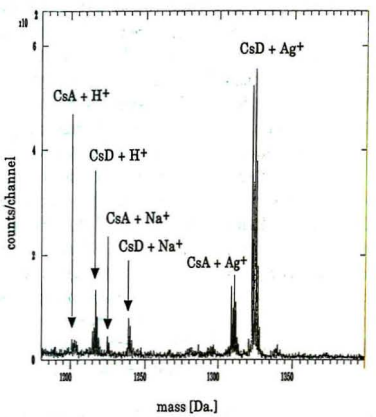

Figure 2. TOF-SIMS spectrum of a blood extract containing 100 ng/mL CsA and 625 ng/mL CsD.

to be 7 ng/mL and the LOQ was found to be 23 ng/mL, both using an initial blood sample of 1 mL. Since the sample is finally reconstituted in 150 μL of MeOH, this results in concentrating the sample by a factor of 6. Only 3 μL of this reconstituted residue is used for TOF-SIMS analysis, which is deposited onto an etched silver substrate with an area of 150 mm^2. The TOF-SIMS ion beam only samples a 50-μm diameter spot; thus, sample consumption is calculated to be in the low-femtomole range. Since sample consumption from the Ag substrate is minimal; saving the standard curve substrates would allow reproduction of the standard curve without extraction of new standard blood samples. Currently, experiments are being conducted to determine the length of time the standard curve extracts are stable on Ag substrates. After storage of the Ag substrates in a desiccator at room temperature for 2 months, the extracts proved to be stable and still generated a linear response. All results reported herein did not utilize this approach.

The plot of the ratio of the peak integral values $(CsA + {}^{107}Ag)^+/(CsD + {}^{107}Ag)^+$ vs CsA concentration was fit using linear least-squares regression. A linear response was obtained over the concentration range 25–2000 ng/mL. The equation of the line is $y = 0.00172x + 0.115$, where y is the intensity ratio and x is the concentration of CsA in nanograms per milliliter. The relative standard deviation of the slope was 0.87% with a correlation coefficient (r_0) of 0.998. The error in the ratio $(CsA + Ag)^+/(CsD + Ag)^+$ was determined to range from 2.3 to 9.0%. Since these errors add in quadrature, i.e., $[(\sigma_{\text{intensity ratio}})^2 + (\sigma_{\text{slope}})^2]^{1/2}$, the accuracy for a single CsA determination is better than 10%. All standard and clinical samples were measured using this calibration curve.

MALDI/TOF-MS. Mass spectra of extracts from blood containing CsA and CsD showed Na-cationized peaks and also weaker cationized peaks of both components with K. These weaker peaks led to an interference because $(CsD + Na)^+$ (1239 Da) and $(CsA + K)^+$ (1241 Da) overlap due to insufficient mass resolution. This interference is a problem only when CsA concentrations exceed 1000 ng/mL. In addition, samples from transplant patients contain metabolites, in particular, the hydroxylated CsA (1241 Da) component interferes with the $(CsD + Na)^+$ peak. Knowing that these interferences exist, the data were analyzed by damped nonlinear least-squares curve fitting (NLLSCF)[31–33] to resolve the overlapping peaks. The methodology to curve fit the envelope involved the use of parameters (e.g., the masses of the components in the envelope and their fwhm) derived from analysis of the components separately. The mass of each component in the system, CsA, CsD, and the hydroxylated metabolite, is already known; thus, the separation between the peaks is also known. A goodness-of-fit parameter (REX% = (maximum residual/peak height) × 100)[34] was used to assist curve fitting. Lower REX% values indicate better agreement between the experimental and theoretical spectra.

An important aspect of quantitative analysis using the MALDI/TOF-MS technique is sample preparation, particularly selecting the matrix. The use of 4-hydroxy-3-methoxycinnamic acid (ferulic acid)[35] gave reproducible and linear response (1.63% RSD_{slope}) over more than two decades of concentration for an insulin/cytochrome c system,[24] with a strong signal from the protonated molecules. Unfortunately, this matrix forms several types of crystals, which leads to extensive sample heterogeneity. This heterogeneity requires identification and use of only one type of crystal, which complicates the analysis. Another common and widely used matrix is 3,5-dimethoxy-4-hydroxycinnamic acid (sinapinic acid);[35] however, this matrix does not yield good shot-to-shot signal reproducibility.[25] Attempts to control the crystallization process have not yet led to any significant improvement.

We found that 2,5-dihydroxybenzoic acid (DHB)[36] can be applied successfully for quantitative analysis. The more homogeneous crystal structures yield strong molecular signals and good shot-to-shot reproducibility, which makes this matrix attractive for quantitative analysis. Another reason to prefer the DHB matrix is that the matrix peaks do not interfere with components to be analyzed. Figure 3 shows the positive-ion

(31) Proctor, A.; Hercules, D. M. *Appl. Spectrosc.* **1984**, *38*, 505.
(32) Ansell, R. O.; Dickinson, T.; Povey, A. F.; Sherwood, P. M. A. *J. Electronanal. Chem.* **1979**, *98*, 79.
(33) Nakamura, R.; Pioch, D.; Bowman, R. G.; Burwell, R. L., Jr. *J. Catal.* **1985**, *93*, 388.
(34) Fiedor, J. N.; Proctor, A; Houalla, M.; Hercules, D. M. *Surf. Interface Anal.* **1993**, *20*, 1.
(35) Beavis, R. C.; Chait, B. T. *Rapid Commun. Mass Spectrom.* **1989**, *3*, 436.
(36) Strupat, K.; Karas, M.; Hillenkamp, F. *Int. J. Mass Spectrom. Ion Processes* **1991**, *111*, 89.

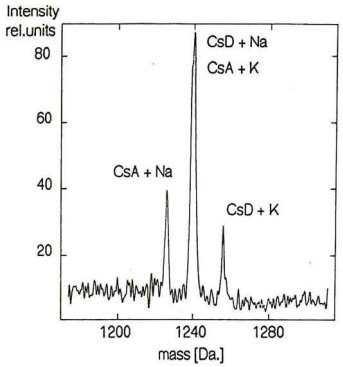

Figure 3. MALDI/TOF-MS spectrum of a blood extract containing 100 ng/mL CsA and 625 ng/mL CsD.

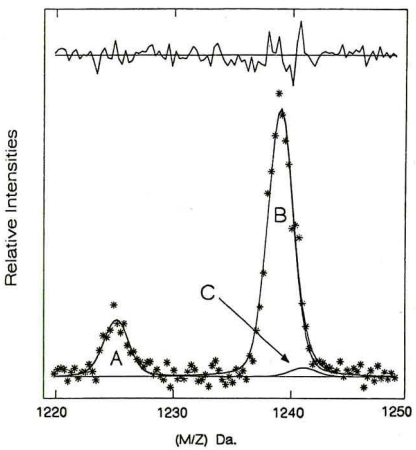

Figure 4. Curve-fitted MALDI/TOF-MS spectrum of a blood extract containing 100 ng/mL CsA and 625 ng/mL CsD: (A) $(CsA + Na)^+$, (B) $(CsD + Na)^+$, and (C) $(CsA + K)^+$.

laser mass spectrum obtained from a blood extract containing 100 ng/mL CsA and 625 ng/mL CsD after preparation in the DHB matrix. The main peaks of CsA and CsD are due to each component being cationized with Na. As mentioned previously, the mass spectrum also contains weaker cationized peaks of both components with K. The curve-fitted spectrum for the same standard sample is shown in Figure 4. The peak at 1225 Da was fit with only one peak, $(CsA + Na)^+$ (A). The envelope with the centroid at 1239 Da was fit using two peaks, one due to $(CsD + Na)^+$ (B) and the other to $(CsA + K)^+$ (C). The $(CsA + K)^+$ peak contributes less than 4% to the overall fit; i.e., the intensity is never substantial. The LOD was determined to be 10 ng/mL for this technique. Since we only use about $^1/_{30}$ of the crystal, the absolute detection limit is estimated to be in the low-femtomole range.

A plot of the ratio of integral values of $(CsA + Na)^+/(CsD + Na)^+$ vs CsA concentration resulted in a linear response from 25 to 2000 ng/mL. The equation of the line was $y = 0.00195x + 0.0858$, where y in the intensity ratio and x is the concentration of CsA in nanograms per milliliter. The relative standard deviation of the slope is 1.36% and $r_0 = 0.997$. The error in the intensity ratio ranges from 3 to 10%. These errors also add in quadrature, allowing an accuracy of a single determination better than 11%. All standard and clinical sample concentrations were determined using this curve.

Table 1. Comparison of Standard Samples

std sample conc (ng/mL)	TOF-SIMS mean conc (ng/mL)	TOF-SIMS CV (%) (RE (%))	MALDI mean conc (ng/mL)	MALDI CV (%) (RE (%))
150	149	5.0 (0.67)	150	8.1 (0)
1500	1468	3.5 (2.1)	1504	4.0 (0.27)

Standard Samples. The therapeutic range of CsA in blood is difficult to establish;[37] however, the range of 25–2000 ng/mL covers all patient groups. Monitoring of trough levels, i.e., just before the next dose, appears to be the most practical approach. For patients doing well, the typical trough levels of CsA in whole blood range from 100 to 300 ng/mL by the HPLC method.[2] The accuracy and precision of the standard HPLC method has been previously documented;[38–40] the accuracy reported for the HPLC method was typically better than 10% and the coefficient of variation ranged from 5 to 15%, depending on sample concentration. The results reported in this paper are compared with the HPLC statistics cited above. Spiked blood samples were used to determine the precision and accuracy of measurements using the TOF-SIMS and MALDI/TOF-MS methods. The real blood samples were first analyzed by a nonspecific method, FPIA, to give an estimate of the CsA concentration. This method overestimates the CsA concentration by a factor of 1–10, depending on when the sample was collected (metabolism increases with time) and whether the liver is functioning properly (most metabolism occurs in the liver), because it measures some CsA metabolites.[41]

Table 1 shows the results from standard samples measured by both TOF-MS analytical methods. The TOF-SIMS results from the five samples were averaged and the mean concentration used to determine the accuracy and precision when multiple extractions of the same sample are carried out. The accuracy (RE) ranged from 0.67 to 2.1% with CVs ranging from 3.5 to 5.0%. The above results provide information about the distribution of error in the measurement of a single sample. This information can be used to determine the confidence interval of the mean ($CIM_{95\%}$). The $CIM_{95\%}$ is defined as follows:

$$\mu = \bar{X} \pm tS/N^{1/2}$$

where μ is the true concentration of the sample, $\bar{X}$ the experimental mean, t is the t statistic at a confidence level of 95%, and $S/N^{1/2}$ is the standard error in the mean. For the 150 ng/mL sample, the $CIM_{95\%}$ is $\mu = 149 \pm 9$ ng/mL. The value of a single CsA determination would be, at worst, 149 ng/mL − 9 ng/mL = 140 ng/mL. Assuming that μ is known exactly since it is a standard sample, the accuracy (RE) of

(37) Bowers, L. D. *Clin. Biochem.* **1991**, *24*, 81.
(38) Holt, D. W.; Marsden, J. T.; Johnston, A. *Transplant. Proc.* **1990**, *22*, 1234.
(39) Bowers, L. D. *Transplant. Proc.* **1990**, *22*, 1150.
(40) Wong, P. Y.; Mee, A. V.; Glenn, J.; Keown, P. A. *Clin. Biochem.* **1991**, *24*, 59.
(41) Burckart, G. J.; Jain, A.; Diven, W.; Venkataramanan, R.; Starzl, T. E. *Transplant. Proc.* **1990**, *22*, 1319.

a measurement at this concentration would be 6.7%. Similarly, for a 1500 ng/mL sample, the $CIM_{95\%}$ is $\mu = 1468 \pm 64$ ng/mL. The value of a single CsA determination at this level, at worst would be 1468 ng/mL – 64 ng/mL = 1404 ng/mL, which corresponds to an accuracy of 6.4%. All of these results are within the TOF-SIMS standard curve statistics.

The MALDI/TOF-MS results were interpreted in the same way as the TOF-SIMS results. The accuracy (RE) was 0% for 150 ng/mL and 0.27% for 1500 ng/mL with CVs ranging from 4.0 to 8.1% when multiple extractions are carried out. For a single extraction of a sample with 150 ng/mL, the $CIM_{95\%}$ is $\mu = 150 \pm 15$ ng/mL, allowing a minimum accuracy of a single CsA determination of 10%. The 1500 ng/mL sample resulted in a $CIM_{95\%}$ of $\mu = 1504 \pm 74$ ng/mL, allowing a minimum accuracy of one CsA determination of 5.2%. All of these results are within the MALDI/TOF-MS standard curve statistics.

The mean concentrations given by each technique can be compared to determine whether they are statistically different or not using the *t* test at the 99% confidence level. For both the 150 and 1500 ng/mL standard samples, the mean concentrations by the two TOF-MS methods were not statistically different.

Comparison of TOF-MS Statistics with HPLC Statistics. As previously mentioned, HPLC has an accuracy of better than 10% with CVs ranging from 5 to 15%, depending on sample concentration. By comparison, the TOF-SIMS method has proved to be accurate within 10% with CVs ranging from 3.5 to 5.0%. The MALDI/TOF-MS method has been proven to quantify CsA with an accuracy of 11% or better with CVs ranging from 4.0 to 8.1%. On the basis of the small number of samples run, the TOF-SIMS method appears to have both accuracy and percision comparable to HPLC. Similarly, the MALDI/TOF-MS method appears to be slightly less accurate than HPLC, but the precision looks somewhat better.

Samples from Transplant Patients. *TOF-SIMS.* Figure 5, from top to bottom, shows the positive secondary-ion mass spectrum of transplant sample 1 (A), the theoretical isotopic distribution of $(CsD + Ag)^+$ (B), that of the CsA hydroxylated metabolite (C), and a composite of components B and C at 85 and 15%, respectively. Note that the TOF-SIMS spectral pattern (A) is very similar to the $CsD + Ag^+$ theoretical pattern (B) but does not match it exactly, indicating the presence of another component. The most pronounced difference between spectra A and B is in the relative intensities at 1325 and 1328 Da. This difference in intensity is most likely due to the CsA hydroxylated metabolite. This metabolite does not cause interference with CsA concentration determinations because when the CsD integral is calculated, only the $(CsD + {}^{107}Ag)^+$ is used and the difference in mass between $(CsD + {}^{107}Ag)^+$ and $(CsA - H + OH + {}^{107}Ag)^+$ is 2 Da, which is mass resolved in the TOF-SIMS. Although (C) resembles the TOF-SIMS spectral pattern (A) less than (B), it appears that (C) may also be present. When a composite theoretical spectrum is created with 85% B and 15% C, the theoretical and experimental spectra now look almost identical. This indicates that the TOF-SIMS is detecting CsA and its metabolites simultaneously, providing additional information about the sample.

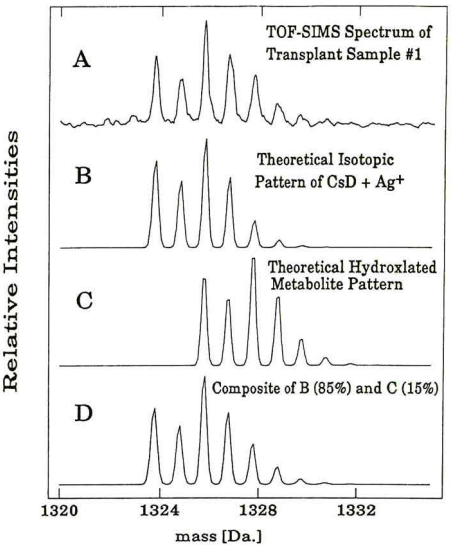

Figure 5. TOF-SIMS spectra.

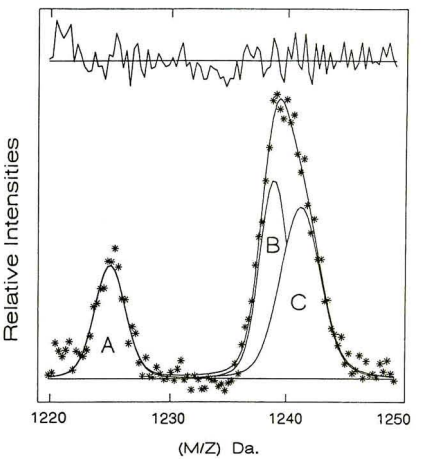

Figure 6. Curve-fitted MALDI/TOF-MS spectrum of transplant sample 1: (A) $(CsA + Na)^+$, (B) $(CsD + Na)^+$, and (C) $(CsA + K)^+$ and (CsA hydroxylated metabolite + $Na)^+$.

MALDI/TOF-MS. Figure 6 shows the curve-fitted positive-ion laser mass spectrum of transplant sample 1. The peak at 1225 Da (A) is fit with only one peak, indicating no interference from metabolites. Recall that in the standard sample (Figure 4) the fitted peak at 1241 Da (C) is very small (<2%) relative to the same peak (41%) in the transplant sample spectrum in Figure 6. The increase in intensity of the fitted peak with the centroid at 1241 Da in the transplant sample is attributed to the hydroxylated metabolite of CsA. Hence, like TOF-SIMS, MALDI/TOF-MS can provide metabolite information, at least in principle.

Comparison of Analytical Methods. Table 2 shows the concentration of CsA in blood samples from transplant patients

Table 2. Comparison of Transplant Patient Samples

	CsA (ng/mL)			
sample	FPIA	HPLC	TOF-SIMS	MALDI/TOF-MS
1	703	188	180	174
2	608	110	120	138
3	922	212	160	166
4	699	581	543	520
5	715	228	198	286

as measured by FPIA, HPLC, and both TOF-MS methods. As expected, FPIA overestimated the CsA concentration in all samples when compared to the results of the other methods, due to its lack of specificity. The HPLC and both TOF-MS results indicate that FPIA overestimated CsA concentrations by a factor of 1.2–5.8. This is consistent with previously reported results.[41]

Comparison of the TOF-MS methods indicates that samples 1–4 gave the same results by both, taking into account the expected error in this concentration range; however, sample 5 did not. This is explained by the curve-fitting results of the MALDI/TOF-MS spectra. We found that the experimental spectrum must have a resolution of about 400 (fwhm) to obtain meaningful results from NLLSCF. Sample 5 is the only spectrum out of the five samples with a resolution below 400 which resulted in a large range where the REX% was minimized, which led to a large uncertainty in the CsD peak area. The result reported was calculated by averaging all of the curve fits when the REX% was minimized.

A correlation plot of the HPLC data vs the TOF-SIMS method was obtained and resulted in a correlation coefficient of 0.992 with a y intercept of –5.5. Similarly, the MALDI/TOF-MS method correlated with the HPLC results giving a correlation coefficient of 0.968 with a y intercept of 37. Hence, taking into account the uncertainty of the measurements, both TOF-MS methods agree with the HPLC results.

In conclusion, we have documented that CsA can be quantified in blood by two TOF-MS methods. The TOF-MS methods developed to quantify CsA potentially offer many advantages. First, both TOF-MS methods have lower detection limits than HPLC. Second, since both TOF-MS methods consume very little sample, the extraction of a standard curve is unnecessary on a routine basis. Third, the simultaneous detection of CsA metabolites can offer more information about each transplant patient, and potentially, the metabolites can be quantified. Last, HPLC methodology requires extensive sample preparation due to other components in the blood absorbing UV radiation, but both TOF-MS methods potentially allow elimination of some extraction steps due to the high specificity of these methods. Work on this latter point is continuing.

CONCLUSIONS

Quantitative CsA data have been obtained from TOF-SIMS and MALDI/TOF-MS spectra for synthetic and real blood samples. The intensity ratio of (CsA/CsD) is reproducible [CVs = 3–5% (TOF-SIMS) and 4–8% (MALDI-TOF-MS)] and standard samples are within experimental error (ca. ±10%) of the standard curve. The influence of TOF-SIMS and MALDI/TOF-MS instrumental parameters and other factors influencing desorption and ionization were overcome by using an internal standard. The accuracy of both TOF-MS methods was better than 11% for blood samples from transplant patients.

ACKNOWLEDGMENT

This work was supported by the National Science Foundation under Grant CHE-9022135. D.C.M. thanks Andrew (Jack) Sharkey for valuable discussions from the onset of this project. We also thank Prof. A. Benninghoven and the Münster group for their help in the TOF-SIMS work.

Received for review September 22, 1993. Accepted April 26, 1994.[⊗]

[⊗] Abstract published in *Advance ACS Abstracts,* June 1, 1994.

Anal. Chem. **1994,** *66,* 2369–2373

Open Channel Electrochromatography on a Microchip

Stephen C. Jacobson, Roland Hergenröder, Lance B. Koutny, and J. Michael Ramsey*

Chemical and Analytical Sciences Division, Oak Ridge National Laboratory, Oak Ridge, Tennessee 37831-6142

A glass microchip having a channel with a cross section of 5.6 μm high and 66 μm wide was fabricated using standard photolithographic and etching techniques. The surface of the channel was chemically modified with octadecylsilane to function as the stationary phase for open channel chromatography. Electroosmotic flow was used to "load" the sample into the microchip and to "pump" the mobile phase during the experiments. For electric field strengths in the separation column from 27 to 163 V/cm, the linear velocity for the electroosmotic flow ranged from 0.13 to 0.78 mm/s. Detection was performed using direct fluorescence for separation monitoring and indirect fluorescence for void time measurements. Plate heights as low as 4.1 and 5.0 μm were generated for unretained and retained components, respectively.

Compact, reliable, and inexpensive instrumentation is desirable for a number of chemical measurement problems including field surveys, on-line process control, and remote sensing. One approach to this problem is the microfabrication of conventional chemical instrumentation. Micromachining using standard lithographic and etching techniques is one method for fabricating these miniature devices.[1] Chemical separation devices appear to be particularly amenable to microfabrication. Micromachined substrates have been produced for gas chromatography,[2] liquid chromatography,[3] and capillary electrophoresis.[4-9] In the case of liquid chromatography, no experimental demonstration has been presented. Liquid chromatography is a common method for separating and analyzing neutral species. Implementing liquid chromatography on a microchip simply requires packing of the separation channel with a separation phase or chemically modifying the channel wall for open channel operation. The latter approach was taken here. The reduced dimensions of microchip separation devices have the potential advantage that the contribution of the resistance to mass transfer decreases as the dimensions of the channel decrease.[10] Consequently, shorter columns and higher mobile-phase velocities can be used, resulting in shorter analyses times.

An important issue to resolve is the method by which to pump the mobile phase during the experiments. The technically simplest method to implement on the microchip substrate is electroosmosis[11,12] because no moving parts are required. In capillary liquid chromatography, electroosmotic "pumping" of the mobile phase has been demonstrated for both packed[13,14] and open[15] capillaries. By pumping the mobile phase with electroosmosis, the flow profile of the mobile phase is nearly flat. Conversely, pressure-driven capillary liquid chromatography has a Poiseuille flow profile, and consequently, the resistance to mass transfer for the mobile phase is approximately 2 times higher for a pressure-driven system than an electroosmotically driven system.[16] Experimental verification of this has been demonstrated.[14] The benefits of the electroosmotic flow also are seen in the manipulation of the sample during injection on a microchip. By loading the sample onto the column with electroosmotic flow, valveless, time-independent, nonbiased injections can be made with high reproducibility.[8]

In the case of open tubes, as the diameter of the capillary decreases, the resistance to mass transfer for the mobile phase decreases, but other problems arise. The amount of sample that can be injected without overloading the column is proportional to the surface area of the capillary and may fall below the limits of detection. Detection for path length dependent schemes becomes instrumentally prohibitive. Also, injection and detection volumes must be scaled proportionally to prevent excessive contributions to band broadening. One solution is to fabricate columns that have a high aspect ratio, i.e., channel width to channel height. This affords improved mass transfer in one dimension while the sample load, detection path length, and detection volume are maintained in the other dimension. For a flat flow profile comparable plate heights between a capillary and a channel with a high aspect ratio are obtained if the height of the channel is approximately 0.6 times the diameter of the capillary.[17] Using field flow fractionation (FFF) technology, channels with aspect ratios up to 1500 have been fabricated, chemically modified, and used for gas[18] and liquid chromatography.[19,20]

(1) Manz, A.; Fettinger, J. C.; Verpoorte, E.; Lüdi, H.; Widmer, H. M.; Harrison, D. J. *Trends Anal. Chem.* **1991,** *10,* 144.
(2) Terry, S. C.; Jerman, J. H.; Angell, J. B. *IEEE Trans. Electron Devices* **1979,** *26,* 1880.
(3) Manz, A.; Miyahara, Y.; Miura, J.; Watanabe, Y.; Miyagi, H.; Sato, K. *Sens. Actuators* **1990,** *B1,* 249.
(4) Manz, A.; Harrison, J.; Verpoorte, E. M. J.; Fettinger, J. C.; Paulus, A.; Lüdi, H.; Widmer, H. M. *J. Chromatogr.* **1992,** *593,* 253.
(5) Harrison, D. J.; Manz, A.; Fan, Z.; Lüdi, H.; Widmer, H. M. *Anal. Chem.* **1992,** *64,* 1926.
(6) Seiler, K.; Harrison, D. J.; Manz, A. *Anal. Chem.* **1993,** *65,* 1481.
(7) Harrison, D. J.; Fluri, K.; Seiler, K.; Fan, Z.; Effenhauser, C. S.; Manz, A. *Science* **1993,** *261,* 895.
(8) Jacobson, S. C.; Hergenröder, R.; Koutny, L. B.; Warmack, R. J.; Ramsey, J. M. *Anal. Chem.* **1994,** *66,* 1107.
(9) Jacobson, S. C.; Hergenröder, R.; Koutny, L. B.; Ramsey, J. A. *Anal. Chem.* **1994,** *66,* 1114.
(10) Golay, M. J. E. In *Gas Chromatography*; Desty, D. H., Ed.; Butterworths: London, 1958; p 36.
(11) Burgreen, D.; Nakache, F. R. *J. Phys. Chem.* **1964,** *68,* 1084.
(12) Rice, C. L.; Whitehead, R. *J. Phys. Chem.* **1965,** *69,* 4017.
(13) Jorgenson, J. W.; Lukacs, K. D. *J. Chromatogr.* **1981,** *218,* 209.
(14) Knox, J. H.; Grant, I. H. *Chromatographia* **1987,** *24,* 135.
(15) Tsuda, T.; Kazuhiro, N.; Nakagawa, G. *J. Chromatogr.* **1982,** *248,* 241.
(16) Martin, M.; Guiochon, G. *Anal. Chem.* **1984,** *56,* 614.
(17) Giddings, J. C. *J. Chromatogr.* **1961,** *5,* 46.
(18) Martin, M.; Jurado-Baizaval, J.-L.; Guiochon, G. *Chromatographia* **1984,** *16,* 98.

0003-2700/94/0366-2369$04.50/0
© 1994 American Chemical Society

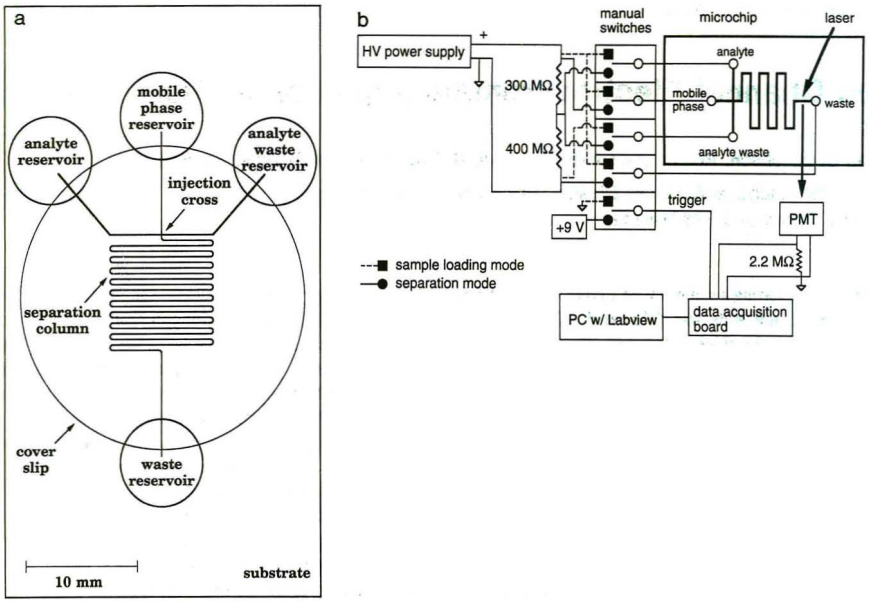

Figure 1. (a) Schematic of the microchip with a serpentine column geometry. (b) Diagram of the high-voltage switching apparatus and detection/data acquisition system.

In this paper, a microchip was fabricated to perform electrochromatography in open channels. Laser-induced fluorescence was used to monitor the separations directly and the void time indirectly. The mechanisms for band broadening are discussed, and calculated values for flat flow profiles are compared to experimental values.

EXPERIMENTAL SECTION

The channels on the glass microchip substrate were fabricated using standard photolithographic techniques and chemical wet etching.[21] The micromachined substrate and cover plate were joined using a direct bonding technique as described previously.[8] Figure 1a shows a schematic of the column design implemented for the experiments. The serpentine column geometry has enclosed column lengths of 6.4 mm from the buffer reservoir to the injection cross, 9.4 mm from the analyte and analyte waste reservoirs to the injection cross, and 171 mm from the waste reservoir to the injection cross. The serpentine column design enables a long column length to be fabricated within a compact area. On this microchip a separation column length of 165 mm is fabricated within a 8 mm × 8 mm area. Only an 11-mm straight separation column design could be fabricated in the same space.

Because the substrate is glass and the channels are chemically wet etched, an isotropic etch occurs; i.e., the glass etches uniformly in all directions, and the resulting channel geometry is trapezoidal. Figure 2 shows the profile of the channel cross section with dimensions of 5.6 μm high and 72 μm wide at the top and 60 μm wide at the bottom. The dimensions were obtained using a profilometer (Alpha-Step 200, Tencor Instruments). The aspect ratio for the channel is

$$\beta = w_{0.5}/h \tag{1}$$

where $w_{0.5}$ is the channel width at half-height and h is the channel height. From the channel profile in Figure 2, $w_{0.5}$ and h are 66 and 5.6 μm, respectively, corresponding to an aspect ratio of 12.

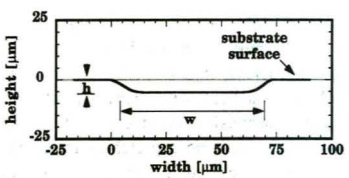

Figure 2. Measured profile of channel cross section with $h = 5.6$ μm and $w_{0.5} = 66$ μm.

After bonding the cover plate to the substrate and thereby enclosing the channels, the reverse-phase coating was chemically bonded to the walls of the channels.[22] First, the waste reservoir was affixed to the substrate via epoxy to act not only as a reagent vessel but also as a connection to a helium supply. The column was treated with 1 M sodium hydroxide and then rinsed with water. The column was dried at 125 °C for 24 h while being purged with helium at a gauge pressure of

(19) Martin, M.; Jurado-Baizaval, J.-L.; Guiochon, G. *C.R. Acad. Sc. Paris, Ser. II* **1982**, *295*, 579.
(20) Giddings, J. C.; Chang, J. P.; Myers, M. N.; Davis, J. M.; Caldwell, K. D. *J. Chromatogr.* **1983**, *255*, 359.
(21) For example: Ko, W. H.; Suminto, J. T. In *Sensors*; Gopel, W., Hasse, J., Zennel, J. N., Eds.; VCH: Weinhein, Germany, 1989; Vol. 1, pp 107–168.
(22) For example: Jorgenson, J. W.; Guthrie, E. J. *J. Chromatogr.* **1983**, *255*, 335.

approximately 50 kPA. A 25% (w/w) solution of chlorodimethyloctadecylsilane (ODS, Aldrich) in toluene was loaded into the waste reservoir and pumped into the channel with an overpressure of helium at approximately 90 kPa. The ODS/toluene mixture was pumped continuously into the column throughout the 18-h reaction period at 125 °C. The channel was rinsed with toluene and then with acetonitrile to remove the unreacted ODS.

The separations were monitored on-microchip via fluorescence using an argon ion laser (351.1 nm, Coherent Innova 90) for excitation and a photomultiplier tube (PMT, Oriel 77340) to collect the fluorescence signal. The PMT, with collection optics, was situated below the microchip with the optical axis perpendicular to the microchip surface. The laser was operated at approximately 20 mW, and the beam impinged upon the microchip at a 45° angle from the microchip surface and parallel to the separation channel. The laser beam and PMT observation axis were separated by a 135° angle. The power supply (Spellman CZE1000R) for the electrophoresis was operated between +0.63 and +3.8 kV relative to ground. Figure 1b shows a diagram of high-voltage switching apparatus and detection/data acquisition system. The high-voltage switches and leads were interlocked to prevent electrical shock. Platinum electrodes were inserted into the reservoirs for electrical contact. Higher voltages could not be utilized due to limitations of the manual switching apparatus (4 kV). The analytes used for the experiments were coumarin 440 (C440), coumarin 450 (C450) and coumarin 460 (C460, Exciton Chemical Co., Inc.) at 10 μM for the direct fluorescent measurements of the separations and 1 μM for the indirect fluorescent measurements of the void time. A sodium tetraborate buffer (10 mM, pH 9.2) with 25% (v/v) acetonitrile was the buffer in all experiments. Due care must be exercised with the Coumarin dyes because the chemical, physical, and toxicological properties have not been fully investigated.[23]

The microchip was operated under a "pinched sample loading" mode and a "separation" mode as described previously.[8] The sample is loaded into the injection cross via a frontal chromatogram traveling from the analyte reservoir to the analyte waste reservoir, and once the front of the slowest analyte passes through the injection cross, the sample is ready to be analyzed. The analyte flowing through the injection cross is both defined and confined by electroosmotic pumping of the buffer from the buffer and the waste reservoirs toward the analyte waste reservoir. To switch to the separation mode, the applied potentials are merely reconfigured by manually throwing a switch. Now the primary flow path for the separation is from the buffer reservoir to the waste reservoir. In order to inject a small analyte plug into the separation column and to prevent bleeding of the excess analyte into the separation column, the analyte and the analyte waste reservoirs are maintained at 57% of the potential applied to the mobile-phase reservoir. This three-way flow forces the excess analyte to pull away from the injection cross and prevents analyte from bleeding into the separation column. This method of loading and injecting the sample is time-independent, nonbiased, and reproducible.

A separation length of 58 mm was used for all experiments. At this distance the analytes were baseline resolved for all linear velocities, and the analysis times were not excessive. The void times were estimated indirectly by having C440 and C450 in the mobile phase and injecting a water plug. The composition of the injection plug therefore was 5 mM sodium tetraborate with 25% acetonitrile.

(23) Exciton Chemical Co., Inc.

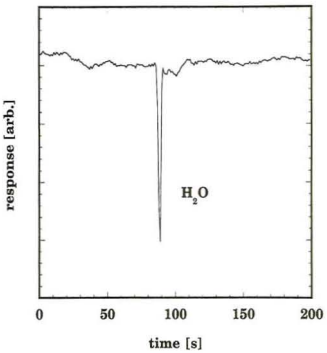

Figure 3. Indirect chromatogram of H_2O for void volumn measurement with u = 0.65 mm/s.

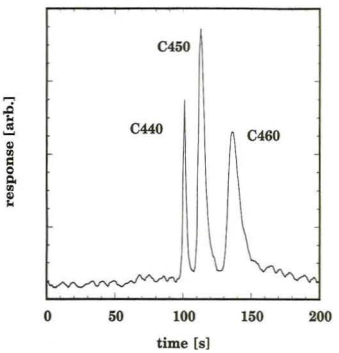

Figure 4. Chromatogram of C440, C450 and C460 with u = 0.65 mm/s.

RESULTS AND DISCUSSION

An indirect chromatogram of water at a linear velocity of 0.65 mm/s is depicted in Figure 3. Indirect fluorometry was a simple method for determining the mobile-phase velocity which was pumped electroosmotically. The presence of the low concentration of coumarins in the mobile phase was assumed not to affect the electroosmotic velocity. The highest linear velocity was 0.78 mm/s for an electric field strength in the separation column of 162 V/cm. This value compares well with the literature[15] and corresponds to a volumetric flow rate of 0.3 nL/s. In Figure 4, a chromatogram of the coumarins is shown for a linear velocity of 0.65 mm/s. The retention ratios and efficiency data from this separation are listed in Table 1. For C440, 11 700 plates were observed, which corresponds to 120 plates/s. The most retained component, C460, has an efficiency nearly 1 order of magnitude lower than C440, 1290 plates. The undulating background in the chromatograms is due to background fluorescence from the glass substrate and shows the power

Table 1. Retention and Efficiency Data for Chromatograms in Figures 3 and 4

compound	R	N	H (μm)
H_2O	1.0	13800	4.2
C440	0.91	11700	5.0
C450	0.79	2950	19.7
C460	0.64	1290	44.8

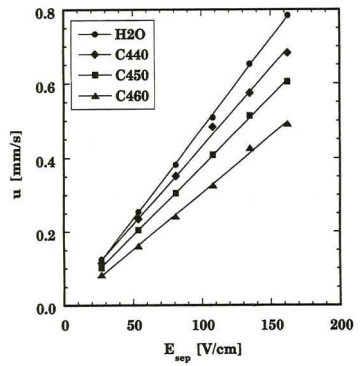

Figure 5. Variation of the linear velocity (u) with the electric field strength in the separation column (E_{sep}) for H_2O, C440, C450, and C460 with linear fits (lines).

instability of the laser. This, however, did not hamper the quality of the separations or detection. A compilation of the separations is plotted in Figure 5 as the variation of the linear velocities with the electric field strength in the separation channel. This figure demonstrates that over the span of time taken to perform the separations, no change in the column dynamics was observed; i.e., the bonded phase was stable. Also, the separation selectivity, α, can be calculated[24]

$$\alpha_{j,i} = (t_{Rj} - t_0)/(t_{R,i} - t_0) \tag{2}$$

where t_R is the elution time of a retained molecule, t_0 is the elution time of an unretained marker, i designates a less retained molecule, and j designates a more retained molecule. For the data in Figure 5, $\alpha_{C450,C440} = 2.44 \pm 0.13$ and $\alpha_{C460,C450} = 2.19 \pm 0.10$. This demonstrates that the separation selectivity is independent of the separation field strength.

The most important measure of a separation system is the plate height. The significant contributions to the total plate height for this system are

$$H_{tot} = H_{inj} + H_{det} + H_{geo} + H_{diff} + H_m \tag{3}$$

where H_{inj} is from the injection plug length, H_{det} is from the detector observation length, H_{geo} is from the column geometry, H_{diff} is from axial diffusion, and H_m is from mass transfer for the mobile phase. The contribution to the plate height from Joule heating is considered negligible for these experiments because the power dissipated was well below 1 W/m[25] and from resistance to mass transfer for the stationary phase because the film thickness formed from monochlorosilanes is small relative to the channel dimensions.[26]

The plate heights for the injection plug length, detector observation length,[27] and column geometry[8] are constant contributions for a given experiment and can be written

$$H_{inj} = l^2_{inj}/(12L_{sep}) \tag{4}$$

$$H_{det} = l^2_{det}/(12L_{sep}) \tag{5}$$

$$H_{geo} = n(w\theta)^2/(12L_{sep}) \tag{6}$$

where l_{inj} is the length of the injection plug, l_{det} is the detector observation length, L_{sep} is the separation length, n is the number of turns, w is the width of the channel, and θ is the angle of the turn. The band distortion due to a turn in the serpentine column geometry has been observed experimentally to be equal to the difference in the path lengths between the inside and outside of the channel.[8] Other phenomena such as electric field effects or eddy flow have not been observed, although these contributions are quite feasible.

The velocity-dependent terms of the plate height are axial diffusion and resistance to mass transfer to the mobile phase. For axial diffusion, the expression is[28]

$$H_{diff} = 2D_m/u \tag{7}$$

where D_m is the diffusion coefficient of the analyte in the mobile phase and u is the linear velocity of the mobile phase. The resistance to mass transfer for the mobile phase with infinitely parallel plates and plug flow is given by[17]

$$H_{m,h} = C_{m,h}u = {}^1/_6(1-R)^2h^2/D_m u \tag{8}$$

where R is the retention ratio, i.e., the void time, t_0, divided by the retention time of the analyte, t_R, and h is the height of the channel. The analogous expression for a capillary of diameter, d, is[17]

$$H_{m,d} = C_{m,d}u = {}^1/_{16}(1-R)^2d^2/D_m u \tag{9}$$

The ratio of eqs 8 and 9 is

$$H_{m,h}/H_{m,d} = {}^8/_3h^2/d^2 \tag{10}$$

Under conditions where the mass-transfer term dominates, comparable plate heights are produced by rectangular channels and capillaries when $h \approx 0.6d$. Consequently, with a rectangular channel geometry having a high aspect ratio, high efficiency is feasible without sacrificing detection path length or injection and detection volumes.

The constant contributions to the plate height for these experiments are calculated. The length of the injection plug is approximately 300 μm,[8] which corresponds to $H_{inj} = 0.13$ μm. The detection is on-microchip, and the channel length

(24) Karger, B. L.; Snyder, L. R.; Horvath, C. *An Introduction to Separation Science*; John Wiley and Sons: New York, 1973.
(25) Monnig, C. A.; Jorgenson, J. W. *Anal. Chem.* **1991**, *63*, 802.
(26) Knox, J. H. *J. Chromatogr. Sci.* **1980**, *18*, 453.
(27) Sternberg, J. C. *Adv. Chromatogr.* **1966**, *2*, 205.
(28) Giddings, J. C. *Dynamics of Chromatography, Part I: Principles and Theory*; Marcel Dekker: New York, 1965; Chapter 2.

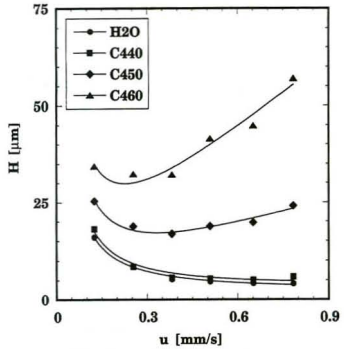

Figure 6. Variation of the plate height (H) with the linear velocity (u) for H_2O, C440, C450, and C460. Lines are eq 11 fitted to the experimental data.

Table 2. Fitted and Calculated Plate Height Coefficients for Figure 6

compound	D_m (mm²/s)	C_m (s)	$C_{m,h}$[a] (s)
H_2O	9.7×10^{-4}		
C440	1.0×10^{-3}	1.9×10^{-3}	4.2×10^{-5}
C450	1.4×10^{-3}	2.4×10^{-2}	2.3×10^{-4}
C460	1.6×10^{-3}	6.4×10^{-2}	6.8×10^{-4}

[a] Equation 8.

illuminated is equal to the laser spot size. Thus, l_{det} = 100 μm, and H_{det} = 0.014 μm. The contribution to the plate height from the column geometry is H_{geo} = 0.53 μm, which is calculated for one turn with an angle $\pi/2$ plus seven turns with an angle π and width of the channel at the top equal to 72 μm. The sum of all the constant contributions is 0.67 μm.

The experimental plate height data are plotted versus the linear velocity of the mobile phase in Figure 6. The following equation is fitted to these data:

$$H_{tot} = 2D_m/u + C_m u + 0.67\ \mu m \qquad (11)$$

with the determined coefficients listed in Table 2. The constant, 0.67 μm, is taken from experimental parameters rather than being determined in the fitting procedure to lend consistency to the values D_m and C_m. The values of the diffusion coefficients are slightly higher than expected (0.001 mm²/s); however, the number of data points in the low velocity region is few.

Equation 8 assumes infinitely parallel plates or, from a practical standpoint, rectangular channels with a large aspect ratio, e.g., $\beta > 400$, whereas $\beta = 12$ for this experiment. The calculated values for $C_{m,h}$ with a channel height of 5.6 μm with D_m = 0.001 mm²/s are listed in Table 2. The experimental values are 2 orders of magnitude larger than the calculated values for the channel. This difference may be attributed to the trapezoidal geometry of the channel cross section (Figure 2). The probability of a molecule contacting the bonded phase in the corners of the channel is higher than in the rest of the channel. If this is the case, then the band broadening would increase with increasing retention as observed. The cross section of the channel can be divided into three regions approximated by a right triangle on each end and a rectangle in the center. With this simple picture, the surface-to-volume ratio is 0.81 mm^{-1} for the triangular regions and 0.33 mm^{-1} for the rectangular region. Consequently, the velocity distribution of retained molecules for the trapezoidal channel geometry would be broader than in the case of infinitely parallel plates, leading to band broadening. The extent of this contribution is under further investigation.

In conclusion, the prospect of microchip devices for the separation of neutrals using electroosmotic pumping is promising. The band-broadening effects of the trapezoidal channel cross section on the separations require more study in order to improve the efficiencies. Ultimately, microchips with micromachined channels having a height of 1 μm and a width of 50 μm could offer the benefits of small contributions from resistance to mass transfer for the mobile phase with reasonable values for the injected volume, detection path length, and detection volume. The contribution of the serpentine column geometry to the total plate height ranges from 1 to 13%, depending on the analyte and the linear velocity of the mobile phase. This contribution can be minimized by decreasing the width of the channel, the angle of the turns, and the number of turns per unit length.

ACKNOWLEDGMENT

This research was sponsored by the U.S. Department of Energy (DOE), Office of Research and Development. Oak Ridge National Laboratory is managed by Martin Marietta Energy Systems, Inc. for the U.S. Department of Energy under Contract DE-AC05-84OR21400. Also, this research was sponsored in part by an appointment for S.C.J. to the Alexander Hollaender Distinguished Postdoctoral Fellowship Program sponsored by the U.S. DOE, for L.B.K. to the DOE Laboratory Cooperative Postgraduate Research Training Program, and R.H. to the ORNL Postdoctoral Research Associate Program. These programs are administered by the Oak Ridge Institute for Science and Education and ORNL. The authors acknowledge many useful discussions with Drs. Roswitha Ramsey and Georges Guiochon.

Received for review Janurary 4, 1994. Accepted April 14, 1994.[⊗]

[⊗] Abstract published in *Advance ACS Abstracts,* May 15, 1994.

Anal. Chem. **1994,** *66,* 2374–2381

Target Factor Modeling of Migration Behavior in Capillary Electrophoresis

Rachhpal S. Sahota† and Morteza G. Khaledi*

Department of Chemistry, North Carolina State University, Raleigh, North Carolina 27695-8204

This paper describes a target factor analysis based technique to model migration behavior in capillary electrophoresis (CE). The technique is effective in reducing the initial number of experiments required for modeling, as well as in recognizing the optimum conditions for running these experiments. The technique can be applied to optimize any number of parameters. The usefulness of the technique is demonstrated via both the experimentally obtained and the simulated data sets. Examples are provided to describe optimization of one and two parameters.

The introduction of various new separation mechanisms has broadened the scope of applications of capillary electrophoresis (CE). Micelles, cyclodextrins, complexing reagents, and organic modifiers include some of the recent introductions aimed at controlling solute migration and selectivity in CE. The choice of the type and concentration of these buffer modifiers can play an important role in improving the quality of CE separations. Besides water, a number of nonaqueous solvents can be used, advantageously, for specific applications.[1] The nature of the bulk solvent, supporting electrolytes, ionic strength, pH, temperature, the dimensions, and the surface chemistry of the capillary can all significantly influence the optimization process. Any attempt to optimize these parameters, through either brute force or trial and error methods, can be a frustrating endeavor. Development of effective methodologies, for modeling solute migration, and for optimization, is therefore important for a wider acceptance of CE.

In chromatography, two basically different approaches are popular for systematic optimization of separations. The first is the sequential approach. Simplex optimization falls into this category. In this approach, one selects a criterion for evaluating the goodness of a separation. The experimental parameters are changed sequentially to improve separation at each step, until an optimum is reached.[2] In the second approach, migration behavior of individual components is modeled as a function of the experimental parameters. The space of the experimental parameters is then searched for the global optimum.[3] The migration models can range from entirely empirical, regression-based approaches to physical models where the migration of a solute is defined in terms of physical properties of the solute and the separation system.

† Current address: Analytical Drug Development, Procter & Gamble Pharmaceuticals, Norwich, NY 13815.

(1) Sahota, R. S.; Khaledi, M. G. *Anal. Chem.* **1994,** *66,* 1141.
(2) Morgan, S. L; Deming, S. N. *J. Chromatogr.* **1975,** *112,* 267.
(3) Schoenmakers, P. J. *Optimization of Chromatographic Selectivity. A Guide to Method Development*; Elsevier: Amsterdam, 1986.

The area of capillary electrophoresis is so far lacking in attempts at developing efficient optimization strategies. Only a small number of reports have appeared in the literature that describe efforts at systematic optimization.[4–6] Most application reports have used trial and error approaches to achieve the desired separations. Since efficiencies of CE separations are high, such approaches often yield adequate results. However, a systematic approach to optimization should be considered in order to fully take advantage of the power of CE for the separation of complex mixtures.

Modeling of Electrophoretic Behavior in CE. Several models describing electrophoretic migration have been reported in the literature.[7–16] These models are derived either from fundamental equations describing electroneutrality, mass transport, dissociation equilibria, and conservation of mass and charge[7] or from phenomenological considerations of the mobility of completely ionized species and the fraction of any such species under the given experimental conditions.[11–16] Models have also been described to include additional phenomena of solute retention during an electrophoretic migration (e.g. partition of the solute into micelle in micellar electrokinetic chromatography (MEKC).[10–15] The proponents of such physical or semiempirical models have advocated their accuracy in describing the electrophoretic migration. There are, however, some practical problems associated with these approaches. The physical models describing zone electrophoresis usually include complex procedures for integration of the transport equations.[17] Also, the number of buffer modifiers, required to resolve difficult mixtures, may increase with increasing complexity of the mixture. Accordingly, the models, that include additional mechanisms of solute retention, will be complex.[4] Simplification may introduce

(4) Quang, C.; Khaledi, M. G. *J. Chromatogr.* **1994,** *659,* 459.
(5) Romano, J.; Jandik, P.; Jones, W. R.; Jackson, P. E. *J. Chromatogr.* **1991,** *546,* 411–421.
(6) Kuhr, W. G.; Yeung, E. S. *Anal. Chem.* **1988,** *60,* 2642–46.
(7) Bier, M.; Palusinski, O. A.; Mosher, R. A.; Saville, D. A. *Science* **1983,** *219,* 1281–1287.
(8) Mosher, R. A.; Dewey, D.; Thormann, W.; Saville, D. A.; Bier, M. *Anal. Chem.* **1989,** *61,* 362–66.
(9) Grossman, P. D.; Colburn, J. C.; Lauer, H. H. *Anal. Biochem.* **1989,** *179,* 28–33.
(10) Terabe, S.; Otsuka, K.; Ando, T. *Anal. Chem.* **1985,** *57,* 834.
(11) Ghowsi, K.; Foley, J. P.; Gale, R. J. *Anal. Chem.* **1990,** *62,* 2714–21.
(12) Khaledi, M. G.; Smith, S. C.; Strasters, J. K. *Anal. Chem.* **1991,** *63,* 1820–30.
(13) Strasters, J. K.; Khaledi, M. G. *Anal. Chem.* **1991,** *63,* 2503.
(14) Smith, S. C.; Khaledi, M. G. *J. Chromatogr.* **1991,** *586,* 221.
(15) Khaledi, M. G.; Quang, C.; Sahota, R. S.; Strasters, J. K.; Smith, S. C. Controlling Migration Behavior in Capillary Electrophoresis: Optimization Strategies for Method Development. In *Capillary Electrophoresis Technology*; Guzman, N. A., Ed.; Marcel Dekker, Inc.: New York, 1993.
(16) Smith, S. C.; Khaledi, M. G. *Anal. Chem.* **1993,** *65,* 193.
(17) Heinrich, J.; Wagner, H. *Electrophoresis* **1992,** *13,* 44–49.

0003-2700/94/0366-2374$04.50/0
© 1994 American Chemical Society

uncertainties in such models. Schoenmakers and Blaffert[18] have provided an elaborate account of model inaccuracies on selectivity optimization procedures. They examined several suggested models from the literature, depicting migration behavior in chromatography; none described the data with any reasonable accuracy. In empirical modeling on the other hand, predictions are based on the experimental data obtained under a limited set of experimental conditions. Recently, we reported successful application of empirical modeling for optimization of CE separation of a mixture of 14 metal cations. All components were completely separated in less than 4 min.[4] The modeling approach does not involve any explanation of the underlying mechanism of migration. As long as the variation due to a given parameter is embedded in the training set, it would be included in the model. All regression-based and factor analysis-based approaches fall into the category of empirical modeling. Although commonly employed in HPLC, empirical modeling has not been popular for optimizations in CE.

This report describes a target factor analysis (TFA) based procedure for modeling migration in capillary electrophoresis (CE). Target factor analysis has found many applications in chemistry. A detailed description of target transformation, along with a thorough discussion on the areas of application of factor analysis, is given by Malinowski and Howery.[19] The usefulness of target factor analysis has already been shown in predicting retention behavior in GC and in HPLC.[20-23]

Theory. This report describes a specific procedure, for applying factor analysis to retention modeling. The details of the theory of target factor analysis can be found elsewhere.[19,20] However, for the sake of completeness, a brief account of the factor analysis process is given here.

Let [D] represent an $\mathbf{m} \times \mathbf{n}$ data matrix that contains CE mobility at different buffer compositions, where **m** is the number of solutes in the mixture and **n**, mobility values at n different conditions, represents the dimensionality of the measurement space. Using factor analysis we can decompose [D] as

$$[\mathbf{D}] = [\mathbf{R}][\mathbf{C}] \tag{1}$$

where the $\mathbf{n} \times \mathbf{n}$ column matrix [C] represents the loadings and is composed of n eigen vectors. The $\mathbf{m} \times \mathbf{n}$ row matrix [R] represents scores and is a product of [D] and $[\mathbf{C}]^{-1}$.

If a smaller number, say **k**, of principal components can account for most of the variance in the data, [D] can be reproduced within reasonable error using only **k** eigen vectors from [C]. Accordingly dimensions of [R] will be reduced to $\mathbf{m} \times \mathbf{k}$. In other words, the migration behavior in CE can be fully described using k dimensions which leads to a fewer number of experiments. Equation 1 can then be rewritten as

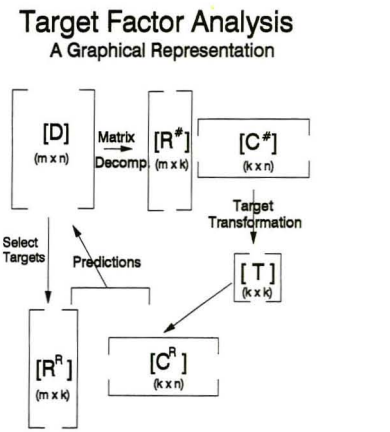

Figure 1. A schematic representation of the process of target factor modeling.

$$[\mathbf{D}^{\#}] = [\mathbf{R}^{\#}][\mathbf{C}^{\#}] \tag{2}$$

Here [D#] is the regenerated data matrix using only k eigen vectors and [R#] is the $\mathbf{m} \times \mathbf{k}$ row matrix. Each row of [R#] represents a data point in the space of the k principal components. The **k** column values of a row of [R#] represent k coordinates for that data point in this space. [C#] is the $\mathbf{k} \times \mathbf{n}$ column matrix, and each row of [C#] describes the position of a new principal component axis with respect to the original **n** axes.

[R#] and [C#] give us abstract solutions. The objective of target transformation is to convert these abstract solutions into real, physically meaningful solutions. In the target transformation phase, [R#] is then replaced by an $\mathbf{m} \times \mathbf{k}$ matrix $[\mathbf{R}^{\mathrm{R}}]$ of the real or physically meaningful coordinates. To reproduce the data matrix using $[\mathbf{R}^{\mathrm{R}}]$, one has to replace [C#] by $[\mathbf{C}^{\mathrm{R}}]$ and eq 2 becomes

$$[\mathbf{D}^{\mathrm{R}}] = [\mathbf{R}^{\mathrm{R}}][\mathbf{C}^{\mathrm{R}}] \tag{3}$$

$[\mathbf{D}^{\mathrm{R}}]$ is intended to be as close to [D#] as possible. This transformation is brought about by a transformation matrix [T]. Equation 4 depicts the relationship of the matrices [R#] and [C#] with the matrices $[\mathbf{R}^{\mathrm{R}}]$ and $[\mathbf{C}^{\mathrm{R}}]$ via [T]. The data

$$[\mathbf{D}^{\#}] = [\mathbf{R}^{\#}][\mathbf{T}][\mathbf{T}]^{-1}[\mathbf{C}^{\#}] \tag{4}$$

matrix $[\mathbf{D}^{\mathrm{R}}]$ reproduced by eq 3 depends upon the choice of $[\mathbf{R}^{\mathrm{R}}]$ and can be very different from [D#], the matrix reproduced via eq 2. The goal of target transformation is to choose $[\mathbf{R}^{\mathrm{R}}]$ so as to minimize the difference between [D#] (or in fact [D]) and $[\mathbf{D}^{\mathrm{R}}]$. A schematic diagram describing the process is given in Figure 1. Detailed discussions on searching optimal $[\mathbf{R}^{\mathrm{R}}]$ from the available choices and computing the transformation matrix [T] can be found in ref 19.

Predictions. Let the $\mathbf{m} \times \mathbf{n}$ matrix [D], in Figure 1, represent CE data, where each row represents a different solute.

(18) Schoenmakers, P. J.; Blaffert, T. *J. Chromatogr.* **1987**, *384*, 117–133.
(19) Malinowski, E. R.; Howery D. G. *Factor Analysis in Chemistry*; John Wiley & Sons: New York, 1980.
(20) Lochmuller, C. H.; Breiner, S. J.; Reese, C. E.; Koel, M. N. *Anal. Chem.* **1989**, *61*, 367–375.
(21) Bergman, G.; Gotze, H.-J.; Hermann, A.; Zinn, P. *Chromatographia* **1991**, *32*, 259–64.
(22) Howery, D. G.; Williams, G. D.; Ayala, N. *Anal. Chim. Acta* **1986**, *189*, 339–51.
(23) Huber, J. F. K; Welte, S.; Reich, G. *Anal. Chim. Acta* **1985**, *177*, 1.

The columns of [D] would then represent mobilities of these solutes under different conditions. A row y of [D], would thus correspond to the migration behavior of the yth solute as a function of buffer composition and a point $d_{y,x}$, of [D] would give the mobility of the yth solute under conditions corresponding to the xth column of the [D] matrix. From eq 3, if matrix [D^R] represents [D] with reasonable accuracy, the point $d_{y,x}$ can be computed by multiplying the yth row of [R^R] with the xth column of [C^R]. In [R^R] matrix with k columns, the yth row of [R^R] would represent k real or physically meaningful descriptors of the yth solute. If the original data matrix [D] is used as a source of columns for [R^R], it will represent mobilities of the yth solute under k sets of conditions. These can be referred to as the "core mobilities" of solute y and can be thought of as the most representative, k-size set of [D]. The matrix [C^R] has k rows and n columns. The rows of [C^R] represent loadings and the columns the experimental conditions. Hence, using core mobilities, the mobility of a solute y can be predicted under any conditions, if the loadings corresponding to that set of conditions are available. The rows of [C^R] can thus be modeled as a function of the experimental parameters to obtain loadings at any given set of conditions within the parameter space of the training data set. This TFA procedure for prediction of migration behavior in CE and MEKC was adapted from the previously reported application of TFA in HPLC by Lochmuller and co-workers.[20]

EXPERIMENTAL SECTION

Apparatus. Experiments were carried out on a homemade CE system described earlier[12] and on a Beckman P/ACE System 2100 instrument. The home made system used a 0–30 kV high-voltage power supply (Series EH, Glassman High Voltage, Inc.,Whitehouse Station, NJ) and a variable-wavelength UV detector (Model 200, Liner Instruments, Reno, NV). The capillary temperature was controlled by jacketing the capillary in light mineral oil. The mineral oil was circulated using a constant temperature circulator (Type K2-R, Lauda, Germany). Electropherograms were recorded with an electronic integrator (Model SP4200, Spectra-Physics, San Jose, CA). The Beckman system embodied a 0–30 kV high-voltage built-in power supply, a selectable, fixed wavelength UV detector, and the GOLD software for system controlling and data handling. The capillary was inserted in the system in a cartridge format. The temperature, in the P/ACE 2100, was controlled using a fluorocarbon-based cooling fluid. The electropherograms were recorded on an IBM PS/2 Model 55 SX computer.

All capillaries were obtained from Polymicro Technologies (Phoenix, AZ) and had an i.d. of 50 μm and an o.d. of 375 μm. The length of the capillary was as described in the text. In all experiments, the temperature was set at 25 °C. The eluting components were detected using absorbance at 214 nm. Electropherogram labeling and data analysis were performed, on a 80386-microprocessor-based PC (Northgate Computer System, Inc., Plymouth, MN), using Quattro Pro (Borland International Inc., Scotts Valley, CA) and Free Lance (Lotus Development Corporation, Cambridge, MA) software.

Reagents and Chemicals. All chemicals were purchased from the standard suppliers and were of analytical grade.

Table 1. The Phenols and Their pK_a Values for the Training and the Test Data Sets in pH Optimization

training set			test set		
entry	phenol	pK_a	entry	phenol	pK_a
1	4-phenylphenol	9.55	9	4-chlorophenol	9.43
2	4-propylphenol	10.28	10	4-hydroxyacetamide	9.99
3	4-iodophenol	9.20	11	(4-hydroxyphenyl)-ethyl alcohol	10.12
4	4-hydroxybenzamide	9.23			
5	4-bromophenol	9.34	12	4-fluorophenol	9.89
6	4-phenoxyphenol	10.70	13	4-methoxyphenol	10.20
7	phenol	9.99	14	4-*tert*-butylphenol	10.23
8	4-ethylphenol	10.00			

Procedures. In the P/ACE 2100 system, the samples were injected using pressure injection mode. The duration of an injection was 1 s. In the homemade system, the samples were injected by inserting the upstream end of the capillary in the sample vial and lifting the vial, approximately 5 cm above its normal position, for 5 s.

Simulated Data. Simulated data sets were used, along with the experimentally obtained data to validate the target factor modeling approach. Verified phenomenological models were used to create the simulated data. Normally distributed random noise (0–10% of the average of all the data values in the set) was added to the simulated data to mimic the actual experimental conditions. The target factor analysis as well as the simulation programs were written in Turbo Pascal version 6.0 (Borland International Inc., Scotts Valley, CA). The models used for simulating different data sets are described at appropriate places in the text.

RESULTS AND DISCUSSION.

One Parameter Modeling: pH Effect in CE. The electrophoretic mobility of a solute depends on the charge it carries. For weak acids and bases, the charge on the solute is a function of the pH of the medium and the dissociation constants of the dissociable groups on the solute. The mobility of a typical monobasic compound varies with pH in a sigmoidal manner.[16] Separation of a mixture of such compounds will depend on the choice of the pH; optimization essentially means selecting a pH that gives the optimum separation.[16]

The first set of solutes contained a mixture of 15 para-substituted phenols. The phenols and their pK_a values are given in Table 1. The first eight phenols in Table 1 were used as a training set and the remaining six were used as a test set. The experimental mobilities for each of the eight phenols in the training set were obtained in the pH range of 8.0–12.0. The data matrix [D] was 8 × 8 dimensional. Each row represented a phenol and each column represented phenol mobilities at a different pH. On factor analysis, only two factors explained most of the variation in the data. Since the objective of empirical modeling is to model mobility as a function of a small number of experimentally observed mobilities, columns of [D] should provide ideal targets for target transformation. The mobility columns corresponding to pH 9.5 and 11.5 provided the most suitable pair of targets in our analysis. The loadings, modified on target transformation, were plotted as a function of pH. Figure 2 shows the resulting plot.

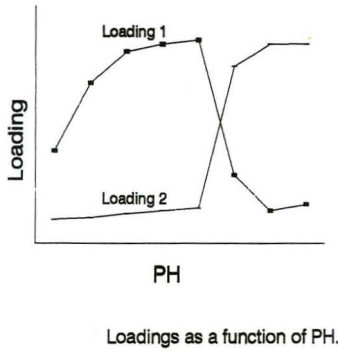

Figure 2. A plot of the loadings, as a function of pH, for the phenol data set.

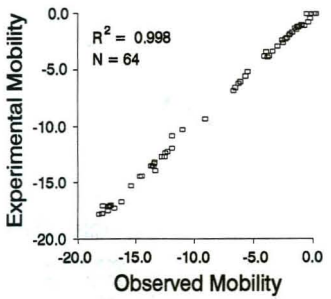

Figure 3. Predicted vs experimentally observed mobilities for the phenol data set.

Predictions. From eq 3, any point $d_{y,x}$ of [**D**] can be predicted by multiplying row y of [$\mathbf{R}^R$], i.e. the two core mobilities for phenol y at pH 9.5 and 11.5, with column x of [$\mathbf{C}^R$], which in this case represents the loadings corresponding to column x of [**D**]. In other words, mobility of y at pH x is given as

$$d_{y,x} = \mu_{9.5}L_1 + \mu_{11.5}L_2 \qquad (5)$$

Where μ represents the experimental mobility and L_n represents the nth loading corresponding to pH x. To predict the mobility of a phenol at any pH within the experimental pH range of the training set, the loadings for that pH should be evaluated. This can be done through interpolation using the graph in Figure 2. Figure 3 gives a comparison between the experimentally observed and the predicted data. As seen from the Figure, there is a good agreement between the two sets of data (R^2 = 0.998, x coefficients = 0.999).

Optimizing a Separation. A separate test set of six phenols (phenols 9–14 in Table 1) was used to further validate the model. The two core mobilities for these six phenols were obtained experimentally at pH 9.5 and 11.5. The loadings which have been obtained from the eight phenol training data set (Figure 3) were used for optimizing the separation of this phenol mixture. Minimum resolution was used as the criterion for evaluating the separation. The optimum pH for the separation of this mixture was found to be 11.0. Figure 4 shows the experimentally observed (a) and the predicted (b) electropherograms at that pH.

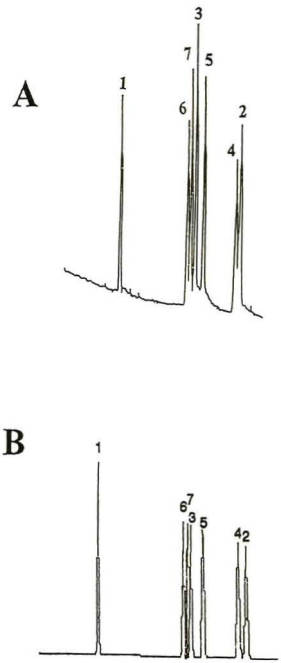

Figure 4. Experimentally observed (A) and the predicted (B) electropherograms for the test set of phenols: (1) acetophenone—the electroosmotic flow marker, (2) *p*-chlorophenol, (3) *p*-hydroxyacetamide, (4) (*p*-hydroxyphenyl)ethyl alcohol, (5) *p*-fluorophenol, (6) *p*-*tert*-butylphenol, (7) isopropyl alcohol.

Comparison with the Phenomenological Model. Electrophoretic mobility of monobasic compounds in CE as a function of pH can be described by the following phenomenological model:[16]

$$\mu_o = \frac{\mu_A - \{K_a/[H^+]\}}{1 + K_a/[H^+]} \qquad (6)$$

The mobilities of three acidic compounds with different pK_a values are shown, as a function of pH, in Figure 5. In order to have a wide range of mobility patterns in the training sets, we simulated three data sets (data set 1, data set 2, and data set 3) using eq 6.

Each data set contained four subsets with each subset containing ten compounds. The pK_a values for all compounds were chosen randomly within an arbitrarily chosen range for each subset. The four pK_a ranges chosen for the four subsets were 5–6, 6–7, 7–8, and 8–9, respectively. The mobility of the completely ionized species was randomly selected for each compound, within the range –17 and –7 cm^2/kV min. The pH ranges of 3–12, 3–8, and 7–12 were used to create data sets 1, 2, and 3, respectively. Figure 5 exemplifies the mobility patterns in the three data sets. Up to 10%, normally distributed random noise was incorporated in the data set. In factor analysis of all three cases, three factors seemed to explain most of the variation in the data. Figure 6 shows the

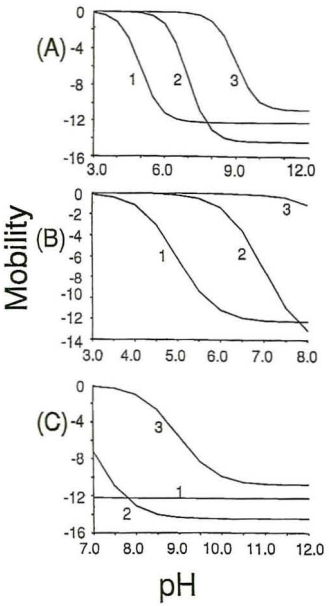

Figure 5. Mobility of three acidic compounds with different pK_a values (1: pK_a = 5.0, 2: pK_a = 7.0, 3: pK_a = 9.0) in three different ranges (A: 3–12, B: 3–8, C: 7–12) of pH.

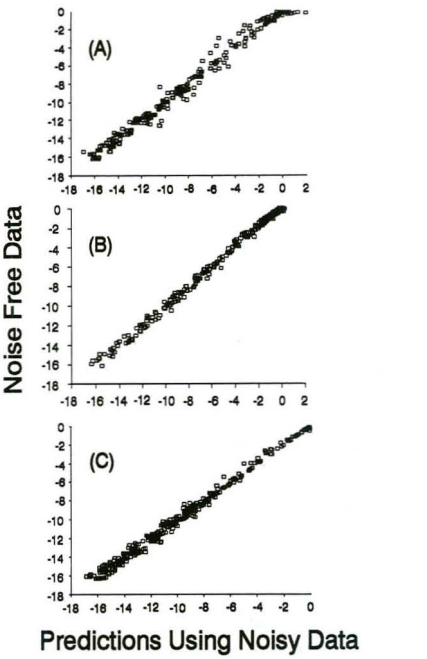

Figure 6. A comparison between the original and the predicted data for three simulated data set 1 (A), 2 (B), and 3 (C) for acidic compounds. Data sets 1, 2, and 3 are defined in the text.

comparison between simulated and predicted data for the three data sets. A t_{paired} test was performed on the data sets. The hypothesis that the predicted and the original data have the same averages can be accepted at $\alpha = 0.05$ level in all three cases. Relatively small standard deviations of the residuals (0.38, 0.12, and 0.27 for data sets 1, 2, and 3, respectively) and high correlation among the predicted and the experimentally observed data (r^2 = 0.994, 0.998, 0.995; x coefficients = 0.995, 0.999, and 0.996 for data sets 1, 2, and 3, respectively) show the predictions to be good.

Table 2 shows a comparison between the TFA predicted and the originally simulated mobilities (using eq 6) for three compounds with different pK_a values (col. A: pK_a = 5.0; col. B: pK_a = 7.0; col. C: pK_a = 9.0) in the pH range of 7–12. Data set 3 was used as a training set. The three compounds were not included in the training data set. The boldfaced numbers represent the actual predicted points whereas the normal face numbers represent the core values used to make the predictions. In all three cases, a t_{paired} test showed that at α = 0.05 level, the predicted and the observed values have the same average. The relatively small standard deviations of the residuals (0.41, 0.32, and 0.19) show that the predictions are good. Although the three predicted compounds have different mobility patterns, the training data set contained enough compounds to represent each kind of mobility pattern. To see the effect of reducing the number of representative compounds in the training set, a fourth data set was created. In this set, one compound had a pK_a of 5.0. The remaining compounds had pK_a in 7–9 range. The predictions for that single compound with pK_a of 5.0 are shown in column D of Table 2. Although a t_{paired} test allows us to accept the hypothesis that predicted and the observed values have the same average, a higher standard deviation of the residuals (0.81) shows the predictions to deteriorate, especially in the lower pH range (see column D in Table 2).

Table 2. A Comparison between the Predicted and the Simulated Mobilities for Three Compounds with Different pK_a Values[a]

A pK_a = 5.0		B pK_a = 7.0		C pK_a = 9.0		D pK_a = 5.0	
obsd	pred	obsd	pred	obsd	pred	obsd	pred
−12.19	−12.19	−7.22	−7.22	−0.11	−0.11	**−12.18**	**−10.04**
−12.27	**−12.74**	**−10.97**	**−9.99**	**−0.34**	**−0.31**	−12.26	−12.26
−12.30	**−12.60**	**−13.13**	**−12.46**	**−1.00**	**−0.35**	**−12.29**	**−12.81**
−12.31	−12.31	−14.00	−14.00	−2.65	−2.65	−12.30	−12.30
−12.31	**−12.21**	**−14.30**	**−14.52**	**−5.47**	**−5.90**	**−12.30**	**−12.02**
−12.31	**−12.26**	**−14.39**	**−14.51**	**−8.27**	**−8.52**	**−12.30**	**−12.14**
−12.31	−12.31	−14.43	−14.43	−9.86	−9.86	−12.30	−12.30
−12.31	**−12.33**	**−14.44**	**−14.39**	**−10.50**	**−10.38**	**−12.30**	**−12.37**
−12.31	**−12.34**	**−14.44**	**−14.37**	**−10.72**	**−10.55**	**−12.30**	**−12.40**
−12.31	**−12.34**	**−14.44**	**−14.37**	**−10.79**	**−10.61**	**−12.30**	**−12.41**
−12.31	**−12.34**	**−14.44**	**−14.37**	**−10.81**	**−10.63**	**−12.30**	**−12.41**

[a] Column A, pK_a = 5.0; column B, pK_a = 7.0; column C, pK_a = 9.0; column D, same compound as in column A but when there were not enough representative compounds of this type in the training set. The bold face numbers represent the TFA predicted values whereas the normal face numbers represent the core mobility values used to make predictions.

Two Parameter Modeling: pH and Micelle Concentration in MEKC. The target factor modeling technique described above can be easily extended to optimize two or more numbers of parameters. For analysis purposes, the matrix can be set up in the same way as in the single parameter case. The rows of the data matrix represent different compounds and the columns represent different sets of experimental conditions.

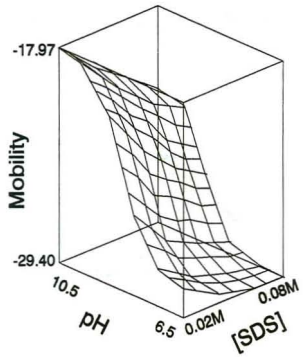

Figure 7. Mobility of an acidic compound as a function of pH and SDS concentration.

As an example, in MEKC, the mobility of an acidic compound, μ, can be described by the following model:[12]

$$\mu = \frac{\mu_{HA} + \mu_{A^-}(K_{a,app}/[H^+])}{1 + (K_{a,app}/[H^+])} \quad (7)$$

where μ_{HA} and μ_{A^-} are the mobilities of the uncharged and the charged species, respectively, and $K_{a,app}$ is the apparent acid dissociation constant in the anionic micellar media. Figure 7 shows the electrophoretic mobility of a typical acidic compound as a function of the two important variables, pH and micelle concentration, sodium dodecylsulfate (SDS).

To test the TFA technique on two-dimensional data, a data set was simulated using the model given by eq 7 above. The data set had 40 rows representing 40 acidic compounds and 24 columns representing pH and SDS concentration ranges of 5.5–10.5 and 20–80 mM, respectively. Normally distributed random noise (0–10%) was added to the simulated data. Three factors explained most of the variation in the data. The results of a comparison between the predicted and the simulated data is shown in Figure 8A. A t_{paired} score of 1.38 (N = 960), correlation of r^2 = 0.98 (x coefficient = 0.985), and a standard deviation of 0.42 for the residuals represent good prediction capabilities.

Eliminating Noise from Data. During the factor analysis step, the factors that correspond to the highest variation in data are retained. The variation accounted for by the deleted factors is usually insignificant and often represents noise in the data. Deleting noise is sometimes better as it can lead to better predictions. To see the correlation of predictions with the noise-free data, we plotted the predicted data against noise-free simulated data. The predictions were made by using the simulated data with added noise as described before. The resulting plot is shown in Figure 8B. All the prediction evaluators including t_{paired} (0.576), standard deviation of the residuals (0.34), correlation coefficient r^2 (0.986), and x-coefficient of correlation (0.993) had better values than before. In other words, the predicted data correlated better with the original noise-free data than with the noisy data used to make the predictions.

The next two-dimensional data set was obtained experimentally. The migration is described in terms of migration

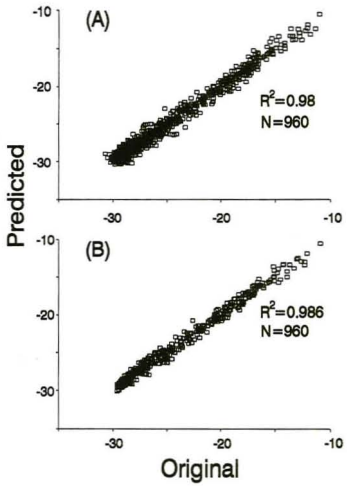

Figure 8. A comparison between the predicted and the simulated mobilities with (A) and without (B) added noise for the MEKC data set.

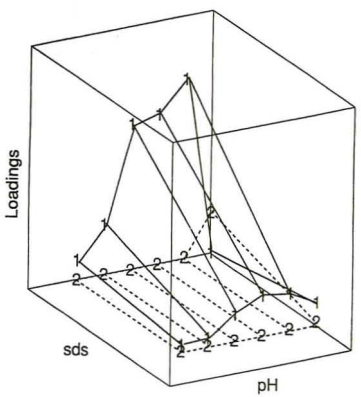

Figure 9. The plot of the two loadings, for the two-dimensional MEKC data set, as a function of pH and SDS concentration.

factors.[12] The migration factors for 12 substituted phenols were obtained as a function of pH and SDS concentration. The data set contained 20 columns, representing a pH range of 8 to 11.5 and an SDS concentration range of 20 to 80 mM. On factor analysis, more than 95% of the variation could be explained by only two factors. Target transformation showed that the two columns corresponding to pH 8, SDS concentration 20 mM, and to pH 10 SDS concentration 80 mM, provide the best pair of targets. The corresponding plot of the target-modified loadings is given as a function of pH and SDS concentration in Figure 9. Based upon this plot of the loadings and the two core vectors, the migration factors for all phenols were predicted at all conditions. A comparison of the observed and the predicted migration factors is given in Figure 10. Three points in the plot seem obvious outliers. The correlation of 0.96 shown in the figure does not include these outliers. These three points were noted as outliers even when we used

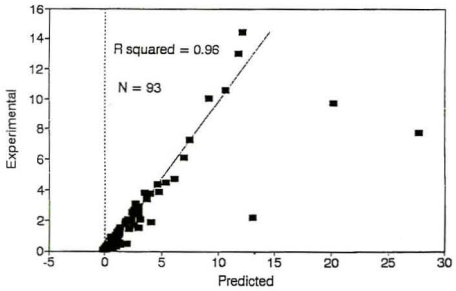

Figure 10. A comparison between the predicted and the experimentally observed migration factors for the two-dimensional MEKC data set.

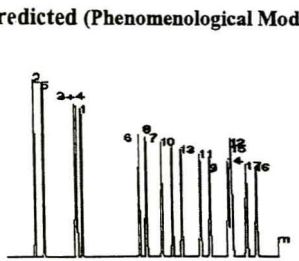

Figure 11. Three chromatograms for 17 aromatic amines. The chromatogram A was predicted using the phenomenological model described in eq 11, the chromatogram B was obtained experimentally, and the chromatogram C was predicted using the target factor modeling approach. The data for this figure were taken from ref 24.

a semiempirical model to predict the migration of these compounds.

The migration of a cationic solute differs from that of an anionic solute.[24] This is due to the electrostatic attraction between the cationic solutes with the anionic surfactant in monomeric and aggregate forms. The mobility of a cationic solute can be expressed as a function of pH and SDS

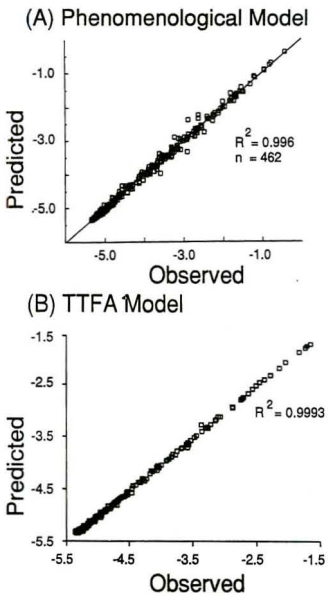

Figure 12. A comparison between the experimentally obtained mobilities and those predicted using the semiempirical (A) and the target factor based (B) approaches, for the 17 aromatic amines. The data for this figure were taken from ref 24.

concentration using the following model.[24]

$$\mu = \frac{\left(K^{m}_{BH+} + \frac{K_a}{[H^+]}K^{m}_{B}\right)[M]\mu_{mc} + \mu_{BH+}}{1 + K^{m}_{HB+}[M] + K_{ip}CMC + \frac{K_a}{[H^+]}(1 + K^{m}_{B}[M])} \quad (11)$$

This semiempirical approach was used, along with the target factor analysis approach, to model the mobility for a set of 17 aromatic amines obtained at 15 different conditions of pH and SDS concentration. Figure 11 shows three MEKC chromatograms predicted and observed at pH 11 and SDS concentration of 50 mM. The chromatogram B was obtained experimentally and chromatograms A and C were predicted using the semiempirical model given above and the target factor approaches, respectively. Figure 12 shows a comparison between the experimentally obtained mobilities and those predicted using the semiempirical (A) and the target factor based (B) approaches.

CONCLUSIONS

Modeling of migration behavior is important for efficient optimization of a separations system. Although physical models are the most desirable, a lack of understanding of all the factors that may influence a practical separation makes it more difficult to derive and implement such models. Semiempirical models on the other hand are of more practical

(24) Quang, C.; Strasters, J. K.; Khaledi, M. G. *Anal. Chem.* **1994**, *66*, 1646.

value. However, the complexity of the models will increase drastically with the number of parameters which reduces their practical utility. Purely empirical models are often the only practical solution to many practical situations. Target factor analysis approach exemplifies a case of empirical modeling that uses a minimum number of initial experiments to optimize a separation. The use of target factor approach to model the electrophoretic behavior has been shown for one and two parameters. The approach is, however, directly extendible to any type and number of parameters.

ACKNOWLEDGMENT

The authors gratefully acknowledge funding from the National Institutes of Health (FIRST Award, GM38738) and the loan of a PACE 2100 CE unit from Beckman Instruments.

Received for review May 21, 1993. Accepted March 25, 1994.[⊗]

[⊗] Abstract published in *Advance ACS Abstracts,* May 15, 1994.

Anal. Chem. **1994,** *66,* 2382–2389

Postcolumn Radionuclide Detection of Low-Energy β Emitters in Capillary Electrophoresis

Scott Tracht, Verna Toma,† and Jonathan V. Sweedler*

Department of Chemistry, University of Illinois, Urbana, Illinois 61801

A postcolumn radionuclide detection system for capillary electrophoresis (CE) is described. Eluant from an electrophoresis capillary is directed onto a peptide binding membrane that has been previously coated with a solid scintillator. The membrane is moved in a preselected pattern relative to the fixed capillary outlet during electrophoresis. Light emission from scintillation is imaged onto a charge-coupled device (CCD) using a series of 35-mm camera lenses. Detection of two low-energy β^- emitters (^{35}S and ^{3}H) not previously reported for capillary electrophoresis is demonstrated. The separation efficiencies are similar to those obtained with on-line UV detection. The response for ^{35}S-labeled methionine is linear ($r^2 = 0.996$) from 66 amol to 11 fmol. Detection limits are 88 zmol (0.03 Bq) for ^{32}P-labeled analytes, 17 amol (0.94 Bq) for ^{35}S-labeled analytes, and 8 fmol (8.5 Bq) for ^{3}H-labeled analytes.

Radioisotopes have been used as an analytical tool in biochemical applications for a number of years. This method of labeling and detection offers attomole sensitivity and unprecedented selectivity. Because of these features, radionuclide detection is extensively used for a variety of separation techniques such as liquid chromatography and slab gel electrophoresis.[1,2] The ability to selectively label particular compounds in matrices such as a living cell allows extremely complex samples to be investigated using conventional separation methods. In addition, the ability to label a small fraction of a particular compound can be important. For example, labeling newly synthesized peptides in a cell (by introducing radiolabeled precursor for a short period) allows the dynamics of peptide synthesis and transport to be studied in ways that other detection schemes do not allow.[3,4] Because the analysis of small amounts of complex mixtures of biologically important molecules is among the strong points of capillary electrophoresis, a natural progression is to combine radionuclide detection with capillary electrophoresis.

Kaniansky and co-workers first demonstrated on-column detection of the radionuclides ^{32}P, ^{14}C, and ^{99}Tc for capillary isotachophoresis.[5,6] Their system consisted of 300 μm i.d. capillaries and a plastic scintillator/photomultiplier tube combination to detect β^- particles. They reported a detector efficiency of 15% and a 6 pmol (16 Bq) LOD for ^{14}C using a large (210 nL) detector cell. Altria reported CE separations and detection of radiolabeled pharmaceuticals containing ^{99}Tc, a β^- emitter with a 6-h half-life.[7] Pentoney and Zare demonstrated ^{32}P detection in an on-line capillary electrophoresis system;[8,9] they reported three different approaches, including the use of coincidence detection with nearly a 100% detector efficiency for ^{32}P. In their systems, a 100 μm i.d. capillary and relatively large injections of between 60 and 80 nL were used. With this approach, the reported LOD was approximately 40 amol during a standard CE run. Several additional reports have investigated the detection of energetic β^- and γ emitters,[10,11] and several on-column approaches have been commercialized.[12,13]

However, almost all previous work has used on-column detection and is not suitable for detection of two of the most important nuclides for biological work—^{3}H and ^{35}S. One of our long-term goals is to detect ^{35}S-labeled methionine and cysteine containing peptides from subsections of a cell, and we need the ability to detect these weak β^- emitters. The inherent problem with these radionuclides is that a β^- particle has insufficient energy to penetrate the capillary wall.[14] This leaves two approaches to detect these emitters: placing a scintillator in the running buffer or on the capillary wall, or using postcolumn detection. In this report, we describe a postcolumn membrane/scintillator that allows peptides and other relatively small molecules labeled with ^{32}P, ^{3}H, or ^{35}S to be detected.

In radionuclide detection, the longer one can observe the sample, the lower the limit of detection. In capillary electrophoresis, typical peak widths are only several seconds wide, and so only a several-second observation is possible without limiting separation efficiency. In order to detect a radiolabeled analyte, the probability of observing a peak must be high—in other words, several decays must be observed, even in background-free situations.[15] As a 3-amol sample of

† Present address: Eli Lilly and Co., Indianapolis, IN 46254.

(1) Andrews, A. T. *Electrophoresis*, 2nd ed.; Oxford Science Publications: Oxford, 1990; Chapter 2.
(2) Reich, A. R.; Lucas-Reich, S.; Parvez, H. *Prog. HPLC* **1988,** *3,* 1–10.
(3) Lloyd, P. E.; Schacher, S.; Kupfermann, I.; Weiss, K. *Proc. Natl. Acad. Sci. U.S.A.* **1986,** *83,* 9794–9798.
(4) Church, P. J.; Lloyd, P. E. *J. Neuroscience* **1991,** *11,* 618–625.
(5) Kaniansky, D.; Rajec, P.; Švec, A.; Havaši, P.; Macášek, F. *J. Chromatogr.* **1983,** *258,* 238–243.
(6) Kaniansky, D.; Rajec, P.; Švec, A.; Marák J.; Kovaľ, M.; Lúčka, M.; Franko, Š.; Sabanoš, G. *J. Radioanal. Nucl. Chem.* **1989,** *129,* 305–25.
(7) Altria, K. D.; Simpson, C. F.; Barij, A.; Theobald, A. Presented at the 1988 Pittsburgh Conference, New Orleans, February 1988. Paper no. 642.
(8) Pentoney, S. L.; Zare, R. N.; Quint, J. F. *Anal. Chem.* **1989,** *61,* 1642–47.
(9) Pentoney, S. L.; Zare, R. N.; Quint, J. F. *Analytical Biotechnology: Capillary Electrophoresis and Chromatography*; Horvath, C., Nikelly, J. G., Eds.; ACS Symposium Series No. 434; American Chemical Society: Washington DC, 1990; pp 60–89.
(10) Westerberg, G.; Lundquist, H.; Kilar, F.; Longstrom, B. *J. Chromatogr.* **1993,** *25,* 319–325.
(11) Gordon, J. S.; Vasile, S.; Hazlett, T.; Squillante, M. *IEEE Trans. Nucl. Sci.* **1993,** *40,* 1162–64.
(12) Isco, Inc. Product Guide, *Instruments for Chromatography and Electrophoresis*; Lincoln, NE, 1993.
(13) Raytest USA. *Radiodetection in CE*; Wilmington, DE, 1992.
(14) Knoll, G. F. *Radiation Detection and Measurement*, 2nd ed.; John Wiley: New York, 1989.

0003-2700/94/0366-2382$04.50/0
© 1994 American Chemical Society

^{32}P has an activity of 1 Bq (one decay/s), the best possible LODs are on the order of 8 amol for a 1-s observation time.

In previous work by Pentoney,[9] the detection efficiency of their most sensitive coincidence detector is nearly 100%. Therefore, further improvements are difficult using an on-line approach. One of the few methods available to further improve LODs is to observe the analyte for a longer time. Pentoney and co-workers increased the observation time by lowering the applied potential during the transit of a peak of interest past the detector. Using the flow programming approach, they demonstrate an improvement in LODs of more than an order of magnitude. As they note, one must know precisely when the peak of interest will reach the detector. Using the flow programming method for samples containing a number of analytes eluting over a wide time range can be problematic.

An advantage of postcolumn detection is that it isolates detection conditions from the separation conditions—the separation can be optimized independently of the observation of the membrane. Even the low efficiency (typically only a few percent) of photographic film used in autoradiography can produce superior results to coincidence detection because of the long observation times possible.

Using a postcolumn detector requires collecting effluent fractions. The collection of CE effluent is complicated by the fact that the end of the capillary must be electrically connected to complete the electrophoresis circuit. Membrane fraction collection in CE was first demonstrated by Huang and Zare using a CE system grounded before the outlet with an on-column frit.[16] The outlet end of the capillary made contact with a moving piece of filter paper, and fluorescently labeled amino acids were visualized and detected using photographic film. Hjertén and co-workers[17] and Carson and colleagues[18] demonstrated improved versions in which a capillary touched a moving, grounded membrane to complete the circuit. In both systems, a circular membrane was rotated to produce a phonograph-like recording of the capillary effluent. In the report by Hjertén, a sample of radioactive iodine labeled human growth hormone was separated and eluted onto a membrane. The membrane was then cut into 20 sections and the pieces counted in a γ counter. In these previous reports, the separation efficiency for the protein separations was less than 20 000 plates; whether this was due to heterogeneity in the samples, interactions of the analyte with the capillary wall, or zone spreading caused by the membrane fraction collection was not determined.

We also use a membrane to collect the capillary eluant. A variety of membranes were tested for this application; although a number of protein binding membranes are available, few are available which bind smaller molecules such as small peptides. We are using a prototype membrane (Immobilon Psq/CD Experimental) from Millipore Corp. with a high surface area and a hydrophilic cationic polymer (which should bind the carboxylic acid group of the peptides). Malcolm Pluskal of Millipore reports that it quantitatively binds small peptides.[19]

(15) Currie, L. A. *Anal. Chem.* **1968**, *40*, 586–93.
(16) Huang, X.; Zare, R. N. *J. Chromatogr.* **1992**, *516*, 185–89.
(17) Eriksson, K.-O.; Palm, A.; Hjertén, S. *Anal. Biochem.* **1992**, *201*, 211–15.
(18) Cheng, Y.-F.; Fuchs, M.; Andrews, D.; Carson, W. *J. Chromatogr.* **1992**, *608*, 109–16.

Table 1. Physical Properties of Selected Radionuclides

nuclide	half-life (d)	mode of decay	emission (MeV)	mol/Bq (amol)
^{77}Br	2.4	β^-	0.361	0.49
^{32}P	14.2	β^-,γ	1.71	3
^{125}I	57	γ	0.149	12
^{35}S	87	β^-	0.167	18
^{3}H	4500	β^-	0.019	930
^{14}C	2.03×10^6	β^-	0.156	4.30×10^6

In our case, the membrane binding properties are complicated by the desire to pretreat the membrane with a scintillator such as PPO (2,5-diphenyloxazole) and a wavelength shifter (perylene). Using PPO and perylene, we can detect ^{32}P-, ^{35}S-, and ^{3}H-containing analytes. The membrane has a series of glowing analyte bands after the CE run, with the light emission from each analyte in proportion to the amount of radionuclide present. However, the PPO/perylene scintillator mix is hydrophobic and changes the ionic binding properties of the membrane.

Another complication is the requirement for an efficient CE separation, as we wish to separate complex mixtures of similar peptides. Thus, the choice of membrane/scintillator is extremely important for the success of this radionuclide detection approach. In preliminary work, a nonoptimized membrane/scintillator system was used, and the resulting separation efficiency was poor, most likely due to postcolumn band broadening.[20] We currently use the membrane dry, electrically connect the capillary outlet to ground, and then raster the membrane lightly across the stationary capillary. Using this approach, we obtain up to 100 000 theoretical plates for peptides and amino acids with improved detection limits for radionuclides.

Once the bands are deposited onto the membrane and dried, the next step is to image the membrane and quantitatively measure the light emission from each band. In order to accomplish this, we use a series of 35-mm camera lenses coupled to a cooled, scientific charge-coupled device (CCD). CCD detectors are now used for a number of measurements in spectroscopy[21–23] and are well suited to this detection system. The characteristics that make CCDs well suited for measuring photon emission from small points of light in the night sky, low dark current, and read noise also make them the detector of choice for measuring light emission from the membrane.

With membrane observation times between 1 and 2 h, the LODs for single-labeled compounds are 88 zmol (0.03 Bq) for ^{32}P, 17 amol (0.94 Bq) for ^{35}S, and 8 fmol (8.5 Bq) for ^{3}H. The reasons for the great variation in LODs for the different nuclides are twofold: the lifetime of the radionuclide and the energy of the β particle. Table 1 lists the activity and lifetimes for several commonly used radionuclides. A further advantage of this postcolumn method is that after the detection procedure, the membrane is still intact, and the measurement

(19) Malcolm Pluskal (Millipore/Waters). Private communication, July 1993.
(20) Sweedler, J. V.; Fuller, R.; Tracht, S.; Timperman, A.; Toma, V.; Khatib, K. *J. Microcolumn Sep.* **1993**, *5*, 403–412.
(21) Sweedler, J. V.; Bilhorn, R. B.; Epperson, P. M.; Sims, G. R.; Denton, M. B. *Anal. Chem.* **1988**, *60*, 327A–335A.
(22) Sweedler, J. V. *Crit. Rev. Anal. Chem.* **1993**, *24*, 59–98.
(23) *Charge Transfer Devices in Chemistry*, Sweedler, J. V., Ratzlaff, K. L., Denton, M. B., Eds.; VCH: New York, 1994.

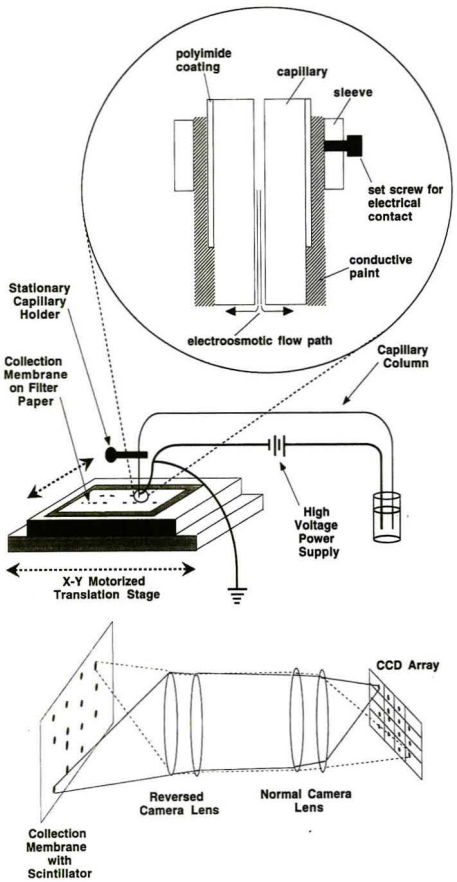

Figure 1. (A, Top) Schematic diagram of the capillary electrophoresis/membrane fraction collector system. The detail shows the end-column electrical connection that completes the electrophoresis circuit. (B, Bottom) Membrane imaging system. Two 35-mm camera lenses image the membrane from the 2.5 cm by 2.5 cm membrane containing the eluant from the CE run onto the 1 cm by 1 cm CCD array.

can be repeated many times to decrease the LODs (with a corresponding increase in analysis time). In addition, many analytes are available with multiple radiolabels, which can further lower the obtainable LODs.

EXPERIMENTAL SECTION

CE System. The radiochemical detection capillary electrophoresis system is shown in Figure 1. With the exception of the membrane fraction collection system, the CE system is similar to previous systems.[24] The entire system is contained within a Plexiglas box with interlocks. A 75 μm i.d. fused silica capillary (Polymicro, Phoenix, AZ) was used for all experiments. All injections use gravity injection with a 9-cm height displacement for 10 s; the injection volume is calculated to be ~5 nL under these conditions.[25] A 20-kV potential was applied to the injection end for all separations using a Bertan high-voltage power supply (Model 230, Bertan, Hicksville, NY).

In order to facilitate membrane fraction collection, a silver electrode is fabricated on the outside of the outlet end of the capillary. The electrode is constructed by painting conductive silver paint (GC Electronics; Rockford, IL; Part No. 22-202) on the last centimeter of the capillary. The coating is heated to 125 °C for 2 h to improve durability. The electrical connection to the power supply, shown in the detail of Figure 1, is maintained with a nonconductive collar that holds a conductive screw against the electrode coating. Connection to ground is made with an alligator clip attached to the screw. This arrangement allows the CE circuit to be maintained with no electrolyte at the outlet end (except that provided by electroosmotic flow). Such painted electrodes have been used daily for several months with no degradation in performance.

CE separation conditions and parameters are optimized using a Waters Quanta 4000 CE system with UV detection. Nonderivatized amino acids and peptides are detected using the standard Waters detector set at 185 nm. In order to allow comparisons of the membrane collection system with this on-column detection system, the capillary diameter and length, the applied voltage, and injection conditions are kept nearly equivalent in both systems.

Membrane Fraction Collection. The eluant is directed onto a membrane that has been impregnated with a solid scintillate by physical contact of the end of the capillary. The membrane is moved in a preselected pattern relative to the fixed outlet of the capillary during the CE separation.

The membrane is moved by fastening the membrane onto an XY translation stage with the stage position controlled using linear translation motors and a manipulator controller from Newport (Model 860CM2 controller, Model 860SA motors, and 230 stages, Newport Research Corp., Irvine, CA). The membrane movement is programmed using Lab Windows (Version 2.2.1 from National Instruments; Austin, TX) driving a Lab PC card (National Instruments; Austin, TX) in a Northgate 80486 33-MHz IBM AT compatible computer, which also controls the electrophoresis power supply.

Highly efficient light collection optics are available for small-membrane areas, leading to low LODs; on the other hand, too small a membrane can reduce separation efficiency. As a compromise, we use a 2.5 cm by 2.5 cm membrane to record a 16-min capillary output trace. Figure 2 shows an image of a fraction collection membrane when the running electrolyte contains a small amount of ^{35}S-labeled methionine and the membrane has been pretreated with a scintillator, thus allowing the capillary trace to be visualized. The membrane movement is 2.5 cm/min for all separations. The width of the trace is approximately 0.6 mm for ^{3}H- and ^{35}S-labeled amino acids and peptides, and slightly wider for ^{32}P analytes.

A number of membranes and scintillator materials have been evaluated. The membrane performs two different tasks—binding the analytes and emitting photons. Beckman's XtalScint membrane, which uses a yttrium silicate scintillator coated onto a fiber support back, has the highest light emission

(24) Sweedler, J. V.; Shear, J. B.; Fishman, H. A.; Zare, R. N.; Scheller, R. H. *Anal. Chem.* **1991**, *63*, 496–502.

(25) Jandik, P.; Bonn, G. *Capillary Electrophoresis of Small Molecules and Ions*; VCH: New York, 1993; Chapter 3.

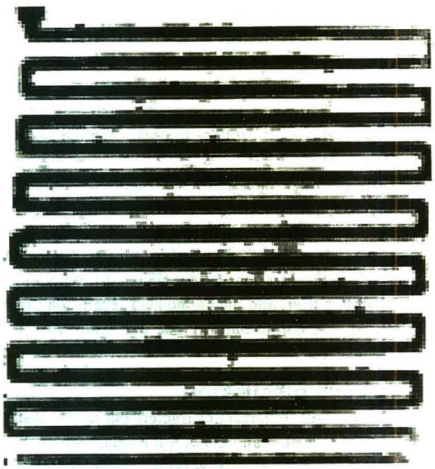

Figure 2. Image of the membrane when the buffer contains radiolabeled methionine, showing the path of the outlet end of the capillary. Each horizontal line represents 1 min.

of any tested scintillator/membrane. Although the scintillation response is excellent, the number of theoretical plates for a peptide separation has never been more than 1000.[20] In addition, the underlying fibrous support is easily torn by the motion of the capillary.

Several membranes designed for blotting proteins and peptides from slab gels have been evaluated. We find that scintillation response and peptide binding is highest with Immobilon Psq/CD (experimental) from Millipore coated with PPO. Binding and response are related in that more tightly bound peptides generally occupy a smaller area of the membrane and light from scintillation is therefore concentrated in a smaller area on the CCD. Although the Millipore membrane also produces broad peaks when prewetted with running buffer (as is commonly done), it produces much narrower peaks than any other tested membrane when used dry and moved lightly across the capillary end. The use of dry membranes is possible in this system, as opposed to previous membrane collection systems, because of the end-column grounding method.

Scintillation efficiency of the membrane is optimized with compounds commonly used for liquid scintillation counting. After the screening of several compounds, PPO has been selected as the scintillator. However, PPO has a light emission below 400 nm at a wavelength that the CCD has poor quantum efficiency. Because of the much higher quantum efficiency of the CCD at longer wavelengths, perylene, with an emission in the 450–500-nm region, is used as a wavelength shifter. The optimum membrane soak solution is 0.1 g of PPO and 0.5 mg of perylene per mL of diethyl ether. Although ether is chosen as the solvent because it solubilizes the scintillators and does not degrade the membrane coating significantly, a pure ether treatment extracts some membrane as it reduces the membrane weight by ~4%. The membrane is soaked in the ether solution for 5 min and in allowed to dry for 15 min at room temperature before use. Membranes are treated and used the same day.

Detection. The membrane is imaged onto the CCD using two standard Nikon 35-mm camera lens, as shown in Figure 1B. The lenses provide approximately 2.7:1 image reduction, so that a 2.5-cm membrane can be imaged by a 1-cm CCD. The camera lens near the membrane, a Nikon 135-mm f2.0 lens, is used in reverse, and the lens near the CCD, a Nikon 50-mm f1.2 lens, is operated in the normal direction. Both lenses are focused to infinity and set to maximum aperture. The reversed lens collects light from the membrane and collimates it, while the second lens focuses the collimated light onto the CCD. The overall collection efficiency of the system is equivalent to ~f2.5 and represents a compromise between light collection efficiency from a point on the membrane and the membrane area.

A liquid nitrogen cooled 16-bit CCD is used to detect the light emission from the membrane. The CCD is a PM512 controlled with a CH260 camera controller (Photometrics Ltd., Tucson, AZ). It has a low read noise and dark count rate, allowing multiple-hour integration times of the membrane emission. The CCD is controlled using PMIS 2.0 software, also from Photometrics. CCD readout is a very flexible process, with variable analog gain, binning, bias procedures, and a variety of postacquisition image processes available to improve performance. For this work, the binning is set to 4 serial by 4 parallel, resulting in 128 by 128 point images of the membrane. Even with a read noise floor of approximately 10 e^-, this system is usually read-noise limited. Thus the binning results in improved detection limits while acceptable spatial resolution of the membrane is still maintained. For all data presented here, the CCD temperature is maintained at −110 °C, and the membrane exposure time (for signal integration) is varied from 15 min to 2 h.

CCD detectors respond to cosmic rays and background radiation. As these events are very energetic, each event can produce thousands of electrons.[22,23] These events limit the maximum practical observation time to under 4 h. The electrophoretic bands are several detector elements wide in both the X and Y dimensions and so can be distinguished from intense cosmic ray induced "point spikes". A software routine written in the PMIS macro language removes the spikes and uses a median filter to improve the signal-to-noise ratio. All spikes 100 counts greater than the average of the eight neighboring detector elements are removed and replaced with an average of the eight neighboring elements. The median filter, consisting of the average of the eight neighboring pixels, is applied to the entire image. Both the raw data and the raw background data are treated by the same algorithm before background subtraction. Figure 3 shows raw and processed membrane images for a separation of tritiated amino acids, with both images having the same intensity scale. The images have been reversed so that the lighter areas indicate less light and darker areas indicate more light. Figure 3A is background-substracted only and shows a large number of single- and double-detector element spikes denoted by the appearance of dark spots. The lack of spots in Figure 3B demonstrates the efficiency of the spike removal routine.

Once the images have been processed as described above, the CCD rows containing the capillary trace are extracted and a standard electropherogram is reconstructed using Excel for Windows. For each electrophoretic row, three rows of

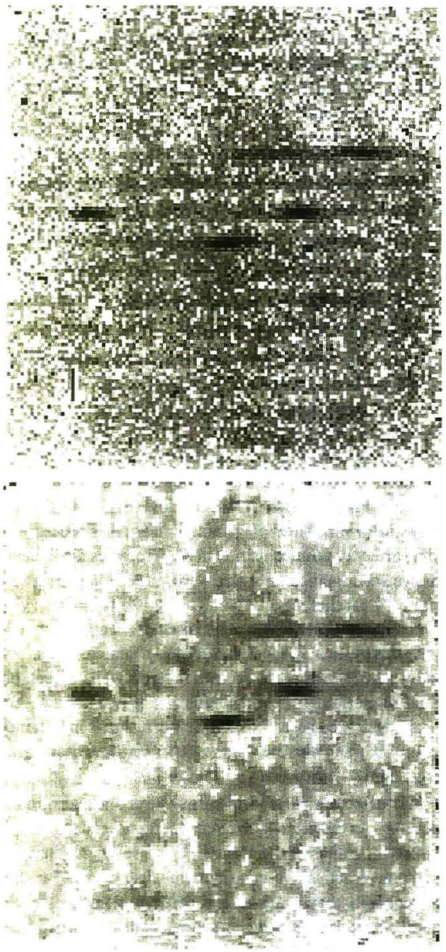

Figure 3. (A, Top) Raw image of the membrane for a separation of five tritiated amino acids. (B, Bottom) Processed image of the membrane after spike removal and median filtering.

CCD data are exported into an Excel spreadsheet, summed into a single row, and plotted against time. All signal-to-noise calculations are based on peak height. For the membrane images shown, images are exported as an 8-bit TIFF to Corel Photo-Paint for reversal and printing.

Reagents. Radiochemicals are from Amersham Co. (Arlington Heights, IL). The [^{35}S]methionine (Catalog No. SJ.1515) is in an aqueous solution stabilized with 2-mercaptoethanol and pyridine-3,4-dicarboxylic acid. The [^{35}S]-cysteine (Catalog No. SJ.232) is in an aqueous solution containing potassium acetate and dithiothreitol. The non-stabilized cysteine is used to radioactively label peptides, as the stabilizers could interfere in the derivatization reaction. The tritium-labeled amino acid mixture (Catalog No. TRK.550) and α-^{32}P-labeled ATP (Catalog No. PB.10384) are also from Amersham. All amounts of radionuclide are based on the manufacturer specifications adjusted for radioisotopic decay.

Cysteine-containing peptides are labeled with [^{35}S]cysteine by forming a disulfide linkage. Benzofuroxan is used to form the disulfide bond.[26] The reaction is completed in the running buffer. Peaks are identified by reacting the peptides individually with [^{35}S]cysteine and comparing the retention times of the individual labeled peptides to peak retention times of the peptide mixture.

The peptides were purchased from Sigma Chemical Co. (St. Louis, MO) and American Peptide Co. (Sunnyvale, CA). All other chemicals are from Aldrich Chemical Co. (Milwaukee, WI). Borate buffer is used for all separations; the peptide and ATP separations used a pH 8.4, 61.5 mM (total borate) borate buffer, and the amino acid separation used a pH 10.0, 50 mM borate buffer. The pH is adjusted with sodium hydroxide.

RESULTS AND DISCUSSION

Two of the most important characteristics of this system are separation efficiency and LOD. Individual radionuclides are expected to have greatly varying characteristics and different optimum conditions, and so each radionuclide is discussed separately. The amounts of sample injected and LODs are reported in terms of mass as opposed to concentration as all membranes are dried after fraction collection before imaging and so the mass of the analyte is the important parameter.

Sulfur-35. ^{35}S is one of the most important radionuclides because it is used in biological systems to label methionine- and cysteine-containing peptides and proteins. Figure 4 shows the electropherogram of 66 amol (3.7 Bq) of ^{35}S-labeled methionine. The LOD, calculated using three injections, each based on the sum of three 1-h image exposures, yields a detection limit for ^{35}S methionine of 17 amol (0.94 Bq). This can be further improved using longer integration times or multiple exposures.

The linearity of response of the membrane has been tested using a series of injections of ^{35}S-labeled methionine. The exposure time for all but the 66-amol injection is 15 min. The membrane produced by the 66-amol injection is exposed for 1 h and the results converted to a 15-min equivalent exposure (the background-corrected results are divided by 4). The system response is determined by summing the peak in the image and subtracting an equivalently sized background signal from the membrane image between the traces (see Figure 2). The response versus labeled methionine is shown in Figure 5; the scintillator response is linear from 66 amol to 11 fmol (r^2 = 0.996). The response of the membrane for the highest mass injected, 33 fmol, has a significant deviation from the best-fit line. This injection represents injecting the straight methionine standard solution from Amersham; whether the deviation is caused by a matrix effect or membrane saturation has not been determined. Five replicate injections of the 0.67 fmol (37 Bq) standard gave a mean of 1560 counts with a RSD of 15%. This uncertainty is most likely caused by the manually timed gravity injections and irreproducibility in membrane coating.

In order to demonstrate a separation of labeled peptides, we separated a series of cysteine-containing peptides and linked radiolabeled cysteine to the peptides with the formation of a

(26) Shipton, M.; Brocklehurst, K. *Biochem. J.* **1977**, *167*, 799–810.

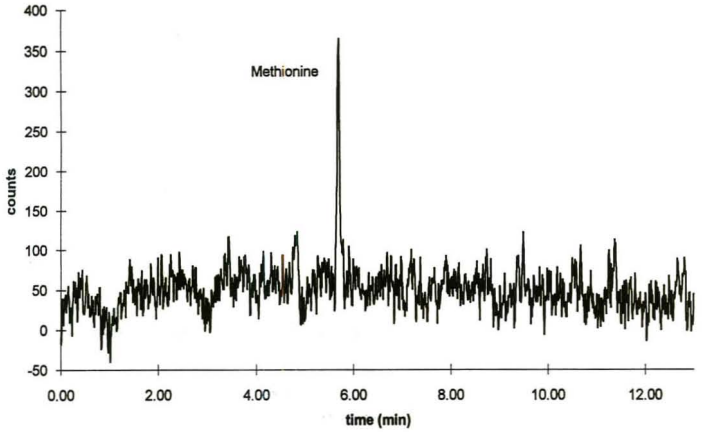

Figure 4. Reconstructed electropherogram of 66 amol of ^{35}S-labeled methionine.

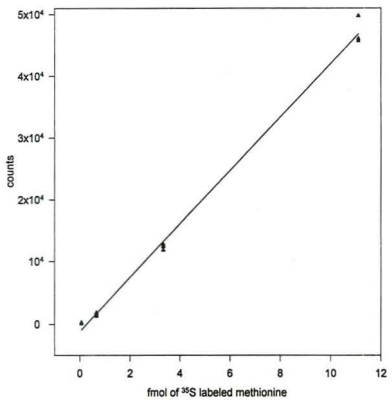

Figure 5. Response of the system as a function of labeled methionine injected onto the capillary.

disulfide bond. Figure 6A,B shows the separation of four peptides with the electropherogram obtained using a single 1-h exposure of the membrane. The high efficiency separation demonstrates that peptides containing between 4 and 10 amino acids can be separated and detected with this system.

A total of 3 fmol of radiolabeled sulfur has been injected in the electropherogram shown in Figure 6, and so the integrated peak area of all peaks is from this 3 fmol of ^{35}S. With the assumption of equal response for all ^{35}S-containing compounds, several peptides are present in the 100–200 amol range. The broad peak between 9 and 10 min is due to impurities in the [^{35}S]cysteine. The radiochemical purity specification is 90% for this lot when purchased and degrades during storage due to interaction of the sample with the β^- emission. Other unidentified peaks are thought to be products of disulfide formation between radiolabeled cysteine and other thiol-containing impurities and degradation products.

We compared data from UV detection to the radiochemical detection using similar capillary, buffer, and injection parameters to determine the effect of the membrane fraction collection on postcolumn band broadening. Table 2 lists the efficiency of the CE separations for both systems. The number of theoretical plates (~60 000) for [^{35}S]methionine indicates that the separation efficiency is typical of on-line CE separations. For the cysteine-containing peptides, the number of theoretical plates for the radiolabeled peptides (~110 000 for C*-CDPGYIGSR-NH_2) compared to on-line UV detection (~40 000) under these conditions indicates that the peptides bind to the membrane with little postcolumn broadening.

Tritium. Tritium is one of the lowest energy β^- emitters used in biological investigations. Because of the ubiquitous nature of hydrogen, it can be used to label most compounds of biological interest. Its detection is much more difficult than the other radionuclides; for example, autoradiography of tritium in gels is problematic because the low-energy β^- particles do not penetrate the gel to expose the film. Liquid scintillation counting is one of the most successful approaches to detect this radionuclide.

We have separated and detected a mixture of five tritium-labeled amino acids. The resulting electropherogram is shown in Figure 7. The lysine peak is not completely resolved and is broader than the other amino acid peaks. Both the membrane and the lysine carry a positive charge at the separation pH. This likely reduces the lysine binding interaction relative to that of the other amino acids. A CE run using UV detection at 185 nm does not show the lysine peak broadened relative to that of other amino acids. Because of the peak overlap and broadening, the peaks for lysine and proline are omitted from the calculation of average tritium detection limits and separation efficiency. For leucine, phenylalanine, and tyrosine, the average detection limit is 8 fmol of ^{3}H for a 1-h exposure.

Phosphorus-32. ^{32}P is commonly used to label nucleotides and monitor the phosphorylation of proteins. Unlike ^{35}S and ^{3}H, there are previous reports of the detection of ^{32}P using CE, allowing comparison of detection limits. An electropherogram of approximately 300 zmol of ^{32}P-labeled ATP is shown in Figure 8, yielding an 88-zmol (0.03 Bq) LOD for a single 2-h exposure. This represents nearly a 2 order of magnitude decrease in LODs compared to previous work.[8,9]

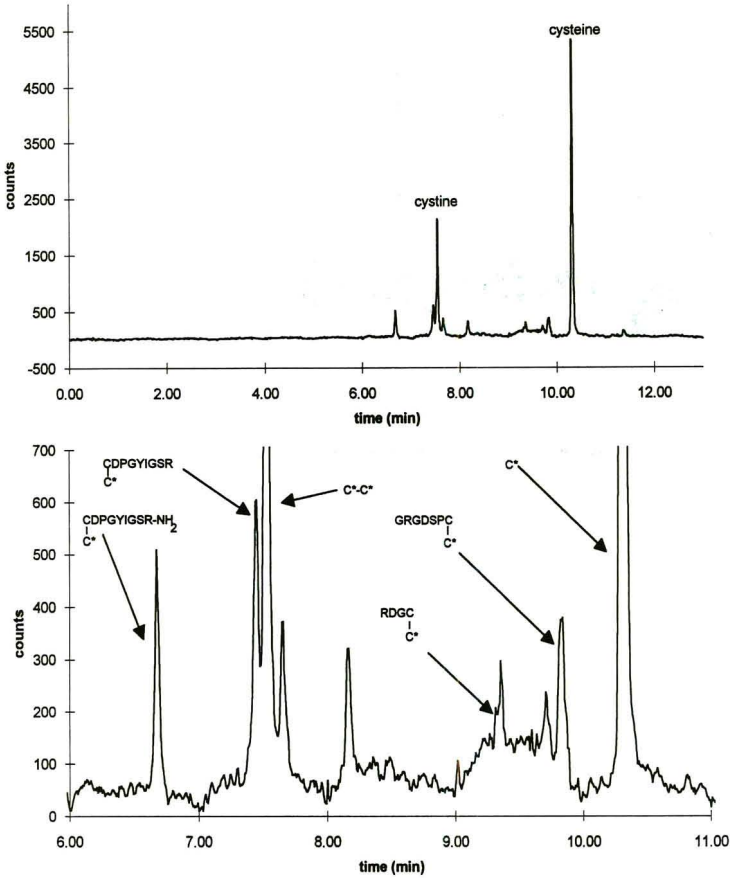

Figure 6. (A, Top). Electropherogram of [^{35}S]cysteine-labeled peptides. (B, Bottom) Detail of the electropherogram. A total of 3 fmol of ^{35}S is injected onto the CE column.

Table 2. Summary of Results

nuclide	chemical form	detection limit (amol of nuclide)	theoretical plates: radiochemical detection	theoretical plates: UV detection
^{32}P	ATP	0.09	80 800	not tested
^{35}S	Met	17	60 000	not tested
^{35}S	peptides	17	110 000	30 000
^{3}H	Phe	8000	70 000	30 000
^{3}H	Tyr	8000	70 000	40 000

In conclusion, we have demonstrated a novel radionuclide detection system that enables weak β emitters to be analyzed with excellent limits of detection and high separation efficiency. One of the limitations of the system is that the membrane binding properties only allow a select range of analytes to be examined. The Millipore Immobilon Psq/CD (Experimental Section) works well for peptides and most amino acids, but not for positively charged amino acids. A wide range of protein binding membranes are commercially available, and it is only in the area of analyzing small ions that potential problems arise due to the lack of a suitable membrane.

The current LODs of the membrane fraction collection system represent large improvements compared to on-line CE radiochemical detection systems. Unlike the on-line systems, the light collection efficiency and membrane scintillator efficiency are far from their theoretical limits in the postcolumn system, and so additional improvements should be possible. As one example, a tapered image reduction fiber (optical minifier) is being examined to improve light collection efficiency approximately 10-fold. Increases in light collection should yield a linear improvement in detection limit until the scintillation process from a single radionuclide decay produces enough photons to bring the event over the CCD read-noise level, an approximately 100-fold improvement.

The 15% RSD between replicate methionine injections is, at least in part, due to difficulties in reproducibly applying scintillator to the membranes. We are currently investigating using a second capillary to deliver a known amount of radiolabeled standard at a preset distance from the separation capillary. The advantages of the approach are severalfold. This will allow variations in scintillator efficiency to be normalized between membranes and will greatly facilitate automated routines to find and reconstruct the electrophero-

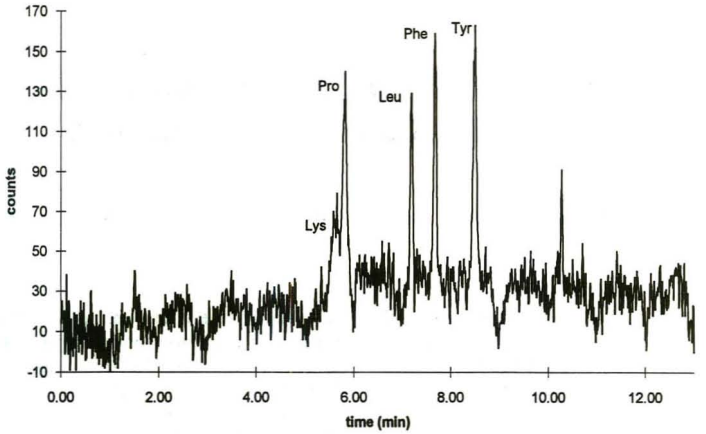

Figure 7. Electropherogram of a tritium-labeled amino acid standard solution. Each amino acid is present with equal activity.

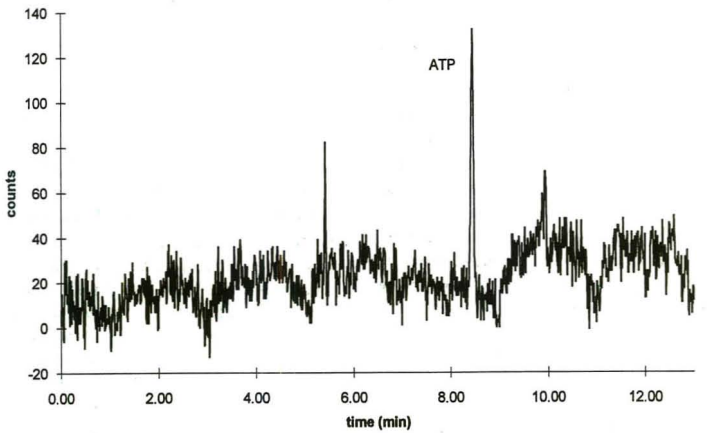

Figure 8. Electropherogram of a 300-zmol injection of ^{32}P-labeled ATP.

grams from the images. Lastly, the light collection efficiency from the camera lens pair is not uniform across the membrane; a smaller fraction of the emission from a point at the corner of a membrane is collected than from a point in the center. The main effect of this variation in collection efficiency is a "curved" baseline that "peaks" once per minute (corresponding to one pass across the membrane). This effect is visible in Figures 6 and 8. Although the use of analyte standards allows quantitative analysis to be performed even with this effect, a second capillary will allow the effect of nonuniform light collection efficiency across the membrane to be corrected.

Even without these refinements, the current system affords flexibility in the trace-level assay of a variety of radionuclides. A significant advantage of this detection approach is that it is nondestructive. If the LODs reported are not low enough for a particular assay, the membrane can be repeatedly imaged, with the limitation being the stability of the scintillation process and the eventual decay of the radionuclide. This ability affords unprecedented flexibility in dynamically obtaining the required LODs after the CE separation has been performed.

ACKNOWLEDGMENT

We thank Dr. Malcolm Pluskal of Millipore for providing the membranes for this research and for many useful discussions, Garret Forbes of the University of Illinois Chemistry Department for his help in examining a number of scintillator coatings, and Dr. Steven Pentoney, Jr. of Beckman Instruments for many helpful discussions. In addition, the donation by Millipore of the Quanta 4000 CE system is gratefully acknowledged. This work was supported by the National Institute of Mental Health (1R03 MH49640), a National Science Foundation Young Investigator Award (CHE 92-57024), the David and Lucile Packard Foundation, and the Searle Scholars Program/Chicago Community Trust.

Received for review November 22, 1993. Accepted April 13, 1994.[⊗]

[⊗] Abstract published in *Advance ACS Abstracts,* June 15, 1994.

Anal. Chem. **1994,** *66,* 2390–2396

Eluent Modifiers for the Liquid Chromatographic Separation of Carboxylic Acids Using Conductivity Detection

John Morris and James S. Fritz*

Ames Laboratory, U.S. Department of Energy, and Department of Chemistry, Iowa State University, Ames, Iowa 50011

It has long been held that chromatographic separation of carboxylic acids requires (a) the use of a gel-type column of fairly large dimensions and (b) an acidic aqueous eluent to repress ionization of the analytes and thereby give sharp peaks. The present work shows that neither of these conditions is necessary. Excellent separations of aliphatic carboxylic acids were obtained on macroporous resin columns using a predominantly aqueous eluent with no added acid. Addition of an alcohol, such as 1-butanol, to an aqueous mobile phase has a dramatic effect on the chromatographic separation of carboxylic acids. The alcohol is believed to coat the surface of a macroporous polystyrene–divinylbenzene resin and establish a dynamic equilibrium between the mobile and stationary phases. This increases the hydrophilicity of the resin surface and reduces the hydrophobic attraction of the analytes for the resin phase. The eluent systems have a very low background conductance, thus giving a very sensitive conductometric detection. The presence of carbonic acid (from atmospheric carbon dioxide) in the eluent was found to play a role in the retention mechanism of the carboxylic acid analytes.

Weak inorganic and organic acids of fairly low molecular weight are often separated and determined by ion-exclusion chromatography (IEC). Such separations are usually performed on sulfonated macroporous (gel) resin columns of fairly large dimensions. Several reviews have been published on IEC.[1-5] The separation mechanism is considered to be the partitioning of solute acids between the predominantly aqueous eluent and water inside the resin gel. However, several authors have identified a mixed-mode mechanism in which partitioning also occurs due to hydrophobic attraction of the sample solutes for the polymeric resin matrix.[6-8]

Hydrophilic organic acids can also be separated on smaller resin columns containing lightly sulfonated macroporous (nongel) polymeric resins.[8,9] Following accepted theory, these separations were performed with an eluent containing sulfuric acid. The purpose of the acid is to repress ionization of the carboxylic acids being separated so that the mechanism of separation would be predominantly interaction of the molecular solute acid with the resin matrix (i.e., hydrophobic attraction). Separations using macroporous resins offered some real advantages over traditional separations performed on gel resins. Separations were much faster (on much smaller columns), and the rigid nature of these resins provided the additional ability to carry out gradient elution with an organic solvent such as acetonitrile.

Detection of the separated carboxylic acids was by UV absorbance (at 210 nm) or refractive index. These methods are rather insensitive; typical sample concentrations were 20–2000 ppm. Unless an additional suppression device is used, the use of sulfuric acid in the eluent severely limits the use of conductivity detection because a small detection signal must be measured on top of a large background.

Equilibrium constant calculations indicate that alkane carboxylic acids are extensively ionized (69–97%) in predominantly aqueous solutions at the low concentrations generally used in liquid chromatography. It is questionable whether added sulfuric acid is really effective in converting the solute acids to the unionized molecular form. In fact Tanaka and co-workers[10] were able to obtain good separations of alkane carboxylic acids on gel-type resins with a carboxylic acid functional group using eluents containing a neutral hydrophilic chemical additive but no added acid.

In the present work, it was found that small straight-chain alcohols added to an aqueous eluent have a dramatic effect on the chromatographic behavior of small polar compounds such as the alkane carboxylic acids. The alcohols are believed to coat the surface of the polymeric resin owing to a dynamic equilibrium between the mobile and stationary phases. In favorable cases, low parts per billion (ppb) injected concentrations were easily detected by conductivity detection. In separations involving the carboxylic acids, carbonic acid, found naturally in the eluent, was discovered to have a noticeable effect on the retention mechanism of the separated acids.

EXPERIMENTAL SECTION

Apparatus. The chromatographic system consisted of a LKB 2156 solvent conditioner, a LKB 2249 HPLC gradient pump (LKB, Bromma, Sweden) with a mixing chamber volume of 0.5 mL, a Rheodyne 7125 injector (Rheodyne, Berkeley, CA) equipped with a 20-μL loop, a Dionex CDM-3 conductivity detector (Dionex, Sunnyvale, CA), and a Fisher Recordall Series 5000 recorder (Fisher Scientific/Instrument Lab, Itasca, IL). The data acquisition system consisted of a Keithley Chrom 1-AT acquisition board (Keithley MetraByte

(1) Gjerde, D. T.; Mehra, H. *Advances in Ion Chromatography*; Century International: 1989; Vol. 1, p 139.
(2) Haddad, P. R.; Jackson, P. E. *Ion Chromatography*; Elsevier: Amsterdam, 1990; p 195.
(3) Fritz, J. S. *J. Chromatogr.* **1991,** *546,* 111.
(4) Tanaka, K.; Ishizuka, T.; Sunahara, J. *J. Chromatogr.* **1979,** *174,* 153.
(5) Glód, B. K.; Kemula, W. *J. Chromatogr.* **1986,** *366,* 39.
(6) Jupille, T.; Gray, M.; Black, B.; Gould, M. *Am. Lab.* **1981,** *13* (8), 80.
(7) Smith, R. E. *Applications of Ion Chromatography*; CRC Press: Boca Raton, FL, 1988; p 69.
(8) Lee, D. P.; Lord, A. D. *LC-GC* **1987,** *4,* 261.
(9) Morris, J. B.; Fritz, J. S. *LC-GC* **1993,** *11* (7), 513.

(10) Tanaka, K. Personal Communications, Mar and Oct 1992.

0003-2700/94/0366-2390$04.50/0
© 1994 American Chemical Society

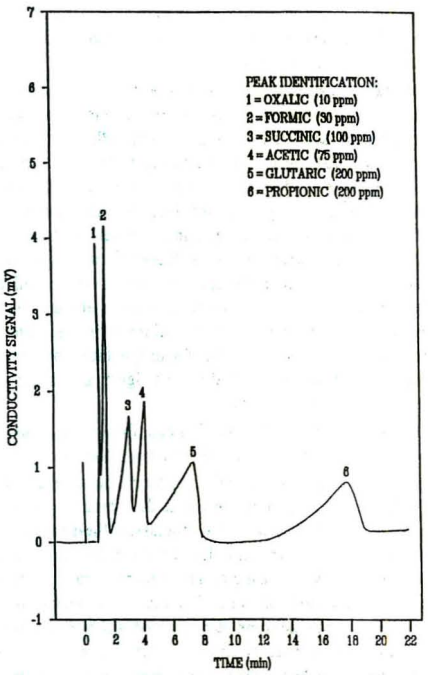

Figure 1. Chromatographic separation on sulfonated PS-DVB resin column (150 × 4.6 mm) of 0.25 mequiv/g exchange capacity. Eluent conditions: deionized water. Detection is conductivity with an output range of 30 μS full scale. Flow rate is 1.0 mL/min. Peaks are as identified.

Corp., Taunton, MA) and Labtech Notebook software (Laboratory Technologies Corp., Wilmington, MA). The ion-exclusion columns used in this study were columns prepared in our lab using 5-μm underivatized macroporous polystyrene–divinylbenzene resin (Sarasep Inc., Santa Clara, CA), and the same resin functionalized with a sulfonic acid group at 0.25 mequiv/g exchange capacity. A Shandon HPLC packing pump (Shandon Southern, Sewichley, PA) was used for column packing. A Hamilton PRP-X100 (Hamilton Co., Reno, NV) trimethylammonium anion-exchange column of 0.19 mequiv/g exchange capacity was used to remove carbonic acid from the eluent.

Reagents and Chemicals. The organic eluent modifiers used for the chromatographic separations were reagent grade. Stock solutions of the organic acids were prepared from reagent-grade materials. Eluents were prepared daily using the reagent-grade organic modifiers and water. A Barnstead Nanopure II system (Sybron Barnstead, Boston, MA) was used to further deionize distilled water for all eluents and sample mixtures.

RESULTS AND DISCUSSION

Effect of Organic Modifiers. Several carboxylic acids were separated chromatographically on a lightly sulfonated polymeric resin column. An aqueous eluent was used with varying amounts of various alcohols or other organic liquids as modifiers. Figure 1 shows the separation of six carboxylic acids using only water as an eluent. A couple of things should be noticed from this chromatogram. First, the elution order of the separated acids is different than in previous work using sulfuric acid in the eluent. In this case, succinic acid elutes before acetic acid. This elution order is not surprising since succinic acid is a dicarboxylic acid and would have a high percentage of ionization in a water eluent. The second item of interest is the poor peak shape, especially for glutaric and propionic acids. Elution of butyric and valeric acids was prohibitively long.

Addition of a small amount of methanol to the eluent improved the peak shape and reduced retention times of the acid solutes. The amount of methanol was increased until an optimized separation was achieved with an eluent containing 60% methanol/40% water. Baseline resolution was obtained in less than 6 min for a mixture containing formic acid (1 ppm), acetic acid (15 ppm), propionic acid (30 ppm), butyric acid (50 ppm), and valeric acid (75 ppm). There was a dramatic increase in sensitivity using conductivity detection compared to either UV or RI detection.

The same optimization procedure was followed, and a similar separation of the same five acids was obtained with an eluent consisting of 40% ethanol/60% water. Using the same detector output range, injected concentrations ranged from 0.2 (formic) to 6.0 ppm (valeric) for peaks of the same magnitude.

An optimized separation of the five alkane carboxylic acids was also obtained with an eluent consisting of 20% propanol/80% water. The same detector response was seen for injected concentrations from 0.25 (formic) to 2.00 ppm (valeric), again using the same detector setting.

Figure 2 shows the optimized separation of the same acid mixture using an eluent of 5% butanol/95% water. Notice that the acids are still essentially baseline resolved, and the separation is complete in approximately 5 min. Again, the sensitivity is improved as the injected concentrations range from 0.25 (formic) to 0.50 ppm (valeric).

A few points should be considered with the use of this series of straight-chain alcohols. The first is that the detection sensitivity continues to improve as the chain length of the alcohol increases. In the series of alcohol additives (from methanol to butanol), the sensitivity increases as the percentage of alcohol modifier decreases (the percentage of water increases). The percentage of ionization of the carboxylic acids is higher with the higher percentage of water in the eluent. In the case of a pure water system, a calculation showed the acids to be approximately 69–97% ionized for the concentrations injected.

The use of organic modifiers other than straight-chain alcohols was investigated. These included cyclohexanol, dimethylformamide, tetrahydrofuran, methyl ethyl ketone, 2-ethoxyethanol, and acetonitrile. Some of these were effective in reducing the retention times of the carboxylic acid analytes and sharpening the peaks (see Table 1). In some cases, new peaks were observed resulting from impurities in the organic modifiers. While the organic modifiers had relative merits, the best appeared to be the straight-chain alcohols.

Mechanism of Alcohol Modifiers. The effect of methanol and ethanol on the chromatographic separations could possibly be explained by stronger solvation of the sample solutes in the

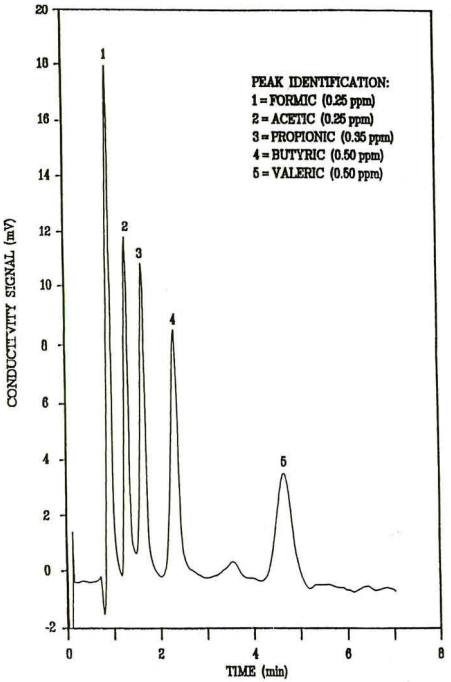

Figure 2. Chromatographic separation on sulfonated PS-DVB resin column (150 × 4.6 mm) of 0.25 mequiv/g exchange capacity. Eluent conditions: 5% butanol/deionized water. Detection is conductivity with an output range of 3 μS full scale. Flow rate is 1.0 mL/min. Peaks are as identified.

Table 1. Retention Times for Formic, Acetic, Propionic, Butyric, and Valeric Acids for Optimized Concentrations of Various Modifiers in Binary Water Eluents[a]

	t_R (min)				
eluent modifier	formic	acetic	propionic	butyric	valeric
water (100%)	1.35	3.90	17.90		
methanol (60%)	1.35	1.90	2.30	3.05	4.95
ethanol (40%)	1.15	1.90	2.45	3.55	6.35
propanol (20%)	0.90	1.45	1.95	2.55	4.65
butanol (5%)	0.85	1.25	1.65	2.30	4.70
pentanol (1%)	0.90	1.10	1.40	1.90	3.75
tert-butanol (5%)	0.80	1.10	1.85	3.55	8.50
cyclohexanol (2%)	1.45	1.90	2.60	4.10	
dimethylformamide (15%)	1.35	2.05	3.70	8.40	
tetrahydrofuran (1%)	0.85	0.95	1.25	2.00	5.35
methyl ethyl ketone (2%)	0.90	1.05	1.25	1.75	3.90
2-ethoxyethanol (10%)	0.95	1.20	1.70	2.80	7.85
acetonitrile (20%)	0.90	1.35	1.75	2.40	4.40

[a] Separations performed on a lightly sulfonated resin column (150 × 4.6 mm) of 0.25 meq/g exchange capacity. Detection was conductivity. Flow rate was 1.0 mL/min.

liquid eluent. In this connection, it should be noted that in a binary aqueous system the majority of methanol exists as a methanol–water complex up to a maximum of approximately 60% methanol.[11] In HPLC separations, the capacity factor is thought to be a function of "free" methanol rather than the total methanol content of the eluent. For our carboxylic acid separations with propanol–water and especially with butanol–water, the amount of modifier in the eluent is too small to adequately explain the observed effects on the basis of increased solvation in the liquid phase.

Several authors have found that a portion of the organic solvent in organic water eluents is adsorbed onto the surface of a bonded-phase silica commonly used in HPLC.[12–17] This creates a so-called "third phase" that can alter the partitioning of sample solutes and thereby affect their capacity factors. However, this effect may not be very large with the commonly used eluents such as methanol, acetonitrile or tetrahydrofuran mixed with water. McCormick and Karger[13] found that only 2% (by volume) of a modifier of somewhat higher molecular weight in a methanol–water or acetonitrile–water eluent was more strongly adsorbed by the stationary phase. They concluded that the concentration of hydrophobic modifiers in the stationary phase is believed to be a significant factor in determining polar selectivity.

Slaats et. al. studied distribution equilibria of deuterated solvents between the mobile and stationary phases.[15]

Scott and Simpson studied the adsorption of aliphatic alcohols, aldehydes, and carboxylic acids in binary mixtures with water by ODS-2 silica.[16] They found that the distribution coefficient increases exponentially with the carbon number of the moderator. When using an aliphatic moderator having a chain length of four or five carbon atoms, the surface of a bonded phase could be completely covered with a monolayer. They stated further that the chromatographic characteristics of the surface could be changed by choosing appropriately active groups.

Adsorption of a layer of alcohol on the polymeric resin surface is believed to explain the dramatic effects observed in our separations of carboxylic acids. Butanol has the highest distribution coefficient of the alcohol moderators studied, and only a low concentration in the aqueous eluent is needed to coat the resin surface. Partitioning of the various solute acids between the predominately aqueous eluent and the coated resin surface is much different than it is with an uncoated polystyrene surface.

Effect of Resin Sulfonation. Our separations up to this point were performed on lightly sulfonated polymeric resins. The small amount of sulfonic acid groups makes the resin surface more hydrophilic so that analyte species can approach and interact more readily with the resin matrix. It is conceivable that the sulfonic acid substituent may also affect the separation of analytes by converting the carboxylate anions to molecular carboxylic acid at the resin surface. This idea was tested by performing the separations under identical conditions but using an underivatized resin column. With an aqueous eluent containing 5% v/v butanol, only small differences were noted in the chromatograms obtained on the sulfonated and unsulfonated resin columns. While separations with lightly sulfonated resins tended to be slightly better than with unsulfonated resins, these results suggest that the sulfonic acid group does not play a vital role in the separation process.

(11) Katz, E. D.; Lochmüller, C. H.; Scott, R. P. W. *Anal. Chem.* **1989**, *61*, 349.
(12) Knox, J. H.; Pryde, A. *J. Chromatogr.* **1975**, *112*, 171.
(13) McCormick, R. M.; Karger, B. L. *J. Chromatogr.* **1980**, *199*, 259.
(14) McCormick, R. M.; Karger, B. L. *Anal. Chem.* **1980**, *52*, 2249.
(15) Slaats, E. H.; Markovski, M.; Fekete, J.; Poppe, H. *J. Chromatogr.* **1981**, *207*, 299.
(16) Scott, R. P. W.; Simpson, C. F. *Faraday Symp. Chem. Soc.* **1980**, *15*, 69.
(17) Lau, Y. M.; Simpson, C. F. *Anal. Proc. (London)* **1988**, *25* (3), 86.

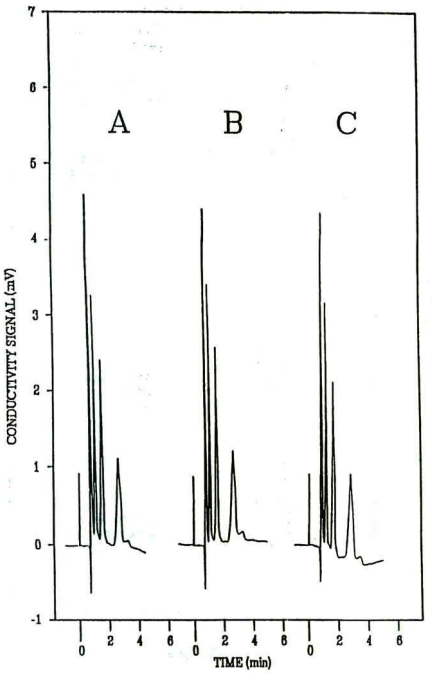

Figure 3. Successive injections of (A) formic acid (3.25×10^{-6} M), acetic acid (6.66×10^{-6} M), propionic acid (1.08×10^{-5} M), and sodium butyrate (9.08×10^{-6} M); (B and C) sodium formate, sodium acetate, sodium propionate, and sodium butyrate in the same respective concentrations. Separations performed on underivatized PS-DVB resin column (150 × 4.6 mm). Eluent conditions: 4% butanol/deionized water. Detection is conductivity with an output range of 10 μS full scale. Flow rate is 1.0 mL/min. The elution order of the analytes is as listed.

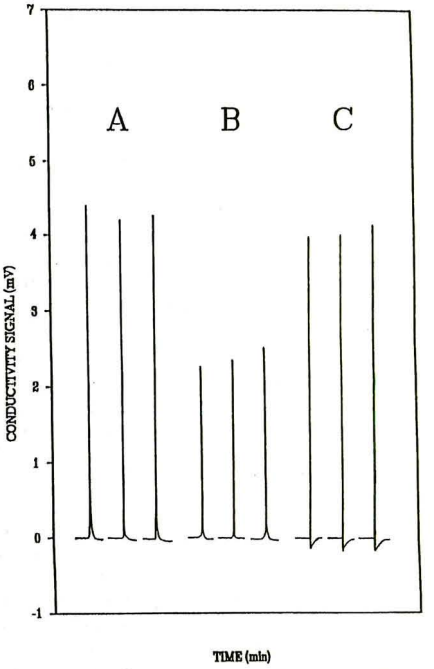

Figure 4. Three successive injections of (A) formic acid (3.25×10^{-6} M), (B) sodium formate (3.25×10^{-6} M), and (C) sodium formate (3.25×10^{-6} M) after treatment with carbon dioxide. Flow injection analyses are performed with the detector connected directly to the injection valve. Eluent conditions: 4% butanol/deionized water. Detection is conductivity with an output range of 30 μS full scale. Flow rate is 1.0 mL/min.

In an effort to find additional information about the retention mechanism, we investigated the chromatographic behavior of sodium salts of these alkane carboxylic acids. An underivatized column was chosen to avoid introducing any source of acid into our system. A simple ion exchange would take place on a sulfonated resin, converting the salt to the acid. Figure 3A shows the separation of formic acid, acetic acid, propionic acid, and sodium butyrate on an underivatized resin column using a 4% butanol/water eluent. Figures 3B,C shows the successive separations of the sodium salts of these same acids at the same concentrations. Comparison of the chromatograms reveals no great differences. The salts behave almost the same as the acids, possibly indicating that the salts are being converted to acids.

Effect of Carbonic Acid. In reviewing our complete chromatographic system, no source of acid other than carbonic acid (or CO_2) could be found. Since the analyte acids are weaker carboxylic acids, it is possible that carbonic acid could have an effect on the retention mechanism. It was also shown in previous work that carbonic acid has a substantial capacity factor.[9] In other words, the carbonic acid spends a significant amount of time residing on the surface of the polymeric resin. In this particular case, the carbonic acid could be a natural impurity that works to our advantage.

A series of experiments were performed to further elucidate the effects of the carbonic acid in the eluent. First, approximately 100 mL of the eluent mixture (4% butanol/water) was placed in a beaker and the pH was measured. Initially, the pH was close to neutral (pH 6.8). With time, however, the pH gradually drifted toward more acidic pH values. As the solution stands exposed to the atmosphere, one would expect continuous absorption of carbon dioxide and a more acidic pH with the resultant formation of carbonic acid. Even though our eluent is sparged and kept under a blanket of helium, it would be very difficult to completely remove all carbonic acid. Any amount present in the water–alcohol mixture will equilibrate with the resin.

The next experiments were performed after removing the analytical column and connecting the conductivity detector directly to the injection port. This configuration allowed us to do some flow injection analyses. Figure 4 shows the detection signal obtained from the equal concentration injections of formic acid (A), sodium formate (B), and sodium formate after treatment with carbon dioxide (C). The magnitude of the conductivity signal was lower for equal concentration of the salt compared to the acid. This is expected based on the theoretical limiting equivalent conductances for the two species (i.e., $H^+ = 350$, $Na^+ = 50$, and the formate anion is the same for both). Notice, however, that the magnitude of the signal for the salt treated with carbon dioxide

closely approximates the signal obtained for the injected acid. This suggests that there is conversion of the salt to the acid species by the carbonic acid present in the solution. Similar results were obtained when the same experiment was performed on the other carboxylic acids such as acetic and propionic acids.

Additional experiments were needed to provide information as to whether the effect of the carbonic acid is a solution or a surface phenomena. Closer examination of previous chromatograms using various organic mobile-phase modifiers showed a small consistent system peak at approximately 3.5 min. Depending on the retention times of the analyte acids, this system peak can show up as a small shoulder on another peak or possibly coelute in some cases. The system peak became very noticeable when the amplification of the acquired detection signal was increased. The system peak was identified by injection of only carbonic acid which gives a peak at the same retention time. The origin of the system peak is believed to be the carbonic acid that elutes after disruption of the established mobile-stationary phase equilibrium, which occurs with the injection of the acid mixture.

Using the original system configuration, an anion-exchange column in the hydroxide form was placed in-line between the pump and the injection valve. In this manner, the anion-exchange column should act as a filter to remove any carbonic acid from the mobile phase prior to the separation column. Figure 5A shows the separation of formic through butyric acids under established eluent conditions prior to the insertion of the anion-exchange column. Notice the background conductance of 904 nS. Flow was then stopped, and the anion-exchange column was placed in-line. As flow was resumed, injections were made at timed intervals and background conductances were recorded. Considering the low dead volume of the system, the mobile phase should be free of carbonic acid after a couple of minutes. The background conductance signal, however, decreased more gradually indicating that the carbonic acid was slowly being washed off the column. The background signal stabilized after 30 min to a significantly lower value of 177 nS. Figure 5B shows the separation of the same mixture at this time. The resolution of the acid analytes was noticeably decreased. This indicates that the carbonic acid plays a role in the retention mechanism of the weak acid analytes. As the carboxylic acids approach the resin surface predominantly as anions, the carbonic acid could convert them to the molecular acids. This would then help facilitate separation of these alkane carboxylic acids based on the length of the hydrocarbon portion of the molecules. Finally, the anion-exchange column was removed from the system. The background conductance gradually increased toward the original value. Figure 5C shows a separation of the same mixture when the background had stabilized 30 min after removal of the anion-exchange column. The resolution of the acid species and the background signal had returned to the same value as the original chromatogram.

If the eluent was allowed to sit exposed to the atmosphere for a 12-h period, the background conductance roughly doubled (1.5–3.0 μS) and injection of the standard mixture resulted in a fluctuating conductivity signal. After a period of time, the signal would again stabilize. As expected, the eluent was taking up increasing amounts of carbon dioxide from the

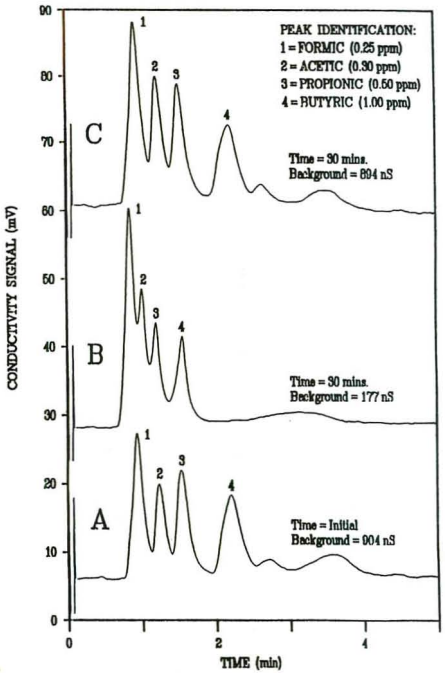

Figure 5. Chromatographic separation on sulfonated PS-DVB resin column (150 × 4.6 mm) of 0.25 mequiv/g exchange capacity. (A) initial separation, (B) separation after 30 min with anion-exchange column (hydroxide form) in-line between pump and injection valve, and (C) separation 30 min after removal of anion-exchange column (initial configuration). Eluent conditions: 4% butanol/deionized water. Detection is conductivity with an output range of 3 μS full scale. Flow rate is 1.0 mL/min. Peaks are as identified.

atmosphere. As time passed, the increased carbonic acid content in the eluent gave an increased background signal. Similar signal fluctuations were seen in experiments where carbonic acid was injected in large amounts. After the column became heavily loaded with the carbonic acid, an injection led to severe disruption of the established equilibrium until it stabilized at a new level.

Freshly deionized water was used to prepare an eluent, which was then equilibrated for approximately 1 h. The background conductance returned to near the original value of 1.5 μS, and a separation of the standard mixture returned to normal.

The presence of carbonic acid in the eluent appears beneficial for separation of the alkane carboxylic acids, when it is in moderate and controlled quantities. This does not present a problem for most HPLC systems that are equipped with a degassing module. For normal operation, the alcohol/water eluent can be prepared without any special treatment. Whatever small amount of carbonic acid that exists naturally in the alcohol or water will establish an equilibrium between the mobile and stationary phases. This proves to be sufficient for separation of the alkane carboxylic acids. A reasonable estimation of the carbonic acid content can be obtained by monitoring the background conductance signal. The total amount of carbonic acid remains constant when the eluent is

Table 2. Quantitative Results Showing Linear Dynamic Range and Linearity for Formic, Acetic, Propionic, and Butyric Acids on Underivatized Resin Column (150 × 4.6 mm) Using a 4% Butanol/Water Eluent[a]

acid	linear dynamic range (M)	corr coeff	slope
formic	1.0×10^{-6}–5.0×10^{-4}	0.9991	1.07
acetic	1.0×10^{-6}–5.0×10^{-4}	0.9998	0.92
propionic	1.0×10^{-6}–5.0×10^{-4}	0.9996	0.95
butyric	5.0×10^{-6}–5.0×10^{-4}	0.9993	0.89

[a] Detection is conductivity at 3 μS full scale.

protected from contact with the atmosphere as is the case with helium degassing.

Attempted Separation of Sulfonic Acids. Next, the behavior of alkane sulfonic acids and their respective sodium salts was investigated. On the basis of the success of the separation of the alkane carboxylic acids, it was thought that a similar series of sulfonic acids could also be separated. No separation was achieved for the alkane sulfonic acids or their sodium salts when using the binary alcohol/water eluent system. All acids in the series eluted with the same retention time. This was not surprising, considering the strength of these acids. The sulfonic acid is a much stronger acid than the carboxylic acid and, consequently, is not going to be affected in the same manner by the presence of the carbonic acid. The highly ionized alkane sulfonic acids will be strongly solvated by the aqueous eluent and have very fast chromatographic elution. This was evidenced by the identical retention times irregardless of the length of the hydrocarbon portion of the molecule. This was further confirmation that the role of carbonic acid on a retention mechanism was a phenomenon unique to the weaker carboxylic acids.

Quantitative Chromatographic Determinations. A series of chromatographic separations was run at varying concentrations of formic, acetic, propionic, and butyric acids in order to determine the approximate limits of detection and the linear dynamic range (see Table 2). An unsulfonated resin column was used in conjunction with an aqueous eluent containing 4% v/v butanol. The concentration of each analyte acid ranged from 2.5×10^{-7} to 1.0×10^{-2} M. Good separations with well-formed peaks were obtained for analyte concentrations of 1×10^{-3} M and below. Significant peak fronting occurred at 5.0×10^{-3} and 1.0×10^{-3} M concentrations, indicating some overloading. The peak shapes were very poor at 5.0×10^{-3} and 1.0×10^{-2} M concentrations with severe fronting. A chromatogram at an intermediate concentration (1×10^{-5} M of each analyte) is shown in Figure 6.

Linear plots of peak area vs concentration were obtained for each of the four analytes studied over most of the concentration range studied. The plot for formic acid had a linear regression correlation coefficient of 0.9995 between 1×10^{-6} and 5×10^{-4} M. A slight deviation from linearity was noted at 5×10^{-7} and at 1×10^{-3} M. Similar plots were obtained for acetic and propionic acids. The calibration plot for butyric acid had a nonlinear region at the two lowest concentrations owing to interference from the overlapping carbonic acid peak. However, the butyric acid calibration plot was linear between 5×10^{-6} and 5×10^{-4} M. It should be possible to alter chromatographic conditions to minimize carbonic acid interference at very low butyric acid concentrations.

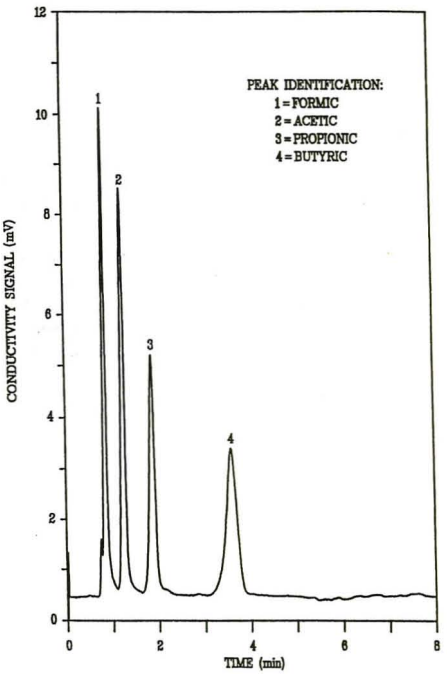

Figure 6. Chromatographic separation on underivatized PS-DVB resin column (150 × 4.6 mm). Eluent conditions: 4% butanol/deionized water. Detection is conductivity with an output range of 3 μS full scale. Flow rate is 1.0 mL/min. Injected concentration for all acids is 1×10^{-5} M, and peaks are as identified.

Limits of detection were estimated to be approximately 1×10^{-7} M for acetic and propionic acids and 5×10^{-8} M for formic acid, which has a somewhat sharper peak. This corresponds to approximately 2 ppb for formic acid, 6 ppb for acetic acid, and 7 ppb for propionic acid.

CONCLUSIONS

Carboxylic acids and other polar compounds are often separated by ion-exclusion chromatography on gel-type ion-exchange resin columns. It has always been considered necessary to add a strong acid to the aqueous eluent to ensure that the carboxylic acid analytes are in the molecular form. We now conclude that separations of carboxylic acids can be performed on columns containing either underivatized or lightly sulfonated macroporous resins. The separation mechanism appears to be largely a hydrophobic attraction between the analytes and the resin. If a suitable alcohol or other organic moderator is added to the aqueous eluent, no strong acid is necessary. Excellent sensitivity and low detection limits are now possible for carboxylic acids using an ordinary conductivity detector.

The function of the organic moderator is to coat the resin surface and make it less hydrophobic. Butanol is more efficient than the lower straight-chain alcohols because it has a higher partition coefficient, and lower concentrations in the eluent are thereby needed to effectively coat the resin. This concept may find extensive use for many other types of HPLC

separations. In some cases, the addition of surface modifiers may have clear advantages over chemically derivatized resins. It may be possible to alter the properties of a single resin by the appropriate choice of a chemical moderator in the eluent. This would make it possible to "fine tune" conditions to optimize the separation of interest.

Carbonic acid is another example of a chemical moderator that may be present in the eluent. Gas sparging does not remove low concentrations of CO_2 from liquid eluents. Unless special treatment methods are employed, it is likely that aqueous organic eluents will contain low concentrations of dissolved CO_2, which may function as carbonic acid. The possible effects of carbonic acid on HPLC seem not to have been considered previously, at least in the separation of carboxylic acids. Our results indicate that carbonic acid (or CO_2) from the eluent can adsorb onto the resin surface and change the retention times of carboxylic acid analytes.

ACKNOWLEDGMENT

The authors wish to thank D. T. Gjerde of Sarasep, Inc. for providing the polymeric resin used in this work. We also thank Dan Lee of the Hamilton Co. for the gift of the anion-exchange column used in this research. This work was supported by Supelco Inc. Work was performed in the Ames Laboratory, which is operated by Iowa State University for the U.S. Department of Energy under Contract W-7405-Eng-82.

Received for review January 3, 1994. Accepted May 4, 1994.®

® Abstract published in *Advance ACS Abstracts,* June 1, 1994.

Anal. Chem. **1994**, *66*, 2397–2403

Enhanced Extraction of Phenobarbital from Serum with a Designed Artificial Receptor

Jane N. Valenta, Robert P. Dixon,† Andrew D. Hamilton, and Stephen G. Weber*
Department of Chemistry, University of Pittsburgh, Pittsburgh, Pennsylvania 15260

The primary goal of this work was to determine whether artificial receptors that function on the basis of molecular recognition have analytical capabilities. As an example of such a receptor, we have chosen one directed toward barbiturates. Chloroform enriched with this artificial receptor (1 mM) can extract more than 90% of the phenobarbital from a 20 μM phenobarbital solution in human control serum using a volume ratio (organic/serum) as small as 0.5. In the absence of this receptor, the volume ratio must be greater than 10 to achieve similar extraction efficiencies. In addition to volume ratio, the role of pH, receptor concentration, and solvent type are discussed. The experimental results are found to be in good agreement with predictions based on chemical equilibria. Through the use of this and other similar receptors, the amount of organic solvent used in extractions can be minimized.

Liquid–liquid[1,2] and solid-phase[3] extractions have been used extensively in chromatography for sample preparation. Solvent extraction is a convenient method for isolating an analyte or group of analytes from a complex matrix such as blood serum. The extracting solvent offers a very limited degree of selectivity and so it is not uncommon to find interfering species in the extract. The lower the degree of selectivity of the extraction step, the greater the demands placed on the selectivity of the ensuing chromatographic determination. From a practical standpoint, an extraction should extract selectively the analyte of interest and concentrate it in a minimum number of steps.

Historically, the extraction of ions has benefited from the use of transition metal chelating agents[4] that can selectively extract metal cations from aqueous solution. Recently Bartsch and co-workers[5–8] have turned attention to the more difficult problem of alkali and alkaline earth metal ion extractions. A series of crown ether derivatives was synthesized and systematically studied for their ability to extract alkali and alkaline earth metal cations from aqueous solution into chloroform.[5–8]

There has been very little effort directed toward molecularly selective extractions. Antibodies have been used in the extraction of drugs[9] for example. Artificial receptors offer a flexible strategy for small-molecule extractions. Though the selective extraction of butylamines,[10] creatinine,[11] and the amino acids phenylalanine, tryptophan, and tyrosine[12] have been demonstrated, there have been to our knowledge no systematic investigations of the molecularly selective extraction of any organic species.

The system that we are currently investigating represents the larger class of artificial receptors that are based on hydrogen bond-directed molecular recognition.[13–17] In this work, an enhanced extraction medium has been developed based on an artificial receptor molecule[18] that binds specifically to 5,5-disubstituted barbiturates (Figure 1). The cavity of the receptor molecule is lined with hydrogen-bonding groups that are complementary to the hydrogen-bonding groups of barbiturates. The binding interactions of the receptor–barbital complex have been evaluated in $CDCl_3$ by ^1H NMR and a formation constant (K_f) value of 2.08×10^4 M^{-1} has been determined.[18] This formation constant is large enough that practical application of the receptor may be considered.

The purpose of this paper is to investigate the analytical capabilities of a synthetic receptor for the enhanced extraction of phenobarbital from serum. In particular, the use of such receptors should make extractions possible with less organic solvents. There are several questions that arise in conjunction with this, or any other attempt to use hydrogen bond-directed molecular recognition in this manner. This barbiturate receptor is relatively polar. Binding to barbiturates is favored in nonpolar solvents and weakened in polar solvents. Thus, it is important to determine whether a practically useful concentration of a rather polar receptor can be achieved in an extraction medium that favors binding. In addition to solubility being an issue, the presence of additional hydrogen-bonding substrates (e.g., water and serum components) which may interfere with phenobarbital–receptor binding is a concern as well. Another aspect of the extraction that needs to be addressed is pH. Traditionally, the adjustment of pH of the aqueous sample has been used to control selectivity but the

† Current address: Department of Chemistry, Northwestern University, Evanston, IL 60208.

(1) Poole, S. K.; Dean, T. A.; Oudsema, J. W.; Poole, C. F. *Anal. Chim. Acta* **1990**, *236*, 3.
(2) Furton, K. G.; Rein, J. *Anal. Chim. Acta* **1990**, *236*, 99.
(3) Krishnan, T. R.; Ibraham, I. *J. Pharm. Biomed. Anal.* **1994**, *12*, 287.
(4) Fritz, J. S.; Schenck, G. H. In *Quantitative Analytical Chemistry*; Allyn and Bacon, Inc.: Boston, MA 1979; pp 425–433.
(5) Strzelbicki, J.; Bartsch, R. A. *Anal. Chem.* **1981**, *53*, 1894.
(6) Charewicz, W. A.; Heo, G. S.; Bartsch, R. A. *Anal. Chem.* **1982**, *54*, 2094.
(7) Walkowiak, W.; Kang, S. I.; Stewart, L. E.; Ndip, G.; Bartsch, R. A. *Anal. Chem.* **1990**, *62*, 2022.
(8) Walkowiak, W.; Ndip, G.; Desai, D. H.; Lee, H. K.; Bartsch, R. A. *Anal. Chem.* **1992**, *64*, 1685.
(9) Miyairi, S.; Shimada, H.; Awata, N.; Goto, J.; Nambara, T. *T. Pharm. Biomed. Anal.* **1994**, *12*, 389.
(10) Chang, S. K.; Jang, M. J.; Han, S. Y.; Lee, J. H.; Kang, M. H.; No, K. T. *Chem. Lett.* **1992**, *10*, 1937.
(11) Buhlmann, P.; Badertscher, M.; Simon, W. *Tetrahedron* **1993**, *49*, 595.
(12) Rebek, J., Jr.; Nemeth, D. *J. Am. Chem. Soc.* **1985**, *107*, 6738.
(13) Lehn, J. M. *Science* **1985**, *227*, 849.
(14) Cram, D. J. *Agnew. Chem., Int. Ed. Engl.* **1988**, *27*, 1009.
(15) Izatt, R. M.; Bradshaw, J. S.; Pawlak, K.; Bruening, R. L.; Tarbet, B. J. *Chem. Rev.* **1992**, *92*, 1261.
(16) Rebek, J., Jr.; Askew, B.; Killoran, M.; Nemeth, D.; Lin, F. T. *J. Am. Chem. Soc.* **1987**, *109*, 2426.
(17) Hamilton, A. D. In *Advances in Supramolecular Chemistry*; Gokel, G. W., Ed.; JAI Press, Inc.: Greenwich, CT, 1990; Vol. 1, pp 1–64.
(18) Chang, S. K.; Hamilton, A. D. *J. Am. Chem. Soc.* **1988**, *110*, 1318.

0003-2700/94/0366-2397$04.50/0
© 1994 American Chemical Society

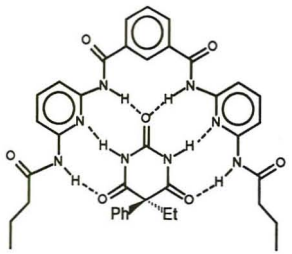

Figure 1. Structure of the barbiturate receptor and the hydrogen-bonding interactions between barbiturate receptor and phenobarbital.

effects of pH on binding are not known. This paper not only addresses these issues but it evaluates the experimental results in light of equilibrium considerations.

EXPERIMENTAL SECTION

Binding Studies. *Reagents.* Spectrophotometric grades of chloroform and methylene chloride were purchased from Mallinckrodt Specialty Chemicals Co. (Paris, KY) and Aldrich Chemical Co. (Milwaukee, WI), respectively. Barbital, amobarbital, and phenobarbital were purchased from Sigma Chemical Co. (St. Louis, MO). The details of the barbiturate receptor synthesis have been described elsewhere.[18] The barbiturate receptor solutions were placed in an ultrasonicator for 10 min to hasten the dissolution of the receptor in chloroform.

Apparatus. UV absorbance measurements were made using either an IBM 9420 UV–vis spectrophotometer or Hewlett-Packard 8450A diode array spectrophotometer. Quartz cuvettes with path lengths of 0.1 and 1.0 cm were purchased from Fisher Scientific (Pittsburgh, PA).

Procedure. Two different experimental approaches were pursued to determine the dissociation constant (K_d) for receptor complexes involving barbital, amobarbital, and phenobarbital. In the first set of experiments, the concentration of receptor was held constant while the concentration of barbiturate was varied. For these experiments, 1.0-cm path length quartz cells were used and the total receptor concentration was held constant between 40 and 75 μM. In the second set of experiments, a series of dilutions was made in which the concentrations of receptor and barbiturate were very similar. Concentrations ranged from 0 to 505 μM for the barbiturates and the receptor. Linear calibration plots for receptor and receptor–phenobarbital solutions were obtained for the concentration ranges studied. At concentrations beyond 121 μM, spectrophotometric quartz cells of 0.1-cm path length were necessary. In the wavelength range where there is no interference from the barbiturate absorption ($\lambda_{max} \cong 240$ nm), there is a large absorption band at 302 nm in the receptor. This absorption band shifts to 305 nm upon formation of the receptor–substrate complex. The maximum difference in absorptivities of the receptor and the receptor–substrate complex is 318 nm. The concentration of the RS complex was determined by directly measuring absorbance changes at either 316 or 318 nm or by measuring the absorbance changes occurring at 318 and 290 nm by difference spectroscopy. Representative UV spectra for difference measurements are

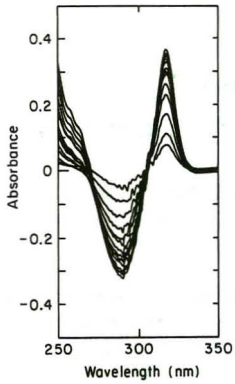

Figure 2. Representative UV spectra for a solution containing 5.90–319 μM phenobarbital and 65 μM receptor in methylene chloride.

Table 1. Difference in Molar Absorptivities for Receptor–Barbiturate Complex and Receptor Solutions in Chloroform and Methylene Chloride

substrate	solvent	$\Delta\epsilon_{316}$ (L/mol-cm)	$\Delta\epsilon_{318}$ (L/mol-cm)	$\Delta\epsilon_{maxmin}$ (L/mol-cm)
barbital	chloroform	4780		8310
barbital	methylene chloride	6260		10400
amobarbital	chloroform	4820		8640
amobarbital	methylene chloride	6030		10400
phenobarbital	chloroform	5230	5410	8880
phenobarbital	methylene chloride	5910	6130	10700

shown in Figure 2. The molar absorptivities for the receptor at 318 nm in chloroform and methylene chloride are 12 700 and 12 300 L mol^{-1} cm^{-1}, respectively. Thus for the single-wavelength measurement, the absorbance must be corrected for the concentration of free receptor in solution. The concentration of the RS complex can be calculated for the single wavelength measurements by using

$$[RS] = (A^{T}_{\lambda 1} - A^{R}_{\lambda 1})/(b\Delta\epsilon_{\lambda 1}) \quad (1)$$

where [RS] is the concentration of receptor–barbiturate complex, $A^{T}_{\lambda 1}$ is the baseline-corrected absorbance of a solution containing the barbiturate receptor, barbiturate, and receptor–barbiturate complex at λ_1, b is the path length, $A^{R}_{\lambda 1}$ is the baseline-corrected absorbance of a solution containing only the barbiturate receptor at λ_1, and $\Delta\epsilon_{\lambda 1}$ is the difference in molar absorptivities for the barbiturate–receptor complex and barbiturate receptor ($\epsilon_{RS} - \epsilon_R$) at λ_1. The molar absorptivity (ϵ_{RS}) for each of the barbiturate–receptor complexes is determined from spectroscopic studies in which the barbiturate substrate is in sufficient excess compared to the receptor concentration such that all of the receptor present in solution is converted to receptor–barbiturate complex. Values of $\Delta\epsilon_{\lambda 1}$ can be found in Table 1. For the dual-wavelength measurements [RS] is calculated as,

$$[RS] = \Delta A_{maxmin}/b\Delta\epsilon_{maxmin} \quad (2)$$

where ΔA_{maxmin} is the difference between the absorbance at 318 nm and that at 290 nm ($A_{318} - A_{290}$), and $\Delta\epsilon_{maxmin}$ is the

difference in molar absorptivities of the RS complex at 318 and 290 nm ($\epsilon_{318} - \epsilon_{290}$). Table 1 lists $\Delta\epsilon_{maxmin}$ values obtained from binding studies carried out in chloroform and methylene chloride.

Spectroscopic Studies. *Reagents.* Control serum Type I-A was purchased from Sigma Chemical Co. The serum was reconstituted as directed. Spectral grade chloroform was purchased from Mallinckrodt Specialty Chemicals Co. The buffer solutions for the pH range 3–10 were prepared daily with water passed through a Milli-Q water purification system (Millipore, Bedford, MA). The buffers for pH 3–8 (citrate–phosphate), pH 9 (borax–HCl), and pH 10 (borax–NaOH) were prepared according to ref 19. Citric acid (Aldrich Chemical Co.), sodium phosphate, dibasic (EM Science, Gibbstown, NJ), sodium borate, 10-Hydrate (J. T. Baker Inc., Phillipsburg, NJ), sodium hydroxide, and hydrochloric acid (Mallinckrodt Specialty Chemicals Co.) were used as received.

Apparatus. The UV absorbance measurements were made using either an IBM 9420 UV–VIS spectrophotometer or Hewlett-Packard 8450A diode array spectrophotometer. Spectrophotometric quartz cuvettes with a path length of 1.0 cm were purchased from Fisher Scientific.

Procedure. Aqueous solutions of phenobarbital ($\cong$100 μM) were transferred to a scintillation vial containing an equal volume of extracting solvent (chloroform, 200 μM barbiturate receptor–chloroform, or 1 mM barbiturate receptor–chloroform). The contents of the vials were mixed gently for a few seconds using a Vortex-Genie (speed control 1, Scientific Industries, Bohemia, NY), vented, and placed on a shaker (setting 4, Eberbach Corp., Ann Arbor, MI) for 30 min. The samples were removed from the shaker, and after a short period of time, the layers separated. The aqueous and organic layers were then transferred to clean vials. All of the extractions were carried out at ambient temperature (22.7 ± 1.76 °C) and examined in duplicate.

Measurements. The UV absorbance spectra of barbiturates are pH dependent. Aqueous solutions of phenobarbital were examined by UV spectroscopy prior to and after each extraction as a function of pH. The percentage of phenobarbital extracted at each pH value was based on changes in absorbance at a predetermined analytical wavelength. All UV measurements were baseline corrected.

Chromatographic Studies. *Reagents.* The mobile-phase buffer was prepared from stock solutions of 0.50 M potassium phosphate, monobasic (EM Science) and 0.45 M phosphoric acid (EM Science). The pH of the buffer solution was adjusted to pH 4.3 using a 1 M NaOH solution. The mobile phase consisted of (v/v %) 65% 20 mM phosphate buffer–21% methanol (Mallinckrodt Chemical Specialty Co.)–14% acetonitrile (EM Science). All of the solvents were filtered prior to use. The organic solvents were filtered through Teflon filters (pore size 0.45 μm), while the aqueous solvents were filtered through cellulose ester filters (0.45-μm pore size). The aqueous solutions were prepared daily using Milli-Q water.

Apparatus. The chromatographic system consisted of a Waters 600E pump, Hewlett-Packard 1050 autosampler, an Alltech precolumn (Brownlee RP-18 New Guard Cartridge), a Hypersil ODS C_{18} 15 × 4.6 (cm × mm) column, 5-μm packing, and a Waters 990 diode array detector. Data were acquired using a Waters 990$^+$ Version 6.22A data acquisition program. Experiments were carried out at ambient temperature. The chromatographic conditions were as follows: wavelength of detection for phenobarbital 196 nm, flow rate 1.0 mL min^{-1}, and injection volume 50 μL. The average chromatographic run time was 10 min.

Procedure. Twenty micromolar solutions of phenobarbital in aqueous buffer (pH 8, 2 × 10^{-3} M KH_2PO_4–5 × 10^{-4} M NaOH) and serum were extracted with chloroform and 1 mM receptor–chloroform solutions, respectively. The volume ratio (V_{org}/V_{aq}) ranged from 0.25 to 10. The extraction procedure was carried out in an identical manner as described above in the spectroscopic studies procedure section with the exception that the extraction time was increased from 30 min to 1 h. The serum samples were centrifuged (Adams analytical centrifuge, Clay-Adams, Inc., New York, NY) after each extraction in order to completely separate the two layers. The aqueous and organic layers were placed in separate test tubes. The aqueous layers for pH 8 solutions were filtered and examined directly by reversed-phase HPLC. The organic extracts (of known volume) for both the pH 8 solutions and serum samples were placed on a reaction block set (temperature setting 55 °C, nitrogen purge) for 5 min; the dried residue was then reconstituted with mobile phase, placed in an ultrasonicator for a few minutes to resolubilize completely the residue, filtered, and examined by reversed-phase HPLC. The chromatographic procedure for phenobarbital determination was adapted and modified from a method previously described in the literature by Gerson et al.[20]

Measurement. The percentage of phenobarbital extracted was calculated on the basis of the changes in peak height prior to and after each extraction. Phenobarbital standards were prepared daily in mobile phase and placed randomly among the samples on the autosampler. A calibration curve was prepared for each set of runs. There were day-to-day variations in retention times, but these variations on the average were less than 30 s.

RESULTS AND DISCUSSION

Equilibrium Considerations. The dissociation constants (K_d) for the receptor–barbiturate complexes in chloroform and methylene chloride were determined using the following equation:[21]

$$(R_t + S_t) = (R_tS_t)/[RS] + [RS] - K_d \qquad (3)$$

where R_t is the total receptor concentration, S_t is the total barbiturate concentration, and [RS] is the concentration of barbiturate complex present in solution. Linear regression of $(R_t + S_t)$ on $(R_tS_t)/[RS] + [RS]$ in eq 3 leads to K_d. A representative example of this approach is given in Figure 3. Table 2 lists K_d values for barbital, amobarbital, and phenobarbital in chloroform and methylene chloride. These data show that binding is more favorable in methylene chloride than chloroform. One plausible explanation is that chloroform is more acidic than methylene chloride. As such, it is more

(19) *Lange's Handbook of Chemistry*; Dean, J. A., Ed.; McGraw-Hill Book Co.: New York, 1985; pp 69–82.

(20) Gerson, B.; Bell, F.; Chan, S. *Clin. Chem.* **1984**, *30*, 105.

(21) Connors, K. A. In *Binding Constants, The Measurement of Molecular Complex Stability*; John Wiley and Sons: New York, 1987; pp 147–157.

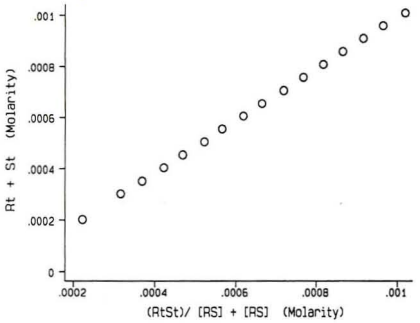

Figure 3. Representative curve fit for binding studies. Dilution experiment: [receptor] and [phenobarbital] range 0–505 μM in chloroform; b = 0.1 cm; dual-wavelength measurement (spectral subtraction).

Table 2. Dissociation Constants for Barbiturate–Receptor Complexes in Chloroform and Methylene Chloride

substrate	$K_d \pm s$[a] (M) chloroform	$K_d \pm s$[a] (M) methylene chloride
barbital	$4.67 \pm 0.670 \times 10^{-5b}$	$4.80 \pm 0.236 \times 10^{-6c}$
amobarbital	$2.49 \pm 0.503 \times 10^{-5b}$	$1.14 \pm 0.816 \times 10^{-5c}$
	$3.70 \pm 0.328 \times 10^{-5b}$	
phenobarbital	$2.18 \pm 0.153 \times 10^{-5c}$	$1.20 \pm 0.440 \times 10^{-5b}$
	$1.99 \pm 0.400 \times 10^{-5b}$	

[a] $\pm s$ denotes standard deviations. [b] Denotes constant [R] experimental approach. [c] Denotes dilution experimental approach.

competetive in its interactions with substrate and receptor than methylene chloride. A more thorough investigation of solvent effects on binding is warranted, and this investigation has been initiated and will be reported in the future.

In a simple extraction, phenobarbital equilibrates between an aqueous and an organic phase. The completeness of the extraction depends on two equilibria, the acid dissociation of phenobarbital and partitioning of the neutral phenobarbital between the two phases. The partition coefficient, K_p refers to the partitioning of the neutral form of phenobarbital (SH_2) between the two phases and does not account for the ionized forms of phenobarbital (SH^- and S^{2-}). More relevant to the extraction is the the distribution of all forms of phenobarbital between the two phases. The distribution coefficient, D_c, is defined in eq 4, where K_{a1} is the first acid dissociation constant

$$D_c = K_p/(1 + K_{a1}/[H^+]) \quad (4)$$

of phenobarbital. Note that eq 4 does not take into account the second acid dissociation constant of phenobarbital. The pK_a values for phenobarbital[22] are 7.3 and 11.8, respectively. The second pK_a value has been omitted from all theoretical treatments because all experiments were carried out at pH values less than 10, and therefore, the concentration of S^{2-} is always negligible.

The completeness of the extraction is based on the fraction of phenobarbital remaining (q) in the aqueous phase. It is

(22) Chao, M. K. C.; Albert, K. S.; Fusari, S. A. In *Analytical Profiles of Drug Substances*; Florey, K., Ed.; Academic Press, Inc.: New York, 1978; Vol. 7, p 374.

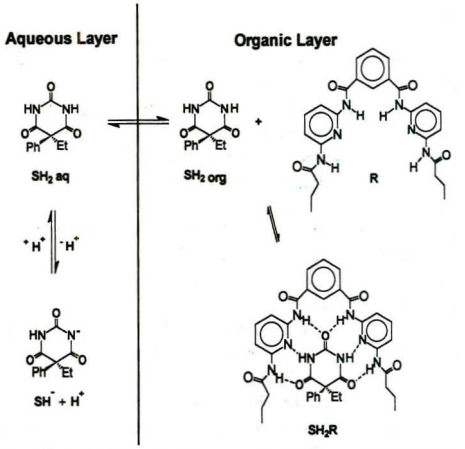

Figure 4. Schematic diagram of an extraction of phenobarbital in the presence of barbiturate receptor.

defined by eq 5, where Φ is the volume phase ratio ($V_{organic}/V_{aqueous}$). Thus, the amount of phenobarbital extracted from the aqueous layer for a simple extraction depends on pH explicitly, solvent type through K_p, and phase volumes explicitly.

$$q = 1/(D_c\Phi + 1) = (1 + K_{a1}/[H^+])/(K_p\Phi + 1 + K_{a1}/[H^+]) \quad (5)$$

The system becomes slightly more complex with the introduction of an artificial receptor molecule for phenobarbital into the overall extraction scheme (Figure 4). The enhanced extraction efficiency arises from the binding interactions between phenobarbital and the barbiturate receptor. If the total number of moles of receptor (R) is in excess, there is no partitioning of the phenobarbital–barbiturate receptor complex between the two phases, and the receptor is insoluble in the aqueous phase, then the simple relationship, eq 6, can be

$$q = 1/[D_c\Phi\,(1 + K_f[R_t]_{org}) + 1] \quad (6)$$

derived in which K_f is the formation constant for the phenobarbital–barbiturate receptor complex ($K_f = K_d^{-1}$) and $[R_t]$ is the total concentration of barbiturate receptor present in the organic phase. Equation 6 not only takes into account the dependence of the extraction on pH, solvent type, and phase volumes but also accounts for the influence of receptor concentration and the binding constant for the complex.

In the following sections, this equation will be used to predict the efficiency of the extraction for a given set of experimental conditions. Distribution coefficients (D_c) values were calculated for pHs ranging from 2 to 11 by taking the D_c value of 4.16 obtained from the literature[22] at pH 3.4 and using eq 4. A formation constant (K_f) value of 4.59×10^4 M^{-1} was determined from the phenobarbital–barbiturate receptor binding studies carried out in our laboratory (Table 2). Equations 5 and 6 were used to calculate the theoretical fraction of phenobarbital remaining (q) after each extraction

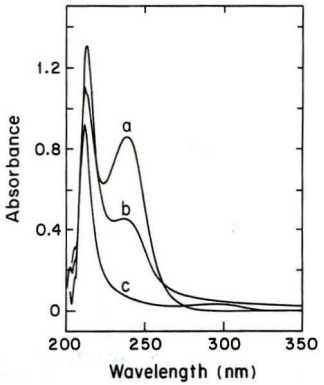

Figure 5. Qualitative demonstration by UV spectroscopy of phenobarbital extraction: aqueous layer prior to extraction (a); aqueous layer after extraction with chloroform (b); aqueous layer after extraction with 896 μM barbiturate receptor (c). Conditions: initial $[\text{phenobarbital}]_{aq}$ = 105 μM; Φ = 1.0.

as a function of pH, receptor concentration, volume phase ratio, and solvent type. It is important to note that there are no adjustable parameters in eq 6. Values are either obtained from the literature or from experiments carried out in our laboratory.

Qualitative View. A qualitative demonstration of phenobarbital extraction is given in Figure 5. Figure 5 shows a fairly complete extraction of phenobarbital from aqueous solution at pH 8 in the presence of receptor (curve c) while only about half of the phenobarbital could be extracted with chloroform (curve b). Curve a represents the concentration of phenobarbital present initially in the aqueous layer prior to extraction. The presence of receptor in the extracting solvent, chloroform, has a remarkable effect on the quantity of phenobarbital extracted from aqueous solution. Curve c also shows that only a small fraction, about 0.1%, of the receptor is extracted into the aqueous phase (peak near 300 nm).

Quantitative Studies: Influence of pH and Receptor Concentration. The efficiency of the extraction was determined based on absorbance changes prior to and after each extraction as a function of pH and receptor concentration. The theoretical and experimental percentages of phenobarbital extracted as a function of pH are given in Figure 6. The solid lines represent the predicted results in the absence and presence of 0.2 and 1 mM receptor (eq 6) while the experimental results are represented by symbols. The results for the chloroform extractions in the absence of barbiturate receptor are interpreted fairly straightforwardly because the first acid dissociation constant for phenobarbital is 5×10^{-8} M (pK_a = 7.3). As the pH of the solution increases, the solubility of phenobarbital in the aqueous phase increases through increased ionization. This limits the amount of phenobarbital available in its neutral form. However, when the organic phase contains 1 mM barbiturate receptor, complex formation stabilizes the neutral form of the solute. This results in the appearance that the pK_a shifts to a more basic value. From a quantitative standpoint, at pH values of $\leq$7, the ratio of phenobarbital extracted in the presence and absence of 1 mM barbiturate

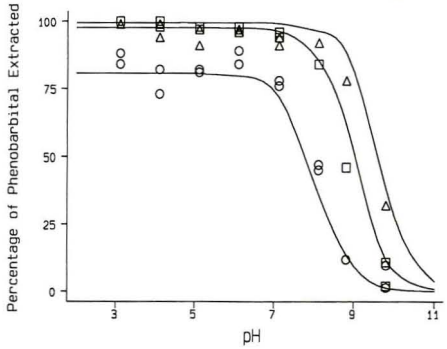

Figure 6. Comparison of experimental and theoretical data as a function of receptor concentration. Plot of percentage of phenobarbital vs pH: chloroform (○); 200 μM receptor (□); 1 mM receptor (△); theory (solid line). Conditions: initial $[\text{phenobarbital}]_{aq} = \cong 100$ μM; Φ = 1; K_f = 4.59×10^4 M^{-1}.

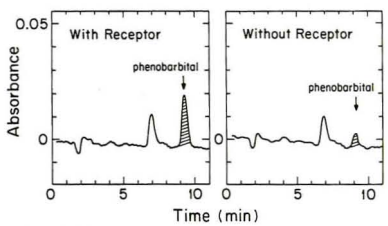

Figure 7. Qualitative demonstration by RP-HPLC of phenobarbital extraction from serum. The direct injection of chloroform layers following extraction. Conditions: initial $[\text{phenobarbital}]_{serum}$ = 129 μM; [receptor] = 1 mM; Φ = 1; injection volume 10 μL; flow rate 1 mL min^{-1}; detection wavelength 196 nm.

receptor is 1.2:1. At these pH values, the extraction is only slightly enhanced in the presence of receptor because the solvent alone extracts a significant amount of the barbiturate. On the other hand, at pH values greater than 7, the effect of the receptor is more pronounced. As expected, a higher concentration of receptor leads to higher extraction yields. There is an advantage to having a wider range of pH over which the extraction is acceptable because the chance of finding selectivity against interfering organic species is more likely the wider the available pH window. This is an important practical consideration when one is analyzing for trace levels of phenobarbital in serum. The theoretical and experimental results are in very good agreement with one another in Figure 6.

Quantitative Studies: Influence of Phase Ratio. Reversed-phase high-performance liquid chromatography was used to investigate the effects of volume on extraction efficiency. Representative chromatograms for the organic extracts of serum in the presence and absence of receptor are given in Figure 7. In these chromatograms, two distinct peaks are present; one peak represents phenobarbital while the other represents one or more serum interferences. The chromatograms demonstrate that the magnitude of the phenobarbital peak is influenced by the presence of receptor, while the magnitude of the interfering peak is not. This illustrates the selectivity of the receptor for phenobarbital over this (these) particular interference(s) arising from serum.

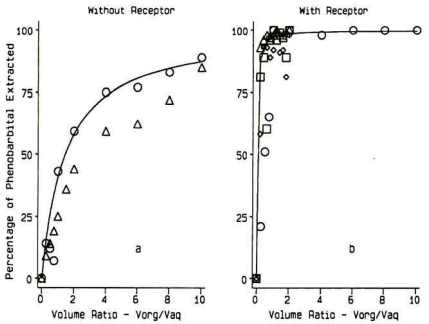

Figure 8. Comparison of experimental and theoretical data in the absence (a) and the presence (b) of 1 mM receptor. A plot of percentage of phenobarbital extracted vs phase ratio: absence of receptor (a) pH 8 buffer (O), serum (Δ), and theory (solid line); presence of 1 mM receptor (b) pH 8 buffer aqueous layer day 1 (O), pH 8 buffer aqueous layer day 2 (Δ), pH 8 buffer organic layer day 2 (□), serum (◇), and theory (solid line). Conditions: initial [phenobarbital] = 20 μM; Φ = 0–10; $K_f = 4.59 \times 10^4$ M^{-1}; [receptor] = 1 mM.

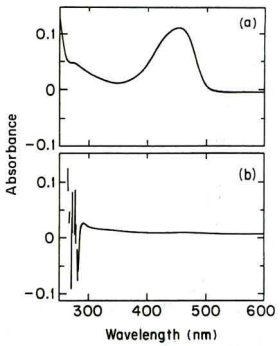

Figure 9. Comparison of UV–visible spectra for serum extractions carried out with chloroform (a) and toluene (b). Conditions: Φ = 1.

A larger volume of extracting solvent than sample is necessary to remove (on the order of 10:1)[23,24] an appreciable quantity of phenobarbital from serum. In this work, we wanted to demonstrate that this was not the case when receptor-enriched solvent was used. Twenty micromolar solutions of phenobarbital (pH 8 buffer or serum) were prepared and extractions were carried out with chloroform and 1 mM receptor–chloroform using volume ratios ranging from 0.25 to 10. A buffer of pH 8 was chosen for two reasons: (1) experiments had shown that at pH values below 7 the receptor had minimal effect on extraction efficiency, and (2) the pH of the serum samples upon reconstitution was 8. Figure 8 represents the extraction results for aqueous and serum solutions of phenobarbital in the absence and presence of receptor. The solid lines represent the predicted percentages of phenobarbital extracted as a function of volume ratio. The symbols represent the experimental results. In the case of the chloroform extractions (Figure 8a), a volume ratio greater than or equal to to 10 is necessary to extract an appreciable quantity (≅80%) of phenobarbital from aqueous or serum solutions. On the other hand, for extractions carried out in the presence of 1 mM receptor (Figure 8b), a volume ratio of 0.5 was more than sufficient to extract at least 90% of the phenobarbital present in the original sample. Also, Figure 8a shows that it is more difficult to extract phenobarbital in the absence of receptor from serum, possibly due to interactions between phenobarbital and serum proteins.

In Figure 8b, note the shape of the experimental results for pH 8 buffer extractions involving 1 mM barbiturate receptor. The data points for this curve represent RP-HPLC results for both the aqueous and organic layers following extraction. A considerable discrepancy between the theoretical and experimental results is evident for a few points at volume ratios less than 1. In particular, four data points stand out. Three of these four data points represent aqueous extracts obtained on the same day while the other data point represents the organic extract obtained on a different day. At this point in time, we have rationalized this discrepancy in terms of incomplete extractions. At volume ratios less than 1, the total surface area of the organic layer is much less than the total surface area of the aqueous layer. Thus, the extraction may require much longer extraction times than 1 h or perhaps require a more vigorous shaking to ensure complete mixing of the two layers. A similar discrepancy can be seen in Figure 8a at volume ratios less than 1.

Solvents. Solvent was another important experimental consideration. It was felt that use of a hydrophobic solvent such as toluene in place of chloroform would limit the number of interferences arising from serum in the extract. Experimentally, this was found to be true and is shown spectroscopically in Figure 9. In Figure 9, serum samples extracted with chloroform were found to contain a higher absorbance from interfering species than those extracted with toluene. While certainly the level of the interference from nonanalyte molecules in a sample depends on the analytical technique used, it is clear that there is less colored material extracted by toluene than by chloroform. In addition to minimizing polar interferences, we also anticipated that smaller quantities of phenobarbital would be extracted (in the presence and absence of receptor) for a number of reasons. First, phenobarbital has a very limited solubility in toluene. The literature reports distribution coefficient values for phenobarbital of 0.552 (toluene) vs 2.35 (chloroform) at pH 7.4.[22] Second, the solubility of the barbiturate receptor is extremely limited in toluene (≅5 vs ≅500 mg/L in chloroform).

The receptor's limited solubility in toluene has prevented us from taking a closer experimental examination of receptor-enriched toluene. Thus, the receptor molecule will require synthetic modification if it is to be employed successfully in toluene. However, we can gain some insight from eq 6. In theory, as the solubility of the modified receptor increases in toluene, one can expect extraction efficiencies equal to those of receptor-enriched chloroform. However, as seen in theoretical plot given in Figure 10, extractions carried out between pH 8 and 10 with receptor-enriched toluene will require a much higher concentration of receptor to achieve extraction efficiencies equal to those of receptor-enriched chloroform. For the sake of illustration, we have taken the formation

(23) Papadoyannis, I. N. *HPLC in Clinical Chemistry*; Academic Press: New York, 1976; pp 242–260.
(24) Baselt, R. C. *Analytical Procedures for Therapeutic Drug Monitoring and Emergency Toxicology*, 2nd ed.; PSG Publishing Co., Inc.: Littleton, MA, 1987; pp 26–39.

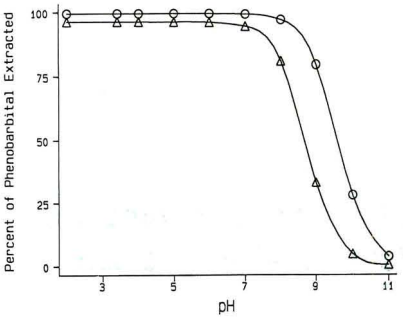

Figure 10. Comparison of theoretical results for receptor-enriched solvent from equation 6 to illustrate the effects of changing solvent. A plot of percentage of phenobarbital extracted vs pH: receptor-enriched chloroform (O); receptor-enriched toluene (Δ). Conditions: $K_f = 4.59 \times 10^4\ M^{-1}$; [receptor] = 1 mM; $\Phi = 1$.

constant for the phenobarbital–barbiturate receptor complex in toluene to be equal to its value in chloroform. Theoretical calculations indicate that the concentration of the receptor in toluene will have to be on the order of 8 mM in toluene, compared to 1 mM in chloroform, to achieve similar extraction efficiencies between pH 8 and 10. This increase in receptor concentration is necessary to overcome the differences in the distribution coefficient, D_c.

CONCLUSIONS

Receptor-enriched solvent extracts phenobarbital from serum with high efficiency. Chloroform enriched with this artificial receptor (1 mM) can extract more than 90% of the phenobarbital from a 20 μM phenobarbital solution in human control serum using a volume ratio (organic/serum) as small as 0.5. In the absence of this receptor, the volume ratio must be greater than 10 to achieve similar extraction efficiencies. This work clearly demonstrates the selectivity of the barbiturate receptor for phenobarbital over serum interferences.

Our initial concerns regarding pH and water were found to be unwarranted; however, receptor solubility still remains a key issue. The future of this artificial receptor depends principally on synthetic modification to improve receptor solubility. The building of even better artificial receptors with even greater solubilities in nonpolar solvents such as toluene will produce even more dramatic extraction results as a function of [receptor], pH, volume ratio, and solvent type.

ACKNOWLEDGMENT

This work was supported by the Material Research Center at the University of Pittsburgh, which is funded through AFOSR and the Office of Naval Research (to A.D.H.). We express our gratitude to PPG Industries, Inc., for their educational support (to J.N.V.) and Gerald Feulmer (PPG Industries, Inc.) for his assistance with the HPLC experiments.

Received for review January 3, 1994. Accepted April 20, 1994.[⊗]

[⊗] Abstract published in *Advance ACS Abstracts,* June 1, 1994.

Anal. Chem. **1994,** *66,* 2404–2408

Ion Chromatography as Potential Reference Methodology for the Determination of Total Calcium and Magnesium in Human Serum

Linda M. Thienpont,*,† Jean E. Van Nuwenborg,† and Dietmar Stöckl‡,§

Laboratorium voor Analytische Chemie, University of Ghent, Harelbekestraat 72, B-9000 Gent, Belgium, and Institut für Standardisierung und Dokumentation im medizinischen Laboratorium e.V. (INSTAND e.V.), Johannes-Weyer Strasse 1, D-40225 Düsseldorf 1, Germany

The potential of ion chromatography to serve as a new reference method principle for the determination of total calcium and magnesium in human serum was investigated. Sample pretreatment consisted of acidic dilution and filtration. Detection was based on conductivity. Mean total coefficients of variation for calcium and magnesium were respectively 0.91% and 1.20% and the mean method bias was +0.06% for calcium and −0.35% for magnesium, as determined with five control materials from the Community Bureau of Reference and the National Institute of Standards and Technology. These results were comparable to those of the proposed candidate reference methods based on flame atomic absorption spectrometry. Therefore, we consider ion chromatography as a valuable reference methodology for the determination of total calcium and magnesium in human serum.

Reference methods in clinical chemistry serve as a link for transferring accuracy from definitive methods to routine methods, thus making measurement results of routine methods traceable to the "true" quantity of a given analyte in a patient sample.[1] For the determination of total calcium and magnesium in human serum, isotope dilution in combination with thermal ionization mass spectrometry was used as the measurement principle for definitive methods,[2,3] providing the accuracy base for those two analytes. Afterwards, a reference method for calcium based on flame atomic absorption spectrometry (FAAS) was developed by Cali et al.[4] This candidate reference method was assessed by Pickup et al.,[5] as well as in the interlaboratory trial organized by the Community Bureau of Reference (BCR) of the Commission of the European Communities.[6] For magnesium, a reference method was proposed only recently by Külpmann et al.,[7] also using FAAS. Although FAAS is generally accepted as the reference method principle, a second reference method principle for the determination of electrolytes in serum is desirable because it is recommended that two independent methods of analysis be used for the certification of reference materials.[8] As ion chromatography (IC) has been applied successfully for the determination of serum electrolytes,[9–12] we investigated its potential for use as a reference method, encouraged by its application for the certification of calcium and magnesium in simulated rainwater by the National Institute of Standards and Technology (NIST).[13,14] Another reason for investigating the potential of IC was its flexibility. Also, clinically important monovalent cations such as sodium and potassium or anions such as chloride or phosphate can be analyzed with the same equipment.

Here, the development and validation of IC methods for total calcium and magnesium are presented. We developed two separate methods to keep analysis time short and because reference methods are often applied to selected problems where simultaneous determination of calcium and magnesium is not demanded. The methods are not intended to substitute for routine methods used in clinical laboratories. The requirements for method accuracy and precision were derived from their intended application for target setting in the German

† University of Ghent.
‡ INSTAND e.V.
§ Present address: Laboratorium voor Analytische Chemie, University of Ghent, Harelbekestraat 72, B-9000 Gent, Belgium.

(1) Tietz, N. W. *Clin. Chem.* **1979,** *25,* 833–9.
(2) Moore, L. J.; Machlan, L. A. *Anal. Chem.* **1972,** *44,* 2291–6.
(3) Bowers, G. N., Jr; Fasset, J. D.; White V. E. *Anal. Chem.* **1993,** *65,* 475R–9R.
(4) Cali, J. P.; Bowers, G. N., Jr.; Young, D. S. *Clin. Chem.* **1973,** *19,* 1208–13.
(5) Pickup, J. F.; Jackson, M. J.; Price, E. M.; Brown, S. S. *Clin. Chem.* **1974,** *20,* 1324–30.
(6) Brown, S. S.; Healy, M. J. R.; Kearns, M. *J. Clin. Chem. Clin. Biochem.* **1981,** *19,* 395–426.
(7) Külpmann, W. R.; Ruschke, D.; Büttner, J.; Paschen, K. *J. Clin. Chem. Clin. Biochem.* **1989,** *27,* 33–9.
(8) Trahey, N. M. *NIST Standard Reference Materials Catalog 1992–93*; Special Publication 260; National Institute of Standards and Technology, U. S. Government Printing Office: Washington, DC, 1992; p 5.
(9) Nordmeyer, F. R.; Hansen, L. D.; Eatough, D. J.; Rollins, D. R.; Lamb, J. D. *Anal. Chem.* **1980,** *52,* 852–6.
(10) Rehfeld, S. J.; Loken, H. F.; Nordmeyer, F. R.; Lamb, J. D. *Clin. Chem.* **1980,** *26,* 1232–3.
(11) Shintani, H. *J. Chromatogr.* **1985,** *341,* 53–63.
(12) Matsuhita, S. *Anal. Chim. Acta* **1985,** *172,* 249–55.
(13) Han, K.; Koch, W. F. *LC-GC* **1988,** *9,* 56–60.
(14) Koch, W. F. *J. Chromatogr. Sci.* **1989,** *27,* 418–21.

0003-2700/94/0366-2404$04.50/0
© 1994 American Chemical Society

Table 1. Precision and Accuracy Data of the Proposed IC Method for the Measurement of Calcium in Five Certified Human Serum Reference Materials

control serum	certified concn (mmol/L)	uncertainty[a] (%)	measd concn (mmol/L)	uncertainty[b] (%)	deviation from target (%)	CV (n = 12) (%)
CRM 303	2.472	±0.77	2.478	±0.68	+0.26	1.07
CRM 304	2.201	±0.86	2.197	±0.57	–0.19	0.89
SRM 909	3.013	+2.92/–1.59	3.024	±0.49	+0.36	0.77
SRM 909a-1	2.322	±1.77	2.315	±0.74	–0.32	1.17
SRM 909a-2	3.338	±1.41	3.345	±0.40	+0.20	0.63

[a] For CRM 303/304, the uncertainties are given at the 95%/95% statistical tolerance interval (measurement-/dry-mass variabilities); for the SRM 909, at the 95%/97% interval; for the SRMs 909a-1 and a-2, at the 99%/95% interval. [b] These values include the measurement- (n = 12) and the dry-mass variability (n = 4) at the 95% statistical tolerance interval.

external quality assessment (EQA) scheme.[15] Emphasis was put on the use of primary Standard Reference Materials (SRMs) for calibration and accuracy assessment of the methods through the use of five certified matrix reference materials from the NIST and the BCR. Sample pretreatment necessary for the determination of total ion concentrations (e.g., release of ions from their binding to proteins) was evaluated, with special attention to the need for destruction of the organic matrix. In addition, a rigorous calibration and measurement protocol was followed.[16]

EXPERIMENTAL SECTION

Instrumentation. Ion chromatography was done with a Model DX-100 ion chromatograph from Dionex Corp. (Sunnyvale, CA). A 25-μL loop was used for injection. Chromatographic separation was done on two Ionpac CS10 Guard Columns (50 mm × 4 mm i.d.), installed in series, and connected with a Cation Self-Regenerating Suppressor-I system (CSRS-I, 4 mm) used in the chemical suppression mode. Detection was based on conductivity. All the above equipment were from Dionex. Integration of the chromatographic signals was performed with a C-R5A integrator from Shimadzu (Kyoto, Japan). An Elgastat Maxima Analytical water purification system from Elga Ltd. (Bucks, U.K.) was used to produce water of ultrapure quality (18.2 MΩ). Microwave digestions were performed in a closed-vessel pressure-controlled system, Model MDS-2000 from CEM (Matthews, NC). Weighings were done with an AT261 Deltarange balance (accuracy 0.02 mg) from Mettler Toledo (Greifensee, Switzerland). The density of serum was determined with a Model DMA 35 densitometer (accuracy 1 mg/mL) from A. Paar KG (Graz, Austria).

Materials. The following chemicals were used: DL-2,3-diaminopropionic acid monohydrochloride (DAP·HCl), 65% nitric acid, strontium chloride hexahydrate, manganese(II) chloride tetrahydrate, iron(II) chloride tetrahydrate, cobalt(II) chloride hexahydrate, nickel(II) nitrate hexahydrate, zinc(II) nitrate hexahydrate, copper(II) chloride dihydrate, and lead(II) nitrate, all from Fluka (Buchs, Switzerland); tetrabutylammonium hydroxide (TBA)OH (40% solution in water) from Riedel-de Haën (Seelze, Germany); 30% hydrochloric acid Suprapur from Merck (Darmstadt, Germany). Filtrations were done with Acrodisc LC13 PVDF filters with an 0.45-μm pore size from Gelman Sciences (Ann Arbor, MI). For filtration and injection, 1-mL Plastipak syringes from Becton Dickinson (Dublin, Ireland) were used. Pipeting was done using 1-mL and 200-μL pipet tips from Eppendorf (Hamburg, Germany). To exclude external contamination at any stage of the IC analysis, no glassware was used and hand contact of vials, etc., was avoided. It was even necessary to rinse and dry all vials and containers before use. All vials and containers used were of polypropylene from Nalgene (Hereford, U.K.).

Standard Materials. For calibration, standard materials of certified purity from the NIST (Gaithersburg, MD) were used, i.e., calcium carbonate (SRM 915) and magnesium gluconate dihydrate (SRM 929). For each element, three standard solutions (I–III) were prepared. To keep the weighing time short, we did not attempt to reach "round" concentrations such as 2.000 mmol/L. Calcium carbonate was dissolved in a 0.5% aqueous hydrochloric acid solution in a concentration of 2–2.2 mmol/L calcium (accurate to the third decimal); magnesium gluconate dihydrate was dissolved in water in a concentration of 1.0–1.1 mmol/L magnesium (accurate to the third decimal). Before use, the respective standard solutions were cross-checked against each other. Deviations of less than 0.6% (on the basis of six measurements) were accepted. The standard solutions were stored in 500-μL portions in polypropylene vials at –20 °C and discarded after two freezing/thawing cycles. The CRM 303 and CRM 304 lyophilized sera from the BCR[16,17] (Brussels, Belgium), and the SRM 909, SRM 909a-1, and SRM 909a-2 lyophilized sera from NIST, were reconstituted on a gravimetric basis and according to the manufacturer's instructions (for SRM 909, procedure B was followed). The deviation of the volume of water used for reconstitution from the prescribed volume was taken into account and the maximum acceptable deviation was set to 0.5%. The certified concentrations of the sera are listed in Tables 1 and 2. After reconstitution, the sera were stored in 500-μL portions in polypropylene vials at –20 °C. Each aliquot was discarded after two freezing/thawing cycles.

Method. All volumes were chosen to give masses of >25 mg to keep weighing errors below 0.1%. The pipeted volumes were calculated from the density of the solutions and the masses pipeted. For serum sampling, a volume representing approximately 88 nmol of calcium (25–40 μL of sample) and 50 nmol of magnesium (25–60 μL) was weighed in and further diluted with a 2 mmol/L hydrochloric acid solution under

(15) Stöckl, D.; Reinauer, H. *Scand. J. Clin. Lab. Invest.* **1993**, *53* (Suppl. 212), 16-8.

(16) Stöckl, D.; Reinauer, H. *Clin. Chem.* **1993**, *39*, 993–1000.

(17) De Leenheer, A. P.; Yeoman, W. B.; Colinet, E. S. *The certification of total calcium in two lyophilized serum materials CRM No. 303 and 304*; Commission of the European Communities, Community Bureau of Reference, BCR Information Report, 1986; EUR 10627 EN.

Table 2. Precision and Accuracy Data of the Proposed IC Method for the Measurement of Magnesium in Five Certified Human Serum Reference Materials

control serum	certified concn (mmol/L)	uncertainty[a] (%)	measd concn (mmol/L)	uncertainty[a] (%)	deviation from target (%)	CV (n = 12) (%)
CRM 303	1.131	±1.95	1.123	±0.94	–0.67	1.48
CRM 304	1.850	±1.62	1.845	±0.62	–0.26	0.98
SRM 909	1.210	+4.13/–2.48	1.212	±0.65	+0.14	1.02
SRM 909a-1	0.868	±1.84	0.869	±0.95	+0.08	1.50
SRM 909a-2	1.846	±1.52	1.827	±0.65	–1.03	1.03

[a] See Table 1.

gravimetric control. The dilutions were individually adapted to give similar peak heights for standards and samples. Dependent on sample concentration, dilutions ranged from approximately 80- to 180-fold. Samples SRM 909a-1 and a-2 were measured after 25–200-fold dilution to investigate whether the different degree of dilution affected method accuracy. After 1 h of equilibration, the acidified sample was filtered. The filter device was prerinsed three times with water and finally with the sample so that the first 500 μL of filtrate was discarded (care should be taken to make the syringe air-free). In this way, any change in sample concentration by filtration was prevented. The filtrate was used for injection without further treatment (25 μL, containing approximately 0.50 nmol of calcium or 0.26 nmol of magnesium, respectively). The standards were diluted 100-fold and otherwise treated the same way as the samples.

For calcium, microwave digestion (under a closed hood) was evaluated additionally. A 300-μL aliquot of serum was weighed and an appropriate amount of an aqueous strontium chloride hexahydrate internal standard solution was added, so that a 1/1 response ratio for calcium to strontium (measured as peak heights) was obtained. The solution was transferred into a destruction vessel, and 1 mL of a 65% solution of nitric acid and 5 mL of water were added. Destruction was done under pressure-controlled conditions (7 min at a pressure of 160 psi), and the vessels were opened after approximately 5-min cooling time. Completeness of destruction was verified by adding concentrated sulfuric acid, followed by additional heating. After digestion, the residue was diluted with water (the final dilution was 1000-fold) and 25 μL was injected. The standards were treated in exactly the same way as the serum aliquots.

The conditions for ion-exchange chromatography of calcium were as follows: elution at a flow rate of 1 mL/min with a combined eluent of 4 mmol/L DAP·HCl and 40 mmol/L hydrochloric acid; for magnesium, the composition of the eluent was changed to 2 mmol/L DAP·HCl and 40 mmol/L hydrochloric acid at a flow rate of 1 mL/min. In both methods, the same suppression eluent consisting of 100 mmol/L (TBA)OH at a flow rate of 3 mL/min was used.

Analysis and Measurement Protocol. For the analysis of the lyophilized SRMs and the CRMs, four different vials were used to compensate for the variation in the dry-mass content in each vial. The concentration measured for each SRM or CRM serum was always calculated from 12 independent measurements performed on 4 different days. This means that every day three serum aliquots (A–C) from each SRM or CRM were analyzed, together with the three standards (I–III). The measurement scheme of the serum samples and standards was as follows: standards I–III; sample 1A, sample 1B, sample 1C; second injection of standards I–III; sample 2A, sample 2B, sample 2C; third injection of standardsI–III etc. The calculations of the serum samples were based on the duplicate injections of the standards encompassing them.

Precision, Accuracy and Detection Limit. The precision of the proposed IC methods for calcium and magnesium was estimated as overall precision (n = 12, triplicates of four independent series). The accuracy of the methods was estimated from the results obtained for the five certified sera mentioned above. The detection limit was determined with a diluted processed serum sample.

Safety Considerations. The methods demand no specific safety precautions. Lyophilized control sera of human origin have to be handled as potentially infectious. General guidelines for work with acids and bases have to be respected. Microwave digestion has to be performed under a closed hood.

RESULTS AND DISCUSSIONS

The above described methods are intended for use as reference methods in clinical chemistry. As it is generally accepted that the precision and accuracy requirements of reference methods depend on their application, they will be different for, for example, method evaluation or target setting in quality control. For the development of the here described methods, we aimed at reaching the requirements necessary for target setting in the German EQA scheme.[19] There the total allowable error (TAE) of a reference method value for calcium (magnesium) shall not exceed 2% (2.4%). The TAE includes the limit for bias and the statistical 95% confidence interval. For a method CV of 2% and 12 measurements, the 95% confidence interval is ±1.27%, which results in a bias limit of 0.73% for calcium and 1.13% for magnesium.[15] To comply with this concept, every reference method value was calculated from 12 independent measurements.

For the determination of total electrolyte concentration, attention should be paid to the release of the bound ion fraction from proteins. This was realized by dilution of the serum sample with 2 mmol/L hydrochloric acid. The dilution of the samples was individually adapted (see Method) to the concentration of the respective standards. Dilutions between 25- and 200-fold did not affect the accuracy of the procedure

(18) Thienpont, L. M.; De Leenheer, A. P.; Colinet E. S.; Dirscherl, C. D. *The Additional Certification of Magnesium (II) and Lithium (I) in the Lyophilized Serum Materials CRM 303 and CRM 304*; Commission of the European Communities, Community Bureau of Reference, BCR Information Report, 1992; EUR 14186 EN.

(19) Richtlinien der Bundesärztekammer zur Qualitätssicherung in medizinischen Laboratorien, *Dt. ÄArztebl.* **1988**, *85*, A699–A712.

(see Method). In this way, always the same amount of Ca^{2+} (for the samples to be analyzed for calcium), and of Mg^{2+} (for those to be determined for magnesium), was finally injected into the IC system. The dilution was controlled gravimetrically; therefore, errors less than 0.1% were introduced by this step. Precipitated proteins were removed by filtration, which did not alter the concentration of the analytes in the sample (see Method). Injection of 25 μL of filtrate was found appropriate for reliable quantification by means of peak height measurements, because substance amounts representing 300-fold (200-fold) the detection limit (S/N 3) for calcium (magnesium) were injected. The detection limits were 1.7 pmol for calcium and 1.3 pmol for magnesium.

For the determination of calcium, alternatively microwave digestion with strontium as internal standard was applied for sample pretreatment (see Method). But first results showed no advantage to the much simpler and cheaper acid treatment and therefore it was not investigated further.

During method development, emphasis was put on baseline separation of Ca^{2+} and of Mg^{2+} ions, respectively, from other cations also present in serum and on a short total analysis time. We therefore used different eluents for the analysis of calcium and magnesium. In addition, the conventional combination of a guard/analytical column (the latter with dimensions of 250 mm × 4 mm i.d.) was substituted by two guard columns (= 2 × 50 mm × 4 mm i.d.). The eluent for calcium analysis was 4 mmol/L DAP•HCl and 40 mmol/L hydrochloric acid, which resulted in good separation of the Ca^{2+} ions from the monovalent ions and Mg^{2+}, and a retention time of 5.35 min (Figure 1) (Sr^{2+}, used as internal standard for the microwave digestion experiments eluted at 7.8 min under the same conditions). In the same chromatogram, an unexpected peak is observed at 3.2 min (identical to the peak at 5.5 min in Figure 2). Chromatography of Mn^{2+}, Fe^{2+}, Co^{2+}, Ni^{2+}, Cu^{2+}, Zn^{2+}, and Pb^{2+} revealed that the peak might represent Co^{2+}, Ni^{2+}, or Pb^{2+}. But as in our methods the sample is not in contact with metals, these possibilities seem unlikely. Another explanation would be the presence of an organic cation, which we did not further investigate as the peak did not disturb quantification.

For baseline separation of Mg^{2+}, we used 2 mmol/L DAP·HCl and 40 mmol/L hydrochloric acid, resulting in a chromatographic profile as shown in Figure 2 (retention time of magnesium, 4.2 min; calcium, not shown, eluted at 9.4 min). The retention times in our system were considerably lower than with a conventional column combination using the same eluents (approximately 19 min for calcium and 16 min for magnesium[20]). Alternatively, faster elution could have been achieved by increasing the strength of the mobile phase, but with the drawback of increased suppressor flow rate and decreased baseline stability. Chromatographic analysis of acid-treated serum samples did not reveal baseline disturbance or higher background conductivity than the analysis of the standards (see Figures 1B and 2B). Long-term stability was reached by rinsing the ion-exchange columns after approximately 150 injections of serum samples, as generally recommended by the manufacturer.[20] The bracketing measurement and calculation protocol (see Analysis and Measurement Protocol) was necessary to compensate for a slight unidirectional drift in the chromatographic system during the day, being 3% (5%) for calcium (magnesium) during 21 injections.

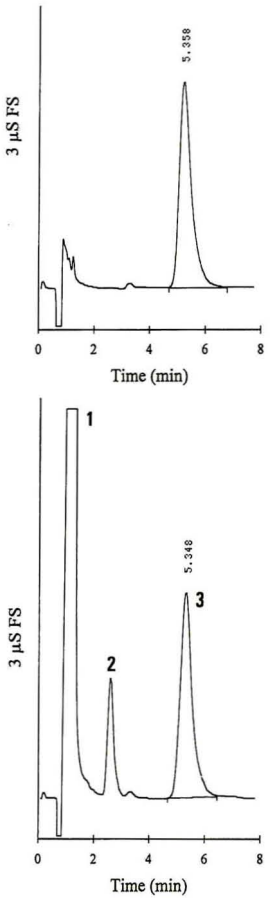

Figure 1. Chromatogram obtained for a calcium standard (retention time, 5.35 min) (A, top) and for calcium in the CRM 303 serum (B, bottom). The designated peaks in chromatogram B represent (1) monovalent cations, (2) Mg^{2+}, and (3) Ca^{2+}. For chromatographic conditions, see the Experimental Section.

The precision and accuracy reached for the IC methods for calcium and magnesium are shown in Tables 1and 2, for the measurements of the five certified serum reference materials. The coefficients of variation (CVs) listed were calculated from the 12 measurements performed on four different days. On each day, three independent serum aliquots were processed and each sample was measured once. Therefore, the imprecision data include the within- and between-day errors of weighing, variations introduced during sample pretreatment, errors during IC measurements, and the variation in dry mass of the lyophilized controls. The maximum CV for total calcium and magnesium was 1.17% and 1.5%, respectively. These maximum CVs and 12

(20) *Installation instructions and troubleshooting guide for the IONPAC CS10 analytical column*; Dionex Corp.: Sunnyvale CA, 1991; Document No. 034341, revision 02.

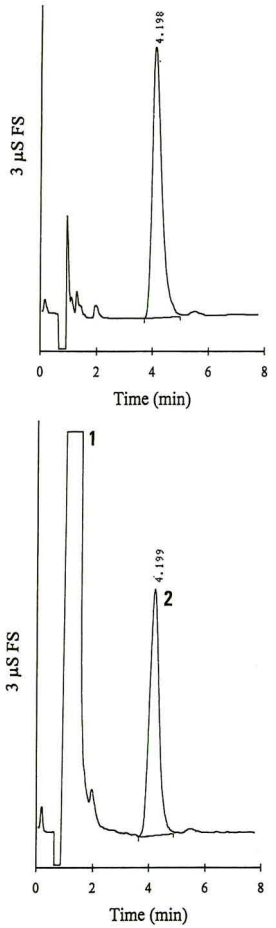

Figure 2. Chromatogram obtained for a magnesium standard (retention time, 4.2 min) (A, top) and for magnesium in the SRM 909a-1 serum (B, bottom). The designated peaks in chromatogram B represent (1) monovalent cations and (2) Mg^{2+}. For chromatographic conditions, see Experimental Section.

measurements yield a 95% confidence interval around the mean of 0.74% for calcium and 0.95% for magnesium (calculated from *t*-statistics). The mean deviation of the measured from the certified concentrations (method bias) was + 0.06% for calcium and –0.35% for magnesium (calculated from the data in Tables 1and 2). Combination of the method bias with the above calculated confidence interval results in a maximum total error of 0.80% for calcium and of 1.30% for magnesium. Both values are below the TAE limits required for target values in the German EQA scheme (see discussion above). All concentrations determined for the reference materials are well within their stated uncertainty limits (Tables 1and 2).

The accuracy and precision reached for the IC methods for total calcium and magnesium are comparable to those of the proposed candidate reference methods based on FAAS. For the FAAS method of calcium, a mean CV of approximately 0.8% and a maximum deviation of 0.5–1% from certified materials were reported[6] (for our IC method the mean CV was 0.91%, the maximum deviation was +0.36%). For the FAAS method of magnesium, a mean CV of 0.5% and a deviation of –1.4% from the SRM 909 certified value was reported[7] (for our IC method the mean CV was 1.2%, the maximum deviation was –1.03%). The higher CV in our method may be because the dry-mass variabilities of the lyophilized sera are included, while in the FAAS method pooled sera were used. In addition, we determined the values on four different days, while in the FAAS method the results were obtained on one day in four different runs.

CONCLUSION

We have developed two IC methods which enable us to reliably determine total calcium and magnesium in lyophilized human serum reference materials. The sample pretreatment procedure is very simple, and the overall analysis time is reasonable. From the precision and accuracy obtained, we suggest that, for the analysis of total calcium and magnesium in human serum, IC principally may be considered as a valuable reference methodology.

ACKNOWLEDGMENT

This research was supported by the Research Fund of the University of Ghent under Grant 01116692. The authors are grateful to CEM (Beun De Ronde, the Netherlands) for technical and practical support in microwave digestion.

Received for review December 17, 1993. Accepted April 19, 1994.[⊗]

[⊗] Abstract published in *Advance ACS Abstracts,* June 1, 1994.

Anal. Chem. **1994,** *66,* 2409–2411

Improved Method for the Determination of the Oxygen Isotopic Composition of Cellulose

Peter E. Sauer
INSTAAR and Department of Geological Sciences, University of Colorado, Boulder, Colorado 80309-0450

Leonel d. S. L. O. Sternberg*
Biology Department, University of Miami, Coral Gables, Florida 33124

A modification of a chemical preparation procedure for oxygen isotope analysis of cellulose has been developed which yields greater precision and requires less time for sample preparation. In the place of isoquinoline, zinc is used to remove HCl from the reaction products of the sample and $HgCl_2$. The two methods give systematically different results because isoquinoline biases measurements by contaminating the sample with additional CO_2. For the zinc method, precision is ±0.2‰ (1σ standard deviation) compared with ±0.9‰ for the isoquinoline method.

The stable isotopes of oxygen in organic material are of interest to plant physiologists[1] and paleoclimatologists[2] who use isotopic ratios to constrain water relations and climate models. Because changes of only 1–2‰ may be of biological or climatic importance, it is desirable to improve analytical precision better than the ±0.9‰ variability of existing techniques. Natural changes in $^{18}O/^{16}O$ ratios are small, and oxygen isotope ratios are expressed in δ notation as per mil (‰) variation from a standard:

$$\delta^{18}O = [(R_{sample}/R_{standard}) - 1] \times 1000‰ \quad (1)$$

in which R is the $^{18}O/^{16}O$ ratio in the sample or standard, respectively. In this paper, the standard used for all measurements is standard mean ocean water (SMOW).

Because different plant components have different isotopic compositions, a single compound is usually isolated for analysis. Cellulose $(C_6H_{10}O_5)_n$ is traditionally chosen because it is relatively easily isolated, it is a major component of plant material, and its resistance to chemical alteration subsequent to synthesis allows it to preserve its original isotopic composition. The method presented here was developed and tested for cellulose, but in principle it could be used for oxygen isotopic analysis of any carbohydrate.

To measure the oxygen isotopic composition of cellulose, it is necessary to convert all the oxygen in the sample to CO_2 without introducing any additional oxygen. Combusting cellulose with an excess of mercuric chloride in vacuum provides insufficient oxygen to oxidize all the carbon to CO_2, and a significant portion of the oxygen combines to form CO. The CO is converted to CO_2 by using a 5000-V spark chamber partially submerged in liquid nitrogen; immediate condensation of the newly formed CO_2 shifts the reaction equilibrium toward the formation of additional CO_2. Hydrogen also poses a problem during pyrolysis because it reacts with oxygen to form H_2O. This source of error is eliminated by adding $HgCl_2$ to the combustion ampule.[3] The chlorine gas evolved when the ampule is heated reacts with hydrogen to form HCl and prevents the formation of H_2O. The HCl must be removed from the sample before it is loaded into the mass spectrometer. In earlier methods, HCl was removed using either a nickel reaction vessel[4] or organic bases such as quinoline and 5,6-benzoquinoline.[3] Isoquinoline is commonly used today.[5] An amalgalm of zinc has also been used for the determination of the $\delta^{18}O$ of inorganic compounds, but precision was poor by modern standards (±30‰).[6] No test of the zinc amalgalm method has been performed on organic compounds to determine whether it can distinguish the small isotopic changes of interest to plant physiologists or paleoclimatologists.

To minimize the handling and generation of isoquinoline waste (which is toxic), a single batch of isoquinoline (15–20 mL) is normally used to process several dozen samples.[5] Unfortunately, gases dissolve in isoquinoline, and the procedure for removing CO_2 from the reaction vessel is time-consuming, involving a number of heating and cooling steps. A small amount of CO_2 always remains in solution trapped within the isoquinoline. Thus, the analysis is very sensitive to the condition of the isoquinoline, which changes as samples are processed. A drift of 2.2‰ in the determination of standards was observed over a period of several weeks of heavy use of the preparation system (Table 1).

(1) Sternberg, L. d. S. L. *Stable Isotopes in Ecological Research;* Springer-Verlag: New York, 1989; pp 124–141.
(2) Burk, R. L.; Stuiver, M. *Science* **1981,** *211,* 1417–1419.
(3) Rittenberg, D.; Ponticorvo, L. *Int. J. Appl. Radiat. Isot.* **1956,** *1,* 208–214.
(4) Thompson, P.; Gray, J. *Int. J. Appl. Radiat. Isot.* **1977,** *28,* 411–415.
(5) Sternberg, L. d. S. L. In *Plant Fibers;* Linskens, H. F., Jackson, J. F., Eds.; *Modern Methods of Plant Analysis, New Series 10;* Springer-Verlag: New York, 1989; pp 89–99.
(6) Anbar, M; Guttmann, S. *Int. J. Appl. Radiat. Isot.* **1959,** *5,* 233–235.

0003-2700/94/0366-2409$04.50/0
© 1994 American Chemical Society

Table 1. $\delta^{18}O_{SMOW}$ Values of Sigma Standard Obtained over a 2-Week Period Using the Isoquinoline Method[a]

	$\delta^{18}O_{SMOW}$
	29.3
	29.0
	29.8
	30.5
	30.2
	30.5
	30.0
	29.6
	29.6
	29.2
	28.3
mean ± 1 SD	29.5 ± 0.7

[a] Long-term drift of the determinations may result from the changing condition of the isoquinoline. It is reasonable to expect these changes during normal sample processing because (1) the amount of isoquinoline decreases with each sample processed, as it is converted to the chloride salt, (2) isoquinoline degrades through time, and (3) the amount and isotopic composition of the CO_2 retained from each sample changes as different samples are processed.

METHODS

Only the new aspects of this procedure are described here in detail. Additional details including a description of the preparation vacuum line were described earlier by Sternberg.[5] Cellulose is first isolated from plant material according to the Jayme and Wise method, described by Green.[7] An aliquot of 6–10 mg of cellulose is sealed in a Vycor breakseal ampule with 0.375 g of $HgCl_2$ and is baked for 6 h at 550 °C, producing a mixture of CO_2, CO, and HCl. The breakseal ampule is loaded in a vacuum line fitted with a spark chamber. Carbon monoxide is converted to CO_2 in a 5000-V spark chamber.[5] Two grams of zinc is loaded into a 9-mm-o.d., 10-cm-long Vycor ampule and evacuated. While still under vacuum, the zinc is heated for approximately 1 min with a blue flame from a glass-blowing torch. The flame is applied only to the bottom portion of the ampule where the zinc is located. A portion of the zinc sublimes and condenses as a purified coating higher on the ampule wall. As the vapor pressure of the zinc rises, the zinc pellet suddenly jumps several centimeters up into the ampule and sticks to the ampule wall. At this point, the flame is removed and the ampule is allowed to cool. This process removes oxides and provides a clean zinc surface which will react with the HCl. The mixture of HCl and CO_2 from the spark chamber is then frozen into the ampule for a period of 5 min, then sealed, and baked for 2 h at 200 °C. This ampule is reloaded onto the extraction line. Carbon dioxide is frozen in a liquid nitrogen trap, and H_2 and other residual gasses are pumped away. The volume of CO_2 is measured manometrically to determine yield. Finally, the pure CO_2 is cryogenically transferred to a Pyrex ampule for transfer to the mass spectrometer. A mass scan for HCl within the CO_2 being transferred indicated that zinc completely removed HCl from the combustion products.

RESULTS

Replicates of three standards (Table 2) and 22 other samples (Figure 1) were measured with the old and the new improved method. The repeatability of the measurement is substantially improved: standard deviations of replicate analyses are 0.2‰ for the improved method using zinc as opposed to 0.2–0.9‰ using the isoquinoline method.

Table 2. $\delta^{18}O_{SMOW}$ Values of Three Cellulose Samples Using Isoquinoline or Zinc as the Agent To Remove HCl

	$\delta^{18}O_{SMOW}$[a]	
sample	isoquinoline	zinc
Sigma[b]	29.1 ± 0.9 (20)	29.3 ± 0.2 (19)
LS9[c]	24.3 ± 0.2 (5)	24.3 ± 0.1 (4)
RL10[d]	15.9 ± 0.8 (5)	13.3 ± 0.2 (5)

[a] The number of replicate analyses is shown in parentheses. [b] Sigma is ground cellulose from Sigma Chemical Co. (Sigmacell, type 100, lot 58F0697). [c] LS9 is cellulose isolated from *Potomogeton* from Equador. [d] RL10 is cellulose isolated from *Warnsdorfia exannulata*, an aquatic moss, from Baffin Island, Canada.

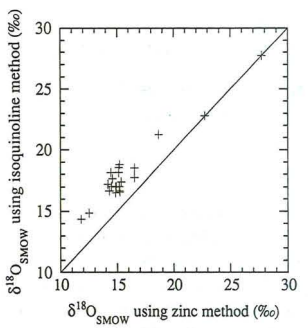

Figure 1. Comparison of results of the zinc and isoquinoline methods. Solid line represents expected values if both methods would give the same results.

The two methods for preparing samples do not always yield the same results (Table 2, Figure 1). Although both methods produced identical results for LS9 ($\delta^{18}O$ = 24.3‰) and Sigma (29.3‰), the isoquinoline method gave higher $\delta^{18}O$ values for samples having lower $\delta^{18}O$ values (RL10 and field samples). This suggests the isoquinoline may be providing additional oxygen, which biases the analysis. To test this possibility, we measured the $\delta^{18}O$ of CO_2 gas evolved from the isoquinoline as it sat under vacuum overnight. Although the amount of gas evolved was small, its composition ($\delta^{18}O$ = 19‰) could account for the tendency of the isoquinoline to produce misleading values (Figure 1).

This test did not replicate the conditions of normal sample processing, however, in which substantial amounts of HCl come into contact with the isoquinoline. To test the effect of HCl on the gas derived from the isoquinoline, we introduced 200 μmol of pure HCl into the isoquinoline and again measured the $\delta^{18}O$ of the evolved CO_2. This test yielded 9 μmol of CO_2 (from an isoquinoline volume of 15–20 mL) with a $\delta^{18}O$ of +34‰. Such an amount of CO_2 could seriously contaminate samples, which typically produce 100–150 μmol of CO_2, especially samples with $\delta^{18}O$ values very different from +34‰. Because many factors may affect the amount and the isotopic composition of CO_2 gas given off by the isoquinoline during routine sample preparation, the impact of the CO_2 released from isoquinoline will have both a memory effect and a systematic bias which cannot be eliminated. Instead, it is

(7) Green, J. W. *Methods of Carbohydrate Chemistry;* Academic Press: New York, 1963; Vol. 3, pp 9–21.

better to remove HCl gas without the use of organic compounds.

A comparison of preparations using zinc from two sources showed no differences in measured $\delta^{18}O$ values. The $\delta^{18}O$ value of the Sigma standard using zinc from Mallinckrodt was determined at 29.4 ± 0.2 (n = 4) and using zinc from Aldrich at 29.3 ± 0.2 (n = 12).

In conclusion, using zinc to remove the HCl from the HCl–CO_2 gas mixture has several advantages over the isoquinoline method. The new method is more precise, removing a significant source of CO_2 contamination. Differences between analyses performed by different workers and long-term variation, two problems with the use of isoquinoline, are eliminated. The use of zinc takes less time per sample, primarily because this approach avoids the multiple heating and cooling steps required to get the dissolved CO_2 gas out of the isoquinoline. Finally, this new method is cleaner, preventing the introduction of organic reactants into the vacuum line and generating less toxic waste.

ACKNOWLEDGMENT

We thank Professor Carl Hoff, Department of Chemistry, University of Miami, for suggesting the use of zinc. This research was funded by NSF Grant ATM-9122974 and a Student Research Grant from the Geological Society of America. This is publication 421 from the program in Ecology, Behavior and Evolution of the Department of Biology, University of Miami, Coral Gables, FL, and contribution 9 from the Paleoclimate of Arctic Lakes and Estuaries (PALE) Program.

Received for review December 2, 1993. Accepted April 11, 1994.[•]

[•] Abstract published in *Advance ACS Abstracts,* May 15, 1994.

Anal. Chem. **1994,** *66,* 2412–2416

Binding Studies of Vancomycin to the Cytoplasmic Peptidoglycan Precursors by Affinity Capillary Electrophoresis

Jinping Liu,*,† Kevin J. Volk,† Mike S. Lee,‡ Michael Pucci,§ and Sandra Handwerger‖

Analytical Research & Development and Anti-Infective Microbiology, Bristol-Myers Squibb Pharmaceutical Research Institute, Wallingford, Connecticut 06492, Analytical Research & Development, Bristol-Myers Squibb Pharmaceutical Research Institute, Princeton, New Jersey 08543, and Laboratory of Microbiology, Rockefeller University, New York, New York 10021

The ability of vancomycin to bind three cytoplasmic peptidoglycan precursors in bacterial species was studied using affinity capillary electrophoresis (ACE). The ACE binding assay was established with the normal precursor, UDP-*N*-acetylmuramyl-L-Ala-D-Glu-L-Lys-D-Ala-D-Ala, from *Staphylococcus aureus* 209P under conditions where vancomycin served as substrate ligand included in the buffer system. This precursor was found to bind to vancomycin with a binding constant of $1.6 \times 10^{-5}\,M^{-1}$ (or a dissociation constant of 62.5 μM) obtained from Scatchard plots. No migration shifting was observed under the same conditions for the other two precursors from *Leuconostoc mesenteroides* VR1 and *Lactobacillus casei* 7469, suggesting structural modifications at the stem peptide terminus. The reduction of their affinity to vancomycin is consistent with proposed structures, UDP-*N*-acetylmuramyl-L-Ala-D-Glu-L-Lys-(L-Ala)-D-Ala-D-lactate and UDP-*N*-acetylmuramyl-L-Ala-D-Glu-L-Lys-D-Ala-D-lactate, from *L. mesenteroides* VR1 and *L. casei* 7469, respectively, based on mass spectrometry. This rapid technique provides additional evidence in the understanding of one mechanism of bacterial resistance.

The glycopeptide family of antibiotics such as vancomycin has been the focus of considerable interest during recent years in regard to a novel mechanism of bacterial resistance.[1] The specific molecular recognition abilities of vancomycin to the D-alanyl-D-alanine terminus of stem pentapeptides present in bacterial peptidoglycan is the basis of vancomycin's action.[2,3] The antibiotics form a complex with the D-alanyl-D-alanine termini of peptidoglycan precursors at the cell surface, leading to inhibition of transglycosylation and transpeptidation reactions in the cell wall layer.[3,4] However, transmissible high-level resistance to glycopeptide antibiotics in *Enterococcus faecium* has recently been recognized,[5–8] which is associated with production of a 38-kDa membrane-associated protein VanA. VanA is a ligase of broad substrate specificity responsible for the synthesis of a number of mixed dipeptides, D-Ala-X, which could be incorporated into peptidoglycan precursor,[9] resulting in structural alteration and possible reduction of its affinity to vancomycin. In vitro studies using analogs of peptidoglycan stem pentapeptides have shown that replacement of the terminal D-alanine by other D-amino acids reduces vancomycin binding affinity 10–1000-fold, and substitution of hydroxyl acids reduces binding to an even greater extent.[2,9]

Various binding assays and structural studies of abnormal precursors provide useful information in understanding molecular recognition in the mechanism of resistance. We have previously studied a cytoplasmic peptidoglycan precursor in resistant *E. faecium* using microcolumn LC and ion spray mass spectrometry techniques.[10] A component was separated from the extraction mixture and the structure was identified as UDP-*N*-acetylmuramyl-L-Ala-D-Glu-L-Lys-D-Ala-D-lactate. The C-terminus was altered from D-alanine to D-lactate, resulting in a 1 amu increase resolved by ion spray mass spectrometry (MS). Studies on other bacterial species, such as *Leuconostoc*, *Pediococus*, and some *Lactobacillus*, displaying a high level of resistance to glycopeptides, have also revealed similar results.[11] In conjunction with these studies, we have recently incorporated a novel binding assay to investigate the binding affinity of vancomycin to these precursors and provide additional evidence for the identification of altered peptidoglycan precursors.

Affinity capillary electrophoresis (ACE) has been recently demonstrated as a useful approach for studying receptor–ligand interaction and the determination of their binding constants or the dissociation constants of formed complexes.[12–16] For example, binding of the negatively charged arylsulfonamide ligands to carbonic anhydrase resulted in its increased mobility.[12] Affinity interaction between enzyme and cofactors,[13] protein–sugar,[14] and peptide–drugs[15,16] using ACE has also been demonstrated. An ACE assay as an alternative screening technique for identifying a tight-binding ligand for

† Analytical Research & Development, Bristol-Myers Squibb Pharmaceutical Research Institute, Wallingford, CT.
‡ Bristol-Myers Squibb Pharmaceutical Research Institute, Princeton, NJ.
§ Anti-Infective Microbiology, Bristol-Myers Squibb Pharmaceutical Research Institute, Wallinford, CT.
‖ Rockfeller University.

(1) Courvalin, P. *Antimicrob. Agents Chemother.* **1990,** *34,* 2291–2296.
(2) Nieto, M.; Perkins, H. R. *Biochem. J.* **1971,***123,* 789–803.
(3) Sheldrick, G. M.; Jones, P. G.; Kennard, O.; Williams, H.; Smith G. A. *Nature* **1978,** *271,* 789–803.
(4) Nagarajian, R. *Antimicrob. Agents Chemother.* **1991,** *35,* 605–609.
(5) Johnson, A. P.; Uttley, A. H. C.; Woodford, N.; George, R. C. *Clin. Microbiol. Rev.* **1990,** *3,* 280–291.

0003-2700/94/0366-2412$04.50/0
© 1994 American Chemical Society

a receptor in a small peptide library was described.[17] In addition, an affinity approach using the high-performance capillary electrophoresis (HPCE) format for peptide mapping and evaluation of glycopeptide microheterogeneity was also recently demonstrated.[18]

This novel ACE approach inherits the advantages of HPCE, such as high separation efficiency, high sensitivity, and rapid analysis time. An attractive feature of ACE is its unique ability to assess the study of receptor–ligand interactions with only small amounts of nonradiolabeled samples required. The basis for performing ACE is that a charged ligand substrate can be added into the buffer at various concentrations. An appropriate receptor, upon introduction into the column, will interact to a certain extent with the ligand in terms of their bioaffinity during the electrophoretic run. This in turn induces a change in the electrophoretic mobility of the receptor due to its association with the charged ligand. Measurement of the migration shifting as a result of the change in charge status before and after the formation of the complex allows for the determination of binding constants based on Scatchard analysis. Purification prior to injection is not necessary as long as the component to be analyzed in the sample matrix can be separated from other species. This is especially beneficial when samples are available in limited quantities, such as from physiological fluids, tissues, or cell wall extractions. Simultaneous determination of binding constants for each individual component within a sample mixture is also possible. In the present study, ACE is utilized to examine the binding affinity between vancomycin and two modified peptidoglycan precursors extracted from *Lactobacillus casei* 7469 and *Leuconostoc mesenteroides* VR1, respectively, and a normal precursor isolated from *Staphylococcus aureus* 209P as a reference material.

EXPERIMENTAL SECTION

Apparatus. All affinity capillary electrophoretic experiments were performed with a Beckman P/ACE Model 2100 CE system (Fullerton, CA). An untreated fused silica capillary (Polymicro Technology, Phoenix, AZ), 57.3 cm × 50 μm i.d., with an effective separation length of 50.6 cm was employed. The operating temperature for the capillary chamber was set at 25 °C and thermostated by circulating a liquid coolant. The components were monitored with the UV detector at a wavelength of 254 nm. Data were collected and analyzed with Beckman System Gold software.

Reagents. Vancomycin, bacitracin, glycine, and Tris were purchased from Sigma (St. Louis, MO). Mesityl oxide was obtained from Aldrich (Milwaukee, WI).

Extraction of Peptidoglycan Precursor. Cytoplasmic pools of UDP-linked peptidoglycan precursors were extracted as previously described.[10,11] Briefly, bacterial cultures were grown to midlogarithmic phase and bacitracin was added to a final concentration of 100 μg/mL to accumulate precursors. After 1 h, cultures were chilled rapidly, and cells were harvested by centrifugation and extracted with cold trichloroacetic acid (final concentration 5%) for 30 min. The supernatant fluid was separated by gel filtration (Sephadex G-25; Pharmacia, Alameda, CA) with water elution. Hexosamine-containing fractions were identified by the assay of Ghuysen et al.,[19] pooled, and lyophilized.

Procedures. All binding assays were performed using an open-tubular ACE system. The running buffer consisted of 0.2 M glycine and 0.03 M Tris at a pH = 8.30. A 25 mM vancomycin stock solution was used as ligand substrate added into the running buffer. A neutral marker, mesityl oxide (0.2 mg/mL), was utilized to serve as a reference for the measurement of relative migration times as reported.[12] A 10-μL aliquot of each peptidoglycan precursor was mixed with 10 μL of mesityl oxide and used directly for injection without further sample purification. Pressure injection was utilized with a duration time of 20 s, which represents about 20 nL of sample volume injected. Affinity interaction between vancomycin and precursors can be examined through the measurement of migration shifting. The determination of binding constants, or dissociation constants, was carried out by preparing a series of running buffers containing appropriate concentrations of vancomycin ligand. Scatchard analysis illustrates the relationship between ligand concentrations and receptor's migration times.

RESULTS AND DISCUSSION

Extensive studies on molecular recognition between vancomycin and various small peptides with a D-alanine-D-alanine terminus and structurally modified variants have been conducted by other techniques.[2] It is known that the three amide linkages and the free terminal carboxyl group are essential for vancomycin binding. Modification or replacement of these functional groups by other structural moieties may significantly reduce their interaction with vancomycin. A model system used in this study is a normal pentapeptide precursor isolated from *S. aureus* 209P with a molecular mass of 1149 Da as determined by ion spray MS.[11] The proposed structure of this precursor together with its binding to vancomycin is displayed in the following diagram:

(6) Leclercq, R.; Derlot, E.; Duval, J.; Courvalin, P. *N. Engl. J. Med.* **1988**, *319*, 157–161.
(7) Nicas, T. I.; Wu, C. Y. E.; Hobbs, J. N.; Preston, D. A.; Allen, N. E. *Antimicrob. Agents Chemother.* **1989**, *33*, 1121–1124.
(8) Shlaes, D. M.; Bouvet A.; Devine, C.; Shlaes, J. H. *Antimicrob. Agents Chemother.* **1989**, *33*, 198–203.
(9) Bugg, T. D. H.; Wright, G. D.; Dutka-Malen, S.; Arthur, M.; Courvalin, P.; Walsh, C. T. *Biochemistry* **1991**, *30*, 10408–10415.
(10) Handwerger, S.; Pucci, M. J.; Volk, K. J.; Liu, J.; Lee, M. S. *J. Bacteriol.* **1992**, *174*, 5982–5984.
(11) Handwerger, S.; Pucci, M. J.; Volk, K. J.; Liu, J.; Lee, M. S. *J. Bacteriol.*, in press.
(12) Avila, L. Z.; Chu, Y.-H.; Blossey, E. C.; Whitesides, G. M. *J. Med. Chem.* **1993**, *36*, 126–133.
(13) Chu, Y.-H.; Avila, L. Z.; Biebuyck, H. A.; Whitesides, G. M. *J. Med. Chem.* **1992**, *35*, 2915–2917.
(14) Honda, S.; Taga, A.; Suzuki, K.; Suzuki, S.; Kakehi, D. *J. Chromatogr.* **1992**, *597*, 377–382.
(15) Carpenter, J. L.; Camilleri, P.; Dhanak, D.; Goddall, D. A. *J. Chem. Soc., Chem. Commun.* **1992**, 804–806.
(16) Chu, Y.-H.; Whitesides, G. M. *J. Org. Chem.* **1992**, *57*, 3524–3525.
(17) Chu, Y.-H.; Avila, L. Z.; Biebuyck, H. A.; Whitesides, G. M. *J. Org. Chem.* **1993**, *58*, 648–652.
(18) Rush, R. S.; Derby, P. L.; Strickland, T. W.; Rohde, M. F. *Anal. Chem.* **1993**, *63*, 1834–1842.
(19) Ghuysen, J. M.; Tipper, D. J.; Strominger, J. L. *Methods Enzymol.* **1966**, *8*, 684–699.

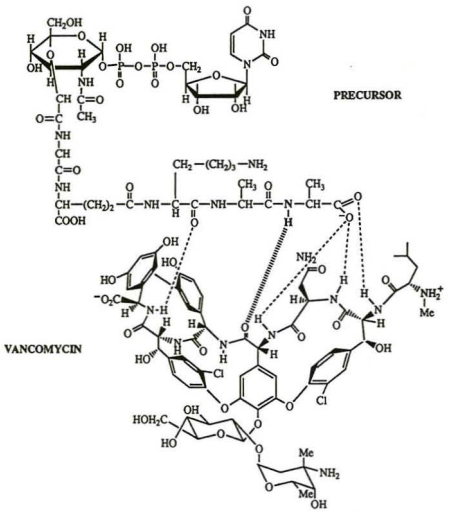

The precursor consists of a UDP-*N*-acetylglucosamine substructure linked with a pentapeptide chain which terminates in the dipeptide D-alanine-D-alanine. Affinity interaction between the precursor and vancomycin is mediated by a series of five hydrogen bonds between the dipeptide backbone and the glycopeptide. Structural modification generally occurs within the dipeptide substructure. Previous investigations revealed structural alteration at the C-terminus where the amide linkage (highlighted) was modified into a ester linkage, thus preventing vancomycin binding.[10,11] Studies from microcolumn LC/ion spray MS also indicated a Lys-Ala-Ala (m/z 289) substructure from this precursor.[11] Peptidoglycan transglycosylase and transpeptidase add pentapeptide precursor to the growing cell wall and catalyze the cross-linking of the peptide moieties.[9] The interaction between vancomycin and the pentapeptide precursor is crucial for the inhibition of these two enzymes. In this study, the binding behavior of the standard precursor with vancomycin serves as a binding "template" for the subsequent studies of the other precursors. Two general approaches can be utilized for these experiments. For example, the peptidoglycan precursor can serve as the substrate ligand added into the operating buffer, while vancomycin is used as the probe for monitoring migration shifting. Typically, the amount of substrate ligand required in buffer is larger than the amount of receptor probe. Since the sample size obtained from precursor extraction was limited, vancomycin was selected as the substrate ligand for this study. The second approach would employ vancomycin as the substrate ligand while the peptidoglycan precursor is used as the probe.

Buffer selection is one of the important parameters in many HPCE applications. The criteria for choosing a proper buffer depend on the specific application. In an ACE binding assay, perhaps one of the most important concerns is that the buffer composition does not participate in the interaction between receptor and ligand. Various additives, widely used in other HPCE applications, should generally be avoided to prevent interferences. Biological buffers are preferred to facilitate

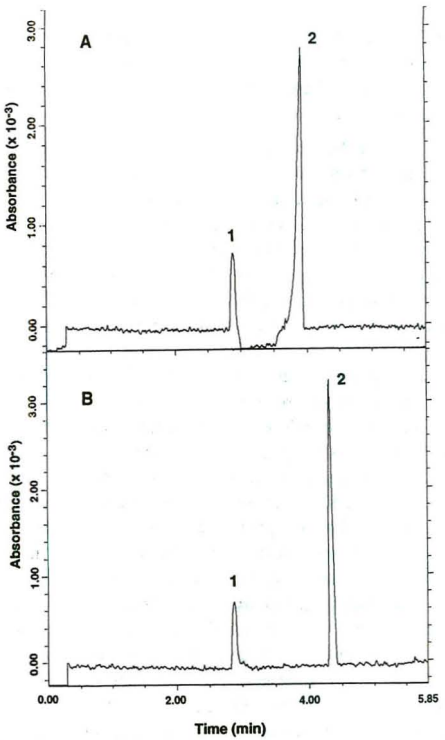

Figure 1. Evaluation of vancomycin binding to pentapeptide precursors from *S. aureus* 209P by affinity capillary electrophoresis: 1, neutral marker; 2, UDP-*N*-acetylmuramyl-L-Ala-D-Glu-L-Lys-D-Ala-D-Ala. Buffer: in upper traces (A), 0.2 M glycine/0.03 M Tris (pH = 8.30) and additional 25 μM vancomycin, and in lower traces (B), 0.2 M glycine/0.03 M Tris (pH = 8.30) without addition of vancomycin. Sample injection, 20 s; operating voltage, 25 kV (7 μA).

the interactions between biomolecules. A common buffer consisting of 0.2 M glycine/0.03 M Tris (pH = 8.30), as recommended in the literature,[12,13] is thus selected in the present studies. Figure 1 shows two electropherograms indicating migration shifting of the precursor peak with and without the presence of vancomycin in the buffer. The neutral marker, mesityl oxide as a component in the sample mixture, has the same migration time (2.88 min) under both conditions. Upon the addition of 25 mM vancomycin to the buffer, the precursor peak shifts toward the reference peak corresponding to a shift in migration time from 4.3 to 3.9 min, as indicated in Figure 1B. The complexation between the precursor and vancomycin resulted in a reduction of net charge and the complex is thus "dragged" toward the cathode direction (or detection window) somewhat faster than the unbound component due to electroosmotic flow generated under present experimental conditions. This type of shifting in binding assay has also been observed by other laboratories.[12] The observed change in mobility of the complex suggests that the normal pentapeptide precursor, UDP-*N*-acetylmuramyl-L-Ala-D-Glu-L-Lys-D-Ala-D-Ala from *S. aureus* 209P, bound to vancomycin. As expected, the formed complex has a mobility different from the original free precursor. The terminal

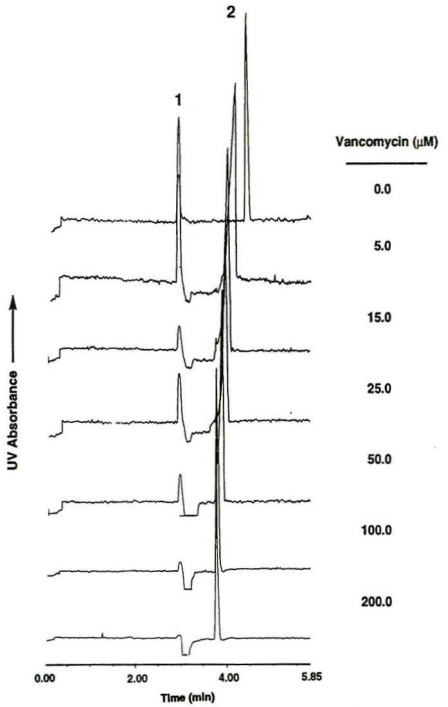

Figure 2. Affinity capillary electrophoresis of pentapeptide precursors from *S. aureus* 209P using 0.2 M glycine/0.03 M Tris (pH = 8.30) containing vancomycin with concentrations ranging from 0 to 200 μM. Instrumental conditions are the same as in Figure 1.

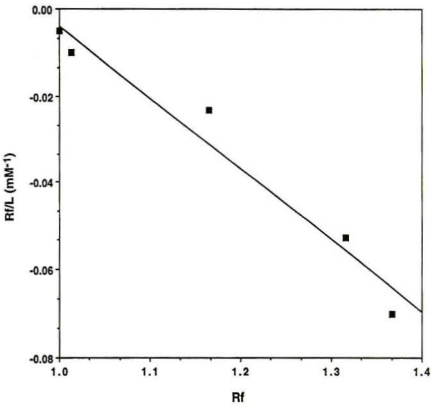

Figure 3. Scatchard plot from data obtained in Figure 1 for determination of the binding constant for precursor from *S. aureus* 209P.

dipeptide D-Ala-D-Ala provides the required amide linkages and free carboxyl group to form a complex with vancomycin through a series of hydrogen bonds. It should be pointed out that the precursors studied here are cytoplasmic extracts; thus there are no standards that can be used for peak identification. These extracts were prepurified by gel filtration prior to other analyses, and the major components were identified by ion spray mass spectrometry.[11] There is only a single component which appeared in both the microcolumn LC chromatogram and the CE electropherogram for the normal peptidoglycan precursor from *S. aureus* as demonstrated in Figure 1. We thus assumed this precursor as a "reference" in CE separations for the identification of other precursors, which are major components in extracts, based on their migration time since they are structurally similar.

In order to determine the binding constant, a series of buffers containing various concentrations of vancomycin ranging from 0 to 200 μM were used. As shown in Figure 2, an increase of vancomycin concentration results in gradual migration shifting of the precursor toward the reference peak. Binding saturation was observed at a concentration of about 200 μM vancomycin. It was also observed that peak broadening occurred at some intermediate concentrations. This is generally caused by the retardation of migrating molecules due to their frequent interactions with the ligand in the region of intermediate status. Receptor–ligand binding interaction in biological studies is generally a thermodynamic equilibrium process. The kinetic rate (or *on* and *off* rates) is one of only a few variables that affects electropherograms, especially while the dissociation time falls into the same magnitude as the migration time of the receptor. Relaxation times between free receptor and its saturated complex with the ligand appear to take longer in the range of intermediate substrate concentrations, reflecting the slow process of equilibration between species with different migration times, which results in slightly broader peaks. The precursor peak becomes sharper at the saturating concentrations of the ligand. Similar results were also reported by simulation studies of this phenomenon.[12] The possible reason for the decrease of peak height of the neutral marker may be due to the evaporation of mesityl oxide, which is miscible with common organic solvent and evaporates slowly. It should be emphasized that this change has no effect on the measurement of the relative migration time as long as the migration time of the neutral marker remains unchanged and measurable. Based on some assumptions, such as the monovalent interaction between the receptor and the ligand, achieved equilibrium during the electrophoretic run, and no significant alteration of the binding interaction associated with surface absorption of the capillary column, equations relating the migration time to binding constant were proposed for Scatchard analysis in ACE studies.[12,14] A Scatchard plot derived from these experiments (Figure 3) displays linearity with a correlation coefficient of 0.97. The binding constant, K_b, measured is 1.6×10^{-5} M^{-1} and the dissociation constant, K_d, was found to be 62.5 μM, which compares well with those obtained from other assays for structurally similar compounds.[2,9]

In conjunction with mass spectrometry studies[10,11] aimed at determining whether the mechanism of resistance was similar in intrinsically resistant bacteria, the ability of vancomycin to bind to cytoplasmic peptidoglycan precursors isolated from *L. mesenteroides* VR1 and *L. casei* 7469 was investigated using ACE. Figure 4 displays two electropherograms obtained from strain VR1 under the same conditions for the standard precursor from strain 209P as indicated in Figure 1. The cell extract was injected directly without further

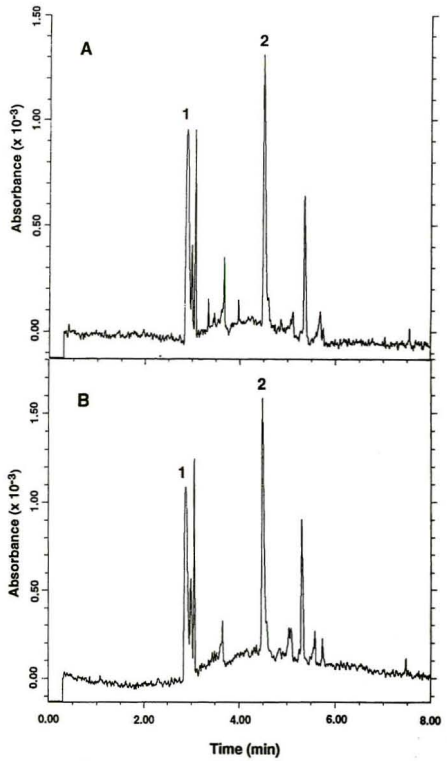

Figure 4. Evaluation of vancomycin binding to pentapeptide precursors from *L. mesenteroides* VR1 by affinity capillary electrophoresis: 1, neutral marker; 2, UDP-*N*-acetylmuramyl-L-Ala-D-Glu-L-Lys-(L-Ala)-D-Ala-D-lactate. Instrumental conditions are the same as in Figure 1.

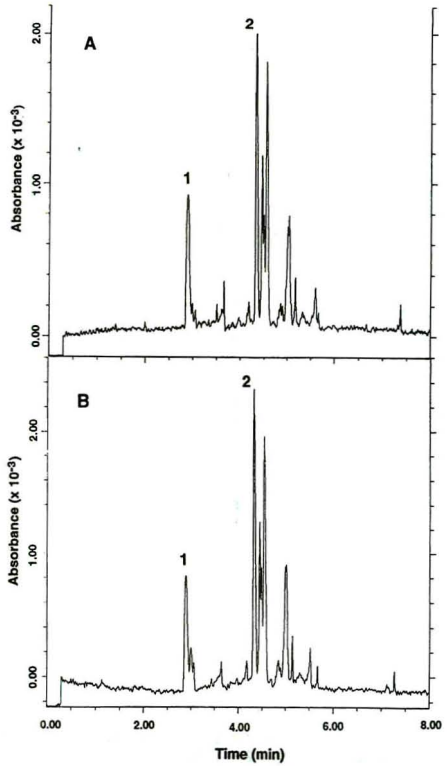

Figure 5. Evaluation of vancomycin binding to pentapeptide precursors from *L. casei* 7469 by affinity capillary electrophoresis: 1, neutral marker; 2, UDP-*N*-acetylmuramyl-L-Ala-D-Glu-L-Lys-D-Ala-D-lactate. Instrumental conditions are the same as in Figure 1.

purification and the precursor peak was identified by ion spray MS.[11] No migration shifting was observed under these conditions, which indicates that the bioaffinity of this precursor to vancomycin has been reduced to a great extent, suggesting a structural modification occurred at the terminating amino acid. A similar lack of migration shift was also obtained for the precursor from *L. casei* 7469, as shown in Figure 5, supporting an alteration of the C-terminus. The C-terminal amide hydrogen of D-Ala-D-Ala was reported to be a crucial binding site involved in the formation of hydrogen bonds, which binds specifically to the carbonyl oxygen of the (*p*-hydroxyphenyl) glycine residue located at the "core" center of vancomycin.[20] The modified structure resulting from the incorporation of a depsipeptide terminating in D-lactate no longer possesses this amide linkage and thus loses its capacity to be a hydrogen-bond donor and the affinity to vancomycin. This substitution of the amide NH for oxygen has been reported to result in at least 1000-fold lower binding,[2,9] which is not detectable by this assay in current studies.

Previous results obtained from microcolumn LC/ion spray MS revealed a structural alteration of an amino acid near the C-terminus for each precursor.[11] A component with a molecular mass of 1150 Da present in precursor extract from *L. casei* 7469 was detected, while the component found in extract from *L. mesenteroides* VR1 possesses a molecular mass of 1221 Da. Substructures corresponding to Lys-Ala-lactate (m/z 290) and Lys-(Ala)-Ala-lactate (m/z 361) were also identified from these two precursors. The proposed structures for peptidoglycan precursors are UDP-*N*-acetylmuramyl-L-Ala-D-Glu-L-Lys-D-Ala-D-lactate for *L. casei* 7469 and UDP-*N*-acetylmuramyl-L-Ala-D-Glu-L-Lys-(L-Ala)-D-Ala-D-lactate for *L. mesenteroides* VR1. The replacement of an amide linkage by an ester linkage due to the production of the peptidoglycan precursors terminating in D-alanyl-D-lactate results in a decreased ability for the formation of a hydrogen bond, thus preventing vancomycin binding. Present results obtained from ACE binding assays are consistent with the proposed modification at the stem peptide terminus, providing additional evidence in the studies of bacterial resistance to glycopeptide antibiotics.

Received for review December 10, 1993. Accepted April 14, 1994.[•]

(20) Williamson, M. P.; Williams, D. H.; Hammond, S. J. *Tetrahedron* **1984**, *40*, 569–577.

[•] Abstract published in *Advance ACS Abstracts*, May 15, 1994.

Anal. Chem. **1994,** *66,* 2417–2419

Isolation of Marine Dissolved Organic Matter: Evaluation of Sequential Combinations of XAD Resins 2, 4, and 7

Rubén J. Lara* and David N. Thomas

Alfred Wegener Institute for Polar and Marine Research, Am Handelshafen 12, D-27570 Bremerhaven, Germany

The sorptive behavior of resins XAD2, -4, and -7 for dissolved organic carbon (DOC) derived from marine phytoplankton was compared. The resins were arranged in varying sequences, which proved to be critical for determining the efficiency of DOC isolation. The sequence XAD7/2/4 allowed the isolation of a very high percentage of DOC (65%) from the seawater matrix. A mixed bed of the same resins showed a significantly lower recovery (39%). Varying amounts of the material adsorbed by the individual resins could not be recovered by NaOH/methanol elution. The percentage of DOC firmly retained by each resin was 32, 21, and 2% in XAD2, XAD4, and XAD7, respectively.

Characterizing the nature of dissolved organic matter (DOM) in seawater by direct analysis typically accounts for less than 15% of the total.[1] Alternatively, DOM can be isolated from seawater, thereby providing improved analytical conditions in regard to ionic strength and concentration levels. Various methods have been employed to isolate DOM: the adsorption of DOM from acidified seawater onto XAD resins has proved to be useful, even though these are selective for mainly hydrophobic compounds. Some workers use a combination of XAD and ion-exchange resins to recover the hydrophilic fraction of DOM and, hence, achieved almost 100% recovery of dissolved organic carbon (DOC).[2] Unfortunately this methodology is not appropriate for high-salinity matrices such as seawater. Tangential-flow ultrafiltration through 1000-Da cutoff filters only recovers approximately 30% of DOM in seawater.[1] Currently there is much speculation about the amount and form of DOM in the world's oceans. However, our understanding of the generation of this pool, its transformation by the trophic network, and the humification of organic matter in the water column is hindered by these technical difficulties.

Lara and Thomas[3] presented results from a study following the humification of DOC recently produced by laboratory diatom cultures. It was found that ca. 30% of the material adsorbed by the XAD2 resin used for DOC fractionation could not be recovered by standard NaOH/methanol elution. In an attempt to separate and operationally delimit the nature of this tightly bound DOM fraction, we subsequently compared the sorptive behavior of three different XAD resins arranged in varying sequences. Our main research is orientated toward nitrogenous compounds and organic acids in the humification of marine DOM, and so the combination of XAD2, XAD7, and XAD4 is most appropriate. According to the manufacturers product information (Serva, Heidelberg, Germany) XAD7 should have good adsorptive properties for polypeptides and enzymes, and XAD4 for small molecules, including low-molecular-weight acids.[4] XAD7 and XAD8 have been shown to have the best performances for soil fulvic acid.[4] XAD8 and XAD2 have similar performances for marine humics, XAD2 being preferred to XAD8 because of lower bleed.[5,6]

EXPERIMENTAL SECTION

^{14}C radiolabeled DOM was produced by cells of the Antarctic diatom *Thalassiosira antarctica* grown in Antarctic seawater as described in Lara and Thomas.[3] Thus, the terms "DOM" or "DOC" used to discuss results from the present study refer to algal-derived material. The seawater containing 7 month old DO^{14}C was filtered through cellulose nitrate filters (0.2 μm, Sartorius) and acidified to pH 2 with HCl. Subsequently, 100-mL samples were passed through 3 series each comprising column combinations containing respectively 5 mL of the XAD resins 2, 4, and 7 (particle size: 0.3–1.0 mm) as described in Figure 1. Thereafter, the resin was washed with 50 mL of 0.01 N HCl. The retained DOM was fractionated by eluting with 150 mL of 0.2 N NaOH (hydrophobic acid fraction, HbA), 75 mL of distilled water (H_2O fraction), and 100 mL of methanol (hydrophobic neutral fraction, HbN). The fraction not retained by the resin was termed hydrophilic (Hl). The radioactivity of subsamples of each fraction was measured in triplicate subsamples by liquid scintillation counting. The results are expressed as percentages of the total activity applied to the column series.

RESULTS AND DISCUSSION

The analytical approach used here permitted a direct measurement of the carbon retained by the resins. In a comparison of those resins at the beginning of the fractionation scheme (Figure 1), XAD4 retained 34% less carbon than XAD2. Strong sorption was ca. 10–15 times lower on XAD7 (2% of the DO^{14}C) compared to XAD4 and -2, respectively. Considering only XAD2 and -4, it is evident that, despite the different amount of DO^{14}C tightly retained (32% and 21%, respectively), HbA was almost the same for both, but HbN

(1) Benner, R.; Pakulski, J. D.; McCarthy, M.; Hedges, J. I.; Hatcher, P. G. *Science* **1992,** *255,* 1561–1564.
(2) Leenheer, J. A. *Environ. Sci. Technol.* **1981,** *15,* 578–587.
(3) Lara, R. J.; Thomas D. N. *Mar. Chem.*, in press.
(4) Aiken, G. R.; Thurman, E. M.; Malcolm, R. L.; Walton, H. F. *Anal. Chem.* **1979,** *51,* 1799–1803.
(5) Fu, T.; Pocklington, R. *Mar. Chem.* **1983,** *13,* 255–264.
(6) Thurman, E. M.; Aiken, G. R.; Ewald, M.; Fischer, W. R.; Förstner, U.; Hack, A. H.; Mantoura, R. F. C.; Parsons, J. W.; Pocklington, R.; Stevenson, F. J.; Swift, R. S.; Szpakowska, B. *Humic Substances and their Role in the Environment*; J. Wiley & Sons: Chichester, U.K., 1988; pp 31–43.

0003-2700/94/0366-2417$04.50/0
© 1994 American Chemical Society

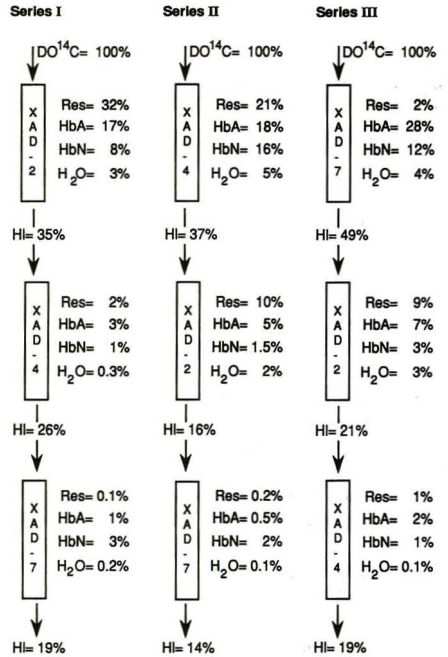

Figure 1. Resin sequences of three fractionation series. Key: Res, fraction tightly retained by the resin; HbA, hydrophobic acid fraction; HbN, hydrophobic neutral fraction; H_2O, fraction eluted with distilled water; HI, hydrophilic fraction. Results from each series are listed as a percentage of total $DO^{14}C$ in the unfractionated sample.

was significantly higher for XAD4. It would seem therefore that XAD-2 firmly binds a part of HbN. However, if XAD2 and -7 are compared, the difference in the firmly bound fraction is mainly reflected in the much higher HbA fraction from XAD7. From this, one would conclude that XAD2 firmly retains a part of HbA, which seems contradictory to the comparison between XAD2 and -4. The differences in the firmly bound fraction are partially reflected in the different HbA and HbN fractions but also in the HI counts which increase in the sequence XAD2 < XAD4 < XAD7. From this comparison it seems that XAD2 may also be retaining a part of the hydrophilic compounds. This clearly indicates that the operational delimitation of the sorptive characteristics of the fraction strongly bound by XAD2 is not straightforward. Thurman[7] indicated that, because of interaction between aromatic rings on the resin and in humics, these elute poorly from styrene–divinylbenzene resins such as XAD2. However, in the present study this is not a likely explanation. It does not seem realistic that 30% of the carbon present in phytoplankton exudates or in its degradation products is part of aromatic structures.

The difference between XAD7 and -2 or -4 was not just a higher carbon content in the HbA fraction but also (due to the extremely low amount tightly retained by XAD7) higher $DO^{14}C$ in the hydrophilic fraction. In series III the hydrophilic fraction from XAD7 was passed through XAD2. This showed that, although XAD7 yielded by far the highest HbA, its hydrophilic fraction still contained a significant amount of HbA substances that could be adsorbed by XAD2 and be subsequently recovered in the NaOH eluate. Assuming that the sum of HbA in both resins in series III represents 100% of the humic and fulvic acids in the sample, then XAD2 in series I recovered only 49% and XAD7 in series III about 80%.

A column rinse after extraction of humics from seawater is necessary to avoid precipitation of insoluble salts during alkaline elution. This rinse is made using distilled water acidified at the same pH of the sample (pH 2), thereby avoiding desorption of a DOM portion. However, the radioactivity in the acid wash was on average about 5% of the total carbon, similar to that recovered by H_2O elution. This amount of carbon greatly exceeds (ca. 10 times) that expected to come from cross contamination from the preceding sample. The existence of such a hydrophobic basic fraction in XAD extracts has been mentioned by others,[8,9] although no explanation has been proffered. The recoveries from the acid rinses are not included in Figure 1, since the radioactivity in these was not measured in all instances.

Considering the fraction of organic acids associated with humics on XAD4 in series II as compared to XAD2 in series I, the carbon content in the alkaline eluates does not seem to reflect a more efficient adsorption/desorption by XAD4. On the other hand, the H_2O fraction from XAD4 contains ca. 100% more counts than the one from XAD2, which might be a reflection of the increased capacity of XAD4 for small organic acids.

Not only the type but also the sequence of the resins proved to be important. In series I, the HbN fraction from XAD4 and -2 together recovered 9% of the total $DO^{14}C$, whereas in series II these resins recovered 17%. Whether or not the substances contained in HbN should be considered humic or not is controversial. Nevertheless, this fraction represents a substantial portion of the total DOC. The different percentages of DOC isolated from seawater by each series are strongly determined by the resin sequence as seen in the summary given in Table 1. The high efficiency of series III and the degree of tight sorption of DOM of each resin suggested that the "ideal" sequence would be XAD7/4/2, i.e. in order of decreasing elution efficiency. This was tested in an additional experiment, although without further improvement, the overall DOC recovery being ca. 65%, including the acid rinse.

Mixed beds of XAD resins have been succesfully used by Van Rossum and Webb[10] for the extraction of organics from water. The significant difference in performance among the three series raised the question about the efficiency of a mixed bed of the three resins. This was tested using a mixed bed containing 5 mL of each XAD2, -4, and -7, compared with a column containing 15 mL of XAD2. The percentage of "humic" DOC (HbA) was practically the same in both cases, 18 and 17% for the mixed bed and XAD2, respectively (Table 1). The percentage of $DO^{14}C$ firmly retained by the columns

(7) Thurman, E. M. *Organic geochemistry of natural waters*; Nijhoff/Junk Publishers: Dordrecht, The Netherlands, 1985; Chapter 10.

(8) Kukkonen, J.; McCarthy, J. F.; Oikari, A. *Arch. Environ. Contam. Toxicol.* **1990**, *19*, 551–557.

(9) Bourbonniere, R. A. *Org. Geochem.* **1989**, *14*, 97–107.

(10) Van Rossum, P.; Webb R. G. *J. Chromatogr.* **1978**, *150*, 381–392.

Table 1. Summary of Results from Each Series as a Percentage of Total $DO^{14}C$ in the Unfractionated Sample

	series				
	I (XAD2/4/7)	II (XAD4/2/7)	III (XAD7/2/4)	mixed bed (XAD2 + 4 + 7)	XAD2 (15 mL)
% DOC in HbA	21	23	37	18	17
% DOC in HbN	12	19	16	13	11
% DOC in H_2O	3	7	7	3	2
% DOC in acid rinse	n.m.	n.m.	5	5	4
% DOC recovered	36[a]	49[a]	65	39	34
% DOC on resin	34	31	12	33	41
% DOC in final HI	19	14	19	22	22
sum	89	94	96	94	97
% unaccounted DOC	11[a]	6[a]	4	6	3

[a] This refers to the effect of losses in the acid rinse, which was not measured (n.m.) for series I and II. Thus, the values cited are probably slightly underestimated for "% DOC recovered" and overestimated for "% unaccounted DOC".

was lower for the mixed bed (33%) compared with 41% for XAD2 alone. However, the latter was not much greater than the 32% for only 5 mL of XAD2 in series I, especially considering that the amount of resin was three times higher. This points again to the importance of resin sequence compared to mixed beds. It appears that the influence of XAD2 in the amount of carbon firmly bound is fundamental for the overall efficiency of the mixed bed.

Including the acid rinse, the combination XAD7/2/4 in series III recovered 65% of algal-derived DOC. This is substantially more that the 5–15% considered to be a usual recovery of DOM from seawater using XAD resins.[1] However, it must be taken into account that the behavior of the algal DOM used in this study might differ from truly marine DOM, especially from the deep ocean. The use of radiolabeled DOC in this study permitted an accurate investigation of the performance of XAD7, -4, and -2 at low, oceanic DOC concentrations. Despite the potential contamination due to bleed of XAD7,[4] if the released compounds do not interfere with the substances of interest being specifically investigated, this resin can be a useful alternative for extraction and characterization of marine DOM, especially in productive surface waters.

CONCLUSIONS

The percentage of $DO^{14}C$ firmly retained by each resin was 32, 21, and 2% in XAD2, XAD4, and XAD7, respectively. A result of this is that the sequence of the individual resins in a series is critical for the overall efficiency in isolating algal DOM from seawater: the percentage of $DO^{14}C$ recovered by each series was inversely related to the percentage of carbon tightly bound by it. The main difference among the series is that the unrecoverable $DO^{14}C$ is much lower for series III. XAD7 adsorbs reversibly components of the HbA fraction which are irreversibly adsorbed by XAD2 and, to a lesser extent, by XAD4. According to the properties of XAD7, these components might be polypeptides or enyzmes. The combination XAD7/2/4 allowed the isolation of a very high percentage of $DO^{14}C$ (65%) from the saltwater matrix, and we would recommend the use of this combination, whose effectivity might be further enhanced by the use of reverse flow elution. The combination of this procedure (XAD) and ion-pair extraction of HI onto solid phases[11] may considerably increase the amount of isolated DOM. The series XAD7/4/2 showed a similar performance and might be more useful for other chromatographic applications. A mixed bed of all three resins had no substantial improvement over that of XAD2 alone, and the overall efficiency of the mixed bed was evidently strongly influenced by the amount of carbon firmly bound by XAD2. The precise operational characterization of the fraction strongly bound by XAD2 remains elusive.

ACKNOWLEDGMENT

We thank M. Baumann for making his algal cultures available. This is contribution No. 707 of the Alfred Wegener Institute for Polar and Marine Research.

Received for review November 15, 1993. Accepted March 30, 1994.[●]

(11) Brauch H.-J. *Fresenius J. Anal. Chem.* **1992**, *343*, 6–7.

[●] Abstract published in *Advance ACS Abstracts*, May 15, 1994.

Anal. Chem. **1994,** *66,* 2420–2423

Enzymatic Profiling of Immobilized Cells Using CZE

Karen J. Miller and Fred E. Lytle*

Department of Chemistry, 1393 Brown Laboratories, Purdue University, West Lafayette, Indiana 47907-1393

Baker's yeast cells (*Saccharomyces cerevisiae*) were immobilized on a CZE capillary using a midcapillary frit of novel design. The frit was constructed using a single 50-μm particle with "through pores". Cells trapped on the capillary were profiled using different amino acid β-naphthylamide–aminopeptidase substrates. These substrates were introduced sequentially and metabolized for 1 min. After incubation the hydrolysis products were withdrawn by electrophoresis and detected by laser-induced fluorescence. An aminopeptidase profile was produced using just 500 cells. The new CZE-based method was found to have several significant advantages over the older cuvette/fluorometer method.

The small sampling and detection volumes of CZE make it a useful tool for the study of cells. As examples, individual neurons[1-3] and single human erythrocytes[4,5] have been examined. In these studies, chemical components were assayed by withdrawing cytoplasm,[1,2] by homogenizing single cells prior to injection,[3] or by lysing the cell within the capillary.[2,4,5] Recently, the separation of intact bacteria using CZE was reported by Ebersole and McCormick.[6] They found that >90% of the population remained viable after 1 h under electrophoretic conditions. In this technical note, we report the immobilization of microorganisms within a capillary in order to characterize those cells.

In many fields of microbiology, the rapid and accurate identification of microorganisms is critical. Physical descriptions are inadequate for distinguishing individual cells due to a lack of morphological diversity.[7] Instead, microorganisms are often identified by characterizing the biomolecules within them.[8] Aminopeptidase (AP) profiling catalogs microorganisms by characterizing their aminopeptidase enzymes.[9-11] These enzymes are profiled by measuring their substrate specificity. This specificity is determined by mixing the intact cells with nonfluorescent L-amino acid β-naphthylamide substrates and quantifying the fluorescent enzymatic product, β-naphthylamine. The metabolic response of the cells to uptake of individual amino acids is used to generate a metabolic profile that is taxonomically unique to the organism.

The most recent advance in this methodology utilized macroscopic immobilization of the microorganisms of interest.[11] In this method, the cells were trapped on a nylon filter. Subsequently, an aminopeptidase substrate solution was deposited on the filter and allowed to incubate in contact with the cells. The enzymatic products and unused substrate were then pulled into a cuvette by vacuum, and the fluorescence was measured using a laser-based fluorometer. The process was repeated for as few as 8 to as many as 23 different substrates. With immobilization, the same aliquot of cells could be used for all tests, instead of requiring a separate aliquot of cells for each substrate as had been done previously.[9] By requiring fewer cells for testing, the total time for cell growth and analysis was reduced from 6–10 to 3–7 h.[11] The most significant limiting factor in this procedure was the large detection volume of the cuvette and the resultant dilution of the fluorescent tag.

In the present study, we have immobilized cells within a CZE capillary. Many significant advantages have resulted. In the CZE-based method, there is little to no dilution of the enzymatic product, making it possible to profile just 500 cells with 1-min incubation times. The method is less labor intensive than other published approaches and can utilize an autosampler. It also does not require a separate assay of the fluorescent background for each substrate. Finally, the CZE approach does not subject the cells to desiccation at any time during the analysis.

EXPERIMENTAL SECTION

Chemicals. The aminopeptidase substrates L-alanine, L-arginine, glycine, L-histidine, *trans*-hydroxy-L-proline, L-leucine, and L-lysine β-naphthylamides and L-cystine di-β-naphthylamide were purchased from Sigma. Stock solutions were prepared to 10^{-3} M in methanol. Working solutions were prepared to 10^{-4} M by dilution with 10 mM pH 8.0 phosphate buffer. All solutions used in preparing the yeast cells, constructing the frit, and profiling were degassed and filtered (0.45-μm nylon filter) just prior to use. All solutions were prepared in a laminar-flow hood to avoid particulate contamination. Solutions were kept covered whenever possible.

Cells. *Saccharomyces cerevisiae* (baker's yeast) Type II dry yeast was purchased from Sigma. A 30-mg aliquot of the yeast was dissolved in 10 mL of 10 mM pH 7.0 phosphate buffer at 37 °C. Cells were centrifuged at 1500 rpm for 5 min and the supernatant was discarded (centrifuge washed). Cells were resuspended in 3 mL of buffer and centrifuge washed another two times. After the final removal of supernatant, cells were resuspended in buffer to original volume. Cell density was determined by dissolving 30 mg of yeast in 100 mL of the same buffer and counting cells using

(1) Olefirowicz, T. M.; Ewing, A. G. *Anal. Chem.* **1990**, *62*, 1872–1876.
(2) Olefirowicz, T. M.; Ewing, A. G. *Chimia* **1991**, *45*, 106–108.
(3) Kennedy, R. T.; Oates, M. D.; Cooper, B. R.; Nickerson, B.; Jorgenson, J. W. *Science* **1989**, *246*, 57–63.
(4) Hogan, B. L.; Yeung, E. S. *Anal. Chem.* **1992**, *64*, 2841–2845.
(5) Lee, T. T.; Yeung, E. S. *Anal. Chem.* **1992**, *64*, 3045–3051.
(6) Ebersole, R. C.; McCormick, R. M. *Bio/Technology* **1993**, *11*, 1278–1282.
(7) Amann, R.; Ludwig, W.; Scleifer, K.-H. *FEMS Microbiol. Lett.* **1992**, *100*, 45–50.
(8) Donzel, A.; Hamilton S. *Bio/Technology* **1993**, *11*, 793–796.
(9) Coburn, J. T.; Lytle, F. E.; Huber, D. M. *Anal. Chem.* **1985**, *57*, 1669–1673.
(10) Coburn, J. T.; Forbes, R. A.; Freiser, B. S.; Becker, L.; Lytle, F. E.; Huber, D. M. *Anal. Chim. Acta* **1986**, *184*, 65–76.
(11) Hughes, K. D.; Lytle, F. E.; Huber, D. M. *Anal. Chem.* **1989**, *61*, 1656–1600.

0003-2700/94/0366-2420$04.50/0
© 1994 American Chemical Society

a hemacytometer and microscope.[12] Five weighings with three measurements each were averaged to give a cell density of $(19.5 \pm 3.55) \times 10^6$ cells/mg.

Capillary. Fused silica capillary, 360-μm o.d., 75-μm i.d., was purchased from Polymicro Technologies. The length of capillary used was 37 cm total, 27 cm to detector. A restriction was made in the capillary 19 cm from the injection end. The restriction was made by clamping the capillary across the mouth of a caliper. This section was heated to the softening point using a methane torch. The capillary was pulled by opening the caliper 4–5 mm. A protective sleeve was placed over the restriction to prevent breaking the capillary at the very fragile restriction. The sleeve was constructed using a 40-mm length of stainless steel tubing (1.59-mm o.d., 0.76-mm i.d.). A window 3 cm by 0.5 mm was cut through the tubing allowing visual inspection with a microscope. The sleeve was held in place by threading two small pieces of septum along the capillary and positioning these pieces snug against either side of the sleeve.

Capillary Frit. POROS OH-150 50-μm spherical particles were obtained from PerSeptive Biosystems (Cambridge, MA). They were sized using a 45-μm sieve to remove particle fragments and then suspended in water. The frit was constructed by dipping the injection end of the empty capillary into the suspension of particles. Suspended particles were drawn into the capillary by capillary action. The capillary was then inspected under a microscope (120×) to assure that just one particle was drawn into the capillary. If more than one particle was within the capillary, vacuum was applied to remove the solution, and the process repeated. Once one particle was within the capillary, positive pressure was applied at the injection end to force it into the restriction. The capillary (with frit) was then rinsed with methanol, water, and buffer using positive pressure and in that order.

Loading Cells on Capillary. The cells were placed onto the capillary by electrokinetic injection; 12 kV was applied for 2 s. Buffer was then run for 10 min at 325 V/cm. Vacuum was then applied to the detection end of the capillary to draw cells adhering to the capillary walls toward the frit. The ideal number of cells for profiling was determined empirically. Cells were loaded onto the capillary and then assayed for aminopeptidase activity using a high-activity substrate such as alanine βNA or leucine βNA. If the signal for a 1-min incubation was at least 20 times above the noise, the cell number was judged to be sufficient for the detection of weaker activity substrates. If an excessive number of cells was used, flow was blocked causing the electrophoretic current to cease.

CZE Instrumentation. The laser-induced fluorescence instrumentation used has been described previously.[13] During incubation a shutter isolated the photomultiplier from the sample chamber. The data were collected without time-gated detection by integrating the first 40 ns of the fluorescence decay. Temporal resolution was not used because the major component of the blank was β-naphthylamine. That is, the blank had the same fluorescence lifetime as the signal. The origins of this background will be explained in the Results and Discussion section.

(12) Tuite, J. *Plant Pathological Methods: Fungi and Bacteria*; Burgess Publishing: Minneapolis, MN, 1969; p 183.
(13) Miller, K. J.; Lytle, F. E. *J. Chromatogr.* **1993**, *648*, 245–250.

CZE Profiling. Aminopeptidase profiles were generated by replacing the electrophoresis buffer with the β-naphthylamide substrate solution. Each substrate was run for 3.5 min at 325 V/cm. Then the electrophoretic potential was removed for 1 min to allow the substrate to incubate in contact with the cells. During the incubation time, the working substrate reservoir was replaced with the next substrate solution. Following incubation of the final substrate, buffer was run and incubated in contact with the cells to check for reagent carryover.

Filter-Based Method. Aminopeptidase profiles were generated by use of the large immobilization apparatus procedure described in ref 11. In this procedure, the cells are incubated in 1 mL of substrate and rinsed with 4 mL of buffer for each test. The following modifications were made: The buffer used was pH 8.0 10 mM phosphate buffer, incubation time was reduced from 3 to 1 min, and the filter used was Gelman FP-Vericel membrane, 25-mm diameter with 0.45 μm pore size; 5×10^6 yeast cells were profiled.

RESULTS AND DISCUSSION

The critical part of the on-capillary cell immobilization procedure is the POROS OH-150 particle. POROS OH-150 particles are poly(styrene–divinylbenzene) spheres with a hydrophilic coating.[14,15] These particles are manufactured for use as packing materials in high-speed HPLC columns. They contain "through pores" approximately 1 μm in diameter that allow mobile phase to "perfuse" through the particle. It is believed that perfusion is the major source of flow when a single particle is used as a frit. However, the frit is not permanently bound to the capillary. If the frit should become plugged and need to be replaced, the particle can be removed by applying positive pressure to the detection end of the capillary. A new particle can then be inserted into the same capillary.

S. cerevisiae (baker's yeast) was selected as the test organism for this study primarily for the convenience of preparing cell solutions from the solid culture without subculturing. Also, the yeast cells are larger in diameter than *Pseudomonas aureofaciens*, the bacteria used in previous aminopeptidase profiling studies.[11] *S. cerevisiae* are 5–10 μm in length and 3–5 μm in diameter[16] while *P. aureofaciens* are 1.9–2.8 μm in length and 0.7–0.8 μm in diameter.[17] The yeast cells are therefore less likely to pass through or plug the pores of the frit. The alanine aminopeptidase activity of yeast cells was found to be 7 times greater than that of *P. aureofaciens* using conventional methodology.[9]

Figure 1 is a micrograph of the frit with yeast cells trapped on the injection side. The micrograph was taken under static conditions. Most of the cells have drifted upstream. Under flow conditions, the cells become closely packed at the frit. Too many cells will block the electrophoretic flow and two few cells may not be detected; therefore, an optimum quantity must be determined. The procedure for determining this

(14) Afeyan, N. B.; Fulton, S. P.; Regnier, F. E. *J. Chromatogr.* **1991**, *544*, 267–279.
(15) Mu, N.; PerSeptive Biosystems, personal communication, 1993.
(16) *Encyclopedia of Food Science and Technology*; Hui, Y. H., Ed.; Wiley: New York, 1992; Vol. 4, p 2879.
(17) *Bergey's Manual of Systematic Bacteriology*; Holt, J. G., Ed.; Williams & Wilkins: Baltimore, MD, 1984; Vol. 1, p 165.

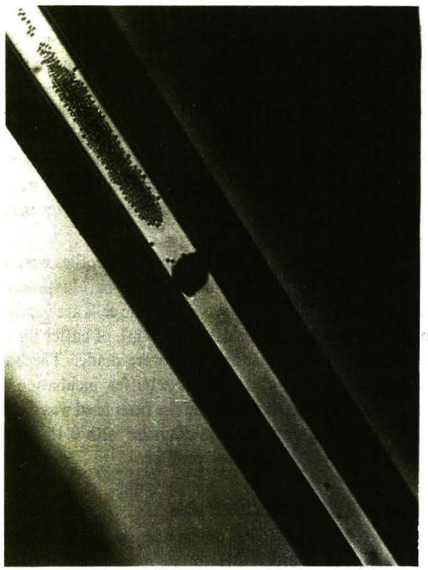

Figure 1. Micrograph of capillary frit with approximately 500 yeast cells trapped upstream of frit. Frit is approximately 50 μm in diameter. Cells have been stained with methylene blue. The capillary is surrounded by a protective sleeve.

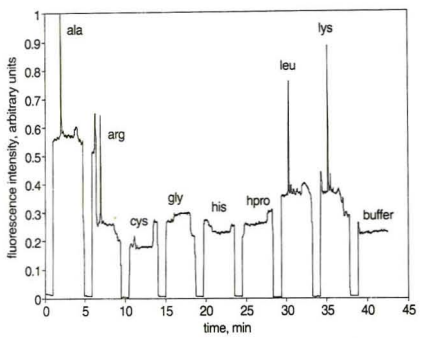

Figure 2. Electropherogram showing the aminopeptidase profile of approximately 500 immobilized yeast cells. Each aminopeptidase substrate was incubated with the cells for 1 min.

quantity is described in the Experimental Section. For aminopeptidase profiling yeast, the ideal number was found to be 500–1500.

The electropherogram for the aminopeptidase profile of approximately 500 yeast cells is shown in Figure 2. The incubation time was 1 min for each substrate. During the incubation time, the shutter to the detector was closed and the injection end of the capillary was transferred to the next substrate. In this way, the sampling "down time" was used for incubation. Closing the shutter caused the large drops seen in the response. The same 500 cells were profiled three times over 4 h. The standard deviation in relative fluorescence response averaged over four substrates (Ala, Arg, Leu, and Lys) was 11.8%.

The baseline in Figure 2 varies from substrate to substrate. This is caused by two factors. First, different rates of

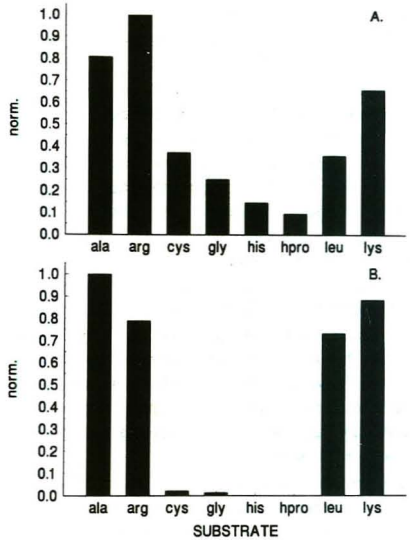

Figure 3. Aminopeptidase profiles of *S. cerevisiae*: (A) performed by filter/cuvette method using 5×10^6 cells and (B) performed by CZE method using 500 cells.

autohydrolysis for each substrate lead to a different concentration of free βNA in each substrate solution. Second, enzymatic product is formed by the cells under constant potential conditions ("on the fly"). This constant potential fluorescent product is detected as a higher baseline.[18] Therefore, the more active substrates, e.g., alanine and lysine, tend to have higher baselines. Although spurious peaks can be seen in the electropherogram (Figure 2), they do not cause problems in data interpretation. This is because the signal due to enzymatic incubation with the substrate will occur at a well-defined time after application of the electric potential.

Although the origin of several of these spurious features has not yet been determined, the leading peak with arginine and lysine is due to a known experimental artifact. In preliminary experiments, when the photomultiplier shutter was left upon during incubation, a large photoproduct peak was observed. The width of this peak matched the duration of incubation. It was concluded that during incubation, when the solution is static, the laser is sufficiently intense to photochemically hydrolyze a measurable amount of β-naphthylamine. Under flow conditions, the product of this undesired reaction is small compared to substrate autohydrolysis. The spurious peaks in Figure 2 are residual, accumulated photoproduct observed by the detector. The tail of the artifact peak was detected when timing mismatches occurred during the manual application of voltage to the capillary and changing of the position of the photomultipler shutter.

S. cerevisiae cells were also profiled using the filter immobilization procedure in ref 11. The results are shown in the histogram of Figure 3A. Peak areas from the electropherogram in Figure 2 were used to generate the histogram

(18) Miller, K. J.; Leesong, I.; Bao, J.; Regnier, F. E.; Lytle, F. E. *Anal. Chem.* **1993**, *65*, 3267–3270.

in Figure 3B. The differences in the weaker hydrolyzed substrates are caused, at least in part, by the decreased in cell concentration for Figure 3B.[11] Though there are similarities in the profiles, it is clear that data obtained using different methods are not interchangeable. A separate library of profiles will need to be assembled for profiles obtained using CZE.

CZE profiling has several advantages when compared to the previous filter-immobilization cuvette-based method in ref 11. First, the new approach provides useable profiles with 500 yeast cells, far fewer than the previous method, which required a minimum of 500 000 bacteria. Part of this large reduction is due to the higher activity of the yeast cells. However, the majority of the improvement is a result of the subnanoliter detection volume of the CZE capillary. The CZE method does not dilute the fluorescent enzymatic products whereas the cuvette-based method dilutes the enzymatic products in order to fill the sampling cuvette.

The CZE method is also easier to perform manually and much easier to automate. Once the cells are loaded onto the capillary frit, all that is required for profiling is switching to a new substrate every 3.5 min. This can easily be performed with an autosampler. The period required for substrate sampling is then used as the incubation time, resulting in no overall deadtime. In contrast, the filter-immobilization method requires many cycles of substrate introduction and withdrawal as well as rinsing and filling of the sampling cuvette. This procedure is not as easily automated with common laboratory devices.

A third advantage of CZE is that it does not require separate fluorescence assays of each substrate prior to enzymatic hydrolysis. The fluorescence "blank" for each substrate is the baseline prior to each peak. In the prior method, each substrate was assayed for fluorescence background in a separate measurement.

In addition, the CZE-based method uses milder conditions since cells are never allowed to dry and pressure is not applied during profiling. In the filter-immobilization method, vacuum was applied for every substrate and rinsing/dilution buffer. This may be a deleterious factor for fragile cells.

There are disadvantages to the CZE technique. The midcapillary frit is more difficult to assemble than the filter immobilization apparatus of ref 11. It also becomes plugged more easily by solution particulates. Extra precautions were taken in order to reduce particulate contamination. These measures are detailed in the Experimental Section. In the near future, larger diameter POROS particles will be available commercially.[15] Use of these larger particles should help to alleviate these problems. Glass capillary connectors with tapered internal diameters will be used to hold the particle eliminating the need for a restriction in the capillary. These particles should have more "through pores" and therefore be less likely to plug.

The next step in this work is the profiling of bacteria. Some difficulties are anticipated due to their smaller size. However, POROS particles with smaller pore sizes are available. Additional method development work is expected.

ACKNOWLEDGMENT

The authors are indebted to the following people and organizations: Continuum, Inc. for the laser used in these studies, Dr. Ning Mu and PerSeptive Biosystems for providing the POROS particles, and Dr. Don M. Huber and Dr. Fred E. Regnier of Purdue University for advice and assistance. This work was supported by the National Science Foundation Grant CHE-8822878.

Received for review December 17, 1994. Accepted May 1, 1994.®

® Abstract published in *Advance ACS Abstracts,* June 1, 1994.

Author Index

Abuaf, P., 2356
Adusumalli, V., 2356
Alam, M. K., 2293
Altland, D. E., 2302
Amudi, N. M., 2318

Bakker, E., 2250
Barnes, P. A., 2226
Barnes, R. M., 2279
Boroumand, F., 2260
Brodbelt, J., 2330

Callis, J. B., 2293
Charsley, E. L., 2226
Chen, Y. H., 2348
Colorado, A., 2330
Corkum, N., 2356
Crowther, J., 2356

Diven, W., 2362
Dixon, R. P., 2397
Dohmeier, D. M., 2285
Dorman, F. D., 2285

Fishman, H. A., 2318
Fritz, J. S., 2390
Frye, G. C., 2201
Fu, B., 2250

Gao, D., 2245
Gnedenko, B. B., 2240
Goldstein, G., 2356
Gusev, A. I., 2362

Hamilton, A. D., 2397
Handwerger, S., 2412
Hayes, J. M., 2336
Hercules, D. M., 2302, 2362
Hergenröder, R., 2369
Hill, H. H., Jr., 2348
Hittle, L. R., 2302

Ito, H., 2313

Jacksier, T., 2279
Jacobson, S. C., 2369
Jordan, K., 2356
Jorgenson, J. W., 2285

Kashina, S. B., 2232
Kaufman, S. L., 2285
Khaledi, M. G., 2374
Koutny, L. B., 2369

Lara, R. J., 2417
Lee, M. S., 2412
Lee, T. T., 2318
Lemire, G. W., 2272
Lewis, K. C., 2285
Li, J.-Z., 2245
Liu, J., 2412
Luckenbill, B. K., 2348
Lucy, C. A., 2220
Lytle, F. E., 2420

Martin, S. J., 2201
Matsuo, T., 2313
Matsuoka, M., 2267
Merritt, D. A., 2336
Meyerhoff, M. E., 2250
Miller, K. J., 2420
Morris, J., 2390
Moser, J. E., 2260
Muddiman, D. C., 2362
Mukherjee, T., 2356

Namba, R., 2267

Parkes, G. M. B., 2226
Proctor, A., 2302, 2362
Pucci, M., 2412

Ramsey, J. M., 2369
Ryabov, A. D., 2240

Sahota, R. S., 2374
Sakurai, T., 2313
Sauer, P. E., 2409
Sausa, R. C., 2272
Sawada, T., 2267
Scheller, R. H., 2318
Senturia, S. D., 2201
Simeonsson, J. B., 2272
Sternberg, L. d. S. L. O., 2409
Stöckl, D., 2404
Sweedler, J. V., 2382

Takamatsu, T., 2267
Takamoto, R., 2267
Thienpont, L. M., 2404
Thomas, D. N., 2417
Tolan, J., 2356
Toma, V., 2382
Tracht, S., 2382

Udischas, R., 2279

Valenta, J. N., 2397
van den Bergh, H., 2260
Van Nuwenborg, J. E., 2404
Venkataramanan, R., 2362
Volk, K. J., 2412

Wang, H.-C., 2279
Weber, S. G., 2397
Wittmer, D., 2348

Yamamoto, S., 2267
Yang, V. C., 2250
Yatsimirskaya, N. T., 2232
Yatsimirsky, A. K., 2232
Yeung, K. K.-C., 2220
Yu, R.-Q., 2245
Yun, J. H., 2250

Zare, R. N., 2318
Zarrin, F., 2285
Zheng, G.-D., 2245

introducing A NEW

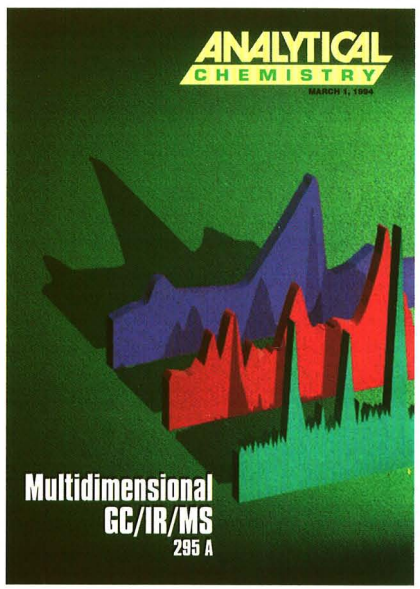

Analytical Chemistry

Since 1929, *Analytical Chemistry* has been at the forefront of this dynamic field. Now, this peer-reviewed journal sets a new standard for comprehensive coverage as the world of measurement science enters new frontiers.

Along with the cutting-edge research, state-of-the-art applications, and instrumentation methods you've come to rely on, discover our new research highlights from other international journals, late-breaking industry news, reviews of analytically oriented software, and objective product reviews.

Make *Analytical Chemistry* your one-stop resource. Call 1-800-333-9511 to subscribe today.

ANALYTICAL CHEMISTRY

It's all you need to analyze.

Safety Update!

Now, all versions of Sigma-Aldrich Material Safety Data Sheets are arranged in 16 chapter format. And the new Windows *version provides you with another choice of software. Over 66,000 complete, printable data sheets are available on a compact disc or magnetic tape. The CD-ROM version gives the user access to chemical structures. Subscribers receive a new database, quarterly, with new products and updated safety information.*

Compact Disc Subscribers receive quarterly updates, on a new CD-ROM, which include new products and updated safety information. Search fields include Sigma, Aldrich or Fluka catalog numbers, CAS registry number, molecular formula, and over 430,000 names and synonyms including RCRA and DOT numbers. Subscription may be licensed for single user or network.

IBM Mainframe or Vax Version Subscribers are supplied with magnetic tape, updated each quarter. Database is licensed for multi-user/multi-site. IBM Mainframe version features a batch search and print program for distribution of MSDS information. VAX software available with search fields including Sigma, Aldrich or Fluka catalog numbers, CAS registry number, names, synonyms and molecular formula.

To order	USA/Canada	Outside USA/Canada
Sigma Customers	800-325-3010	314-771-5750
Aldrich Customers	800-558-9160	414-273-3850

For license agreement, demo program and additional information, please contact our Data Products Department at 1-414-273-3850 or 1-800-231-8327.

IBM is a registered trademark of International Business Machines Corp. PC-XT, PC-AT and PS/2 are registered trademarks of International Business Machines Corp. Apple is a registered trademark and Macintosh is a trademark of Apple Computers, Inc. Microsoft and MS-DOS are registered trademarks of Microsoft Corp. Hercules is a trademark of Hercules Computer Technology. VAX,VMS and VAXcluster are trademarks of Digital Equipment Corporation.

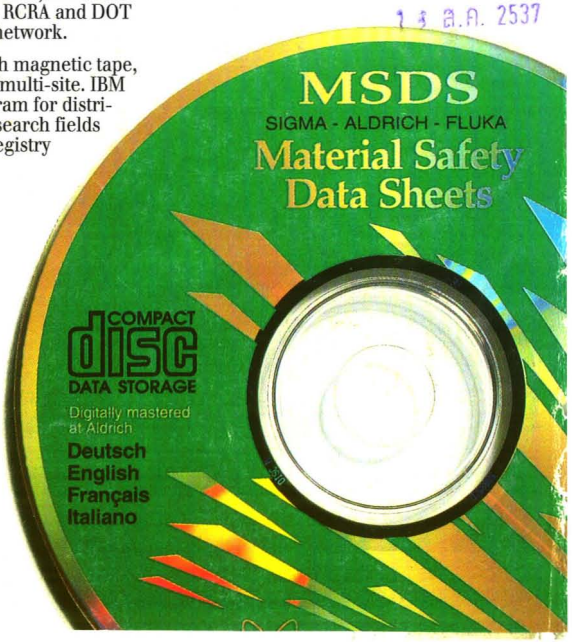

SIGMA-ALDRICH™
Techware
FROM BENCHTOP TO BOOKSHELF

CIRCLE 2 ON READER SERVICE CARD